

AKADEMIA GÓRNICZO-HUTNICZA IM. STANISŁAWA STASZICA W KRAKOWIE

FIELD OF SCIENCE: Engineering and technology

SCIENTIFIC DISCIPLINE: Chemical engineering

DOCTORAL DISSERTATION

Glassy carriers of sulphur for agricultural applications

Author: mgr inż. Anna Berezicka

First supervisor: dr hab. inż., prof. AGH Magdalena Szumera
Auxiliary supervisor: dr inż. Justyna Sułowska

Completed at: AGH University of Krakow,
Faculty of Materials Science and Ceramics
Department of Ceramics and Refractories

Kraków, 2025

Acknowledgements

First and foremost, I would like to extend my deepest gratitude to my supervisors – **Dr habil. Eng. Magdalena Szumera, Professor at AGH University of Krakow**, for what is now the ninth year of her unwavering support, extending not only to scientific matters but also to the challenges of everyday life, for the fruitful and truly inspiring collaboration, for her optimism, and above all for her contagious enthusiasm, which helped me through moments of doubt, as well as for her tireless sharing of experience that opened the door to a remarkable scientific journey – and to **Dr Eng. Justyna Sułowska**, for her scientific guidance, for pointing me towards the right research path, for creating opportunities that allowed me to spread my wings in the world of science, and for her invaluable advice and the time she devoted to me.

I would also like to express my sincere thanks to **Dr Eng. Piotr Jeleń** for his professional support, valuable advice, and assistance with measurements and their analysis. My gratitude extends as well to the staff of the Faculty Laboratory of Scanning Microscopy and Microanalysis at the Department of Ceramics and Refractories, Faculty of Materials Science and Ceramics of AGH University of Krakow, and especially to **Dr Eng. Agnieszka Wojteczko**, who tirelessly devoted long hours to the analysis of my samples and consist-ently offered valuable guidance. My sincere appreciation further goes to **Dr Eng. Sebastian Komarek** for his inexhaustible patience in the analysis of my samples. I am equally thankful to other members of the Faculty of Materials Science and Ceramics for their assistance in conducting the research and for their helpful comments and suggestions.

Finally, I wish to express my heartfelt gratitude to **Dr habil. Eng. Dorota Rutkowska-Żbik, Professor at the Jerzy Haber Institute of Catalysis and Surface Chemistry, Polish Academy of Sciences**, and to **Dr Eng. Mariusz Gackowski** of the same institute, for their invaluable help in carrying out the spectroscopic measurements.



NARODOWE CENTRUM NAUKI

This research was funded by the National Science Centre, Poland, under the SONATA 14 project no. 2018/31/D/ST8/03148 and the PRELUDIUM 22 project no. 2023/49/N/ST11/00299.

Table of contents

Acknowledgements 2

Glossary of key terms and abbreviations 6

Summary in Polish 9

Summary in English 10

Study background 12

List of scientific publications comprising the thematic series, including complete bibliographic information 14

1 Glassy carriers of macro- and microelements for agricultural applications 15

1.1 Problem statement 15

1.2 Fertilisation practices and the role of synthetic agrochemicals in modern agriculture 17

1.3 Alternative solutions to conventional synthetic fertilisers 22

1.4 The concept of glassy carriers of macro- and micronutrients 26

2 Glass structure – conventional view 29

2.1 Zachariasen's theory and its evolution 30

2.2 Dietzel's field strength concept 32

2.3 Continuous random network versus crystallite model 33

3 Requirements imposed on the vitreous carriers of macro- and micronutrients .. 35

(1) High resistance to neutral or slightly basic aqueous environments, to minimize nutrient loss through leaching by rainwater or irrigation, while maintaining enhanced solubility under acidic conditions, such as those typically found in the rhizosphere; 36

(2) Controlled and gradual nutrient release, allowing for the long-term supply of essential ions encapsulated within the glassy matrix in synchrony with the demand of the growing plant; 36

(3) Tailored chemical composition, providing adequate concentrations of macro- and micronutrients essential for plant growth, while also promoting a fragmented (open) glass structure that facilitates water ingress and ion exchange; 36

(4) Fully amorphous structure, with minimal or no crystalline phases, as the presence of such phases may hinder he uniform and predictable release of nutrients into the surrounding medium. 36

3.1 High resistance to water combined with preferential dissolution in acidic environments 36

3.2 Prolonged release of nutrients 38

3.2.1 Kinetics of glass alteration 38

3.2.2 Formation of Surface Alteration Layers 41

3.2.3 Strategies for prolonged nutrient release from glass fertilizers 42

3.3 Optimized chemical composition and structural design of glassy carriers for macro- and micronutrient delivery 45
3.3.1 Stage I 47
3.3.2 Stage II and Stage III 56
3.3.3 Role of network formers in modulating glass alteration 61
3.3.4 Role of network modifiers in modulating glass alteration 64
3.4 Amorphous nature – its influence on glass alteration and nutrient release 66
4 Macro- and microelements essential for plants and their Functions 68
4.1 Phosphorus 68
4.2 Potassium 68
4.3 Magnesium and calcium 69
4.4 Silicon 70
4.5 Sulfur as the fourth, recently recognized, essential macronutrient 70
4.5.1 Incorporation and influence of SO_3 in glasses 72
5 Research objective and hypothesis 83
6 Subject of the study 84
7 Experimental Design 85
8 Results and discussion 90
8.1 Visual inspection of acquired materials 90
8.2 Control of the chemical composition of the synthesised materials 91
8.3 Verification of the amorphous nature of the acquired samples 93
8.4 Sulfate capacity of the obtained materials 96
8.5 Homogeneity of the acquired materials 97
8.6 Analysis of thermal behaviour of the samples representing the XS_6PM system 102
8.6.1 High-temperature X-ray diffraction (HT-XRD) analysis 104
8.7 Estimation of thermal stability of XS_6PM glasses 106
8.8 Study of devitrification products within the XS_6PM glass system 108
8.9 Raman Imaging analysis 110
9 Structural studies of glasses representing the XS_6PM system 114
9.1 Raman spectroscopy study 115
9.2 FTIR spectroscopy study 120
9.3 MAS-NMR spectroscopy study 123
9.4 X-ray absorption spectroscopy study 127
9.5 Summary of the first part of the studies on sulfur-bearing silicate-phosphate glasses 132

10 Melt fritting procedure as a way of widening the glass-forming range of materials 134
11 Fritted sulfur-bearing glasses – guide to the published manuscripts 138
11.1 Verification of the amorphous nature of the fritted materials 139
11.2 Control of the chemical composition 143
11.3 Sulfate incorporation efficiency within selected glass systems 144
11.4 Thermal behaviour of the fritted samples 145
11.4.1 Influence of melt-cooling technique on thermal behaviour of selected glasses 148
11.4.2 Influence of sulfur addition on thermal behaviour of selected glasses 155
11.5 Structure of the fritted samples – general view 158
11.5.1 Evolution of the structure of the multicomponent silicate-phosphate glasses with increasing sulfate content 159
11.6 Chemical activity of sulfur-bearing silicate-phosphate glasses 162
11.6.1 The ‘in vitro’-like experiment 162
11.6.2 The ‘in vivo’-like experiment 165
11.6.3 Alteration of sulfur-bearing glasses in less acidic soil (pH 5.5-6.5). 168
12 Structure of glasses after dissolution in citric acid solution 186
13 Sulfur-bearing glass and conventional fertilizers – comparison 191
14 Lifecycle of vitreous sulfur carriers 193
15 Summary of the obtained results 197
Glass composition vs sulfate capacity 199
Sulfate addition vs. the glass properties 201
16 Future plans 203
17 References 204

Glossary of key terms and abbreviations

Disclaimer: The author would like to emphasize that, in the present thesis, while acknowledging that various terms describing phenomena that alter the physicochemical properties of glass (e.g., weathering, corrosion, alteration, degradation, and deterioration) exhibit distinct meanings, these terms are used interchangeably for simplicity. However, for clarity, the following section provides definitions of the terms and abbreviations frequently used in this thesis.

Alteration: any physical or chemical change in glass;

Bridging Oxygen (BO): an oxygen atom shared by two polyhedra in a glass network;

Chemical resistance (of glass): the ability to withstand the destructive influence of chemical solutions;

Congruent dissolution: a dissolution process where the constituents of the glass are released stoichiometrically and simultaneously, with the stoichiometric ratio of constituents in solution being the same as in the originating material;

Corrosion: degradation or deterioration caused by external (e.g., environmental conditions) and/or internal factors (e.g., glass chemical composition); a term generally used pejoratively in the context of partial or complete loss of material functionality, microstructure, and/or shape;

Dissolution: process where the solid glass material transforms into aqueous species;

Hydration: the process in which water enters the glass through void spaces between oxygens in the structure as an intact molecular species;

Hydrolysis: the reaction between water and metal-oxygen bonds in the glass, breaking network-forming bonds and forming hydroxyl groups;

Incongruent dissolution: a dissolution process characterized by the selective leaching and non-stoichiometric release of different elements, leaving less-soluble reaction products that form an alteration layer, which may be either crystalline or amorphous;

In vitro (Latin for *in glass*): a term traditionally associated with medical research, where studies occur outside living organisms, typically with cells or biological molecules in non-biological environments. In the context of this study, the soil environment is considered a "living entity". Thus, ‘in vitro’ conditions refer to laboratory-based experiments conducted outside the soil system, such as dissolution studies of glass fertilizers in simulated environments (e.g., solutions mimicking root exudates)[1];

In vivo (Latin for *within the living*): a term traditionally associated with medical research where studies occur within living organisms. In the context of this study, aligned with soil science, the soil environment is considered a "living entity" due to its complex biological activity and interactions with microorganisms. Thus, ‘in vivo’ conditions refer

[1] To underscore the distinction from traditional biological applications, terms ‘in vitro’ and ‘in vivo’ are presented in quotation marks throughout the manuscript to highlight their adapted use in studying glass fertilizers under controlled soil conditions.

to experimental conditions simulating those occurring in the soil, such as incubation studies where glass fertilizers interact with acidic peat/universal substrate to simulate real-world scenarios[1];

Leaching: the initial degradation step involving the selective removal of alkali- and alkaline-earth metal ions, which are ionically bonded to the silica framework;

Network: the backbone of the glass structure formed (in silicate-based glasses) by silicon-oxygen tetrahedra, along with other network forming polyhedra when present;

Network connectivity (NC): a numerical value describing the average number of bridging oxygen atoms per network-forming element;

Network former: a compound in the glass, typically silicon, phosphorus, or boron, that continues the glass network through connections with other compounds, including itself, bridged by oxygen atoms;

Network modifier: a compound in the glass, typically alkali or alkaline earth metal ion, that forms weaker bonds with oxygens compared to network formers and disrupts the continuous network, forming non-bridging oxygens;

Q^n_T**:** a notation in glass science, where *Q* refers to "quaternary," and *n* specifies the number of BO atoms (implying 4−n NBO ions) in a given tetrahedral unit (e.g., SiO_4/PO_4 tetrahedra);

Rhizosphere: the region of soil surrounding plant roots, where the chemistry and microbiology are influenced by plant growth, respiration, and nutrient exchange;

Saturation: a condition in a solution where no more of a particular solid can be dissolved. Saturation is temperature-dependent and always relative to both the concentration of a species in solution and a particular solid in question;

Slow-release fertilizer: according to the Association of American Plant Food Control Officials (AAPFCO), slow-release fertilizers are fertilizing media characterized by delayed nutrient availability and delivery following application, with a slower rate of macro-/microelement release compared to conventional fertilizers, providing nutrients in a readily available form;

Sulfate capacity: the maximum sulfur content that can be incorporated into the glass matrix following a controlled heating and melting regime, without inducing precipitation of a sulfate-bearing crystalline phase. This term differs from sulfur solubility, which requires the establishment of equilibrium between dissolved and atmospheric sulfur species, a rare occurrence in practical applications;

S/V: the ratio of the surface area of a sample to the volume of the solution;

Weathering: deterioration through mechanical effects, reactions resulting from the contact with water/atmospheric gases/sunlight etc. or via activities of living organisms.

Abbreviations:

CFS – Cation Field Strength index;

ΔC_p – Heat capacity change;

Δi_G – Gorlich ionicity value;

DSC – Differential Scanning Calorimetry;

EDS – Energy Dispersive X-ray Spectroscopy;

FTIR – Fourier Transform Infrared Spectroscopy;

ICP-AES – Inductively Coupled Plasma Atomic Emission Spectroscopy;

MAS-NMR – Magic Angle Spinning Nuclear Magnetic Resonance;

SEM – Scanning Electron Microscopy;

T_c – Crystallization temperature;

T_g – Glass transition temperature;

T_m – Melting temperature;

T_x – Onset of crystallization effect;

XAS – X-ray Absorption Spectroscopy;

XRD – X-ray Diffraction;

XRF – X-ray Fluorescence.

Summary in Polish

Niniejsza rozprawa doktorska, podsumowująca cykl wydanych publikacji naukowych, podejmuje tematykę wieloskładnikowych szkieł krzemianowo-fosforanowych, reprezentujących układ SiO_2-P_2O_5-K_2O-MgO-CaO, w kontekście ich potencjału dla zastosowań jako szkliste nośniki siarki w agrotechnice. Omawiane na stronach tejże pracy materiały stanowią propozycję rozwiązania narastającego problemu degradacji i wyjaławiania środowiska glebowego, wskutek wciąż postępującej intensyfikacji zabiegów rolnych napędzanej stale rosnącą liczbą mieszkańców naszej planety. Sam dodatek siarki jest natomiast podyktowany niedawno rozpoznanym zagrożeniem zubożenia tego ekosystemu w biodostępną formę siarki – siarkę siarczanową, mianowaną czwartym, po azocie, fosforze oraz potasie, kluczowym składnikiem pokarmowym niezbędnym dla prawidłowego wzrostu i rozwoju roślin. W świetle tych wyzwań, podjęto próbę zaprojektowania, otrzymania oraz optymalizacji składu chemicznego wieloskładnikowych nawozów szklistych oraz oceny ich potencjału do inkorporacji ugrupowań siarczanowych przy zastosowaniu szerokiej palety dostępnych technik badawczych (techniki pozwalające wstępną ocenę zdatności materiałów: XRD, XRF; obszerny zestaw metod pozwalających na wgląd w strukturę szkieł: spektroskopia Ramana, FTIR, MAS-NMR, XAS; analiza termiczna z zastosowaniem metody DSC; oraz metody weryfikujące aktywność glebową potencjalnych nawozów szklistych: SEM-EDS, ICP-AES). Analiza uzyskanych wyników prowadzona jest dwu-perspektywicznie: z punktu widzenia wpływu tegoż niekonwencjonalnego dodatku (siarczanów) na właściwości badanych materiałów a także – pod kątem wpływu składu chemicznego szkieł na ich zdolność do inkorporacji siarczanów, w dążeniu do rozwikłania relacji: skład chemiczny – struktura – właściwości szklistych nośników siarki.

Nadmienić należy, iż niniejsza praca, pomimo posiadania formy cyklu publikacji, nawiązuje nieco do kompozycji tradycyjnej rozprawy, charakteryzując się konwencjonalnym podziałem na:

I. Część literaturową, której kolejne podrozdziały poruszają oraz rozwijają poszczególne wymagania, nakładane na szkliste nośniki jonów użytecznych w kontekście ich planowanego zastosowania w agrotechnice;

II. Część eksperymentalną, która nie tylko stanowi przewodnik po wydanych publikacjach naukowych tworzących wspomniany cykl, ale również zawiera dodatkowe wyniki badawcze, dopełniające dyskusję nad charakterystyką otrzymanych materiałów.

Część eksperymentalna przedstawionej rozprawy poprzedzona jest rozdziałem wskazującym cel pracy oraz postawioną hipotezę badawczą stanowiącymi odpowiedź na wyzwania zdefiniowane w części o charakterze przeglądu literaturowego.

Co istotne, zaprezentowana w niniejszej pracy ścieżka badawcza stanowi swego rodzaju przewodnik do charakterystyki materiałów szklistych pełniących rolę rezerwuaru składników użytecznych dla roślin, prowadząc do wytypowania najbardziej obiecujących układów, najpełniej wpisujących się w wymagania stawiane nawozom szklistym. Niewątpliwą nowością naukową prezentowanej rozprawy jest dogłębny opis zachowania ugrupowań siarczanowych w strukturze wieloskładnikowych szkieł krzemianowo–fosforanowych – tematyka o niebagatelnym znaczeniu nie tylko dla materiałów funkcjonalnych jakimi są badane szkła nawozowe, ale również dla wielu dziedzin nauki, począwszy

od przemysłu szklarskiego, przez nauki o Ziemi od geochemii po wulkanologię, aż po immobilizację odpadów radioaktywnych.

Summary in English

This doctoral dissertation, which consolidates a cycle of peer-reviewed scientific publications, explores the development and characterization of multicomponent silicate-phosphate glasses within the SiO_2–P_2O_5–K_2O–MgO–CaO system, with particular emphasis on their potential application as vitreous carriers of sulfur for agricultural use. The materials discussed herein are proposed as a response to the increasingly pressing issue of soil degradation and nutrient depletion, which stems from the intensification of agricultural practices driven by the continuously rising global population. The incorporation of sulfur is motivated by the growing recognition of a widespread depletion of bioavailable sulfur – specifically, sulfate species – in terrestrial ecosystems. Sulfate has recently been acknowledged as the fourth essential macronutrient for plants, alongside nitrogen, phosphorus, and potassium, being indispensable for proper growth and physiological development.

In view of these challenges, this work undertakes the design, synthesis, and compositional optimization of sulfur-bearing multicomponent glass fertilizers, accompanied by a thorough assessment of their structural and functional attributes using an extensive suite of analytical techniques (these include: XRD and XRF for initial material characterization; Raman, FTIR, MAS-NMR, and XAS for structural insights; DSC for thermal behaviour; and SEM-EDS as well ICP-AES to evaluate their agrochemical reactivity and nutrient release potential).

The obtained results are analysed from a dual perspective: first, to assess the influence of this unconventional additive (i.e., sulfate) on the physicochemical properties of the examined glass matrices; and second, to determine how the overall chemical composition affects the ability of these glasses to incorporate sulfate species, to elucidate the intricate relationship between composition, structure, and properties in the context of sulfate-enriched vitreous systems.

Although structured as a cumulative dissertation, this work also retains certain features of a traditional monograph, as it is divided into the following major sections:

I. A literature review, which systematically outlines the functional requirements for glass-based ion carriers tailored for agricultural applications;

II. An experimental section, which not only guides the reader through the published articles that comprise the dissertation but also presents additional research findings that further enrich the discussion on the properties of the synthesized materials.

The experimental part is preceded by a chapter defining the main objective of the study and the research hypothesis formulated in response to the scientific and technological challenges identified in the literature review.

Importantly, the investigative approach adopted in this dissertation serves as a methodological framework for the comprehensive characterization of glass materials intended to act as reservoirs of plant-available nutrients. It also facilitates the identification of the most promising compositional systems that best meet the stringent requirements of glass-

based fertilizers. a key scientific novelty of this work lies in the in-depth description of the behaviour of sulfate groups within complex silicate-phosphate glasses – a subject of considerable relevance not only for the development of functional fertilizing materials but also for a broad range of scientific disciplines, spanning from industrial glass science, through Earth sciences – including geochemistry and volcanology – to the immobilization of hazardous and radioactive waste.

Study background

Ever since U.S. President Franklin D. Roosevelt famously stated in 1937 that "The nation that destroys its soil, destroys itself," this declaration has been echoed time and again in discussions surrounding environmental sustainability. Yet, nearly a century later, the condition of the Earth's most vital natural resource has not improved; on the contrary, it has deteriorated alarmingly, ushering in what many now recognize as an unprecedented soil crisis. While the indispensability of fertilizers in sustaining global food production is unquestionable, their excessive and often inefficient application – leading to nutrient loss, volatilization, fixation, and the depletion of soil organic matter – has been identified as a major contributor to soil degradation. Thus, there is an urgent need to mitigate these adverse effects by complementing conventional fertilization strategies with alternative approaches that not only enhance nutrient use efficiency and deliver essential elements in accordance with plant demand but also contribute to the restoration of soil health and functionality.

Indeed, soil is far from an inert substrate – it is a dynamic, living ecosystem inhabited by a myriad of organisms engaged in symbiotic interactions to ensure nutrient cycling and availability. Plants, alongside a multitude of rhizospheric microorganisms such as bacteria and fungi, actively mediate the mobilization of nutrients from soil minerals through the secretion of a complex mixture of organic acids, sugars, enzymes, and inorganic ions. It is through a deeper understanding of these natural mechanisms that the concept of glass fertilizers emerged – a result of numerous attempts to emulate the ability of biotic parts of soil ecosystems to mobilize the beneficial elements from minerals, present in the rhizosphere zone. This concept raises however a fundamental question: why is it advantageous to encapsulate essential nutrients within a glassy matrix rather than deliver them in the form of traditional soluble fertilizers?

The answer lies in the unique properties of glass. Existing in a higher-energy state relative to its crystalline analogue, glass is inherently more susceptible to alteration in aqueous environments (Chapter 1). Furthermore, the flexible network of vitreous materials allows for the incorporation of diverse constituents that seldom coexist within a single crystalline phase, enabling simultaneously the fabrication of complex materials. Unlike conventional mineral fertilizers, which often exhibit rapid nutrient release followed by leaching of the unused part, or crystalline soil minerals, which weather too slowly to meet plant demands, glass fertilizers are supposed to offer a controlled, gradual release of nutrients – closely aligned with plant uptake rates.

This capability for regulated nutrient delivery is intimately linked to the structure of the glass itself, which in turn is a function of its chemical composition (Chapter 2). There is a fine balance between chemical inertness and activity, since even minor adjustments in glass composition can significantly alter the coordination environment, network connectivity, and ionic clustering – factors that collectively determine the material’s dissolution behaviour and – in the present instance – agronomic efficacy. To ensure that glass fertilizers integrate seamlessly into the soil ecosystem – responding to biological signals without disturbing the delicate biogeochemical equilibrium – a profound understanding of the composition-structure-property relationship is imperative. Hence, the materials must be precisely engineered to meet these criteria.

Despite the conceptual simplicity of glass fertilizers, their fabrication is far from trivial. For a glass to function effectively as a carrier of plant-available nutrients, it must

satisfy stringent requirements – discussed in detail in Chapter 3. Notably, the activity of such materials cannot be evaluated solely through the lens of materials science; equal consideration must be given to plant nutritional requirements and prevailing soil deficiencies. This necessitates the intentional incorporation of specific macro- and micronutrients within the glass matrix – tailored to address current agricultural challenges (Chapter 4).

In alignment with these principles, researchers at AGH University of Krakow have developed a range of glass fertilizer formulations, each targeting a distinct issue in contemporary agriculture. One particularly pressing concern is the widespread depletion of sulfur in topsoil – an element long assumed to be abundantly available. The importance of sulfur in plant nutrition has only gained full recognition in recent decades, following substantial reductions in atmospheric SO_2 emissions mandated by international and national legislation. While these regulations have significantly improved air quality, they have simultaneously limited the main source of sulfur for plants, necessitating targeted interventions to counteract emerging deficiencies. The growing prevalence of sulfur-deficient soils and its critical role in plant metabolism have now elevated this element to the status of the "fourth major nutrient," alongside nitrogen, phosphorus, and potassium (Chapter 5).

In light of the foregoing, this thesis focuses on the following aspects, as revealed by the research presented herein:

I. To propose a solution to the dual challenges of (i) nutrient loss through leaching from highly soluble conventional fertilizers and (ii) increasing sulfur deficiency in agricultural soils, by developing sulfur-bearing multicomponent glass fertilizers;

II. To elucidate the composition–structure–property relationships of these fertilizers in order to optimize their design for slow-release performance under local temperate climate conditions.

Although substantial progress has been made in understanding the structure of glasses designed for specialized applications, the scientific literature remains sparse with respect to sulfur-containing vitreous materials – particularly regarding the correlation between their structure and functional properties such as dissolution rate. Moreover, existing studies on structure–property relationships have largely focused on bioactive glasses intended for medical use, while, despite superficial similarities between bioactive and soil-active glasses, their intended applications and performance requirements differ markedly. Thus, a comprehensive approach that combines detailed structural analysis of sulfur–containing glass formulations with dissolution testing under environmentally relevant conditions represents a scientific novelty. Given the current knowledge gap, elucidating the structure–property–function paradigm for sulfur-bearing multicomponent glass fertilizers may contribute significantly to the development of controlled-release materials for sustainable agriculture and environmental protection.

List of scientific publications comprising the thematic series, including complete bibliographic information

1. Berezicka, A.*, Sułowska, J., Jeleń, P., Komarek S., Szumera M., Effect of sulfur addition on glass-forming ability, structure and thermal stability of multicomponent silicate-phosphate glasses, *J Therm Anal Calorim*, 2024, 149, 10405–10427, https://doi.org/10.1007/s10973-023-12866-y
2. Berezicka, A.*; Sułowska, J.; Szumera, M., Alteration of Sulfur-Bearing Silicate-Phosphate (Agri)Glasses in Soil Environment: Structural Characterization and Chemical Reactivity of Fertilizer Glasses: Insights from 'In Vitro' Studies, *Molecules*, 2025, *30*, 1684, https://doi.org/10.3390/molecules30081684s. 32-37
3. Berezicka, A.*; Wojteczko, A.; Sułowska, J.; Szumera, M., Alteration of Sulfur-Bearing Silicate–Phosphate (Agri)Glasses in Soil Environment: Chemical Interactions and Biological Response, *Molecules*, 2025, *30*, 1790, https://doi.org/10.3390/molecules30081790

* Corresponding author

1 Glassy carriers of macro- and microelements for agricultural applications

1.1 Problem statement

The Green Revolution programme, initiated by the Food and Agriculture Organization of the United Nations (FAO), played a pivotal role in addressing many of the challenges faced by global agricultural production during the twentieth century [1–3]. The comprehensive implementation of modern agricultural technologies – ranging from the selection of high–yield crop varieties to the application of advanced fertilisation methods and plant protection strategies – resulted in a dramatic increase in crop yields, which in turn contributed to a gradual alleviation of the widespread famine that had afflicted large parts of the world at that time [1]. Within only a few decades, this programme led to more than a threefold rise in global cereal production, while the land area under cereal cultivation expanded by merely around 15% relative to the early 1960s (Fig. 1). In parallel, there was a marked decline in extreme poverty, an increase in food caloric availability, and a reduction of pressure on natural ecosystems due to a limitation of land conversion for agricultural purposes [1–3].

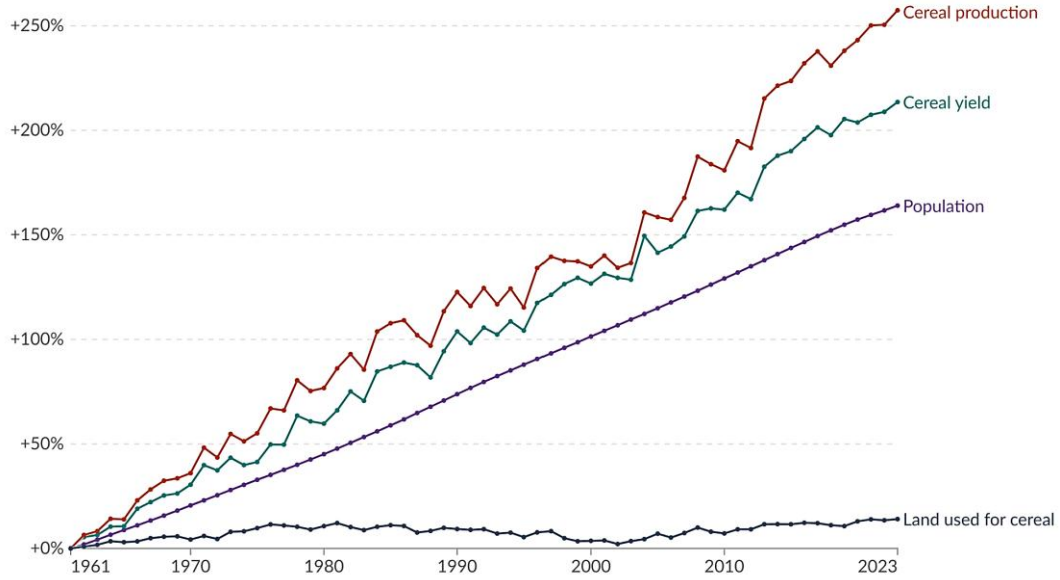


Fig. 1. Chart illustrating four variables: total cereal production; average cereal yield; land area dedicated to cereal production; and total population. These are expressed as indices relative to their respective values in 1961 (i.e., 1961 = 0). It can be observed that global cereal production has grown at a considerably faster pace than the population, which implies that cereal production per capita has increased despite global demographic growth [4].

Nevertheless, alongside these undeniable benefits, the intensification of agricultural production triggered by the Green Revolution has also been associated with profound and, in many cases, irreversible changes to the natural environment [1]. Technological progress, which made it possible to achieve high yields with only a limited expansion of arable land, was primarily based on the massive and intensive use of mineral fertilisers and chemical plant protection agents, often applied in quantities exceeding the actual requirements of crops. This practice has disrupted the delicate biogeochemical balance of both soil and aquatic ecosystems: nutrients not absorbed by plants or soil microorganisms

are inevitably leached into surface and groundwater or become immobilised in stable mineral complexes, thereby decreasing their bioavailability [3,5,6]. Furthermore, intensive exploitation of arable soils combined with the abandonment of regenerative practices – such as leaving crop residues in the field to replenish nutrients – is recognised as a major factor contributing to soil depletion, which manifests as a steady decline in organic matter content, alterations in soil structure and water retention capacity, and a gradual loss of fertility [1,2].

It is important to stress that these processes tend to be self–reinforcing: the degradation of soil and the subsequent loss of its natural fertility necessitate increasing applications of fertilisers and plant protection products, a portion of which is irretrievably lost through leaching, immobilisation, or volatilisation. Consequently, the ongoing intensification of agricultural production requires ever-higher inputs of agrochemicals, which further exacerbates the problem and locks agricultural systems into a vicious cycle of escalating dependence on synthetic inputs [3,5–7].

The destabilisation of one of the fundamental components of the biosphere–soil–undoubtedly triggers a cascade of effects that propagate through other ecosystems. The degradation of soil structure and its microbiome undermines the integrity of the biosphere, leading to a decline in genetic diversity and a reduction in the complexity of trophic networks. It should be emphasised that soils are home to approximately 25% of all living organisms on Earth, and their capacity to sustain life depends on a network of delicate biological and chemical interactions that are irreversibly disrupted by intensive farming practices [8–11]. This underscores the urgent need to adopt more sustainable strategies for managing agricultural resources, including regenerative farming systems, controlled-release fertilisers, and agrotechnical methods that minimise the negative environmental footprint of agricultural activity.

As mentioned earlier, a considerable fraction of synthetic fertilisers and plant protection agents that remain unused by crops is inevitably transported into the hydrosphere. Due to their detrimental role in the eutrophication of water bodies – and, in extreme cases, in the development of oceanic anoxia – this process poses a serious threat to the stability of aquatic ecosystems [1,3,7,12–17]. It is currently estimated that agricultural activity accounts for roughly 66% of anthropogenic nitrogen emissions and 38% of anthropogenic phosphorus emissions into the environment, clearly demonstrating the decisive contribution of intensive agricultural practices to both soil degradation and water eutrophication [3,7,8].

Among the multitude of consequences associated with the progressive degradation of soils [11], particular attention must be paid to its impact on the climate change phenomena observed in recent decades. As the largest terrestrial reservoir of carbon stored in the form of soil organic matter, soils play a key role in the global carbon cycle. Their capacity to store and sequester carbon is strongly influenced by factors such as mineral composition, texture, biodiversity of soil organisms, and even cultivation techniques [11,18,19]. However, as a result of the intensive exploitation of soil resources, the ensuing erosion disrupts this fragile equilibrium, leading to the release of carbon bound in organic matter into the atmosphere and, consequently, contributing to progressive global warming. This mechanism takes the form of a feedback loop, since the resulting climatic changes promote extreme weather events, including alternating periods of drought and heavy rainfall, which in turn intensify soil erosion [2,8,10,18,19].

These interlinked processes not only impair the ability of ecosystems to maintain homeostasis but also exert a profound impact on global food production. Current estimates suggest that climate change has already reduced caloric food availability by approximately 1%, while projections indicate that by 2050 the global per capita food supply may decrease by as much as 3.2% [8,20]. Moreover, the loss of soil biodiversity, brought about by intensive agricultural practices, leads to a decline in soil productivity, since soil microorganisms play a pivotal role in nutrient cycling, plant protection against pathogens, and the maintenance of soil fertility. Numerous studies have demonstrated that a more complex soil biota enhances resistance to environmental stress, improves nutrient use efficiency, and ultimately supports higher crop yields [8,10,20,21].

In view of these challenges, it is imperative to take action aimed at both the restoration of degraded soils and the protection of those that still retain their natural fertility. Continuous efforts are needed to explore and implement new technological and agronomic solutions that can ensure the long-term health of this essential ecosystem, which is vital not only for feeding a growing global population but also for mitigating climate change and safeguarding the biodiversity of our planet.

1.2 Fertilisation practices and the role of synthetic agrochemicals in modern agriculture

As outlined in Section 1.1, modern agriculture is confronted with an unprecedented challenge: feeding a continually growing global population while relying on an increasingly depleted and nutritionally impoverished soil ecosystem, without which this goal cannot be achieved. The rapid rise in human numbers, combined with only a marginal expansion of arable land (Fig. 1), has inevitably led to a considerable decline in the per capita availability of cultivable land. Under such conditions, the available areas are exploited with maximum intensity, and the use of inputs that restore the nutrient balance of exhausted soils becomes indispensable.

Today, the application of fertilisers and plant protection products is regarded as an integral part of soil resource management in agronomy, substantially enhancing the efficiency of agricultural operations. The conventional classification of such inputs distinguishes three principal categories (Fig. 2): (i) mineral (synthetic, inorganic) fertilisers, produced through chemical transformations or processing of natural mineral raw materials; (ii) natural and organic fertilisers, a broad class derived exclusively from organic sources, such as compost or livestock manure; and (iii) mixed fertilisers, which combine properties of both mineral and organic inputs [22,23].

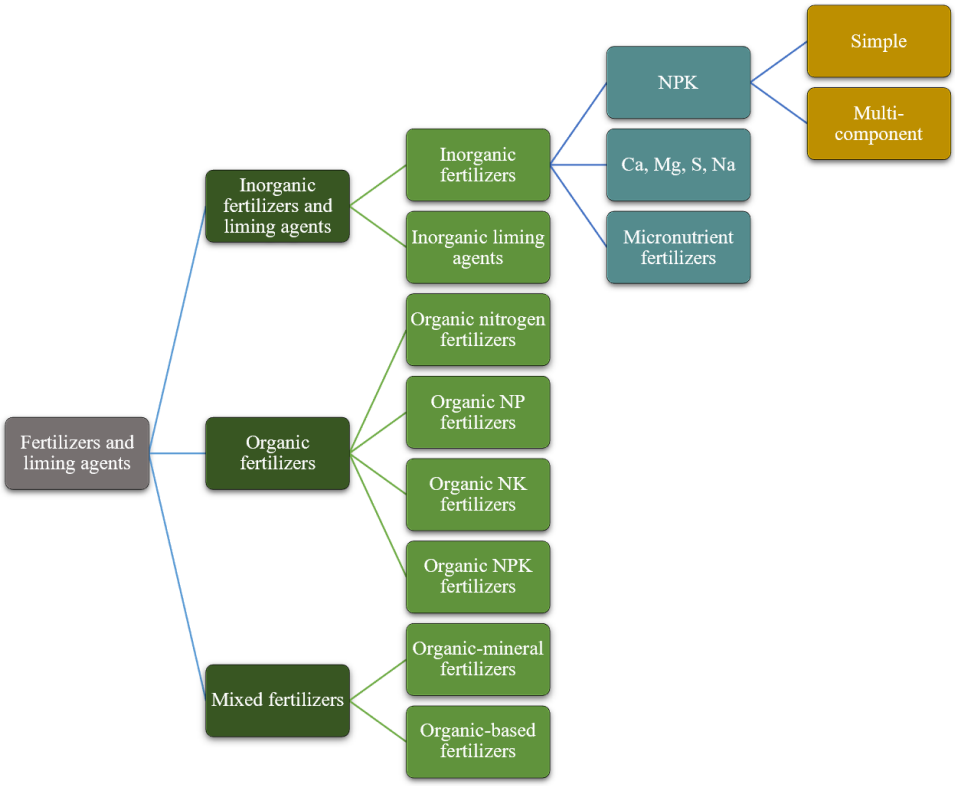


Fig. 2. Main classes of fertilising materials, based on [24].

Although contemporary concepts of sustainable agriculture promote the wider use of alternatives to conventional mineral fertilisers, the latter still account for the largest share of fertiliser consumption, both globally and in Poland. This predominance is readily explained by their well-documented effectiveness in increasing crop yields, their rapid and predictable action – which allows for timely corrective measures – and their ease of application and formulation tailored to specific crop requirements. An additional factor is the long-standing reliance on conventional fertilisers, a practice deeply embedded in agricultural history, making any transition towards sustainable soil management strategies dependent on time-consuming verification of new methods and their demonstrated efficiency.

In fact, the widespread use of artificial fertilisers in Poland dates back to the early twentieth century, when the average consumption was approximately 19 kg per hectare of agricultural land. Over subsequent decades, this figure grew steadily, with only temporary slowdowns during the world wars. Following the post-war restructuring of agriculture, based on collectivisation and the establishment of large state-owned farms (PGR), the drive to increase yields brought with it an intensification in the production and use of agrochemicals. National policies aimed at ensuring food security encouraged abundant use of artificial fertilisers, which at their peak reached 182 kg/ha. Alongside these fertilisers, plant protection products were also extensively applied to safeguard crops against pests and weeds [22].

a profound shift came with the economic transformation of 1989. Liberalisation, coupled with the dissolution of state-owned farms, led to a decline in agricultural production and a dramatic reduction in the use of fertilisers (Fig. 3**Błąd! Nie można odnaleźć źródła odwołania.**). These structural changes in the agricultural sector were accompanied by a gradual increase in environmental awareness among landowners, resulting in the

abandonment of farming on marginal soils and a more rational approach to fertiliser application. a new turning point occurred with Poland's accession to the European Union, which, through direct subsidies, reinvigorated the purchasing power of the agricultural sector. This time, however, the growth in agricultural output proceeded more gradually and was guided by the principles of sustainable development and organic farming. The use of synthetic fertilisers became subject to strict regulations aimed at protecting soils, preventing nutrient leaching into surface waters, and preserving biodiversity [22].

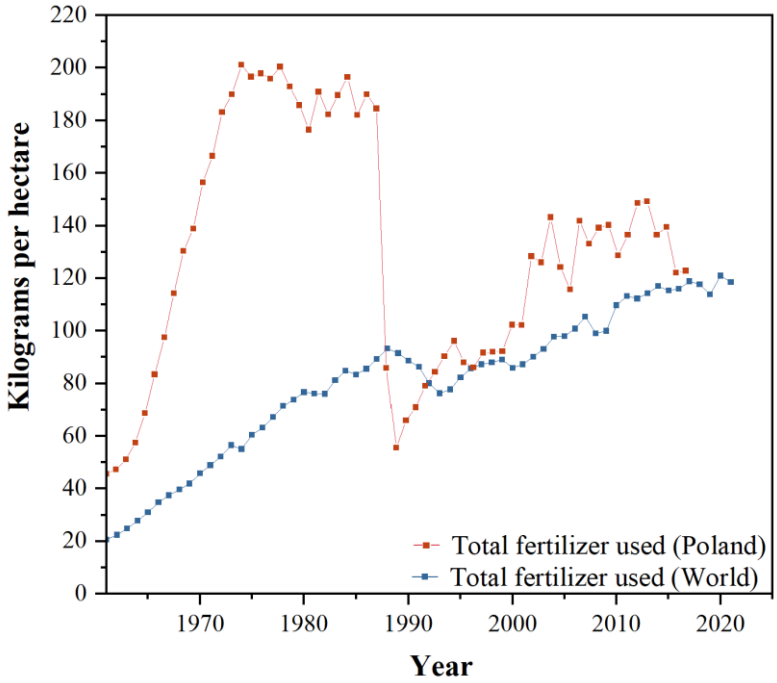


Fig. 3. Consumption of artificial fertilisers in Poland from 1961 to 2021, expressed in kg/ha; the World data are added for comparison (based on [4]).

According to the European standard PN-EN 13535, the category of inorganic fertilisers comprises materials "[…] applied to soil specifically for the purpose of crop nutrition, in which the declared nutrients are present in the form of inorganic salts obtained by extraction and/or through physical and/or chemical industrial processes" [24]. This group includes:

- **NPK fertilisers**, which occur either as *simple* formulations containing a single, concentrated, and usually readily available nutrient (nitrogen, phosphorus, or potassium), or as *compound* fertilisers combining two or more nutrients (NP, NK, PK, and NPK);
- **fertilisers containing secondary nutrients** such as Ca, Mg, Na, or S;
- **micronutrient fertilisers**, providing trace elements including B, Co, Cu, Fe, Mn, Mo, or Zn;
- **liquid fertilisers**, formulated as solutions or suspensions;
- **chelating agents**, synthetic aminopolycarboxylate (APCA) compounds capable of forming stable, water-soluble complexes [25].

However, despite the indisputable importance of synthetic fertilisers as a cornerstone of modern agriculture and a guarantee of global food security, the detrimental consequences of their excessive and unbalanced use cannot be disregarded (Fig. 4).



Fig. 4. Consequences of unsustainable application of synthetic mineral fertilisers.

As stressed earlier (Section 1.1 and Fig. 4), the improper use of fertilisers entails serious consequences not only for the natural environment but also for human health. This problem was recognised by European countries even prior to the formal establishment of the European Union, leading to the adoption of the Nitrates Directive (Council Directive 91/676/EEC), aimed at protecting water resources from nitrate pollution of agricultural origin. This regulation is widely regarded as the most important EU initiative designed to mitigate the adverse impacts of inappropriate fertiliser use and to enhance nitrogen-use efficiency [26]. Further regulatory measures include the introduction of CE labelling (Conformité Européenne) for fertilising materials, which certifies compliance with EU requirements, particularly those concerning environmental and human safety, and is a prerequisite for placing such products on the European market [27]. Additionally, Regulation (EU) 2019/1009 of the European Parliament and of the Council of 5 June 2019 represents a key component of the Union's Circular Economy Action Plan. It harmonises rules for fertilisers produced from organic or recycled materials, reflecting the principles of a circular economy, in which waste is transformed into valuable plant nutrients [27,28].

Among the most recent policy initiatives is the Farm to Fork Strategy, introduced in 2020 as an integral part of the European Green Deal. This ambitious programme seeks to transform the EU food system into a more sustainable, environmentally friendly, and climate-neutral model by 2050 [29]. One of its key objectives is to reduce nutrient losses by 50% and, consequently, to lower the use of synthetic fertilisers by 20% by the year 2030. The strategy also promotes the adoption of digital technologies and innovative solutions to improve efficiency and sustainability in food production [29–31]. The significance of the European Union's vision of sustainable agriculture is evident, given that the global use of mineral fertilisers remains highly inefficient (Fig. 5). Estimates suggest that the losses of the three primary macronutrients supplied to soils – N, P, and K – amount to approximately 40–70%, 80–90%, and 50–90%, respectively [32,33].

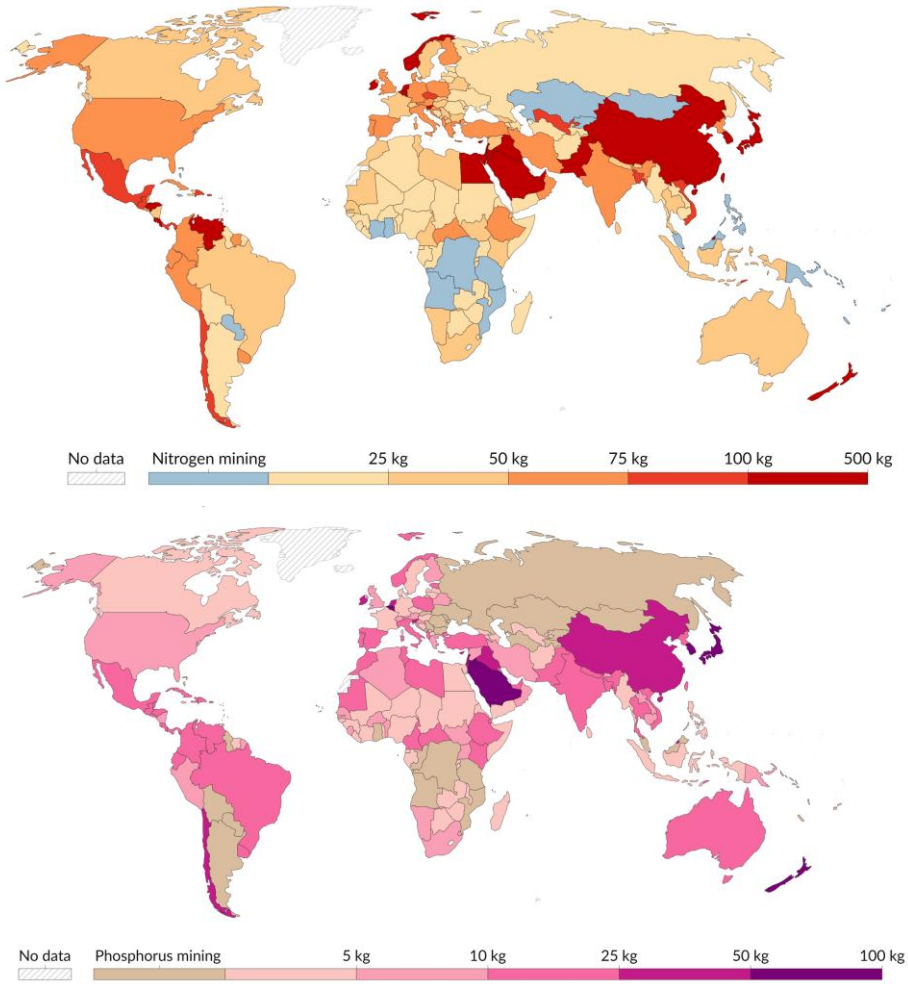


Fig. 5. Global distribution of excessive nitrogen (upper map) and phosphorus (lower map) application per hectare of cropland.

At the same time, the concerns expressed by farmers regarding the potential negative effects of these strategies and regulations on yields and market competitiveness are not unfounded. Consequently, the search for modern solutions compatible with sustainable soil management practices must be accompanied by a gradual, carefully balanced implementation, replacing part of conventional fertilisers and supported by efforts to raise public and professional awareness.

1.3 Alternative solutions to conventional synthetic fertilisers

In response to the growing challenges described above, a wide range of innovative approaches are being continuously explored and tested, with the aim of at least partially substituting conventional fertilisers. Among the most widely adopted strategies is the use of compost, a natural fertiliser obtained through the partial microbial decomposition of organic waste. Numerous studies have demonstrated that the incorporation of compost into soil significantly enhances fertility, as it introduces not only essential macro- and micronutrients but also improves the physicochemical properties of soils and stimulates the development of a diverse and active soil microbiota. The organic matter derived from plant and animal residues acts as a structural binder, stabilising soil aggregates, improving water retention and aeration, and facilitating root growth. Furthermore, organic amendments exert a beneficial influence on microbial community dynamics by increasing both the abundance and activity of soil microorganisms and by suppressing the incidence of phytopathogens [34–36].

It must be emphasised, however, that the effectiveness of such organic amendments depends on the mineralisation of the added organic matter by the soil microbiome. Through this biologically mediated process, the raw organic substrate undergoes aerobic decomposition and stabilisation, leading to the formation of humus enriched with mineral compounds (e.g., nitrate, sulfate, phosphate, hydrogen phosphate, calcium, potassium ions) [36,37]. Since this transformation is relatively slow (requiring several months) and the nutrient content of compost is generally lower than that of synthetic fertilisers, organic amendments alone have not yet reached an application level comparable to that of inorganic inputs [38]. Increasingly, however, integrated fertilisation systems are being implemented, combining organic and mineral nutrient sources to reduce dependence on synthetic fertilisers while sustaining high crop productivity and maintaining long-term soil fertility [35,39,40].

The search for alternatives to mineral fertilisers is also motivated by the finite nature of the resources required for their manufacture. The production of nitrogen-based fertilisers relies on natural gas, while phosphorus-based fertilisers are derived from phosphate rock, both of which are non-renewable resources [41–43]. In this context, bone meal – an agricultural by-product rich in phosphorus and calcium – has gained attention as a renewable nutrient source. a related material, meat-and-bone meal, is considered even more valuable because, in addition to phosphorus and calcium, it contains nitrogen derived from protein residues [41,44]. The main limitation associated with nitrogen-rich bone meals lies in the rapid mineralisation of nitrogen compounds: organic nitrogen is first converted to ammonium (NH_4^+), which is then oxidised to nitrite (NO_2^-) and subsequently to nitrate (NO_3^-), a highly mobile form that is prone to leaching losses. To mitigate these losses, the use of nitrification inhibitors must be adopted, thereby improving the nitrogen-use efficiency of such fertilisers [45].

In addition to traditional organic inputs, growing interest has been directed towards controlled-release fertilisers, a group of unconventional nutrient carriers designed to synchronise nutrient release with plant uptake. The principal objective of these formulations is to ensure an extended nutrient supply while minimising losses due to leaching and volatilisation, thereby improving the efficiency of nutrient use [46].

A prominent subcategory of such materials includes coated fertilisers, the rate of nutrient release of which is modulated by the virtue of the outer layer, either polymeric or

sulphur-based. Depending on the type of such outmost material, the coating may be broadly divided into two groups: (i) biodegradable ones, made from materials such as polysaccharides, aliphatic polyesters (e.g., polylactide – PLA, polycaprolactone – PCL), polyvinyl alcohol, poly(3-hydroxybutyrate-co-3-hydroxyhexanoate), or bio-based polyurethanes; and (ii) non-biodegradable ones, including ethylcellulose, polyvinyl acetate, and epoxy resins [47–53]. Notably, one of the earliest and most widely known examples of this approach is sulfur-coated urea (SCU), known to exhibit a substantially higher nitrogen-use efficiency than conventional urea due to the gradual release of nitrogen from the coated granules, reducing nutrient losses and environmental impact [54]. Nonetheless, SCU materials are not without drawbacks: the brittleness of the sulphur shell often leads to cracking and premature nutrient release, whereas the manufacturing process of SCU is more complex than that of uncoated urea, as it requires precise control over coating thickness and often the incorporation of additives such as waxes or polymers to enhance durability and performance [55]. For this reason, recent research has shifted towards the development of biodegradable coatings derived from natural materials as more environmentally benign alternatives [56].

The design of biodegradable coatings is further driven by the need to minimise the accumulation of persistent residues in soils. Therefore, one promising direction involves the use of hydrogels as coating materials. Hydrogel-based composites combine high water and nutrient retention in the rhizosphere with a capacity for controlled nutrient release, enabling the reduction of irrigation frequency and fertiliser application rates. Due to their exceptional sorption properties, even the addition of 1 g of hydrogel to 50 g of soil can increase its water-holding capacity by 99–101% [56]. An equally important and, from the agronomic perspective, highly valuable attribute of hydrogel-based materials is their intrinsic capacity to control the temporal profile of nutrient release, a property that not only reduces the frequency of fertiliser application but also significantly mitigates the risk of nutrient leaching into surface waters. Over the past years, a remarkable diversity of hydrogel formulations has been developed, differing in their physicochemical characteristics such as the type of ionic charge they bear (anionic, cationic, non-ionic, amphoteric, or zwitterionic), the method of crosslinking employed in their synthesis (chemical or physical), and even in their morphological architecture, which may assume the form of a continuous polymer matrix, thin films or finely dispersed microspheres [57]. In the majority of currently studied systems, two principal structural strategies are adopted for the incorporation of fertilisers into polymeric carriers (Fig. 6): in the reservoir-type configuration, a fertiliser core is surrounded by a polymer coating which acts as a semi-permeable barrier, while in the matrix-type configuration the fertilising agent is homogeneously distributed throughout the bulk of the polymeric material, forming a composite granule [56].

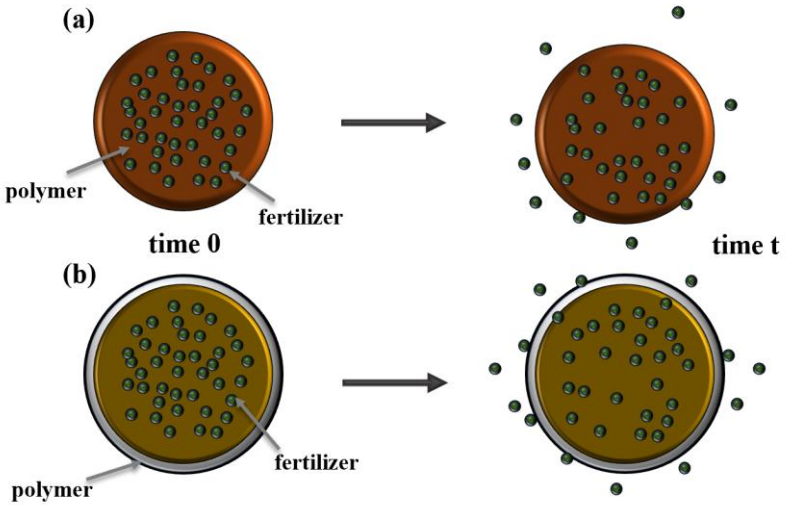


Fig. 6. The most common polymer–fertiliser configurations: (a) matrix type, in which the fertiliser is evenly dispersed within the polymer matrix, and (b) reservoir type, where a central fertiliser core is enclosed by a polymeric coating.

The kinetics of nutrient release from such systems are governed by three primary mechanisms – diffusion, swelling, and erosion – which may occur independently or operate simultaneously in a complex sequence. In reservoir-type systems, the saturated core acts as a steady source of nutrients, which first diffuse through the polymeric shell and then gradually migrate into the surrounding soil. As long as the core remains saturated, a constant concentration gradient is maintained across the coating, which ensures a controlled, almost zero-order release rate [58]. In contrast, in matrix systems, nutrient release initially occurs at the granule surface, but as the outer layers are depleted, the process progressively extends deeper into the structure. a characteristic phenomenon often observed in these systems is the so-called *burst release* – a rapid discharge of nutrients during the initial contact of the granule with water, which is subsequently followed by a slower, stabilised release phase [56].

An useful property exploited by these polymeric composites is their capacity for water-induced swelling: upon contact with moisture, the polymeric network absorbs water and expands, increasing the spacing between polymer chains and facilitating nutrient diffusion through the swollen structure. This ability to undergo significant volumetric expansion in moist environments has been deliberately harnessed as a means of modulating the rate of nutrient delivery, irrespective of whether the fertiliser is organised in a matrix- or reservoir-type configuration. There are also systems in which polymer degradation (erosion) controls the release profile: in these cases, the crystallinity and chemical composition of the polymer define the rate at which the matrix disintegrates, thereby regulating nutrient availability over time [56].

Recent research efforts have also focused on optimising the internal architecture of these systems by designing highly crosslinked polymer networks, which both refine the release profile and improve water penetration. The introduction of nanofillers, such as clay minerals or nanosilica, into the coating has proven to be particularly effective, as these additives form additional nodes within the polymeric structure, improving water retention and prolonging nutrient delivery by slowing down the mobility of water and nutrients within the composite [59–61].

Apart from such structural modifications, the thickness and multilayering of the polymer coating are also crucial parameters in achieving the desired release dynamics. For instance, xanthan gum matrices modified with hydroxypropyl methylcellulose (HPMC) create an additional gel-like barrier that slows the penetration of soil solution into the granule and thus delays fertiliser dissolution [62].

A particularly innovative and rapidly emerging branch of this research field involves nanofertilisers, a group of advanced materials that draw on the unique chemical and physical properties of nanostructures. The rapid growth of interest in nanofertilisers observed in recent years stems largely from the inefficiency of conventional fertilisers, which are often applied at rates that greatly exceed the actual nutrient uptake capacity of plants, thereby causing both environmental harm and economic losses [32,33,63].

Nanofertilisers offer a remarkably wide spectrum of possible formulations, ranging from nanostructured forms of macro- and micronutrients themselves to nanoscale carriers engineered to deliver nutrients in a controlled manner [33]. Indeed, they can be synthesised from a broad variety of materials, including minerals such as zeolites, metals (Cu, Ag, Al, K, Zn, Fe, Na, Mn, Ca), non-metallic elements (C, N, Si), and even unconventional plant-based precursors, such as grapevine extracts or banana peels [32,63–65]. The exceptional surface-area-to-volume ratio of these nanostructures results in a high density of reactive sites, which in turn facilitates close interaction with plant roots – owing to their nanoscale dimensions, these particles are able to pass through the epidermis and endodermis of root tissues, subsequently entering the xylem and being transported to aerial parts of the plant [33]. Furthermore, nanoparticles can be surface-functionalised with specific ligands or chemical groups, which enables targeted binding to receptors on plant cell membranes, and consequently – increases the efficiency of nutrient uptake while simultaneously minimising the risk of over-fertilisation and allowing much lower application rates [33,63].

Despite their extraordinary promise, the introduction of nanofertilisers into agricultural practice is associated with significant uncertainties: the very same high reactivity that enhances their efficacy also promotes aggregation within soil matrices, limiting their mobility and favouring accumulation. Furthermore, their tendency to interact with soil components may result in an immobilisation, reducing bioavailability. Concerns have also been raised about their potential toxicity, known to become more pronounced with decreasing particle size, increasing concentration, and prolonged persistence in soils. For now, the complexity of soil environments makes predicting their long-term behaviour and ecological consequences extremely challenging [33,63,66]. Experimental evidence already suggests that nanoparticles can have deleterious effects on plants, soil microbiota, aquatic organisms, and even human health. Studies indicate that accumulation of nanoparticles on plant cell walls or intracellular organelles can trigger oxidative stress [67], disrupt chlorophyll synthesis and photosynthetic efficiency [68] or interfere with electron transport in chloroplasts and mitochondria, and induce excessive production of reactive oxygen species, ultimately disturbing cellular homeostasis [69,70]. Furthermore, the leakage of such nanoparticles into water bodies poses an additional risk to aquatic ecosystems [33,71], and, importantly, their potential entry into the human food chain is a concern that cannot be underestimated [33].

For these reasons, while nanofertilisers undoubtedly hold significant potential as a component of next-generation sustainable agriculture, their safe use requires a thorough

evaluation of risks, including detailed studies of their life cycle and environmental interactions in complex and dynamic soil systems.

Finally, given the fact that according to the EU Regulation of 2019, a fertilising product is defined as any substance, mixture, microorganism, or other material applied to plants for the purpose of supplying nutrients or improving nutrient-use efficiency [27], this broad category encompasses not only the materials discussed above but also another emerging solutions in this field, namely glass fertilisers.

1.4 The concept of glassy carriers of macro- and micronutrients

The concept of using vitreous materials as carriers of macro- and micronutrients originated from the observation of processes occurring spontaneously in nature and the attempt to reproduce them under controlled conditions. Volcanic activity, while often associated with catastrophic phenomena, massive energy release and hazards for humans and climate, also gives rise to some of the most fertile soils on Earth, known as andosols. These soils owe their exceptional productivity to the abundance of volcanic glass, a metastable phase which, being highly susceptible to weathering, undergoes progressive alteration that enriches the soil with a wide spectrum of plant-essential macro- and micronutrients [72–74]. Inspired by this natural model, glass fertilisers are designed as engineered analogues of natural volcanic glass: materials whose composition, structure, and mode of action mimic the slow, controlled release of nutrients observed in nature as magma-derived glass weathers.

A fundamental feature of these glassy systems is the mechanism by which they interact with the soil environment. Once introduced into the rhizosphere, the glassy carriers, much like the minerals from which natural soils are derived, are subjected to a continuum of transformation processes that progressively convert them into more stable phases. These transformation pathways collectively fall under the domain of weathering processes, which may be classified as chemical, physical, or biological. In the case of chemical weathering, the reactive medium is water enriched with oxygen and/or carbon dioxide, forming weak acids and creating a solution capable of dissolving gases and solids with increased aggressiveness. This promotes hydrolytic and dissolution reactions that lead to the gradual mobilisation of nutrient ions contained in the solid phase. Physical weathering, in contrast, is driven by mechanical factors such as temperature fluctuations and water flow, which fragment the solid material, exposing new reactive surfaces and thereby accelerating subsequent chemical reactions. Finally, biological weathering stems from the activity of living organisms, whether through mechanical disruption by root penetration or through biochemical action via the secretion of organic ligands, acids, and enzymes that enhance mineral dissolution [75,76].

Although all three mechanisms participate in the transformation of soil minerals, the biological component is considered predominant in agroecosystems, as the rhizosphere constitutes a hotspot of intense biochemical activity driven by plant roots, soil microorganisms, and symbiotic fungi. Root systems and their microbial partners secrete a wide range of low-molecular-weight organic acids and chelating agents which, either by exchanging hydrogen ions for cations embedded in the solid matrix or by forming stable metal–ligand complexes, greatly facilitate the release of nutrients from both natural minerals and synthetic glassy reservoirs [77]. This secretion is strongly stimulated under nutrient-limiting conditions because plant development is tightly regulated by internal molecular signals, and the biochemical composition and quantity of root exudates vary in accordance with the nutrient status of the plant. Changes in nutrient availability influence the concentration of key plant hormones, such as cytokinins and abscisic acid, which in

turn modulate exudation patterns, giving rise to species-specific and nutrient-specific responses (Tab. 1) [77,78].

Tab. 1. Examples of chemical compounds identified in plant root exudates [78].

Amino acids	**Organic acids**	**Sugars**	**Vitamins**	**Purines / Nucleosides**	**Enzymes**	**Inorganic ions and gases**
asparagine aspartic acid cysteine cystine glycine glutamic acid histidine isoleucine leucine lysine methionine ornithine proline serine threonine tryptophan valine α-alanine β-alanine	aconitic aldonic succinic citric erythronic fumaric glycolic glutaric malic malonic butyric lactic formic acetic pyruvic oxalic tetronic valeric	arabinose deoxyribose fructose galactose glucose xylose maltose oligosaccharides raffinose rhamnose ribose	biotin niacin pantothenic acid riboflavin thiamine	adenine cytidine guanine uridine	amylase phosphatase (acid/alkaline) invertase protease	CO_2– carbon dioxide H^+ – hydrogen ion (proton) H_2 – molecular hydrogen HCO_3^- – bicarbonate ion OH^- – hydroxide ion

For instance, in soils deficient in micronutrients such as Fe, Cu, Mn or Zn, actively growing roots produce increased amounts of phytosiderophores – specialised chelating compounds capable of mobilising these metals from insoluble soil complexes, thereby increasing their bioavailability [79–81]. Similarly, in environments where the bioavailable pool of phosphorus is limited – due to its strong tendency to form insoluble precipitates with Mg^{2+}, Ca^{2+}, Al^{3+} and Fe^{3+}, or to be adsorbed onto clay minerals and oxides [82] – plants enhance the exudation of organic acids such as oxalic, citric, malic, and succinic acids, which complex the bound phosphates, lower their local saturation and stimulate further dissolution [83–85]. Some species, for example lupine, also upregulate the production of phosphatases – enzymes that hydrolyse organic phosphorus compounds – while in the rhizosphere of others (e.g., alfalfa), phenolic compounds are secreted that can solubilise both macro- and micronutrients [81,86].

This ability to actively mobilise nutrients is not restricted to plant roots alone: soil microorganisms and mycorrhizal fungi display similar mechanisms. The release of mineral-bound elements may be either a passive by-product of microbial metabolism or a deliberate strategy to acquire essential nutrients. The processes involved mirror those in plants: the secretion of organic and inorganic acids (such as in sulfur-oxidising bacteria [87]), chelating compounds, and even redox reactions that utilise metals released from minerals as electron acceptors during anaerobic respiration [88,89].

Of particular significance are mycorrhizal fungi, which form symbiotic associations with plant roots. In exchange for photosynthates, fungi supply their host plants with nutrients obtained through biochemical weathering of mineral particles. Remarkably, these symbiotic fungi act as biosensors: they are able to discriminate between minerals, even selecting particles with high surface-to-volume ratios or those enriched in the limiting nutrient, thereby increasing the efficiency of nutrient acquisition under conditions of scarcity [77,90–92].

Apart from active biochemical dissolution, indirect mechanisms also enhance nutrient release. Carbon dioxide produced by root respiration dissolves in soil water to form carbonic acid, which dissociates into hydrogen and bicarbonate ions, acidifying the soil solution and accelerating weathering reactions [84,85]. Similarly, the formation of bacterial biofilms on the surface of mineral grains promotes the local dissolution of minerals by maintaining microenvironments with distinct chemical conditions. Laboratory experiments under iron-deficient conditions have shown that biofilms covering biotite flakes are capable of locally mobilising Fe, but also K and Mg, while simultaneously retaining these ions within the biofilm, thus preventing them from diffusing away from the colony. As a consequence, bacterial communities associated with mineral surfaces grow larger and accumulate a greater amount of essential nutrients than those living in the surrounding soil [93].

These insights reveal the extraordinary ability of the soil biota to mobilise nutrient elements from recalcitrant sources and highlight the compatibility of glass fertilisers with this natural biological machinery. By carefully tailoring their composition, glassy carriers can be made to undergo the same processes as native soil minerals, releasing nutrients gradually in response to biologically generated cues.

A particularly advantageous characteristic of vitreous carriers of useful ions is that nutrient release occurs primarily in the rhizosphere and is strongly triggered by root activity, rather than by plain contact with water. Their slow dissolution, controlled by ion exchange in weak organic acids secreted by plants and soil microbes, ensures that in pure aqueous environments the leaching of nutrients remains negligible [94–97]. This property prevents the uncontrolled washout of fertilisers into groundwater or surface waters, while enabling a plant-demand-driven delivery of nutrients via exudate-induced local dissolution. Of utter importance is the fact that the final product of the weathering of glassy carriers is an inert, porous silica gel, which not only avoids disturbing the biogeochemical balance of soils but can even improve soil structure, enhance water retention, and immobilise toxic heavy metals [95,98,99].

Nonetheless, certain limitations must be considered before the widespread implementation of such materials. Their production is energy-intensive, although this drawback can be partly alleviated by adjusting the glass composition – e.g., increasing the fraction of P_2O_5 and network modifiers to lower melting temperatures – or by incorporating recycled glass cullet in a circular-economy approach. Experimental attempts to harness solar energy for glass melting are also ongoing, though currently limited to laboratory scales [100]. Another potential limitation lies in their relatively slow release rate, which may be insufficient for high-yield, short-cycle crops. Consequently, their application is envisioned as complementary to conventional fertilisers, thereby reducing the doses of synthetic agrochemicals, or as a nutrient source for long-lived plants, horticulture, organic farming, or for the rehabilitation of degraded soils. For these reasons, large-scale field trials under realistic agronomic conditions are essential to fully validate the agronomic potential of glassy fertilisers.

In principle, the promising functionality of glassy nutrient carriers stems from the intricate elasticity of vitreous network, typically based on silica but modified to accommodate a broad suite of macro- and micronutrients. To fully appreciate how the composition of glass translates into its structure, dissolution behaviour, and agronomic efficiency, it is essential first to understand the nature of the amorphous state and the structural evolution of a silica network from a fully polymerised vitreous SiO_2 to a carefully engineered material tailored to release essential ions in a controlled and plant-responsive manner.

2 Glass structure – conventional view

In order to grasp the intricate relationship between the chemical composition of glass, its resulting structure, and the way atomic ordering governs reactivity in aqueous environments, it is first necessary to present the conventional view of the vitreous network. In crystalline solids, structure is defined by long-range periodicity, where atoms, ions, or molecules are arranged in symmetric patterns that repeat along the three spatial axes and can be fully described by a unit cell. Glasses, in contrast, lack such repeating order, and no unit cell can be identified. Yet if structure is interpreted more broadly as the spatial arrangement of atoms, glasses may equally be regarded as structured solids, since they display a pronounced short-range order, extending over one or two interatomic distances, and a medium-range order manifested through recurring motifs such as rings, chains, and angular correlations over distances of up to ~20 Å. They should therefore not be seen as chaotic, but as non-crystalline solids in which the absence of long-range periodicity coexists with significant local organisation [101,102].

In silicate glasses, the fundamental structural motif is the silicon–oxygen tetrahedron [SiO_4], in which the small, highly charged Si^{4+} ion forms strong, directional bonds with oxygen, producing a tetrahedral geometry with characteristic bond lengths and angles. Paradoxically, it is not silicon but oxygen that plays the dominant structural role: owing to its abundance and large ionic radius, oxygen defines the framework within which cations are accommodated. The structural description of silicates is therefore an analysis of how cations fit into oxygen polyhedra, with their coordination numbers and bond distances largely determined by ionic size and charge. In practice, this leads to the concept of coordination polyhedra (Fig. 7), which constitute the common language of structural models for both crystals and glasses [101,102].

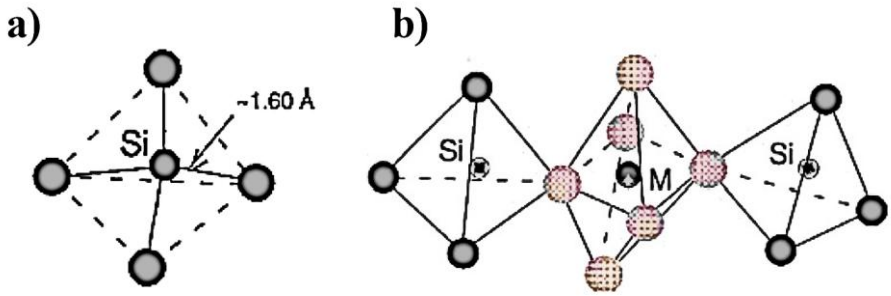


Fig. 7. SiO_4 tetrahedron (a); connectivity of Si tetrahedra through non-bridging oxygen to another cation M coordinated in an octahedron (b).

An excellent example of the structural dominance of [SiO_4] units is provided by Mg_2SiO_4 glass. Despite magnesium ions being present in twice the molar amount of silicon, the network is controlled by a framework of isolated, regular tetrahedra, while Mg^{2+} occupies distorted polyhedral sites ($4 \leq n \leq 6$), acting essentially as a space-filling charge compensator. This illustrates the ability of strong Si–O bonds to dictate structural organisation, relegating other cations to subordinate roles. Depending on the Si/O ratio, these tetrahedra may be fully connected, as in pure silica where every oxygen bridges two silicon atoms to form a continuous three-dimensional network, or completely isolated, in which case all oxygens are non-bridging. Between these extremes, the extent of

polymerisation is expressed by the number of non-bridging oxygens per tetrahedron, conventionally described by the Q^n notation (Fig. 8) [101].

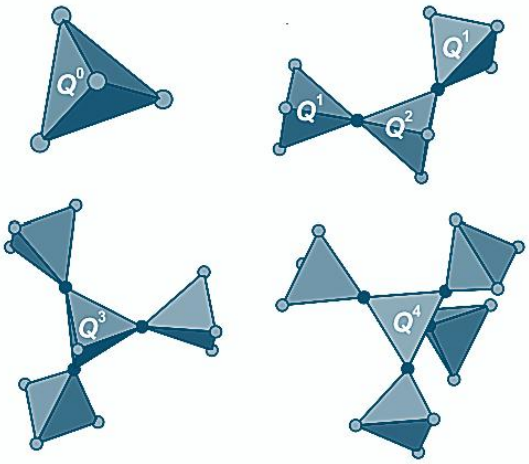


Fig. 8. Schematic illustrating various silicon-oxygen structural units, parallel with progressive depolymerisation of silicate networks as the number of non-bridging oxygens increases.

Here, Q^4 represents fully polymerised tetrahedra, while Q^0 denotes isolated units; intermediate species such as Q^3 or Q^3 define partially connected networks. This simple scheme, originally devised for crystalline silicates, has become indispensable for interpreting glass structure, particularly when combined with spectroscopic techniques such as MAS-NMR or Raman spectroscopy [103,104].

Ultimately, this view leads to the model of a continuous silicon–oxygen framework in which metal cations occupy interstitial positions to compensate the residual negative charge of terminal oxygens. Formalised by **Zachariasen** and refined by **Warren**, this so-called random network model Fig. 8) remains the classical and widely accepted description of the structure of simple inorganic glasses[102,105].

2.1 Zachariasen's theory and its evolution

Building upon the early observation of Goldschmidt—who noted that glass formation requires cations of tetrahedral coordination with radius ratios to oxygen between 0.2 and 0.4 – Zachariasen proposed a more comprehensive explanation of why certain oxides vitrify rather than crystallize upon cooling. Although originally conceived as an interpretation of glass formation mechanisms, his model rapidly became the cornerstone of modern glass science and one of its most cited contributions. The essential insight was that glass-forming oxides differ structurally from those that crystallize: instead of adopting close-packed lattices, they construct irregular, non-periodic frameworks of corner-linked polyhedra. These disordered but continuous networks, topologically comparable to crystalline frameworks yet devoid of long-range periodicity, account for the isotropic physical properties that define glasses.

To formalize this view, Zachariasen formulated structural rules which may be condensed into four premises: (1) all oxygen atoms and network cations occupy equivalent positions; (2) there is no long-range ordering of [SiO_4] units; (3) polyhedra link only through their corners; and (4) the resulting arrangement forms a three-dimensional, interconnected, but non-periodic network [101].

The practical consequences of this model can be clearly seen in simple systems: in pure SiO_2 each oxygen atom bridges two tetrahedra to produce a fully polymerised

framework, whereas the addition of large cations (e.g., Na^{+}, Ca^{2+}) disrupts Si–O–Si bonds, creating non-bridging oxygens while the modifier cation occupies the resulting cavity (Fig. 9).

On this basis, oxides were classified into three categories according to the electronegativity of the cation and the character of the cation–oxygen bond [101,102,106]:

- **Network formers (Group I):** cations that create bonds with a fractional ionic character close to 50% (Si, B, P, Ge, As). These elements produce stable networks on their own, forming polyhedra with coordination numbers of 3 or 4.
- **Intermediates (Group II):** cations of slightly lower electronegativity (e.g., Ti, Zn, Pb, Al), which cannot form a glass independently, but can substitute network-forming cations. They may behave either as network formers (adopting coordination 4) or as modifiers (6–8) depending on the overall composition.
- **Network modifiers (Group III):** cations with very low electronegativity (e.g., Na, K, Ca, Ba) which form highly ionic bonds with oxygen. They do not participate in building the network but occupy interstitial sites and disrupt the network by converting bridging oxygens into non-bridging ones.

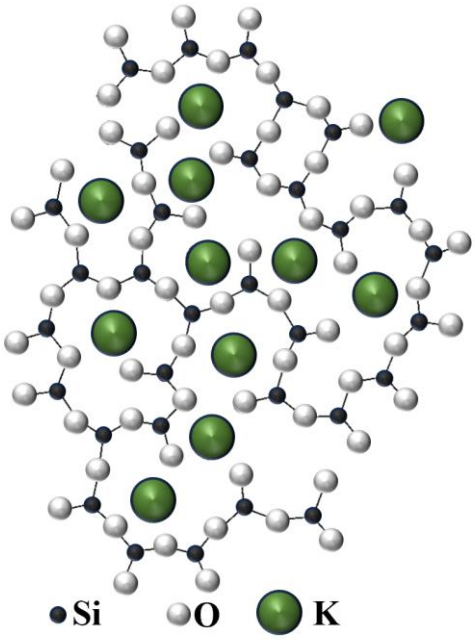


Fig. 9. Schematic representation of the structure of a simple potassium silicate glass based on the Zachariasen-Warren theory: the silicate network is built of interconnected SiO_4 tetrahedra, partially depolymerised due to the presence of potassium ions that create non-bridging oxygens.

This classification elegantly explains the compositional dependence of many physical properties: increasing concentrations of large cations progressively depolymerise the network, lowering viscosity and glass-transition temperature, broadening the melting interval, and enhancing electrical conductivity. Nevertheless, certain oxide systems reveal discontinuities in these property–composition trends, demonstrating that although the random network model remains a powerful conceptual framework, it does not fully account for the structural complexity of all glasses [102].

2.2 Dietzel's field strength concept

A significant extension of Zachariasen's work was introduced by Dietzel, who recognized that the influence of a given cation on the network is not solely governed by its size or polarizability but also by the strength of its electrostatic interaction with neighbouring oxygen atoms. This interaction was quantified in terms of the field strength (F) [102]:

$$F = \frac{Z}{a^2} \qquad \text{Eq. (1)}$$

where Z is the cation valency and $a=r_c+r_{O^{2-}}$ – is the sum of the cation and oxygen ionic radii. The field strength reflects the ability of a cation to attract and hold oxygen ligands in a cooling melt.

Dietzel's analysis established a clear correlation between the field strength and the structural role of cations in glasses:

- **Network modifiers:** F ≈ 0.1–0.4
- **Intermediates:** F ≈ 0.5–1.0
- **Network formers:** F ≈ 1.5–2.0

This classification is summarised in Tab. 2, which compiles data on valence, ionic radii, coordination, and field strength for a range of cations.

Tab. 2. Classification of cations according to their field strength (after Dietzel [102]).

Element	Valence Z	Ionic radius r(Å)	Most frequent CN	Ionic distance a(Å)	Field strength Z/a^2	Role in glass structure
K	1	1.33	8	2.77	0.13	Network modifier F ≈ 0.1–0.4
Na	1	0.98	6	2.30	0.19	
Li	1	0.78	6	2.10	0.23	
Ba	2	1.43	8	2.86	0.24	
Pb	2	1.32	8	2.74	0.27	
Sr	2	1.27	8	2.69	0.28	
Ca	2	1.06	8	2.48	0.33	
Mn	2	0.91	6	2.23	0.40	
Fe	2	0.83	6	2.15	0.43	
Mn	2	0.83	4	2.03	0.49	Intermediate F ≈ 0.5–1.0
Mg	2	0.78	6	2.10	0.45	
Mg	2	0.78	4	1.96	0.53	
Zr	4	0.87	8	2.28	0.77	
Be	2	0.34	4	1.53	0.86	
Fe	3	0.67	6	1.99	0.76	
Fe	3	0.67	4	1.88	0.85	
Al	3	0.57	6	1.89	0.84	
Al	3	0.57	4	1.77	0.96	

Ti	4	0.64	6	1.96	1.04	
B	3	0.20	4	1.50	1.34	Network former F ≈ 1.5–2.0
Ge	4	0.44	4	1.66	1.45	
Si	4	0.39	4	1.60	1.57	
P	5	0.34	4	1.55	2.10	
B	3	0.20	3	1.63	1.63	

The concept of field strength explains the competition between cations for oxygen coordination during cooling. When two cations in a binary silicate melt possess very similar field strengths, they tend to segregate, forming two distinct phases. By contrast, when their field strengths differ significantly ($\Delta F > 0.3$), a stable glass structure is more likely to form. This principle also accounts for the observation that while silica and phosphorus pentoxide are both excellent glass-formers individually, their binary mixtures frequently phase-separate or crystallise unless quenched rapidly [102].

2.3 Continuous random network versus crystallite model

At the time of its proposal, the **crystallite theory** was conceived as a direct counterpoint to the continuous random network (CRN) hypothesis. While the latter assumes that modifiers are statistically distributed within a disordered, continuous framework, the former envisions glasses as aggregates of submicroscopic crystalline regions –"crystallites" –randomly linked together. According to Lebedev, even nominally pure SiO_2 glass could be regarded as an assembly of ultrafine microcrystalline entities composed of silica, and in more complex systems, of additional silicate phases (Fig. 10) [105].

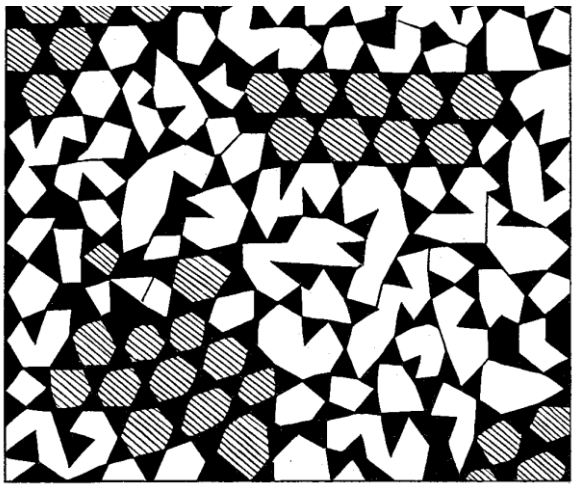


Fig. 10. Schematic illustration of the Lebedev crystallite model: ultrafine microcrystals arranged in a disordered manner, forming a glassy structure.

In multicomponent compositions these crystallites were thought to represent stoichiometric compounds or solid solutions predicted by equilibrium phase diagrams. Although coherent, they were assumed to be heavily distorted and too small to be detected by conventional optical techniques. To emphasise their submicroscopic and strained nature, Lebedev introduced the term "crystallite," and used it to explain abrupt discontinuities or extrema in property–composition relationships that could not be rationalised within the

CRN framework. In later revisions, he acknowledged that glasses might contain both disordered regions and more ordered domains resembling specific compounds [102].

Subsequent experimental evidence suggests that most glasses occupy an intermediate state between these two idealised extremes. Some of the early support for the crystallite hypothesis likely reflected limitations of experimental practice, such as the use of vitreous silica obtained from ground quartz, where the exceptionally high fusion temperature may have preserved remnants of the crystalline lattice within the cores of incompletely melted grains. Such residual fragments could have been mistaken for crystallites rather than ordered domains grown from a homogenised melt [102]. At the same time, the CRN concept is not without weaknesses. Warren, in seeking to substantiate it by analysing X-ray diffraction patterns of vitreous silica, applied the Scherrer equation to the broad principal halo and calculated an average coherent domain size of ~0.77 nm. Since the unit cell dimension of β-cristobalite along the [111] direction is 1.2 nm, this was taken as proof of the absence of periodicity on that scale. Yet this interpretation assumed isotropic growth, whereas β-cristobalite grows anisotropically, particularly along its dense [111] plane, making such a comparison less straightforward [107]. Moreover, the majority of arguments supporting either model derive from diffraction, a technique which yields averaged information and thus cannot decisively resolve nanoscale structural motifs in amorphous solids [105,107,108].

As Görlich emphasised [109], the distinction between the two models lies mainly in the scale of ordering: the crystallite theory implies domains extending over 15–20 Å, while the CRN model confines coherence to the first coordination sphere, i.e., a single SiO_4 tetrahedron. In reality, most glasses exhibit a hybrid structure (Fig. 9, Fig. 10), globally disordered yet interspersed with nanoscale regions of partial ordering. Numerous studies confirm that silicate glasses, though lacking long-range periodicity, display short-range order closely resembling that of their crystalline analogues, while their out-of-equilibrium character is largely expressed at the medium-range scale (0.5–2 nm), where motifs show a non-random organisation [105,107,108]. Spectroscopic evidence strongly supports this hybrid picture. Vibrational data reveal ordered domains within vitreous silica reminiscent of high-temperature α-cristobalite, randomly linked to form heterogeneous regions of varying packing density [105]. Similar domain structures have been identified in more complex glasses: for instance, amorphous kalsilite ($K[AlSiO_4]$) exhibits spectra nearly identical to its crystalline counterpart, and progressive addition of MgO to silicate–phosphate glasses drives structural motifs from cristobalite-like to forsterite-like ordering [105,110].

Comprehensive spectroscopic studies of amorphous silica have shown that the vitreous network is heterogeneous, comprising domains of varying order: some resemble high-temperature cristobalite, while others are enriched in broken Si–O bonds ($Si–O^-$), concentrated in less densely packed regions between ordered domains [105,111]. The introduction of alkali or alkaline-earth modifiers transforms this structure, as continuous breaking of Si–O–Si linkages produces non-bridging oxygens and progressively depolymerises the three-dimensional framework. In modifier-free glasses the network consists almost exclusively of fully polymerised Q^4 tetrahedra, whereas modifier addition shifts the distribution toward less connected units (Q^3, Q^2), according to a systematic scheme [104]:

$$2Q^{(n)}O_{n/2} + O^{2-} \rightarrow 2Q^{(n-1)}O_{(n-1)/2}O^{-}\ (Q = Si, P, B)$$

As the modifier-to-former ratio increases, tetrahedral units with a lower number of bridging oxygens (Q^{n-1}) appear at the expense of those with a higher connectivity (Q^n). This shift, which is approximately proportional to the amount of added modifier, can be quantified by determining the number of bridging versus non-bridging oxygens per network former atom. The resulting parameter, network connectivity (NC) – usually determined by high-resolution MAS-NMR and supported by Raman spectroscopy – provides a powerful measure for correlating composition with properties such as bioactivity, crystallisation tendency, or glass transition temperature [104,112].

The formation of non-bridging oxygens and associated depolymerisation upon modifier addition is well established, yet the extent of these changes depends strongly on modifier type, thermal history, and pressure conditions. a key factor is the field strength of the cations, which governs Q-species distribution: for example, lithium silicate glasses show higher proportions of Q^2 and Q^4 units than sodium silicates, as Li^+ tends to cluster around Q^2 units and enrich adjacent regions in Q^4 tetrahedra. More generally, increasing field strength shifts the equilibrium $2Q^n \rightarrow Q^{n-1} + Q^{n+1}$ towards the right [113]. Modifier cations may also display selective charge compensation. At low phosphorus content, Na^+ and Ca^{2+} show little preference, but with higher P_2O_5 content, Ca^{2+} increasingly associates with phosphate groups, leading to Ca-rich phosphate clusters, illustrating simultaneously that modifiers are often heterogeneously distributed [114]. Cation site geometries in glasses are likewise complex: coordination numbers are usually lower than in crystals, and unusual states, such as five-fold Mg^{2+}, are common [115,116]. a given cation may occupy multiple sites, and the presence of low-field-strength species such as K^+ can lower the average coordination number of others, thereby influencing partial molar volumes [115].

In general, modifiers reduce network connectivity, causing viscosity and glass transition temperature to drop, while density, refractive index, and thermal expansion rise. Electrical conductivity, controlled by alkali mobility, increases by orders of magnitude with alkali oxide content [101]. et these trends are often non-linear, and threshold effects can reverse them.

Altogether, such complexities make glasses both technologically indispensable and scientifically captivating. They reveal the limits of simplified models such as the random network or crystallite hypotheses: unlike crystals, glasses lack a unique structure, even within a single specimen. a nuanced understanding of this structural diversity is therefore essential for linking composition to properties and for designing glasses with tailored functionalities, including controlled reactivity in biological or environmental contexts.

3 Requirements imposed on the vitreous carriers of macro- and micronutrients

As discussed in the preceding section, the structure of a vitreous material plays a critical role in determining its properties, influencing whether the material exhibits high chemical durability or distinctive chemical activity. This distribution of elements within the vitreous matrix is, in turn, directly modulated by the glass composition, governing at the same time the material's functional performance. Like any material designed for a specific application, glass fertilizers must exhibit a set of well-defined properties to effectively fulfil their intended role.

In the case of glass fertilizers, which are deliberately designed as nutrient carriers for plants, the material must satisfy a precisely defined set of functional requirements in order to perform its role effectively. From this perspective, the key criteria that must be met by such materials include:

(1) **High resistance to neutral or slightly basic aqueous environments**, to minimize nutrient loss through leaching by rainwater or irrigation, while maintaining enhanced solubility under acidic conditions, such as those typically found in the rhizosphere;

(2) **Controlled and gradual nutrient release**, allowing for the long-term supply of essential ions encapsulated within the glassy matrix in synchrony with the demand of the growing plant;

(3) **Tailored chemical composition**, providing adequate concentrations of macro- and micronutrients essential for plant growth, while also promoting a fragmented (open) glass structure that facilitates water ingress and ion exchange;

(4) **Fully amorphous structure**, with minimal or no crystalline phases, as the presence of such phases may hinder he uniform and predictable release of nutrients into the surrounding medium.

The following sections discuss these requirements in detail, with particular emphasis on their significance for the functionality of glass-based fertilizers.

3.1 High resistance to water combined with preferential dissolution in acidic environments

It is well established that the chemical resistance of glass is controlled by a broad spectrum of factors. These include not only the intrinsic features of the material itself, such as its chemical composition, microstructure, and surface state, but also external variables like the chemical nature of the contacting medium, the duration of exposure, and the temperature at which the interaction occurs.

Given the specific conditions prevailing within the rhizosphere, where the mobilization of nutrients from soil minerals is largely driven by the acidic exudates of plant roots and associated microorganisms, glass fertilizers should be formulated so that they release macro- and micronutrients primarily when exposed to acidic solutions that mimic these natural exudates. At the same time, such materials must exhibit very limited interaction with pure water, thereby minimizing leaching losses into groundwater or surface reservoirs and preventing the permanent immobilization of plant-available elements.

Although the mechanisms governing the reaction of aqueous solutions with amorphous materials have been investigated for decades, they remain complex and incompletely understood due to their dependence on numerous interrelated factors. Nevertheless, several fundamental processes are generally recognized as the main contributors to the overall interaction of water with glass [117]:

- **Interdiffusion**, whereby molecular water, primarily in the form of H^+ or H_3O^+ ions, diffuses into the glass and undergoes ion exchange with alkali (K^+, Na^+, Li^+) or alkaline earth (Mg^{2+}, Ca^{2+}, Ba^{2+}) cations, resulting in the formation of an alkali-depleted reaction layer;

- **Hydration**, involving the penetration of molecular water into the glass without concurrent ion exchange, which leads to structural swelling and the formation of a hydrated layer;
- **Hydrolysis**, encompassing a cascade of reactions that cleave chemical bonds, both those linking network-forming oxides with network-modifying cations (e.g., Si–O–K) and those forming the framework itself (e.g., Si–O–Si). Hydrolysis also results in the release of network-forming species into the solution;
- **Condensation**, in which silanol groups (Si–OH) produced during previous steps condense to regenerate Si–O–Si bridges;
- **Precipitation of secondary phases**, occurring when the solution becomes oversaturated with components released from the glass. These secondary products may also form through reactions between released ions and components of the environment, sometimes creating surface layers that act as partial diffusion barriers.

It should be highlighted, however, that the sequence, intensity, and consequences of these reactions depend strongly on the glass composition as well as on environmental parameters [118]. Among these processes, ion exchange and hydrolysis are generally considered to be the most critical for long-term glass integrity, as their rates are strongly controlled by the pH of the contacting solution, a relationship illustrated schematically in Fig. 11 **Błąd! Nie można odnaleźć źródła odwołania.**[119].

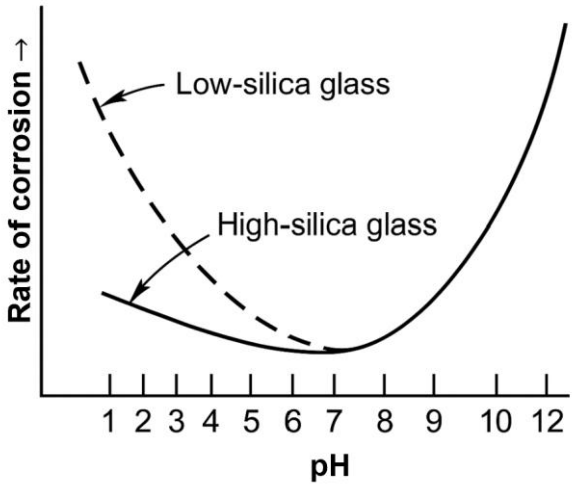


Fig. 11. Dependence of the glass corrosion rate on the pH of the contacting solution.

In acidic solutions, ion exchange dominates: protons (H^+ or H_3O^+) from the surrounding medium replace alkali or alkaline-earth cations, forming Si–OH bonds with the glass network. The extent of this reaction depends on the depth of proton penetration, which in turn is controlled by composition, temperature, and the duration of exposure, and the resulting ion-depleted layer may reach several micrometres in thickness [119]. For high-silica glasses, Si–OH groups formed in this manner can undergo condensation to produce a thin hydrated barrier, which slows further attack. Such a protective effect, however, is largely absent in glasses rich in network-modifying oxides; the lower silica content prevents the development of a coherent surface gel, leaving the material more vulnerable [120]. Importantly, the structural framework of Si–O–Si bonds remains intact under these

conditions—the corrosion selectively affects the Si–O–M linkages, where M denotes alkali or alkaline-earth metals[2] [119].

In contrast, when neutral water interacts with glass, the same ion exchange process occurs but proceeds at a significantly slower rate. The resulting hydrated, alkali-depleted layer rarely exceeds 50 Å and generally exhibits high stability, effectively shielding the inner regions of the material [120]. Under conditions of limited water availability, however, this mechanism can change dramatically. Rapid ion exchange depletes the thin surface film of protons, raising the local pH, and shifting the mechanism toward that typical of alkaline solutions – one of the most aggressive scenarios for the integrity of glass [121]. In such conditions, at pH values above 9, hydrolysis of the glass network becomes intense: hydroxide ions attack Si–O–Si linkages, and the glass dissolves congruently, releasing all of its constituents into the medium [119]. Although newly formed silanol groups can, in principle, re-condense into a silica-rich gel, this gel is not protective under alkaline conditions, gradually dissolving into the solution [122].

It is generally acknowledged that in Poland, the most common soil types – brown, podzolic, and lessive soils – are predominantly acidic in nature [123]. Moreover, the pH in the rhizosphere typically deviates from that of bulk soil, ranging from slightly acidic to near-neutral, due to biological activity [124,125]. For this reason, although localized alkaline conditions cannot be completely excluded (for instance, due to the accumulation of a thin film enriched in leached modifiers on the surface of a glass granule), the typical scenario is exposure to solutions with pH < 7 or close to neutral. Under these conditions, ion exchange remains the principal process, ensuring a controlled release of nutrients while preserving the integrity of the silica-rich glass network. Because the mobilization of macro- and micronutrients is then triggered by root exudates – in other words, "on demand" by the plant – the risk of overfertilization is significantly reduced.

3.2 Prolonged release of nutrients

3.2.1 Kinetics of glass alteration

As emphasized previously, a fundamental requirement for glass-based fertilizers is the long-term, gradual release of the nutrients encapsulated within the vitreous matrix into the surrounding environment. Consequently, any evaluation of glass formulations intended as sustained nutrient carriers for plants must be based on a careful analysis of their alteration kinetics under conditions representative of their final application. As described in the preceding sections, regardless of the specific chemical composition, any glass exposed to a reactive aqueous environment responds to external factors through a cascade of coupled processes occurring at the atomic scale. These involve interactions between the solution and the solid surface through a series of mechanisms such as adsorption and desorption, ion exchange, hydrolysis of chemical bonds followed by their reformation, Ostwald ripening of the hydrated gel layer, precipitation of secondary phases, and transport of both reactants and products across the altered layer. The interplay of these mechanisms governs the release of constituents into the surrounding medium, giving rise to a characteristic time-dependent behaviour that can generally be divided into three stages, schematically illustrated in Fig. 12.

[2] An exception may be hydrofluoric acid, known for its aggressive reaction with glass, even at low temperatures, leading to the release of SiF_4 and fluorides [122].

When a pristine glass surface comes into contact with a dilute aqueous solution, the interaction begins with a rapid, feedback-free corrosion process at an initial rate denoted as r_0 (often referred to as the forward rate). This first period, known as Stage I, corresponds to the maximum dissolution rate attainable under given pH and temperature conditions. It is initially dominated by interdiffusion between protons (H^+/H_3O^+) and the alkali or alkaline-earth cations bound within the network, but very quickly becomes governed by the hydrolytic cleavage of Si–O–X linkages (where X represents Si, Al, Zr, B, etc.). In this phase, dissolution is typically linear with time and occurs congruently, i.e., all glass constituents are released in proportions similar to those in the parent glass. Only in glasses that are strongly depolymerized or in acidic conditions is the behaviour markedly different, with modifiers such as Na or K released more rapidly than Si due to the fast kinetics of H^+/Na^+ exchange.

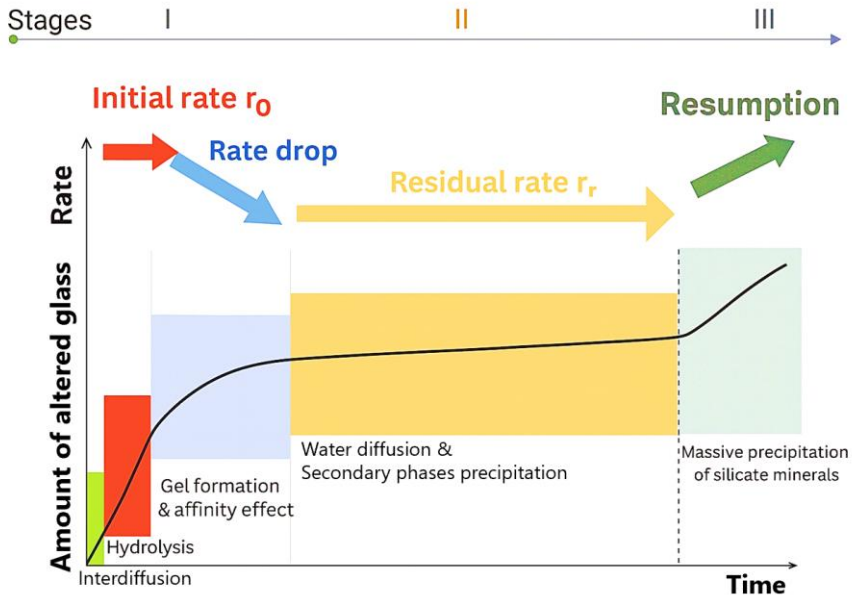


Fig. 12. Schematic representation of the three main stages of silicate glass corrosion [126].

At the macroscopic level, the value of r_0 depends on both intrinsic factors (glass structure and composition) and extrinsic conditions (pH, temperature, ionic strength of the solution), whereas mechanistically, the initial rate reflects the combined effects of adsorption, ion-exchange, and hydrolytic reactions occurring at the molecular scale. Importantly, in this regime the solution remains undersaturated with respect to all possible phases, so no protective or secondary layers can form. It is now well established that:

(1) The molecular level processes are complex, as involve not a single bond but the cooperative rearrangement of a local atomic environment, including at least the second coordination shell around the hydrolysed site;

(2) Ion exchange or the removal of a network cation induces local reorganization of the structure, involving coordination changes of neighbouring cations, the generation of silanol (Si–OH) groups, and proton or water molecule diffusion;

(3) Ion-exchange and hydration processes are inherently coupled with the progressive hydrolysis of ionic-covalent bonds within the network.

As the dissolution continues, the silicon concentration in the contacting solution gradually increases until a quasi-steady state is attained. At this point, the driving force for further dissolution diminishes and the rate drops dramatically to a much slower, nearly constant value referred to as the residual rate (Stage II). This regime is usually several orders of magnitude slower than r_0. During Stage II, dissolution becomes incongruent: a hydrated, silica-rich alteration layer (gel) forms on the surface through the re-condensation of hydrolysed silica species (or alternatively: dissolution-precipitation mechanism of silica particles), and this layer selectively retains certain elements, while others are slowly released. Over time, the porosity of this gel tends to decrease as a result of structural rearrangement, and the layer develops passivating properties that impede the ingress of water and slow the release of components.

The drastic reduction in dissolution rate during this stage is now considered to result from the combined action of two effects: (i) a **thermodynamic effect**, associated with the decreased chemical affinity of the silicate network for further hydrolysis as the solution approaches saturation with respect to silica (or other released glass components), and (ii) a **transport-limiting effect**, caused by the silica-rich gel acting as a diffusion barrier that hinders the migration of water and reactive species. During the transient phase between Stages I and II, concentrations of glass constituents in the solution rise until the solution becomes essentially saturated with respect to the alteration layer. Then, the residual rate, r_r, is noted – a low (3 to 5 orders of magnitude lower than r_0) and stable alteration rate that can persist over long timescales (Fig. 12). Interestingly, for glasses with a low fraction of non-bridging oxygens—such as natural obsidians or aluminosilicate glasses—the residual rate regime has, in some cases, not been detected, most likely because the compact structure prevents significant water diffusion into the bulk of the glass. If, on the other hand, water can diffuse into the solid, alteration, although slowly, may still proceed through ion exchange, hydrolysis reactions, and local rearrangements.

Even after the residual regime has been established, under certain conditions a renewed acceleration of alteration—commonly termed Stage III—can occur. This resumption of corrosion is most frequently attributed to the precipitation of secondary crystalline or poorly crystalline phases, such as zeolites or calcium silicate hydrates (C–S–H). The nucleation and growth of these phases, which form at the expense of the protective silica gel, disrupt the passivating layer and restore access of water to the underlying glass. Additionally, other factors are known to trigger Stage III resumption of alteration – these include cracking or detachment of the alteration layer, as well as an increase in the reactive surface area. Remarkedly, the amorphous and crystalline secondary products of glass-solution interaction undergo sequential evolution on the altered glass surface, which is well explained by the Ostwald rule of stages. According to this rule, a system tends to evolve through a series of intermediate, metastable states before ultimately reaching the most thermodynamically stable one, potentially once again slowing down the further alteration processes [127].

The occurrence of Stage III is strongly dependent on both the glass composition and the external conditions. It is particularly favoured in glasses containing high concentrations of alkali modifiers and is promoted by conditions such as elevated temperatures (above 90 °C), high pH (>10.5), and large glass-surface-area-to-solution-volume (S/V) ratios. Under much milder conditions, however, Stage III is rarely observed; many systems remain indefinitely in the Stage II regime, exhibiting extremely low alteration rates. When alteration does resume, the rate r_{res} is consistently lower than the forward rate r_0,

but can nonetheless significantly exceed the residual rate maintained during Stage II [127].

3.2.2 Formation of Surface Alteration Layers

The long-term durability of glass is governed by the combined effects of its kinetic behaviour and the thermodynamic stability of its oxide constituents. In a perfectly balanced state, when the chemical potentials of species within the glass surface and those in the surrounding solution become equal, no net transfer of mass can occur. However, a glassy solid is, by nature, a untastable material that exists far from thermodynamic equilibrium, and therefore tends to undergo chemical reactions aimed at reaching a new, more stable state [119]. In practice, most silicate glasses – particularly those enriched in alkali oxides [128] – when subjected to contact with water, undergo a sequence of coupled processes: diffusion of water into the surface layers, ion exchange between hydronium or protonated species and the network-modifying cations, hydrolysis of iono-covalent Si–O–M bonds (M = Si, Al, Zr, Fe, Zn, etc.), condensation of partially detached units, and precipitation of crystalline or poorly crystalline phases. These reactions progress until a quasi-stationary state is reached. As a consequence, a subsurface altered zone forms, differing significantly from the bulk composition, with a thickness that may range from a few nanometres to several centimetres depending on the glass composition and environmental conditions [126,129,130].

The precise mechanisms by which this surface alteration layer (SAL) develops remain a matter of considerable debate, and two fundamentally distinct conceptual models are currently under discussion. According to the first model, the SAL represents a product of solid-state repolymerization within a hydrated glass layer. This layer is generated through diffusion-controlled ion exchange, in which mobile network-modifying cations (e.g., Na, Li, Ca) are replaced by protons from the solution, resulting in the formation of silanol (Si–OH) groups. These groups can subsequently condense, releasing water and reorganizing into a more polymerized structure that minimizes the free energy of the system. The newly formed layer exhibits increased porosity, and in some cases may act as a passivating interface where the pores are partially sealed, reducing further ingress of water and slowing down corrosion [131,132]. The alternative model attributes SAL formation to interface-coupled dissolution–precipitation (ICDP) reactions. Here, an amorphous silica layer is precipitated directly from the solution as the glass dissolves congruently at a sharp, advancing interface. The thermodynamic driving force is the difference between the solubilities of the glass constituents and amorphous silica [129]. It is postulated, however, that both concepts may apply under different conditions, as the dominant mechanism depends strongly on glass composition and environmental factors such as pH, flow regime, and temperature [133].

Irrespective of the precise route, the altered layer attains a steady-state thickness once the system approaches a condition of diffusion-limited dissolution. For glasses with highly polymerized networks, such as borosilicate glasses (Duran, Pyrex), the formation of a dense, silica-rich layer drastically slows down further corrosion. Similarly, when the available solution volume is small and rapidly becomes saturated with respect to the released elements, further glass dissolution is essentially halted (a phenomenon sometimes referred to as the "solubility limit" or concentration equilibrium across the water–glass interface) [128,134]. Besides the intrinsic chemical structure, the duration of each corrosion stage depends critically on external factors. In fast-flowing environments, the

solution remains undersaturated, maintaining Stage I dissolution for extended – potentially indefinite – periods. In contrast, under static or poorly circulated conditions, the system rapidly transitions to Stage II, with the possible passivation effects.

3.2.3 Strategies for prolonged nutrient release from glass fertilizers

The deliberate tailoring of the composition of glass fertilizers must therefore take these factors into account, with particular attention to the profound influence of solution pH on corrosion behaviour. When glass is exposed to an aqueous medium, proton–metal exchange reactions progressively leach cations from the network-modified regions of the glass. The depth of this leached zone depends on both solid-state properties and environmental conditions. Typically, at pH values between 2 and 5, almost all network modifiers (Na^+, C^{2+}, Mg^{2+}) are readily removed, whereas Si remains relatively unaffected. Within the range of $5 < pH < 9$, leaching mainly involves monovalent and divalent modifiers, whereas trivalent cations, such as Al^{3+}, remain essentially immobile. At pH values above 9, the rate of cation leaching diminishes, but nucleophilic attack by hydroxyl groups leads to direct depolymerization of the silicate network, a process that becomes particularly pronounced at $pH > 12$ [135]. Ab initio molecular orbital calculations by Xiao and Lasaga [136] have shown that pH not only controls which bonds are attacked but also alters the activation energy of siloxane (Si–O–Si) hydrolysis. Hydrolysis catalysed by hydroxyl ions proceeds with an activation barrier of 18.9 kcal mol^{-1}, whereas proton-catalysed hydrolysis (via H_3O^+) requires 24 kcal mol^{-1}. In contrast, an uncatalyzed process in pure water requires a significantly higher activation energy of 29 kcal mol^{-1}, emphasizing the catalytic roles of both acids and bases.

Since under acidic conditions, glasses experience rapid cation exchange, creating a leached, silica-rich alteration layer, in such environment the advancing reaction front progresses inward as mobile species are replaced by protons, releasing cations incongruently into the surrounding solution. Near-neutral environments, in contrast, promote a slower, more uniform dissolution that favours the development of a protective hydrated layer which limits further corrosion [137].

For glass fertilizers, this means that over the intended lifespan in soil, exposure to natural moisture (rainfall or irrigation) should result only in a very shallow alteration of the outermost surface – on the order of a few tens of nanometres – driven primarily by dealkalization and hydration [138]. Once the solution in contact becomes saturated with respect to the alteration products, a steady state is reached and the reaction front ceases to advance deeper into the material. At this stage, further dissolution is essentially halted unless the environmental conditions change, and the hydrated layer stabilizes with a thickness typically in the range of 20–30 nm [128,132].

Selective leaching of network modifiers in multicomponent glass compositions can be described in terms of proton-exchange reactions such as [138]:

$$Si - O - K^+ + H_3O^+ \rightarrow Si - OH + K^+ + H_2O \quad \text{Eq. (2)}$$

$$Si - O - K^+ + H^+ \rightarrow Si - OH + K^+ + OH^- \quad \text{Eq. (3)}$$

and the extent of such processes can be quantitatively expressed using ion-exchange equilibrium constants [138]:

$$K = \frac{[Si - OH][K^+]}{[Si - O - K^+][H^+]} \quad \text{Eq. (4)}$$

According to this relation, the degree of ion exchange is influenced by several factors: the concentration of K^+ (or other modifiers) in the surrounding solution, the pH (with more acidic conditions favouring exchange), and the equilibrium constant, which defines the relative affinity of protons for anionic sites within the network [138]. It is therefore expected that under the exposition to the root and microorganisms' acidic exudates, the ion exchange will be driven by the high concentrations of exogeneous protonated species (H^+ as well as H_3O^+) in the exudates. In such conditions, imposed by plant and/or soil biota, the exchange between glass network-modifying cations and protons in the solution will constitute a preferred mechanism of glass alteration with its kinetics exceeding significantly the hydrolysis rate of the silicate network. Since ion-exchange reactions create voids which water can penetrate, the reaction front is expected to be progressing towards the bulk glass leaving the hydrated porous silica rich altered layer [138]. Furthermore, it is assumed that the macro- and microelements mobilization will be minimized together with the cease of exudation, as well as once the concertation of the released modifier cations in the contacting solution will be significant enough to impose a chemical affinity effect. The components of root exudates themselves, as citric or acetic acids, are also believed to enhance useful elements mobilization. Since the organic ligands can form soluble organic-metal complexes, the effective concentration (chemical activity) of cations present in the contact solution is reduced which furthers accelerates the leaching process [135]. However, as soon as exudate production decreases or the solution becomes enriched in the released cations, a temporary thermodynamic balance is established, slowing down the process.

From a practical perspective, for glass fertilizers it is desirable to **prolong the controlled release of nutrients over the entire growth cycle of the plant**, ensuring a consistent supply of ions without creating peaks of high concentration. This controlled release can be achieved through two primary mechanisms:

I. the formation of a condensed hydrated silica gel layer at the superficial dealkalized glass area, and

II. the precipitation of secondary phases at the interface between the glass and the surrounding soil solution.

The first mechanism is favoured in glasses with a high silica content and a greater proportion of Q^3 units in the network, as the higher degree of polymerization reduces the activation energy required for condensation. The resulting hydrated silica layer strongly limits diffusion: the mobility of water molecules within this gel has been shown to be approximately thirty times lower than in bulk water, due to the extensive interactions between water molecules and the silicate network [139].

Meanwhile, the second mechanism that contributes to the slowdown of nutrient release is the precipitation of secondary phases – the process that modifies the chemical composition of the surrounding solution (or, in some cases, surface gel composition), which in turn influences further glass alteration rate. Indeed, numerous experimental observations have reported that the nucleation of such secondary phases may, under certain conditions, be accompanied by a temporary acceleration of glass dissolution. However, this

phenomenon primarily occurs when the precipitated phases are composed of elements that constitute the backbone of the alteration layer itself (notably Si and Al). In this particular instance, the silicon required for these precipitates is supplied either directly from the alteration gel or from the solution. The consumption of silica from the gel tends to make the layer more porous and less compact, which facilitates the transport of both reactants and reaction products, whereas, in the latter case, the depletion of dissolved Si destabilizes the gel. Regardless of their origin, both these phenomena lead to renewal and acceleration of the overall corrosion process.

For this reason, glass fertilizers must be carefully designed so that the precipitation of secondary phases involves mainly the most mobile glass components, without affecting the continuity of the fundamental Si–O–Si network. Such a controlled crystallization ensures that the secondary phases act as a temporary reservoir of useful elements, and/or (when forming a dense and continuous outer layer) a diffusion barrier, restricting the access of fresh water to the glass surface and thereby contributing to a temporary increase in durability, rather than intensifying leaching. In this scenario, the precipitation layer serves as a regulatory interface, moderating the elemental concentrations in the solution at the interface to the residual glass (Fig. 13).

A crucial requirement for these secondary phases is that they remain soluble in mildly acidic environments, which ensures that, in the rhizosphere where root exudates periodically acidify the surrounding medium, the immobilized nutrients can be remobilized and made available to plants “on demand,” while avoiding their permanent sequestration within stable and insoluble crystalline structures. Therefore, the careful selection of glass components, systematic studies of their crystallization behaviour, and long-term investigation of glass-soil interactions are essential to ensure that these materials fulfil their intended role as slow-release fertilizers.

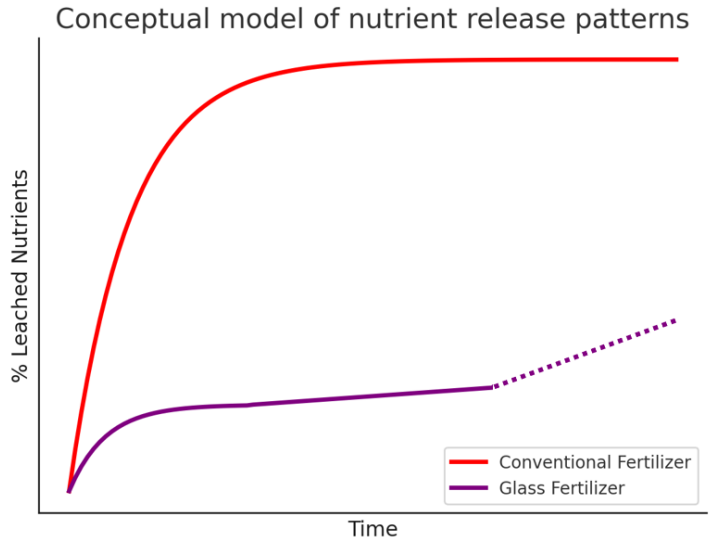


Fig. 13. Conceptual model of the release patterns of nutrients from conventional as well as vitreous fertilizers; the dotted line represents the rate resumption as a consequence of mobilization of useful ions from the secondary phases.

It should also be emphasized that the predominance of either of the two protective mechanisms—silica gel formation or precipitation of secondary phases – depends strongly on the soil microenvironment. a high and continuous supply of moisture favours

the growth of a hydrated silica gel, while limited and intermittent water availability leads more readily to the precipitation of secondary phases once local saturation is achieved. Regardless of the specific conditions, both mechanisms, acting alone or in combination, enable a prolonged and stable release of macro- and micronutrients over extended periods, in synchrony with plant demand.

3.3 Optimized chemical composition and structural design of glassy carriers for macro- and micronutrient delivery

It is important to emphasize that the alteration mechanism of glasses, as outlined in the preceding sections, has been presented in a simplified manner consistent with the widely accepted framework for silicate glasses. In reality, however, the alteration of silicate-based glasses is a highly complex and nuanced phenomenon. It is influenced not only by the intrinsic properties of the glass – such as its chemical composition, short- and medium-range structural order, and bonding environments – but also by a wide range of external environmental factors. These include temperature, pH, redox potential (Eh), solution chemistry, and numerous interrelated parameters (Fig. 14). Given the immense variability and dynamic nature of biotic soil environments – characterized by seasonal changes, sudden weather events, and the activity of countless microbial and plant species – environmental conditions can only be predicted to a limited extent. In contrast, the material-related characteristics, particularly composition and the resulting structure, can and should be meticulously engineered. By doing so, it becomes possible to design glass materials capable of releasing nutrients or functional components in response to 'plant demand', allowing them to integrate harmoniously into the complexity of soil ecosystems.

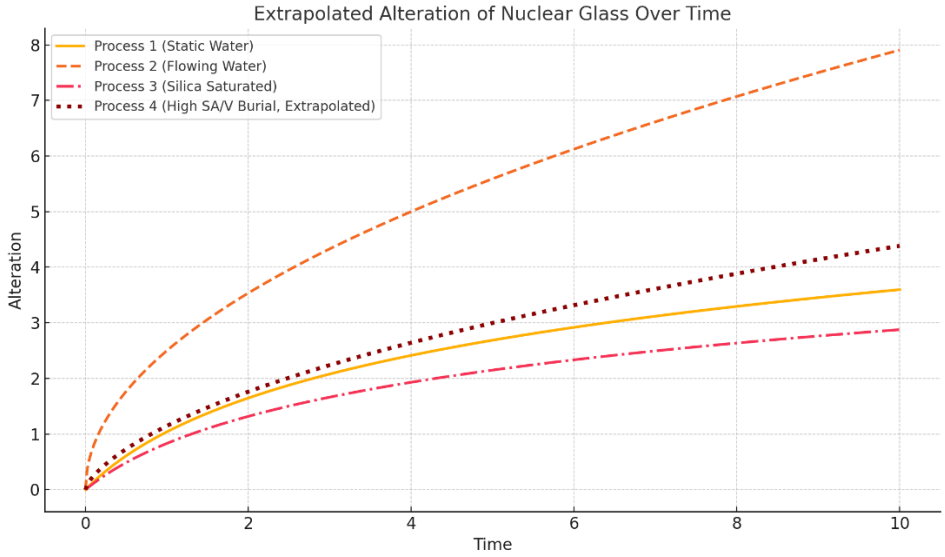


Fig. 14. Conceptual alteration behaviour of silicate glasses in aqueous environments under different conditions, based on [140].
***Process 1** represents glass corrosion in static water, leading to a decelerating alteration rate as silica saturation is approached.*
***Process 2** corresponds to alteration in rapidly flowing water, where continuous removal of dissolved species prevents saturation, resulting in sustained high alteration rates.*
***Process 3** shows alteration in silica-saturated solutions, where reaction rates are minimal.*
***Process 4** illustrates alteration under high surface area-to-volume (SA/V) conditions, such as burial environments, where initial rates may be elevated but slow over time due to localized saturation.*

As discussed earlier, although the vast majority of glasses undergo some degree of transformation when exposed to aqueous environments, the extent of this alteration is strongly dependent on the composition of the glass network – specifically, the identity, proportion, and interactions of the constituent components. Extensive research in the field of glass corrosion has consistently demonstrated that glass composition significantly influences each stage of the alteration process, as illustrated in Fig. 12.

Each component incorporated into the glass matrix affects its structure in a characteristic manner, governed by factors such as ionic radius, charge, and chemical affinity with other constituents. These structural modifications, in turn, have a direct impact on the dissolution behaviour of the glass, emphasizing the central role of the composition–structure–property relationship in determining the performance of glassy materials in practical applications.

A notable example is provided by Mascaraque et al., who applied the Phillips−Thorpe topological constraint theory to show that the topology of the glass network is a key determinant of chemical durability. Their findings revealed a clear correlation between glass stability in aqueous media and network topology, across a broad spectrum of glass systems – including phosphate, silicophosphate, borophosphate, silicate, borosilicate, aluminosilicate, and aluminoborosilicate compositions [141,142]. According to the concept presented in their works, in a three-dimensional atomic network, each atom has three degrees of freedom, which are progressively constrained by the formation of chemical bonds. These constraints can be categorized into two primary types: bond-stretching (BS) constraints, associated with the interatomic distances (e.g., Si–O or P–O bonds), and bond-bending (BB) constraints, which arise from angular relationships between three atoms (e.g., O–Si–O or O–P–O angles). The nature and number of constraints introduced by each network-forming component depend on its coordination environment and concentration. For example, each bridging oxygen atom contributes two BS constraints, while non-bridging oxygens contribute only one. BB constraints are typically associated with bridging oxygens, as non-bridging oxygens do not maintain stable angular geometry at ambient conditions. Network-modifying cations (e.g., Na^+) contribute one BS constraint per metal–oxygen bond. Glass networks can be quantitatively characterized by the number of topological constraints per atom, denoted as n_n, which reflects the overall rigidity of the network. Systems with $n_n < 3$ are considered *flexible*, as they possess internal degrees of freedom that allow for local deformations. Networks with $n_n = 3$ are *isostatic*, representing an optimal balance – rigid yet free from internal stress. Conversely, networks with $n_n > 3$ are *stressed-rigid*, with high connectivity that introduces internal eigenstress and prevents structural relaxation.

Mascaraque et al. evaluated the bulk dissolution rate (D_r) of various glass compositions across a range of pH conditions and reported a linear relationship between D_r and n_n, confirming that dissolution behaviour is directly influenced by network topology. From an energy landscape perspective, each topological constraint acts like an energy well or elastic spring, resisting deformation. a lower n_n indicates fewer constraints and a more accessible energy landscape, enabling atoms to rearrange more readily. As a result, flexible glasses exhibit lower energy barriers for structural reorganization, which facilitates local compaction during ion exchange and enhances the susceptibility of the network to hydrolytic attack. In contrast, stressed-rigid networks are structurally

immobilized, limiting their ability to adapt locally and thus improving chemical durability [141–143].

This flexibility, as interpreted through the lens of topological constraint theory, is fundamentally dictated by glass composition. It determines how open or compact the network is, and consequently, how readily it can accommodate external species or the transient products of hydrolysis reactions. As previously emphasized, the chemical composition of the glass significantly influences every stage of the alteration process – from initial water adsorption on the surface, through network breakdown, to the eventual crystallization of secondary phases in the altered subsurface region.

3.3.1 Stage I

In the initial stage of alteration, the rate-limiting step for most glasses is the ingress of water molecules into the vitreous network, and consequently, the influence of chemical composition is closely tied to the resulting structural characteristics of the reacting material [130].

As outlined earlier, water can enter a glass surface through two fundamentally different mechanisms. It may either diffuse as an intact molecule through the voids present between oxygen atoms in the network or react with the glass matrix via hydrolysis and subsequent condensation of metal–oxygen bonds, following the general reaction scheme [138]:

$$H_2O + M - O - M \rightarrow M - OH + HO - M \rightarrow M - O - M + H_2O \quad \text{Eq. (5)}$$

The dominant pathway for water penetration depends on the relative rates of these two processes. The efficiency of molecular diffusion is primarily governed by the steric limitations imposed by the size of the voids in the glass structure – in silicate-based materials, this void size reflects the distribution of interconnected silicate tetrahedral rings [138].

Experimental studies indicate that molecular water diffusion becomes significant only when the structural voids exceed approximately 0.7 nm in diameter (compared to the 0.28 nm kinetic diameter of a water molecule). This value effectively separates two distinct diffusion regimes: above this threshold, diffusion behaves as in a liquid, with apparent diffusion coefficients on the order of 10^{-9} m^2/s, whereas below it diffusion slows dramatically to less than 10^{-15} m^2/s, corresponding to solid-state transport. Consequently, glasses characterized by high degrees of polymerization – typically silica-rich glasses with a high proportion of Q^3 units – tend to be more compact, and water can enter primarily through reactions involving hydrolysis of bridging bonds rather than by free molecular diffusion. Under these conditions, the advance of water into the glass proceeds in parallel with network hydrolysis, with the overall kinetics governed by both the distribution of local structural units and the chemical properties of the external medium, including pH (which can vary locally depending on the surface-area-to-volume ratio). The structural arrangement influences local bond strain and, in turn, the reactivity of silica, while also affecting the rate of ionic exchange. Glasses of this type – predominantly high-silica materials – commonly exhibit a rapid initial rate decrease associated with the development of a hydrated, Si-rich, porous alteration layer on the surface. This layer gradually evolves into a relatively dense and passivating gel that restricts further transport, enabling the system to enter Stage II, characterized by low residual dissolution rates. The ease of forming such

a passivating barrier increases with the polymerization of the glass, as the re-condensation of hydrolysed Si–O–Si linkages is facilitated within more interconnected frameworks [126,138].

This hydrated surface layer significantly impedes the migration of aqueous species, with the diffusion coefficient of water through the gel reported to be approximately thirty times lower than in bulk water at ambient conditions – this marked reduction is attributed to interactions between diffusing molecules and the constraining network at the gel–glass interface. Importantly, isotopic tracer studies (e.g., using ^{29}Si and ^{18}O) have provided direct evidence that this compact alteration layer restricts transport of both water molecules and dissolved glass constituents. Over time, pore structures within this layer tend to coalesce and close, further reducing transport and limiting contact between the reactive fluid and the pristine glass. In this manner, this phenomenon of local reorganization within the gel layer, sometimes referred to as pore ripening, results in a progressive decrease in its reactivity toward water. In contrast, when the structural network contains voids sufficiently large (greater than ~0.7 nm) relative to the size of water molecules, H_2O can diffuse through the material almost as readily as through a liquid. Such conditions typically correspond to glasses with a lower degree of polymerization, often characterized by a relatively low silica content and a higher concentration of alkali or alkaline-earth oxides, since the presence of larger elements, expanding the network, enables water to penetrate without its substantial disruption. Under these circumstances, ion exchange becomes the dominant mechanism of element release, superseding network hydrolysis. During Stage I, the alteration rate is then controlled by the inward diffusion of water, and incongruent release of network-modifying species proceeds at a rate faster than that of silicon, particularly under acidic conditions, due to rapid H^+/M^+ exchange [126,138].

In the context of glass-based fertilizers, the design objective is to tailor the glass structure so as to promote controlled penetration of water through appropriately sized structural voids, thereby enabling a gradual mobilization of nutrients encapsulated within the vitreous matrix. The size and distribution of these voids, which dictate the migration of water and hydrated species, are intrinsically linked to the chemical composition of the material and thus constitute a key factor in engineering its functional performance.

3.3.1.1 Fragmented network

The transport-related properties of silicate glasses, including their ability to release ions into the surrounding medium, are profoundly influenced by the local atomic arrangement and by the overall degree of network polymerization – both of which are primarily determined by chemical composition [144]. As outlined earlier, the incorporation of network-modifying oxides, particularly those containing alkali metals such as sodium or potassium, disrupts Si–O–Si linkages and gives rise to non-bridging oxygen atoms. These NBOs are charge-compensated by modifier cations, which become associated with the surrounding oxygen atoms, forming coordination polyhedra whose geometry reflects the ionic radius and field strength of the respective cation [145–147].

When the content of network-modifying oxides is sufficiently high, individual non-bridging oxygens may be simultaneously coordinated to multiple alkali ions. This results in the emergence of modifier-rich regions – often referred to as “channels” – within the glass network. These channels act as preferential, energetically favourable pathways for ion transport, enabling migration via a series of thermally activated, short-range hops between adjacent coordination polyhedra rather than through direct long-range diffusion. Because the local structure and energy landscape vary for sites associated with different

ionic species, ions preferentially occupy sites previously vacated by a species of the same type. Migration into a site associated with a different species requires a local rearrangement of the network, which introduces an additional energy barrier. This phenomenon underpins the well-documented mixed-alkali effect (MAE), a structural mechanism that has been exploited in glass design to reduce ionic mobility and suppress the rate of corrosion in certain silicate systems [145,148–150].

Nevertheless, it has been repeatedly demonstrated that the activation energies associated with ion release from reactive glasses are typically much lower than those predicted for conventional hopping mechanisms. This observation indicates that classical models of ion transport, developed primarily for highly polymerized, silica-rich glasses, cannot fully capture the dissolution dynamics of depolymerized, low-silica glasses used in ion release applications [147].

In these latter systems, the relationship between ion release and electrical conductivity is fundamentally altered. For example, in glasses with a low degree of connectivity, the diffusion coefficients inferred from leaching experiments may exceed those calculated from electrical conductivity by factors of 10^4–10^5. This striking discrepancy suggests that in depolymerized glasses, ionic transport mechanisms differ substantially from those operating in more compact networks [145,147,151–153].

These differences arise from the structural flexibility of open, fragmented silicate frameworks, which allow the network to undergo local distortions that transiently stabilize modifier ions in metastable interstitial positions. As a result, transport can proceed via interstitial mechanisms rather than being limited to vacancy-mediated hopping, which dominates in more rigid high-silica structures. In addition, the disrupted network structure of depolymerized glasses facilitates more rapid water ingress, which, in turn, promotes exchange reactions between modifier cations and protons (H^+, H_3O^+), accelerating dissolution and the mobilization of glass constituents [145,152,153].

The fundamental distinction between conventional silicate glasses and compositions intentionally designed for ion release lies in the degree of network fragmentation. While traditional glasses exhibit highly connected, crosslinked frameworks dominated by Q^3 and Q^4 units, reactive and bioactive compositions display a more open, chain-like structure in which Q^2 species predominate, with a smaller contribution from Q^3. This depolymerization is achieved through the incorporation of substantial quantities of alkali and alkaline-earth oxides, which break Si–O–Si bridges and generate additional non-bridging oxygens. The resulting increase in free volume and network flexibility facilitates the deeper penetration of water molecules and leads to markedly different alteration behaviour. These trends have been confirmed by ^{29}Si MAS-NMR analyses, which consistently show that bioactive and ion-releasing glasses contain a larger proportion of Q^2 units, in contrast to the more polymerized structures of conventional high-silica glasses. The structural openness of such depolymerized glasses also explains their sustained release behaviour: dynamic dissolution studies of bioactive compositions – originally developed for biomedical applications – demonstrate a continuous release of modifier ions from the bulk of the glass, in contrast to high-silica glasses, which show an initial burst release confined to the near-surface region, followed by negligible further leaching. Moreover, the enrichment of the glass surface with mobile modifiers increases hydrophilicity, enhancing water adsorption and facilitating ion-exchange processes that trigger dissolution. The strong affinity of these exposed ions (e.g., Na^+, Ca^{2+}) for water molecules initiates rapid H^+/M^+ exchange, while the abundance of non-bridging oxygens further promotes

water-glass interactions, as NBO sites are more reactive and hydrophilic than bridging oxygens [153–155].

In addition to the concentration of modifiers, the type of modifying cation exerts a profound influence on the dissolution behaviour of glasses. The electronegativity and field strength ($F = Z/a^2$) of alkali metals determine their bonding characteristics and mobility within the network: modifiers with high field strength, such as Li^+, form stronger bonds with oxygen, thereby reducing ion mobility and leaching, whereas those with lower field strength, such as K^+, are more weakly bound and more easily exchanged [144]. This principle is exemplified by modifications of the classical Hench 45S5 bioactive glass: full replacement of sodium by lithium leads to a more compact glass network, as the smaller ionic radius of Li^+ allows closer packing of SiO_4 tetrahedra, resulting in reduced ionic mobility. Conversely, substitution with potassium, which has a larger ionic radius, pushes the tetrahedra apart, creating a more open structure that enhances ion mobility and decreases the activation energy for K^+ self-diffusion. Thus, despite having similar overall network connectivity, these glasses exhibit markedly different dissolution and diffusion characteristics solely due to the nature of the modifier cations [144].

The incorporation of alkaline-earth network modifiers has also a marked influence on the degradation behaviour of silicate-based glasses. While these divalent cations, much like their monovalent counterparts, are susceptible to ion exchange with exogenous protonated species from the surrounding solution, their diffusion through the vitreous network is considerably slower – often by an order of magnitude – than that observed for monovalent modifiers [156]. Their comparatively higher field strength enhances electrostatic interactions with the surrounding non-bridging oxygens and with other migrating species, thereby impeding both their own mobility and that of other diffusing ions [151]. This strong electrostatic binding often results in the accumulation of alkaline-earth cations within the altered subsurface gel layer, further contributing to the retardation of ion transport [130]. Moreover, although the introduction of such modifiers disrupts Si–O–Si bridges and depolymerizes the network, their presence is frequently associated with improved chemical durability and enhanced stability. This is because divalent cations form stronger bonds with non-bridging oxygen sites compared to monovalent species, which reduces their tendency to be leached out, thereby enhancing resistance to aqueous attack [157,158].

A widely adopted strategy in the design of reactive glasses is the deliberate combination of two or more network-modifying oxides with the purpose of tuning dissolution behaviour and controlling the release rate of functional ions. On one hand, partial substitution of one alkali oxide for another with a different ionic radius alters the local packing of the silicate network—manifested in changes to the molar volume and oxygen density – without necessarily changing the overall network connectivity. The replacement of a large modifier cation by a smaller one (e.g., $K^+ \rightarrow Na^+$ or $Na^+ \rightarrow Li^+$) results in a more compact, tightly packed glass structure with reduced free volume, whereas substitution with a larger cation expands the network, increasing its openness. This variation strongly influences water ingress, the kinetics of ion exchange, and ultimately the rate of glass alteration. As a result, glasses enriched with potassium exhibit enhanced ion release due to their more open structure, while lithium-enriched glasses, characterized by higher structural compactness, display reduced mobility of modifiers and slower degradation. An analogous trend is seen among alkaline-earth elements: replacement of calcium (Ca^{2+}) by magnesium (Mg^{2+}) leads to greater compaction and lower solubility, while substitution

with strontium (Sr^{2+}) exerts a comparatively modest effect owing to the closer ionic size of Sr^{2+} to Ca^{2+} [144,159–161].

On the other hand, the simultaneous incorporation of two or more alkali or alkaline-earth species frequently leads to non-linear behaviour, characterized by reduced ion mobility and a significant slowdown in surface corrosion – a phenomenon widely recognized as the briefly mentioned above – mixed-alkali effect (or mixed-alkaline earth effect). This effect, well-documented in glass science, originates from the disruption of continuous ion migration pathways by the co-existence of chemically distinct modifier cations. As the energetic landscapes of adjacent modifier sites become mismatched, the efficiency of ion hopping decreases, thereby lowering ionic conductivity and diffusivity. The resulting slowdown in ion release is often accompanied by a diminished pH increase in the surrounding medium and, in many cases, an extension of the glass service life compared to single-alkali (alkaline-earth) compositions. In addition to improving durability, mixed-alkali systems are also advantageous from a processing standpoint, as the suppression of crystallization broadens the working temperature range, facilitating high-temperature forming [150,162].

However, the magnitude and even the presence of the mixed-alkali effect seems to depend strongly on the connectivity of the silicate framework: whereas in highly polymerized silicate glasses, where ion migration is dominated by vacancy hopping within narrow channels, the MAE is consistently expressed through a significant reduction in ion release, in depolymerized, open-framework glasses this effect becomes less pronounced. Such disrupted networks, characterized by abundant modifier cations and a large fraction of non-bridging oxygens, provide multiple pathways for ion migration that diminish the extent to which ion transport is disrupted by heterogeneity. Molecular dynamics simulations confirm that in such systems, divalent cations such as Ca^{2+} may occupy sodium-rich pathways, reducing the mobility of Na^{+}, but the impact is much less significant than in polymerized networks [145,162]. Furthermore, studies have demonstrated that the manifestation of the MAE also depends on the characteristics of the surrounding solution. Specifically, the effect becomes more pronounced under conditions dominated by ion exchange—typically at lower pH levels (<9), where alkali ion leaching is the principal corrosion mechanism. In contrast, under conditions favouring congruent network dissolution, the MAE is considerably less apparent. Under static corrosion environments, the coexistence of multiple alkali species has been shown to slow the rate of dealkalization and delay the onset of network breakdown, thereby enhancing the chemical durability of the glass [163].

It is also increasingly recognized that the spatial distribution of modifier cations – particularly in multicomponent silicate-phosphate glasses – plays a critical role in determining the energetics of bond breaking and the rates at which structural fragments are released [164].

Molecular dynamics simulations conducted by Tilocca and co-workers demonstrated that sodium and calcium exhibit preferential interactions with phosphate units rather than with silicate tetrahedra. At low phosphorus concentrations, both cations migrate toward phosphate sites, depleting the silicate network of modifiers. As the P_2O_5 content rises, this preference becomes more selective, with calcium ions showing a markedly stronger affinity for phosphate, leading to the formation of calcium-phosphate-rich domains. The more covalent Ca–O–P bonds are more resistant to hydrolysis than the more ionic Na–

O–P bonds, thereby reducing the dissolution rate of these domains under aqueous conditions [114,157,165].

Complementary NMR studies, examining the structural role of modifier cations within the silicate subnetwork of silicate-phosphate glasses, further revealed that calcium preferentially associates with non-bridging oxygens of Q^2 silicate units, while sodium remains linked to Q^3 units. This produces a heterogeneous network composed of relatively soluble Na–Q^3 domains and more durable Ca–Q^2 regions, with the solubility of the former modulated by the distribution of the latter [157]. Similar preferential coordination is observed in glasses containing both calcium and magnesium: Mg^{2+} tends to stabilize silicate-rich domains, while Ca^{2+} forms bonds with phosphate groups. As phosphate groups are more acidic and thus more susceptible to hydrolysis, Ca-rich phosphate regions dissolve more rapidly, releasing Ca^{2+} and phosphate ions, whereas Mg–Si linkages remain more resistant. This differential behaviour stems from structural differences between silicate and phosphate tetrahedra: while both are tetrahedrally coordinated, silicate units form four strong and directional, ionic-covalent Si–O bonds, whereas phosphate tetrahedra contain one shorter polar P=O bond and exhibit greater electron delocalization, enhancing their reactivity. Consequently, water preferentially attacks P–O–Ca linkages, accelerating the release of Ca^{2+} and phosphate relative to Mg^{2+} and silicate [166]. The pronounced preference of Ca to associate with orthophosphate domains may, in certain cases (as observed for higher silica, lower alkali glasses), lead to significant degree of Ca/P aggregation with the formation of Ca-rich phosphate regions, separated from the silica-based phase. This phenomenon has been shown to enhance the chemical durability of multicomponent silicate glasses by the virtue of immobilizing soluble species [164].

The preceding discussion underscores the complex interdependence of composition, structure, and chemical activity in multicomponent silicate-based glasses. The presence, type, and distribution of network modifiers govern the architecture, compactness, and connectivity of the glass network, thereby dictating the pathway by which water interacts with the surface and penetrates the bulk. Ultimately, the early stages of alteration – ion exchange, hydrolysis, and the formation of hydrated surface layers – are controlled as much by the elemental composition as by the resulting vitreous framework architecture. While silica content appears to be a primary determinant of durability (data compiled by Gin [126] indicate that glass durability generally increases with higher Si content, Tab. 3), it is clear that the interplay of multiple constituents introduces additional, non-linear effects that govern the initial dissolution rate (r_0) and the long-term behaviour of the glass in a corrosive environment.

Tab. 3. Glass composition and initial dissolution rate (r_0) of some common silicate glasses (based on [126].

Component / Parameter	**ISG**	**SON68**	**Albite glass**	**Basaltic glass**	**Obsidian**	**Roman glass**	**Soda-lime**	**Pyrex**	**Bioglass 45S5**	**E**
					Glass Composition in mol%					
SiO_2	60.1	52.7	75	61.6	83	72.4	72.9	81.0	46.1	57.0
B_2O_3	16.0	14.0	---	---	---	---	---	13.0	---	6.1

Al_2O_3	3.8	3.4	12.5	10.9	8.2	1.1	1.0	2.0	---	8.8
P_2O_5	---	---	---	0.1	---	---	---	---	2.6	---
Fe_2O_3	---	3.0	---	5.1	0.6	0.1	---	---	---	---
Na_2O	12.6	11.4	12.5	3.2	3.9	19.4	12.3	4.0	24.4	0.6
Li_2O	---	4.6	---	2.5	---	---	---	---	---	---
K_2O	---	---	---	---	2.9	---	---	---	---	---
CaO	5.7	5.0	---	14.6	1.0	5.4	7.2	---	26.9	19.6
MgO	---	---	---	---	0.3	---	6.6	---	---	6.5
BaO	---	0.3	---	---	---	---	---	---	---	---
SrO	---	0.2	---	---	---	---	---	---	---	---
ZrO_2	1.7	1.5	---	---	---	---	---	---	---	---
MoO_3	---	0.9	---	---	---	---	---	---	---	---
TiO_2	---	---	---	---	0.1	---	---	---	---	0.4
ΣRE_2O_3	---	0.9	---	---	---	---	---	---	---	---
Other	2.0	2.0	---	2.0	---	1.5	<1	---	---	<1
Initial dissolution rate r_0 in $g \cdot m^{-2} \cdot d^{-1}$ in the (T, pH) [b]										
T (°C)	90	90	90	90	157	90	87	90	37	90
pH	9	9	9	8.4	7[a]	9.5	9[a]	7[a]	7[a]	9
r_0	8.2	0.3	0.26	0.8	6×10^{-3}	5.9	7.7	0.5	45	4.6
Initial dissolution rate r_0,calc at 90°C, pH 9 from the measured value										
r_0,calc	8.2	0.3	0.26	1.4	2×10^{-3}	2.5	23	3	>8000	4.6

Footnotes:

- [a]pH at room temperature;
- $\sum RE_2O_3$ = sum of rare earth oxides;
- Uncertainty on r_0 is ~50% (except for Bioglass and Obsidian);
- r_0,calc determined using activation energy E_a = 60 kJ·mol^{-1} and η = –0.4 when needed;
- [b]conditions given in the [126].

In summary, the mechanisms underlying the early degradation of glass are fundamentally shaped by compositional choices that dictate structural packing and network fragmentation. These factors, in concert, determine whether alteration proceeds predominantly through interdiffusion and ion exchange or whether it transitions to a regime dominated by hydrolysis and network dissolution.

3.3.1.2 Hydrolysis

Simulation studies reveal that the variation in activation energies for the hydrolysis of different Q^n (Si) species is influenced not only by the accessibility of H_2O pathways –

shaped by the degree of network fragmentation – but also by the extent of inherent strain within the glass matrix [138,167].

In dry amorphous silica (a-SiO_2) surface can be populated with four types of Si sites classified according to their number of bridging oxygen atoms: Q^1, Q^2, Q^3, and Q^4, characterised by the presence of between one and four Si–O–Si bridges (siloxanes). Dissolution progresses through the sequential depolymerization of these sites, eventually liberating silicic acid ($Si(OH)_4$) into solution and producing an isolated Q^0 site in solution. Each step of this process corresponds to the rupture of a Si–O–Si bridge, accompanied by a progressive reduction in connectivity from Q^4 to Q^0. Although it is often assumed that sites with a lower number of bridging oxygens (e.g., Q^1) are more reactive due to their weaker network constraints, simulation data obtained using the potential of mean force (PMF) method indicate that the rate-limiting transformations are in fact the $Q^3 \rightarrow Q^2$ and $Q^2 \rightarrow Q^0$ transitions, both of which exhibit activation energies of approximately 58.6 kJ·mol^{-1}. Surprisingly, the conversion of a Q^4 unit to a Q^3 site displays a lower average energy barrier (~44.8 kJ·mol^{-1}) than even the final $Q^1 \rightarrow Q^0$ step (~52.7 kJ·mol^{-1}) [138,167].

Hydrolysis of a Si–O–Si bond proceeds via nucleophilic attack, predominantly by hydroxyl ions (OH^-), and involves the formation of a transient, fivefold-coordinated transition state in which the silicon atom adopts a trigonal bipyramidal configuration [138,167]:

$$Si - O - \underset{OH}{\overset{OH}{Si}} - OH + OH^- \rightarrow Si - O - \underset{OHOH}{\overset{OH}{Si}} - OH \rightarrow Si - O^- + Si(OH)_4 \qquad \text{Eq. (6)}$$

The creation of this activated complex requires substantial bond-angle distortions. In the tetrahedrally coordinated environment typical of silicate networks, the O–Si–O angles are close to 109°. To form the pentacoordinated intermediate, these angles must rearrange: the in-plane angles widen toward 120°, whereas the angle between the bridging oxygen and the Si–O plane contracts to approximately 90°. Such angular deformations introduce strain, representing an energetic barrier to the reaction.

Although one might expect that highly polymerized regions dominated by Q^4 units would present the greatest resistance to bond cleavage due to their dense, tightly interconnected structure, these fully connected units often harbor significant pre-existing angular strain. This intrinsic distortion lowers the additional energy required for rearrangement and can therefore make Q^4 siloxane bonds unexpectedly vulnerable to hydrolytic attack. In contrast, Q^1 species, which contain a single bridging oxygen and three terminal silanol groups, offer a much more flexible local environment. When a water molecule attacks these sites, only minimal structural adjustments are needed to form the transition state, and as a result, the activation energy for hydrolysis in these regions is relatively low [167].

In the context of glass fertilizers, which primarily interact with acidic (or mildly mildly) environments such as those created by root exudates, network hydrolysis is not expected to dominate the overall alteration process. Under these conditions, the primary mechanism involves proton-driven interdiffusion, whereby modifier cations are replaced by exogenous H^+ or H_3O^+ species. Nevertheless, soil is a dynamic and heterogeneous medium, and there are conditions – particularly during prolonged dry periods – when the local environment around the glass may become progressively alkaline. The limited water content in such scenarios causes the thin liquid film on the glass surface to become rapidly depleted in protons, resulting in a local pH increase and the subsequent predominance of

OH^--mediated hydrolysis. In these cases, the rates of network dissolution are strongly influenced by both the nature and spatial distribution of Q^n structural species within the glass matrix [138].

It is important to emphasize, however, that in consistently acidic environments, hydrolysis plays only a minor role. In such conditions, the activation energy for glass alteration decreases with falling pH, reflecting the dominance of ion-exchange processes By contrast, the activation energy tends to remain nearly constant at less acidic to alkaline pH, suggesting that a change from dissolution through hydrolysis to ion exchange occurs at low pH [141].

3.3.1.3 Interdiffusion

Selective leaching of alkali and alkaline earth cations from the glass matrix, a process central to its early-stage alteration, depends not only on the chemistry of the contacting solution but also on the density and accessibility of ion-exchange sites exposed at the glass surface or formed within the near-surface structure as corrosion progresses. Extensive studies on pure silica, bioactive, and borosilicate glasses have consistently shown that water molecules exhibit a markedly stronger affinity for modifier cations and for non-bridging oxygen atoms than for the more stable Si–O–Si linkages. Upon adsorption and dissociation of water, these preferred sites are rapidly protonated, resulting in the formation of M–OH and NBO–H groups, where M denotes a mobile network-modifying cation such as K^+, Na^+, Ca^{2+}, or Mg^{2+} [126,138].

Given that non-bridging oxygen sites are the primary loci for ion-exchange reactions, as the concentration of network modifiers increases, the number of NBO sites rises, and with them the overall susceptibility of the glass to ion exchange. This facilitates deeper penetration of water into the glass, as alkali or alkaline earth cations are removed from their coordination environments and replaced by water molecules, which then propagate into the bulk. This coupled process of ion exchange and water ingress ultimately accelerates the formation of hydrated, silanol-rich layers that mark the onset of further alteration [138].

The quantity of non-bridging oxygen atoms is therefore a critical structural parameter influencing glass dissolution rates. For a given type of network modifier, glasses richer in NBOs invariably show faster reaction kinetics with aqueous environments. However, glasses containing the same overall modifier fraction but different types of cations (e.g., Na^+ versus K^+) exhibit markedly distinct reactivities. This behaviour can be rationalized in terms of both structural packing effects and the chemical nature of the M–O bond. In general, the lower the field strength of the modifier cation, the more reactive the glass: for instance, lithium silicate glass ($30Li_2O{\cdot}70SiO_2$) reacts with water at 60 °C approximately twenty times more slowly than its sodium analogue ($30Na_2O{\cdot}70SiO_2$), whereas potassium-rich glass ($K_2O{\cdot}3SiO_2$) is roughly six times more reactive than the corresponding sodium composition [138].

Besides the already mentioned network expansion effect related to the replacement of a smaller ion, such as sodium (ionic radius ~102 pm), with a larger one, such as potassium (138 pm) which reduces packing density and facilitates faster ion migration, the type of modifier dictates the character of the M–O bond. While lithium–oxygen bonds are more covalent and hence more resistant to hydrolysis, sodium–oxygen and then potassium–oxygen bonds display higher degree of ionicity, thus are more easily cleaved during aqueous attack. This trend directly correlates with the rate of cation release into solution [138,162]. Notably, the same relationship applies to alkaline earth network modifiers,

where the rate of cation leaching decreases with increasing ionic charge and field strength [127].

3.3.2 Stage II and Stage III

As outlined in the preceding sections, following the initial phase of rapid release of glass constituents – whose nature and intensity depend strongly on both the chemical composition and structure of the glass as well as on environmental parameters, particularly the pH of the contacting solution – the overall dissolution rate decreases dramatically and enters a so-called residual regime (Stage II) with the dissolution rate typically several orders of magnitude lower than the initial rate [168]. Whereas the influence of composition on the early, high-rate stage of corrosion has been thoroughly studied, its impact on the kinetics and mechanisms at advanced stages of alteration remains less extensively explored.

The general consensus is that the observed deceleration in dissolution is governed by two key phenomena. The first is a thermodynamic effect, often referred to as chemical affinity, arising from the progressive reduction in the difference between the chemical potential of the solid and that of the solution as the latter becomes enriched with dissolved species. The second mechanism involves the progressive development of a hydrated alteration layer (commonly called a gel), which gradually acts as a diffusion barrier to the transport of reactive species. Several models have been proposed to describe the origin of this passivating layer. At one extreme, the dissolution–reprecipitation model postulates that the glass dissolves congruently within a thin film of interfacial water and that the gel forms via precipitation of sparingly soluble species. At the other end of the spectrum, the leaching model regards the gel as a residual, restructured skeleton of the parent glass left behind after selective removal of weakly bonded constituents (such as alkalis and boron). An intermediate approach, frequently termed the hydrolysis–condensation model, suggests that preferential hydrolysis of less strongly bonded network species is followed by in situ condensation of partially depolymerized silica, producing a progressively densified, hydrated network. In practice, these mechanisms are not mutually exclusive: modern studies suggest that the relative importance of these processes depends on the glass composition, environmental conditions, and the extent of alteration, while the gel undergoes a time-dependent reorganization that typically reduces its porosity and enhances its protective capability [169]. In the absence of a dense, passivating alteration layer, or when a non-protective (porous) gel is formed, the dissolution continues at the relatively high initial rate (Stage I). Conversely, when conditions favour gel consolidation, the growth of this interfacial layer limits mass transfer between the glass and the surrounding medium, resulting in a stable, low residual rate. While dissolution at Stage I often proceeds congruently, Stage II is marked by incongruent dissolution because silicon and certain other species (notably Al, Zr, and Ca) are retained within the hydrated layer, leading to the development of a silica-rich gel [126,168,169].

The degree to which the gel impedes further corrosion depends strongly on the initial glass composition. High silica content is particularly beneficial, as the retention of silicon within the altered layer (quantified by the retention factor f_{Si}) is considered one of the key parameters controlling its passivating capacity [170]. Additionally, Al and Zr, which exhibit low solubility, tend to be immobilized within this layer, producing a dense, mixed Si–Al–Zr hydrated film that significantly hinders further glass dissolution [131,170]. Interestingly, calcium – typically a network modifier that accelerates glass degradation

when incorporated in significant amounts – can also accumulate within this layer when Ca^{2+} ions are present in the contacting solution. Under such conditions, calcium participates in the co-precipitation of a calcium–silicate-rich gel with pronounced passivating properties. This effect is most evident in confined, near-saturation environments with pH around 9, where the presence of calcium in solution has been shown to suppress alteration rates substantially [171,172].

Charge-compensating-requiring species incorporated into the gel also play a significant role in its evolution. For example, when $[AlO_4]^-$ species are present, they can attract alkali cations according to a preferential order of $K > Cs > Na \gg Li$, as demonstrated by Collin et al. [173] This selective affinity has been explained in terms of a balance between the strength of hydration of the cation and its electrostatic attraction to the negatively charged species in the gel. Less strongly hydrated ions such as K^+ and Cs^+ exhibit a greater propensity to occupy these sites, whereas strongly hydrated ions (e.g., Li^+) remain preferentially bound to their hydration shells [173]. Also, aluminium itself alters gel properties – its presence strengthens the passivating effect of the gel through its ability to reinforce Si–O bonds, making them more resistant to hydrolysis and thereby enhancing the chemical durability of glass [174].

Studies also show that over time, the gel layer undergoes a progressive structural reorganization that drives it toward a state of lower free energy, marked by a more polymerized silica framework and reduced porosity. Experiments have shown that glasses with initially high contents of network modifiers (i.e., more depolymerized structures) tend to produce gels that become more polymerized over time, because the enhanced leaching of modifiers generates abundant silanol groups that facilitate condensation [131,175,176]. Importantly though, this specific layer not necessarily has to display protective properties. Indeed, the densified and matured gel may act as a molecular sieve, allowing the passage of water only through small pores, which eventually become closed. However, when the gel is immature, with a high density of open pores larger than the size of a water molecule, water can diffuse relatively freely, and the layer offers little protection [175].

Notably, the altered layer also serves as a template for the precipitation of secondary crystalline phases, as the gel surface, rich in reactive silanol groups (Si–OH), provides energetically favourable sites for heterogeneous nucleation (Fig. 15).

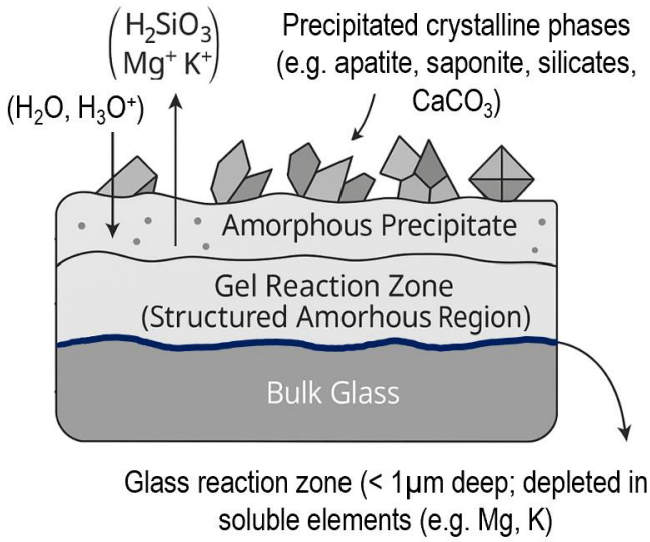


Fig. 15. Reaction zones in silicate glass in contact with aggressive solution; based on the [177].

The alteration layers that develop in the subsurface regions of glasses exposed to corrosive environments are predominantly amorphous and therefore thermodynamically unstable. Therefore, not only they, over time, undergo progressive reorganization and densification, which involves a gradual transformation toward more polymerized Q^4-type silicate units, but also, may ultimately serve as precursors for crystalline phases, as has been observed in naturally weathered glasses [130,176].

The precipitation of secondary crystalline phases is particularly significant because it is often linked to a renewed increase in the glass alteration rate. As already indicated, this acceleration occurs when crystallization proceeds at the expense of the hydrated gel, thereby compromising its passivating function, or when the nucleation of these phases modifies the chemical composition of the solution, reducing the concentration of dissolved species and increasing the driving force for further dissolution. In such circumstances, the alteration process enters Stage III of glass corrosion. The mechanism most frequently invoked to explain this phenomenon involves the nucleation and growth of secondary products that consume network-forming elements (notably Si and P) from either the alteration layer or the surrounding solution, thus sustaining the breakdown of the glass [130].

While spontaneous, homogeneous precipitation of secondary phases on a glass surface can occur under conditions of strong supersaturation, the hydrated silicate layer that forms during Stage II generally provides a far more favourable substrate for heterogeneous nucleation, even at low supersaturation levels. This behaviour arises from the high concentration of reactive silanol groups (Si–OH) present at the altered surface as a result of ion exchange between network-modifying cations and protons in the contacting medium. Hydrolysis further enhances this surface reactivity by breaking Si–O–Si bonds according to the reaction: $Si–O–Si+H_2O \rightarrow 2Si–OH$, increasing the population of nucleation sites. The subsequent deprotonation of these silanol groups ($Si–OH \rightarrow SiO^- + H^+$) generates negatively charged surface species that readily complex with multivalent cations from the solution. These complexes ($[SiO^- \cdots M^{2+}]^+$) attract anions, such as phosphates, which assemble into stable clusters that grow into crystalline nuclei [178,179]:

$$H_2O + PO_4^{3-} \leftrightarrow HPO_4^{2-} + OH^- \equiv SiO^- \cdots Ca^{2+} + HPO_4^{2-} \rightarrow \equiv SiO^- \cdots Ca^{2+} \cdots HPO_4^{2-} \quad \text{Eq. (7)}$$

This mechanism has been extensively described for the precipitation of apatite on the surface of bioactive glasses and, given the similar chemical composition, is highly relevant for glass fertilizers, whose surfaces are frequently found to be populated with phosphate-rich secondary phases [95].

The types of secondary phases that ultimately crystallize are strongly influenced by the original glass composition. For instance, alteration of multicomponent borosilicate glasses, such as those used in nuclear waste immobilization, often yields smectite-type clay minerals, calcium–silicate–hydrate (C–S–H) phases, rare-earth phosphates, and zeolites, whereas the surfaces of bioactive glasses are typically covered by calcium hydroxycarbonate apatite [178,180,181]. However, this crystallization process is also profoundly controlled by the characteristics of the solution, including its ionic composition, pH, temperature, and the ratio of exposed glass surface area to the volume of solution (S/V). Notably, most of the secondary phases commonly reported on altered silicate glasses precipitate preferentially under alkaline conditions. Therefore, glasses rich in alkali and alkaline-earth components – whose release elevates the pH of the contacting medium – tend to crystallize such phases more readily than low-alkali compositions. This effect is particularly pronounced under confined conditions, where a high S/V ratio results in the rapid accumulation of leached cations and a localized rise in pH. a well-documented example involves calcium-bearing glasses subjected to atmospheric alteration, on which a calcite crust invariably develops. This behaviour illustrates the strong role of environmental species (e.g., atmospheric carbonates) in governing the formation of secondary phases [126,130,182].

Archaeological glass artifacts also bear testimony to this complex interplay between glass composition and environmental exposure. For example, Franceschin et al. [183] showed that Fe-rich glasses buried in soil undergo long-term alteration processes that promote the precipitation of Fe-based secondary phases at the glass–water interface, facilitated by the simultaneous availability of Fe ions from both the glass and the surrounding soil. Similarly, studies of Mg- and Al-rich aluminoborosilicate glasses demonstrated that Mg-smectites form under a range of conditions (pH > 9), but their structure differs: unsaturated conditions tend to yield dioctahedral smectites, whereas saturated high-S/V conditions favour the formation of trioctahedral varieties enriched in Al and Mg [181].

In the specific case of glass fertilizers, the secondary phases precipitating at the glass–solution interface are expected to act as temporary reservoirs for the nutrients released from the glass, once the solubility limit of those elements has been reached. Previous studies suggest that these phases will predominantly consist of phosphates, which is consistent with the low to moderate P_2O_5 content (typically < 10 mol %) incorporated into the compositions designed at AGH [95,184,185]. Under such conditions, phosphorus is largely present as easily mobilizable orthophosphate units, which can rapidly participate in precipitation processes. Over time, the crystallization of these transient phases is anticipated to slow further release, creating a reservoir of nutrients that remains available until mobilized once again by the acidic exudates of plant roots. It is therefore essential for the development of such glass fertilizers that the secondary phases formed on their surfaces remain soluble under acidic conditions; this ensures that the temporarily immobilized nutrients can be re-dissolved on plant demand. Consequently, careful selection of

glass composition and systematic evaluation of phase stability in soil environments are indispensable steps in the design and optimization of glass-based fertilizers.

Given the above considerations regarding glass behaviour in aqueous environments, Fig. 16 schematically represents the expected alteration kinetics of a vitreous carrier of plant nutrients subjected to intermittent exposure to acidic root exudates, in comparison with a conventional silicate glass.

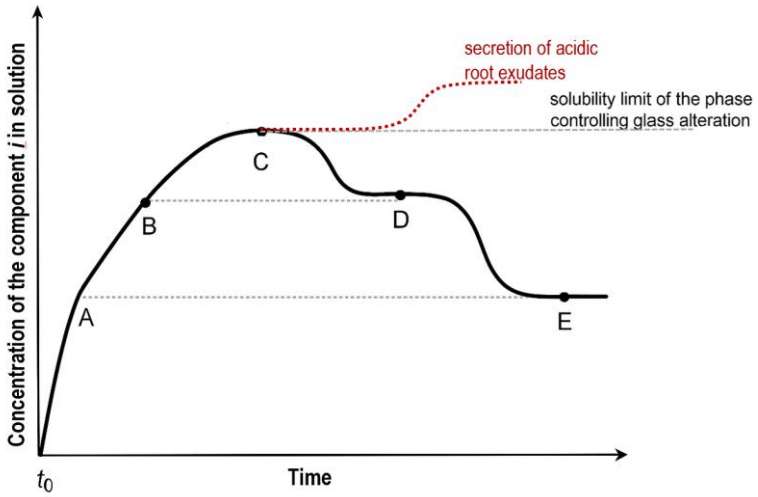


Fig. 16. Conceptual model illustrating the kinetics of alteration of glass fertilizers under root exudate activity compared with conventional silicate glass.

At time t_0, the soil solution in contact with the glass fertilizer is undersaturated with respect to component *i*. This leads to a high initial dissolution rate (steep slope between points a and B in Fig. 16), as described by Equation 7 [168]:

$$r = \frac{1}{v_i}\frac{dm_i}{dt} = \frac{1}{v_i} V \frac{dC_i}{dt} = k_0 \cdot [H^+]^{\eta} \cdot \exp\left(\frac{-E_a}{RT}\right) \cdot \left(1 - \frac{Q}{K}\right) \qquad \text{Eq. (8)}$$

where ν_i is the mole fraction of species *i* in the glass, , m_i its mass released to the solution, C_i the molar concentration of *i* in solution, V the solution volume, k_0 the intrinsic rate constant, η the reaction order with respect to $[H^+]$, E_a the activation energy, R the gas constant, T the temperature, and Q and K the ion activity product and solubility product, respectively.

As dissolution progresses, the concentration of *i* in the solution rises, and when the system approaches its solubility limit, the driving force for further dissolution diminishes (the affinity term $(1 - Q/K)$ tends toward zero). Consequently, the alteration rate decreases significantly, approaching a low residual value (transition from B to C). At point C, a metastable secondary phase begins to precipitate, incorporating element *i* and buffering its concentration in the solution. a dynamic equilibrium is established between glass dissolution and the precipitation of this phase.

In purely abiotic systems, this equilibrium evolves over time through the successive precipitation of increasingly stable mineral phases, in accordance with Ostwald's law. Each newly formed phase is less soluble and more stable than the previous one, so the overall concentration of *i* gradually declines as the system slowly approaches equilibrium with the most stable phase. During this process, glass alteration often involves substantial

supersaturation with respect to various minerals (e.g., quartz, zeolites, feldspars), which appear in sequence as the free energy of the system decreases stepwise.

In the rhizosphere, however, this equilibrium is repeatedly disrupted by root and microbial exudates. These exudates acidify the microenvironment and can chelate or solubilize *i* from the metastable precipitates, remobilizing it into the soil solution. The resulting local undersaturation, compounded by continuous plant uptake, triggers renewed glass dissolution (red dotted line in the Fig. 16), with rates approaching those characteristic of Stage I (not represented in the Fig. 16, demonstrating the conceptual model of glass fertilizer alteration). This cyclical behaviour – precipitation, remobilization, nutrient uptake, and renewed dissolution – can repeat multiple times, maintaining nutrient availability over an extended period.

Unlike the prognosed decline in C_i observed in abiotic systems as the solution moves toward equilibrium, in biologically active soils the concentration of element *i* is expected to oscillate between values defined by points D and C, adopting intermediate values, controlled by the interplay of glass dissolution kinetics, the stability of secondary phases, the intensity of root exudate activity, and nutrient uptake by plants. Over longer timescales, the progressive formation of more stable phases (e.g., crystalline apatite-type phosphates or feldspars) may reduce nutrient release. Nevertheless, as long as these phases remain at least partially soluble under acidic conditions, rhizosphere processes will periodically remobilize nutrients, ensuring sustained fertilizing action of the glass.

It must be emphasized that this conceptual model simplifies the much more complex conditions in real soils, where fluctuating moisture content, microbial colonization, redox gradients, and organic ligands significantly influence the pace and mechanism of glass alteration. Despite these complexities, one factor remains under human control: the glass composition and structure. As dictated by the well-established composition–structure–property relationships, these parameters govern the fundamental mechanisms of glass corrosion, thereby enabling the design of materials with tailored dissolution behaviour to match plant nutrient requirements. Accordingly, the following section presents the most commonly incorporated components of glass fertilizers and outlines their respective roles within the vitreous matrix.

3.3.3 Role of network formers in modulating glass alteration

Network formers constitute the fundamental structural backbone of vitreous materials and decisively govern both their chemical durability and their ability to release ions into the surrounding medium. In glass fertilizers, the most common network-forming oxide is silica (SiO_2), which imparts a mineralogical resemblance to natural soil constituents and volcanic glasses occurring in fertile volcanic soils. The proportion of this oxide is of primary importance, as it determines the future kinetics of ion liberation into the soil solution.

3.3.3.1 SiO_2

The silica content exerts a decisive influence on glass durability by directly controlling the network topology, which in turn governs dissolution rates. An increasing number of topological constraints per atom—radial bond-stretching and angular bond-bending that stabilize interatomic distances and angles—reduces dissolution kinetics, since the enhanced local stiffness raises the activation energy for hydrolytic bond cleavage or, under acidic conditions, for ion exchange between modifiers and protons. Thus, the leaching behaviour of network-forming elements is dictated by the rigidity of the skeletal

framework, with rupture energy per constraint largely determined by the identity and concentration of formers [186].

a higher abundance of Si–O–Si linkages increases network rigidity and atomic packing, reducing the free volume accessible to diffusing water molecules and thereby limiting the transport of mobile species. While silica variation scarcely alters short-range order (bond lengths, coordination numbers), it strongly affects medium-range structure, i.e., the distribution of Q^n units and network connectivity [187]. For instance, raising the silica content from 45 to 65 mol.% shifts the dominant silicon species from Q^2 to Q^3, and increases connectivity from ~1.9 to 2.8, transforming chain-like networks that admit facile water ingress into highly cross-linked frameworks resistant to dissolution [187].

Beyond structural compactness, silica also modulates dynamic properties, particularly ionic mobility. The initial dissolution stage – exchange of modifier cations with protons or hydronium ions – is diffusion-controlled, with alkalis being most mobile. With increasing SiO_2, the diffusion coefficients of modifiers, especially monovalent species, decline systematically, consistent with the lower chemical reactivity of silica-rich glasses. This trend follows the Arrhenius relation [187]:

$$D = D_0 \cdot e^{-E_a/RT} \qquad \text{Eq. (9)}$$

where D represent the diffusion coefficient, D_0 pre-exponential factor, E_a activation energy, T temperature and R gas constant.

Notably, E_a for ion migration changes only marginally (about 6% between 45% and 65% SiO_2), suggesting that slower diffusion arises not from higher energy barriers but from a decrease in D_0. Since D_0 reflects configurational entropy, its decline indicates that highly polymerized, rigid networks offer fewer energetically favourable migration pathways, while less polymerized systems provide greater disorder and hence enhanced ion mobility [186,187].

Although silica is the principal determinant of durability and leaching, secondary network formers are deliberately introduced to impart additional functionality. In Hench-type bioactive glasses, P_2O_5 promotes hydroxyapatite formation, enabling bonding with bone tissue [188]. Analogously, in nutrient-releasing fertilizers, phosphorus favours the precipitation of orthophosphate-based secondary phases enriched in modifiers, which temporarily immobilize macro- and micronutrients and regulate their gradual release. Furthermore, P_2O_5 is widely recognized for its beneficial effect on lowering the melting temperature of glass, a feature of particular significance when considering the industrial-scale production of these materials [189].

3.3.3.2 P_2O_5

The incorporation of additional network-forming species such as B_2O_3, Al_2O_3 or P_2O_5 into a silicate-based glass matrix induces profound modifications within the vitreous structure, which, in turn, exert a direct influence on the chemical durability of the resulting material [141]. Network connectivity may thus be adjusted not only by altering the proportion of the primary network former (e.g., SiO_2) or by varying the type and concentration of alkali and alkaline earth modifiers, but also by deliberately introducing a secondary network former – a strategy that has been showed to translate into the changes in the degree of network polymerization [114].

When P_2O_5 partially substitutes for silica at a fixed level of modifiers, an often counterintuitive increase in silicate polymerization is observed, despite the lower intrinsic

connectivity of phosphate tetrahedra. At P_2O_5 levels typically below 10 mol% and in glasses with less than 50 mol% SiO_2, phosphate species appear mainly as orthophosphate (Q^0) or pyrophosphate (Q^1) units, each containing a high proportion of non-bridging oxygens. These units attract modifier cations, forming local coordination shells and thereby depleting the silicate subnetwork of modifiers; as a result, silicate tetrahedra form additional Si–O–Si linkages, which enhances polymerization and shifts Q-species from Q^1/Q^2 toward Q^3/Q^4 [114,188]. This reorganization improves the durability of the silicate framework, while the simultaneous presence of isolated phosphate units facilitates ion release, creating a dual effect highly relevant for both bioactive and fertilizer glasses. However, if a fraction of phosphorus is incorporated into the network as Si–O–P bonds – a matter still debated – orthophosphate mobility is reduced, leading to slower release [114,152].

The role of P_2O_5 therefore depends strongly on its speciation. Orthophosphate (Q^0(P)) units enhance leachability and controlled nutrient delivery [188], whereas more connected species such as Q^2(P) or Q^3(P) form a distinct phosphate subnetwork that strengthens chemical resistance and reduces ion release [189,190]. At higher P_2O_5 contents, nanoscale phase separation can occur, yielding silica-rich and phosphorus-rich domains enriched in modifiers, particularly in Ca-containing systems, where strong Ca–P affinity promotes CaP clustering. In Hench-type glasses, such clustering appears above ~12 mol% P_2O_5, while at lower concentrations, domains remain too small to alter structure significantly. With increasing phosphorus content, however, these regions expand and promote modifier-rich clustering and, under heat treatment, crystallization of phosphate phases [152,188]. The resulting inhomogeneities decrease overall reactivity by restricting species mobility, making P_2O_5 content a critical compositional variable requiring careful optimization [164,188].

When present as orthophosphate, phosphorus exhibits higher reactivity than silicate groups owing to the localized negative charge on terminal P–O^- bonds, which increases the Lewis basicity of oxygen and renders these units more susceptible to hydration and hydrolysis (Fig. 17). Less electronegative cations further intensify this effect by conferring greater negative charge on their associated oxygens, thereby promoting water coordination and accelerating ion release. Thus, despite the stronger intrinsic P–O bond polarization, phosphate groups – especially Q^0 – are generally more hydrolytically labile than Si–O–Si linkages [156,165,191].

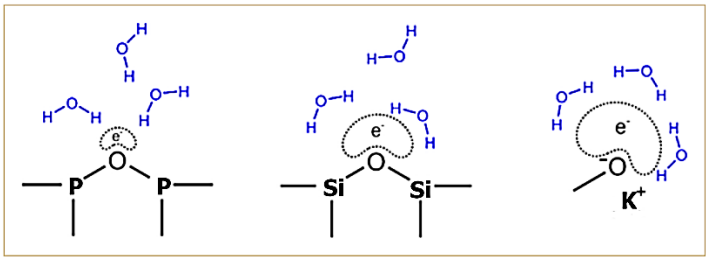


Fig. 17. Dependence of water coordination on the electronegativity of the associated cations. Less electronegative cations (towards the right) increase the Lewis basicity of oxygen, promoting hydration. Based on [156,191].

In addition, phosphate incorporation enhances glass hydrophilicity, facilitating water adsorption and surface interactions [192,193]. According to Rodrigues et al. [194], the extent of water uptake is governed by porosity and hygroscopicity, which control penetration into the surface layer, hydrolysis of P–O–M linkages, and migration of modifier cations. The amount of water absorbed at early stages strongly influences subsequent

alteration: greater hydration accelerates network hydrolysis, promotes cation release, enlarges porosity, and increases silanol content. These silanol groups, being strongly hydrophilic, further enhance water adsorption, establishing a self-reinforcing feedback loop that sustains long-term glass degradation.

3.3.4 Role of network modifiers in modulating glass alteration

A well-established strategy for tailoring glass structure – and thereby its susceptibility to alteration in aqueous or biological environments – is the deliberate adjustment of network modifiers, whose incorporation disrupts the continuity of the framework by converting bridging oxygens, which connect silicate or phosphate tetrahedra through strong iono-covalent bonds, into non-bridging oxygens. This transformation produces Si(P)–O–M linkages, where M denotes a monovalent (M^+) or divalent (M^{2+}) cation, and the progressive introduction of such oxides inevitably lowers network connectivity, reduces structural coherence, and enhances dissolution susceptibility [165,191]. Since Si–O–M bonds undergo hydrolysis at considerably lower energies than Si–O–Si bonds of predominantly covalent character, water penetrating the glass preferentially attacks modifier-rich regions, inducing bond cleavage and gradual network fragmentation [156]. As illustrated in Fig. 17, the propensity of oxygen atoms to undergo hydration largely reflects the electronegativity of the bonded cation: highly electronegative formers such as Si or P withdraw electron density, thereby reducing the basicity and hydration tendency of the associated oxygen atoms, whereas bonds with more ionic character, e.g. O–K, confer greater negative charge and thus stronger Lewis basicity, promoting water coordination and accelerating hydrolysis [156,165,191].

Accordingly, the degradation rate of glassy fertilizers can be deliberately tuned by controlling both the concentration and type of network-modifying oxides, as these parameters strongly affect network topology, rigidity, and chemical resilience [195]. Systematic studies on SSL glasses, for instance, revealed that alkali contents above ~20 wt% combined with ≤ 4 wt% alkaline-earth oxides induce severe surface deterioration, establishing this threshold as the approximate boundary between stable and unstable compositions, since beyond it the silicate network becomes sufficiently depolymerized to allow rapid migration of highly mobile alkali cations. By contrast, moderate increases in the CaO/SiO_2 ratio initially enhance structural stability through additional cross-linking, yet once the CaO content exceeds ~15 wt% the network rapidly destabilizes and the glass undergoes accelerated alteration [119].

It must be stressed, however, that the effect of modifiers is governed not only by concentration but also by the intrinsic chemical nature of the cation – its valence, field strength, and coordination tendencies – which may decisively influence the mechanisms and kinetics of glass–solution interactions, in some cases surpassing compositional effects alone.

3.3.4.1 K_2O

Monovalent network modifiers are generally the first constituents released into solution, a consequence of their low cation field strength and weaker interaction with the glass backbone compared to multivalent cations. Their removal is further promoted by the strong preference of protons or hydronium ions to exchange with monovalent species rather than with divalent ones [156]. The preferential leaching of such modifiers, particularly under acidic conditions [141], generates vacancies subsequently filled by water molecules, thereby advancing the alteration front into the bulk. Since monovalent cations

are characterized by relatively large ionic radii, these voids facilitate deeper water ingress; hence, the presence of potassium – with its larger radius compared to sodium (138 ppm vs. 102 ppm) – enhances the alteration process [156]. This effect is evident in the more pronounced leaching of alkali and alkaline-earth elements from K-rich glasses relative to Na-rich ones [196], confirming that dissolution behaviour is strongly dependent on the type of monovalent modifier employed. Numerous studies further indicate that the reactivity of glass fertilizers systematically increases with higher K_2O contents [110,184] – a trend mirrored by historical observations: medieval Si–K–Ca stained glasses display greater fragility and susceptibility to weathering than conventional silica–soda–lime materials [119].

Beyond facilitating water penetration into a more open and less rigid network, K^+ ions also induce more significant shifts in the pH of contacting solutions during immersion tests [197]. When the pH surpasses the critical threshold of ~9, silicate glasses become markedly unstable, leading to accelerated dissolution, especially in systems with high surface-area-to-volume ratios. Moreover, the structural response of K-rich glasses to ion exchange is distinctive: substitution of large K^+ by much smaller H^+ ions produces strong local compression, unlike in networks containing smaller monovalent cations such as Li^+. Under environmental conditions of alternating wetting and drying, such stress accumulation often results in surface cracking or even partial exfoliation of the altered layers [119].

3.3.4.2 CaO and MgO

While divalent modifiers share with monovalent ones the tendency to accelerate the early stages of dissolution, their role in the vitreous network is far more complex [171]. The general correlation between ionic radius, field strength, and dissolution behaviour remains valid: the lower the field strength, the higher the initial release rate [186,195]. Thus, Ca^{2+} ions, forming stronger bonds with non-bridging oxygens, are released more slowly than monovalent cations such as K^+, and within the alkaline-earth series, Mg^{2+} is typically less mobile than Ca^{2+} owing to its smaller radius, higher field strength, and the more covalent character of Mg–O bonds [165,186,198].

The comparatively low reactivity of divalent species arises both from the less ionic nature of their bonds relative to M^+–O linkages and from their much slower diffusion [165,191]. Migration of modifiers to the surface is a prerequisite for alteration, yet Ca^{2+} is hindered by its rigid pseudo-octahedral coordination with non-bridging oxygens, unlike the more flexible Na^+ environment that allows migration across multiple sites. Even in highly depolymerized matrices, Ca^{2+} retains these restrictions, thereby reducing ion mobility and water ingress, as shown in both experimental studies and molecular dynamics simulations [126,199].

Magnesium, in contrast, does not impose such blocking effects [186], reflecting its more variable coordination behaviour: it can adopt four-, five-, or six-fold environments, with its structural role strongly dependent on the accompanying cations – in potassium-rich systems Mg^{2+} tends toward tetrahedral sites, whereas in Ca-rich ones octahedral coordination dominates, highlighting its borderline character between a classical modifier and an intermediate oxide [116].

Indeed, in MgO-rich and disrupted silicate networks, part of the Mg^{2+} population enters the structure as $[MgO_4]^{2-}$ units, promoting network repolymerization by shifting the Q-distribution from Q^2 to Q^3 species. This dual role – network depolymerizer on one hand and partial former on the other – enhances durability and reduces diffusivity, since the

more covalent Mg–O bonds stabilize the framework compared with the more ionic Ca–O linkages [200–203].

At higher modifier concentrations, however, clustering of non-bridging oxygens around divalent cations can induce phase separation, a process thermodynamically rooted in the positive heats of mixing between SiO_2 and modifiers and microscopically linked to local charge-balanced domains [204–206]. Such effects are particularly marked in CaO–P_2O_5 glasses, where calcium–phosphate-rich clusters lower ion mobility and diminish reactivity [188], and in MgO-bearing systems, where similar clustering around Q^0(Si) units has been reported in aluminosilicate matrices [204,206].

Even without macroscopic demixing, divalent cations shape medium-range order and thereby chemical activity. Increasing MgO content, for instance, promotes a transition from cristobalite-like toward forsterite-like domains (Q^0(Si)), enhancing ion release, while CaO initially stabilizes the network but later accelerates release once Ca–phosphate clusters appear, provided phase separation does not occur [110,207]. Beyond bulk effects, secondary phase formation at the interface must also be considered: Ca^{2+} can participate in the precipitation of calcium silicate hydrate (CSH) within the hydrated silica-rich layer, producing passivating barriers that slow dissolution and extend nutrient release, a feature directly exploitable in fertilizer design [171,208].

In summary, the type and proportion of alkaline-earth oxides exert decisive control over structure, mobility, and reactivity, enabling the fine tuning of glass behaviour between bioactivity and durability. The subtle interplay between Ca^{2+}, Mg^{2+}, other modifiers, and network formers thus constitutes one of the most effective strategies for tailoring the performance of silicate-phosphate glass fertilizers.

3.4 Amorphous nature – its influence on glass alteration and nutrient release

Regardless of the material type, any substance existing outside its thermodynamic equilibrium – i.e., not in its lowest energy state – will, when exposed to a corrosive environment, tend to undergo transformations aimed at minimizing its Gibbs free energy, ultimately evolving into more stable phases. Glass, by virtue of its amorphous, unstable nature, possesses a higher internal energy than corresponding crystalline solids and is therefore inherently more susceptible to transformation under such conditions.

The significantly lower stability of natural glasses compared to their crystalline igneous counterparts under Earth's surface conditions has been long recognized – a difference attributed to the residual excess energy that glasses retain from their molten precursors. As widely acknowledged, a glass is a solid thermodynamically unstable, a direct consequence of the kinetic trapping that occurs during the glass transition. Whereas equilibrium phase transitions are driven by the system's tendency to minimize Gibbs free energy in response to changes in temperature and pressure, kinetic ones arise when the system is cooled too quickly to reach its equilibrium state. In such cases, the structure becomes trapped in a non-equilibrium configuration, characterized by an elevated Gibbs free energy and a pronounced dependence on the thermal history of the material. Consequently, a glass always exists at a higher energy state than a crystalline phase of analogous composition, the latter possessing a periodic and efficiently packed lattice structure [101].

This intrinsic instability has direct implications for chemical activity: amorphous phases generally dissolve at substantially higher rates than crystalline analogues, a phenomenon consistently documented in the literature [209,210]. Beyond thermodynamic considerations, the structural attributes of glasses further contribute to their susceptibility

to chemical attack. Unlike crystalline materials, which display efficient atomic packing with minimal free volume, glasses – particularly those quenched at high rates – contain a considerable fraction of unoccupied space within their network. These voids create pathways for the ingress of water, accelerating hydrolytic attack once the glass is exposed to aqueous environments [152,211]. Molecular dynamics simulations conducted by Perez et al. [212] comparing vitreous albite to its crystalline counterpart highlight this behaviour: while the compact crystalline structure prevents water from diffusing into the bulk, the open, irregular structure of the glass allows water to penetrate. As a result, the dissolution of the crystalline phase is limited to surface reactions, whereas glasses undergo not only surface degradation but also internal ion exchange following water diffusion into the solid. Classical molecular dynamics simulations of water chemisorption on silica surfaces further emphasize this difference. Unlike the more compact and less reactive surfaces of crystalline silicates, the reactive zone in a silicate glass extends into the interior of the solid, its depth controlled by both network connectivity and environmental pH [126].

The susceptibility of glasses to hydrolysis is also governed by the local structure. Parameters such as cluster size, the nature of cluster terminations, and the degree of local hydration all influence reactivity. Pelmenschikov et al. [213], demonstrated that the activation energy for hydrolysis ($E_{hydrolysis}$) increases markedly when a Si–O–Si bond forms part of a highly connected crystalline framework; the more polymerized the structure, the higher the energy barrier to reaction. Experimental data corroborate this observation, showing that the structural disorder intrinsic to glasses – which can be modulated through control of the cooling rate – has a strong effect on the forward dissolution rate, r_0 [214]. This conclusion is further supported by geological evidence: amorphous phases in natural rocks are observed to dissolve at rates at least an order of magnitude faster than the coexisting crystalline components [215]. Consequently, while controlled crystallization through deliberate thermal treatment can be used to enhance the mechanical properties of glass-ceramic materials, uncontrolled or spontaneous crystallization is highly detrimental, particularly for ion-releasing glasses [216,217].

Such unintended crystallization introduces several challenges. Beyond its impact on processing and mechanical integrity, the development of discrete, stable crystalline phases within a glass matrix fundamentally alters its degradation behaviour, reducing the overall reactivity of the material and producing heterogeneity in both dissolution kinetics and ion release profiles. This heterogeneity can lead to spatially uneven reactivity, erratic nutrient release, and premature failure of the material – outcomes that are incompatible with the strict performance requirements of functional glasses [216].

In light of these findings, it becomes clear that glasses, by virtue of their high internal energy relative to crystalline analogues, are inherently predisposed to chemical alteration. This process involves the gradual hydration of the glass structure and its transformation into more stable secondary phases, accompanied by the release of dissolved ionic species. Consequently, fully amorphous glass fertilizers exhibit a pronounced reactivity in aqueous environments, a property that can be exploited to ensure efficient and sustained ion delivery in agricultural applications.

4 Macro- and microelements essential for plants and their Functions

It should be emphasized that the constituents of glass materials designed for soil fertilization or revitalization must not only facilitate the formation of a suitably open and fragmented structure, which enables efficient ion exchange between the cations embedded in the vitreous network and the acidic components of root exudates, but also satisfy the agronomic requirements imposed by the fertilizer sector. In practical terms, this implies that such glasses must incorporate adequate amounts of macro- and microelements that are indispensable for the proper growth and development of plants. For this reason, glass fertilizers developed by researchers at AGH University are typically formulated to include macronutrients such as phosphorus, potassium, magnesium, and calcium, all immobilized within a silicon-based matrix. Furthermore, it is a common practice to supplement the composition with an additional micro- or macroelement—selected either to address the specific nutritional demands of a given crop or to compensate for nutrient deficiencies present in the soil.

4.1 Phosphorus

Energy constitutes the fundamental basis of life, and all living organisms rely on continuous and highly efficient mechanisms of energy transfer to sustain growth, development, and reproduction. Within this framework, phosphorus stands out as one of the primary and irreplaceable macronutrients in plant nutrition because of its central role as a structural component of adenosine diphosphate (ADP) and adenosine triphosphate (ATP)—the molecular energy carriers that drive a vast spectrum of biochemical reactions within plant cells. The high-energy phosphate bonds of ATP directly fuel photosynthesis, which remains one of the most crucial and energy-demanding processes in the biosphere. Beyond its indispensable role in energy metabolism, phosphorus is also a key element of nucleic acids (DNA and RNA), making it essential for the storage, transmission, and expression of genetic information. As a consequence, phosphorus deficiency profoundly disrupts essential physiological functions, including photosynthesis, respiration, energy storage and mobilization, maintenance of membrane integrity, cell division, and genetic continuity. These impairments, in turn, result in growth retardation and a marked decline in plant productivity [218–221].

4.2 Potassium

Potassium, which may constitute as much as 10% of a plant's dry matter, occupies a distinctive position among plant nutrients owing to the fact that, unlike other macronutrients, it does not become incorporated into organic molecules but rather persists in plant tissues almost exclusively as a free ion. This unusual mode of occurrence has historically posed a significant challenge for researchers attempting to elucidate its precise physiological functions. Nevertheless, extensive studies have allowed these functions to be broadly categorized into two principal groups: processes that depend on maintaining a stable intracellular K^+ concentration in metabolically active compartments, and those that involve the dynamic redistribution of K^+ across cellular organelles and tissues. The former encompasses, among others, the activation of a wide range – up to sixty – of enzymes that are central to energy metabolism, protein biosynthesis, and the transport of

solutes, as well as the electrostatic stabilization of negatively charged macromolecules. The latter group includes key regulatory processes such as the control of transmembrane voltage gradients, which are vital for cytoplasmic pH homeostasis, the intracellular partitioning of metabolites and inorganic ions, the regulation of osmotic potential required for cell expansion and stomatal movement, and the coordination of water and solute transport through the xylem. In addition, potassium plays a critical overarching role in enhancing plant tolerance to a broad spectrum of abiotic and biotic stress factors – including drought, salinity, excessive light, low temperatures, and pathogenic attacks – making it a cornerstone element in plant adaptability and defence [222–225].

4.3 Magnesium and calcium

In addition to phosphorus and potassium (as well as not discussed here nitrogen) – undoubtedly the macronutrients most extensively investigated in relation to crop yield and quality – two further elements, historically undervalued in routine soil diagnostics and fertilization strategies, merit closer consideration because of their indispensable contributions to plant growth and development: magnesium and calcium.

The essentiality of magnesium is unequivocally demonstrated by its strategic localization within plant organelles, particularly its central position within the chlorophyll molecule, where it is directly responsible for capturing solar energy during photosynthesis and, as a consequence, for facilitating the assimilation of carbon dioxide in chloroplasts. Notably, despite this primary role, only about 15–35% of the total magnesium absorbed by a plant is incorporated into chlorophyll pigments, indicating that the remaining 65–85% fulfils other, equally fundamental physiological functions. Among these are the facilitation of carbohydrate translocation from source organs to sink tissues, the structural and functional stabilization of ribosomes, and the regulation of genetic information translation through interactions with ribosomal subunits, which ensure correct binding of messenger RNA (mRNA) and transfer RNA (tRNA). Moreover, magnesium plays a pivotal role in phosphate transport and energy metabolism, particularly through the activation of key enzymes, including ATPases and phosphatases – a fact that highlights the intricate interdependence among all the principal macronutrients [226,227].

Calcium, in parallel, serves a dual function in plant physiology, encompassing both structural and signalling roles. In a manner analogous to its role in animals, calcium confers mechanical strength to plant tissues by contributing to the formation and stabilization of cell walls and by maintaining the structural integrity of plasma membranes, thereby reducing cellular vulnerability to both mechanical and environmental stresses. Beyond this structural function, calcium acts as a ubiquitous secondary messenger that regulates numerous developmental and stress-response pathways, including root elongation, pollen tube growth, fertilization, and plant responses to both abiotic and biotic stimuli. For this signalling function to be effective, cytosolic Ca^{2+} concentrations under resting conditions are maintained at extremely low levels, typically around 0.1 μM. Upon recognition of an external stimulus or non-self signal, a transient elevation of cytosolic Ca^{2+} occurs, which initiates a cascade of downstream molecular events that ultimately lead to adaptive or defensive responses. Consequently, the tight regulation of intracellular calcium homeostasis is essential for plants to perceive and respond to environmental cues in a timely and coordinated manner, ensuring their survival and proper development [228,229].

4.4 Silicon

Finally, although silicon is the second most abundant element in the Earth's crust after oxygen, its significance in plant nutrition has historically been underestimated, largely due to its widespread presence in soils and the resulting assumption that plants always have sufficient access to it. For this reason, silicon has long been excluded from the list of essential plant nutrients. Although debate continues over whether silicon should be regarded as an essential or merely a beneficial element, an expanding body of evidence increasingly points to its pivotal contribution to plant resilience under both biotic and abiotic stress conditions. Initially, silicon's beneficial effects were attributed mainly to its capacity to form a rigid mechanical barrier within plant tissues, thereby strengthening cell walls and impeding the penetration of pathogens, including fungal hyphae. However, recent research demonstrates that its functions extend well beyond structural reinforcement and include a wide range of molecular interactions, modulation of plant metabolism, and involvement in intricate signalling networks [230]. Given the predicted intensification of adverse environmental conditions such as drought, salinity, temperature extremes, root-zone hypoxia, and flooding as a consequence of climate change, the incorporation of silicon into fertilization strategies is likely to shift from being optional to an essential practice [230–232]. Moreover, emerging studies indicate that silicon influences nutrient dynamics in the rhizosphere, improving nutrient solubility and facilitating root uptake. These effects are thought to be mediated, at least in part, by silicon-dependent transcriptional regulation of key nutrient transporters, which varies depending on plant species, soil properties, and nutrient status. This regulation has been shown to support the acquisition and internal balance of a broad spectrum of nutrients – including nitrogen (N), phosphorus (P), potassium (K), calcium (Ca), magnesium (Mg), sulfur (S), iron (Fe), zinc (Zn), manganese (Mn), and boron (B) – under conditions of both deficiency and excess [233]. While the mechanistic basis of silicon's interactions with soil components and nutrient uptake remains incompletely understood, there is a growing consensus that its impact extends beyond the plant to the surrounding soil ecosystem. Silicon applications have been observed to improve soil structure, alter pH and organic matter dynamics, and stimulate microbial activity, collectively enhancing conditions that promote nutrient retention and availability. These multifaceted effects underline the importance of silicon as an emerging tool in sustainable crop production systems, where its role encompasses both direct benefits to plant performance and indirect improvements to soil health and rhizosphere functionality [230–232].

4.5 Sulfur as the fourth, recently recognized, essential macronutrient

The importance of sulfur in plant nutrition only came into broad focus once its principal environmental sources had been markedly reduced. Whereas, in the early 1950s, sulfur deficiency was observed only sporadically and was confined to specific soil types, it has now become a widespread and persistent agricultural concern. Between 2000 and 2020, the concentration of plant-available sulfur in soils has been reported to decline by as much as 34–86%, depending on soil type [234]. This depletion can be attributed primarily to improvements in air quality resulting from stricter environmental regulations and the transition of energy production systems away from sulfur-rich fossil fuels, which have significantly reduced atmospheric sulfur deposition across Europe, the United States, and beyond [235,236]. The decline is further aggravated by several factors,

including the replacement of sulfur-containing pesticides with low-sulfur alternatives, the increasing reliance on purified fertilizers such as superphosphate and ammonium sulfate, and the reduced use of traditional farmyard manure, historically a significant source of organic sulfur. In addition, continuous losses of sulfur occur through leaching, soil erosion, and the gradual degradation of soil organic matter, which, in many soils, constitutes up to 95% of the total sulfur pool [234].

Once the physiological symptoms of sulfur deficiency became evident in crops, the element was promptly recognized as the fourth essential macronutrient – following nitrogen, phosphorus, and potassium – a classification that is now firmly supported from both an agronomic and a biochemical perspective [234,237]. Sulfur's crucial function is perhaps most clearly reflected in the biosynthesis of the amino acids cysteine and methionine. These amino acids are not only integral components of proteins but also represent essential dietary constituents for animals and humans, making plants a major source of bioavailable sulfur within terrestrial food chains. Consequently, adequate sulfur availability improves the nutritional quality of crops by enhancing the methionine content of grains, by contributing to bread-making and malting quality, and, indirectly, through the formation of secondary sulfur compounds with bioactive and phytopharmaceutical properties [238]. Beyond its fundamental role in protein synthesis, sulfur is vital to the structure and activity of numerous biomolecules, as approximately 40% of plant enzymes lose their catalytic efficiency under sulfur-limited conditions. This is primarily due to the indispensable role of sulfhydryl (-SH) functional groups, which participate in redox reactions, facilitate the detoxification of xenobiotics, and form stable complexes with both physiologically essential and potentially toxic metals [239].

Equally critical is sulfur's involvement in photosynthesis. Its deficiency leads to a rapid reduction in chlorophyll content and, consequently, to a decline in efficiency of this oxygen-producing process. Actually, a first visible sign of sulfur shortage is chlorosis occurring mainly in young leaves which produce insufficient amounts of chlorophyll and lipids which in turn leads to reduction of photosynthetic activity and an overall decline of metabolism [236,240].

Perhaps most compelling is the biochemical interdependence between nitrogen and sulfur assimilation pathways. As both nutrients are indispensable for protein synthesis, a lack of sulfur not only reduces the efficiency with which plants utilize nitrogen but also causes the accumulation of nitrates in the soil, which in turn increases the risk of nitrogen leaching through precipitation [237,239].

In addition to its fundamental metabolic roles, sulfur is also instrumental in fortifying plant defence mechanisms against both abiotic and biotic stressors. Under conditions of drought, salinity, temperature extremes, or pathogenic attack, plants experience elevated levels of reactive oxygen species (ROS), exacerbating oxidative stress. In response, plants have evolved complex defence mechanisms, many of which rely on sulfur-containing compounds – including glutathione (GSH), phytochelatins (PCs), ATP sulfurylase (ATPS), hydrogen sulfide (H_2S), methionine, cysteine, and various protein thiols, that play central roles in mitigating such damage by scavenging ROS and maintaining redox homeostasis [241].

Historically, the sulfur requirements of crops were largely met by atmospheric deposition originating from industrial emissions. However, with the advent of clean-air technologies and strict emission controls, agricultural systems have transitioned from passive atmospheric enrichment to the deliberate and agronomically managed application of

sulfur. Although this shift represents an environmentally beneficial outcome, it also necessitates careful planning, as excessive sulfur application, as evidenced in studies of acid rain, can lead to adverse effects, including soil acidification, water contamination, and the mobilization of toxic metals [235]. Consequently, sulfur fertilization must be based on precise dosing strategies, carefully matched to plant requirements and delivered in appropriate chemical forms to maximize agronomic benefits while avoiding ecological harm.

4.5.1 Incorporation and influence of SO_3 in glasses

Although the essential function of sulfur in plant nutrition has now been firmly established, its role as a constituent or co-participant within the vitreous framework remains comparatively poorly understood, despite the fact that its application in glassmaking predates its recognition as a nutrient. It is therefore unsurprising that sulfur was not included in the section devoted to classical network formers and modifiers, for while the influence of the major network components such as SiO_2, P_2O_5, K_2O, MgO, and CaO on the chemical reactivity of silicate–phosphate glasses – though strongly dependent on specific compositions and relative proportions – is broadly acknowledged and can, to a certain degree, be predicted, the manner in which sulfur incorporation alters these properties still poses a number of open questions his uncertainty primarily stems from the relatively scarce body of experimental data concerning the behaviour of sulfur within glass matrices, a consequence of its long-standing marginal status as a structural component of glass. Indeed, much of the available knowledge regarding this element originates from the Earth and planetary sciences, where sulfur has been investigated in the context of magmatic systems, thus providing most of the insights into its behaviour in silicate melts (Fig. 18). Until the very end of the twentieth century, studies of sulfur in glass technology were almost exclusively limited to its function as a fining agent, used to promote the removal of gaseous inclusions from molten glass. In the form of sodium sulfate, sulfur introduces a substantial amount of gas during the decomposition of the batch, while simultaneously contributing sodium to soda–lime–silicate melts. The pronounced sensitivity of sulfur solubility to temperature and melt composition plays a decisive role in this fining process. During melting, sulfates preferentially dissolve in alkali-rich regions of the melt; as silica progressively dissolves into these zones, the solubility of sulfates diminishes, which in turn drives the release of gaseous species, as described by the reaction [106,242]:

$$Na_2SO_4 + xSiO_2 \rightarrow Na_2O \cdot xSiO_2 + SO_3 \qquad \text{Eq. (10)}$$

The resulting SO_3 rapidly decomposes to SO_2 and O_2 according to the following reaction:

$$2SO_3 \rightarrow 2SO_2 + O_2 \qquad \text{Eq. (11)}$$

The liberated SO_2 diffuses into adjacent bubbles, whereas O_2 either dissolves back into the melt or migrates into the bubbles, facilitating their growth and eventual ascent to the melt surface.

The liberated SO_2 diffuses into adjacent bubbles, whereas O_2 either dissolves back into the melt or migrates into the bubbles, facilitating their growth and eventual ascent to the melt surface (Fig. 18).

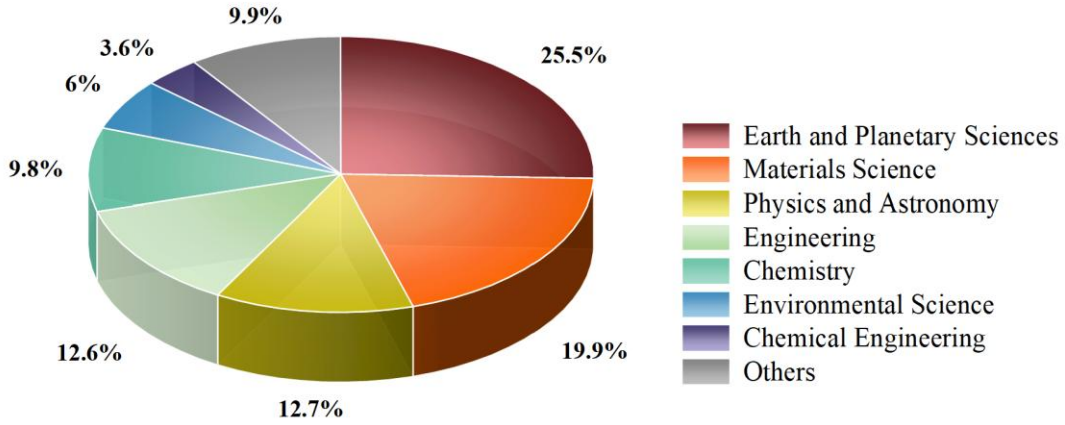


Fig. 18. Scopus search results for the query "sulfur in silicate glass" (documents by subject area).

It was only towards the close of the last millennium that the focus of research broadened, as the pressing issue of nuclear waste immobilisation through vitrification brought renewed attention to the role of sulfur in silicate and other oxide-based glasses (Fig. 19).

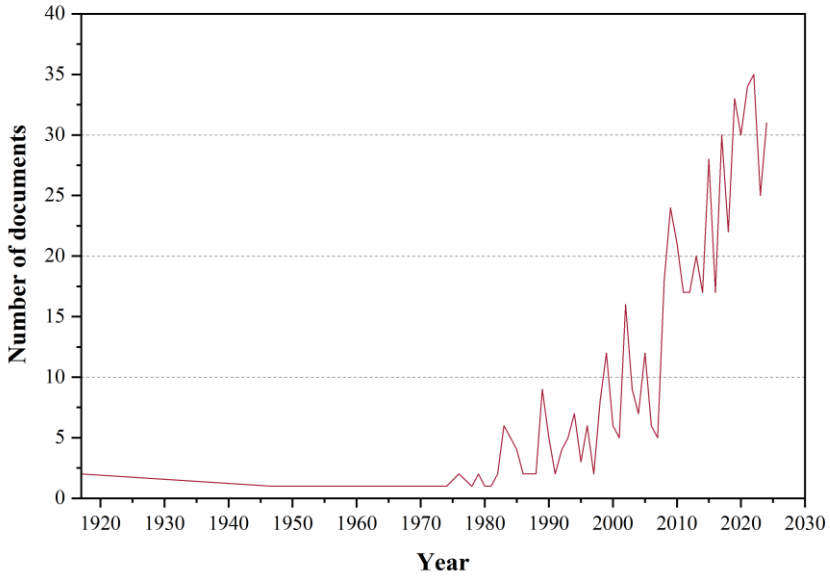


Fig. 19. Number of documents published per year from 1917 to 2024 related to sulfur in silicate glasses (data extracted from the Scopus database).

From that point onward, the incorporation of sulfur into glass-forming systems and its influence on the structure and properties of the resulting materials became a topic of increasing scientific interest. These investigations soon revealed that sulfur presents a significant challenge in efforts to produce fully amorphous, homogeneous glasses with a predetermined sulfur content. Reports indicate that, under conditions typical of conventional Joule-heated melters, 40–70 wt% of sulfate species may volatilise, with the extent of this loss controlled by melt temperature, ambient pressure, oxidation–reduction conditions, and melt viscosity [242]. Even earlier, in the context of sulfur employed for fining, it had been recognised that the equilibrium described by Eq. (2) exhibits strong temperature

dependence: a reduction in temperature can lead to the reabsorption of SO_2 into the melt, forming dissolved sulfate species. In fining operations this phenomenon is undesirable, as it consumes oxygen from the melt to generate sulfate, thereby drawing oxygen from nearby bubbles, reducing their internal pressure, and ultimately causing their contraction and disappearance [106]. Furthermore, the solubility of sulfur in silicate melts is profoundly influenced by redox conditions [242–244]. It is now widely accepted that sulfur dissolves in these systems as both sulfide and sulfate species. Under relatively reducing conditions, sulphides dominate, whereas more oxidising conditions favour the incorporation of sulfur as sulfates. This behaviour is governed by reactions involving the interaction of sulfur with the gas phase, where Eq. (13) describes dissolution under reducing conditions, while Eq. (14) applies to dissolution under oxidising conditions [243]:

$$SO_2(g) + O^{2-}(melt) \leftrightarrow S^{2-}(melt);\ \Delta H > 0 \qquad \text{Eq. (12)}$$

$$SO_2(g) + \frac{1}{2}O_2(g) + O^{2-}(melt) \leftrightarrow {SO_4}^{2-}(melt);\ \Delta H < 0 \qquad \text{Eq. (13)}$$

Despite the fact that sulfur most commonly occurs in the oxidation states –2 and +6, it is capable of existing in a wide variety of forms in both natural and synthetic systems. These include species containing sulfur in a single valence state, such as sulfate, sulfide, sulfite (SO_3^{2-}), dithionite ($[O_2S–SO_2]^{2-}$), and elemental sulfur (S^8), as well as compounds in which sulfur atoms exhibit multiple oxidation states within the same molecule, such as thiosulfate ($[S–SO_3]^{2-}$), polythionates ($[O_3S–(S_n)–SO_3]^{2-}$), metabisulfite ($[O_2S–SO_3]^{2-}$), or polysulfides ($[S–(S_n)–S]^{2-}$). Owing to this remarkable diversity of sulfur-bearing species, the mechanisms governing its solubility and speciation in silicate melts and glasses are inherently complex [245]. In the case of glasses developed as controlled-release carriers of nutrients for agricultural purposes, the chemical form of sulfur present in the glass matrix is of paramount importance for two fundamental reasons, each closely related to the chemical reactivity of the material. First, the structural role of sulfur depends strongly on its speciation; every form is expected to interact differently with the glassy network, inducing distinct structural rearrangements that may, in turn, influence the kinetics and extent of ion release into the surrounding medium. Second, the chemical form of sulfur released from the glass matrix determines its bioavailability to plants, as only sulfate ions can be effectively assimilated by plant tissues [236,238,246]. For this reason, melting and heat treatment under oxidising conditions are generally preferred to ensure that sulfur is predominantly incorporated as sulfate, thus satisfying the nutritional requirements of plants.

Nevertheless, even under conditions that are nominally favourable for the dissolution of sulfate species, it was already proposed in the mid-twentieth century that the $[SO_4]^{2-}$ group, due to its highly symmetrical structure, is not easily distorted and therefore is poorly suited to the glass formation [247]. Although an amorphous material containing sulfate as the sole anionic species can be obtained employing very high cooling rates, such sulfate systems rarely vitrify with ease. As previously mentioned, effective glass formation is associated with a rapid increase in melt viscosity during cooling, prior to the onset of crystallisation. Such an increase is typically linked to the presence of large, complex structural units that form when a substance exhibits a strong tendency towards polycondensation (network polymerisation). The glass-forming ability of inorganic systems is therefore closely related to the nature of their chemical bonding. It has long been

recognised that substances with bonds of a purely ionic, purely covalent, or metallic character show little tendency to form glasses. In contrast, good glass formers are characterised by the presence of bonds of mixed character, intermediate between ionic and covalent or metallic and covalent (Fig. 20). The high degree of covalency in the S–O bond – approximately 80 %, compared with roughly 57 % for the Si–O bond – places sulfur outside the compositional field traditionally associated with systems that vitrify easily (Fig. 21) [248].

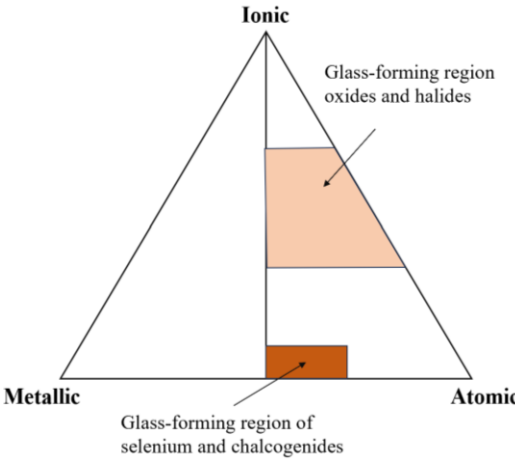


Fig. 20. Glass-forming regions within the bond-type triangle.

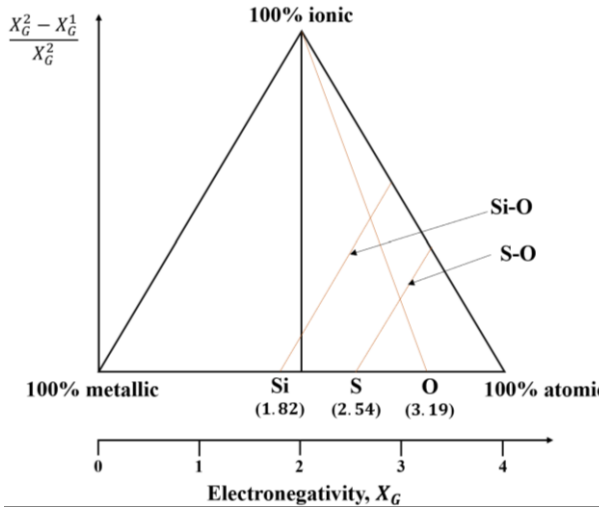


Fig. 21. Position of selected bonds in the bond-type diagram proposed by Görlich. The location of the S–O bond (with a covalency of approximately 80 %) lies considerably closer to the covalent apex compared with the Si–O bond (~57 % covalency), which explains the relatively low glass-forming tendency of sulfur-containing systems compared to classical silicate glasses.

It has therefore been proposed that the vitrification of sulfates can be facilitated by increasing the compositional complexity of the glass. This approach follows the concept that introducing several different cations with varying field strengths promotes subtle distortions of the coordination polyhedra, which, in turn, enhances the ability of the system to form a glass. Furthermore, compounds that on their own do not readily vitrify can often be induced to form glasses when their composition involves a combination of cations exhibiting sufficiently diverse field strengths. This principle has been successfully applied to sulfate-containing systems, for example by surrounding $[SO_4]^{2-}$ groups with strongly polarizing hydrogen ions (H^+) and weakly polarizing potassium ions (K^+). Such an arrangement disrupts the symmetry of the sulfate tetrahedra and has been shown to enable the formation of sulfate-based glasses [247,249]. Nevertheless, even in highly multicomponent glass formulations specifically designed to favour glass formation – such as those developed for the immobilization of nuclear waste—the amount of sulfur that can be successfully incorporated into silicate-based melts is consistently reported to be rather limited. In borosilicate glasses, which are widely studied for this purpose, the sulfur content rarely exceeds 0.6–3 mol %, while in alumino–phosphate systems the upper limit is approximately 7.8 mol % [250–252]. This behaviour reflects the intrinsically poor miscibility of sulfur species in silicate-based melts. Upon cooling from high temperatures, at which the melt behaves as a homogeneous liquid, the system eventually crosses a critical

temperature below which phase separation becomes thermodynamically favourable [106]. Under such conditions, the sulfate-rich phase tends to segregate from the silicate matrix, a process that can be anticipated from the classical considerations of Dietzel concerning the effect of cation field strength on the stability of cooling melts. According to this theory, during cooling, cations compete for coordination with oxygen ions to achieve the densest possible packing. If two species of high field strength are present, demixing occurs, resulting in the formation of distinct, immiscible phases that lower the free energy of the system [106]. In the case of silicon and sulfur, which possess field strengths of 1.57 and 2.60 respectively, there is a low affinity to form a stable combined oxide phase [249,253]. Consequently, liquid–liquid immiscibility may develop during cooling, giving rise to a stratified system with a sulfate-rich layer – characterized by lower viscosity— floating atop the silicate-rich phase. This immiscibility is further accompanied by a preferential partitioning of alkali and alkaline-earth cations (and, if present, rare-earth elements) into the sulfate-rich phase. Studies have shown that this partitioning is not random, but correlates with electronegativity: the partition coefficient increases as the electronegativity of the cation decreases [254,255]. While this phenomenon is of fundamental importance in geological processes, such as magma degassing and ore deposit formation, it is undesirable for materials intended for agricultural applications, including glass-based fertilizers. In such cases, the separated sulfate phase commonly crystallizes as alkali or alkaline-earth sulfates, which are highly water-soluble and would therefore release their constituents almost immediately upon contact with soil moisture. This interpretation is supported by the observation that evidence for sulfate inclusions in natural quenched magmas is exceptionally scarce [255,256]. Even when a discrete sulfate phase is not clearly visible on the surface of a solidified melt, crystalline sulfate precipitates can still form within the glassy bulk. Although such inclusions do not cause the immediate, rapid ion release associated with surface-segregated sulfates, they compromise the homogeneity and amorphous character of the glass, which in turn affects the controlled ion release that such materials are designed to achieve.

Despite this strong tendency of sulfur to segregate during cooling, a given glass-forming system possesses a certain threshold for the amount of sulfur it can retain in solution before reaching saturation. Beyond this limit, sulfide or sulfate species (depending on the prevailing redox conditions) begin to exsolve [257]. This value, often referred to as the sulfide or sulfate capacity of the melt, depends on several parameters, including the oxygen fugacity (fO_2), which governs the oxidation state of redox-sensitive elements and thereby controls the speciation of sulfur, as well as temperature, pressure, and overall glass composition [257,258]. It is important to emphasize that a reliable determination of the sulfate solubility limit in a particular system requires that the melt be in equilibrium with the surrounding atmosphere, and that the partial pressure of sulfur species be strictly controlled. However, such conditions are rarely met in practical applications. For this reason, it is more practical to refer to sulfur incorporation, i.e., the amount of sulfur that remains dissolved in the glass after a controlled melting and fining process [259]. Under these conditions, even though fluctuations in furnace atmosphere occur during melting due to the release of SO_x from the batch, it can be assumed that similar melting protocols lead to comparable atmospheric conditions, and thus differences in the amount of sulfur incorporated into the glass are primarily attributable to variations in composition rather than atmosphere [259].

The effect of composition on this solubility threshold has been demonstrated in numerous studies. The pioneering work of Papadopoulos [260], who investigated the solubility of SO_3 in soda–lime–silica melts under various temperatures and atmospheric conditions, led to the first quantitative model describing sulfate capacity based on the activities of bridging oxygens, non-bridging oxygens, and free oxide ions in the melt. Under equilibrium, the relative proportions of these species are related as follows:

$$O^0 + O^{2-} \overset{K_a}{\leftrightarrow} 2O^- \quad \text{Eq. (14)}$$

Meanwhile, sulfate species, after dissociation according to the general reaction:

$$R_xSO_4 \leftrightarrow R_xO_y + SO_3 \quad \text{Eq. (15)}$$

are incorporated into the melt network via the reaction:

$$SO_4^{2-} \overset{K_b}{\leftrightarrow} SO_3 + O^{2-} \quad \text{Eq. (16)}$$

$$SO_3 + O^{2-}(melt) \rightarrow SO_4^{2-}\ (melt) \quad \text{Eq. (17)}$$

From these relationships, it follows that the sulfate capacity of a melt is directly proportional to the availability of free oxide ions, which is itself strongly influenced by the NBO concentration (Eq. (15)).

Combining these factors, the activity of $[SO_4]^{2-}$ in the melt can be expressed as:

$$[SO_4^{2-}] \propto \frac{p_{SO_3} \cdot [O^-]^2}{K_a K_b [O^0]} \quad \text{Eq. (18)}$$

$$a_{SO_4^{2-}} \propto \frac{f_{SO_2} \cdot [NBO]^2 \sqrt{O_2}}{[BO]} \quad \text{Eq. (19)}$$

where $[SO_4]^{2-}$ represents the sulfate content dissolved in the melt and pSO_3 is the partial pressure of SO_3 in the furnace. Under conditions of constant pressure, sulfate solubility thus depends on the ($[NBO]^2/[BO]$) ratio, a parameter directly linked to the glass structure [242,250,259]. t follows that an increase in the proportion of non-bridging oxygens, at the expense of bridging oxygens, enhances sulfate incorporation, and this can be readily achieved by adjusting the concentration of network modifiers in the glass melt.

Indeed, experimental studies by Ooura and Hanada [261] have confirmed that in binary alkali–silicate and ternary alkaline-earth–lime–silica glasses, sulfate solubility increases with the amount of network-modifying oxides, with the most significant effect observed for M_2O-type modifiers. Not only the concentration of network modifier, but also its type has been proven to impact the assimilation of $[SO_4]^{2-}$ species within the silicate-based network. For a constant content of SiO_2 and alkali oxides, replacing the alkaline-earth component systematically changes the sulfate capacity according to the trend [261]:

BaO > SrO > PbO > CaO > MgO > ZnO

This relationship highlights the role of cation field strength, a parameter introduced by Dietzel to describe the effects of glass composition on structure and properties in terms of valence, ionic radius, and bond length. Subsequent studies have shown that systems containing modifiers with low CFS display a greater ability to incorporate sulfate species. This behaviour was attributed to the fact that low-CFS cations are less effective competitors for oxygen coordination, thereby allowing sulfur species to achieve a higher concentration of free oxide ions and increasing the sulfate capacity [102,259].
In addition to the network modifiers, the nature of the network formers themselves has a marked effect on the ability of the glass to accommodate sulfate. According to Stefanovskii [262], he sulfate capacity of a given vitreous matrix depends strongly on the compatibility of the chemical parameters of the host cations with the sulfate anion. These parameters include cation–oxygen bond energy, field strength, polyhedral size and polarizability, and overall bond character. On the basis of these factors, a compatibility series has been established, ranking cations according to their tendency to form stable associations with sulfate tetrahedra:

S^{6+} (IV) – P^{5+} (IV) – V^{5+} (IV) – B^{3+} (III) – Si^{4+} (IV) – B^{3+} (IV) – Al^{3+} (IV) – Zn^{2+} (IV)

In systems containing a single network modifier, the degree of compatibility between ions is greater when their positions in the above series are closer to one another. Consequently, sulfate tetrahedra are expected to be more compatible with phosphate tetrahedra than with silicate units. By extension, the concentration of a given network former strongly influences the incorporation of $[SO_4]^{2-}$ species, as a higher content of network-forming oxides not only reduces the proportion of non-bridging oxygens but also increases the overall compactness of the glass network, thereby decreasing the size and abundance of structural voids that could potentially accommodate sulfate tetrahedra [243,251,263].

Remarkedly, the existence of a composition- and atmosphere-dependent threshold for sulfate capacity complicates the selection of components for glass fertilizers. Formulations must simultaneously meet several requirements: they are supposed to supply essential nutrients to plants, form a network structure that facilitates controlled ingress of soil solution and ion exchange, as well as shall allow for the incorporation of a sufficient amount of sulfur species to satisfy plant needs throughout the growth cycle.

The integration of sulfur into the vitreous framework is challenging not only because of the risk of crystallisation and phase separation, or the potential for an undesirably rapid release of soluble sulfate species, but also due to the structural perturbations that sulfur may impose on the arrangement of other network components. The addition of any new component to a glass composition inevitably affects the structure of the network, not only through direct interactions between the cation and the glass-forming units but also through cation–cation interactions, and these changes have profound implications for the resulting structure–property relationships [249].

As noted earlier, S^{6+} in the $[SO_4]$ complex has an exceptionally high Dietzel field strength of 2.60, which exceeds those of the main constituents of typical glass fertilizers: P^{5+} (2.1), Si^{4+} (1.57), Mg^{2+} (0.45), Ca^{2+} (0.33), and K^{+} (0.13) [249,253]. Although, according to the classical Zachariasen model, this would place sulfur in the category of network formers, it is worth noting that its CFS value surpasses the conventional range for these group of glass components ($Z/a^2 \approx 1.5–2$). Based solely on this high field strength, it is generally assumed that linkages between S and another strong cation such

as Si are unlikely to form because polyhedra associated with strong cations tend to avoid sharing oxygen atoms; instead, these cations compete for coordination with oxygen to achieve the densest possible packing [102,248]. By analogy, linkages involving P–O–S bonds would also not be expected to form preferentially. Instead, sulfur species are more likely to associate with cations of lower field strength and higher coordination numbers.

Indeed, a number of studies point to a certain structural independence of $[SO_4]^{2-}$ groups within the glassy network [264,265], although there is also evidence that sulfur may form linkages of a P–O–S or B–O–S-type [266–268], and may interact, particularly at low concentrations, with the silicate subnetwork [252,269]. As summarised in Tab. 4, the literature provides a range of sometimes contradictory findings regarding the impact of sulfur incorporation on the degree of polymerisation of the glassy network – a particularly important property for glass fertilizers because a network dominated by Q^2 (Si) chain structures is believed to be the most conducive to water penetration and glass–solution interaction [152]. Similarly, considerable discrepancies exist in the reported influence of sulfur on the thermal properties of glasses, which are critical for processing and for scaling up production of such materials for soil amendment. While some researchers suggest that sulfate species interact strongly with the glass network, others argue that these interactions are negligible and that sulfates merely occupy existing voids in the matrix without significantly modifying the structure [243,245,250–252,263,264,266,270–273]. Nevertheless, a more detailed examination of the studies summarised in Tab. 4 reveals patterns that shed light on these effects.

Tab. 4. Summary of literature reports on the property-related effects of sulfur incorporation into silicate- and phosphate-based glasses.

Glass composition	**Sulfate capacity**	**Polymerisation degree**	**Glass transition temperature [°C]**	**Ref.**
SiO_2-Li_2O/Na_2O-CaO/BaO	6.4 mol.%	Increase	–	Vaishnav [264]
SiO_2-B_2O_3-Al_2O_3-Na_2O	1.85 mol.%	Increase	Increase 402→474	Xu [263]
CaO–MgO–Al_2O_3–SiO_2	0.81 mol.%	Strong increase	–	Morizet [243]
Na_2O–SiO_2	1.25 mol.%	Decrease	–	Tsujimura [245]
SiO_2-B_2O_3-Na_2O-BaO	3 mol. %	Decrease	Decrease 534→497	Mishra [252]
SiO_2– B_2O_3–Na_2O-Al_2O_3-CaO-Fe_2O_3	0.44 mol.%	Decrease	Increase 565→584	Manara [250]
SiO_2-B_2O_3-Na_2O-Al_2O_3-V_2O_5	0.82 mol.%	Increase	Increase 486→509	Saini [270]
P_2O_5-Na_2O	17 mol.%	Decrease	Decrease 275→220	Sokolov [266]
SiO_2-B_2O_3-Na_2O-Li_2O-	1.87 mol.%	–	Decrease 545→ 550	Wu [271]

Al_2O_3-CaO-TiO_2-MgO				
P_2O_5-Fe_2O_3-Al_2O_3-Na_2O	3.89 mol.%	Decrease	–	Stefanovsky [251]
SiO_2-Al_2O_3-B_2O_3-Na_2O-CaO	0.8 mol. %	Increase	Increase 526→ 543	Lonergan [272]
P_2O_5-Li_2O	18.2 mol.%	Decrease	Decrease 305→256	Hémono [273]

A substantial proportion of studies reporting a depolymerising effect of sulfur (incorporated as sulfate species) on the glass network – such as those conducted by Sokolov et al. [266], Stefanovsky et al. [251] and Hémono et al. [273] – were performed under conditions in which sulfur was introduced at the expense of network formers. Consequently, the observed effects may, at least in part, be linked to the reduced connectivity of the primary glass-forming network caused by a lower concentration of network-forming oxides, rather than to sulfur itself. While Sokolov and co-workers reported that the addition of sulfate species to phosphate glasses promotes the depolymerisation of polyphosphate chains (a process in which both metal cations and sulfate groups participate, with the latter binding to the chains as terminal groups and possibly forming P–O–S linkages), Hémono et al. argued that sulfur incorporation results in the coexistence of two separate networks – Li_2O– P_2O_5 and Li_2O–SO_3 – while Stefanovsky interpreted the results as evidence of the structural individuality of $[SO_4]^{2-}$ groups within phosphate glasses. Comparable findings have been reported for silicate-based glasses, where sulfate species were added in increasing quantities. In the studies of Manara et al. [250] sulfur incorporation was likewise associated with a reduction in network connectivity, but, as in the previous examples, this coincided with a decrease in SiO_2 content. Interestingly, however, the reduction in network connectivity was accompanied by an increase in the glass transition temperature, which the authors attributed to the occupation of structural voids by sulfate species thought to hinder the relaxation and rearrangement of the silicate network, thereby influencing its dynamic behaviour during heating and cooling.

More definitive insight can be gained from investigations where sulfur content was systematically varied while the remainder of the glass composition was held constant. Wu et al. [271], who observed a decrease in T_g, but since the difference between the base sample and the one of the highest sulfur content was only 5°C it was treated as negligible. Xu et al. [263], on the other hand, demonstrated an opposite tendency in glass transformation temperature in relation to sulfur content. Together with T_g increase, an augmentation of degree of network polymerization of the silicate network was recorded and explained by the removal of NBO- forming Na^+ by SO_4^{2-} from the silicate network. Interestingly this effect also involved boron-oxygen subnetwork, as reformation of borosilicate ring structures, along with $^{[3]}B$ to $^{[4]}B$ conversion was observed. Similar conclusions, highlighting the preferential association of sulfate species with network-modifying cations, were drawn by Saini et al. [270], Lonergan et al. [272] as well as Vaishnav et al. [264].

Interesting thoughts on the influence of sulfur addition on the evolution of silicon-oxygen subnetwork were made by Morizet's et al. study [243], who observed strong polymerisation action of sulfate on the anorthite-diopside glass composition marked as

a decrease in the abundance of Q^2 units accompanied by an increase in Q^4 units. This behaviour was interpreted as evidence that sulfate groups interact with available non-bridging oxygens in depolymerised melts. No such effect, however, was observed for fully polymerised haplogranitic compositions (NBO/T = 0), suggesting that the influence of sulfate species is limited to depolymerised glass networks. Additionally, in these experiments, only the silicon environments were significantly affected, while the coordination of aluminium remained unchanged. Surprisingly, however, in a subsequent study, Morizet et al. [269], reported a slight decrease in T_g with increasing sulfur content, and proposed a revised interpretation of their earlier results. They argued that the apparent increase in polymerisation observed in ^{29}Si MAS NMR spectra does not correspond to true polymerisation, but rather reflects the formation of Si–O–S bonds during SO_2 dissolution. This mechanism, as suggested by authors, alters the spectral signature of silicon and mimics the presence of more polymerised Q^n units by consuming non-bridging oxygens to form $[SO_4]^{2-}$ groups. Consequently, while the NMR data indicate an increase in polymerisation, the observed decrease in T_g (as measured by DSC) suggests that this effect does not correspond to an actual increase in Si–O–Si linkages but instead to geometric rearrangements in the glass structure [243,269].

A very different perspective was provided by Mishra et al. [252], who, while keeping the base glass composition unchanged, reported a decrease in both the degree of polymerisation and T_g upon increasing sulfur content. They argued that, at low sulfate concentrations, $[SO_4]^{2-}$ species interact with Si–O–Si bonds, resulting in depolymerisation, which in turn leads to an increase in the abundance of Q^2 units at the expense of Q^3 units. This depolymerising effect reduces the rigidity of the borosilicate network, thereby lowering the energy barrier for structural relaxation and decreasing T_g.

A similar decrease in polymerisation was observed by Tsujimura et al. [245], but only when Na_2SO_4 was used as the sulfur source for Na_2O–SiO_2 melts. When elemental sulfur and graphite were used instead, the opposite trend – a more polymerised structure – was reported. The depolymerising effect of Na_2SO_4 was attributed to its partial conversion to polysulfides (Na_2S_x), which have a lower Na/S ratio, leading to the release of additional Na_2O and a corresponding change in the network structure. In contrast, the glasses produced from native sulfur-doped batches were enriched in polymerised units due to the preferential partitioning of sodium into the coexisting fluid phase.

Taken together, these diverse results indicate that the influence of sulfur on glass structure is a highly complex phenomenon, strongly dependent on the overall composition of the glass, the oxidation state of sulfur, and the melting conditions. This body of evidence leaves many open questions, both from a fundamental materials science perspective – relevant for fields as diverse as nuclear waste immobilisation, magmatic processes, or solid-state electrolytes – and from the perspective of applied research. Key questions include: What is the precise structural role of sulfate species within the glass network, and how does it depend on composition? Do sulfate groups form stable linkages with network formers, or do they behave as structurally isolated species occupying the interstitial voids of the glass? Do they exhibit specific preferences for second-shell neighbours? To what extent do they influence the evolution of network polymerisation and thermal behaviour during processing?

For applications such as glass-based fertilizers, additional questions emerge: Will typical laboratory melting conditions ensure that sulfur is incorporated predominantly in the sulfate form, which is assimilable by plants? Will the presence of sulfur affect the ion-

release kinetics, potentially inducing a burst release, or will it alter the amorphous structure in a way that changes the dissolution behaviour? These questions highlight the need for a comprehensive understanding of the structural role of sulfur in glass, which is essential not only for designing effective glass fertilizers but also for advancing knowledge in a wide range of scientific disciplines.

5 Research objective and hypothesis

In response to the growing concern over soil contamination caused by the excessive and inefficient use of conventional mineral fertilizers, and in view of the urgent need to provide a reliable source of sulfur without inducing soil acidification through the accumulation of unused sulfur species, the overarching goal of this doctoral thesis is to optimize the chemical composition of glasses within the SiO_2– P_2O_5–K_2O–MgO–CaO–SO_3 system, thereby enabling their application as slow-release vitreous carriers of sulfate ions for agricultural use.

To accomplish this goal, the following specific objectives have been defined:

I. To determine the appropriate proportions of network formers and modifiers that allow for the successful synthesis of fully amorphous glass compositions with most promising sulfur-retention;

II. To attain a detailed understanding of the structure of sulfur-bearing silicate-phosphate glasses with a special emphasis on the distribution of sulfur species, in order to enable effective control over the chemical activity of these materials;

III. To elucidate the mechanisms underlying the chemical activity of these glasses, with particular attention devoted to the processes occurring in the near-surface region during interaction with soil environment;

IV. To evaluate capability of developed materials to engage with rhizosphere-mediated processes for nutrient mobilization under conditions simulating the temperate climate typical of local agroecosystems and, consequently, assess their potential to act as effective vitreous carriers of plant-available ions.

A key challenge addressed in this work arises from the increased tendency of sulfur-containing glasses to undergo spontaneous crystallization during cooling – a process that, when extensive, compromises the amorphous nature of the material and thereby its functionality as a slow-release nutrient carrier. In light of this, the central research hypothesis of the thesis posits that an appropriately engineered glass composition within the SiO_2–P_2O_5–K_2O–MgO–CaO–SO_3 system will yield an amorphous product capable of sustained release of essential nutrients under mildly acidic conditions, as encountered in the rhizosphere, while exhibiting sufficient resistance to leaching under neutral aqueous conditions.

6 Subject of the study

The subject of the research undertaken within the framework of this doctoral study encompassed multicomponent silicate-phosphate glasses belonging to the SiO_2–P_2O_5–K_2O–MgO–CaO system. These materials were designed to serve not only as matrices capable of enclosing sulfur species but also, of equal importance, as potential sources of biologically essential macro- and micronutrients for plants and soil microbiota, gradually releasing their constituent elements into the surrounding environment. Both objectives simultaneously constituted the principal rationale for selecting the relative proportions of the individual components in the formulations intended for direct contact with soil.

The long-standing investigations conducted by the research team at AGH University of Krakow on vitreous fertilizer materials provided a fundamental basis for the compositional design of these sulfur-bearing glass matrices. These studies have demonstrated that:

- the SiO_2 content in glassy carriers of macro- and micronutrients typically ranges between 35 and 50 mol%, with higher concentrations – approximately 60 mol% – resulting in significantly reduced reactivity in soil environments [95,274];
- the chemical reactivity of such materials tends to increase with rising P_2O_5 and K_2O contents [185,275];
- even slight variations in the mutual quantitative ratios of the principal glass constituents—SiO_2, P_2O_5, CaO, and MgO – can induce pronounced changes in their dissolution behaviour [185,276];

However, it must be emphasized that, in line with the central aim of this dissertation – namely, to assess the influence of sulfur incorporation on the properties of silicate-phosphate glasses – the compositional variability of the remaining components was deliberately minimized. Accordingly, fixed concentrations of SiO_2, K_2O, and the alkaline earth modifiers MgO and/or CaO were maintained. Moreover, drawing on evidence suggesting that an increase in phosphorus content has a more pronounced effect (as compared to potassium) on enhancing the release of glass constituents into solution [275], two distinct P_2O_5 concentrations were selected. The phosphate content was adjusted at the expense of the total amount of alkaline earth oxides (MO). Within each compositional series characterized by a fixed phosphate level (6P or 10P), the nature of the MO-type oxide was systematically varied, guided by prior indications that the specific identity of this modifier may significantly influence the sulfur-loading capacity of the tested glasses [261]. The nominal chemical compositions of the sulfur-encapsulating glass matrices are presented in Tab. 5.

Tab. 5. Chemical composition of silicate–phosphate glasses being the subject of present thesis [mol%].

System	SiO_2	P_2O_5	K_2O	MgO	CaO
	Molar content of oxides [%]				
6PM	41	6	20	33	–
6PC	41	6	20	–	33
6PMC	41	6	20	16.5	16.5
10PM	41	10	20	29	–
10PC	41	10	20	–	29

10PMC	41	10	20	14.5	14.5

Sulfur was introduced into the previously defined silicate-phosphate matrices in progressively increasing amounts, based on the initial assumption that this component would be added in concentrations of 0, 1, 3, and 5 mol%. As such, sulfur was incorporated in excess relative to the remaining constituents, whose total molar fraction was fixed at 100%, in order to evaluate the maximum sulfur capacity of the materials—understood as the highest sulfur content that remains dissolved after controlled heating and melting, without the formation of crystalline sulfate-bearing phases [259].

Throughout this dissertation, the sample nomenclature follows a consistent pattern denoted by the general formula *XS_YP*, where *X* represents the nominal molar content of sulfate sulfur introduced into the glass batch (0, 1, 3, or 5 mol%), while *Y* indicates the molar percentage of P_2O_5 (either 6% or 10%). This designation is further supplemented by a letter – *M*, *C*, or *MC* – which specifies the type of alkaline earth oxide modifier used, thereby distinguishing the different glass series from one another. For instance, a sample labelled *3S_6PMC* corresponds to a glass containing 6 mol% P_2O_5 and both types of MO oxides (MgO and CaO), modified with 3 mol% SO_3:

$$\underbrace{3S}_{\substack{3\ mol.\\ \%\ SO_3}} _ \underbrace{6P}_{\substack{6\ mol.\\ \%\ P_2O_5}} \underbrace{MC}_{\substack{MgO\\ CaO}}$$

7 Experimental Design

The materials constituting the subject of the present thesis were synthesized using a conventional high-temperature melting technique in a chamber-type laboratory electric furnace (Nabertherm). Each glass batch – formulated according to the compositional systems outlined in Chapter 6 (*Tab. 5*) – was prepared from analytically pure (p.a. grade) reagents supplied by Chempur Polska, specifically:

- Silicon dioxide (SiO_2);
- Diammonium hydrogen phosphate ($(NH_4)_2HPO_4$);
- Potassium carbonate (K_2CO_3);
- Magnesium oxide (MgO);
- Calcium carbonate ($CaCO_3$);
- Potassium sulfate (K_2SO_4).

The optimal melting temperature for the synthesized compositions was determined by means of high-temperature microscopy (HSM), which enabled the identification of thermal transitions relevant to melting behaviour of the prepared mixtures. Based on the obtained results, all melting processes were conducted at a fixed maximum temperature of 1450 °C. The complete heating profile developed for the glass synthesis is illustrated in Fig. 22:

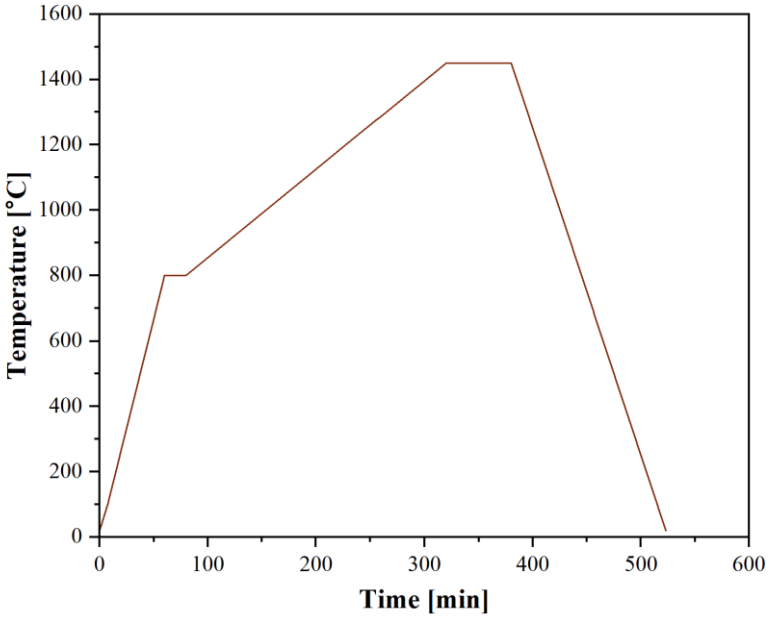


Fig. 22. Heating schedule applied for the preparation of the studied glass compositions.

After melting, the resulting batches were cooled using two distinct methods: pouring onto a metal plate and quenching in cold water to obtain frit. The rationale for employing both approaches, together with a detailed description of each cooling route and the corresponding characteristics of the resulting samples, is discussed in the subsequent chapters of this thesis.

Following synthesis, the obtained glassy materials were subjected to a comprehensive characterization using a wide range of analytical techniques. a detailed account of the methodologies employed is provided in publications **P1**–**P4**, while a summary of the applied procedures is compiled in Tab. 6.

Tab. 6. Overview of analytical techniques applied in the study.

Analytical Method	Purpose of Measurement	Instrument / Software	Measurement Conditions	Data Analysis and Processing
X-ray Diffraction (XRD)	Verification of the amorphous nature of the materials; identification of crystalline phases in devitrified samples	X'Pert Pro MD PANalytical / Highscore Plus software	Bragg–Brentano geometry, 2θ = 10–70°, step size: 0.008°	Verification of the presence of amorphous halo; phase identification via PDF-4+ 2018 database; assignment of reflexes; correlation with thermal events
	Interpretation of thermal effects' origin	PANalytical Empyrean + Anton Paar HTK 1200N (for in situ heating) /	in situ heating from 25°C to 600°C with 100°C increments (25–500°C), and	

		Highscore Plus software	50°C increment (550–600°C)	
X-ray Fluorescence (XRF)	Determination of the chemical composition of obtained materials	ARL Advant'XP Spectrometer / Omnian (standardless analysis)	WDXRF Axios mAX spectrometer equipped with a 4 kW Rhodium (Rh) X-ray tube; normalization of glass compositions to 100%	Comparison of experimental and nominal compositions
Scanning Electron Microscopy with Energy Dispersive X-ray Spectroscopy (SEM-EDS)	Assessment of as-synthesised samples' homogeneity; evaluaton surface microstructure before and after interaction with soil media; elemental analysis (spot measurements)	FEI Nova NanoSEM 200 equipped with EDAX EDS system	High-vacuum mode; backscattered electron (BSE) detector; carbon coating; accelerating voltage: 18 kV	SEM image analysis with EDS spectra; qualitative and semi-quantitative chemical composition analysis (standardless)
Differential Scanning Calorimetry (DSC)	Analysis of thermal properties as a function of sulfate content; determination of thermal stability parameters (GSA)	NETZSCH STA 449 F3 Jupiter (heat flux DSC mode) / Netzsch Proteus software	31 mg powdered samples (grain size: 0.1–0.3 mm); heating rate: 10 °C/min in dynamic air (80 mL/min); reference: Al_2O_3	Analysis of DSC curves; determination of characteristic temperatures (T_g, T_x, T_c, T_m) using Proteus software
Raman Spectroscopy	Structural analysis of the obtained materials; Structural analysis of the materials after exposition to corrosive media	WITec Alpha 300 M+ spectrometer / Opus / Fityk / Origin software	488 nm laser; 1800 grating; 4 accumulations × 20 s; Zeiss LD EC Epiplan 50× objective	Baseline correction (Savitzky–Golay); spectral deconvolution (Gaussian/Lorentzian); Raman mapping (phase distribution)
Mid-Infrared Spectroscopy (MIR)	Structural analysis of the obtained materials	Bruker Vertex 70v vacuum spectrometer / OPUS software	Pellet technique; 128 scans; resolution: 4 cm^{-1}; spectral range: 400–4000 cm^{-1}	Spectral deconvolution via Levenberg–Marquardt algorithm (initial Gauss–Lorentz ratio = 0.5); RMS noise < 0.1 after curve fitting

^{29}Si and ^{31}P MAS-NMR Spectroscopy	Structural analysis of the obtained materials	APOLLO Console (Tecmag) / Origin software	MAS technique; magnetic field: 7 T; spinning frequency: 4–6 kHz	Spectral deconvolution using Gaussian/Voigt functions
X-ray Absorption Spectroscopy (XAS)	Structural analysis of the glass and devitrified samples	PEEM/XAS beamline (SOLARIS National Science Centre) / PyMca, Athena, Origin software	Total electron yield (TEY) mode	Comparative spectral analysis; 'fingerprint method' based on literature data
		XAFS beamline (ELETTRA, Trieste, Italy / PyMca, Athena, Origin software	Fluorescence mode	
Inductively Coupled Plasma–Atomic Emission Spectroscopy (ICP-AES)	Quantitative determination of nutrient release in 'in vitro' dissolution tests	Perkin Elmer Optima Plasma 40	Analysis of leachates using inductively coupled plasma–atomic emission spectrometer	Comparison of nutrient concentrations in leachates vs. original glass composition

Additionally, Tab. 7 provides an overview of the laboratories where the respective investigations were carried out.

Tab. 7. Overview of the laboratories and research facilities where the measurements were performed.

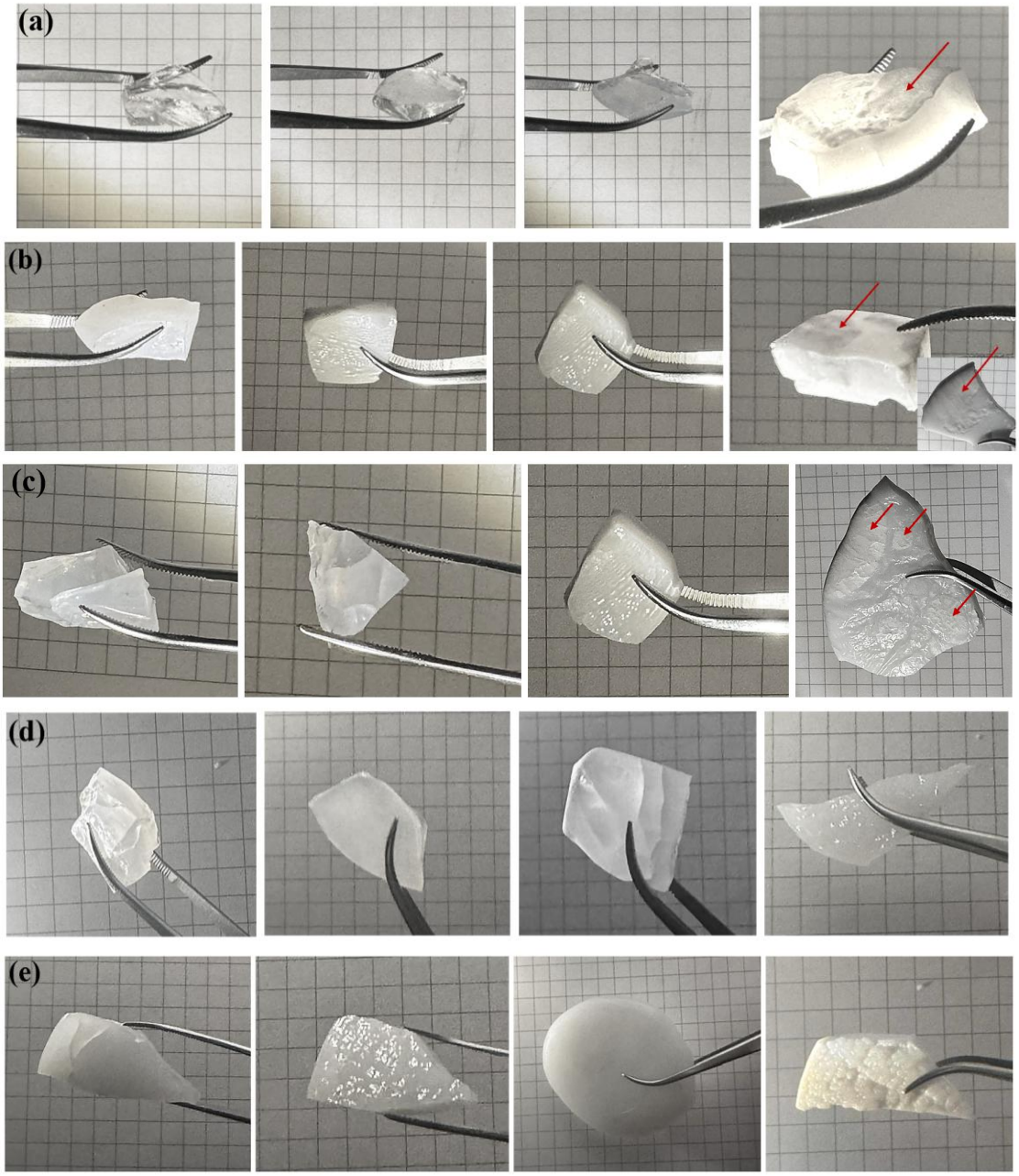
Analytical Method	Laboratory
X-ray Diffraction (XRD)	Faculty of Materials Science and Ceramics, AGH University of Science and Technology, Department of Ceramics and Refractories, X-ray Diffraction Laboratory
X-ray Fluorescence Spectroscopy (XRF)	Faculty of Materials Science and Ceramics, AGH University of Science and Technology, X-ray Diffraction and Fluorescence Laboratory Chemical Laboratory of FERROCARBO Ltd.
Scanning Electron Microscopy (SEM)	Faculty of Materials Science and Ceramics, AGH University of Science and Technology, Laboratory of Scanning Electron Microscopy and Microanalysis
Raman Spectroscopy	Faculty of Materials Science and Ceramics, AGH University of Science and Technology, Infrared Structural Research Laboratory
Fourier-Transform Infrared Spectroscopy (FTIR)	Faculty of Materials Science and Ceramics, AGH University of Science and Technology, Infrared Structural Research Laboratory

Solid-State Nuclear Magnetic Resonance Spectroscopy (MAS-NMR)	Institute of Catalysis and Surface Chemistry, Jerzy Haber Institute of the Polish Academy of Sciences
X-ray Absorption Spectroscopy (XAS)	National Synchrotron Radiation Centre SOLARIS, Jagiellonian University in Kraków Elettra Synchrotron Radiation Facility, Trieste, Italy
Differential Scanning Calorimetry (DSC)	Faculty of Materials Science and Ceramics, AGH University of Science and Technology, Laboratory of Thermal Analysis
Inductively Coupled Plasma Optical Emission Spectrometry (ICP-OES)	Faculty of Geology, Geophysics and Environmental Protection, AGH University of Science and Technology, Accredited Hydrogeochemical Laboratory of the Department of Hydrogeology and Engineering Geology

8 Results and discussion

8.1 Visual inspection of acquired materials

All synthesized materials, representing the full range of tested chemical compositions, were subjected to high-temperature processing and the resulting melts were then cast into disk-shaped pellets and cooled to room temperature by direct contact with a metal plate. The obtained samples are shown in Fig. 23.(a)-(f), arranged from left to right in order of increasing sulfur content in their nominal composition: 0S → 1S → 3S → 5S.



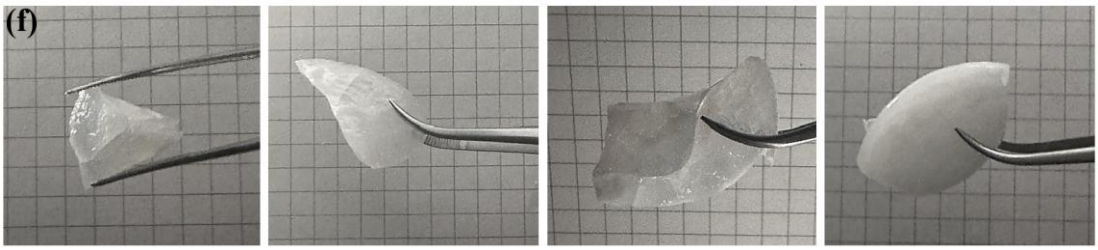


Fig. 23. As-synthesised samples representing all the designed glass systems, arranged from left to right in order of increasing sulfur content in their nominal composition: 0S → 1S → 3S → 5S: XS_6PM (a); XS_6PC (b), XS_6PMC (c), XS_10PM (d), XS_10PC (e), XS_10PMC (f). The surface sulfate phase is marked with a red arrow.

Even a preliminary visual inspection of the materials, carried out with the unaided eye, suggests that most of the samples exhibit a glass-ceramic character. Only those compositions in which MgO was the sole alkaline earth oxide modifier appeared to display optical transparency, which, particularly in the system containing a lower amount of phosphorus pentoxide (XS_6PM), gradually transitioned into translucency (3S_6PM), and subsequently into opacity (5S_6PM), indicating a progressive reduction in visible light transmittance with increasing SO_3 content (Fig. 23.(a)). a similar trend of decreasing light permeability upon sulfur incorporation was also observed in the remaining systems, all of which already exhibited partial optical translucency in their base glass form.

Notably, none of the obtained materials displayed amber discoloration, which is often considered an initial visual indicator of reduced sulfur species [264]. Interestingly, even this straightforward visual assessment offers preliminary insight into the sulfur-loading capacity of the glass matrices, defined – as previously noted – as the maximum amount of sulfur that can be incorporated into the vitreous network without inducing the crystallization of a sulfur-bearing phase. In the majority of reported cases, the literature identifies this phase as a surface-localized sulfate salt layer, which, owing to its lower density relative to the bulk glass, tends to segregate near the outer regions of the final material [242,244,259,277,278]. Indeed, closer observation of the sample surfaces, particularly those within the series characterized by a lower phosphate content (6P), reveals the formation of a distinct surface layer in compositions with higher nominal sulfur contents. This phenomenon is clearly visible in the 5 mol% SO_3 sample of the XS_6PM series and already apparent in the 3 mol% SO_3 samples within the XS_6PC and XS_6PMC systems, as illustrated in Fig. 23. It is important to emphasize, however, that such surface phase separation was observed exclusively in the low-phosphate [6P] series. In contrast, the surface appearance of the samples belonging to the higher-phosphate [10P] family remained consistent with the samples' volumes, with no evidence of surface phase development, as shown in Fig. 23.

8.2 Control of the chemical composition of the synthesised materials

In order to verify the consistency between the intended chemical composition of the designed materials and their actual molar contents, X-ray fluorescence analysis was carried out. The obtained results are summarized in Tab. 8, which presents both the nominal compositions (highlighted in grey) and those measured experimentally via XRF.

Tab. 8. Nominal (in grey) and XRF-determined chemical compositions of the synthesized materials.

Sample	SiO_2	P_2O_5	K_2O	MgO	CaO	SO_3
XS_6PM	41	6	20	33	–	0-5
0S_6PM	36.58	6.97	30.60	22.38	–	–
1S_6PM	35.40	7.09	33.13	20.02	–	1.04
3S_6PM	38.17	7.08	27.61	25.94	–	2.16
5S_6PM	34.67	6.56	32.02	21.70	–	5.88
XS_6PC	41	6	20	–	33	0-5
0S_6PC	30.07	5.04	19.97	–	41.01	–
1S_6PC	26.06	4.65	19.84	–	46.27	0.91
3S_6PC	32.07	5.49	19.58	–	41.83	1.91
5S_6PC	27.61	4.80	20.80	–	43.04	5.08
XS_6PMC	41	6	20	16.5	16.5	0-5
0S_6PMC	29.41	5.24	24.01	8.69	26.53	–
1S_6PMC	34.63	6.09	22.20	11.88	22.21	0.95
3S_6PMC	34.56	6.17	21.99	11.99	23.91	2.23
5S_6PMC	30.63	5.87	24.98	10.75	23.03	8.07
XS_10PM	41	10	20	29	–	0-5
0S_10PM	38.17	11.31	24.55	23.82	–	–
1S_10PM	37.74	11.41	25.05	23.87	–	0.20
3S_10PM	39.16	11.75	24.86	24.83	–	0.28
5S_10PM	39.51	11.87	25.82	25.13	–	0.37
XS_10PC	41	10	20	–	29	0-5
0S_10PC	33.29	9.80	20.30	–	34.71	–
1S_10PC	32.22	9.65	20.53	–	35.73	0.35
3S_10PC	35.48	9.83	20.43	–	32.21	0.39
5S_10PC	33.85	9.63	21.01	–	34.03	0.51
XS_10PMC	41	10	20	14.5	14.5	0-5
0S_10PMC	34.76	10.28	23.10	9.43	20.86	–
1S_10PMC	34.48	10.39	23.20	10.03	20.80	0.18
3S_10PMC	33.74	10.32	24.63	8.90	23.47	0.36
5S_10PMC	35.20	10.60	24.60	9.87	22.21	0.56

A comparison of the theoretical and experimentally determined values for individual glass components reveals several discrepancies, which may be attributed to a variety of factors. Significant deviations in the molar contents of SO_3 can largely be explained by the high volatility of this component, as well as the dependency of its incorporation on the equilibrium established with gaseous SO_2 during melting. This primarily accounts for the systematically lower-than-expected SO_3 levels in most samples. Conversely, the presence of excess SO_3 observed in some of the 5S-type compositions can be attributed to sulfate salt precipitation phenomena – an issue that will be explored in greater detail in Section 8.4) In contrast, the origins of discrepancies in the contents of other components are less readily explained and remain largely speculative. One possible contributing factor is the interaction between the molten glass and the ceramic crucibles during synthesis at high temperatures (1450°C), which may promote bidirectional diffusion processes (i.e.,

crucible ↔ melt). Moreover, potential errors related to the analytical method itself – such as calibration issues or software-based interpretation limitations within the Omnian processing suite – cannot be entirely ruled out. Nevertheless, it is generally accepted that the influence of such technical factors alone is unlikely to account for the magnitude of the discrepancies observed. Given the pronounced tendency of the synthesised materials to undergo surface crystallization – particularly the segregation of phosphate and sulfate phases in peripheral regions of the samples – it is plausible that the primary cause of the observed deviations lies in elemental inhomogeneity within the bulk. In such cases, the analysed fragments may not accurately reflect the average composition of the entire sample, thereby undermining the reliability of the results.

Considering the critical importance of precisely determining the chemical composition of potential sulfur-bearing glass carriers—particularly in the context of evaluating their chemical reactivity—a decision was made to repeat the compositional analysis for a subset of selected materials, specifically those intended for bioactivity studies in soil and biological environments. The results of this targeted reanalysis will be presented in the subsequent chapters of this dissertation.

8.3 Verification of the amorphous nature of the acquired samples

To precisely assess the amorphous nature of the synthesized materials, all samples were subjected to X-ray diffraction analysis. The resulting diffractograms are compiled in Fig. 24.

The obtained diffraction patterns corroborate the preliminary conclusions drawn from visual inspection—only the system containing reduced P_2O_5 content and modified exclusively with MgO from the family of alkaline earth oxides exhibited complete amorphicity, with one exception: in the sample labelled 5S_6PM, a distinct surface layer was detected, corresponding to crystalline potassium sulfate (Fig. 23.(a), Fig. 24.(a)). Despite the high degree of transparency observed in samples of the XS_10PM system, all compositions within this series were found to possess a glass-ceramic character, with $KMgPO_4$ crystallites identified within the glass matrix (Fig. 24.(d)).

It is similarly unsurprising that the XS_6PC and XS_6PMC systems, which displayed progressive loss of transparency – from initial translucency to full opacity with increasing sulfur content – exhibited partial crystallinity. Within these matrices, the presence of the double phosphate phase $KCaPO_4$ was confirmed, accompanied by K_2SO_4 crystallites at sulfur contents of 3 mol% and above (Fig. 24.(b) and Fig. 24.(c)). Crystalline phosphate phases were also detected in samples representing the XS_10PC ($KCaPO_4$) and XS_10PMC ($KCaPO_4$ and $KMgPO_4$) systems, as shown in Fig. 24.(e) and Fig. 24.(f). Notably, no traces of potassium sulfate were identified in any of the glasses belonging to the higher-phosphate [10P] series.

Based on the diffractograms presented in Fig. 24, which clearly demonstrate the glass-ceramic nature of the majority of the synthesized samples, it can be confidently stated that the tendency of the designed materials to undergo spontaneous crystallization during cooling is influenced primarily by three factors:

- the concentration of P_2O_5 in the glass matrix;
- the type of alkaline earth oxide modifier employed (MgO / CaO / MgO + CaO);
- the amount of SO_3 introduced.

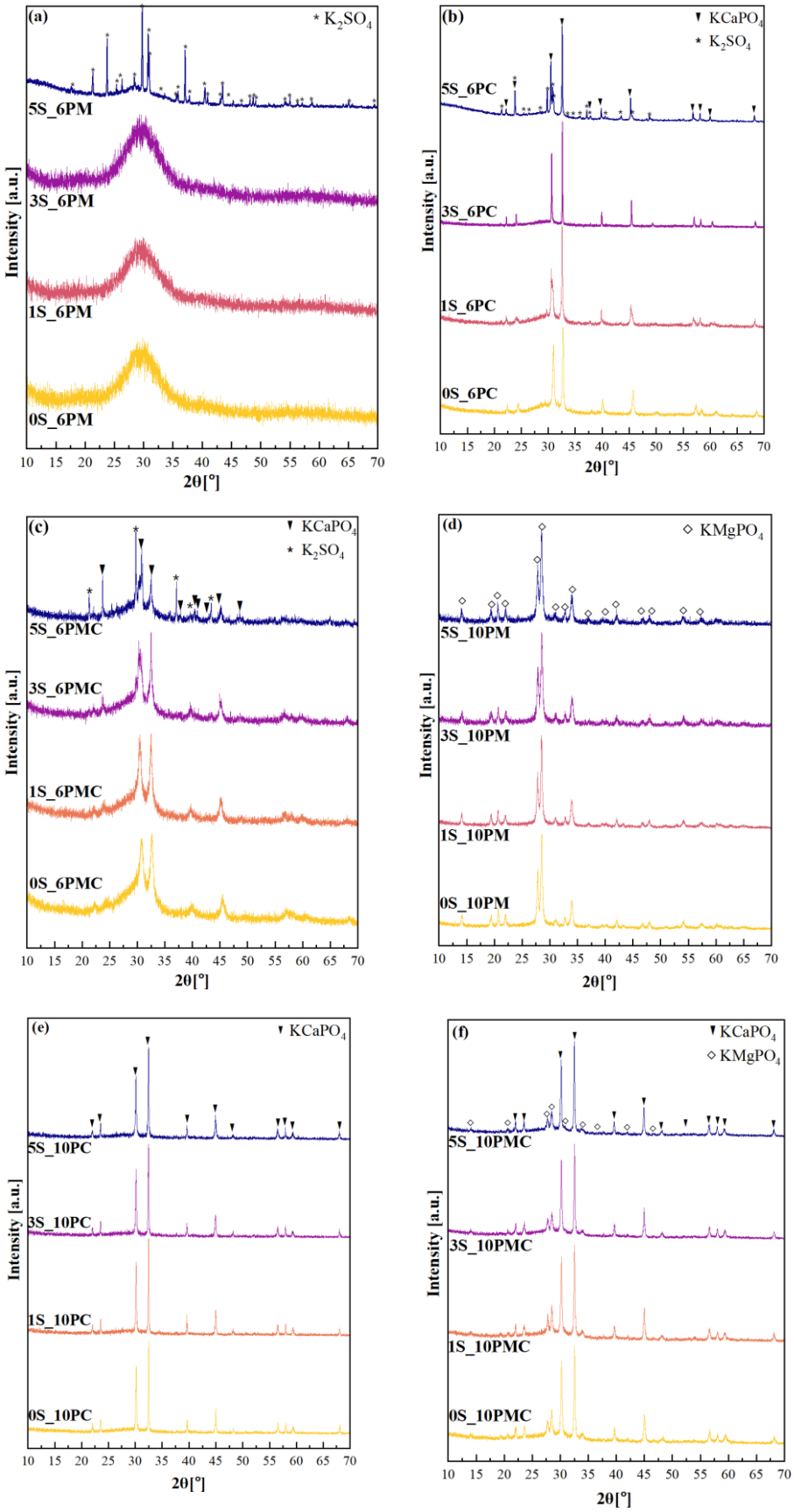


Fig. 24. Diffractograms of samples representing all studied systems (K_2SO_4, ref: 00-044-1414; $KCaPO_4$, ref: 00-033-1002; $KMgPO_4$, refs: 00-050-0149 / 00-050-0151, identified in the XS_10PMC system) [279–281].

The influence of the first factor is particularly evident in the appearance of sharp and well-defined diffraction peaks with high intensity in samples from the [10P] series, in contrast to their low-phosphate counterparts. As previously discussed in the literature review section of this dissertation (Section 3.3.3), this phenomenon likely stems from the intrinsic tendency of phosphates to separate from the silica-rich phase and form orthophosphate domains enriched in network-modifying cations. In Hench-type bioactive glasses, such behaviour was reported to occur when the P_2O_5 content exceeded 12 mol%, whereas in compositions with lower phosphate levels, these domains remained too sparse and poorly developed to induce phase separation [152,188]. This behaviour can be explained by the higher ionic field strength of P^{5+} compared to Si^{4+}, which leads to a preferential association of modifier cations such as Ca^{2+} and Mg^{2+} with the former. The resulting depletion of modifiers in the silica-rich network favours the crystallization of calcium or magnesium orthophosphate phases rather than silicate ones [282]. Although no additional amorphous halo – commonly considered a hallmark of phase separation – was observed in the XRD patterns of the analysed samples, it may nonetheless be inferred that the stronger interaction between modifier cations and P^{5+} ions contributed to the clustering of phosphate-rich regions. This, in turn, promoted the spontaneous formation of crystalline $KCaPO_4$ and $KMgPO_4$ phases, as confirmed by diffraction analysis.

The type of MO-type oxide used also appears to significantly affect the propensity for spontaneous crystallization during melt cooling. Analysis of diffraction peak intensities and background levels suggests that this tendency increases with the CaO content in the glass composition. This may be interpreted in light of the distinct structural roles of MgO and CaO, as outlined in the literature. While CaO acts strictly as a network modifier, promoting depolymerization of the glass structure, the role of MgO is more nuanced and likely concentration-dependent. In certain proportions, MgO behaves as a conventional modifier, but in others, it may participate as a partial glass former, possibly adopting tetrahedral coordination [202,283,284].

Although this aspect will be discussed in more detail in a subsequent chapter, the aforementioned distinction helps rationalize the observed behaviour. The inclusion of CaO likely results in a significant reduction in melt viscosity compared to glasses modified with MgO alone – a hypothesis supported by direct observations of the melt behaviour during quenching – and thus facilitates the rearrangement of melt constituents into crystalline phases. In systems incorporating both MgO and CaO, an additional factor promoting crystallization may be the increased compositional complexity of the melt – a well-known and effective strategy for suppressing long-range ordering. The resultant structural disorder hinders the alignment of constituent ions into an ordered lattice, thereby impeding crystal growth.

Furthermore, based on the progressively reduced visible-light transmittance – manifesting first as increased translucency and then as full opacity with rising sulfur content (Fig. 23) – as well as the declining background intensity in the diffraction patterns of the corresponding samples (especially pronounced in the [6P] series), one may also infer the influence of sulfate concentration on the crystallization tendency of the glasses. If sulfates incorporated into the structure are regarded as heterogeneous nuclei, their presence would significantly lower the energy barrier for crystal growth, allowing nucleation to proceed more readily at pre-existing interfaces – and explaining the observed increasing number of reflections attributed to the presence of crystalline phases within the studied materials (Fig. 24).

8.4 Sulfate capacity of the obtained materials

Based on the XRF results, a comparative diagram was constructed, in which the columns represent the actual SO_3 content measured in the synthesized materials across all investigated systems, while the horizontal lines indicate the nominal amounts of sulfate introduced into the respective glass batches – namely, 1, 3, and 5 mol% (Fig. 25).

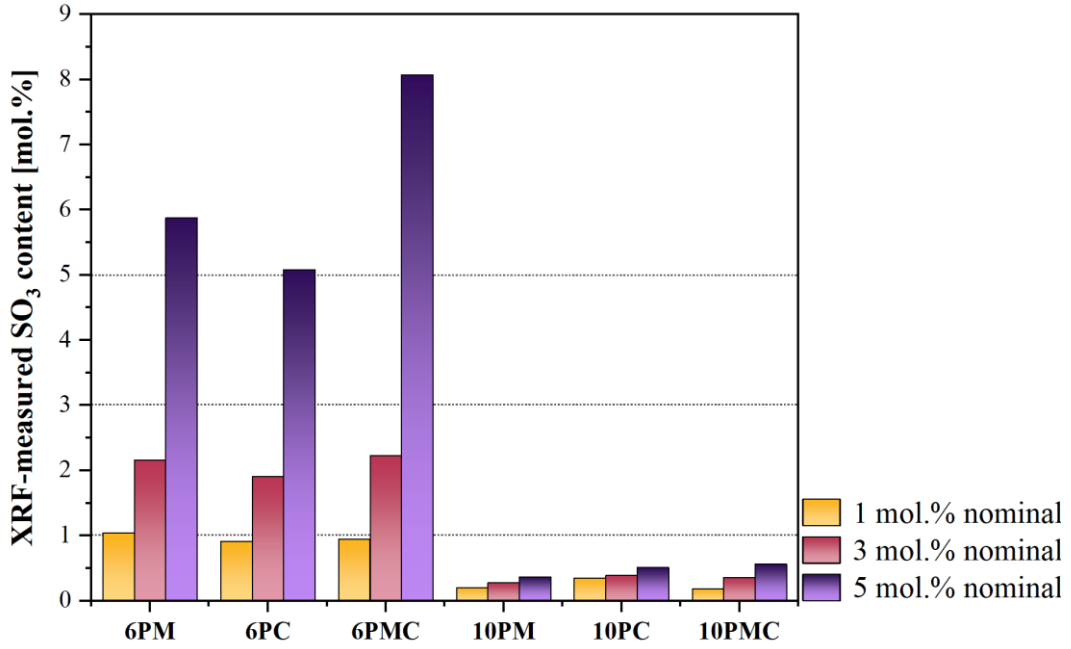


Fig. 25. Comparison of the sulfate retention capacities of samples representing all designed glass compositions.

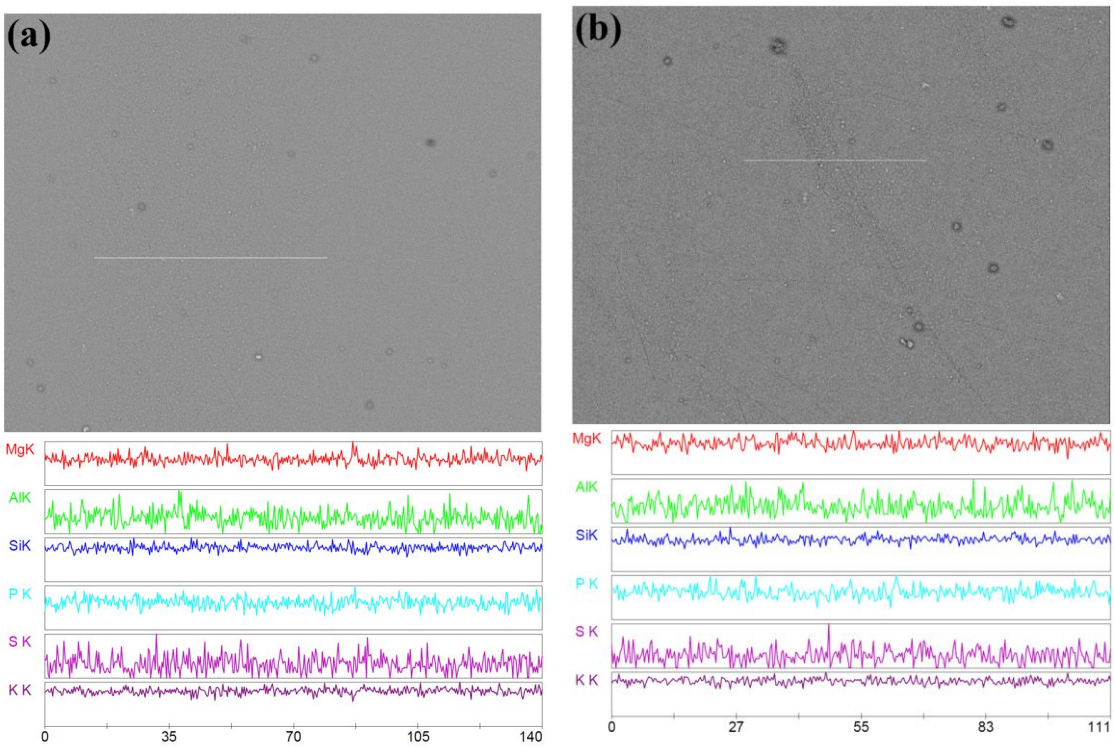
Taking into account the initial visual observations of the obtained materials, the XRD data, and the XRF results presented above, one may reasonably conclude that the sulfur incorporation threshold for the [6P]-type systems is defined by a nominal SO_3 content of 3 mol% for the XS_6PM composition, and 1 mol% for the XS_6PC and XS_6PMC systems. Beyond these values, the precipitation of a crystalline potassium sulfate layer – responsible for binding the excess sulfur—was observed not only with the unaided eye but, more importantly, confirmed by XRD analysis.

The presence of this surface K_2SO_4 layer in samples doped with the highest amounts of SO_3 provides a plausible explanation for the XRF-detected sulfur contents that exceed the nominal values in [6P] compositions. Since the crystalline sulfate phase accumulates at the surface, the uneven distribution of sulfur across the bulk volume leads to an artificial overestimation of its content in localized areas subjected to XRF analysis. By contrast, the glasses representing the higher-phosphate [10P] series exhibited a markedly lower capacity to incorporate sulfate species: in none of the examined compositions did the SO_3 content exceed 0.6 mol% (Fig. 25). Given that no sulfate-rich surface layer was observed on any of these materials (Fig. 23.(e), (f)), it remains unclear whether the measured 0.6 mol% marks the actual sulfate saturation limit of these systems. Nevertheless, in view of the high degree of crystallinity observed in the [10P] glasses and the consistently low levels of incorporated sulfur – rising only marginally with increasing sulfate addition – further attempts to introduce higher SO_3 contents into this family of materials were discontinued.

Considering the outcomes of the preliminary analyses and bearing in mind one of the central objectives of this work – namely, the development of fully amorphous sulfur-bearing glass carriers – only the XS_6PM system was selected for continued investigation. The remaining compositions, which exhibited a pronounced tendency toward spontaneous crystallization, were excluded from further study. Accordingly, the selected system was subjected to in-depth structural and physicochemical characterization, the results of which are presented in the subsequent subsections.

8.5 Homogeneity of the acquired materials

In light of the preliminary indications of compositional inhomogeneity suggested by the XRF results, the first step of the in-depth characterization involved examining the elemental distribution across the selected glass system using Scanning Electron Microscopy. Elemental mapping was performed on polished cross-sections of the samples, and the resulting distributions are presented in Fig. 26.



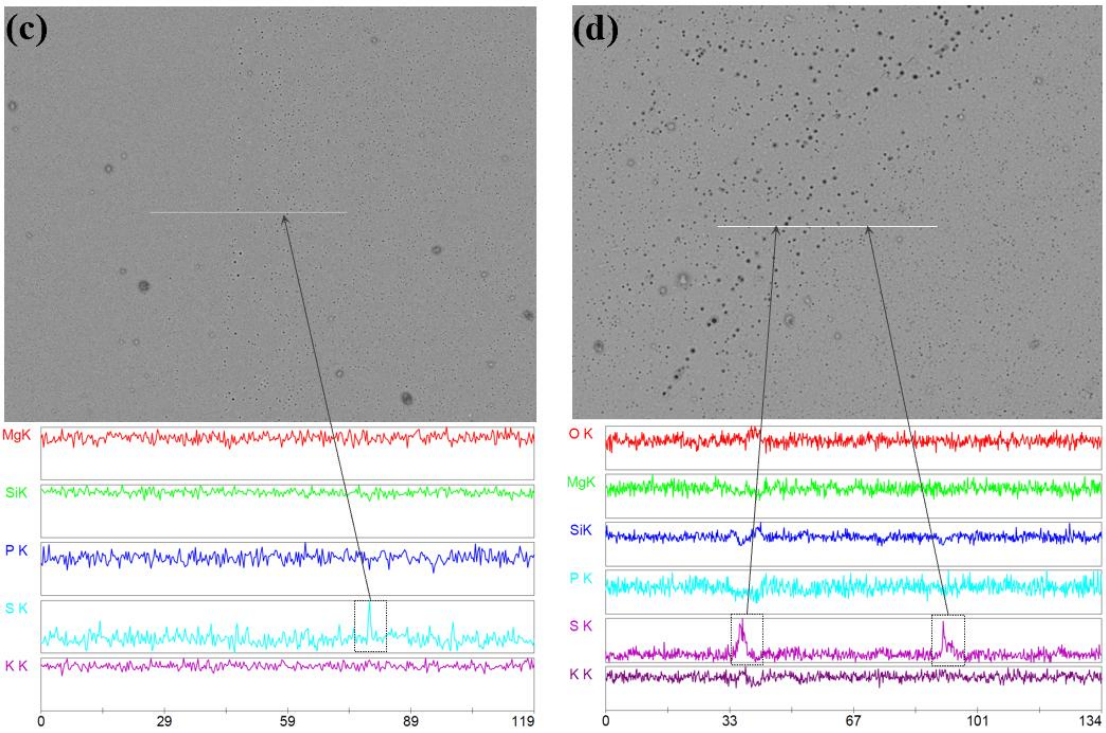


Fig. 26. Elemental distribution maps collected for samples: 0S_6PM (a); 1S_6PM (b); 3S_6PM (c); and 5S_6PM (d), at 1000× magnification, 18.00 kV. Notably, although sulfur has not been detected in the 0S sample, trace amounts may be present; the sulfur content plot is included due to measurement settings.

Analysis of the surface features and, in particular, the elemental maps, indicates a generally homogeneous distribution of glass-forming and modifying oxides across the examined scale of several hundred micrometres. In all cases, the weight percentages of silicon, phosphorus, potassium, and magnesium exhibit only minimal deviations from their respective average values (Fig. 26). The only exception appears to be sulfur—in glasses with elevated SO_3 content, localized regions enriched in this component can be observed, which coincide with a slight increase in potassium content, most notably in the 5S sample, and a corresponding depletion in other glass components. Nonetheless, these regions do not differ in surface morphology from the surrounding matrix (Fig. 26.(c), (d)).

Upon examining the micrographs presented above, it is imperative to highlight two notable features discernible on the surfaces of the investigated materials: specifically, in the surface regions of samples 0S and 1S, distinct bright, spheroidal domains appear to be embedded within the surrounding matrix (Fig. 26. (a), (b)). These spherical formations are absent in the samples containing higher sulfur content – namely, 3S and 5S – where instead, surface features indicative of residual gas bubbles formed during high-temperature melting reactions are clearly observed (Fig. 26 (c), (d)).

In order to further elucidate the nature of these surface heterogeneities, the analysis was extended using higher magnification (5000x) combined with energy-dispersive X-ray spectroscopy, enabling a semi-quantitative estimation of oxide concentrations at selected locations. The corresponding SEM micrographs, along with the EDS spectra recorded at specific surface points, are compiled in Fig. 27.(a)-(d).

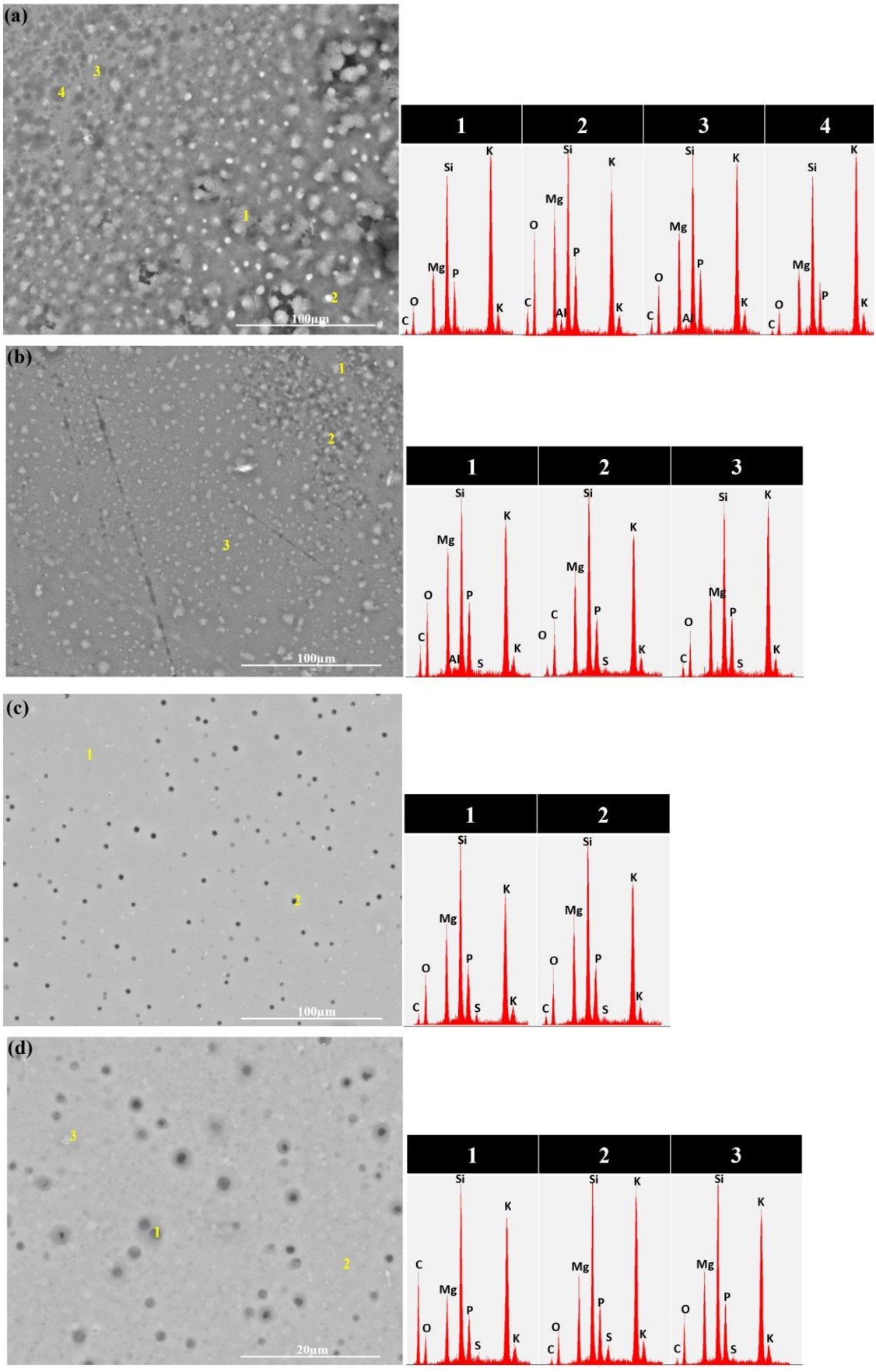


Fig. 27. SEM micrographs and corresponding EDS spectra acquired at selected surface points of the 0S_6PM (a), 1S_6PM (b), 3S_6PM (c), and 5S_6PM (d) samples.

These high-magnification observations indeed corroborate the hypothesis of compositional inhomogeneities in the form of micron-scale bright spherical areas, approximately 1–2 μm in diameter, observed in both the base sample and the one with 1 mol% sulfur addition (Fig. 27. (a), (b)). EDS analysis of these regions (points 1 and 2 for samples 0S_6PM and 1S_6PM, respectively) revealed a locally elevated presence of phosphorus and magnesium, in contrast to point 3 in each sample, where the composition more closely aligns with the nominal glass formulation. Additionally, slightly darker regions enriched in silicon and potassium were identified at points 2 and 4 on the surfaces of samples 0S and 1S_6PM, respectively (Fig. 27. (a), (b)).

Intriguingly, such micro-scale compositional heterogeneities were no longer detectable on the surfaces of the samples with 3 and 5 mol% sulfur loading, instead – residual gas bubbles, remnants of degassing events likely triggered during melting, start to become visible (Fig. 27. (c), (d)). EDS spectra collected from the bubble-containing regions (points 2 and 1 for samples 3S and 5S, respectively) showed no significant deviations from the bulk composition, as confirmed by reference points 1 and 3 in each case. The only compositional irregularity noted in the sulfur-enriched samples was the emergence of localized domains significantly enriched in sulfur, exemplified by point 2 on the surface of sample 5S_6PM, nevertheless, as previously discussed in the context of surface elemental mapping, these sulfur-rich regions are morphologically indistinct from the rest of the surface (Fig. 27.(d)).

The observed trend of diminishing microheterogeneity and enhanced compositional uniformity with increasing sulfate content may be attributed to the well-documented refining behaviour of sulfate species in glass melts—a phenomenon widely exploited in industrial glass technology. Sulfates function as refining agents whose principal role is to eliminate gas bubbles during the production of container or float glass, while also promoting improved melt homogenization. To mitigate secondary bubble formation during the fining process, the addition of a reducing agent to the batch is commonly practiced, enabling reaction with excess sulfate [285,286]. However, since no such reductant was incorporated in the synthesis of the materials examined in this study, residual gas inclusions—particularly in the 3S and 5S samples—bear witness to the degassing events triggered by elevated sulfate concentrations [287]. Despite this, the homogenization of the glass matrix is clearly manifested by the absence of detectable micro-scale inhomogeneities on the examined surfaces. Interestingly also, literature reports affirm the beneficial role of sulfates in enhancing the melting efficiency of glass. For instance, sodium sulfate is known to accelerate the melting of Na–Ca–Si glass by promoting the formation of low-melting eutectic phases, thus lowering the liquidus temperature by approximately 40–50°C compared to conventional soda-lime batches [286].

Microscopic examination of the studied materials reveals that, despite their fully amorphous character confirmed via X-ray diffraction, the samples exhibit a clear tendency toward spatial organization into distinct domains – some enriched in phosphorus and magnesium, and others, though less pronounced, enriched in silicon and potassium. In samples containing the highest sulfate concentrations, point-like regions exhibiting markedly elevated sulfur levels were also identified. While these sulfur-rich zones are morphologically indistinct, it is reasonable to propose the existence of sulfate-based compositional domains at a much finer scale than the phosphate- or silicate-enriched areas described above. The emergence of such partially ordered domains is a well-recognized

phenomenon in glass science. As noted in the introduction, glasses inherently display nano- to submicron-scale structural heterogeneities, which are believed to play a pivotal role in nucleation events and early-stage crystallization processes [288]. Moreover, a growing body of research suggests a strong correlation between the nature of crystalline phases precipitated during thermal treatment and the characteristics of the precursor domains or clusters exhibiting a degree of order extending beyond individual coordination polyhedra (such as [SiO_4] or [PO_4]) [289,290].

Given the aforementioned observations—along with the established thermal instability of several other designed compositions and their pronounced tendency to crystallize during melt quenching on a metallic plate—a detailed thermal analysis of selected XS_6PM samples was undertaken. The thermal stability of glasses, understood as their resistance to devitrification, is of paramount importance from a processing perspective, as it informs the risk of spontaneous crystallite precipitation and defines the range of the glass-forming region. Crucially, the characteristic temperatures derived from differential scanning calorimetry – namely, the glass transition temperature (T_g), the crystallization onset (T_x), the crystallization peak (T_c), and the melting point (T_m) – are known to be highly sensitive to even subtle variations in glass composition [291]. Consequently, the influence of progressive sulfate addition on the XS_6PM system can be effectively monitored through systematic shifts in these thermal events as observed in the corresponding DSC curves.

8.6 Analysis of thermal behaviour of the samples representing the XS_6PM system

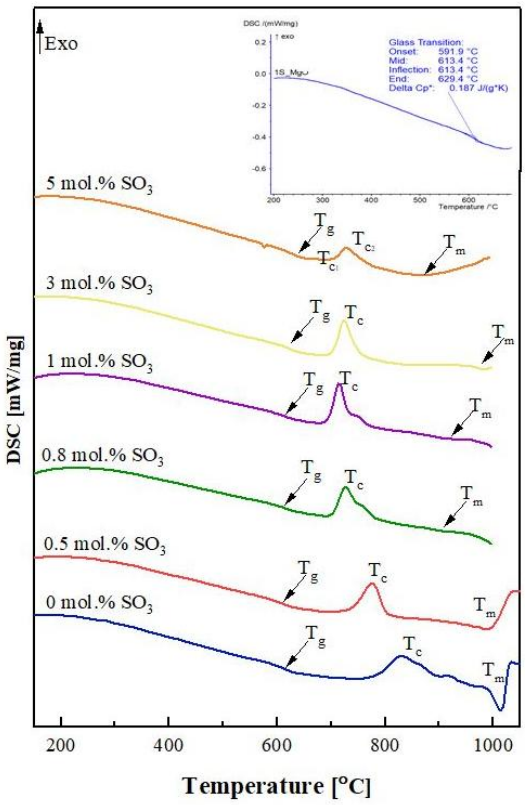


Fig. 28. DSC curves of the sulfate-free and sulfate-bearing glasses from the MgO-system recorded at a heating rate of 10°C/min. Upper-right corner: an exemplary determination of the glass transition temperature in the Proteus Software .

Indeed, as demonstrated by the acquired DSC curves of the samples representing the XS_6PM system, the effect of progressive sulfate addition into the structure of respective samples manifests itself through systematic changes in the positions of glass transition effect, endothermic (T_m) and exothermic peaks (T_c), as illustrated in Fig. 28, and summarized in Tab. 9. In order to enable a more nuanced and reliable interpretation of the thermal evolution induced by increasing sulfate loading, additional samples – specifically 0.5S_6PM and 0.8S_6PM – were synthesized and subjected to differential scanning calorimetry.

From the acquired data on thermal behaviour of the selected system several trends might be deduced. First and foremost, the glass transition temperature increases together with an increase in the sulfate content, while the range of vitreous state transformation ($T_{g_endset} - T_{g_onset}$) systematically decreases (Tab. 9).

Tab. 9. Thermal characteristic of tested samples from the XS_6PM system [279].

No.	Characteristic glass temperatures [°C]*						ΔH [J/g]
	T_g	T_g range	T_x	T_c	T_m	T_c range	
0S_6PM	614	35	785	831	1014	102	63.2
0.5S_ 6PM	612	35	737	776	987	63	64.9
0.8S_ 6PM	613	32	704	727	905	53	69.2
1S_ 6PM	613	37	696	715	919	38	67.2
3S_ 6PM	622	28	704	724	985	47	58.7
5S_ 6PM	636	19	704	728	875	63	32.8

Nevertheless, while the aforementioned tendencies are clearly perceptible, the magnitude of these changes remains relatively modest: a pronounced elevation in T_g, accompanied by a notable contraction of the transformation interval, does not become apparent until the SO_3 content reaches approximately 3 mol%. Although the close dependence of the glass transition temperature on composition is widely recognized, it is rather nuanced, being also influenced by glass thermal history and the cooling rate applied during melt quenching [292]. Above all, the T_g determined via DSC is markedly affected by the concentration and relative proportions of network modifiers to network formers – generally, an increase in the former tends to reduce the glass transition temperature in a near-linear fashion with respect to their molar fraction [292,293]. This behaviour can be rationalized by considering the polymeric nature of silicate-based oxide glasses, which consist of a disordered three-dimensional network of corner-sharing tetrahedra, interconnected via strong, ionic-covalent Si–O–Si bonds. The introduction of network-modifying cations disrupts this connectivity, rendering the network less rigid and thereby reducing the energy required for the transition from a solid to a viscoelastic state [165,184,191,292]. As the ratio of non-directional, predominantly ionic bonds increases at the expense of covalent linkages, the structure becomes more flexible, in contrast to the rigidity imparted by a highly polymerized, bonded network of high degree of covalence [165,191]. Consequently, T_g tends to rise in proportion to the degree of polymerization, as enhanced steric hindrance and limited chain mobility hinder structural rearrangements.

In light of these established correlations between network rigidity and glass transition phenomena, one might preliminarily hypothesize a gradual – albeit subtle – increase in the degree of polymerization accompanying the progressive incorporation of sulfur into the glass structure. This supposition is further supported by the highly covalent character of S–O bonds, which are known to augment network rigidity when introduced in sufficient quantities.

Turning attention to the crystallization behaviour, the exothermic peaks observed in the DSC traces appear equally responsive to sulfate loading: the onset temperature of crystallization (T_x) systematically shifts to lower values with increasing SO_3 content – declining from 785°C for the sulfate-free reference glass, to approximately 740°C at 0.5 mol%, and reaching ~700°C for compositions containing higher levels of SO_3. Additionally, the enthalpy of crystallization evolves in a non-linear fashion: it initially increases, followed by a modest decline upon reaching 1 mol% sulfate, and ultimately drops sharply in the sample doped with 5 mol% SO_3 (Tab. 9). Moreover, the crystallization exotherm becomes progressively broader and less intense at higher sulfate concentrations, as depicted in Fig. 28.

The enthalpy of crystallization, defined as the area beneath the exothermic peak on the DSC curve, may serve as a reliable indicator of the extent to which a glass undergoes crystallization [294]. Based on this parameter, it can be inferred that crystallization proceeds more vigorously in samples containing up to 1 mol% of sulfate, whereas its intensity diminishes noticeably in glasses with higher sulfur content. Given that sulfate concentration constitutes the sole compositional variable across the examined series, the observed modifications in crystallization kinetics must be intrinsically linked to the progressive incorporation of sulfur. Preliminary assumptions regarding the potential role of sulfates as heterogeneous nucleating agents were already proposed during the XRD analysis stage. If one accepts the premise that an increase in sulfate content promotes a higher propensity for spontaneous nucleation within the glass matrix – most likely of phosphate

character, as suggested by the diffraction data – then the remaining amorphous phase would, by extension, exhibit reduced susceptibility to crystallization. This hypothesis aligns well with the observed decline in devitrification intensity at elevated sulfate levels.

In order to further elucidate this apparent decrease in the crystallization potential of sulfate-bearing glasses, a controlled crystallization experiment was conducted. This process was initiated at the temperatures corresponding to the maxima of the exothermic effects recorded in the DSC curves, and the findings from this supplementary thermal treatment are presented and discussed in Section 8.7.

Before proceeding to those results, however, it is important to highlight a noteworthy peculiarity observed in the thermal profile of the 5S_6PM sample—the composition with the highest sulfur content – an additional endothermic event emerges in the temperature range preceding the onset of the glass transition (~ 575°C). The distinct nature of this thermal signal strongly suggests the occurrence of a phase transformation involving one of the structural components of the glass. Given that uncovering the origin of this feature may offer valuable insight into the structural rearrangements induced by sulfate incorporation, its detailed interpretation is provided in the following subsection.

8.6.1 High-temperature X-ray diffraction (HT-XRD) analysis

To elucidate the origin of the distinct endothermic event observed at approximately 577 °C on the DSC thermogram of the sample containing 5 mol% sulfate, high-temperature X-ray diffraction was employed. Therefore, Fig. 29Fig. 29(a) and (b) present a series of XRD patterns recorded over the temperature range of 25–600 °C during the heating and subsequent cooling cycles, respectively.

It is worth noting at the outset that sharp diffraction peaks corresponding to originating from the corundum sample holder used in the XRD instrument, are visible across all diffractograms and are denoted with asterisks in the figures. Aside from this consistent artifact, the HT-XRD results reaffirm the findings obtained from room-temperature XRD analysis (see Section 8.3) confirming that potassium sulfate (K_2SO_4) is the sole crystalline phase present in the 5S_6PM glass at ambient conditions (25 °C).

As the temperature increases, progressive structural changes within the material become apparent through noticeable modifications in the diffraction patterns: of particular relevance is a slight shift of the K_2SO_4 diffraction peaks toward lower 2θ angles, which can be attributed to thermal expansion of the crystalline lattice [295]. More significantly, however, is the appearance of new reflections concomitant with the diminishing intensity of the original diffraction peaks. These emergent features are first discernible at approximately 575 °C, with additional peaks appearing at 2θ positions of 22.0° and 44.9°, indicating the onset of a phase transformation. With continued heating, the intensities of these reflections increase, while some—initially observed at 26.3°, 29.8°, 35.9°, 37.1°, 40.4°, 40.9°, and 48.7° – progressively weaken and eventually vanish above 590 °C. Simultaneously, a minor peak at 28.2° becomes sharper and more pronounced.

Notably, the sample back to room temperature (Fig. 29.(b)), the newly formed reflections revert entirely to their original positions, suggesting a fully reversible structural transition. Collectively, these findings provide a compelling explanation for the thermal events recorded by DSC: at ambient temperature, the K_2SO_4 phase exists in its orthorhombic β-polymorph (space group *Pnma*), which remains stable up to ~575 °C. Beyond this point, it undergoes a transformation into its hexagonal α-polymorph (space group *P6₃/mmc*), which becomes the predominant crystalline phase above 590 °C. The

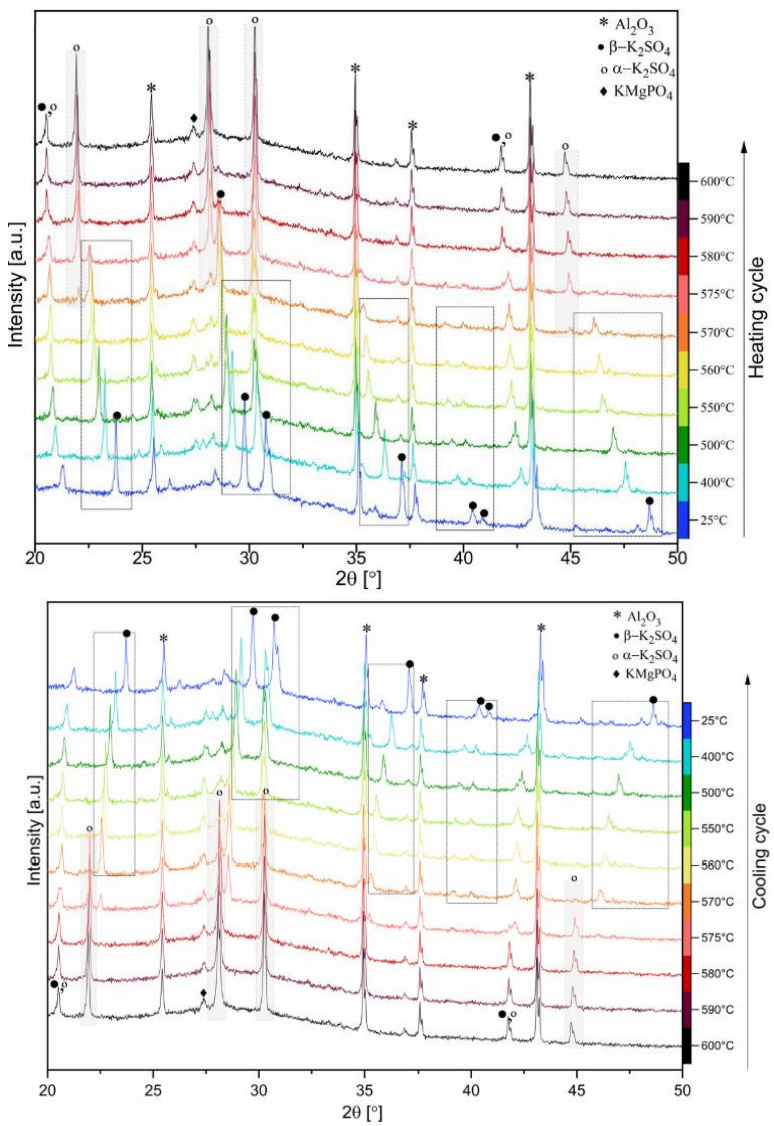


Fig. 29. In situ HT-XRD patterns of the 5S_6PM glass recorded at selected temperatures during (a) heating and (b) cooling cycles. Closed circles, open circles, and closed diamonds denote reflections of β-K_2SO_4, α-K_2SO_4 and $KMgPO_4$, respectively. Peaks marked with an asterisk originate from the Al_2O_3 sample holder [280].

reversibility of this β→α phase transition upon cooling is consistent with the observed endothermic peak on the DSC curve and further corroborated by the HT-XRD results (see Fig. 29, Tab. 10).

Finally, attention should be drawn to a minor diffraction feature observed at 27.4° 2θ, which emerges at temperatures exceeding 400 °C in both heating and cooling profiles (Fig. 29. (a), (b)). Closer examination revealed that this reflection does not correspond to either K_2SO_4 or Al_2O_3. Instead, it is tentatively assigned to a potassium magnesium phosphate phase ($KMgPO_4$), as summarized in Tab. 10. While phase identification based on a single reflection is inherently uncertain, the observed peak position and the broader tendency of comparable glass systems to precipitate orthophosphate phases under thermal treatment suggest that the specific conditions of the HT-XRD experiment – particularly the sustained isothermal exposure at elevated temperatures – may have promoted the localized crystallization of $KMgPO_4$.

Tab. 10 Summary of the HT-XRD results for the 5S_6PM glass sample [279].

Stage	Temperature [°C]	Identified Phases	Reference Code(s)
Initial (RT)	25	Corundum Dipotassium sulfate (VI), Arcanite	98-002-4851 00-024-0703
Heating	600	Corundum (HT)Potassium sulfate (VI) (HT) Potassium Magnesium Phosphate (HT)	98-016-0606 01-070-1227 00-050-0151
Cooling	25	Corundum Potassium sulfate (VI) Potassium Magnesium Phosphate	98-002-4851 00-024-0703 00-050-0146

8.7 Estimation of thermal stability of XS_6PM glasses

In addition to the classical thermal descriptors of glassy systems – namely, the glass transition temperature, the crystallization onset temperature, and the melting temperature – a complementary approach has been developed, wherein the relative positions of these thermal events serve as a basis for assessing the overall thermal behaviour of glasses. Indeed, to facilitate a direct comparison across various glass families, numerous researchers have proposed mathematical formulations that express thermal stability in a quantitative manner [296]. These so-called glass stability (GS) parameters, although originally devised to evaluate a material's resistance to crystallization during heating, have also been postulated to provide insight into the glass-forming ability (GFA) – a property typically evaluated based on the critical cooling rate required to avoid crystallization of the melt [296–298].

In this context, to deepen the thermal characterization of the XS_6PM glass series, a selection of widely used parameters—including those proposed by (K_T) [299], Angell (K_A) [297], Hrubÿ (K_H) [296], Weinberg (K_W) [297] as well as Lu and Liu (K_{LL}) [300]—were calculated, and the results are summarized in Tab. 11, while Fig. 30 graphically illustrates the most GFA-relevant trends.

Tab. 11. Values of selected glass stability parameters for the XS_6PM series [279].

No	Parameter				
	Turnbull (K_T)	**Angell (K_A)**	**Hruby (K_H)**	**Weinberg (K_W)**	**Lu and Liu (K_{LL})**
0S_6PM	0.605	171.6	0.749	0.214	0.482
0.5S_6PM	0.621	124.8	0.500	0.166	0.461
0.8S_6PM	0.677	91.1	0.453	0.126	0.464
1S_6PM	0.667	82.7	0.371	0.111	0.454
3S_6PM	0.632	81.5	0.290	0.103	0.438
5S_6PM	0.727	68.3	0.400	0.105	0.466

Among the earliest and most extensively adopted criteria for evaluating the glass-forming potential of a melt is the reduced glass transition temperature, originally suggested by Kauzmann and subsequently formalized by Turnbull as $K_T = T_g/T_m$) [299]. This

metric rests on the premise that a melt exhibiting high viscosity near T_g tends to vitrify more readily, even in the absence of rapid quenching. Given that oxide glasses typically exhibit a viscosity on the order of 10^{13} Pa·s at T_g [296], it has been proposed that higher K_T values correlate with increased viscosity of the undercooled liquid, which in turn implies a diminished need for extreme cooling rates to suppress crystallization. Moreover, it has been hypothesized that if K_T equals or exceeds the threshold value of approximately 0.67 (or 2/3), the kinetics of homogeneous nucleation are significantly inhibited.

As shown in Tab. 11, the calculated K_T values for the XS_6PM glasses cluster around this critical threshold, suggesting that the compositions studied are indeed capable of forming glasses; however, elevated cooling rates may be necessary to reliably bypass crystallization. Of particular interest is the observation that K_T remains below or near 0.67 for compositions containing up to 3 mol% sulfate, but increases noticeably once the SO_3 content reaches 5 mol%, indicating enhanced GFA. Assuming that K_T values above 0.67 reflect resistance to homogeneous nucleation, and given that only the 5S sample ($K_T \approx 0.73$) exhibits detectable K_2SO_4 crystallites – unlike the other compositions – this trend may signify a threshold sulfate concentration, nominally around 3 mol%, beyond which crystallization is thermodynamically favoured. Additionally, the K_T values provide insight into the predominant crystallization mechanism. Following Zanotto's classification [301], materials with K_T below 0.58–0.60 generally undergo volume (homogeneous) nucleation, whereas those exceeding this value tend to exhibit surface-induced (heterogeneous) crystallization. If this model is applied, the initial samples of the XS_6PM system would crystallize predominantly via homogeneous mechanisms; however, as the sulfate content increases, heterogeneous nucleation appears to become the dominant pathway. While this interpretation is inherently approximate, it aligns with prior indications that sulfate groups in the glass matrix serve as nucleation promoters, thereby facilitating devitrification.

Turning to the Angell parameter, defined as $K_A = T_x - T_g$ [297], this value reflects the temporal and thermal buffer between the onset of structural relaxation and the initiation of crystallization, and the smaller this interval, the higher its tendency to crystallize. According to the data presented in Tab. 11, a consistent decrease in K_A with increasing sulfate content is evidenced, implying a corresponding increase in the crystallization tendency across the XS_6PM series.

Further insight is provided by three additional GS parameters: Hrubý ($K_H = (T_x - T_g)/(T_m - T_x)$) [296], Weinberg ($K_W = (T_x - T_g)/T_m$) [295] and the Lu and Liu measure ($K_{LL} = T_x/(T_g + T_m)$) [298], which, although differing in mathematical form, each integrates all three DSC-derived thermal events (T_g, T_x and T_m) and serves as a comparative index of a glass's resistance to devitrification. It is generally accepted that higher values of these parameters denote superior thermal stability of glass material on heating [300]. Notably, a comprehensive analysis by Nascimento et al. [295], confirmed that these three indicators are also valuable proxies for glass-forming ability, understood as the ease with which a melt can vitrify on cooling.

Accordingly, the parameter values presented in Tab. 11, suggest a consistent decline in both GS and GFA as the sulfate content increases – with the exception of the 5S_Mg sample, which exhibits markedly elevated values of K_H, K_W and K_{LL}. This anomaly is likely attributable to the partially crystalline nature of the sample, where the residual amorphous matrix – having already undergone partial devitrification – displays a higher kinetic barrier to further crystallization, and thus, increased thermal stability.

It must be acknowledged, however, that all such analyses are inherently influenced by the precise determination of T_g, a temperature known to be sensitive to the sample's thermal history and fabrication protocol [300], nevertheless, it is believed that the trends observed in the calculated parameters provide valuable approximations regarding the vitrification potential and devitrification resistance of the studied glasses [295,296,300].

It is clear then that within the XS_6PM system, increasing the sulfate content progressively diminishes both the glass-forming ability and thermal stability of the glasses – up to a compositional threshold of approximately 3 mol% SO_3. Beyond this point, an apparent increase in GS parameters corresponds to the emergence of a crystalline phase, suggesting that sulfate incorporation plays a decisive role in modulating the crystallization tendency of the studied silicate-phosphate glasses (Fig. 30).

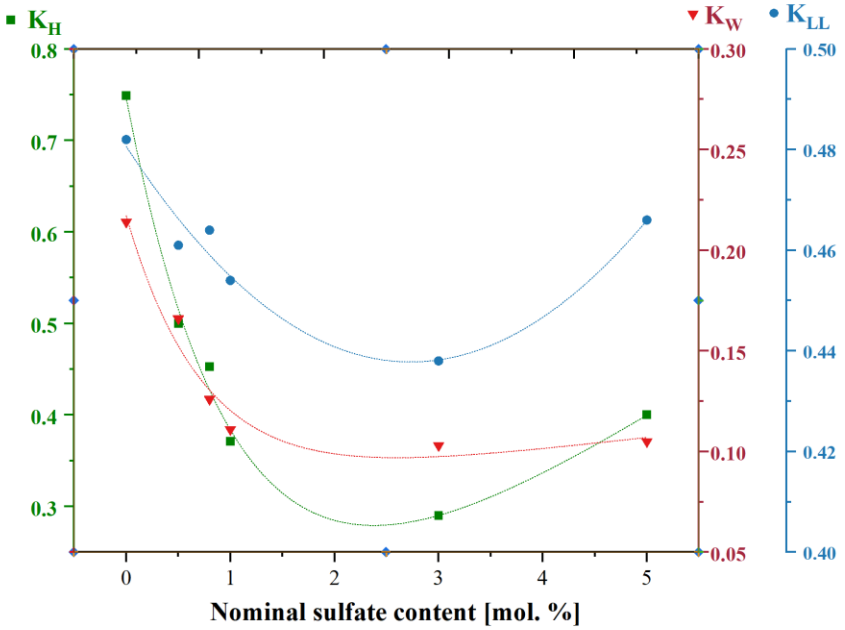


Fig. 30. Calculated values of selected thermal parameters for the XS_6PM glass series: Hrubÿ (green), Weinberg (red),and Lu and Liu (blue); only parameters with a meaningful correlation to glass-forming ability are displayed [279].

8.8 Study of devitrification products within the XS_6PM glass system

Extensive research on multicomponent silicate-phosphate glasses has demonstrated that devitrification proceeds primarily through the reorientation and rearrangement of structural domains under thermal treatment. As discussed in Section 8.6, these domains may act as precursors or nuclei for crystallization, thereby governing the nature of the phases that subsequently emerge [290,303]. Given the strong correlation between the nature of these groupings and the identity of crystalline compounds formed during heat treatment, the products of controlled crystallization can offer critical insights into the internal domain architecture of the studied glasses. This aspect is of particular relevance for glass-based fertilizers, where the spatial arrangement and type of structural domains significantly influence the release dynamics of embedded nutrients in biological environments [302]. To this end, an induced crystallization

protocol was applied[3] *to the as-prepared samples, and the resulting phase assemblages were characterized and summarized in*

Tab. 12.

Tab. 12. Crystalline phases identified in devitrified XS_6PM glass samples based on XRD analysis [279].

SAMPLE ID	DETECTED PHASE (FORMULA)	PHASE ID (ICDD REF.)	ASSIGNED MINERAL NAME
0S_6PM	$K_{1.14}Mg_{0.57}(Si_{1.43}O_4)$	00-044-0089	Potassium Magnesium Silicate
	Mg_2SiO_4	00-004-0769	Forsterite
	$KMgPO_4$	98-005-0926	Potassium Magnesium Phosphate (V) - Alpha
0.5S_6PM	$KMgPO_4$	00-050-0149	Potassium Magnesium Phosphate
0.8S_6PM	$KMgPO_4$	00-050-0149	Potassium Magnesium Phosphate
1S_6PM	$KMgPO_4$	00-050-0149	Potassium Magnesium Phosphate
3S_6PM	$KMgPO_4$	00-050-0149	Potassium Magnesium Phosphate
	$Mg_2P_2O_7$	00-005-0579	Magnesium Phosphate Oxide
5S_6PM	$KMgPO_4$	00-050-0149	Potassium Magnesium Phosphate
	K_2SO_4	00-003-0608	Dipotassium Sulfate

The results reveal that several key factors dictate the crystallization pathways within the XS_6PM system. The first and most apparent is the incorporation of sulfate, which, as previously highlighted in Section 8.3, seems to affect the tendency of studied glasses to crystallise: with increasing SO_3 content, the crystallization temperature decreases, the kinetics of devitrification are altered, and the overall thermal stability of the glass is reduced. a direct consequence of excessive sulfate loading – identified here as 5 mol% SO_3 – is the formation of K_2SO_4, a crystalline phase that emerges distinctly under such conditions. Notably, sulfur is absent from all other crystalline products observed in the devitrified materials, reinforcing the earlier hypothesis that sulfate species exist within the glass as structurally discrete, non-integrated domains (

Tab. 12).

Another decisive factor in the crystallization behaviour is of crystallochemical origin. Prior studies [184,303], have established that the type of crystalline phase formed during devitrification is largely dictated by the bond strength between oxygen and the constituent cations within the chemical linkage, and be quantitatively evaluated by examining the difference in bond ionicity (Δ_{iG}) between oxygen and a given cation. a smaller Δ_{iG} indicates reduced stability of oxygen-centred linkages, which are more prone to disruption during crystallization.

In the present system, the influence of these crystallochemical considerations is particularly evident (

Tab. 12). The Δ_{iG} values for K–O–Si (0.395) and Mg–O–Si (0.241) linkages are significantly lower than those observed within the silicate backbone itself and are also weaker than analogous phosphorus-containing bridges such as K–O–P (0.511) or Mg–O–

[3] The induced crystallization process was performed by subjecting the respective samples to a 24-h heat treatment at temperatures set approximately 10 °C above the maxima of the exothermic effects identified in the DSC curves.

P (0.357). As a result of these variations – and due to stronger acid–base interactions between phosphorus and network-modifying cations – the thermal treatment preferentially facilitates the formation of orthophosphate phases rather than silicate ones. This trend is consistent with the general principle that crystallization in multicomponent glasses typically initiates with compounds composed of the most weakly bound and mobile chemical constituents [303]. The XRD results clearly reflect this behaviour. In sulfate-containing samples, which crystallize at significantly lower temperatures compared to the sulfate-free base glass, only phosphate phases such as $KMgPO_4$ (with additional $Mg_2P_2O_7$ detected exclusively in the 3S_6PM composition) were observed. The 5S_6PM sample also exhibited K_2SO_4, consistent with the earlier discussion. Conversely, in the sulfate-free base glass – crystallizing at the highest temperature when atomic diffusion is more pronounced – both phosphate ($KMgPO_4$) and silicate phases (Mg_2SiO_4 and $K_{1.14}Mg_{0.57}(Si_{1.43}O_4)$) were detected. Given that the difference in ionicity (Δ_{iG}) of the oxygen bridges also reflects the acid-base character of local interactions and the chemical affinity of cations toward oxygen, it is unsurprising that the is K_2SO_4 phase emerges preferentially upon exceeding the sulfate capacity of the glass: the comparison of Δ_{iG} values for S–O–K (0.621), S–O–Ca (0.505), and S–O–Mg (0.467), clearly indicates that K^+ forms the weakest sulfate bonds and thus the most readily crystallizing sulfate phase.

Based on the observed phase assemblages and under the assumption that the aforementioned parallelism between domain structure and crystallization behaviour holds true, it can be inferred that the glass matrix of the XS_6PM system predominantly contains orthophosphate-type domains, most likely of the $KMgPO_4$ variety, accompanied by silicate-based domains composed of isolated tetrahedra (only loosely integrated into the network and therefore exhibit high mobility). Importantly, sulfur does not participate in either of these two domain types but instead seems to form independent groupings resembling K_2SO_4, which precipitate once the sulfate concentration reaches 5 mol%.

While these conclusions are consistent with SEM-based findings, the significance of domain structure – particularly in the context of micro- and macroelement mobility in glassy fertilizers – has prompted further investigation. To this end, the Raman Spectroscopy Imaging (RSI) technique was employed, allowing for spatially resolved identification of structural domains and vibrational signatures. The corresponding results are presented in the following section.

8.9 Raman Imaging analysis

Raman Spectroscopy Imaging was selected as the primary analytical technique to investigate the distribution of crystalline and amorphous clusters within the obtained devitrified samples. This choice was dictated by RSI's exceptional spatial resolution and its capacity to generate chemically specific maps based on spectra collected point by point across the sample surface. Given the particular interest in delineating sulfate-rich domains, the analysis was focused on those glassy materials with the highest sulfur content – specifically, the 3S_6PM and 5S_6PM compositions. The resulting Raman maps, along with representative spectra collected from various regions of the examined profiles, are presented in Fig. 31 and Fig. 32.

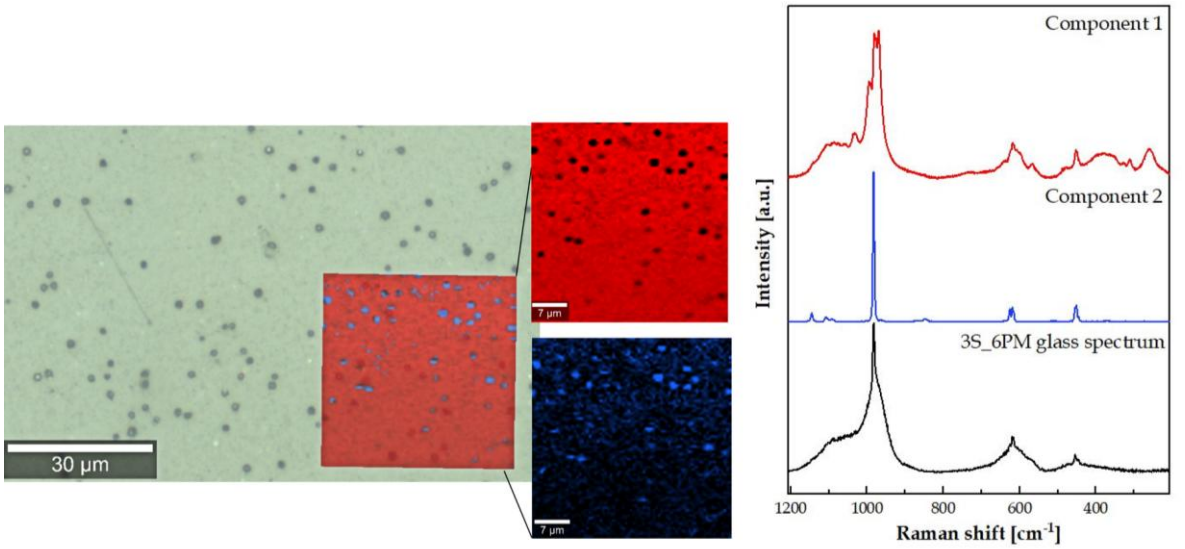


Fig. 31. Raman map of the surface region of the 3S_6PM devitrified sample (left) and the corresponding Raman spectra collected at identified zones (right). The spectral line colours correspond to the spatial regions from which the data were obtained [279].

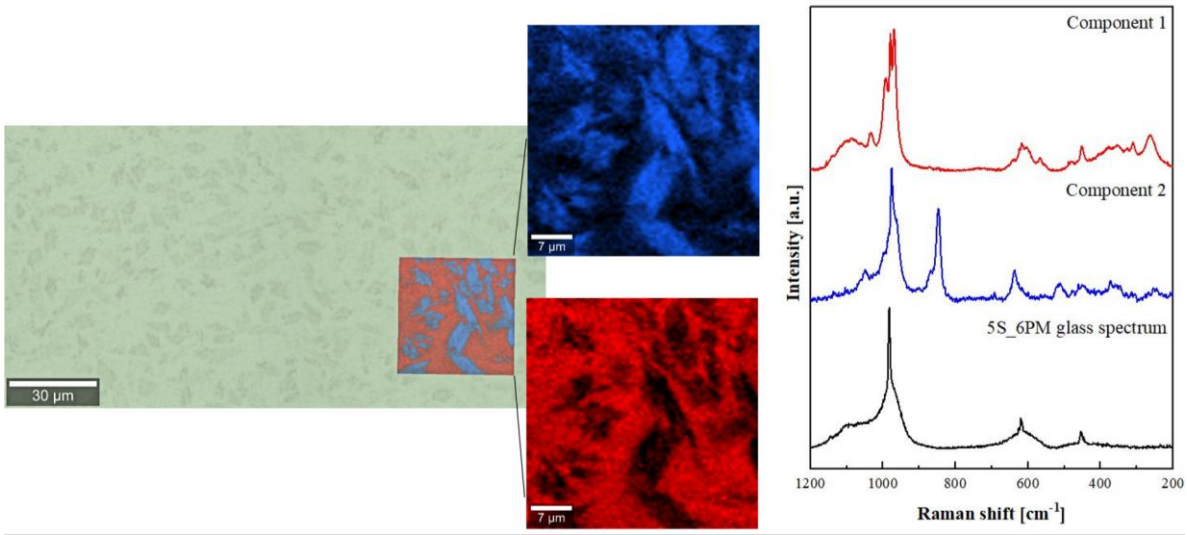


Fig. 32. Raman map of the surface region of the 5S_6PM devitrified sample (left) and the corresponding Raman spectra collected at identified zones (right). Spectral line colours denote the specific surface locations from which measurements were acquired [279].

In order to facilitate comparison and to better visualize structural transformations induced by thermal processing, each spectral set is accompanied by the corresponding Raman spectrum of the initial, as-synthesized glass. Furthermore, to aid the interpretation of the spectral data, a summary of characteristic vibrational modes associated with structural units commonly found in multicomponent silicate-phosphate glasses is provided in Tab. 13, while a more comprehensive analysis of the structural features of the investigated materials is developed in the subsequent section of the present thesis.

Tab. 13. Tentative assignment of Raman bands observed in sulfate-bearing multicomponent silicate-phosphate glasses [279].

Frequency range [cm^{-1}]	**Assignment**
1200 – 850	Symmetric stretching vibrations of Si-O^{-} terminal bonds in silicate units (the higher the number of non-bridging oxygens (NBOs) forming the SiO_4 tetrahedron, the lower is position of the band on the wavenumber scale), as well as symmetric stretching vibrations of P-O bonds within the orthophosphate groups $(PO_4)^{3-}$
700 – 500	Bending motions of Si-O-Si bridges in Q^{2*} structural units, asymmetric bending vibrations of P–O^{-} in orthophosphate groups $(PO_4)^{3-}$
500 – 350	Bending vibrations of O-P-O and P-O^{-} linkages in orthophosphate $(PO_4)^{3-}$ and pyrophosphate $(P_2O_7)^{4-}$ units, respectively
Sulfate-specific Raman vibration modes	
1145	Asymmetric S-O stretching vibration, υ_{as} (S-O)
984	Symmetric S-O stretching vibration, υ_{ss} (S-O)
620	Asymmetric S-O-S bending vibration, δ_{as} (S-O-S)
455	Symmetric S-O-S bending vibration, δ_{ss} (S-O-S)

*In Q^n notation Q represents silicate (or phosphate) tetrahedron, while n is the number of bridging oxygens (BOs) in a given unit.

Preliminary interpretation of the RSI data obtained for both devitrified samples reveals a notable degree of structural similarity. This resemblance arises from the predominance of a common matrix phase – denoted as *Component 1* and marked in red in the Raman maps – which dominates the surface profiles of both compositions. The red Raman spectra associated with this phase exhibit strong similarity across both samples, suggesting that it shares a comparable structural identity, Fig. 31, Fig. 32. The presence of distinct, sharp vibrational bands with narrow full-width at half-maximum, superimposed on broader features typical of an amorphous matrix, implies a partially crystalline character of the dominant phase – an expected consequence of the applied thermal treatment. a closer inspection of the spectral band positions supports the assertion that Component 1 is chiefly amorphous in nature but contains crystalline inclusions of $KMgPO_4$ (identified by intense peaks near 260, 570, 970, 995, and 1030 cm^{-1}) and K_2SO_4 (characterized by bands at approximately 1140, 980, 618, and 453 cm^{-1}) [265,305,306]. Notably, these findings corroborate both the XRD results and the morphological features observed through SEM-EDS method, thereby reinforcing the validity of this interpretation. In addition to the matrix phase, a distinct blue-coloured region (*Component 2*, blue spectrum) was observed within the 3S_6PM sample, manifesting as vacuolar inclusions within *Component 1*, and identified as predominantly crystalline K_2SO_4. In contrast, the 5S_6PM specimen exhibited elongated crystalline structures embedded within the matrix of *Component 1*, similarly denoted as *Component 2* (blue), however, the complex nature of its Raman spectrum, combined with the absence of a matching standard reference in the employed database, hindered unambiguous identification of this phase. Nevertheless, drawing upon literature reports and XRD analyses conducted on other devitrified members of

the XS_6PM system, it can be reasonably proposed that the unidentified elongated crystallites possess the structure of a complex silicate composed of weakly interconnected [SiO_4] tetrahedra. This hypothesis is supported by the presence of intense Raman bands at 975, 850, and 640 cm^{-1}, which are attributed to the stretching vibrations of $Si–O^-$ terminal bonds in Q^2 units, Si–O vibrations in Q^0 units, and Si–O–Si bridging bonds, respectively [307].

Quite unexpectedly, Raman Imaging has proven instrumental not only in mapping crystalline and amorphous domains but also in elucidating the mechanism of sulfate incorporation into the glass network. Particularly striking are the observations made for the 3S_6PM sample, where surface profiles clearly reveal the presence of residual structures attributed to former gas bubbles – features also tentatively identified via SEM in the case of the 5S_6PM composition (Section 8.5) – as illustrated in Fig. 31 and Fig. 32. Notably, the regions corresponding to these bubble-like remnants are enriched in sulfates, a fact clearly evidenced by the associated Raman spectra (*Component 2*, blue spectrum, Fig. 31), which exhibit intense vibrational features characteristic of the $[SO_4]^{2-}$ anion. As discussed in the introductory chapter, sulfates are commonly employed in glassmaking as fining agents, serving as in-situ sources of gaseous species that promote melt clarification [308]. hen introduced into the melt, these compounds preferentially dissolve in alkali-rich regions. Upon reaching temperatures above ~1200 °C – e.g., the decomposition threshold of K_2SO_4 under oxidizing conditions [309] – they undergo thermal dissociation according to the following reaction [310]:

$$K_2SO_4(m) \leftrightarrow K_2O(m) + 4SO_2(g) + \frac{1}{2}O_2 \qquad \text{Eq. (20)}$$

Given the limited solubility of sulfate species in silicate-dominated matrices, only a fraction of the resulting SO_2 becomes structurally accommodated within the network, occupying available free-volume sites and forming isolated sulfate-rich domains. The presence of such inclusions is corroborated by Raman spectra recorded for *Component 1* (Fig. 31 and Fig. 32), where vibrational bands typical of $[SO_4]^{2-}$ units emerge alongside features ascribed to the principal amorphous-crystalline matrix. The remaining SO_2 evolves as gas, generating bubbles within the molten phase. The residual traces of these bubbles—still observable in the 3S_6PM sample—serve as markers of this degassing process.

Given the evident correlation between these regions and the pronounced $[SO_4]^{2-}$ spectral features, it is reasonable to conclude that post-cooling reabsorption of sulfur species from residual gas pockets likely occurred, leading to the localized enrichment in sulfates [102]. Interestingly, although such structures are readily identifiable in SEM micrographs of the 5S_6PM sample, their detection via RSI proved less straightforward: in the Raman surface maps, domains for the 3S_6PM sample associated with sulfate-rich *Component 2* now (for the 5S sample) appear to have been structurally integrated into the silicate matrix – despite both specimens undergoing heat treatment at comparable crystallization temperatures. This observation suggests that sulfate introduction may indeed induce compositional and structural heterogeneities, which, in turn, can act as nucleation sites that facilitate bulk crystallization of the silicate network.

Thermal analysis alone already indicated that sulfur, contrary to classical glass modifiers, does not weaken the vitreous network. On the contrary, its presence necessitates an

increased energy input to induce the transformation from a rigid solid into a viscoelastic state. Nevertheless, the exact role of this unconventional component within the structure of these multicomponent systems remains speculative. The nature of its influence on the evolution and connectivity of the fundamental silico-oxygen framework is yet to be conclusively deciphered.

Moreover, it is evident that sulfate addition adversely affects the thermal stability of the designed vitreous carriers of useful ions with respect to devitrification, and this destabilizing effect can be interpreted from two perspectives. From a technological standpoint, a reduced processing window limits the time available for further treatment, and also indicates a propensity for spontaneous crystallization under suboptimal cooling conditions. Conversely, from the perspective of their potential application in agriculture, decreased thermal stability—which may reflect a weakening of the structural network—could be positively correlated with enhanced solubility in biological solutions [184].

Based on the devitrification behaviour of the XS_6PM glass series, the hypothesis regarding the relationship between crystallized phases and pre-existing domain types appears substantiated. Indeed, within the volume of analysed materials, three distinct domain types can be distinguished: silicate-based groupings; well-defined orthophosphate clusters involving potassium and magnesium cations; and sulfate-rich aggregates. The latter manifest either as dispersed inclusions within the dominant silicate matrix – possibly occupying voids in the network – or as localized accumulations surrounding the vestiges of gas bubbles.

These investigations offer initial insights suggesting that sulfur exhibits a distinct and possibly non-conventional structural role within the framework of the designed multicomponent glasses, as the emergence of clearly differentiated sulfate-rich domains may be indicative of a degree of structural organization not surpassing that typically attributed to short-range order [311]. Accordingly, the following section presents the results obtained through a suite of complementary spectroscopic methods – namely FTIR, Raman, ^{29}Si and ^{31}P MAS-NMR, and XAS, which collectively enable a comprehensive examination of the short-range structural features associated with sulfur incorporation into glasses belonging to the XS_6PM compositional series. The spectroscopic findings are further discussed in the context of elucidating the role of sulfur in modulating the network structure of these complex vitreous materials.

9 Structural studies of glasses representing the XS_6PM system

It is well established that even subtle modifications in glass composition can induce changes in both the fundamental structural motifs and their topological interconnections – factors that may prove pivotal in explaining the non-linear variations observed in the physical and mechanical properties of multicomponent glasses [112]. In order to elucidate the role of sulfur and its distribution within the vitreous framework of silicate-phosphate glasses formulated within the selected XS_6PM system, a comprehensive structural investigation was undertaken. These studies aimed not only to clarify the influence of sulfur incorporation on the evolution of the glass network but also to contribute to a broader understanding of composition–structure–property relationships essential for the rational design of similar materials intended for agronomic applications.

The section begins with an analysis of vibrational spectroscopic data acquired using complementary Raman and Fourier Transform Infrared spectroscopy. These techniques, due to their differential sensitivity to molecular vibrations – Raman spectroscopy being predominantly responsive to changes in polarizability (typically associated with symmetric vibrations), while FTIR is more sensitive to alterations in dipole moment (linked to asymmetric vibrations) – offer a synergistic approach for probing the short-range structural environment. Their combined application is expected to provide insight into the chemical surroundings of sulfur-bearing species embedded within the glass matrix, their effect on the polymerisation state of the main, silicate, materials' subnetwork, as well as allow for a preliminary estimation of the oxidation state of sulfur present in the synthesised materials [312].

Subsequently, solid-state MAS-NMR spectroscopy was employed, specifically targeting the ^{29}Si and ^{31}P nuclei. This technique, owing to its element-specific nature, enables the disentanglement of the structural influence exerted by sulfur on the silicon–oxygen framework from that affecting the phosphorus–oxygen subnetwork.

Both silicon and phosphorus are considered favourable elements for NMR studies of glasses, as they possess NMR-active isotopes with relatively high natural abundances, facilitating high-quality spectral acquisition using commonly available instrumentation. Accordingly, only their spectra were obtained using nearby NMR facilities, whereas sulfur and the remaining constituents of the glass matrix, due to the low natural abundance of their NMR-active isotopes and hence – challenging for NMR analysis – were precluded from their examination within the scope of the present research [312,313]. Nevertheless, given the critical structural roles played by Si and P as network formers, detailed investigation of their coordination environments is expected to yield substantial insight into the overall structural development of the glassy system.

Finally, the section concludes with the presentation of X-ray absorption spectroscopy results, a method known for its exceptional sensitivity to the oxidation state and local coordination environment of specific elements. By scanning the incident X-ray energy across a defined range, it is possible to detect absorption edges – typically K- or L-edges – corresponding to the excitation of core electrons, positions of which are inherently dependent on the chemical speciation and immediate structural surroundings of the absorbing atom. This renders XAS a powerful technique for determining the oxidation state of sulfur and other targeted elements in disordered systems [312].

9.1 Raman spectroscopy study

A preliminary structural assessment of the synthesized materials belonging to the XS_6PM glass system was conducted using Raman spectroscopy, and the resulting influence of progressive sulfur incorporation on the glass network is illustrated in Fig. 33. Notably, to enable a more detailed investigation of the structural evolution, an additional glass composition containing 1.3 mol% SO_3 was prepared and subjected to Raman analysis alongside the primary series.

The interpretation of the spectral features characteristic of the silicate-phosphate glasses under study was carried out relative to the sulfur-free reference composition, the Raman spectrum of which may be conventionally segmented into three principal regions::

I. **Low-frequency region (350–500 cm^{-1}):** This range exhibits a single, low-intensity band centred around 420 cm^{-1}, displaying a subtle asymmetry extending towards higher frequencies (~470 cm^{-1}). The former is commonly attributed to bending

vibrations of O–P–O linkages within isolated orthophosphate units, denoted as Q_P^0 species (~450 cm^{-1})[4], while the higher-frequency shoulder is likely associated with bending vibrations of P–O bonds in pyrophosphate structures Q_P^1 [313–315];

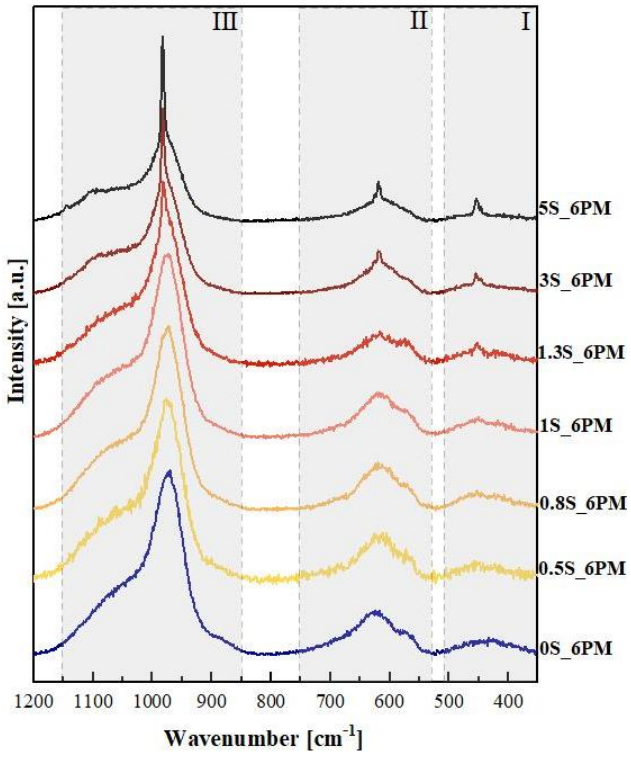


Fig. 33. Raman spectra of sulfur-free and sulfur-bearing silicate-phosphate glasses [280].

[I. **Mid-frequency region (550–750 cm^{-1}):** Dominated by a prominent band near 620 cm^{-1} with an accompanying shoulder around 570 cm^{-1}; the main feature is typically assigned to the bending vibrations of Si–O–Si bridges within Q_{Si}^2 species, while the shoulder is thought to originate from asymmetric P–O$^-$ bending modes in Q_P^0 units [314–321];

[I. **High-frequency region (850–1200 cm^{-1}):** Characterised by stretching vibrations of Si–O$^-$ terminal bonds in Q_{Si}^n tetrahedra, where the specific position of the bands correlates with the number of non-bridging oxygens coordinated to the silicon atom [315,316,321].

Upon progressive incorporation of sulfur into the glass network, additional vibrational bands emerge across all three spectral domains – in the high-frequency region, two distinct features appear at 1145 cm^{-1} and 982 cm^{-1}, while new bands at approximately 618 cm^{-1} and 460 cm^{-1} are observed in the mid- and low-frequency regions, respectively. The assignment of these sulfur-related features was accomplished by comparative analysis with the Raman spectrum of crystalline potassium sulfate (Fig. 34), which exhibits four fundamental vibrational modes associated with the sulfate (SO_4^{2-}) tetrahedron [265,312]:

- Asymmetric S–O stretching vibrations (υ_{as}) at 1145 and 1107 cm^{-1};
- Symmetric S–O stretching vibrations υ_{ss}) centred around 984 cm^{-1};
- Asymmetric bending modes of the S–O–S framework (δ_{as}) near 620 cm^{-1};
- Symmetric bending vibrations (δ_{ss}) around 455 cm^{-1}.

[4] As explained before, in the Q_T^n notation Q refers to the type of tetrahedral unit (here: T refers to Si or P), while the superscript, n, denotes the number of bridging oxygens.

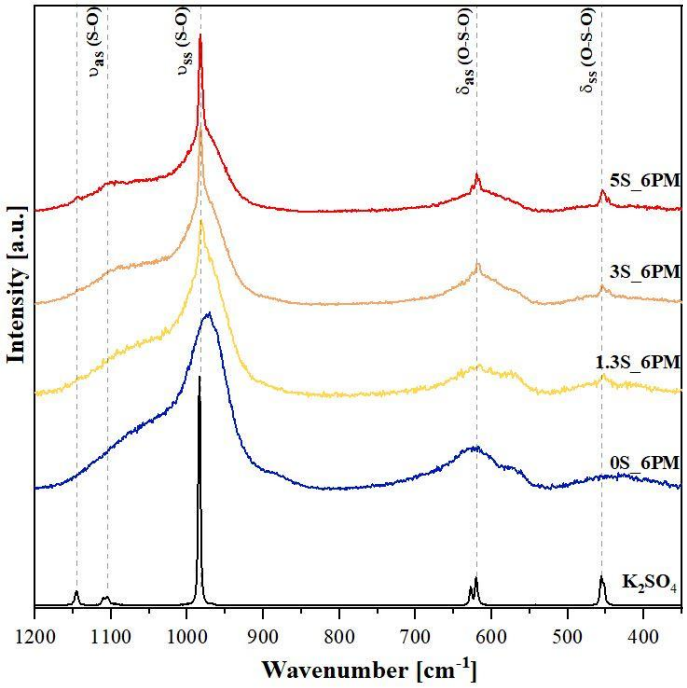


Fig. 34. Raman spectra of selected silicate-phosphate glasses compared with crystalline K_2SO_4. The vibrational bands attributed to sulfur in the glass phase correspond closely to those observed in the crystalline reference, [280].

In geological sciences, the structural identification of elements of interest is frequently accomplished through the fingerprinting approach, which relies on direct spectral comparisons between the measured material and well–characterized model compounds. In the case of sulfur, the positions of characteristic Raman bands are often matched with those of sulfur-bearing crystalline phases to confirm the presence and speciation of sulfur within the glass matrix. Notably, however, due to the distinct coordination environments typical of glasses – marked by their disordered, non–crystalline nature – vibrational bands associated with sulfur may appear shifted by several wavenumbers relative to their crystalline analogues [312]. Taking this into account, and considering the clear correspondence between the sulfur-related bands observed in doped glasses and those characteristic of crystalline potassium sulfate K_2SO_4 [265,313,323], one may put forth the initial assumption that, within the studied silicate-phosphate compositions, sulfur exists exclusively in the form of sulfate anions, appearing to form domains that structurally resemble crystalline sulfate phase. This interpretation is further corroborated by the findings presented in Section 8 – particularly the devitrification studies outlined in subsections 8.8 and 8.9 – which provided compelling evidence for the presence of sulfate-like domains within the vitreous matrix. The progressive intensification and sharpening of the most prominent sulfur-related Raman feature – specifically, the ν_{ss}(S–O) symmetric stretching band – serve as a spectral indicator of increasing local ordering within these sulfate-enriched regions, which parallels the systematic increase in sulfur content, leading to K_2SO_4 crystallization once the sulfate solubility threshold is surpassed. As discussed in Section 8, such structurally pre-formed sulfate domains likely act as heterogeneous nucleation centres, facilitating glass crystallization (including the sulfate-binding phases) under thermal treatment. Due to their strong Raman activity, sulfate species are readily identifiable in spectroscopic analyses, making their detection in glass structures relatively straightforward. In contrast, the identification of reduced sulfur species – such as polysulfides (e.g., S_3^-, S_2^-, S_2^{2-}, S_3^{2-}) – poses significant analytical challenges, given the generally weak and poorly resolved nature of their associated vibrational bands. Nonetheless, the spectral window around 350–400 cm^{-1} is often associated with S–S bond vibrations or the presence of intermediate sulfur species [311]. While such features were not observed in the Raman spectra of the XS_6PM glasses investigated herein,

further insights into the oxidation state and coordination of sulfur will be pursued using oxidation-state-sensitive techniques, specifically XAS.

A more detailed examination of sulfur-induced structural modifications was achieved by deconvoluting the high-frequency region of the Raman spectra for selected glass samples. This spectral region was chosen based on the known limitations of interpreting bands in the lower frequency range, where variations in Si–O–Si bond angles introduce significant ambiguity and hinder reliable band assignment [320]. For the deconvolution process, bands corresponding to Q^n_{Si} units were modelled using Gaussian functions, in accordance with the broad distribution of bond angles and distances within silicate sites. In contrast, sulfate-related bands – due to the relatively narrow distribution of S–O bond lengths and O–S–O angles in SO_4^{2-} tetrahedra – were fitted using Lorentzian functions, reflecting less variable distribution of S-O bond length and O-S-O bond angles [322]. The resulting decomposed spectra, comparing SO_3-free and sulfur-doped silicate-phosphate glasses, are presented in Fig. 35.

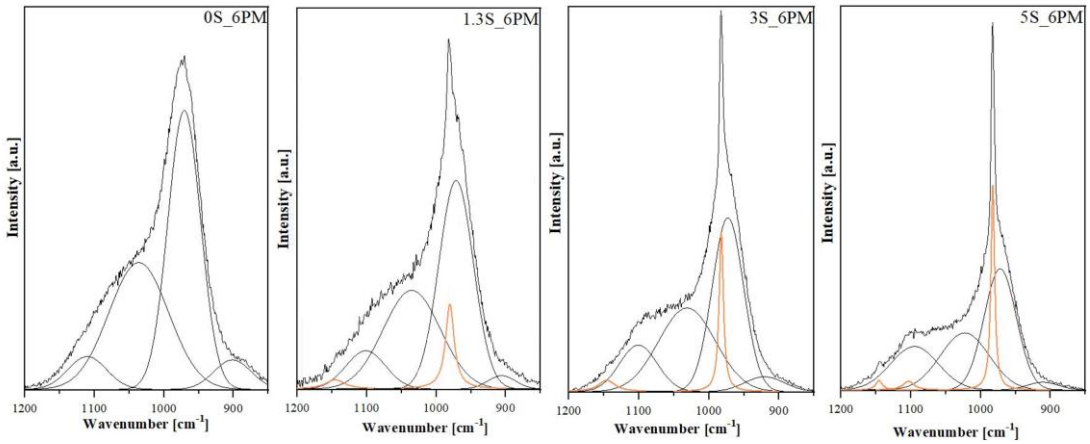


Fig. 35. Deconvoluted Raman spectra of selected silicate-phosphate glasses containing (from left): 0 mol% SO_3,(base glass), 1.3% mol. SO_3, 3% mol. SO_3 and 5% mol. SO_3. Orange bands denote sulfate-related vibrational features, while black ones correspond to various silicate network oscillations [280].

The deconvolution of the high-frequency Raman spectral envelope (800–1200 cm^{-1}) revealed the presence of two distinct sulfate-dependent vibrational bands: the first, a prominent and well-resolved feature observed in all sulfur-doped glasses, appears near 982 cm^{-1} and corresponds to the symmetric stretching (υ_{ss}) vibrations within the of the SO_4^{2-} tetrahedron, whereas the second, an asymmetric stretching vibration (υ_{as}) emerges at approximately 1145 cm^{-1} in samples containing at least 1.3 mol% SO_3, while in the one, loaded with the highest sulfur content, 5S_6PM, appears to be split into two components – an effect likely attributable to crystal field influences within increasingly ordered sulfate domains [323]. It is again worth emphasizing that the gradual increase in sulfate content is accompanied by a systematic intensification, narrowing, and sharpening of the υ_{ss} band, an effect reflecting an increasing degree of short-range ordering within the sulfate-rich regions of the glass, culminating in the onset of crystallization once the sulfate solubility threshold is exceeded.

Beyond sulfate-specific bands, the deconvolution procedure identified four additional peaks within the same high-frequency region. Three of these, centred approximately at 900, 970, and 1100 cm^{-1}, can be confidently assigned to the symmetric stretching modes

of Q^1_{Si}, Q^2_{Si} and Q^3_{Si} units, respectively – each corresponding to silicate tetrahedra containing one, two, or three bridging oxygen atoms [312,313,315], while the fourth band, positioned around 1040 cm^{-1}, of more ambiguous origin, is generally attributed to Si–O stretching vibrations associated with alkali or alkaline earth metal modifiers [326–331].

It must be stressed that while this spectral interpretation – performed using the Fityk software – provided the best fit when assuming four non-sulfur-related components, and was guided by the dominance of silicon as the primary network-forming element, the potential contribution of phosphorus cannot be neglected. Since domain studies of the XS_6PM glass series have clearly demonstrated the presence of orthophosphate-like environments within the amorphous matrix, consequently, it is highly probable that the υ_{ss}(P-O) vibration, typically observed near 960 cm^{-1}, and potentially the weaker υ_{as}(P-O) mode around 1030 cm^{-1}, overlap with the more intense features attributed to silicate units [305]. Thus, a more detailed analysis of the Raman spectra – employing different curve-fitting software – will be presented in subsequent sections. For the purposes of this discussion, however, it is assumed that the dominant influence of sulfur incorporation will manifest most prominently through changes in the silicon-oxygen subnetwork, which forms the structural backbone of the studied glasses.

To roughly estimate the impact of sulfur on the distribution of silicate species, a semi-quantitative approach was adopted: the relative areas of individual Q^n_{Si} bands within the high-frequency region were calculated as ratios of each band's area to the total area under the 800–1200 cm^{-1} envelope. These normalized values were then interpreted as proxies for the relative abundance of Q^n_{Si} species. The results of this analysis are presented in Fig. 36 and Tab. 14.

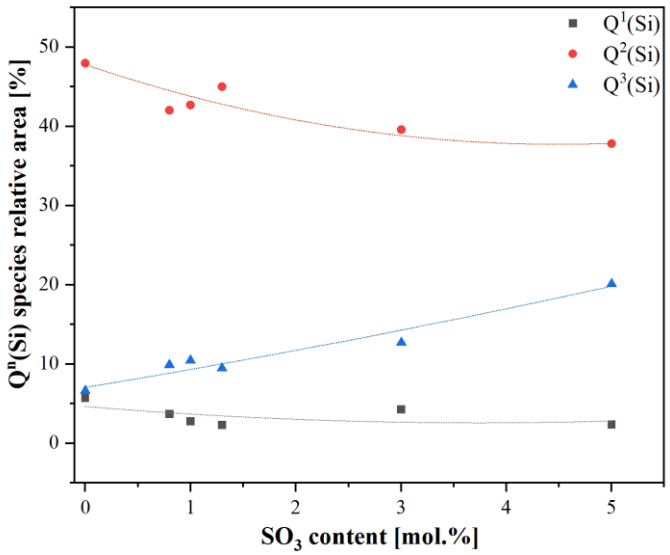


Fig. 36. Relative abundance of Q^n_{Si} units plotted as a function SO_3 content.

Analysis of these data reveals a discernible trend: with increasing sulfate content, the proportion of Q^3_{Si} units raises at the expense of Q^2_{Si} species, suggesting a shift toward greater polymerization of the silicate subnetwork. a modest decline in the abundance of Q^1_{Si} units is also observed, reinforcing the notion of progressive augmentation of Si-O-Si network connectivity driven by sulfur incorporation.

Moreover, the relative area of the ~1040 cm^{-1} band decreases systematically with rising sulfate content. If this feature indeed corresponds to vibrations of Si–O pairs associated with alkali or alkaline earth metal cations, such behaviour could indicate a decreasing proximity of these cations to the silicate units, likely as a result of their preferential interaction with sulfate tetrahedra for charge compensation. Alternatively, if one assumes that in this region indeed the band partially or wholly attributable to asymmetric P–O vibrations is present, then its diminishing intensity may suggest that the incorporation of sulfur not only affects the silicate framework but also perturbs the

phosphate subnetwork. This latter hypothesis will be explored further in the context of MAS-NMR studies presented in subsequent chapters.

Tab. 14. Estimated relative abundance of structural units based on deconvolution of Raman spectra [280].

Glass name	Relative band area [%]		Q^3_{Si}/Q^2_{Si}
	Q^2_{Si}	Q^3_{Si}	
0S_6PM	47.99	6.63	0.14
0.8S_6PM	42.04	9.91	0.24
1S_6PM	42.70	10.48	0.25
1.3S_6PM	45.01	9.48	0.21
3S_6PM	39.60	12.71	0.32
5S_6PM	37.84	20.12	0.53

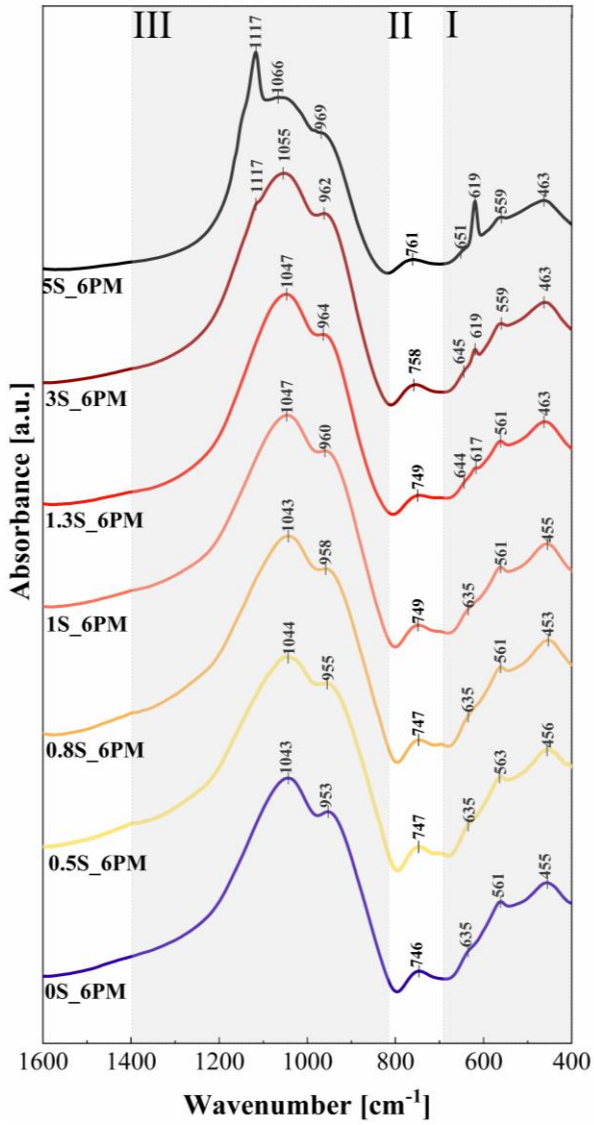


Fig. 37. MIR absorption spectra of studied silicate-phosphate glasses, [280].

9.2 FTIR spectroscopy study

In order to complement the structural insights obtained through Raman spectroscopy, additional spectroscopic investigations were carried out using mid-infrared spectroscopy. The acquired spectra, presented in Fig. 37, offer a valuable extension of the vibrational data, enabling a more comprehensive interpretation of the structural characteristics of the studied silicate-phosphate glasses.

Much like the Raman results, the infrared spectra are dominated by broad, overlapping bands associated with the vibrational modes of silicon-oxygen as well as phosphorus-oxygen bonds, and may, once again, be conventionally divided into three primary frequency domains. The **high-frequency region** (1400–800 cm^{-1}) comprises a complex envelope of bands originating from various stretching vibrations, including those of Si=O, Si–O–Si, Si–O–P, Si–O^-, and P–O linkages [110,331], the **mid-frequency region** (700–800 cm^{-1}) is

characterized by Si–O–Si bending modes, typically associated with bridging oxygens within the silicate framework [315,331], while the **low-frequency range** (400–650 cm^{-1}) includes contributions from both the vibrations of phosphate tetrahedra as well as O–Si–O bending vibrations [110,331,332].

Notably, in contrast to the Raman spectra, sulfur incorporation does not initially produce clearly discernible features in the MIR spectra, with the first sulfate-related band, attributed to the asymmetric bending vibrations (δ_{as}) of $[SO_4]^{2-}$ tetrahedra, becoming evident only upon the addition of at least 1.3 mol% SO_3. Notably, its intensity increases progressively with further sulfur incorporation [251]. and its intensity is notably growing with the increase of sulfate content. a second sulfate-specific vibration, corresponding to the asymmetric stretching mode (υ_{as}) of the $[SO_4]^{2-}$ unit [251], emerges not sooner than in the spectrum of the glass containing 3 mol% SO_3, where it is detected near 1117 cm^{-1}.

It is important to emphasize that the appearance of these sulfate-associated bands is not the sole spectroscopic consequence of increasing sulfur content. Indeed, as the concentration of SO_3 in the glass increases, subtle yet systematic changes are observed in the shape, position, and relative intensity of several spectral features across the full MIR range. To explore these structural modifications more rigorously, a deconvolution approach – analogous to that employed in the Raman spectral analysis – was adopted. The resulting fitted spectra, which provide a clearer resolution of the overlapping vibrational components, are illustrated in Fig. 38 .

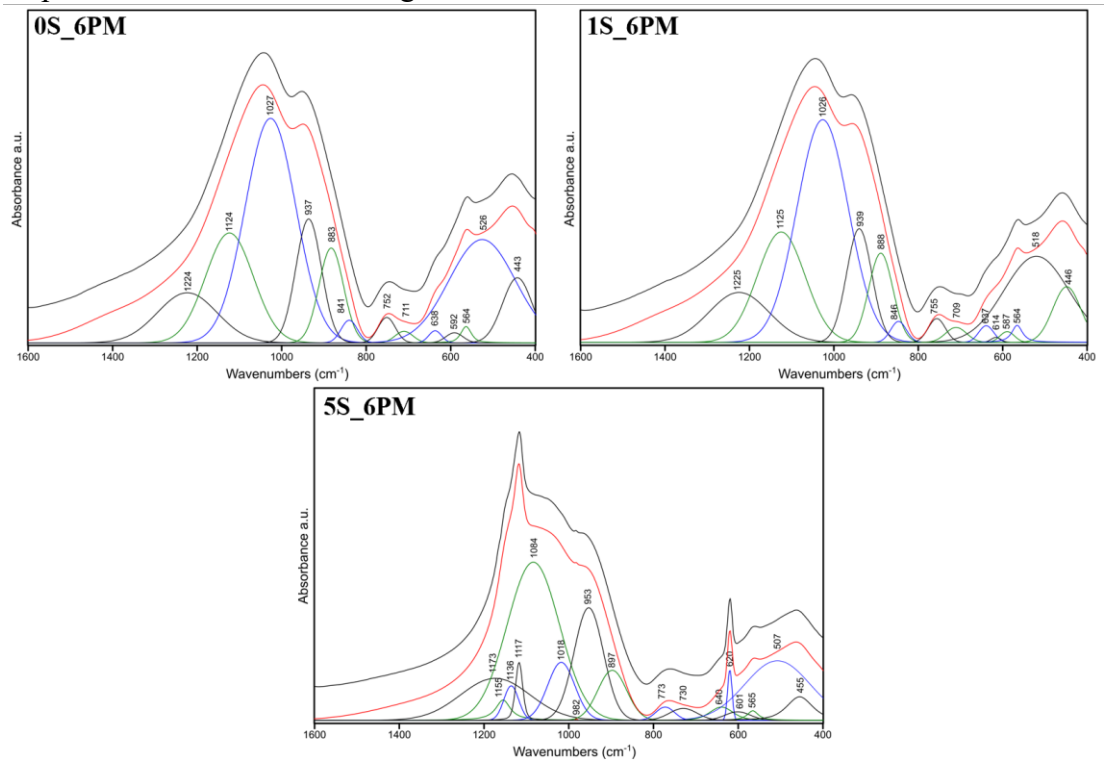


Fig. 38. Deconvoluted mid-infrared (MIR) spectra of selected samples from the XS_6PM system: base glass (upper left), sample containing 1 mol% SO_3 (upper right), and sample doped with 5 mol% SO_3 (bottom panel) [280].

As illustrated in Fig. 38, the comparative analysis of the absorbance spectra obtained via MIR spectroscopy proves to be less diagnostically revealing than the Raman-derived data. In particular, both the number and position of the component bands, as well as their overall profiles, remain virtually unchanged when comparing the sulfate-free base glass

with the specimen doped with 1 mol% SO_3. However, for the glass containing the highest sulfur concentration (5S_6PM), notable spectral alterations emerge across all three principal vibrational regions, suggesting a more pronounced structural effect at elevated sulfate loadings.

I. **Low-frequency region (650–400 cm^{-1}):**

Deconvolution of this range uncovered five distinct component bands, centred at approximately 443, 526, 564, 592, and 638 cm^{-1}. The first of these, near 450 cm^{-1}, is attributed to rocking vibrations of bridging oxygen atoms within O–Si–O linkages [313,332], and exhibits a pronounced shift towards higher wavenumbers with increasing SO_3 content (from 443 to 455 cm^{-1}), indicating a subtle reconfiguration of the silicate framework. The band located near 640 cm^{-1}, according to literature, associated with cristobalite-like domains embedded within the glass matrix, however, remains largely unaffected by sulfur incorporation [110]. The remaining bands in this frequency window are related to the bending modes of O–P–O bonds within PO_4^{3-} tetrahedra [110,316,320,333–336]. Notably, the most intense among these – centred at 526 cm^{-1} – shifts significantly toward lower wavenumbers, a trend that may reflect perturbations within the phosphorus-oxygen subnetwork induced by the presence of sulfate species. When this shift is considered alongside the decreasing intensity of the asymmetric P–O band in the Raman spectrum, it becomes plausible to suggest a slight competitive interaction between $[PO_4]$ and $[SO_4]$ units for charge-balancing K^+ cations. This ionic competition may lead to a subtle redistribution of phosphate species within the vitreous structure [251,337].

II. **Mid-frequency region (800–700 cm^{-1}):**

Although this region primarily reflects the vibrational modes of bridging Si–O–Si linkages, it also encompasses overlapping contributions from P–O–P bonds [110]. While the overall intensities of these features remain relatively stable, a consistent shift towards higher wavenumbers is observed, once again suggesting a changes in polymerization of the glass network.

III. **High-frequency region (1400–800 cm^{-1}):**

This range contains the highest number of closely spaced bands, and thus – constitute the most structurally informative region of the MIR spectrum. Unfortunately, due to the overlapping of vibrational modes originating from both $[SiO_4]^{4-}$ and $[PO_4]^{3-}$ tetrahedra, precise attribution of each component band remains challenging. Nonetheless, bands appearing between 800 and 1000 cm^{-1} are typically linked to $Si–O^-$ stretching vibrations that result from the disruption of Si–O–Si bridges [110,332]. Further specificity is provided by Agathopoulos et al. [313] and Kalampounias et al. [338,339], who assign features in this spectral range to Q^n_{Si} units with varying numbers of non-bridging oxygen atoms. Accordingly, the progressive shift of these bands toward higher wavenumbers may signify a growing dominance of structural units with fewer non-bridging oxygens—an indicator of increasing network polymerization. In contrast, the bands within the 1000–1200 cm^{-1} region – region of the most intense spectral features – are attributed to a combination of Si–O–Si, Si–O–P, and P–O stretching vibrations [110,331]. Importantly, with increasing SO_3 content, not only do these bands undergo shifts toward higher frequencies, but their internal structure also

evolves: initial features located at 1027 and 1124 cm^{-1} become resolved into multiple distinct bands (at 1018, 1084, 1136, and 1155 cm^{-1}). This spectral splitting likely reflects the growing influence of local crystalline ordering on the MIR response [324], consistent with the partial devitrification observed in the 5S_6PM sample. Lastly, the high-wavenumber feature near 1225 cm^{-1} is commonly ascribed to the stretching vibrations of terminal Si=O double bonds [332,340].

Although the introduction of sulfate species does not result in abrupt or dramatic changes in the MIR spectra—suggesting concurrently no abrupt changes in the glass structure—clear trends are nevertheless evident. The progressive shift of vibrational bands toward higher wavenumbers strongly indicates an increasing degree of polymerization within the silicate-phosphate network – conclusion that fully aligns with the acquired Raman data.

9.3 MAS-NMR spectroscopy study

It is well established that the structural characterization of silicate-phosphate glasses using vibrational spectroscopy techniques such as mid-infrared and Raman spectroscopy presents significant challenges, primarily due to the substantial overlap of the vibrational modes associated with Si–O and P–O bonds [183,313]. In light of these limitations MAS-NMR spectroscopy was employed, targeting both silicon and phosphorus nuclei, in order to achieve a more comprehensive elucidation of the influence exerted by SO_3 incorporation on the silicon-oxygen and phosphor-oxygen subnetwork architectures.

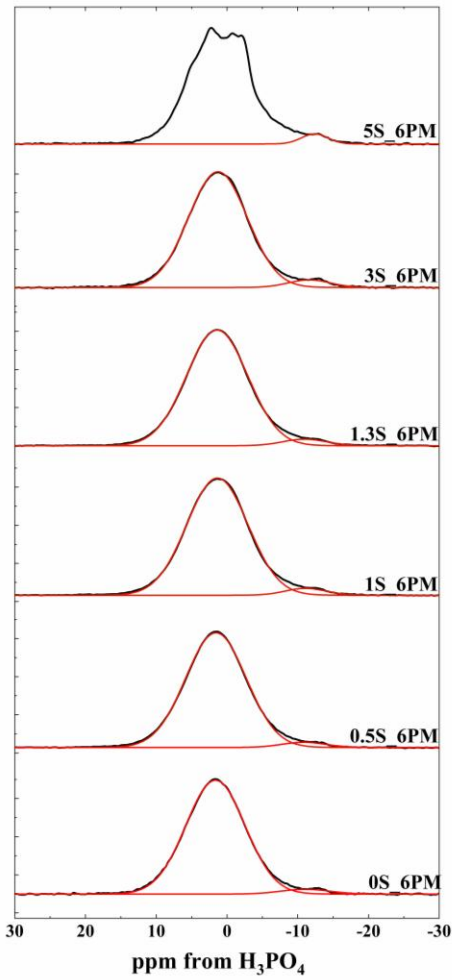


Fig. 39. ^{31}P MAS-NMR spectra of studied silicate-phosphate glasses [280].

In interpreting the acquired spectra, it should be emphasized that all analyses were conducted with reference to the sulfate-free glass sample (0S_6PM). Moreover, spectral deconvolution was performed using a Gaussian fitting model, with the estimated uncertainty in chemical shift positions not exceeding ±0.1 ppm.

The ^{31}P MAS-NMR spectra of selected samples, following Gaussian deconvolution, are presented in Fig. 39Fig. 39, with corresponding spectral parameters detailed in Tab. 15.

The experimental results consistently reveal that, regardless of SO_3 addition, the spectra comprise a superposition of two Gaussian components, indicative of phosphorus atoms occupying two chemically non-equivalent environments. The only notable deviation from this pattern is observed in the 5S_6PM sample, where the introduction of 5 mol.% SO_3 results in the emergence of markedly sharper and narrower peaks, further supporting the hypothesis of increased structural ordering within this specific glass composition.

The predominant spectral feature, characterized by a relatively broad full width at half maximum (FWHM) and positioned within the chemical shift range of approximately +1.8 to +1.4 ppm, is attributed to isolated orthophosphate species, PO_4^{3-} units (Q_P^0), while a distinct shoulder appearing in the –12.3 to –10.7 ppm region corresponds to a minor population of diphosphate species $P_2O_7^{4-}$ (Q_P^1) [341–343]. Much more speculative is precise band assignment in the case of the 5S_6PM spectrum, characterised by the presence of sharper and more pronounced features, alongside the above-mentioned, localised at about: -2.3, -0.9, +2.3 as well as +5.2 ppm, Fig. 39. These features likely reflect the presence of multiple inequivalent orthophosphate sites, each characterized by distinct local environments and varying degrees of structural ordering. Considering that pure crystalline K_3PO_4 exhibits a signal at about +11.7 ppm, whereas Mg_3PO_4 – around 0.0 ppm, the intermediate positions between these values allows to deduce the presence of different levels of participation of the network modifiers cations in charge-compensation of the orthophosphate sites in the tested sample [344,345].

Furthermore, the progressive downfield shift of the signals corresponding to both mono- and diphosphate species, observed with increasing sulfate content, reinforces the notion that SO_3 incorporation indeed alters the configuration of the phospho-oxygen framework. Of particular interest is the observed narrowing of the spectral features and the subtle yet consistent shift in the Q_P^0/Q_P^1 ratio. Specifically, the relative proportion of orthophosphate units exhibits a marginal decline in favour of pyrophosphate species as the sulfate concentration increases, implying a modest enhancement in the formation of bridging P–O–P linkages and thus a slight increase in the connectivity of the phosphate subnetwork [341,343]. It must be underscored, however, that this structural reorganization is relatively minor in magnitude. As indicated by the data summarized in Tab. 15, the relative abundance of Q_P^1 units rises by only approximately 1% upon comparison of the base glass composition with those containing at least 1 mol.% sulfate species attesting to the subtle nature of the sulfate-induced modifications within the phosphate network.

Tab. 15. ^{31}P MAS-NMR parameters of selected glasses from the XS-6PM system [280].

Sample ID	Chemical shift [ppm]	FWHM [ppm][1]	Relative contribution [%]	Type of structural unit
0S_6PM	+1.8	9.8	97	Q_P^0
	-10.9	8.2	3	Q_P^1
0.5S_6PM	+1.7	10.1	97	Q_P^0
	-10.7	7.3	3	Q_P^1
1S_6PM	+1.5	10.1	96	Q_P^0
	-11.0	6.8	4	Q_P^1
1.3S_6PM	+1.5	10.2	96	Q_P^0
	-10.8	7.3	4	Q_P^1
3S_6PM	+1.4	9.8	95	Q_P^0
	-11.5	7.0	5	Q_P^1
5S_6P	-	-	96	-
	-12.3	4.4	4	Q_P^1

[1] *FWHM = Full Width at half Maximum*

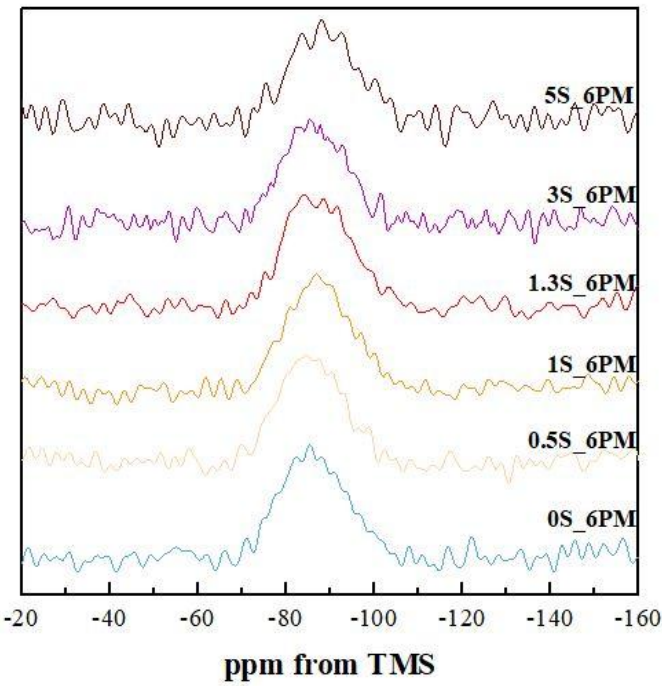


Fig. 40. ^{29}Si MAS-NMR spectra of silicate-phosphate glasses under investigation [280].

Meanwhile, the ^{29}Si MAS-NMR spectra recorded for the entire set of studied silicate-phosphate glasses exhibit a single, characteristically broad resonance spanning the chemical shift range from approximately −60 to –120 ppm, thereby confirming the exclusive presence of silicon atoms in tetrahedral coordination (Fig. 40Fig. 40).

Remarkedly, in the studied system where the sulfate content was systematically increased relative to the base composition, a subtle but consistent downfield shift of the signal maximum was observed – from –84.3 ppm in the sulfate-free sample to approximately –93.9 ppm in the most sulfur-rich variant. This trend is widely recognized as a spectroscopic manifestation of progressive polymerization within the silico-oxygen subnetwork [207].

Given the evident right-skewed asymmetry of the resonances, a deconvolution procedure was applied to enhance spectral resolution and allow for more precise interpretation. The resulting deconvoluted spectra for selected samples are shown in Fig. 41, with a summary of corresponding spectral parameters provided in Tab. 16.

As illustrated therein, the spectra of all analysed glasses reveal the presence of two distinct resonances, assigned—based on their respective chemical shifts– to Q^2_{Si} (–84.3 ppm) and Q^3_{Si} (–94.5 ppm) structural units [346–349]. Upon incremental incorporation of sulfate species into the glass matrix, only minor shifts in the positions of these signals were noted (Q^2_{Si}: –84.3 → –85.0 ppm; Q^3_{Si}: –94.5 → –93.9 ppm). However, particular attention should be paid to the relative intensities of the individual peaks: as the SO_4^{2-} content increases, the contribution of Q^2_{Si} units decreases, while that of Q^3_{Si} units becomes more pronounced. Such a systematic redistribution strongly supports the hypothesis that sulfate incorporation promotes the polymerization of the silicate network by facilitating the conversion of less connected tetrahedra to more extensively cross-linked configurations [346,347].

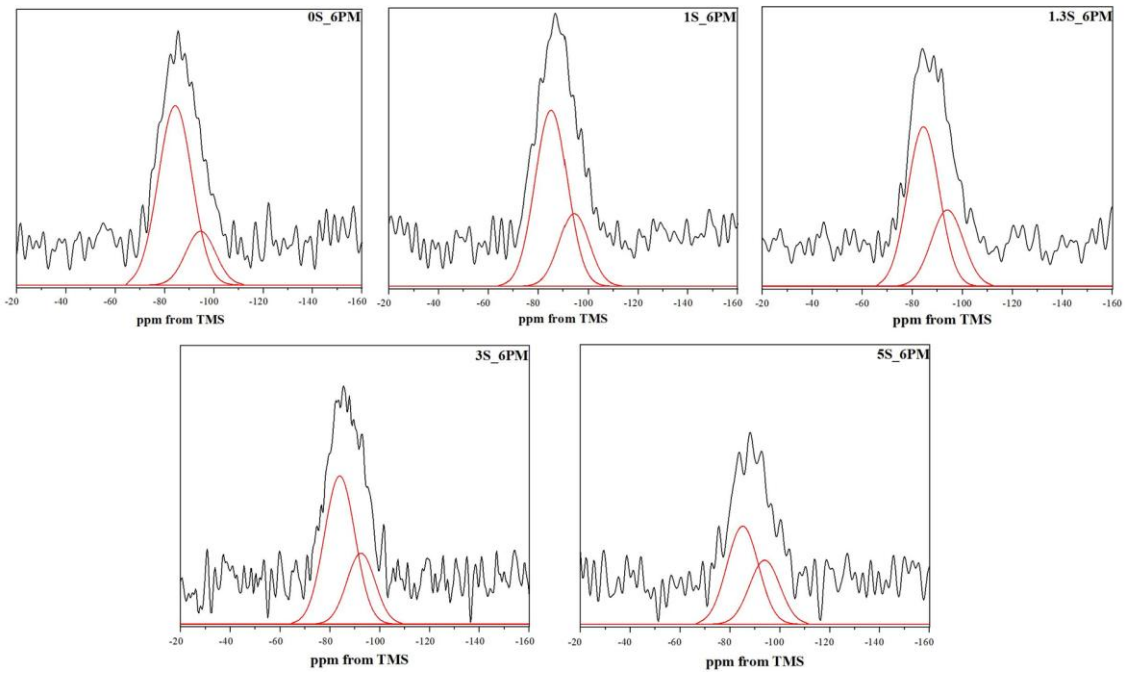


Fig. 41. Deconvoluted ^{29}Si NMR spectra of selected silicate-phosphate glasses [280].

Tab. 16. ^{29}Si MAS-NMR parameters of selected glasses from the XS_6PM system [280].

Sample	Chemical shift [ppm]	FWHM [ppm]	Relative contribution [%]	Type of structural unit
0S_6PM	-84.3	16.1	79	Q^2_{Si}
	-94.5	14.2	21	Q^3_{Si}
1S_6PM	-85.1	15.1	72	Q^2_{Si}
	-94.3	14.0	28	Q^3_{Si}
1.3S_6PM	-84.4	14.9	67	Q^2_{Si}
	-94.0	15.0	33	Q^3_{Si}
3S_6PM	-83.9	14.5	70	Q^2_{Si}
	-92.4	13.3	30	Q^3_{Si}
5S_6PM	-85.0	14.9	61	Q^2_{Si}
	-93.9	14.3	39	Q^3_{Si}

In order to quantitatively assess these structural modifications, the average number of non-bridging oxygens per tetrahedron (NBO/T) and the degree of network connectivity (NC) were calculated for all samples [104,350]. These estimations were derived from both nominal oxide compositions (annotated as 'nom') and experimentally determined values obtained via X-ray fluorescence spectroscopy (marked as 'XRF'), and are presented in Tab. 17.

Tab. 17. Estimated NBO/T and NC values for selected compositions [280].

Sample	$(^{NBO}/_{T})_{nom}$	$(^{NBO}/_{T})_{XRF}$	$\{NC\}_{nom}$	$\{NC\}_{XRF}$
0S_6PM	1.72	1.76	1.72	1.61
1S_6PM	1.67	1.58	1.75	1.65
1.3S_6PM	1.66	1.61	1.79	1.65
3S_6PM	1.58	1.60	1.78	1.68
5S_6PM	1.48	1.64	1.86	1.74

The calculations reveal a consistent trend: as the sulfate content increases, the average number of non-bridging oxygens per silicate tetrahedron decreases, while the number of bridging oxygens—and consequently, the overall network connectivity—rises. This enhanced degree of polymerization may be rationalized by considering the structural role of the $[SO_4]^{2-}$ tetrahedra: their incorporation introduces an excess negative charge into the glass network, which appears to preferentially attract non-tetrahedral modifier cations (such as K^+) into their immediate vicinity. Notably, sulfur's higher cation field strength (CFS) relative to silicon (2.60 vs. 1.57) is more effective in competition for its oxygen environment to achieve densest packing and thus – implies a greater tendency to attract and coordinate with such modifiers [102,249,253]. This preferential association of modifier cations with sulfate units may, in turn, displace potassium ions from the silico-oxygen subnetwork, thereby facilitating the formation of additional Si–O–Si bridges and reinforcing the connectivity of the silicate framework. When these findings are juxtaposed with the relatively modest variations observed in the phosphorus network – reflected in the minor shifts in Q_P^n unit contributions – an asymmetrical action of sulfate units on both studied subnetworks is revealed: the comparable CFS values of phosphorus and sulfur (2.10 and 2.60, respectively, [102]) suggest a more balanced competition for modifier cations as regards the phospho-oxygen subnetwork. Consequently, the structural reorganization induced by sulfate incorporation appears to be more pronounced in the silicon-oxygen part of the network, while changes within the one, formed by the phosphorus remain comparatively limited [262].

9.4 X-ray absorption spectroscopy study

To elucidate the effect of sulfur incorporation on the local atomic environments within glasses belonging to the SiO_2–P_2O_5–K_2O–MgO–SO_3 system, element-specific X-ray absorption spectroscopic techniques were employed. Specifically, measurements were conducted at the sulfur and phosphorus K-edges using the XAFS beamline, and at the magnesium and silicon K-edges via the XAS beamline. The corresponding findings are presented below:

I. Sulfur

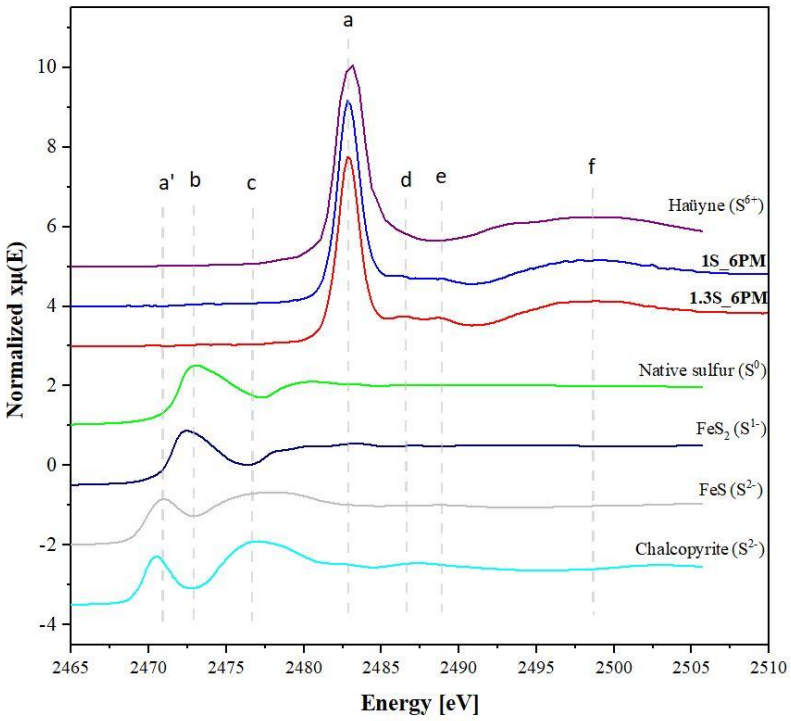


Fig. 42. Normalized XANES spectra at the S K-edge for the analysed glasses alongside selected sulfur-bearing reference compounds. Spectral data for FeS, native sulfur, and chalcopyrite were sourced from Fleet et al. [351,352], while that for haüyne was retrieved from Debret et al. [353]; all reference spectra were extracted using the open-access platform WebPlotDigitizer [354]. Vertical reference markers labelled "a" through "f" were adopted from the aforementioned studies and correspond to the following absorption energies: a' – 2471.01 eV; a – 2482.89 eV; b – 2474.01 eV; c – 2481.01 eV; d – 2486.37 eV; e – 2488.55 eV; and f – 2498.85 eV, [280].

As illustrated in Fig. 42, the spectra of the reference compounds display a systematic shift of the absorption edge with increasing sulfur oxidation state, progressing from metal monosulfides (S^{2-}), through disulfides of the pyrite group (S_1^-), to elemental sulfur (S^0), and ultimately to sulfate species (S^{6+}). This trend, widely recognized in the literature [355,356] is particularly reliable for sulfur in oxygen-rich compounds, wherein the absorber atom is directly coordinated by O^{2-} anions and all cationic species are situated in the second or more distal coordination spheres, in contrast to the behaviour observed in metal sulfides [351]. Against this backdrop, the pronounced spectral resemblance between the investigated glass samples and known sulfate-containing minerals – especially the presence of a distinctive sharp resonance near 2482 eV – strongly suggests that sulfur exists exclusively in its highest oxidation state (S^{6+}) within the studied vitreous matrices, supporting at the same time earlier hypotheses derived from Raman spectroscopic analyses. The intense feature at approximately 2482 eV, denoted as "a" Fig. 42,**Błąd! Nie można odnaleźć źródła odwołania.** is assigned to the transition of the sulfur 1s core electron into the lowest unoccupied antibonding molecular orbitals associated with the sulfur atom [351,357]. Subsequent post-edge resonances, marked "d", "e", and "f", arise from multiple scattering phenomena and reflect the extended coordination environment

beyond the first coordination shell. Their presence in both the studied glass spectra indicates a similar intermediate-range structural motif surrounding the sulfate groups, and at the same time – mirrors this, found in sulfate-bearing reference minerals [351,357]. Collectively, acquired findings confirm that the sulfate species incorporated into the silicate-phosphate glass network retain their structural integrity and exhibit a considerable degree of local order – an interpretation that aligns well with previous spectroscopic observations pointing to the presence of individual sulfate domains within the vitreous framework of tested glasses.

II. Phosphorus

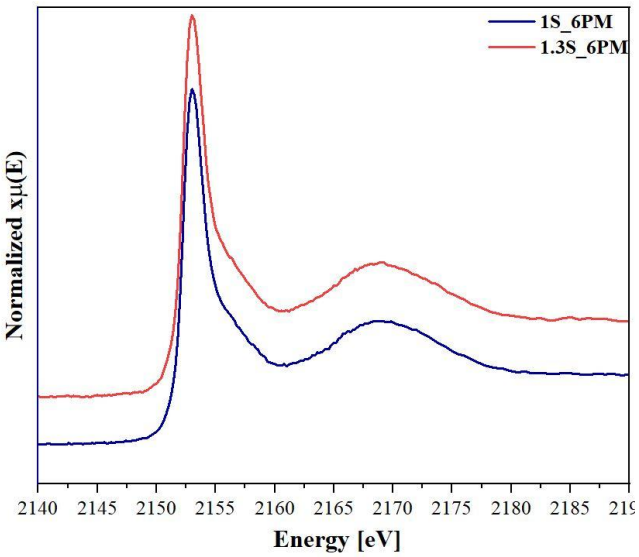


Fig. 43. Normalized XANES spectra at the P K-edge for the investigated glass samples. Reference energy positions for features "a" and "b" correspond to 2152.99 eV and 2168.91 eV, respectively.6 eV; b: 2169,28 eV,[280].

The phosphorus K-edge XANES spectra of the analysed glasses (Fig. 43) display remarkably consistent features across all samples, with each spectrum dominated by a single, intense absorption peak ("a") centred at approximately 2152.99 eV, characterized by a distinct inflection on its high-energy shoulder, referred to as "a1". This principal resonance is accompanied by a secondary, less prominent feature ("b") observed at around 2168.91 eV. Notably, the shape and intensity of the primary K-edge peak closely resemble those reported for crystalline phosphate phases [358], which aligns with the well-established principle that K-edge spectral features tend to converge across compounds containing similarly coordinated absorber atoms, particularly when surrounded by electronegative ligands [359]. Given the tetrahedral T_d symmetry of the PO_4 unit, the most intense transition observed in the spectra can be attributed to the excitation of a P 1s core electron into an unoccupied antibonding state of t_2* symmetry, resulting from the hybridization of phosphorus sp^3 orbitals with oxygen 2p orbitals [359,360]. Additionally, the subtle shoulder detected at approximately 2157 eV, situated on the higher-energy side of the main absorption edge, is a spectral feature commonly observed in a variety of crystalline phosphate minerals; here, in the case of the glasses under study, this feature appears noticeably broadened – a consequence of the inherent structural disorder and statistical variability within the vitreous matrix [358]. Importantly, the energy positions of the main spectral features, including both the white line and the post-edge resonance, remain essentially invariant with increasing sulfur content. Furthermore, the post-edge feature "b", generally associated with shape resonances resulting from multiple scattering events [359,360] also shows no substantial variation in either position or intensity across the studied series. Since alterations in the local chemical

environment surrounding PO_4 tetrahedra would typically manifest as shifts or distortions in the recorded XANES features, the absence of such spectral changes strongly suggests that the closest atomic environment of phosphorus remains largely unaffected by the incorporation of sulfur into the glass structure. This observation is consistent with the notion that modifications introduced by increasing sulfate content are primarily accommodated through the redistribution of charge-balancing modifier cations between the [PO_4], [SO_4] and [SiO_4] units, while the local environment of the phosphate tetrahedra preserved, thereby explaining the spectral invariance observed in the phosphorus K-edge region.

III. Silicon

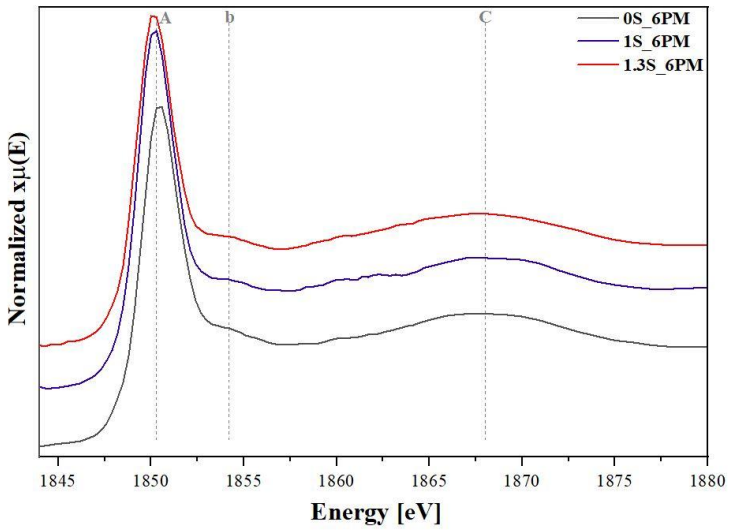


Fig. 44. Normalized X-ray absorption spectra at the Si K-edge for the analysed glass samples. Reference peaks "A", "b", and "C" correspond to the following energy positions: A – 1850.33 eV; b – 1854.23 eV; C – 1868.01 eV, [280].

Fig. 44 resents the Si K-edge XAS spectra acquired for the examined silicate-phosphate glasses. As illustrated, all spectra consistently exhibit three primary features, designated as A, b, and C, with the first of these, peak a – sharp and well-resolved, located at approximately 1850 eV – commonly assigned to the dipole-allowed transition of a Si 1s electron into an unoccupied 3p-like antibonding orbital [361,362]. While the intensity of this so-called "white line" may be influenced by several parameters, such as the symmetry of the local environment, Si–O bond lengths and angles, or the number and nature of neighbouring atoms [361], the minor differences observed in the normalized peak intensities are more plausibly attributed to experimental conditions – specifically, detection mode and surface charging artifacts encountered during measurement – rather than to any intrinsic structural variations. Nevertheless, subtle yet reproducible shifts in the energy position of the white line were recorded across the sample series. Notably, a systematic displacement of the K-edge towards lower energies was observed with increasing sulfur incorporation, shifting from 1850.45 eV in the sulfur-free glass to approximately 1850.16 eV in the sample with the highest SO_3 content. According to the study by Li et al. [362], such edge shifts may reflect a combination of factors, including variations in the O:Si ratio, modifications in the Si–O bond valence, or the influence of cations residing in second or more distant coordination shells. Given the compositional and structural complexity of the studied multicomponent glasses, a definitive attribution remains speculative. However, in light of complementary spectroscopic evidence, it is reasonable to suggest that this shift arises from modifications in the second-shell environment of silicon – likely due to the rearrangement of nearby

cations that indirectly perturb the primary oxygen coordination sphere of the SiO_4 tetrahedra.

The post-edge region of the spectra is notably less pronounced and was therefore interpreted with due caution. The broad feature labelled C, centred near 1867–1868 eV, is attributed to transitions of Si 1s electrons into higher-energy, unoccupied 3d-like states, a spectral signature characteristic of silicon in fourfold coordination [361–363]. In contrast, the assignment of the minor feature b, located around 1854.2 eV – approximately 2 eV above the main absorption edge – is more complex. Fleet et al. [364] previously associated this shoulder with the presence of sixfold-coordinated silicon species; however, in systems where [6]Si is present, one would expect the emergence of two distinct and well-defined post-edge peaks rather than a single, weak shoulder. Consequently, in the case of the glasses under investigation, it is more plausible that this feature originates from multiple scattering events, which are sensitive to the spatial arrangement of atoms beyond the first coordination shell [361–363]. It is of particular interest that Henderson [361] reported an increase in the intensity of this shoulder in glasses with higher Na_2O content, attributing the effect to the enhanced presence of network-modifying cations. Conversely, when RuO_2 was incorporated, a marked decrease in the intensity of feature b was observed, which was interpreted as a result of RuO_2 acting as a network modifier attractor – depleting the silicon coordination environment of sodium and calcium ions [363]. In light of these findings, and considering the attenuated intensity of feature b observed in the present study for sulfate-rich glasses (Fig. 44), it can be inferred that the incorporation of $[SO_4]^{2-}$ units indeed alters the structural order exceeding the one indicated by a single tetrahedron. Such alterations, as also suggested by Raman and IR spectroscopic data, appear to involve a redistribution of network-modifying cations (e.g., K^+) at distances beyond the first coordination sphere, leading to a partial reorganization of the glass network topology. In conclusion, the Si K-edge XAS results provide compelling evidence for subtle changes in the bonding environment of silicon, driven by the presence of sulfate species. These modifications primarily affect the intermediate-range order – particularly the configuration of cations situated in the outer coordination shells—rather than altering the immediate tetrahedral coordination of silicon atoms.

IV. Magnesium

The Mg K-edge XAS spectra obtained for all analysed glass samples reveal an essentially identical overall spectral profile, with the positions of the characteristic features exhibiting negligible variation across the series (Fig. 45). In a manner analogous to the silicon K-edge spectra discussed previously, observed differences in the relative intensities of the principal peaks may stem from subtle experimental influences – such as the detection mode employed – intrinsic to the measurement itself. Nonetheless, given that such deviation was noted exclusively for a single composition, it would be speculative at best to attribute this effect directly to the presence of SO_3.

As evident from the spectra presented in Fig. 45, the absorption envelope spans the energy range of approximately 1305–1390 eV and comprises four distinct features, designated A, B, C, and D. According to earlier interpretations [365–367], peak a corresponds to the dipole-allowed transition of a magnesium 1s electron into an unoccupied bound 3p-like state, peak B, by contrast, is associated with transitions involving the first coordination shell of Mg^{2+} ions. The more complex post-edge features, peaks C and D,

are attributed to multiple scattering effects originating in the extended coordination environment surrounding Mg atoms, as well as shape resonances related to the Mg–O coordination geometry [365–367].

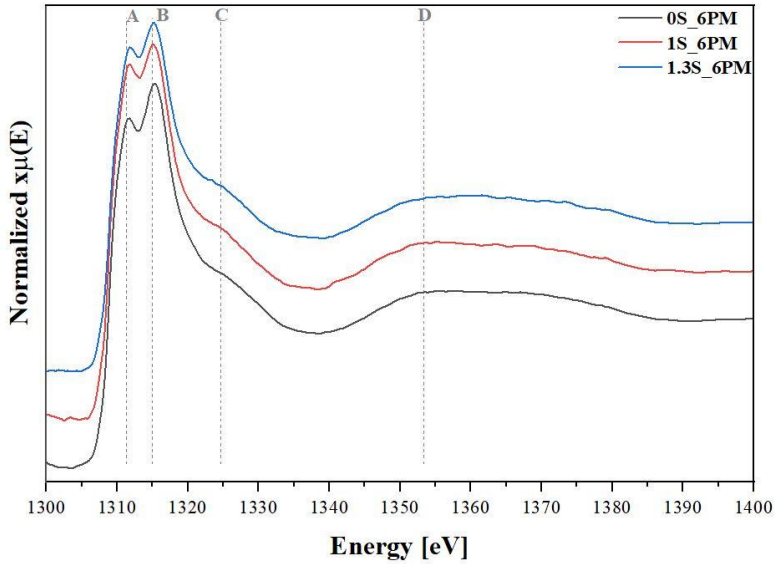


Fig. 45. Normalized X-ray absorption spectra at the Mg K-edge for the investigated glass samples. Reference peaks "A", "B", "C", and "D" correspond to the following energy positions: a – 1311.74 eV; B – 1315.31 eV; C – 1324.59 eV; D – 1353.36 eV, [280].

A careful analysis of the spectral features – including both peak positions and line shapes – strongly indicates that the immediate local environment of magnesium remains invariant regardless of the sulfur content in the glass composition – the incorporation of sulfate groups into the silicate-phosphate network exerts little to no influence on the spatial configuration of magnesium species. This finding lends further support to the hypothesis that sulfate groups interact preferentially with potassium cations, rather than with magnesium – a conclusion that aligns with the interpretations derived from complementary spectroscopic investigations.

9.5 Summary of the first part of the studies on sulfur-bearing silicate-phosphate glasses

The findings presented in Sections 8 and 9 concerning the design and synthesis of sulfur-bearing silicate-phosphate glasses as potential vitreous carriers for sulfur, while promising in certain respects, remain only partially satisfactory. Although the research successfully identified a compositional system that may serve as an effective sulfur carrier for agricultural applications, the overarching objective was to develop a series of glass compositions tailored for diverse soil conditions and crop-specific nutritional demands. Consequently, the inability to obtain fully amorphous materials within several of the designed glass systems constituted a major limitation – one that strongly motivated the author to explore alternative approaches for achieving vitrification of the originally proposed multicomponent matrices. The outcomes of these further investigations are detailed in **Publications P1, P3** and **P4**, together with an additional manuscript (designated here as **P2***). Although **P2*** is still in the process of publication, it represents the second consecutive stage of the research cycle and has therefore been retained in the numbering

scheme. Its inclusion in this dissertation ensures the coherence and continuity of the full series, which is subsequently discussed in detail.

Nevertheless, the comprehensive characterization of the only glass system – XS-6PM – that yielded fully amorphous samples has provided significant insights into the structural role and behaviour of sulfur in such materials. Preliminary assessments (XRD, XRF, SEM-EDS), complemented by thermal analyses (DSC of glasses and XRD/RSI of devitrification products), and followed by detailed spectroscopic investigations, collectively enabled the elucidation of critical phenomena governing sulfur incorporation.

It was demonstrated that tested XS_6PM silicate-phosphate glasses exhibit a marked tendency toward structural organization into orthophosphate-type domains. Importantly, this tendency intensifies with raising sulfur content – factor that leads also to the formation of sulfate domains of increasing degree of ordering. The incorporation of sulfate anions substantially narrows the vitrification range of the materials, reduces their thermal stability, and, beyond a certain compositional threshold, leads to the crystallization of surplus sulfur as discrete phases. Given the high aqueous solubility of these crystalline sulfur-rich phases, and thus their potential environmental impact in agricultural applications, the precise delineation of sulfur capacity limits becomes a matter of utmost relevance.

Moreover, the data acquired from a wide array of spectroscopic techniques consistently confirm that sulfur is incorporated exclusively in the form of sulfate anions – an observation of notable agronomic significance, as only sulfates are readily assimilable by plants. The absence of Si–O–S or P–O–S linkages supports the hypothesis of structural individuality of sulfate species in the glass matrix. Rather than integrating into either the silicate or phosphate subnetworks, sulfate groups are believed to form independent structural entities, spatially isolated and surrounded by a shell of network-modifying cations. This configuration not only segregates sulfate domains from the primary glass network but also depletes the immediate vicinity of the silicate framework in network modifiers, thus promoting the transformation of non-bridging oxygens into bridging ones. As a result, the overall degree of polymerization increases, as evidenced by a progressive shift from Q^2_{Si} to Q^3_{Si} units. Further insight was provided by X-ray absorption spectroscopy, which revealed that sulfur exerts a considerably stronger influence on the local structural environment of silicon than that of phosphorus. In particular, sulfate groups were found to affect the more distant coordination shell constituents of silicon atoms—consistent with the notion that network-modifying cations are drawn away from the silicate domains to stabilize the sulfate units through charge compensation. Although both K^+ and Mg^{2+} ions act as modifiers within the glass network, the XAS data indicate that only potassium participates in the coordination of sulfate groups, with magnesium clearly excluded from such interactions. This observation further substantiates the conclusion that potassium is the principal charge-compensating species in sulfate-rich regions of the glass.

10 Melt fritting procedure as a way of widening the glass-forming range of materials

Motivated by the objective of developing glassy materials with diverse chemical compositions adequate to the specific nutritional demands of different crops – as well as to accommodate varying rates of nutrient release into the soil environment – the author decided to modify the synthesis procedure, drawing upon the foundational principle that virtually any substance may be vitrified, provided a sufficiently rapid cooling rate is applied to the melt.

As elaborated in Chapter 3.4, the formation of an amorphous solid is inherently governed by kinetic factors, wherein a supercooled liquid must be cooled at a rate high enough to prevent the nucleation and growth of crystalline phases [368,369]. When the temperature of a supercooled liquid is reduced to the point where the structural relaxation time exceeds the experimental timescale, the system undergoes a glass transition, thus falling out of thermodynamic equilibrium. The resulting glass, therefore, represents a non-equilibrium state whose physical properties are not only defined by its composition but also strongly influenced by the thermal history of its formation, particularly the cooling or compression rate employed during vitrification [370–372]. Although it is broadly recognized that higher cooling rates enhance the likelihood of producing a fully amorphous material by bypassing crystallization, the precise mechanisms underpinning this relationship remain only partially understood. This knowledge gap primarily arises from the inherent difficulty in characterizing microstructural variations induced by different cooling rates (γ), despite the well-established correlation between such microstructures and the physical properties of amorphous solids. Consequently, elucidating how structural features at short- and intermediate-range order respond to varying γ is essential to understanding how macroscopic glass properties are modulated by thermal processing. However, probing such subtle structural transformations directly at the atomic level remains a formidable challenge, as atoms are both exceedingly small and highly mobile. Despite notable advances in microscopic techniques, the direct visualization of atomic disorder in amorphous solids remains elusive. a noteworthy attempt to address this issue was made by Lu et al. [373], who employed colloidal glass systems to explore the impact of cooling rate on local structural ordering. Through detailed analysis of the radial distribution function (RDF), they demonstrated that slower cooling promotes enhanced local ordering, an observation interpreted within the framework of free-volume theory. Free volume – defined as the spatial region surrounding a particle within which it may move without displacing its neighbours – is effectively "frozen in" during vitrification. According to Lu et al., higher cooling rates entrap more free volume, thereby introducing structural defects that compromise local order; thus, faster cooling is inherently associated with increased structural disorder.

Building upon these insights, Vollmayr et al. [371] conducted a systematic study showing that microscopic structural features exhibit markedly greater sensitivity to cooling rate variations than bulk properties. They demonstrated a logarithmic dependence of the glass transition temperature on γ, while also reporting that properties such as enthalpy, density, and thermal expansion coefficient tend to diminish with decreasing cooling rate. Their findings further revealed that microscopic metrics – including the RDF, bond angle distribution, coordination number statistics, and ring-size distributions – are all significantly influenced by γ. Most prominently, the RDF exhibited substantial dependence on

γ for interatomic distances up to 8 Å, signifying pronounced alterations in both short- and intermediate-range order. Their analysis of Si–O and O–O pair distributions confirmed that slower cooling yields a more ordered network structure. Interestingly, by further analysing the nearest-neighbour pairs, i.e., the Si-O and the O-Si pairs they revealed that in both cases the vast majority of the silicon atoms is surrounded by four oxygen atoms, which can be understood by taking into account that at low pressures silica forms a network of corner-sharing tetrahedra, each of which has a silicon atom in its centre and four oxygen atoms at its corners. Nevertheless, the number of silica atoms that are not fourfold coordinated was about 5% for the fastest cooling rate and diminished quickly to less than 0.5% when the cooling rate is decreased (the silicon atoms that were not fourfold coordinated, were surrounded in most cases by five oxygen atoms while only a very small fraction was surrounded by three oxygen atoms). This observation confirmed again that the local order of the network increases fast with decreasing cooling rate.

Importantly, the local SiO_4 tetrahedral geometry remained largely unaffected by γ, as indicated by the near-constant Si–O bond length. This observation suggests that individual tetrahedra retain their structural integrity, and that variations in density and local order likely arise from changes in the spatial arrangement of adjacent tetrahedra. Supporting this hypothesis, the authors observed that as γ decreases, the O–Si–O bond angle approaches the ideal tetrahedral angle of 109.47°, indicating a progression toward more regular tetrahedral geometry. Simultaneously, widening of the angle between three neighbouring oxygen atoms was interpreted as evidence of structural expansion, implying increased free volume and reduced packing density at lower γ values. These changes collectively suggest that the glass network "opens up" as cooling slows. Moreover, the frequency of six-membered Si–O rings – a structural motif characteristic of β-cristobalite – was found to increase with decreasing γ, reinforcing the idea that intermediate-range order improves under slower cooling conditions [371].

In light of this literature, the author re-synthesized all previously designed glasses using a modified approach, whereby the melt was poured into a cold water-filled basket to achieve a higher cooling rate than attainable via the conventional plate-cooling method. This method, since industrially scalable and devoid of complex instrumentation, was selected to maintain compatibility with large-scale production. For this new synthesis route, a subset of samples – comprising those doped with 1, 3, and 5 mol.% SO_3, along with their respective base compositions (0 mol.% SO_3) – was chosen for reprocessing, based on prior results obtained via plate-cooled samples.

The first and most evident outcome of the modified procedure was the transformation in the morphology of the final product: instead of compact glass pellets, the water-quenched method yielded irregular granules with significantly increased surface development (Fig. 46). This result is entirely consistent with the intrinsic brittleness and poor thermal conductivity of glass, which renders it highly susceptible to thermal shock: during rapid quenching, the outer surface of the glass solidifies and contracts much more rapidly than the interior, generating transient thermal stresses that often exceed the material's tensile strength, thereby leading to fracturing [374].

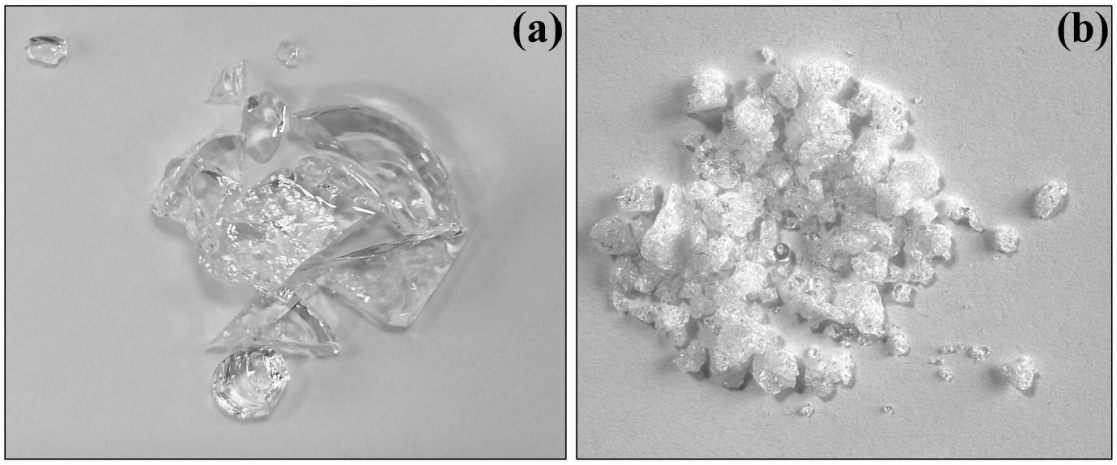
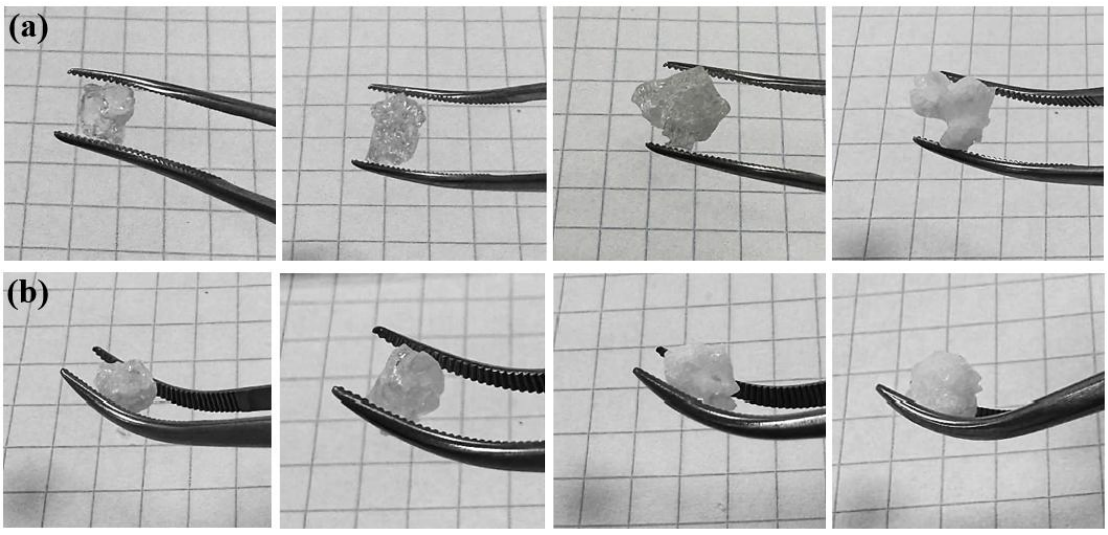


Fig. 46. Final form of glass materials produced by (a) plate-cooling and (b) melt-fritting in cold water.

This newly obtained morphological form is not without consequence for the intended application of these materials. First, the fritted granules possess a significantly higher specific surface area compared to their plate-cooled counterparts, which directly translates into an increased interfacial area in contact with the surrounding soil matrix. Such enhancement promotes faster ion exchange and nutrient release, thus improving the reactivity of the material under agronomic conditions. Secondly, as reported by Gray et al. [375], rapid cooling may introduce residual stresses that leave the material in a less stable, high-energy state. In the context of fertilizer application, such instability may be advantageous, rendering the glass more chemically active upon exposure to the environment. Finally, the spontaneous shattering induced by thermal stress during quenching offers a pragmatic benefit in potential industrial-scale processes, as it significantly reduces the energy required for post-synthesis grinding to obtain fine particulate fractions suitable for use as glass-based fertilizers.

Given the above, representative specimens from both the [6P] and [10P] compositional series, produced via the modified synthesis route, are depicted in Fig. 47



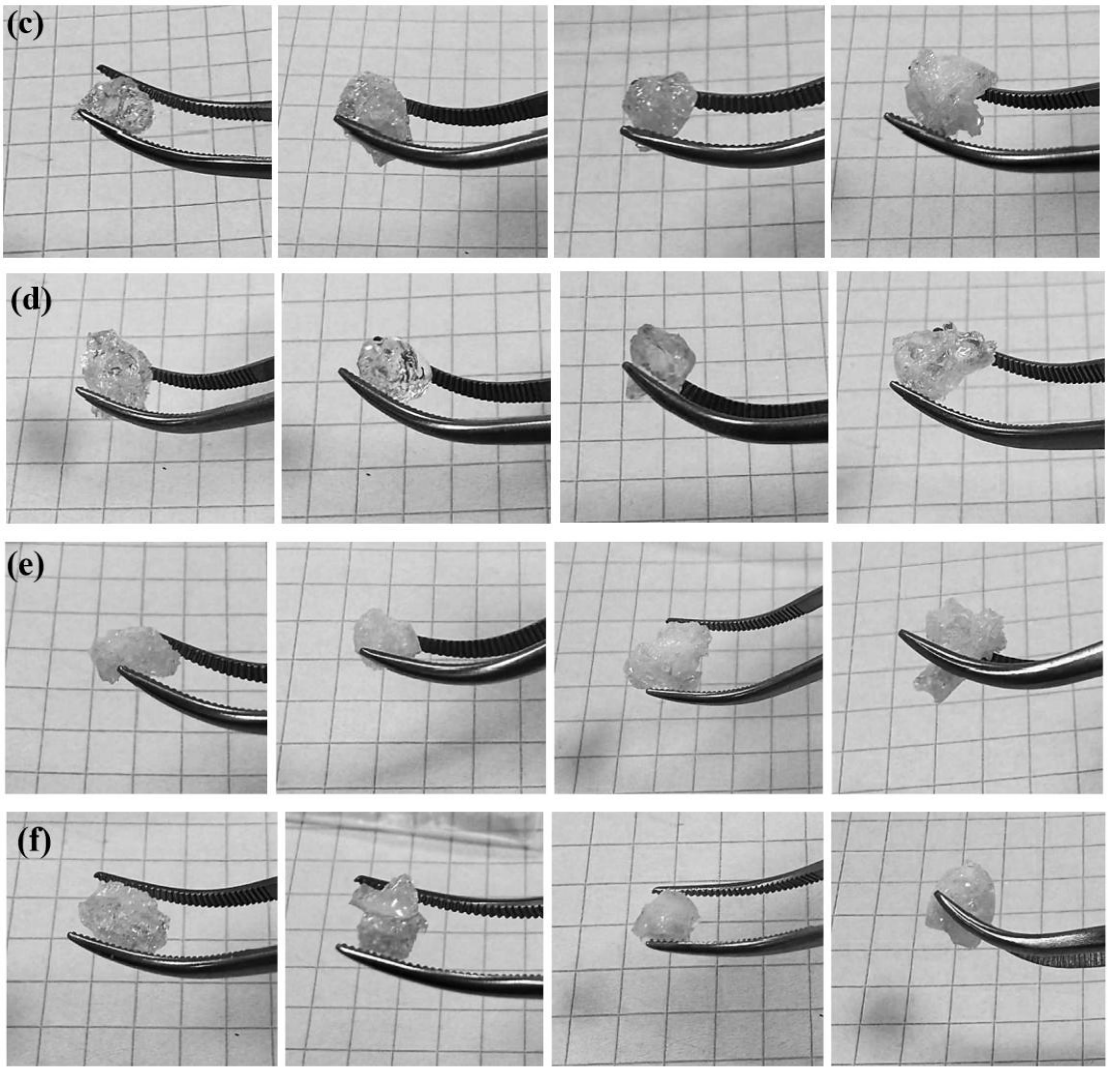


Fig. 47. As-synthesized samples obtained by the fritting method, representing all designed glass systems. The samples are arranged from left to right in order of increasing sulfur content in their nominal compositions (0S → 1S → 3S → 5S): XS_6PM (a), XS_6PC (b), XS_6PMC (c), XS_10PM (d), XS_10PC (e), XS_10PMC (f).

With regard to their visual appearance, none of the newly obtained specimens exhibited any evidence of "sulfate gall," understood here as surface-localized crystalline sulfate phases that differ visually from the bulk glass and typically indicate sulfur oversaturation, as was previously observed in plate-cooled materials. Consequently, the opacity noted in the present fritted glasses – particularly pronounced in the systems with lower P_2O_5 contents – may be reasonably attributed to an increase in overall crystallinity, which, in contrast to the surface-limited phenomena described above, appears to develop homogeneously throughout the bulk of the material.

11 Fritted sulfur-bearing glasses – guide to the published manuscripts

In light of the success achieved in broadening the glass-forming range for materials initially exhibiting a glass–ceramic nature when employing the plate-cooling technique, a decision was made to develop a series of publications presenting the findings related to such materials.

The opening article of this series, entitled *"Effect of sulfur addition on glass-forming ability, structure and thermal stability of multicomponent silicate-phosphate glasses"* (hereafter referred to as **P1** for clarity), reports on the results obtained for the most compositionally complex, successfully amorphized glasses within the SiO_2–P_2O_5–K_2O–MgO–CaO–XSO_3 system (XS_6PMC). This publication, which includes materials synthesized via melt quenching on a metal plate, serves as a conceptual and methodological bridge between both parts of the doctoral research. It underscores the considerable impact that even a relatively modest increase in the cooling rate – achieved through fritting, as compared to ambient-temperature cooling – can have in suppressing spontaneous crystallization (including that of sulfur-bearing phases such as K_2SO_4) and thereby enhancing the potential of the material to attain a fully amorphous state.

The demonstrated enhancement of glass-forming ability in these complex systems prompted a comprehensive characterization using methodologies conventionally employed in preliminary evaluations of vitreous matrices intended for use as controlled-release carriers of plant nutrients. These included: verification of amorphous nature and compositional homogeneity via XRD and XRF analyses, respectively; structural elucidation using FTIR and Raman spectroscopy; and thermal property assessment through DSC measurements. a notable contribution of **P1** is the devitrification study, conducted not only via XRD and Raman Imaging, but also supported by X-ray Absorption Spectroscopy, which enabled insight into the local atomic environments of key elements—particularly silicon, the principal network former, and magnesium, whose coordination state is of particular interest given its ambiguous role as either a modifier or an intermediate oxide, when existing in tetrahedral coordination.

Given the substantial improvement in the degree of amorphization for materials within the XS_10PM system – unique among the [10P] glass series in this regard – the second publication in the series – yet unpublished and therefore designated here as **P2*** – *"Phosphorus influence on sulfate capacity and structural evolution in multicomponent silicate-phosphate glasses"* – undertakes a comparative study between two analogous systems differing primarily in P_2O_5 content: the aforementioned XS_10PM and the XS_6PM composition, which had previously been amorphized via plate cooling and was now re-synthesized through fritting. The comparison focuses on the respective capacities of these matrices to accommodate sulfate groups, and is based on extensive structural analyses employing Raman and FTIR spectroscopy, solid-state NMR (^{29}Si and ^{31}P MAS-NMR), as well as XAS techniques.

The third manuscript in the series, entitled *"Alteration of sulfur-bearing silicate-phosphate (agri)glasses in soil environment: Structural characterization and chemical reactivity of fertilizer glasses. Insights from 'in vitro' studies"* (hereafter referred to as **P3**), integrates materials from all systems identified as promising sulfur carriers for agricultural use. These include: the most compositionally complex XS_6PMC glass (described in **P1**), the XS_6PM composition (re-synthesized by fritting), its CaO-containing variant

– XS_6PC system and the richer in P_2O_5 content XS_10PM formulation, as the one among the [10P] family, exhibiting the largest amorphous phase fraction. The significance of this publication lies in its comparative evaluation of the structural and thermal properties of the selected glasses, as well as their solubility profiles in two media: deionized water and a 2% citric acid solution, the latter widely regarded as a chemical analogue of root exudates. The findings presented in **P3** represent a critical contribution to the development of composition–structure–property relationships for these multicomponent glass systems.

Finally, the selected compositions were subjected to long-term testing under controlled climatic chamber conditions designed to simulate the dynamic environmental variability of the temperate climatic zone typical of Poland. The outcomes of these extended alteration studies are detailed in the fourth manuscript of the series, *"Alteration of Sulfur-Bearing Silicate–Phosphate (Agri)Glasses in Soil Environment: Chemical Interactions and Biological Response"* (referred to as **P4**).

The following subsections present a structured discussion grounded in the four abovementioned publications, outlining their most salient findings and key scientific implications.

11.1 Verification of the amorphous nature of the fritted materials

As demonstrated in publications **P1**, **P2***, and **P3**, the application of the fritting technique enabled a notable extension of the glass-forming range—particularly for the XS_6PC and XS_6PMC systems, where diffraction patterns of their plate-cooled analogues exhibited distinct reflections indicative of residual crystalline phases. Moreover, in the case of the XS_10PM composition, fritting led to a substantial increase in the amorphous fraction, as evidenced by the transformation of well-defined, sharp reflections into broad, low-intensity features on the corresponding diffraction patterns. For comparative purposes, a complete set of diffractograms for all fritted samples across the studied systems is presented in Fig. 48(a)–(f). Additionally, to highlight the structural differences induced by the cooling method, Fig. 49 juxtaposes diffraction patterns of samples from each system modified with 3 mol.% of SO_3, prepared via both plate-cooling and fritting approaches.

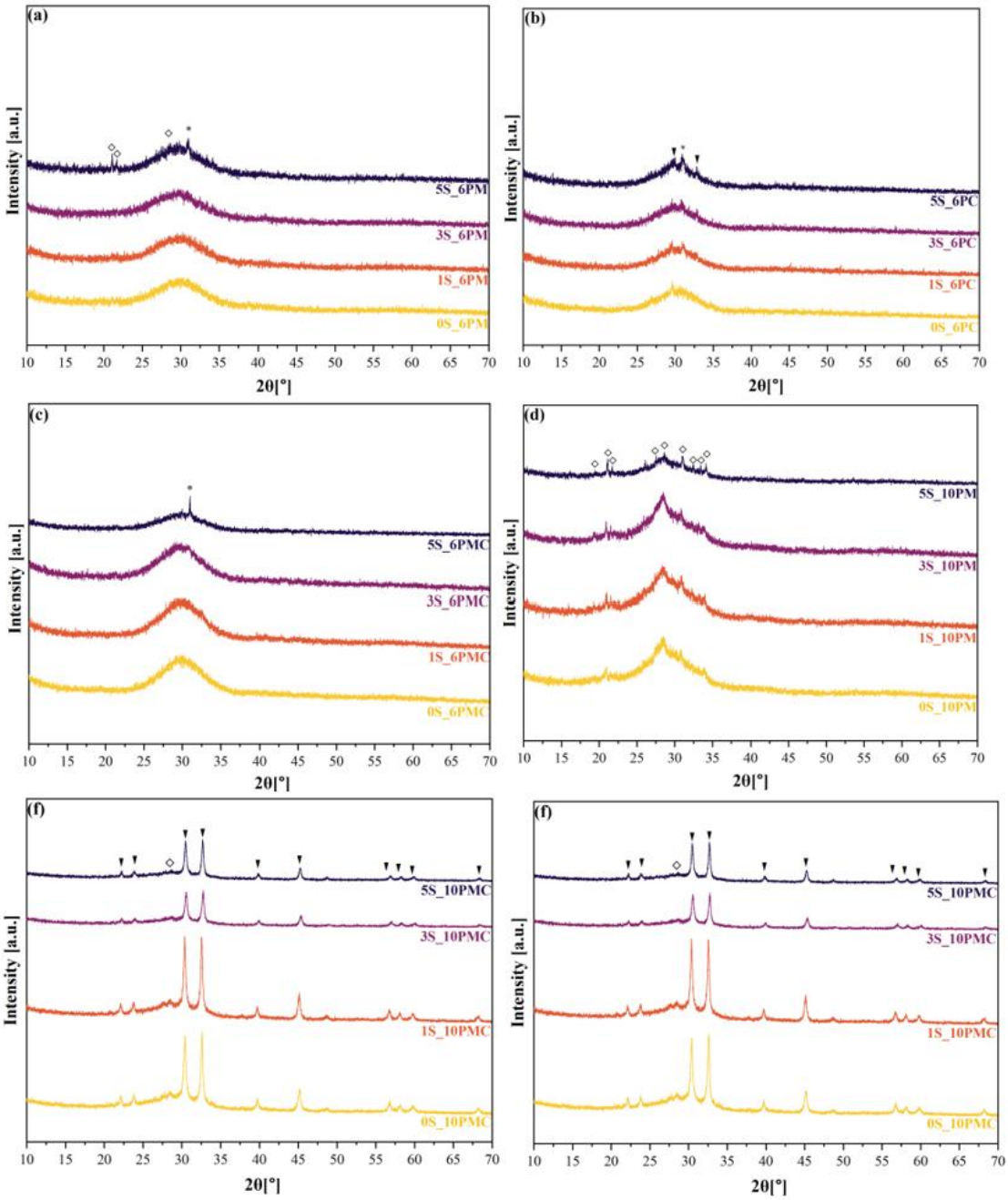


Fig. 48. XRD patterns of all resynthesized and fritted glasses from the XS_6PM (a), XS_6PC (b), XS_6PMC (c), XS_10PM (d), XS_10PC (e), and XS_10PMC (f) systems. Phase markers: elongated triangle – $KCaPO_4$ (00-033-1002), asterisk – K_2SO_4 (00-044-1414), empty inverse square – $KMgPO_4$ (00-050-0149).

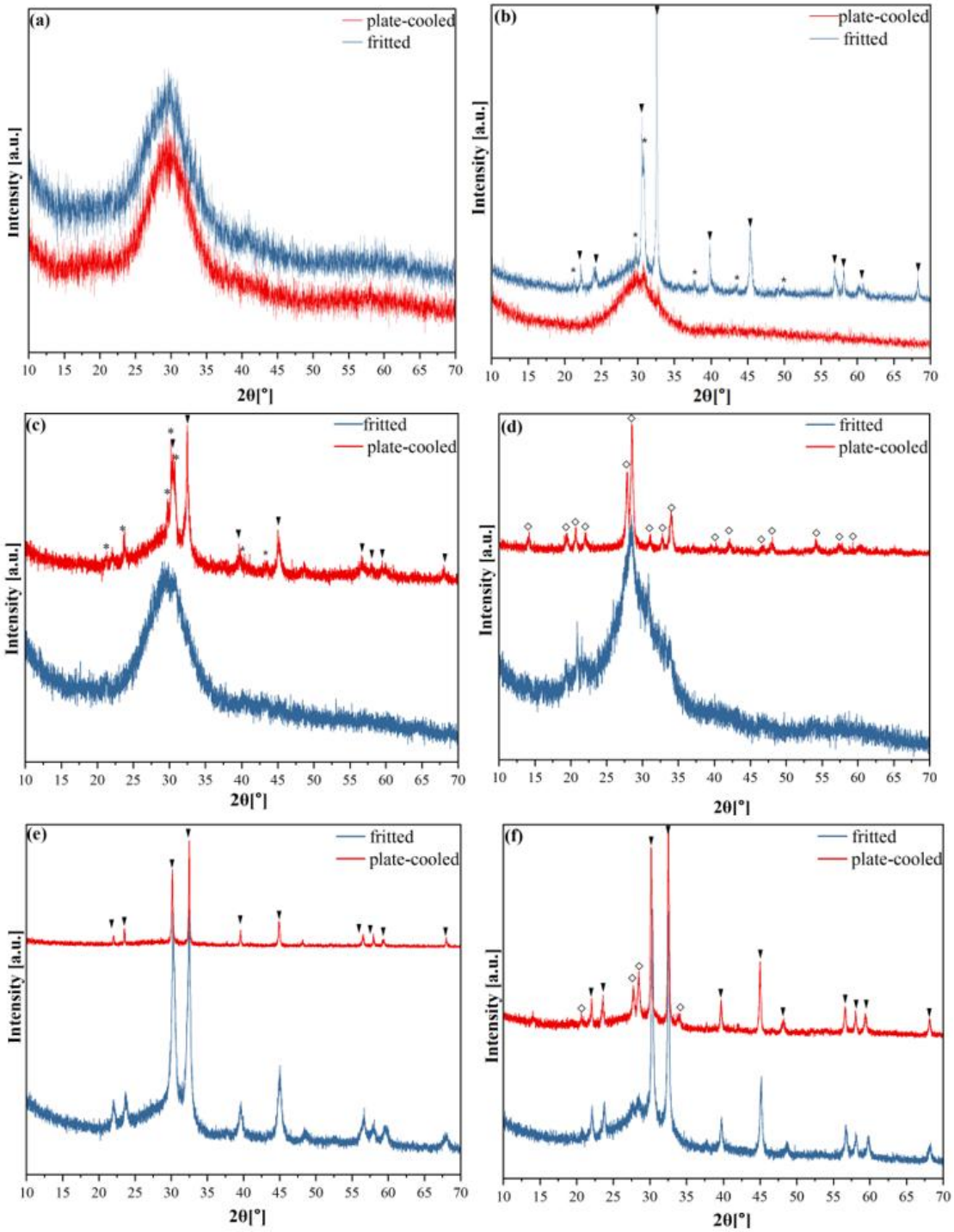


Fig. 49. Comparison of plate-cooled and fritted samples doped with 3 mol.% of SO_3; 3S_6PM (a), 3S_6PC (b), 3S_6PMC (c), 3S_10PM (d), 3S_10PC (e), and 3S_10PMC (f). Phase markers: elongated triangle – $KCaPO_4$ (00-033-1002), asterisk – K_2SO_4 (00-044-1414), empty inverse square – $KMgPO_4$ (00-050-0149).

The diffraction data shown in Fig. 48 and Fig. 49 clearly affirm the superiority of the fritting technique over conventional plate-cooling in terms of enhancing the glass-forming ability of the studied systems. While the latter method was effective in suppressing crystallization only for the XS_6PM composition (until 5 mol.% of sulfate species were introduced), fritting facilitated the production of predominantly amorphous materials even in the XS_6PC and XS_6PMC systems—extending their glass-forming range up to

3 mol.% of SO_3. In compositions enriched with P_2O_5, crystalline reflections were still observed regardless of the cooling method. Nonetheless, these features were noticeably broader in the fritted materials, implying significantly smaller crystallite sizes. This difference was particularly pronounced in the XS_10PM system (Fig. 48(d)), where the elevated background and diffuse diffraction peaks in the fritted samples – relative to their plate-cooled counterparts – attest to their dominant amorphous character and only limited precipitation of $KMgPO_4$ crystallites.

Due to the pronounced intensity of phosphate-related reflections as regards the XS_10PC ($KCaPO_4$) and XS_10PMC ($KMgPO_4$ and $KCaPO_4$) systems, these two formulations were definitively excluded from further investigation, as they failed to meet the requirement of predominantly amorphous character for potential sulfur glass carriers. By contrast, the XS_10PM composition was retained, as the observed reflections were of low intensity and exhibited broad full-widths at half-maximum—indicating the presence of only minor, possibly nanocrystalline inclusions within an otherwise glassy matrix, as emphasized in publication **P3**. Overlapping the amorphous halo, a set of extremely low-intensity reflections was also observed for the XS_6PC system, even in the base sample unmodified with sulfur (Fig. 48(b)). However, their limited intensity strongly suggests that the produced material remains predominantly amorphous. Despite the scarcity of discernible features in the diffraction patterns, a detailed comparison with those of the corresponding plate-cooled sample (Fig. 49(b)) permits a tentative identification of the spontaneously precipitated phase as fine crystallites of $KCaPO_4$. These observations, made during the analysis of the XS_6PC diffraction data, are consistent with previous conclusions highlighting this system's pronounced tendency toward spontaneous crystallization under plate-cooling conditions. This behaviour is most likely attributed to the exclusively network-modifying role of CaO, as opposed to the dual function of MgO – capable of acting both as a modifier and as an intermediate oxide – resulting in diminished network connectivity, reduced melt viscosity, and consequently lower energetic barriers to structural rearrangement and phase ordering.

In addition to selecting materials that meet the criterion of predominant amorphousness for subsequent evaluation as potential vitreous carriers of agronomically beneficial ions, a key outcome of the studies reported in publications **P1**, **P2***, and **P3** was the determination of the sulfate capacity of each glass series – defined here as the maximum sulfur content that can be incorporated into the glass matrix without inducing precipitation of a sulfate-bearing crystalline phase. As outlined in publication **P3**, no diffraction features attributable to crystalline sulfate phases were detected in the fritted materials with nominal SO_3 contents $\leq$ 3 mol.%. Nonetheless, as demonstrated in publications **P1** and **P2***, sulfate crystallization was confirmed when the nominal sulfur content was raised to 5 mol.%, suggesting that this threshold marks the upper sulfate incorporation limit for the studied [6P] compositions.

Although identification of these crystalline phases was based on a limited number of reflections, previous analyses conducted on plate-cooled analogues provide sufficient evidence to ascribe them to the crystalline potassium sulfate phase (Fig. 48(a) – (c)). As emphasized in both **P1** and **P2***, these findings define the sulfate capacity of the examined [6P] systems, wherein the organization of sulfate domains into a crystalline K_2SO_4 phase occurs upon exceeding a 3 mol.% SO_3 content.

It is also worth noting that no XRD reflections attributable to potassium sulfate were detected in any of the systems enriched in P_2O_5 which leaves the sulfate capacity of these

glasses an open and unresolved question. As noted in publication **P2***, the absence of K_2SO_4-related reflections may imply either that the solubility limit of SO_4^{2-} groups in the [10P] matrix has not been surpassed, or that the limit has indeed been reached, but the quantity of precipitated sulfate-bearing phases remains below the detection threshold of XRD technique. Regardless of the explanation, it is evident that the capability to enclose sulfate species is significantly lower for [10P] glasses than the one of their [6P] counterparts.

11.2 Control of the chemical composition

Similarly to the approach adopted for samples obtained via plate-cooling of the melt, an initial compositional assessment was carried out for the fritted materials by means of XRF analysis. This preliminary evaluation targeted representative samples selected for further investigation. The compositional data presented in publications **P1** and **P2*** were acquired using the standardless variant of this technique, and although the measured molar concentrations of individual components were, in general, close to the theoretical values established during batch formulation, certain discrepancies were identified – most notably, an overestimation of K_2O and CaO contents, accompanied by an underestimation of MgO.

Given the necessity of accurately determining the concentrations of elements released into solution during subsequent 'in vitro' dissolution studies, additional XRF analyses were performed using the fused bead method, calibrated against pre-established reference curves. The corresponding results are reported in publication **P3** and summarised in Tab. 18.

*Tab. 18. XRF data derived from fused bead analysis (after **P3**).*

Sample	SiO_2	P_2O_5	K_2O	MgO	CaO	SO_3
XS_6PM	41	6	20	33	–	0-5
0S_6PM	41.42	6.75	20.42	30.17	–	–
1S_6PM	37.39	5.96	19.53	31.72	–	0.84
3S_6PM	40.00	6.92	20.63	32.67	–	1.84
5S_6PM	41.60	6.49	17.69	33.44	–	1.59
XS_6PC	41	6	20	–	33	0-5
0S_6PC	39.11	6.29	18.88	–	33.63	–
1S_6PC	38.28	6.14	17.21	–	35.79	1.00
3S_6PC	37.90	6.46	18.40	–	35.12	2.05
5S_6PC	43.25	6.10	15.03	–	37.42	1.39
XS_6PMC	41	6	20	16.5	16.5	0-5
0S_6PMC	39.91	6.33	18.40	15.46	18.16	–
1S_6PMC	38.20	6.33	19.59	15.53	18.09	0.95
3S_6PMC	38.08	6.64	18.92	16.57	20.15	1.76
5S_6PMC	41.70	6.46	16.41	16.32	20.89	1.40
XS_10PM	41	10	20	29	–	0-5
0S_10PM	38.11	11.01	21.56	29.12	–	–
1S_10PM	39.00	10.89	19.95	28.98	–	0.25

3S_10PM	39.37	11.02	21.14	29.35	–	0.83
5S_10PM	42.29	11.48	22.29	24.71	–	0.48

The data compiled in the above table clearly indicate an improvement in elemental homogeneity throughout the bulk of the fritted materials when compared to the samples obtained by melt quenching onto a metal plate. In the latter case, pronounced deviations from the nominal composition were consistently observed, likely attributable to the uneven spatial distribution of constituents within the cast pellets (see Section 8.2 for further discussion).

Despite the overall improvement, minor compositional divergences between the target and actual values were also noted for the fritted samples. However, in contrast to the previously discussed materials, these deviations are considered acceptable and can most plausibly be attributed to the volatilization of certain species during high-temperature processing, possible interactions with crucible materials, or inherent instrumental uncertainties. As expected, the most significant inconsistency pertains to sulfur content – a deviation that can be readily rationalized by the well-documented high volatility of this element and its limited solubility in silicate-based melts.

11.3 Sulfate incorporation efficiency within selected glass systems

Although preliminary estimates of sulfate capacity were inferred from diffraction data, a more precise quantification of sulfur content in the glasses selected for further evaluation as potential vitreous carriers of this essential nutrient was undertaken using XRF analysis. The corresponding data, detailed in publication **P3**, were employed to graphically represent the experimental sulfate capacity, juxtaposed with analogous samples obtained via plate-cooling of the melt (Fig. 50).

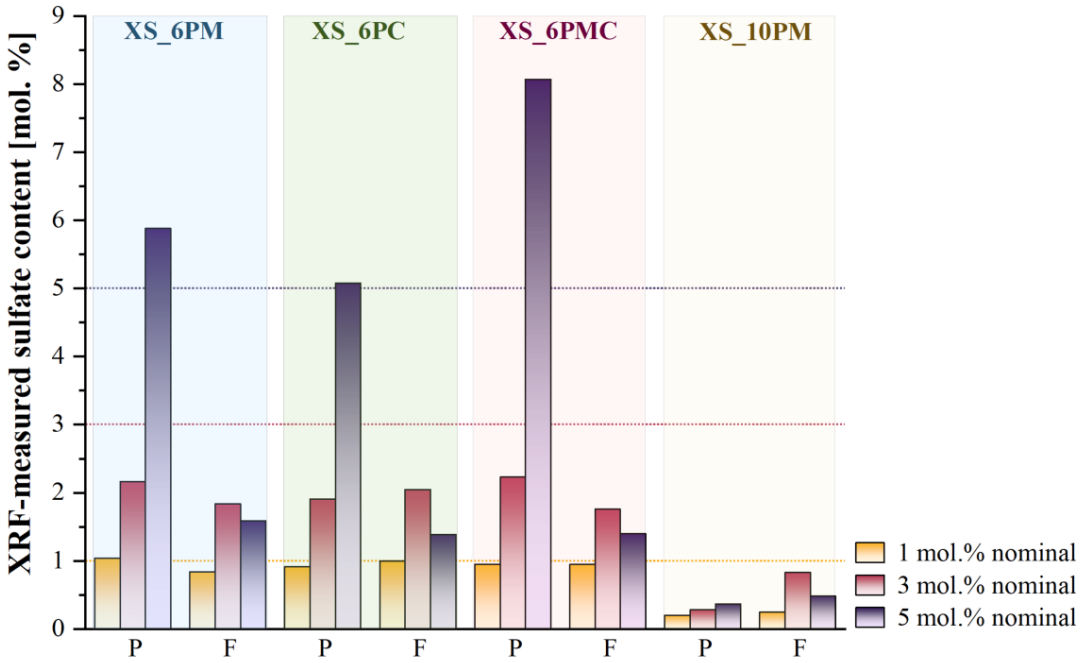


Fig. 50. Comparison of the amounts of sulfate species retained in fritted (F) versus plate-cooled (P) samples for the glass systems selected as potential vitreous carriers of agronomically relevant ions.

It is evident from this comparison that the quantities of sulfur retained within the [6P] series samples modified with 1 and 3 mol% nominal sulfate are comparable between fritted and plate-cooled variants – approximately 1 mol% and 2 mol% measured, respectively. However, a notable divergence is observed for the 5 mol% series (5S). While the plate-cooled 5S_6P specimens exhibit sulfur contents exceeding their nominal value, the corresponding fritted samples show a significantly reduced sulfur concentration, even lower than that measured in the 3S_6P glasses.

As demonstrated in Sections 8.1 and 8.4 as well as briefly noted in publication **P1**, the anomalously high sulfur levels in plate-cooled 5S glasses are attributed to compositional heterogeneity, specifically surface enrichment of crystalline sulfate phases. This accumulation, predominantly near the surface, results in localized regions with elevated sulfur content, which may artificially inflate the measured bulk composition depending on the portion of the sample subjected to analysis. The notably lower sulfur content observed in the fritted 5S_6P samples – when compared to their 3S counterparts – appears considerably more enigmatic. Given that the behaviour of the molten glass prior to quenching is assumed to be analogous in both cases, the origin of this discrepancy must be sought in the cooling method itself. It is therefore plausible to postulate that, in the case of samples with the highest nominal sulfur loading, a segregation of excess sulfur – analogously as in the case of their plate-cooled counterparts – occurs during solidification, likely in the form of a sulfate phase accumulating at the surface of the remaining melt. Considering that fritting involves direct contact between the glass melt and water used as the cooling medium, the most credible explanation is that the precipitated sulfate – owing to its high aqueous solubility – dissolves into the surrounding liquid phase. a similar phenomenon has been observed for the XS_10P system, although on a markedly smaller scale. As in the case of samples cooled on a metal plate, the fritted analogues representing this composition also exhibit significantly reduced actual sulfur contents in comparison to glasses with lower P_2O_5 levels, never exceeding 1 mol.% SO_3 in any instance.

Given this dissolution of the crystallized sulfate phase into the quenching medium, it can be confidently asserted that the SO_3 concentrations determined by XRF for fritted samples correspond exclusively to the fraction genuinely incorporated within the glassy matrix, as opposed to being artificially elevated by surface-enriched crystalline residues.

These findings strongly suggest that the maximum sulfur quantity that can be effectively stabilized within the glass network of [6P]-type systems corresponds to a nominal loading of 3 mol.% – translating to approximately 1.8 mol.% for the XS_6PM and XS_6PMC systems, and around 2.1 mol.% for the XS_6PC composition – SO_3 additions beyond this threshold result in the precipitation of a crystalline K_2SO_4 phase. Notably, the sulfate content identified in the 3S_10PM samples – equimolar in nominal SO_3 to the 3S_6P variants – was more than twofold lower, at approximately 0.8 mol.%. While this does not preclude these materials from serving as potential vitreous sulfur carriers, it undoubtedly influences their optimal agricultural application – rendering them more suitable for crops with lower sulfur demand or for soils characterized by only minor sulfur deficiency.

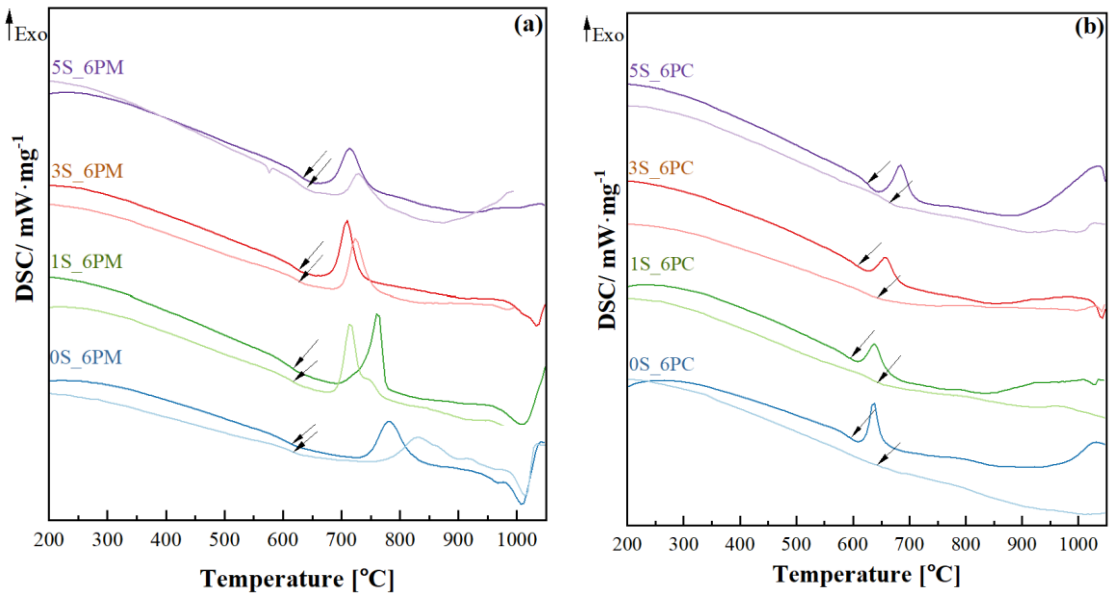
11.4 Thermal behaviour of the fritted samples

The importance of thermal studies of glass materials is proved fundamentally important for several reasons. As emphasized throughout this work, achieving a fully

amorphous state – free from stable crystalline inclusions – is highly desirable for the intended application of these materials as the presence of such crystallites can hinder the controlled release of ions, which is central to the performance of the glasses as nutrient carriers. Accordingly, understanding the thermal behaviour and transition phenomena occurring during heat treatment provides a critical foundation for controlling, and potentially avoiding, undesirable crystallization during glass fabrication at the industrial scale. Furthermore, the thermal response of amorphous materials is intricately linked to their structural characteristics. It therefore serves as a valuable tool for assessing the influence of sulfur on the evolution of the vitreous network and on the formation and distribution of domains structural heterogeneities extending beyond the scale of a single tetrahedron. These domains are often viewed as potential crystallization nuclei and may dictate the identity of the crystallizing phases [288,289]. Importantly, spontaneous devitrification remains the primary factor limiting the compositional range of technically viable glass materials. As such, these detailed thermal studies also provide essential information on the glass-forming ability of sulfur-bearing systems [376]. Also, as stated by Wacławska et al. [377] the results of such an analysis paradoxically may serve as a preliminary indicator of the biochemical activity of silicate- phosphate glasses – an increase in the ability of glass fertilizers for crystallization is a consequence of the weakened framework – a factor also responsible for the increase of their solubility in biological solutions.

Given this significance, thermal investigations of the sulfur-containing glasses representing the systems selected as carriers of plant-available ions were prioritized and presented in detail in Publications **P1** (broad discussion on the thermal behaviour of glasses from XS_6PMC series), as well as **P3** (comparative analysis of DSC results of all the selected materials).

Since in the Manuscript **P3** only the DSC curves of fritted glasses, base as well as loaded with 3 mol.% of SO_3 were presented, in the Fig. 51(a) – (f) thermal signals of all the selected samples are depicted, together with those recorded for samples cooled on a metal plate for comparison purposes. Additionally, the characteristic temperatures associated with glass transition, crystallization, and melting – along with the enthalpy of crystallization (ΔH) – for all samples obtained via both melt-quenching methods are summarized in Tab. 19.



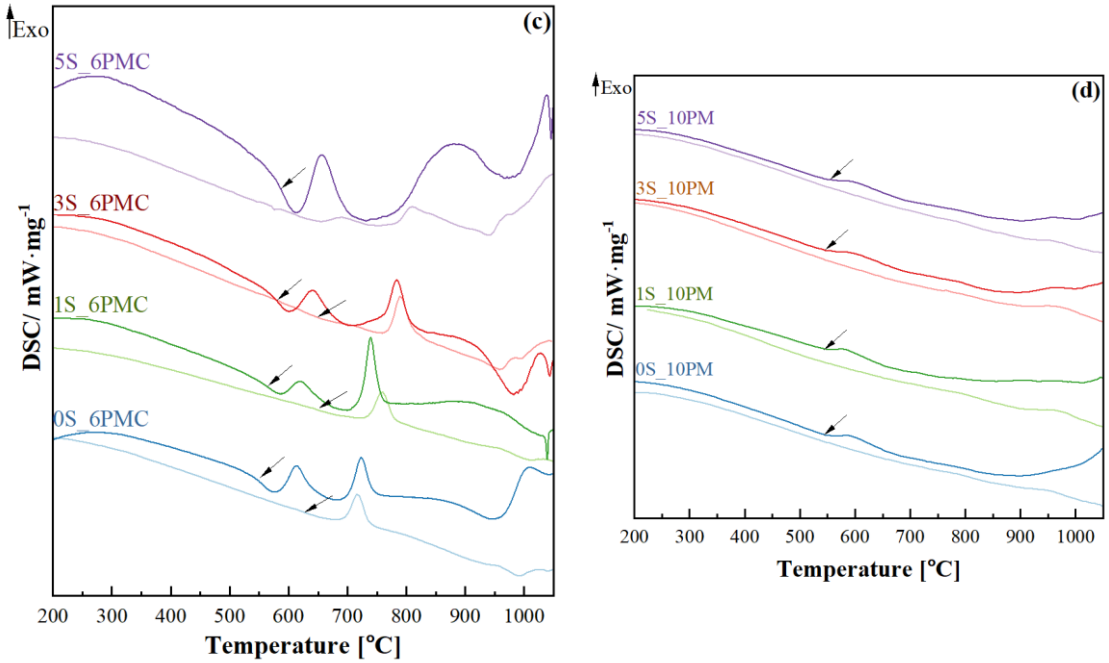


Fig. 51. DSC curves recorded for all synthesized samples representing the glass systems selected as potential vitreous carriers of sulfur for agricultural applications: (a) XS_6PM, (b) XS_6PC, (c) XS_6PMC, (d) XS_10PM. Curves plotted with a bold line style correspond to fritted samples, whereas curves plotted with a thin line style represent plate-cooled samples included for comparison.

Tab. 19. Summary of thermal parameters derived from the DSC analysis for all samples belonging to the glass systems considered as prospective sulfur-containing fertilizers.
***Note:** Rows highlighted in light blue correspond to data obtained for fritted samples, whereas those marked in light orange refer to their plate-cooled analogues.*

Sample ID	Temperature [°C]					T_g range [°C]	ΔH [J/g]
	T_g	T_x	T_c	T_m	Angell (K_A)		
0S_6PM	613	750	782	1009	137.0	32	83.06
	614	785	831	1014	172	35	63.23
1S_6PM	615	741	762	1010	126.2	20	75.75
	613	696	715	919	82.7	37	67.16
3S_6PM	624	689	709	1035	65.1	21	65.7
	622	704	724	985	81.5	28	58.72
5S_6PM	636	687	714	–	50.8	16	52.64
	636	704	728	875	68.3	19	32.83
0S_6PC	595	624	–	–	28.9	21	33.91
	634	–	–	–	–	97	–
1S_6PC	594	615	–	1029	21.1	10	23.08
	636	–	–	–	–	20	–
3S_6PC	608	635	–	1041	26.5	6	22.21
	640	–	–	1043	–	31	–
5S_6PC	626	663	–	–	36.6	3	30.56

	657	–	–	997	–	42	–
0S_6PMC	550	586	613.1	1032	36.1	32	27.84
			723.3				27.45
	627	697	717	986	70.7	21	33.76
1S_6PMC	564	594	618.4	1039	29.5	36	15.68
			739.4				32.46
	649	737	760	1002	88.4	15	42.37
3S_6PMC	584	613	640.7	990	29.4	31	22.1
			783.4	1043			35.6
	649	675	722	956	25.8	11	1.52
			791	995			39.44
5S_6PMC	589	625	656.6	1045	36.3	37	21.98
			879.9				45.2
	–	658	688	942	–	–	6.71
			808	979			35.99
0S_10PM	544	556	589	–	12.1	5	15.03
	–	966	954	–	–	–	7.06
1S_10PM	544	552	575	–	7.3	1	14.06
	–	927	964	–	–	–	18.35
3S_10PM	546	573	600	–	27.0	0.2	9.66
			959	–			4.53
	–	904	968	–	–	–	22.06
5S_10PM	549	601	595	–	51.6	1	24.19
			962	–			4.48
	–	921	960	–	–	–	6.12

* The '-' symbols are placed in table in cases when the identification of the specific glass characteristic temperature was impossible even using the second derivative of the curve.

11.4.1 Influence of melt-cooling technique on thermal behaviour of selected glasses

Since a comparative analysis of the thermal behaviour of fritted versus plate-cooled glasses was not included in any of the published manuscripts comprising the dissertation, the present subsection briefly addresses the influence of the melt-quenching technique on the thermal history of the designed materials.

As observable by the data presented in the Fig. 51(a)-(f), intriguingly, the hallmark endothermic step associated with the transition from a solid glass to a viscoelastic undercooled liquid was either barely detectable or entirely absent in the DSC traces of XS_6PC, XS_6PMC, and XS_10PM plate-cooled systems, even when analysed via second derivative processing. To understand this phenomenon, it is instructive to examine the cooling process leading down to the glass transition region. Upon cooling, a liquid may approach internal equilibrium, provided the rate is sufficiently slow. However, rapid quenching suppresses crystallization by allowing the temperature to drop below the melting point before precipitation of the crystalline phases occurs, enabling access to a metastable supercooled state. In this regime, the structural relaxation time (τ) increases dramatically

with decreasing temperature. Eventually, τ surpasses the observational timescale of the experiment, resulting in the formation of an out-of-equilibrium glass. In this state, molecular motion is insufficient for full configurational rearrangement, and the system becomes kinetically arrested in local energy minima. The temperature at which this kinetic freezing occurs – termed the glass transition temperature – is not a fixed material constant but varies depending on the timescale and thermal history of the measurement. Owing to the inherently unstable and non-equilibrium nature of glassy materials, heating above T_g initiates relaxation towards the supercooled liquid state, accompanied by configurational changes [101].

Relaxation times are thus not solely a function of temperature – they also depend on the degree of structural disequilibrium introduced during formation. As such, the magnitude and sharpness of the DSC-registered glass transition may reflect differences in the extent to which structural relaxation has occurred [101,291,378]. The more abrupt and prominent the endothermic step, the more pronounced the transition in specific heat, ΔC_p, typically associated with fragile glass-forming systems. Such systems exhibit steep viscosity changes near T_g and correspondingly strong discontinuities in macroscopic thermodynamic properties and microscopic structural rearrangements. Conversely, 'strong' glass-formers are characterized by broader T_g regions and more gradual changes in viscosity and ΔC_p [379]. According to this Angell's classification, this behaviour correlates with the nature of atomic bonding – stronger networks yield 'strong' liquids, while weaker bonding favours fragility. It also needs to be noted that following crystallization, the residual melt becomes depleted in mobile, weakly bound structural units (such as orthophosphates, orthosilicates, and network modifiers), and enriched in highly connected species. This compositional shift increases the viscosity of the remaining liquid phase [380,381]. Based on the foregoing analysis, the barely discernible – or entirely absent – glass transition signals observed in the DSC curves of plate-cooled XS_6PC and XS_10PM samples suggest that the glass transition region in these systems may be significantly broadened. This broadening is likely attributable to the increased structural connectivity of the residual melt, resulting from the partial crystallization that depletes the system of the more weakly bonded, mobile constituents. In contrast, samples obtained via the fritting technique – fully amorphous, devoid of crystalline inclusions, and classified as more fragile according to Angell's framework – exhibit a more pronounced departure from equilibrium. Consequently, the degree of structural relaxation, facilitated by the rearrangement of network-forming units, is substantially greater. This is manifested in the form of distinct glass transformation features on the DSC traces recorded for the fritted XS_6PM, XS_6PC, and XS_6PMC systems. For the XS_10PM fritted glass, however, the glass transition remains weakly defined and was only discernible through analysis of the second derivative of the DSC curve (Fig. 51), indicating a more complex relaxation behaviour or partial structural ordering during quenching [191,382,383].

As previously discussed, when a liquid is cooled below its melting temperature, molecular mobility progressively diminishes. If the cooling rate is sufficiently rapid, crystallization can be kinetically suppressed, allowing the system to bypass the equilibrium crystalline state. During this process, the constituent structural units of the melt have limited opportunity to explore lower-energy configurations; slower cooling grants the system more time to undergo configurational rearrangements at each temperature increment, whereas rapid cooling constrains this ability. Consequently, faster cooling rates typically result in higher observed glass transition temperatures, due to the system's reduced

capacity for molecular relaxation [368,369,384]. Such a correlation—namely, the dependence of T_g on the applied cooling rate—is evident only in the case of the fully amorphous XS_6PM system, for which the DSC analysis reveals a modest increase in T_g, not exceeding 5°C (Tab. 19). This limited sensitivity of T_g to cooling rate is consistent with findings reported by Debenedetti et al. [368], who demonstrated that, in practice, changes in T_g of only 3–5°C are typically observed when the cooling rate increases by an order of magnitude. In contrast, for the remaining glass formulations investigated, T_g values are consistently higher for plate-quenched samples compared to their fritted counterparts (Tab. 19). This phenomenon is attributed to the partial crystallinity that develops during plate quenching. The spontaneous nucleation and growth of crystalline phases within the glass matrix inherently alter its composition, rendering the residual amorphous phase more rigid and enriched in structurally interconnected units. These changes stem from the selective incorporation of the more weakly bonded species – such as orthophosphates, orthosilicates, and network modifiers – into the crystalline domains, leaving behind a highly viscous matrix that requires greater energy input to transition from a rigid solid to a viscoelastic state [191,291,305,380,381].

Moreover, the shape and position of the exothermic peaks on the DSC curves further confirm that the crystallization behaviour of the glasses is strongly influenced by the cooling rate. In the case of the XS_6PM system, for instance, the prominent feature corresponding to crystallization shifts towards lower temperatures in the fritted samples compared to their plate-cooled analogues. Notably, not only does the crystallization onset, T_x, appear at lower temperatures, but the enthalpy of the formation of crystalline phases also increases, Tab. 19. Even more significant changes are observed in systems that undergo spontaneous crystallization during plate quenching. For the XS_6PC system, the onset of crystallization becomes discernible, as opposed to the plate-quenched samples, whereas in the XS_6PMC system, crystallization evolves into a two-step process upon heating, a feature also observed for the XS_10PM composition, albeit only in the variants containing the highest sulfur concentrations (3 and 5 mol.%). Additionally, the exothermic crystallization effect in the XS_10PM system is more pronounced in the fritted samples (Fig. 51).

DSC and XRD analyses jointly support the conclusion that these observations stem from the presence of spontaneously formed crystalline phases in the plate-quenched samples. The compositional alteration of the glass matrix – driven by the precipitation of crystalline phases enriched in network modifiers – undoubtedly plays a critical role in modifying both the crystallization pathway and the thermal stability of the material. As illustrated by the DSC traces, fritted samples exhibit a significantly greater tendency toward crystallization, with exothermic events emerging almost immediately following the glass transition (Fig. 51). For example, in the CaO-containing XS_6PMC system, crystallization is clearly observed in fritted samples, whereas no such feature is evident in their plate-cooled counterparts, meanwhile all samples from the XS_6PMC system display a two-stage crystallization profile, a trait shared by high-sulfur-content XS_10PM glasses. The only system exhibiting minimal differences in crystallization behaviour between cooling techniques is XS_6PM, where the sole variation lies in a slight shift of the crystallization onset towards lower temperatures as well as an increase in the enthalpy of this process for the fritted samples (Fig. 51, Tab. 19). These findings clearly indicate that even minor changes in the melt quenching method, despite identical chemical compositions, result in pronounced alterations in thermal stability and crystallization tendency.

This decline in resistance to devitrification, and consequently in the glass processing window, is further corroborated by the calculated values of the Angell stability parameter (K_A), presented in Tab. 19. This parameter – defined already in the Section X as the difference between the crystallization onset temperature and the glass transition temperature ($K_A = T_x - T_g$) – serves as a direct measure of a material's tendency to crystallize, with lower values indicating higher susceptibility to devitrification [297]. It should be noted, however, that K_A values are absent from Tab. 19 for the plate-quenched XS_6PC and XS_10PM samples. In these cases, the absence of detectable crystallization effects and the high uncertainty in T_g determination – due to the shape of the DSC curves—precluded accurate calculations. Although the K_A values are generally higher for the plate-cooled specimens, indicating greater thermal stability, exceptions to this trend do occur (e.g. 1S_6PM sample). These deviations can be attributed not only to the quenching technique but also to compositional variables such as sulfate content and the presence of partial crystallinity.

Crystallization in glasses typically proceeds through two distinct stages: nucleation followed by crystal growth. Nucleation rates often reach a maximum at temperatures slightly above the glass transition temperature, while the rate of crystal growth becomes substantial only at somewhat higher temperatures. Nonetheless, minor crystal growth does occur at nucleation temperatures. Thus, when a sample is held at such temperatures, both the formation and initial growth of nuclei take place simultaneously [380]. In this context, it may be inferred that the plate-quenching technique imposes thermal conditions conducive to spontaneous crystallization within the vitreous matrix, as the melt remains for a longer time interval in the temperature range favourable to structural ordering. In complex, multicomponent systems such as those investigated in the present study, nucleation and subsequent crystallization alter the composition of the residual amorphous phase, which, in turn, influences the kinetics of crystal growth [380]. For instance, in the XS_6PC plate-cooled system, the spontaneous precipitation of the crystalline $KCaPO_4$ phase was identified (Fig. 48). It is also highly plausible that the α-Ca_2SiO_4 phase is present as well, although precise differentiation between these phases via XRD is challenging due to the significant overlap of their characteristic diffraction peaks. As these crystalline phases form, network modifiers (such as Ca) are selectively incorporated into the crystals, leaving behind a melt phase enriched in highly interconnected silicate units. This compositional shift not only leads to an elevated T_g, as discussed earlier, but also likely accounts for the absence of a crystallization signal on the DSC trace for this system. An analogous explanation applies to the XS_10PM-plate-cooled composition, where the $KMgPO_4$ phase crystallizes spontaneously during melt cooling on the metal plate (Fig. 48), and the associated depletion of network modifiers results in a silica-enriched residual glass. By contrast, the XS_6PM plate-cooled system remains predominantly amorphous, with only K_2SO_4 crystallizing once the sulfate solubility limit is surpassed (Fig. 48). Comparing the DSC curves of plate-quenched and fritted samples reveals a key trend: rapid quenching in cold water, which sharply reduces the time the melt spends in the nucleation window near T_g, suppresses the spontaneous crystallization of phases that otherwise precipitate in as-synthesised plate-cooled materials. In general, these very phases then appear as the first to crystallize during thermal analysis of the fritted specimens, manifesting as initial exothermic peaks on the DSC curves (Tab. 20). The only deviation from this trend constitutes the most complex XS_6PMC system for which the $KCaPO_4$ phase was detected as spontaneously precipitated phase within the amorphous matrix of plate-cooled

samples, while the crystalline phase associated with the first crystallization effect on the fritted materials was found to be $CaSiO_4$ (manuscript **P1:**Tab.4). However this may be attributed to the disputable phase identification as regards the as-synthesized plate-cooled materials resulting from the high similarity between reflections positions in both the $KCaPO_4$ as well as $CaSiO_4$ phases (Fig. 52) and partially amorphous nature of the respective sample, making the precise identification more challenging.

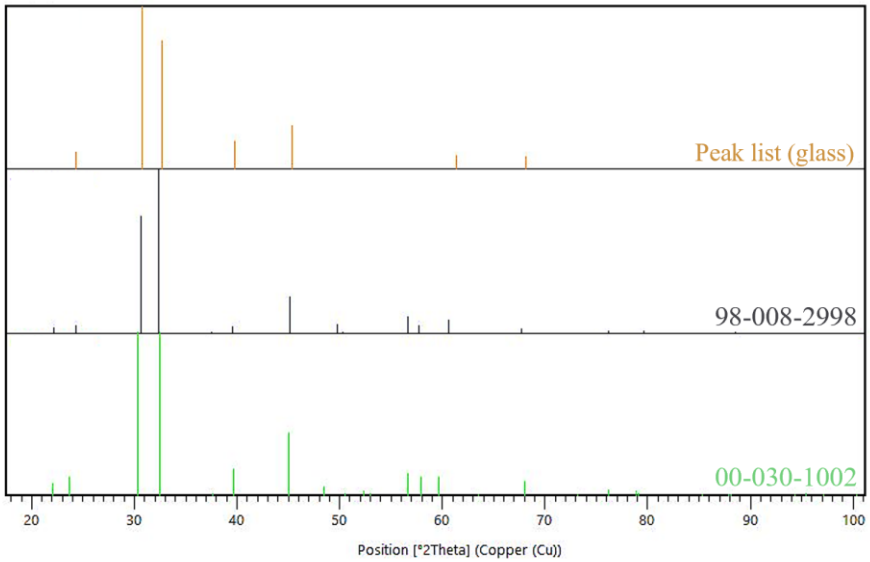


Fig. 52. Comparison of the peak positions corresponding to $CaSiO_4$ (ref. 98-008-2998) and $KCaPO_4$ (ref. 00-030-1002), based on the representative example of the XS_6PMC glass system.

Moreover, in addition to the phases that, depending on the melt-cooling technique, either spontaneously crystallize within the amorphous matrix (as in the plate-cooled samples) or appear only upon subsequent thermal treatment (in the case of fritted specimens), the formation of more compositionally and structurally complex silicate phases was observed exclusively in the heat-treated fritted samples (Tab. 20). This observation aligns with the general understanding that elevated temperatures enhance atomic mobility, thereby facilitating chemical redistribution and enabling the crystallization of phases that are more intricate and often structurally analogous to the original glass network or its intermediate-range domains [305].

*Tab. 20. Crystalline phases identified via X-ray diffraction analysis of thermally devitrified (heat-treated) samples representing the XS_6PM (Fig. 53(a)), XS_6PC (Fig. 53 (b)), XS_6PMC (see Publication **P1:** Fig. 11), and XS_10PM (Fig. 53(c)) fritted glass systems. For comparative purposes, the phases detected in the as-synthesised plate-cooled analogues are also included.*

Sample	Heat-treatment temp. [°C]	Phase	Ref. code	Phases detected in as-synthesised plate-cooled samples
0S_6PM	789	$KMgPO_4$ $K_2MgSi_3O_8$	00-050-0149 00-019-0973	–
1S_6PM	770	$KMgPO_4$	00-050-0149	–

		$K_2MgSi_3O_8$	00-019-0973	
3S_6PM	721	$KMgPO_4$ $K_2MgSi_3O_8$	00-050-0149 00-019-0973	–
5S_6PM	721	$KMgPO_4$ $K_2MgSi_3O_8$	00-050-0149 00-019-0973	K_2SO_4
0S_6PC	645	$KCaPO_4$	00-033-1002	$KCaPO_4$
1S_6PC	645	$KCaPO_4$	00-033-1002	$KCaPO_4$
3S_6PC	662	$KCaPO_4$	00-033-1002	$KCaPO_4$ K_2SO_4
5S_6PC	690	$KCaPO_4$	00-033-1002	$KCaPO_4$ K_2SO_4
0S_6PMC	620	Ca_2SiO_4	98-008-2998	$KCaPO_4$
	730	Ca_2SiO_4 $MgSiO_3$ $CaMgSiO_4$ K_2MgSiO_4 $CaSiO_3$ KH_2PO_4	98-008-2998 98-016-3891 98-020-2285 98-008-32269 98-024-0449 98-002-4683	
1S_6PMC	620	Ca_2SiO_4	98-008-2998	$KCaPO_4$
	730	Ca_2SiO_4 $MgSiO_3$ $CaMgSiO_4$ $CaSiO_3$ KH_2PO_4	98-008-2998 98-016-3891 98-020-2285 98-024-0449 98-002-4683	
3S_6PMC	660	Ca_2SiO_4	98-008-2998	$KCaPO_4$
	785	Ca_2SiO_4 $CaMgSiO_4$ K_2SO_4	98-008-2998 98-020-2285 98-000-2408	K_2SO_4
5S_6PMC	660	Ca_2SiO_4 $MgSiO_3$ $CaMgSiO_4$	98-008-2998 98-016-3891 98-020-2285	$KCaPO_4$
	885	Ca_2SiO_4 $MgSiO_3$ $CaMgSi_2O_6$ K_2MgSiO_4 K_2SO_4	98-008-2998 98-016-3891 98-020-2285 98-008-32269 98-000-2408	K_2SO_4
0S_10PM	585	$KMgPO_4$	00-050-0149	$KMgPO_4$
1S_10PM	585	$KMgPO_4$	00-050-0149	$KMgPO_4$
3S_10PM	585	$KMgPO_4$	00-050-0149	$KMgPO_4$
	965	$KMgPO_4$ $K_{1.14}Mg_{0.57}(Si_{1.43}O_4)$	00-050-0149 00-044-0089	
5S_10PM	585	$KMgPO_4$	00-050-0149	$KMgPO_4$
	965	$KMgPO_4$ $K_{1.14}Mg_{0.57}(Si_{1.43}O_4)$	00-050-0149 00-044-0089	

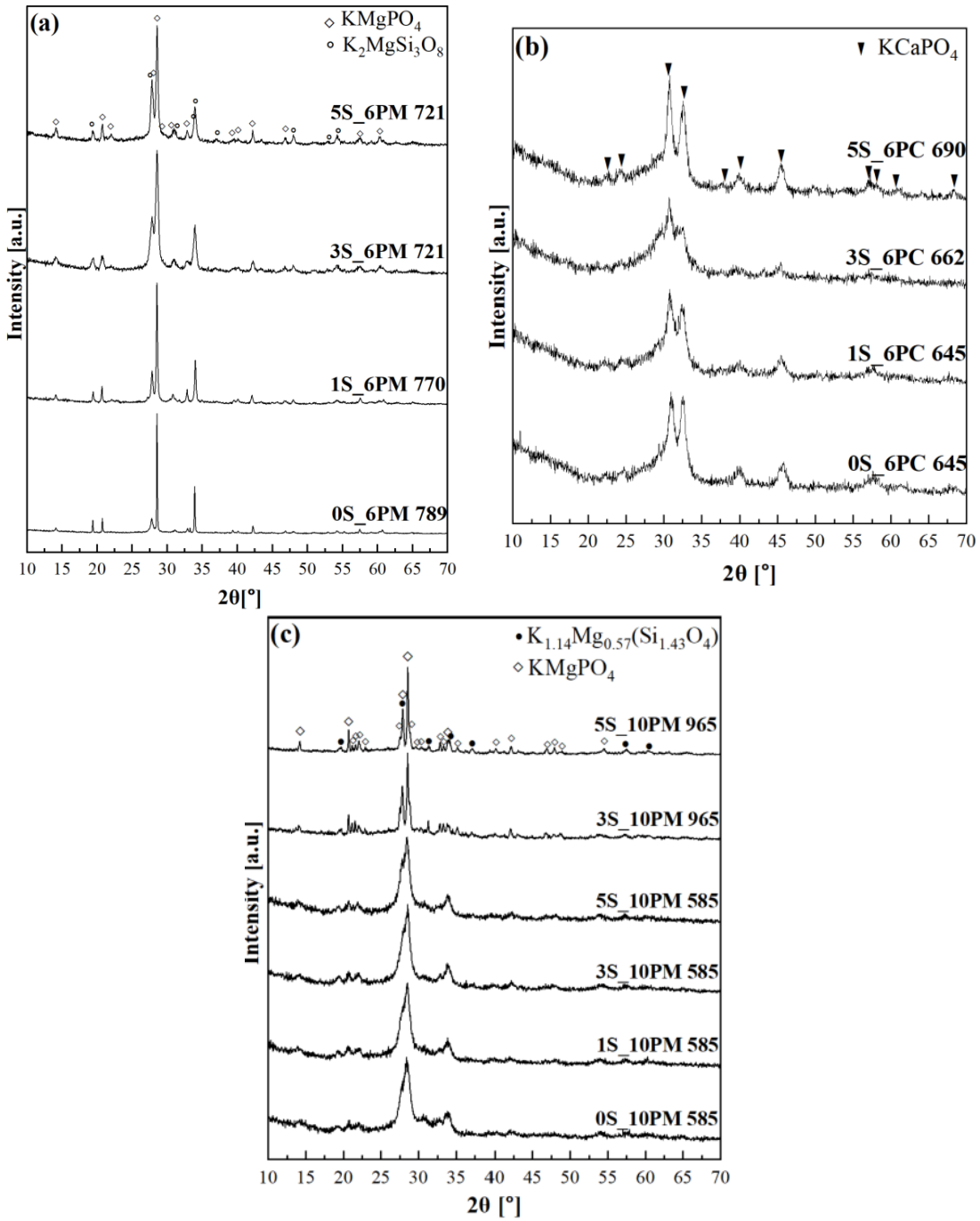


Fig. 53. XRD patterns of devitrified samples representing the XS_6PM (a), XS_6PC (b) as well as XS_6PMC (c) systems.

Thus, it may be one again highlighted that even seemingly minor variations in synthesis route – specifically the quenching method – have substantial impact on the structural organization within the glass and the likelihood of forming fully amorphous products. Fritted glasses, having undergone more abrupt quenching and hence a greater departure from equilibrium, are inherently more prone to devitrification. While such instability is generally undesirable in many glass applications, it may prove advantageous in cases where gradual alteration in soil environments is intended, such as controlled-release fertilizers.

Further analysis of the DSC traces from both processing methods yields another observation, this time concerning sulfate incorporation. As indicated in the Section 8.6, DSC curves for plate-quenched samples exhibit a sharp and well-defined endothermic peak corresponding to the polymorphic transition of β-K_2SO_4 to α-K_2SO_4 at approximately 575 °C – a feature entirely absent in the curves of fritted materials (Fig. 51). This difference clearly indicates a higher concentration of crystalline sulfate phase precipitates in the plate-quenched specimens – although XRD confirms the presence of K_2SO_4 in both sample types, its concentration in fritted samples falls below the detection threshold of DSC. This observation is also consistent with XRF results, which indicate higher sulfur content in the plate-cooled materials. Importantly, this is not due to a higher sulfate capacity in as-produced specimens, but rather to the presence of a superficial crystalline sulfate layer that remains intact in the surface regions 5S plate-cooled samples but dissolves during the fritting process, given the high solubility of sulfate salts in water (see Section 11.3)

11.4.2 Influence of sulfur addition on thermal behaviour of selected glasses

In Publications **P1** and **P3** a number of general trends emerged from the analysis of the thermal behaviour of the selected glass compositions. Most notably, a clear relationship was observed between sulfate content and the glass transition temperature. In the studied systems, increasing sulfur incorporation was reflected on the DSC traces as a progressive shift of the glass transition effect toward higher temperatures, associated with a heightened degree of network polymerization, according to the conclusions made on the plate-cooled samples representing the XS_6PM system. It was supposed that the incorporation of sulfate into the glass structure contributes to the formation of additional Si–O–Si bridges, thereby reinforcing the glass network and increasing the energy required for the transition from a rigid to a viscoelastic state.

As discussed in Sections 3.4 and 8.6, the glass transition is manifested on the DSC curve as a characteristic, step-like change in the molar heat capacity, representing the transition of the glass from a rigid solid into a viscoelastic state. This transformation is driven by stress relaxation within the disordered structure and its magnitude, as expressed by the ΔC_p value, corresponds to the entropy change accompanying the transition and serves as an indicator of the structural rearrangements occurring during this process. Notably, ΔC_p is highly sensitive to the nature and number of network-constituting components, as well as to subtle variations in the chemical composition of the glass [291]. Despite the ΔC_p values for the XS_6PMC system were presented in Publication **P1**, to provide consistency and take advantage of the informative nature of this parameter, the corresponding values for the remaining systems – along with the previously published data for comparison – are compiled in the table below (Tab. 21).

Tab. 21. ΔC_p values measured for the tested glasses.

Sample	ΔC_p [J/gK]
0S_6PM	0.138
1S_6PM	0.104
3S_6PM	0.156
5S_6PM	0.256
0S_6C	0.273
1S_6PC	0.121
3S_6PC	0.177
5S_6PC	0.211
0S_6PMC	0.375
1S_6PMC	0.182
3S_6PMC	0.285
5S_6PMC	0.29
0S_10PM	0.026
1S_10PM	0.01
3S_10PM	0.031
5S_10PM	0.026

Remarkedly, the trend of ΔC_p changes across the compositions is analogous to the one observed for the XS_6PMC glass series, discussed in **P1**, specifically, the introduction of sulfate species initially causes a decrease in ΔC_p across all compositions, followed by an increase once the sulfate content surpasses approximately 1 mol%. This observation aligns with the previously discussed relationship between ΔC_p and the degree of structural relaxation. The initial decrease in ΔC_p in glasses with low SO_3 content may be attributed to the high degree of covalency and directionality of the bonds within the sulfate groupings embedded within the interstices of the glass network. Such linkages induce internal strain within the structure, resulting in a more rigid network that stores higher internal energy and requires comparatively less additional energy to undergo rearrangement during the glass transition. As sulfate content continues to increase, the growing network connectivity raises then the energy required for structural rearrangement during the glass transition and manifesting as an increase in ΔC_p.

To gain a more comprehensive understanding of the role of sulfate species within the structure of tested glasses both manuscripts **P1** and **P3** incorporated an extended discussion on the thermal stability of selected glass series. Notably, this discussion is more extensively developed in Publication **P1**, where the stability of the XS_6PMC system against devitrification is evaluated using three widely recognized empirical parameters: Angell's (K_A), Hruby's (K_H), as well as Weinberg's (K_W) stability criteria. While both K_H and K_W are derived from the trio of characteristic temperatures – glass transition (T_g), onset of crystallization (T_x), and melting point (T_m) – Angell's index is based solely on T_g and T_x. Due to the absence of discernible melting effects on the DSC traces of certain systems (in particular, XS_6PC and XS_10PM), Publication **P3** confines its analysis to the Angell parameter, and for the same reason, the comparative table (Tab. 19) presents only the calculated K_A values for the selected compositions.

As highlighted in both publications, a general trend emerges wherein increasing sulfate content is accompanied by a progressive decline in thermal stability. This tendency is attributed to the incorporation of sulfate units, which – by increasing the number of covalent bonding – render the glass network more rigid and thus more prone to local ordering as an effect of bond rupture. This trend was observed to reverse, beyond certain SO_3-loading threshold, coinciding with an increase in ordering of the internal glass structure, which, due to the change of the remaining melt composition, leads to an improvement in thermal stability.

Furthermore, as discussed in Section 8.6 in the context of plate-cooled XS_6PM glasses, the marked increase in crystallization tendency observed upon sulfate addition substantiates the hypothesis that sulfate species serve as heterogeneous nucleating agents. These entities lower the energy barrier for crystallization, facilitating devitrification. Indeed, it is well-established that the presence of foreign inclusions or internal phase boundaries can significantly reduce the thermodynamic barrier to nucleation, primarily by

diminishing the effective interfacial energy contribution required to form a critical nucleus [376].

In this context, the confirmed presence of the K_2SO_4 phase within the glass matrix – as discernible sulfate clusters exhibiting higher structural organization than the surrounding amorphous phase – provides compelling evidence of their role as potential nucleation sites for the crystallization of orthophosphate and silicate phases. This interpretation coheres with the modern understanding of nanoscale heterogeneity in vitreous systems: although glasses may appear homogeneous at the microscale, they often contain structurally distinct domains at the nanometre scale. Since nucleation and early-stage crystal growth are phenomena initiated on this finer structural level, such heterogeneities exert a critical influence on devitrification behaviour and vary widely depending on the glass composition [288].

According to this paradigm, isolated sulfate groupings may function as primary nucleation centres. This assertion gains further credibility when considering the chemical similarities between sulfur and silicon – both high-field-strength cations with pronounced Lewis acidity and a propensity to form highly covalent bonds with oxygen. These similarities energetically disfavour the formation of mixed SiO_2–SO_3 linkages and instead promote sulfate-rich phase separation from the silicate network [191]. This, in turn, facilitates crystallization of discrete K_2SO_4 domains, a phenomenon also observed by Müller et al. [385], who demonstrated that crystallization is more favourable when the ionic structure of the parent glass resembles that of the emergent crystalline phase. From a thermodynamic standpoint, the ease of K_2SO_4 precipitation an be rationalized through the classical expression for the nucleation barrier W^*, which is governed by the interfacial free energy (σ) and the Gibbs free energy difference per unit volume (ΔG_v) between the glass and its crystalline counterpart:

$$W^* = \frac{16\pi\sigma^3}{3\Delta G_v^2} \qquad \text{Eq. (21)}$$

Structural similarity lowers ΔG_v and hence reduces W^*, favouring nucleation. Indeed, as established on the basis of the Raman study, the local environment of sulfate units within the vitreous framework of tested materials the local environment of sulfate in the glass mirrors that of crystalline K_2SO_4.

In summary of the thermal studies, the crystallization tendency of the studied glasses increases with SO_3 content, whether this crystallization occurs spontaneously during cooling or heat treatment - the domains rich in potassium sulfate appear to initiate and promote matrix crystallization. Furthermore, the incorporation of sulfate raises the energy required for the glass transition (reflected in T_g elevation), primarily due to enhanced Si–O–Si network connectivity and, secondarily, due to the removal of loosely bound orthophosphate/orthosilicate units and modifiers during crystallization. Consequently, the residual glassy matrix becomes structurally depleted in its more mobile, weakly connected constituents, resulting in the more-interconnected silicate phase and hence – higher T_g. Ultimately, incorporation of sulfate species into the vitreous matrix of tested materials reduces the glass-forming range of the compositions and decreased materials' stability. Additionally, if one assumes that indeed there is a direct relationship between the types of crystalline phases detected after glass heat-treatment, and the type of domains

(heterogeneities) present within the vitreous matrix, then the following clusters are present in the materials of studied formulations:

- Orthophosphate-based domains: $KMgPO_4$ and $KCaPO_4$, depending on the type of alkaline-earth network modifier present in a given glass series, dispersed within the silicate matrix;
- Silicate-based groupings: groupings of more complex and not-necessarily stoichiometric composition, which constitute the dominant phase and form the primary framework of the material;
- Independent sulfate-rich domains, constituting the $[SO_4]^{2-}$ units surrounding by K^+ cations.

The coexistence of these domains supports the hypothesis that network-modifier-enriched species – namely, orthophosphate and sulfate units – tend to segregate from the silicate framework during glass formation. These segregated domains, rich in more mobile and reactive species, are likely to govern the initial stages of glass alteration in soil, serving as primary sources of nutrient release. In contrast, the residual silicate matrix functions as a more inert structural reservoir, encapsulating and gradually releasing these active domains over time.

11.5 Structure of the fritted samples – general view

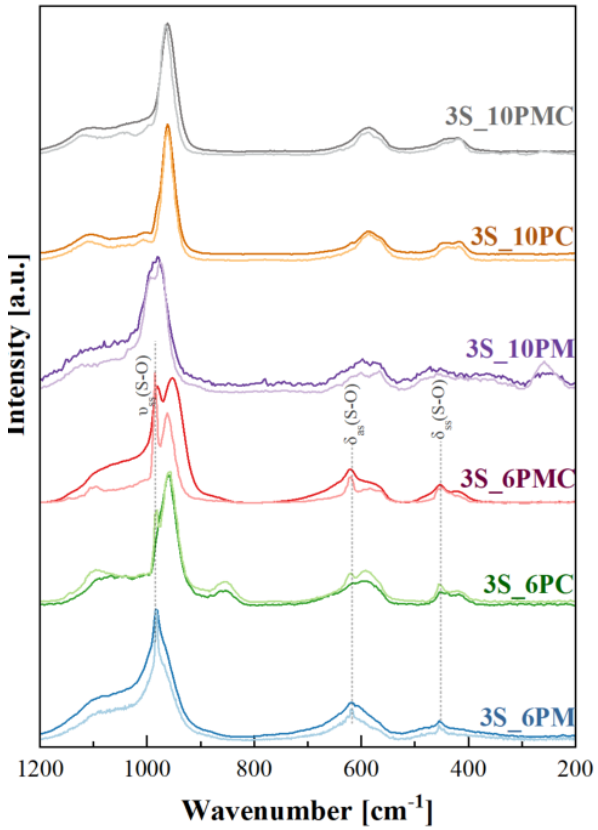


Fig. 54. A comparative evaluation of the Raman spectra collected for the 1S-type fritted (dark lines) and plate-cooled (light lines) variants of all the designed systems.

Just as the capacity to retain an amorphous state or the thermal behaviour of a given system is influenced by external conditions, so too the structure of the synthesized materials seems to be affected by the applied melt-cooling strategy—more specifically, by the rate at which the melt is quenched. As discussed in the Chapter 10, the degree of local order within the glass matrix tends to diminish with increasing cooling rate. This phenomenon is attributed to the higher amount of free volume – interpreted as structural voids or defects – that becomes immobilized in the glass structure under more rapid cooling conditions.

This relationship becomes particularly evident when examining the compiled Raman spectra of the 3S-series glasses across all investigated systems, including those formulations ultimately excluded from further analysis – namely,

XS_10PC and XS_10PMC (Fig. 54). a comparative evaluation of these spectra reveals substantial differences in spectral characteristics between the fritted and plate-cooled variants for most systems.

Nevertheless, a notable exception is observed in the case of the 10P-based compositions, particularly the aforementioned 3S_10PC and 3S_10PMC samples, where the Raman features exhibit a striking degree of similarity regardless of the cooling technique applied. This convergence may be rationalized by considering the partial crystallinity of these systems, which persists irrespective of the melt-cooling approach, thereby yielding relatively sharp and analogous spectral features for both the fritted and plate-cooled counterparts.

Since water-cooling procedure decreased the degree of spontaneous crystallization within the volume of the XS_10PM system, the respective spectral features are slightly broader and less defined compared to the plate-cooled counterpart. Similarly, the spectra collected for the fritted [6P] system samples display deviations when comparing them with these, obtained for melt-quenched samples with the main difference being more broad character of the spectral features registered for the water-cooled melts, suggesting simultaneously more disorder nature of the respective samples. Simultaneously, main, high-wavenumber, spectral bands recorded for the plate-cooled samples tend to be more distinct, reflecting a more homogeneous distribution of local atomic environments, particularly in terms of various Si–O environments. This observation aligns well with the previously discussed relationship between cooling rate and structural organization, where faster cooling leads to increased disorder and a broader distribution of network-forming units.

It should also be noted that vibrational bands commonly assigned to the stretching modes of S-O bonds within the [SO_4] tetrahedra are observed to be less intense in fritted samples compared to their plate-cooled equivalents, likely stems from the enhanced potential for matrix rearrangement and partial crystallization during the slower, more prolonged cooling associated with plate quenching [305,369]. Collectively, these findings corroborate the well-established principle that rapid quenching causes the glass to deviate from thermodynamic equilibrium at a higher temperature, thereby trapping a greater number of high-temperature structural motifs within the final amorphous network. Although slightly, the resulting silicate unit distribution becomes increasingly heterogeneous, as evidenced by the broader high-frequency regions observed in the spectra of fritted glasses [386,387].

Taken together, the Raman and DSC results provide compelling evidence that the structural and physicochemical properties of glass are considerably contingent upon the processing route by which the material is formed. This insight bears critical relevance for the intended functional performance of the designed vitreous fertilizers, as both the degree of network polymerization and the openness of the structure play decisive roles in determining their reactivity and nutrient release behaviour in biological environments.

11.5.1 Evolution of the structure of the multicomponent silicate-phosphate glasses with increasing sulfate content

As previously mentioned and emphasized in the literature review section of this dissertation, the formation of a well-optimized vitreous framework in glassy carriers of agriculturally beneficial ions is of paramount importance in the context of their intended function. For glasses designed to gradually release their constituents into the surrounding

environment, the structural attributes become especially critical due to the nature of the initial stage of the dissolution process – namely, the ingress of water molecules into the glass network. It is widely acknowledged that water can diffuse into the glass matrix only if voids of sufficient size are available – typically greater than ~0.7 nm – which distinguishes glasses exhibiting varied resistance to corrosive environments. In denser, more compact glasses characterized by higher network connectivity, water penetration can only proceed through hydrolysis of robust Si–O–Si linkages. This process is usually accompanied by a reduction in the alteration rate, attributed to the formation of a hydrated, porous, and silica-rich passivating layer at the glass–solution interface. Conversely, glasses displaying lower network connectivity are generally characterized by a higher degree of structural openness, including voids that facilitate water access and enhance the ion exchange process.

Given the critical role of structural organization in sulfur-bearing glassy fertilizers, the evolution of the glass network was systematically investigated using a comprehensive suite of spectroscopic techniques, including Raman spectroscopy, FTIR, MAS-NMR for both ^{29}Si and ^{31}P nuclei, and XAS. The findings and interpretations derived from these methods are presented across several publications forming this dissertation, namely **P1**, **P2***, and **P3**. While the initial structural assessment presented in P1 focused exclusively on the most compositionally complex system – namely XS_6PMC – the subsequent works expanded the scope to explore how compositional variations among the designed materials influenced the evolution of their amorphous networks, always with particular attention paid to the role of sulfur in modulating the vitreous framework. Establishing robust relationships between composition and structure is essential for the fine-tuning of these materials toward controlled, selective, and prolonged release of essential ions under conditions prevailing in the rhizosphere.

The results presented in Publications **P1**–**P3** unambiguously demonstrate that even relatively minor compositional modifications – such as the substitution of the alkaline earth modifier, a 4 mol.% increase in P_2O_5 content, or the incorporation of sulfate species – yield significant and measurable changes in the network connectivity of the resulting glasses. This clearly highlights the potential to modulate the alteration rate through targeted compositional design.

Importantly, as reported in **P2*** and **P3**, all of the studied glass systems share two fundamental structural characteristics. First, based on the analysis of network connectivity (NC), all tested glasses were found to possess silicate networks predominantly composed of Q^2_{Si}-type units, i.e., silicate tetrahedra forming chains or rings, accompanied by a lesser contribution of Q^3_{Si} units responsible for limited two-dimensional network formation. This fragmented, metasilicate-type structure classifies these glasses as inherently susceptible to gradual disintegration under biotic conditions [152]. Notably, the [10P] glass system exhibited the highest calculated NC value (>2.7), slightly exceeding the commonly cited threshold for glass bioactivity. Nevertheless, due to the previously demonstrated in literature high chemical reactivity of phosphate-rich fertilizer glasses, this system was not excluded from further investigation [185].

The second commonality among all studied compositions lies in their structural response to increasing sulfate incorporation. Across all systems, a consistent upward trend in network connectivity was observed with increasing sulfate content. This effect, as documented in Publications **P1** and **P2***, was found to be independent of the specific alkaline earth modifier used or the exact P_2O_5 concentration. However, the magnitude of this

structural change was strongly composition-dependent, reaching its highest expression in the XS_10PM system. Interestingly, the pronounced increase in network connectivity in the XS_10PM glasses, despite their relatively low sulfate content (as compared to other systems), suggests a more complex mechanism at play. It is hypothesized that sulfate addition promotes structural ordering by driving the progressive separation of $KMgPO_4$-like domains from the glass matrix, consequently increasing the connectivity of the remaining silicate network.

Although the evolution of the silicate subnetwork upon sulfate loading followed a broadly analogous pattern across all tested systems, a more differentiated behaviour was observed in the phosphorus-oxygen subnetwork, contingent on the glass composition. Specifically, for the single alkaline earth modifier systems – XS_6PM, XS_6PC, and XS_10PM – a subtle increase in the concentration of Q_P^1 was detected with increasing sulfate content (**P2***, **P3**). In contrast, the opposite trend was observed for the dual-modifier system XS_6PMC, as reported in **P1**.

This contrasting and somewhat enigmatic trend – observed specifically in the most compositionally complex of the studied systems – was preliminarily addressed in Publication **P1**, where it was attributed to the distinct coordination environment of phosphate groups in the various compositions under investigation. It is well established that the degree of polymerization within either the silicon-oxygen or phosphorus-oxygen subnetwork evolves in response to the redistribution of network-modifying cations throughout the matrix. In the studied glasses, the total content of these modifiers was kept constant (with the exception of the 10P composition, where the increase in P_2O_5 occurred at the expense of alkaline earth network modifiers). Consequently, a local deficiency of modifiers in the vicinity of a given subnetwork directly promotes its polymerization. Given their comparable cation field strengths – 2.60 for sulfate tetrahedra and 2.10 for phosphate, as opposed to 1.57 for silicate units [102], – $[SO_4]^{2-}$ and $[PO_4]^{3-}$ groups effectively compete for charge-balancing cations. Due to its higher field strength, sulfur generally outcompetes phosphorus and silicon in attracting these modifiers, thereby promoting an increase in the connectivity of both the silicon-oxygen and phosphorus-oxygen subnetworks. As detailed in Publication **P3**, the dual role of magnesium – acting both as a conventional network modifier and, under certain conditions, as an intermediate cation capable of forming its own subnetwork – contributes to the local deficit of modifiers near orthophosphate units, particularly in the XS_6PM and XS_10PM systems. In contrast, the observed modifier deficiency in the vicinity of $[PO_4]^{3-}$ units within the XS_6PC system may stem from the co-presence of $CaSiO_4$-like domains alongside orthophosphate-rich regions (Notably, XS_6PC is the only system whose Raman spectra exhibit a pronounced band around ~850 cm^{-1}, indicative of isolated orthosilicate Q_{Si}^0 species, Fig. 54). All these factors are believed to ultimately contribute to an increase in the concentration of pyrophosphate (Q_{Si}^1) units across the XS_6PM, XS_6PC, and XS_10PM compositions. In the case of XS_6PMC – where both MgO and CaO are assumed to function primarily as network modifiers [202,388] – the concentration of modifier cations in the proximity of orthophosphate groups appears sufficient to maintain these species predominantly in the form of isolated orthophosphates.

Nevertheless, regardless of the direction of these trends or the specific subnetwork to which they pertain, the observed structural effects were consistently subtle across all systems (**P1**–**P3**). This modest impact is closely linked to both the relatively low levels of sulfur successfully incorporated into the glass structure and the nature of the sulfate

species therein. Based on comprehensive Raman spectroscopic analysis, particularly the fingerprinting approach applied to the plate-cooled XS_6PM samples, it was confirmed (as reported in **P1** and **P2***) that sulfur is retained within the glass matrix primarily as isolated [SO_4^{2-}] species, charge-compensated by surrounding K^+ cations. These sulfate domains reside within the voids of the glass structure, preserving their individuality and not forming common bonds with either the silicon- or phosphorus-based networks, as no evidence for Si–O–S or P–O–S linkages was identified in the structural analyses.

An invaluable tool for elucidating the spatial arrangement of atoms in three dimensions – particularly around selected absorber elements – was X-ray Absorption Spectroscopy, whose results are discussed in Publications **P1** and **P2***. In **P1**, XAS data were acquired at the Mg and Si K-edges for the XS_6PMC system, whereas in **P2***, spectra were obtained for Mg, Si, and K K-edges for the XS_6PM and XS_10PM series, enabling a comparative assessment of systems differing in their P_2O_5 content. From these investigations, it was conclusively established that sulfate incorporation affects the extended coordination environment of both silicon and magnesium atoms without altering their immediate (first-shell) coordination. In contrast, a slight but measurable change was observed in the coordination number of potassium upon sulfate addition, suggesting that sulfate groups preferentially localize near K^+ rather than Mg^{2+} cations within the glass matrix. This observation aligns with the fact that $[SO_4]^{2-}$ tetrahedra do not directly interact with the silicate or phosphate networks, prompting a redistribution of K^+ cations, instead, which reorganize to act as charge compensators for sulfate anions. This reallocation reduces the availability of potassium in the immediate vicinity of both magnesium and silicon coordination spheres, thus explaining the spectral modifications detected in their extended environments.

Nevertheless, the data presented in both the publication **P1** as well as **P2*** unanimously point out to the fact that all the observed alterations in local environments of the studied absorber atoms are rather subtle, as rather low too are the concentrations of sulfate species successfully incorporated into the studied glass matrices.

11.6 Chemical activity of sulfur-bearing silicate-phosphate glasses

11.6.1 The ‘in vitro’-like experiment

As demonstrated in publications **P1**–**P3**, the application of the fritting technique enabled the full vitrification of materials belonging to the XS_6PM, XS_6PC, and XS_6PMC systems, while also substantially enhancing the degree of amorphization in the XS_10PM series. Notably, the data presented in these studies unequivocally indicate that all fritted compositions exhibit a suitable, open, and highly fragmented network architecture. Such a structure, potentially conducive to inward water penetration, is predominantly composed of short silicate chains and rings (Q^2_{Si} units), with a lower contribution from more polymerized species (Q^3_{Si}), as well as Q^1_{Si} units containing a single bridging oxygen atom. Consequently, the subsequent phase of research presented within this publication series focused on extending the established relationships between the chemical composition and structural attributes of the synthesized glasses to include the final functional properties of the resulting products.

As outlined in the introductory chapters of this dissertation, beyond the requirement of achieving an amorphous state and an appropriately depolymerized structure, such materials must also demonstrate the ability to release the ions embedded within the glass matrix under the influence of low-molecular-weight organic acids – the key components

of root and microbial exudates in the rhizosphere. At the same time, however, the glasses must exhibit resistance to pure water to prevent uncontrolled nutrient leaching, which could otherwise lead to over-fertilization and the subsequent eutrophication of aquatic ecosystems. Furthermore, the release of these useful ionic species should proceed in a controlled, gradual manner, slower than in the case of conventional fertilizers, so as to avoid a 'burst release' effect that could result in the loss of nutrients before they are taken up by plants.

In light of these considerations, publications **P3** and **P4** – concluding the research cycle devoted to the development of sulfur-based glassy carriers for agricultural applications – present the results of so-called 'in vitro' and 'in vivo' experiments. The former refers to laboratory protocols simulating the effect of plant root exudates, whereas the latter involves long-term incubation of appropriately ground glass samples in soil matrices typical of Polish agricultural settings – namely, acidic soils – under conditions replicating local temperature and moisture levels characteristic of the temperate climate.

Experimental results reported in **P3** confirm that the solubility of the tested glasses (including selected representatives of the XS_6PM, XS_6PC, XS_6PMC, and XS_10PM systems) in a 2% aqueous solution of citric acid – employed as a rhizosphere-mimicking medium – was significantly higher than in distilled water. In the latter case, none of the constituent elements were released in amounts exceeding 0.5% of their initial concentration in the glass, despite the use of an intensified leaching protocol (involving vigorous agitation and large volumes of leaching medium). The only notable exception to this trend was sulfur, which was leached in quantities reaching up to 5% of its initial content, strongly supporting earlier suppositions regarding the high aqueous solubility of sulfate species. Consequently, glass compositions classified as 5S – characterized by the presence of crystalline K_2SO_4 precipitates – were disqualified as potential sulfur carriers for agronomic purposes due to their propensity for uncontrolled nutrient release associated with the burst effect.

Notably, the ions released in the greatest quantities into the citric acid solution – employed to simulate root exudates – were the network modifiers: K^+, Mg^{2+}, and Ca^{2+}. These species, known to participate in ion exchange processes, are gradually leached from the glass through interdiffusion mechanisms involving their substitution by protons (H^+) originating from the external medium. Following the release of these mobile cations, sulfate and phosphate ions are subsequently liberated – these anionic species, present in the glass as isolated structural units embedded within the voids of the silicate-dominated network, are not bonded into the continuous framework, which facilitates their relatively easy removal. In stark contrast, silica – the principal network former and the most polymerized component of the matrix – was released only in trace amounts over the course of the standard 30-minute 'in vitro' experiment.

Importantly, the data obtained from these experiments allowed for an initial assessment of the relationship between the chemical composition and the chemical reactivity of the synthesized multicomponent glass fertilizers. As shown in publication **P3**, within the [6P] system, the identity of the alkaline earth oxide (CaO, MgO) employed as a network modifier exerted minimal influence on the leaching behaviour of [SO_4^{2-}] and [PO_4^{3-}] species, whose concentrations in the leachate remained comparable across all tested formulations. The only significant variation among these compositions concerned the release of silica, which was the highest in the CaO-containing glass system – attributed to its comparatively lower network connectivity.

Instead, the previously discussed network-polymerizing influence exerted by the incorporation of sulfate species appears to play a predominant role: in all systems containing 6 mol.% P_2O_5, an increase in [SO_4^{2-}] content consistently correlates with a decreased release of these units into the surrounding solution. Although this network-strengthening effect is also reflected in the leaching behaviour of other glass constituents – such as phosphate groups and the most mobile cations (K^+, Mg^{2+}, Ca^{2+}) – its impact is most strikingly evident in the case of silica, where a substantial drop in SiO_2 concentration in the leachate was observed for all glasses exceeding 1 mol.% SO_3. The progressive increase in the number of sulfate units was thus identified as an indirect contributor to the suppression of glass constituents transport, presumably due to the enhanced connectivity of the silicate subnetwork via the formation of additional Si–O–Si linkages.

By contrast, in glasses containing 10 mol.% P_2O_5, the aforementioned sulfate-induced polymerization effect did not manifest as clearly in the release profiles of major ionic species, with the notable exception of silicon. Indeed, in this system, the release of Si into the solution exhibited a slight but measurable decline with increasing sulfur content, once again suggesting the influence of structural reinforcement. However, no comparable tendency was observed for the remaining ions. The inherently high solubility of the 10P-type glasses in acidic media – attributable to their elevated hygroscopicity driven by the increased phosphate content – was found to outweigh the stabilizing effect associated with the enhanced connectivity of the silicate network induced by sulfate incorporation. Nonetheless, the influence of a higher P_2O_5 concentration on glass dissolution was still discernible in the context of silica leaching – the highest degree of network polymerization of this composition translated into the lowest extent of SiO_2 release.

The results presented in publication **P3** also proved particularly valuable in elucidating the alteration kinetics of the investigated materials. Specifically, the increased phosphate content was shown to accelerate the initial dissolution rate, as evidenced by the elevated early-stage release of glass constituents in both acidic and aqueous environments. This intensification of leaching in the initial alteration regime, accompanied by a lower initial rate (V_0) of silica release, indicates a higher chemical reactivity of the 10P system. This behaviour is most likely driven by the greater abundance of structurally isolated [PO_4^{3-}] units – more susceptible to leaching – alongside the concurrently increased polymerization of the Si–O–Si subnetwork, as corroborated by the spectroscopic analyses reported in publications **P2*** and **P3**.

Furthermore, the long-term ion release experiment discussed in **P3** provided valuable insights into the characteristic dissolution regime of these glassy materials, demonstrated to constitute a two-stage kinetic profile commonly observed in aqueous glass alteration studies. The process begins with a rapid initial release phase, governed by a high initial rate, predominantly involving the most mobile cations (K^+, Mg^{2+}), which are exchanged for protons or hydronium ions from the surrounding solution. This interdiffusion results in a compositional gradient near the glass surface, marked by the depletion of these mobile species. In parallel, larger anions such as [PO_4^{3-}] and [SO_4^{2-}], which do not participate in direct ion exchange, were nonetheless released following a similar early-stage trend, by the virtue of their structural role as isolated, non-networked units within the glass matrix. Following this initial phase, the system transitions into a regime characterized by a marked rate drop. From this point onwards, a steady, though non-zero, residual dissolution rate persists. This behaviour was attributed to the inherently fragmented and open nature of the glass network, which promotes rapid leaching from structurally

accessible domains via preferential ion-transport pathways. The remaining portion of ions, however, is sequestered within less permeable regions of the network, where their release becomes dependent on the hydrolysis of robust Si–O–Si bonds – a step that ultimately controls the rate of dissolution in the long-term regime.

Crucially, the mechanism governing the interaction between the synthesized glasses and the leaching solution was preliminarily elucidated in publication **P3**. The predominantly Q^2_{Si}-type Si–O network undergoes only limited hydrolysis, while simultaneously facilitating the inward diffusion of H^+/H_3O^+ ions and the outward migration of mobile glass components (K^+, Mg^{2+}, Ca^{2+}, as well as $[PO_4^{3-}]$ and $[SO_4^{2-}]$). This mechanism is especially pronounced in acidic environments, which inherently promote proton exchange and thus amplify the interdiffusion process.

Nevertheless, the findings presented in **P3** should be interpreted as model-based, since they reflect ion leaching profiles under strongly acidic conditions and dynamic mechanical stirring – factors that, while accelerating ion transport and clearly revealing material behaviour trends, do not faithfully replicate the complexities of natural soil environments. As such, although informative, these conditions are not fully representative of the materials' real-world performance.

To better simulate the intricacies of actual field conditions – such as the presence of exogenous chemical species, seasonal temperature variations, or fluctuations in water content – publication **P4** extended the work initiated in **P3**. This subsequent study aimed to evaluate the materials' functional behaviour and ion release kinetics under environmental conditions more closely mimicking those encountered in natural soil systems.

11.6.2 The 'in vivo'-like experiment

The comprehensive study presented in publication **P4**, integrating SEM imaging with semi-quantitative EDS analysis, underscores the multifaceted nature of glass degradation processes. Of particular significance, from the standpoint of employing these materials as vitreous carriers of essential plant nutrients, was the elucidation of the sequential release pattern of matrix constituents into the soil-like medium.

The experimental findings demonstrated that potassium ions, owing to their low cationic field strength and corresponding high mobility, were leached most readily, diffusing rapidly toward the glass–soil interface. This was followed by the release of sulfate ions, likely attributable to their heightened solubility under acidic conditions. In all investigated compositions, sulfur was detected via EDS up to the third month of incubation, though the duration of its detectability varied depending on the specific glass system under study. The identity of the ions subsequently released was found to be closely governed by both the chemical composition of the glass and that of the surrounding soil. Alkaline-earth network modifiers tended to accumulate transiently within the near-surface regions before co-precipitating with phosphate species to form secondary crystalline phases. Meanwhile, the silica network remained largely unaffected over the course of the experiment, indicating a selective dissolution mechanism. This resulted in the formation of a silica-enriched crust that retained residual, unextracted ions—thus providing strong evidence for an incongruent dissolution pathway. An exception to this trend was observed for the most reactive system, designated [10P], in which no preferential leaching of any specific ion species was noted. Instead, all primary components (K^+, Mg^{2+}, PO_4^{3-}, and SO_4^{2-}) were released simultaneously, although their temporal accumulation within the hydrated silica

layer varied depending on the type of secondary crystalline phases forming at distinct stages of glass incubation.

The experimental framework of **P4** was intentionally designed to expose the glass samples to conditions that mimic natural seasonal fluctuations, thereby enabling more accurate predictions regarding their long-term behaviour in real soil environments. The results revealed a pronounced influence of seasonal variability on the degradation pattern of the potential glass fertilizers. The initial incubation phase, simulating spring conditions, led to the formation of secondary crystalline precipitates on the glass surfaces – precipitates whose nature depended on the particular glass composition. As the temperature increased in the simulated summer phase, processes occurring at the glass–soil interface became markedly intensified. Depending on the system, this was manifested in the emergence of a network of cracked, silica-enriched surface scales with minimal residual mobile ions – indicative of enhanced ion exchange, accelerated leaching, and /or more vigorous secondary phase formation. Subsequent exposure to simulated autumnal conditions, characterized by a temperature decline, triggered the gradual disintegration of the previously formed silica crust. This breakdown exposed deeper regions of the material to the reactive soil solution, effectively pushing the reaction front further into the glass interior. Concurrently, previously formed secondary phases exhibited mechanical decohesion in response to the temperature shift. The final environmental change – representing winter, with diurnal temperature fluctuations oscillating around freezing – further intensified fragmentation, not only of the surface crust but also of entire glass fragments.

These environmental perturbations, as detailed in **P4**, offer a compelling explanation for the layered structure observed in the near-surface regions of the incubated glasses throughout the experiment. Periods of elevated soil moisture promoted interdiffusion, allowing exogeneous hydrogenated species to penetrate the glass while concurrently driving outward migration of mobile constituents. This bidirectional transport gave rise to diffusion (alteration) layers, reminiscent of those described in studies of glass corrosion under aqueous immersion. Following such wet intervals, subsequent dry phases led to the progressive dehydration of the altered zones, mechanically weakening the superficial regions and facilitating their delamination along structurally compromised planes. Beyond moisture cycling, this mechanical separation became particularly pronounced after the transition from summer to autumn, driven by differential thermal expansion between the intact glass core and the weathered outer layer. The brittle, silica-rich surface region – susceptible to fracture both laterally and perpendicularly – formed an interconnected system of microcracks that significantly enhanced water ingress toward the unaltered interior. Yet, the most impactful process was the surface scaling phenomenon itself, which directly accelerated the glass–soil interaction by continuously exposing fresh glass to corrosive conditions. It is postulated that the combination of alternating wet–dry cycles and cyclic temperature fluctuations – both daily and seasonal – establishes a self-reinforcing feedback mechanism. As scaling advances the alteration front deeper into the bulk glass, the increasing contact with soil moisture facilitates further leaching, promoting the formation of a hydrated silica layer. During dry intervals, this layer undergoes contraction and fragmentation, perpetuating the exposure of pristine surfaces and thus sustaining the degradation cycle.

The acidic pH-driven, selective release of mobile components from the glass matrix was observed to rapidly saturate the limited-volume soil solution with released ions. Once the solubility thresholds of these constituents in the surrounding medium were exceeded,

the excess species precipitated onto the outermost glass surfaces, forming a layer of secondary mineral phases that temporarily immobilized the surplus nutrients. As elaborated in publication **P4**, the formation of such a precipitation layer – whose nature was strongly dependent on both the glass composition and the prevailing pH of the soil solution – emerged as a critical factor modulating the kinetics of the glass–soil interaction. Indeed, this superficial zone of crystalline secondary products appears to act as a temporary nutrient reservoir, governing the release rate of elements by sequestering them within its structure.

Remarkably, all secondary phases identified during the study were found to be susceptible to dissolution under acidic conditions – with the notable exception of calcium phosphates belonging to the apatite family – these compounds, known for their low solubility in acidic environments relative to other observed mineral phases, warrant particular attention in the design of CaO-containing vitreous fertilizers, as the re-release of nutrients immobilized within these structures is anticipated to proceed at a significantly slower rate. Nonetheless, the overall low solubility in water of the precipitated phases is believed to effectively limit nutrient runoff. Hence, from an agronomic perspective, such precipitation-driven ion immobilization may be considered an inherent, self-regulating mechanism for the controlled release of nutrients – reactivated through the action of acidic exudates secreted by plant roots and soil microorganisms.

Notably, the surface alteration mechanisms elucidated in publication **P4** exhibit analogies to those widely reported for glass corrosion under aqueous immersion, as the ‘in vivo’-like experiment confirmed the presence of three interconnected processes governing glass degradation in the soil environment: (1) the formation of a thin, adsorbed moisture layer on the glass surface; (2) the simultaneous progression of ion exchange, hydration, and hydrolysis reactions; and (3) the subsequent precipitation of a secondary product layer. These coupled processes collectively define the evolution of the alteration front and contribute to the long-term reactivity profile of the glass.

The experimental results further underscored the critical influence of glass composition on fracture behaviour. In particular, the incorporation of sulfate species was shown to increase network rigidity, rendering the material more susceptible to mechanical degradation and promoting the advancement of the reaction front. These effects manifested at earlier stages and with greater intensity in the sulfur-containing 3S variants relative to their sulfur-free counterparts. Accordingly, the findings suggest that sulfate species indirectly modulate the glass–soil interactions by enhancing the material’s tendency to fracture and facilitating the progressive decohesion of altered surface layers during incubation. This interpretation is well aligned with the thermal and structural data discussed in publications **P1**–**P3**, which reveal a consistent trend of reduced thermal stability and increased network connectivity with rising sulfur content. The resulting structural modifications – primarily the stiffening of the silicate backbone – translate into greater vulnerability to surface cracking and exfoliation, as confirmed by the observed behaviour of the incubated samples.

In the study presented in publication **P4**, only minor variations were observed in the behaviour of the tested materials within the soil environment when comparing compositions belonging to the same series – namely, the 6P group. Nevertheless, within this group, the XS_6PMC variant emerged as the system exhibiting the lowest initial reactivity. This behaviour can be ascribed to the well-established mixed-alkali/alkaline-earth effect, which elevates the activation energy required for ion migration across the glassy

matrix, thereby impeding ionic diffusion. It is, however, indisputable that the specific type of network-modifying alkaline-earth oxide markedly affects the material's interaction with the surrounding soil, primarily by dictating the nature of the secondary crystalline phases that precipitate upon contact. These phases, in turn, govern the dynamics of the ion exchange processes occurring at the glass–soil interface, particularly with regard to the delayed remobilization of essential nutrients temporarily immobilized within their structure.

Among the examined compositional variables, the P_2O_5 content proved to be far more influential in governing glass reactivity than the precise identity of the alkaline-earth modifier. This conclusion is substantiated by the behaviour of the 10P system, which, despite possessing the highest degree of network polymerization, demonstrated the greatest chemical activity. It is well documented that the incorporation of phosphorus pentoxide into silicate-based glass matrices enhances their hygroscopicity while simultaneously diminishing their resistance to ambient moisture. This is primarily due to the inherently labile nature of P–O–P linkages in phosphate-rich structures, which are readily hydrolysed upon exposure to water vapor. Consequently, the pronounced hydrophilicity of $[PO_4^{3-}]$ groups renders these glasses especially vulnerable to moisture-induced degradation: the more water molecules become adsorbed at the surface, the more intense and rapid the hydrolysis and hydration processes become, raising the chemical potential of the interfacial solution and ultimately accelerating the release of mobile cations into the surrounding medium.

The findings outlined in **P4** underscore the multiplicity and complexity of factors governing the processes at the glass–soil interface—many of which exhibit inherently unpredictable behaviour. Among such factors are biotic weathering, known to play a substantial role in the degradation of vitreous materials, and the heterogeneity of local soil mineralogy, which influences the balance between ion release and retention in the subsurface zone of glass fertilizers. Yet, above all, the data emphasize that glass reactivity may be effectively modulated through targeted compositional adjustments. Even seemingly minor modifications – such as varying the type of alkaline-earth network modifier or altering the SO_3 and P_2O_5 concentrations – exert a pronounced influence on the dissolution behaviour and overall chemical reactivity of the final material.

11.6.3 Alteration of sulfur-bearing glasses in less acidic soil (pH 5.5-6.5)

It should be emphasized that, in order to comparatively assess the influence of soil type on the processes occurring at the glass–solution interface, glass samples corresponding to those described in manuscript **P4** were subjected to the action of a universal substrate (pH 5.5–6.5; mineralogical composition determined via XRF analysis – Tab. 22) under 'in vitro' conditions, following a procedure analogous to that employed in the previous study. As in the case of the acidic peat substrate, the selection of this medium was informed by the general characteristics of soils commonly found across Central Europe, with particular consideration given to those prevalent in Poland [123,389,390]. To ensure consistency in data presentation and facilitate direct comparison between the results, SEM micrographs of the glass surfaces obtained after 0.5, 5, 8, and 12 months of incubation are collectively presented in Fig. 59-Fig. 66, whereas Tab. 23 summarizes the morphological changes observed on the external regions of the samples throughout the entire experimental period.

Tab. 22. Chemical composition of the soil substrate used [mol. %].

Soil composition [mol.%]			
SiO_2	8.82	**Fe_2O_3**	3.83
P_2O_5	0.59	**MnO**	0.25
K_2O	1.66	**ZnO**	0.09
MgO	2.24	**SrO**	0.11
CaO	73.31	**ZrO_2**	0.03
SO_3	5.04	**Cl**	1.65
Na_2O	0.30	**Br**	0.09
Al_2O_3	1.31	**PbO**	0.04
TiO_2	0.64		

Tab. 23. Summary of surface characteristics of glass samples after soil incubation, detailing the types of crystalline phases identified and the extent of the surface fragmentation.

Month	0.5	1	2	3	4	5	6	7	8	9	10	11	12
0S_6PM	I	I	I	I	M	E	H	H	M	H	E	E	H
	CP	–	–	CP	CP KM P	CP	CP	CP MP	CP	C P	C P	C P	–
	Localized leaching								Intense leaching				
3S_6PM	I	I	I	I	M	H	E	I	E	E	H	E	E
	CP	CP	KM P	KM P	KM P	CP	CP	CP	CP	C P	C P	C P	CP
	Localized leaching					Intense leaching							
0S_6PC	I	I	N	I	–	I	E	E	E	E	E	E	E
	CP	CP	CP	CP	CP	CP	CP	CP	CP	C P	C P	C P	CP
	Localized leaching					Intense leaching							
3S_6PC	I	M	I	I	I	M	E	E	E	E	E	E	E
	CP	CP	CP	CP	CP	CP	CP	CP	CP	C P	C P	C P	CP
	Localized leaching					Intense leaching							
0S_6PM C	N	I	I	M	I	I	E	H	E	E	E	E	E
	CP	CP	CC	CP	CP	MP CC	CP	CP	CP	C P	C P	C P	CP C C
	Localized leaching							Intense leaching					
3S_6PM C	I	I	I	I	M	H	E	E	E	E	E	E	E
	CP	CP	–	CP	CP	CP	CP	CP	CP	C P	C P	C P	CP
	Localized leaching					Intense leaching							
0S_10PM	E	E	E	E	E	E	E	E	C	C	C	C	C
	KM P	KM P	KM P	KM P	KM P CP	KM P CP	KM P CP	MP KM P	M P CP	C P	C P	C P	CP
	Localized leaching					Intense leaching							
3S_10PM	E	E	E	E	E	E	E	E	C	C	C	C	C

	KMP	KMP	KMP	KMP	KMP	KMP	KMP CP	CP	MP CP	CP	CP	CP	CP MP
	Localized leaching					Intense leaching							

Legend: Types of crystals suggested by the semi-quantitative SEM-EDS analysis: MP—magnesium phosphate, KMP—potassium magnesium phosphate, CP—calcium phosphate, CC—calcium carbonate. Surface condition (fragmentation/cracking): N: no visible cracks—no shading, I: isolated cracks—light pink, M: moderate concentration of cracks—light red, H: high concentration of cracks—red, E: cracks covering the entire surface of all fragments—dark red, C: complete fragmentation of glass pieces—grey. Shaded fields indicate areas where dense layers of crystallites uniformly covered the glass surface.

A comparative analysis of the data compiled in Tab. 23 with those related to the acidic peat incubation (Tab.1, manuscript **P4**) reveals that even relatively small differences in soil pH can exert a pronounced effect on the near-surface alteration processes of the investigated materials. Although surface cracking is also evident on the glasses exposed to the universal substrate, the morphological expression of these features differs notably from that observed in the acidic environment. Specifically, instead of large-scale exfoliations (approximately 100 µm in size) seen in acidic peat conditions (Fig. 55.(b) narrow crack networks are locally observed on the samples incubated in the slightly acidic substrate (Fig. 55(a) and Fig. 56). Notably, these interaction-induced surface features are predominantly visible during the initial half of the incubation period. As the experiment progresses, the near-surface zones of the samples increasingly exhibit the formation of larger-scale, flake-like structures, which begin to resemble the characteristic morphology observed in samples subjected to acidic peat.

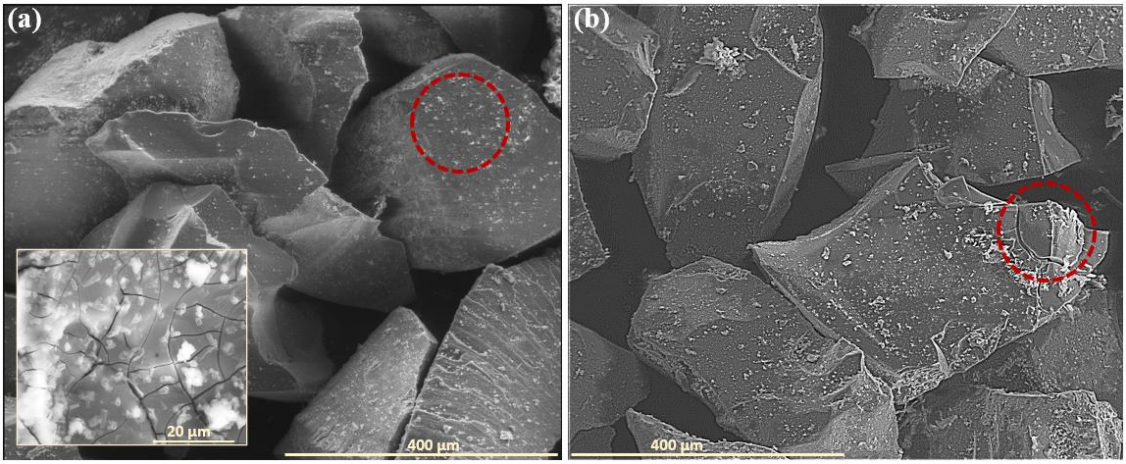


Fig. 55. Types of surface cracking observed on analogous 3S_6P glasses incubated in slightly acidic (a) and acidic (b) soil environments during the spring incubation stage.

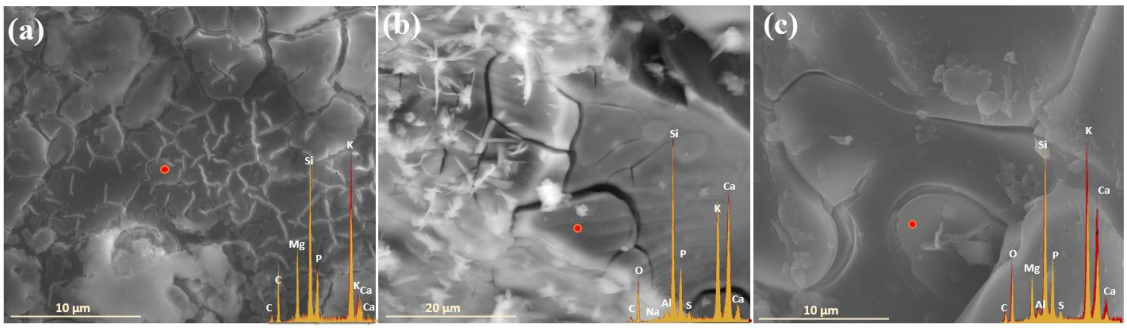


Fig. 56. Crack networks developed on the surface of 3S_6PM (a), 3S_6PC (b), and 3S_6PMC (c) glasses during the spring stage of incubation in slightly acidic soil (universal substrate), along with EDS spectra of selected surface regions (yellow spectra corresponding to intact glasses are added for reference purposes).

Importantly, this observation provides insight into the nature of interfacial processes occurring at the glass–solution boundary. While interdiffusion – dominant during the incubation of glasses in acidic peat – entails the replacement of glass network cations by positively charged species originating from the soil (H^+, H_3O^+), EDS spectra of corroded surface regions (Fig. 56.(a)-(c)) also indicate the occurrence of an additional reaction between the glass constituents and the surrounding aqueous medium. According to Palomar [391], the preservation of the original chemical composition within weathered near-surface zones suggests the complete dissolution of the amorphous network into the surrounding medium, including its silica component. In other words, alongside the ion exchange process, the incubation of glasses in a medium of near-neutral pH is accompanied by the hydrolysis of Si–O–Si linkages, ultimately resulting in the loss of entire surface regions rather than only the most mobile network modifiers. This complete compositional breakdown is evidenced, for instance, by the EDS spectrum of the 3S_6PC glass, taken from an area marked by narrow surface cracking (Fig. 56.(b)), which mirrors the initial stoichiometry of the bulk material. By contrast, chemical analysis of corroded regions in samples from the XS_6PM and XS_6PMC systems reveals a notable enrichment in K^+ and, in the latter case, both K^+ and Ca^{2+} ions, despite a silica content comparable to that of the unaltered glass (Fig. 56.(a), (c)). This upward migration of mobile cations suggests that, although partial network hydrolysis does occur, ion exchange remains the principal interaction pathway at the glass–substrate interface. It must be emphasized, however, that these processes – documented primarily during the early stages of incubation – are highly localized and do not affect the entire surface of the exposed samples.

Interestingly, Palomar [391] also reported the emergence of such phenomena on silicate glasses incubated in neutral or alkaline soils. Her findings, when considered alongside the present results, not only reinforce the notion of a higher [OH^-] concentration in the universal substrate compared to acidic peat but also imply local alkalization of the surrounding solution and a prolonged interaction time at the glass surface, as evidenced by the spatial confinement of these alterations. In fact, the nature of the crystalline phases precipitated at the glass–substrate interface provides additional support for this hypothesis. Calcium phosphate – identified as the dominant secondary product on the surface of all glasses with 6 mol% P_2O_5 content – was consistently observed (Fig. 57.(a)–(d)).

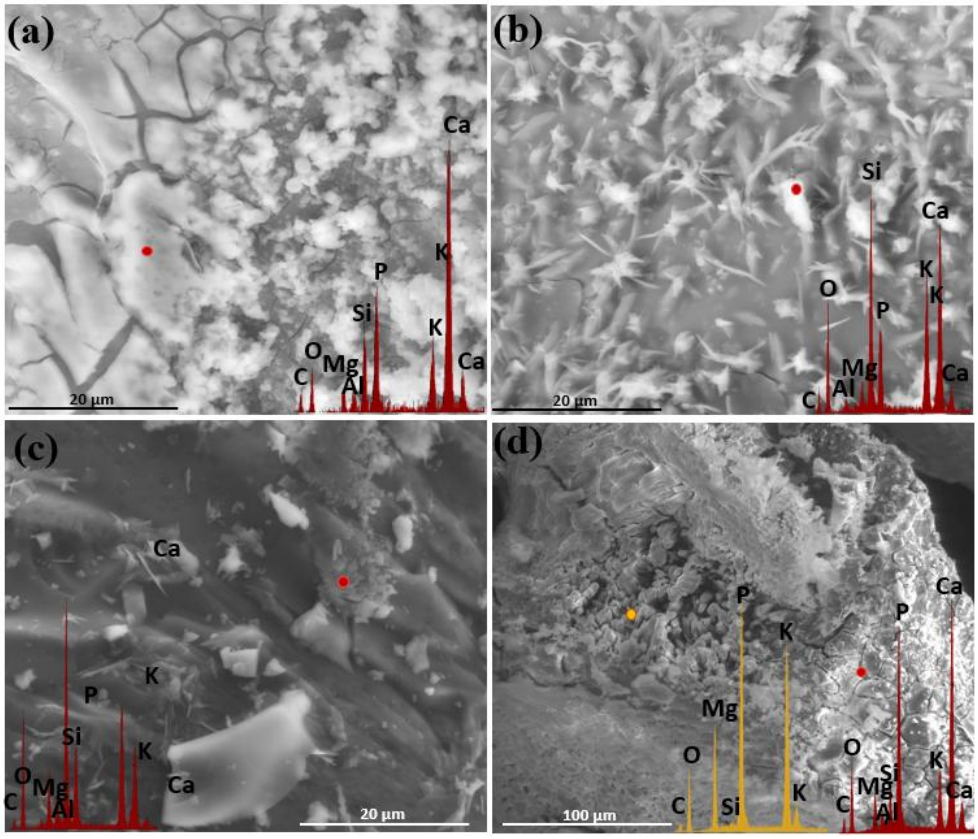


Fig. 57. Calcium phosphate (red spectra) detected on the surface of glasses from the 3S_6PM (a), 3S_6PC (b), 3S_6PMC (c), and 3S_10PM (d) systems. The yellow spectrum in (d) corresponds to the double salt of magnesium and potassium phosphate (SEM images taken during the spring incubation stage).

It is well-established that the precipitation of calcium phosphate phases occurs across a broad pH range: from slightly acidic conditions – favouring the formation of 'desert rose'-like morphologies – through near-neutral pH, which promotes the appearance of amorphous, spherical aggregates, to alkaline conditions, where needle- or rod-shaped forms predominate [392–395]. In view of this pronounced pH-dependence and the characteristic morphology of the secondary phases formed (Fig. 57.(a)–(c)), it is possible to infer the pH of the contact solution interacting with the incubated materials. Star-shaped formations on the surface of XS_6PC glass (Fig. 57.(b)) point to an environment with pH values in the range of 5–6 [394], whereas the amorphous precipitation layers found in MgO-containing systems – XS_6PM and XS_6PMC (Fig. 57.(a), (c)) – are indicative of contact solution pH close to ~7.5 [392]. Furthermore, under comparable near-neutral conditions (pH 7–8), the precipitation of magnesium–potassium phosphate double salts is also thermodynamically favoured. The co-occurrence of both phosphate types in the surface regions of P_2O_5-rich glasses (Fig. 57.(d)) thus reflects the evolving chemical landscape at the glass–substrate interface. This correlation strongly suggests that the presence of MgO in the glass composition contributes to the local alkalization of the surrounding solution. Such behaviour is not unexpected, given that glasses containing CaO as the sole alkaline-earth modifier primarily release K^+ into the environment while promoting the accumulation of Ca^{2+} ions in the near-surface regions (Fig. 56.(b)), which then organize into the crystalline calcium phosphate phases.

This hypothesis is further supported by the work of Chave et al. [171], who reported the enrichment of the corrosion-altered, silica-rich surface layer with calcium cations. Intriguingly, this phenomenon was observed even when Ca^{2+} originated from an external source, highlighting the bidirectional nature of the processes occurring at the glass–solution interface. High calcium concentrations in the universal substrate likely drive inward migration toward glass surfaces devoid of endogenous CaO, such as XS_6PM and XS_10PM, leading to supersaturation of the contact solution and subsequent precipitation of calcium phosphate phases.

In considering the suite of secondary products formed on the surfaces of incubated samples, it is also worth noting the occasional appearance of calcium carbonate and magnesium phosphate phases (Tab. 23, Fig. 58(a), (b)).

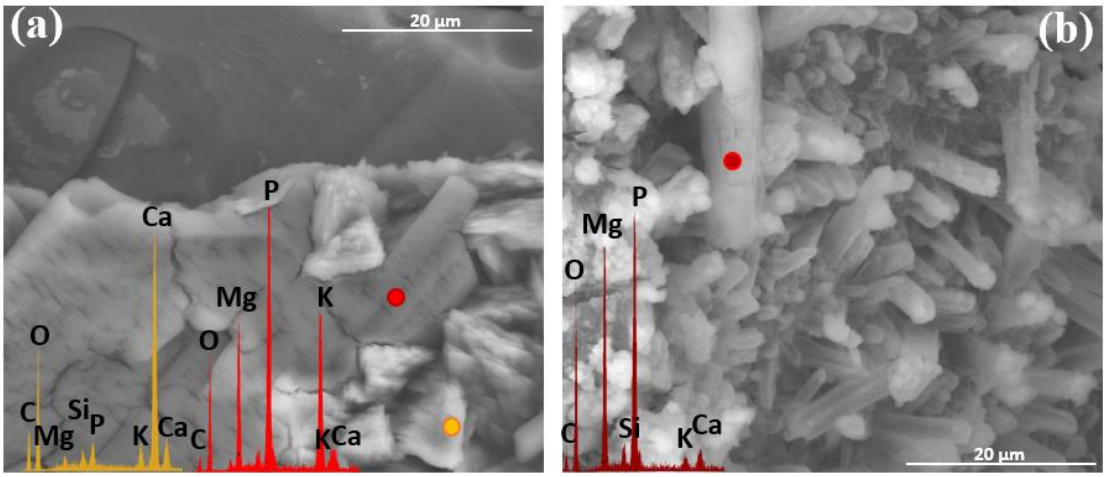


Fig. 58. Sporadically observed secondary phases: calcium carbonate (yellow spectrum) on the surface of 0S_6PMC (a), and magnesium phosphate on 3S_10PM (b); SEM images captured during the summer incubation stage.

It is well established that the precipitation of both identified crystalline phases is favoured under alkaline conditions, particularly within the pH range of 8 to 10 [395–397], which again implies the occurrence of localized and intensified alkalization of the soil solution. This phenomenon likely arises in surface regions of the samples that facilitate prolonged contact between the extractant and the glass, such as areas characterized by enhanced surface roughness or porosity.

A comparison of the data compiled in Tab. 23 with those obtained from the acidic peat incubation experiments (as presented in manuscript **P4**) clearly demonstrates the significant influence of the soil substrate on the progression of surface alteration phenomena. The slightly higher pH of the universal substrate supports more pervasive corrosion of the glass volume, manifested as a network of fine surface cracks; however, these changes remain largely confined to isolated surface regions. More consequentially, the markedly lower concentrations of H^+ and H_3O^+ ions in the universal medium substantially suppress ion exchange processes, which are critical to the controlled release functionality of these glasses when deployed as nutrient carriers. Indeed, none of the glasses incubated in the universal substrate exhibited the early-stage intensification of leaching of mobile constituents that was observed in acidic peat conditions (Tab. 23). This diminished interdiffusion is directly responsible for the lower likelihood of reaching supersaturation in the contact solution with respect to mobile cations, and thus for the reduced tendency toward preferential crystallization of magnesium or magnesium–potassium phosphate phases –

phenomena commonly observed in low-pH environments. In contrast, in the case of the universal substrate, the chemical composition of the soil appears to exert a more decisive influence on the nature of the precipitated secondary phases. Specifically, it not only limits the release of calcium ions from glass compositions containing CaO (e.g., XS_6PC and XS_6PMC), but also promotes the formation of calcium phosphate (CaP) phases on the glass surface.

As shown previously in **P4**, the weathering behaviour of incubated glasses is subject to seasonal variation, a trend that was similarly observed during exposure to the universal substrate. During the early incubation stages simulating spring conditions, the XS_6PM glass surfaces (Fig. 59:0.5 mth) exhibit only limited signs of interaction. In certain areas, a fine network of surface cracking – previously discussed as indicative of [OH^-]-induced attack – becomes visible. EDS analysis of near-surface zones reveals elevated potassium ion concentrations, implying outward migration via ion exchange (0.5 mth, p.2), and thus suggesting a preferential release pathway comparable to that observed under acidic peat incubation. Additionally, the formation of CaP crystals is evident as early as 0.5 months

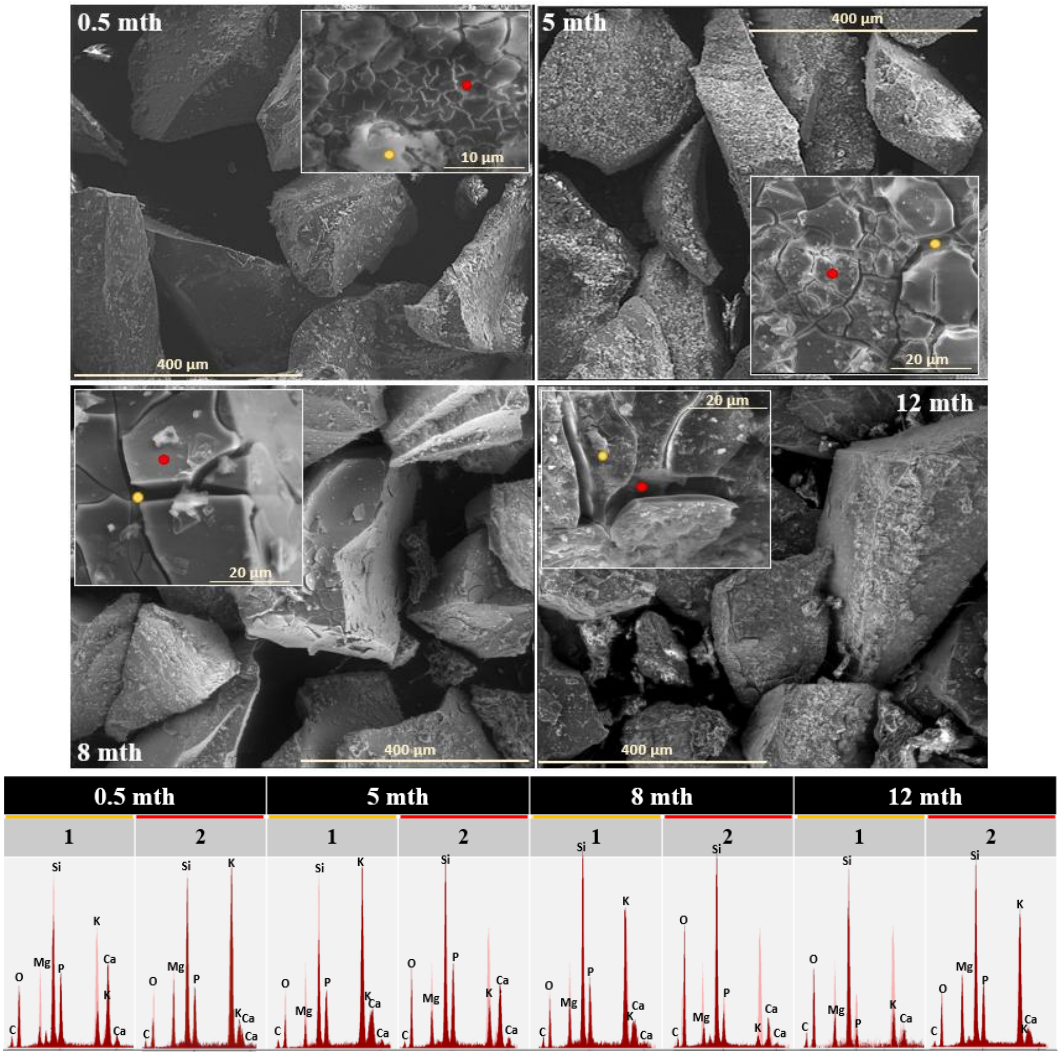


Fig. 59. Morphological evolution of the 0S_6PM glass surface after 0.5, 5, 8, and 12 months of incubation in the universal substrate, accompanied by EDS spectra corresponding to selected surface regions (the light pink spectrum represents intact glass and is included for reference purposes).

(p.1), marking the first signs of soil-induced surface transformation. Notably, throughout the spring period, these processes remain strictly localized and occur in morphologically analogous forms.

However, the transition to simulated summer conditions appears to amplify interfacial activity – much like the behaviour observed in acidic media. The previously confined cracking networks expand to cover substantial surface areas of the glass. Flake-like structures, coated with CaP deposits and depleted in gradually leached potassium and magnesium ions (5 mth, p.2), are also present, though their dimensions remain significantly smaller than those observed during incubation in acidic peat. This discrepancy is likely attributable to differences in the intensity of processes responsible for crack formation. As established in manuscript **P4**, the genesis of such flake-like morphologies is multifactorial; however, one of the principal mechanisms is the extensive dealkalization of the near-surface layer. This chemical transformation introduces disparities in physical properties – particularly thermal expansion coefficients – between the corroded surface and the unaltered glass bulk, ultimately leading to internal stresses, crack propagation, and exfoliation of the altered layer. This, in turn, exposes deeper, unreacted regions of the glass to further corrosion, as illustrated by the potassium-enriched inter-flake zones observed after 5 months of incubation (5 mth, p.1). a similar stress-induced mechanism is likely associated with the overlying layer of crystalline precipitates: temperature fluctuations imposed by experimental conditions may contribute not only to the delamination of the altered glass surface but also to the detachment of secondary product layers. Another factor intensifying surface degradation involves the periodic fluctuations in soil moisture content inherent to the experimental methodology. The cyclic wetting and drying of the silica-enriched surface layer result in repeated expansion and contraction, leading to mechanical damage within the near-surface regions. Taking all these factors into account – and in particular, the markedly lower extent of ion exchange in the universal substrate relative to the acidic medium – it can be concluded that the morphology of the observed flakes serves as a macroscopic indicator of the structural processes occurring within the glass. The reduced degree of surface dealkalization, coupled with localized hydrolysis of Si–O–Si bonds, ultimately gives rise to smaller flake areas compared to those formed during incubation in acidic peat, where more extensive leaching penetrates deeper into the glass volume.

Similarly as it was observed when subjecting glasses to acidic peat, during the incubation of glasses in the universal substrate, the transition from summer to autumn and subsequently to winter conditions was found to intensify the exfoliation of the corrosion-altered surface layer – depleted in the most mobile glass constituents, such as K^+, Mg^{2+}, PO_4^{3-} 8 mth: p.2; 12 mth: p.1) – thereby progressively exposing deeper, previously unaffected regions of the material (8 mth: p.1; 12 mth: p.2). It is important to emphasize that the accumulation of phosphate and exogenous calcium ions at the surface was consistently observed throughout the duration of the experiment, with the sole exception of the final month of incubation.

A comparable behaviour was observed in the early stages of incubation for the glass composition modified by the addition of sulfur (Fig. 60). From the second week onward, a fine network of surface cracks became locally visible, while the EDS spectrum from this region (0.5 mth, p.2) revealed a chemical composition closely resembling that of the unaltered glass. As in the sulfur-free counterpart, the formation of a secondary phase –

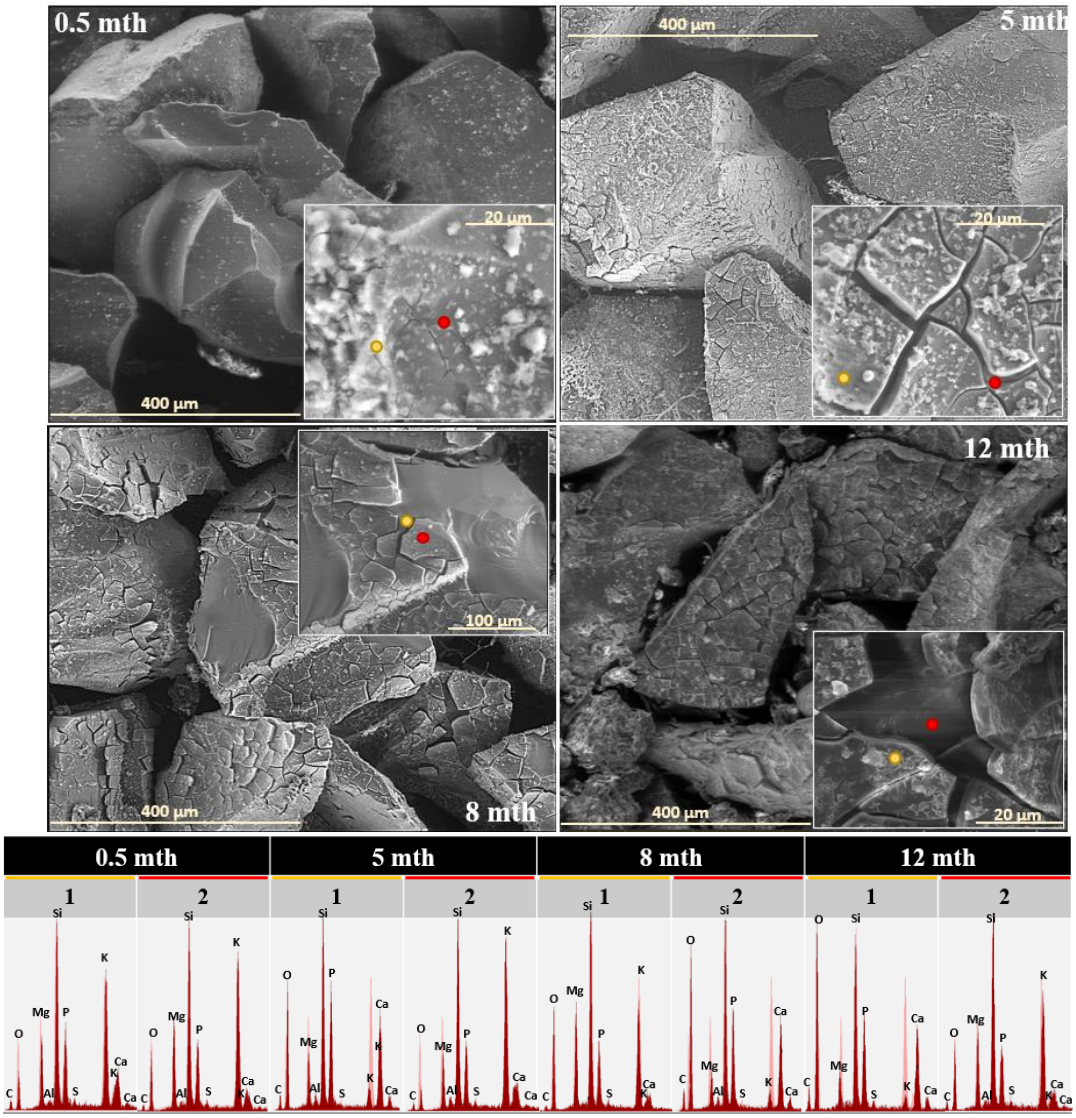


Fig. 60. Morphological evolution of the 3S_6PM glass surface after 0.5, 5, 8, and 12 months of incubation in the universal substrate, accompanied by EDS spectra corresponding to selected surface regions (the bright spectrum represents intact glass and is included for reference purposes).

namely, amorphous calcium phosphate – was already evident at this stage (0.5 mth, p.1). Furthermore, the ion leaching sequence mirrored that previously documented for glasses incubated in acidic peat. In freshly exposed inter-crack areas, an increased potassium concentration was recorded, while the content of other matrix components remained near their original levels. This observation once again points to the preferential outward migration of K^+ ions via interdiffusion (5 mth, p.2).

Based on the EDS spectrum collected from the surface of a detached flake (5 mth, p.1), magnesium and sulfate ions appear to be released next, while phosphate and externally sourced calcium ions accumulate within the silica-enriched corrosion-altered zone. The seasonal shift to autumn and subsequently winter conditions once again exacerbates surface cracking and, in certain areas, leads to the mechanical disintegration of portions of the altered surface layer – the newly exposed regions are characterized by a chemical

composition corresponding closely to that of the unaltered glass (8 mth: p.1; 12 mth: p.2), while the exfoliated flakes exhibit a reduced concentration of mobile elements, with the exception of phosphate and calcium ions (8 mth: p.2; 12 mth: p.1).

Similarly, in the case of glasses containing CaO as an alkaline-earth network modifier, the earliest indications of interaction with the surrounding solution primarily involve the formation of densely packed secondary products on the surface of the incubated specimens (Fig. 61). The morphology and corresponding EDS spectra of these precipitates

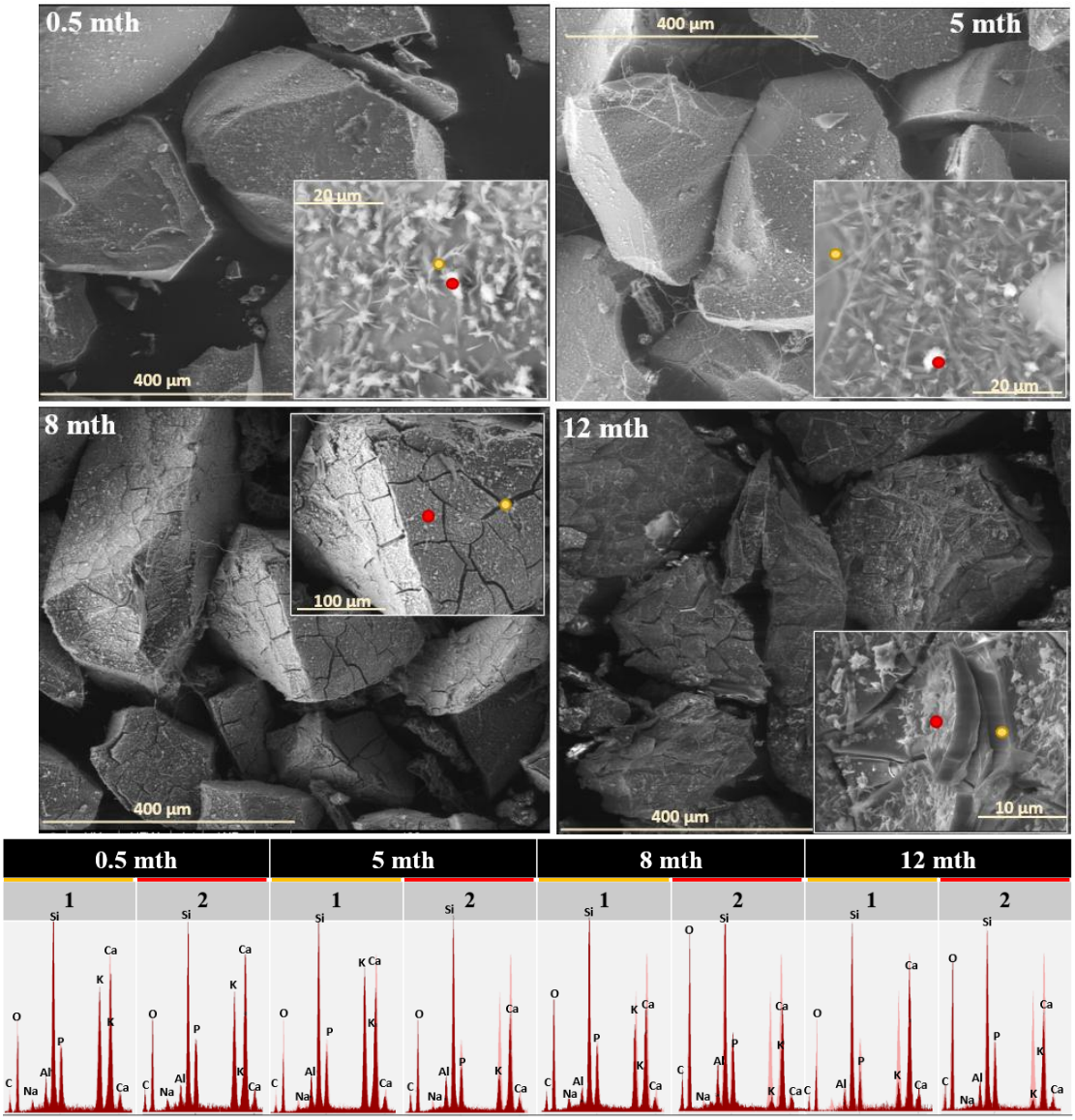


Fig. 61. Morphological evolution of the 0S_6PC glass surface after 0.5, 5, 8, and 12 months of incubation in the universal substrate, accompanied by EDS spectra corresponding to selected surface regions (the bright spectrum represents intact glass and is included for reference purposes).

strongly suggest their classification within the family of calcium phosphates (Fig. 61, 0.5 mth: p.2; 5 mth: p.2; 8 mth: p.2; 12 mth: p.2). It is noteworthy that the chemical composition of areas unaffected by crystallite deposition remains largely comparable to the initial glass matrix, although a slight depletion of potassium ions is evident, indicating

partial release of this constituent into the external medium (Fig. 61, 0.5 mth: p.1; 5 mth: p.1; 8 mth: p.1; 12 mth: p.1).

The preferential leaching of potassium is further corroborated by the analysis of a structurally analogous, sulfur-doped sample (Fig. 62, 0.5 mth), wherein EDS data acquired from interstitial regions demonstrate the migration of both K^+ and Ca^{2+} ions toward the near-surface zones (Fig. 62, 0.5 mth: p.2). While potassium ions, along with $[SO_4]^{2-}$ undergo progressive release into the surrounding environment, calcium ions, in the presence of phosphate groups, tend to precipitate, giving rise to star-shaped CaP structures (Fig. 62, 0.5 mth: p.1).

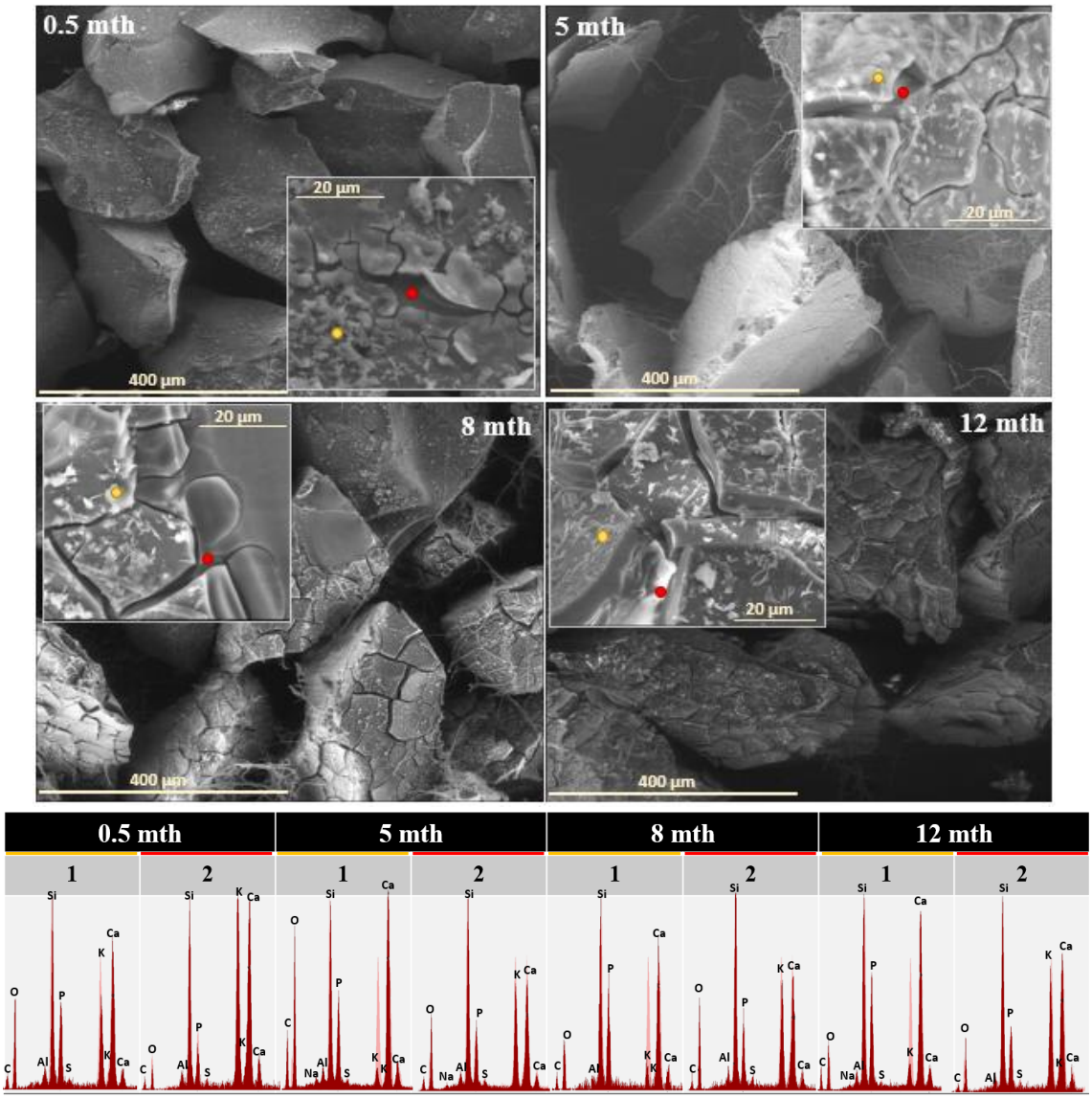


Fig. 62. Morphological evolution of the 3S_6PC glass surface after 0.5, 5, 8, and 12 months of incubation in the universal substrate, accompanied by EDS spectra corresponding to selected surface regions (the bright spectrum represents intact glass and is included for reference purposes).

In both glass systems, the transition to summer conditions and the associated temperature increase does not result in as pronounced a surface alteration as was observed during exposure to peat substrate. Although a gradual intensification of surface degradation is discernible, the chemical composition of the cracked regions indicates only marginal

enhancement of the leaching process, which continues to involve primarily K^+ ions and, in the case of the sulfur-doped sample, also $[SO_4]^{2-}$ species (Fig. 61, Fig. 62, 5 mth: p.1). Notably, in both cases, the near-surface zones are covered with dense CaP-type deposits (Fig. 61, Fig. 62, 5 mth: p.1), while the inter-lamellar regions still retain a chemical composition closely resembling that of the pristine glass. It is not until the experimental conditions shift toward autumnal temperatures that a marked intensification of near-surface disintegration occurs, progressively affecting the entirety of the incubated fragments. Despite the increased extent of alteration and the visible advancement of the reaction front into the bulk, the ion-exchange mechanism remains selective, involving almost exclusively K^+ ions (Fig. 61, Fig. 62, 8 mth: p.1) with the exposed areas beneath the degraded surface still chemically similar to the unaltered glass (p.2).

Further temperature decline appears to exert no significant influence on the ion-exchange dynamics. Potassium continues to be the sole ion subjected to leaching – alongside $[SO_4]^{2-}$ in sulfur-doped systems – whereas calcium remains immobilized in the near-surface regions (Fig. 61, Fig. 62, 12 mth: p.1). a distinct manifestation of winter incubation conditions is the observable exfoliation of corroded surface layers, which seems to play a pivotal role in the intensification of surface processes (Fig. 61, Fig. 62, 12 mth: p.2).

Analogous to the observations made for samples exposed to acidic peat, glasses from the XS_6PMC series also appear to interact with the universal substrate in a delayed manner compared to the remaining systems (Fig. 63, Fig. 64, Tab. 23).

On the surface of the base glass, no visible traces of weathering processes are detected at early incubation stages (EDS point analysis at 0.5 mth: p.1,2 corresponds to the initial composition, Fig. 63), aside from sporadic calcium phosphate precipitates observed at a later stage (Fig. 63, 5 mth: p.2). In contrast, the sulfur-modified sample exhibits not only such crystalline phases (Fig. 64, 0.5 mth: p.2) but also localized microcracks, particularly along edges exposed to soil solution. The chemical composition of these fractured regions suggests a low-intensity ion exchange process occurring within the structurally altered zones, with minor leaching of K^+ and Mg^{2+} ions accompanied by the release of sulfate units (Fig. 64, 0.5 mth: p.1). The aforementioned processes persist throughout the spring incubation period with limited intensity and predominantly local character. Despite an initially delayed onset of interaction with the incubation medium – relative to other studied systems – an increase in temperature appears to intensify surface processes to a greater extent than observed in glasses containing CaO as the sole alkaline-earth network modifier. Both the base glass and its sulfur-doped counterpart exhibit a pronounced increase in crack formation, resulting in the development of distinct flake-like features within the near-surface regions. Given that the corresponding EDS spectra reveal reduced concentrations of K^+ and Mg^{2+} (Fig. 63, Fig. 64, 5 mth: p.1), and in the case of the 3S_6PMC sample, also $[SO_4]^{2-}$ species (Fig. 64, 5 mth: p.1), it may be inferred that the formation of such flakes is correlated with the extent of leaching of mobile glass constituents. This hypothesis is further supported by existing literature [121], which confirms that preferential detachment tends to occur in regions with physicochemical properties distinct from those of the glass bulk. As in the other examined systems, the near-surface domains of these samples appear increasingly susceptible to mechanical degradation under autumnal conditions, as evidenced by the propagation of cracks across the entire sample surface (Fig. 63, Fig. 64). a comparative EDS analysis of the flake surface and the

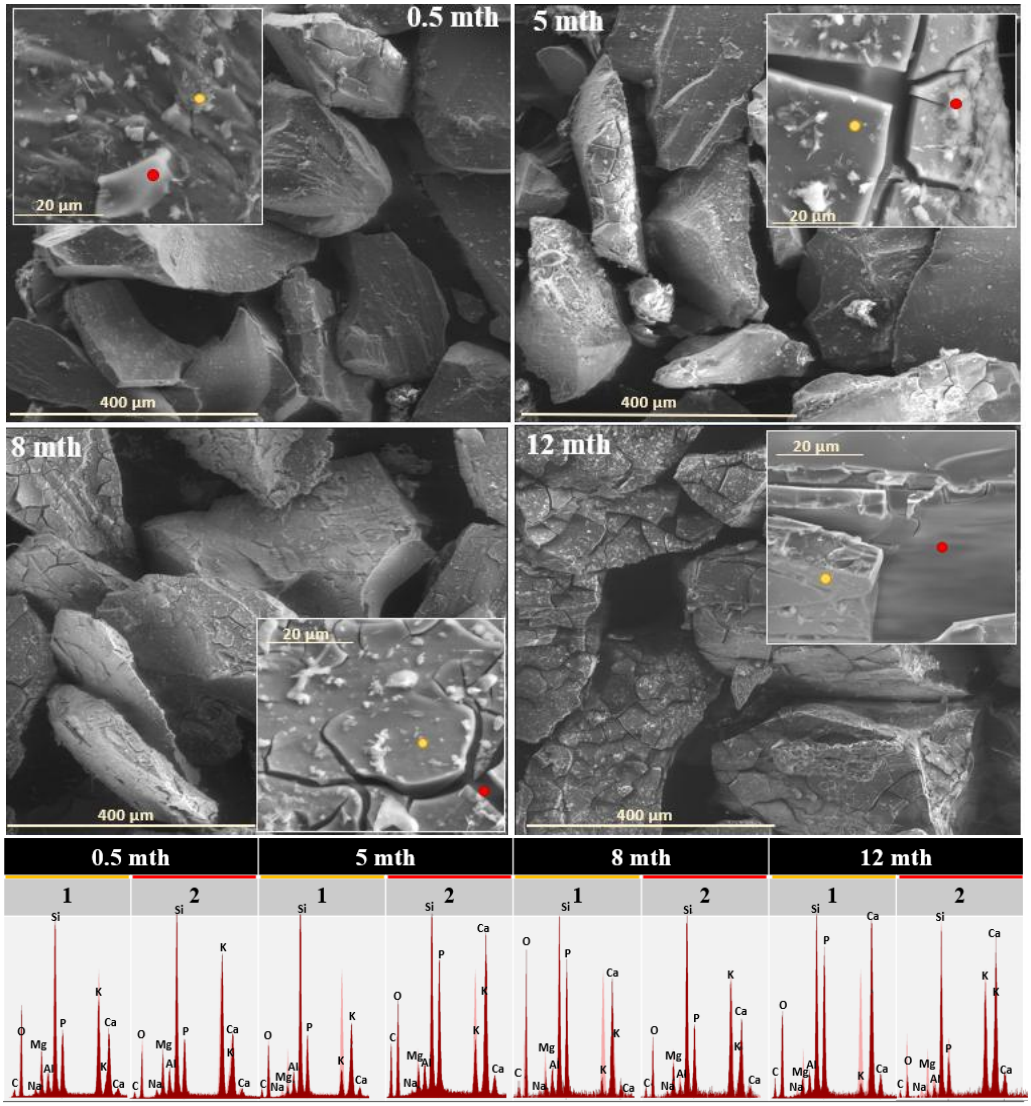


Fig. 63. Morphological evolution of the 0S_6PMC glass surface after 0.5, 5, 8, and 12 months of incubation in the universal substrate, accompanied by EDS spectra corresponding to selected surface regions (the bright spectrum represents intact glass and is included for reference purposes).

areas exposed between fractures – for both the base and sulfur-modified compositions ((Fig. 63, Fig. 64, 8 mth: p.1, p.2), demonstrates the accumulation of Ca^{2+} and $[PO_4]^{3-}$ ions in the outer layers of the incubated samples, accompanied by leaching of the remaining mobile elements. Although the interstitial zones of 3S_6PMC retain elevated levels of both potassium and calcium, the EDS spectrum collected from the outermost layer confirms the release of potassium via interdiffusion.

Further temperature reduction promotes the exfoliation of corrosion-affected surface regions but does not significantly alter the prevailing reaction mechanisms at the solid–liquid interface. The leaching of mobile ions continues, while calcium ions accumulate in the outer glass layer (Fig. 63, 12 mth: p.2., Fig. 64, 12 mth: p.1)., and subsequently co-precipitate with phosphate units, forming CaP-type crystalline deposits (Fig. 63, 12 mth: p.1, Fig. 64, 12 mth: p.2).

Similar to observations in acidic peat substrate, the universal substrate reveals the highest reactivity in samples with elevated P_2O_5, content, regardless of sulfur modification. As early as two weeks into the incubation, both base and sulfur-doped compositions become densely coated with a compact layer of magnesium-potassium double phosphate

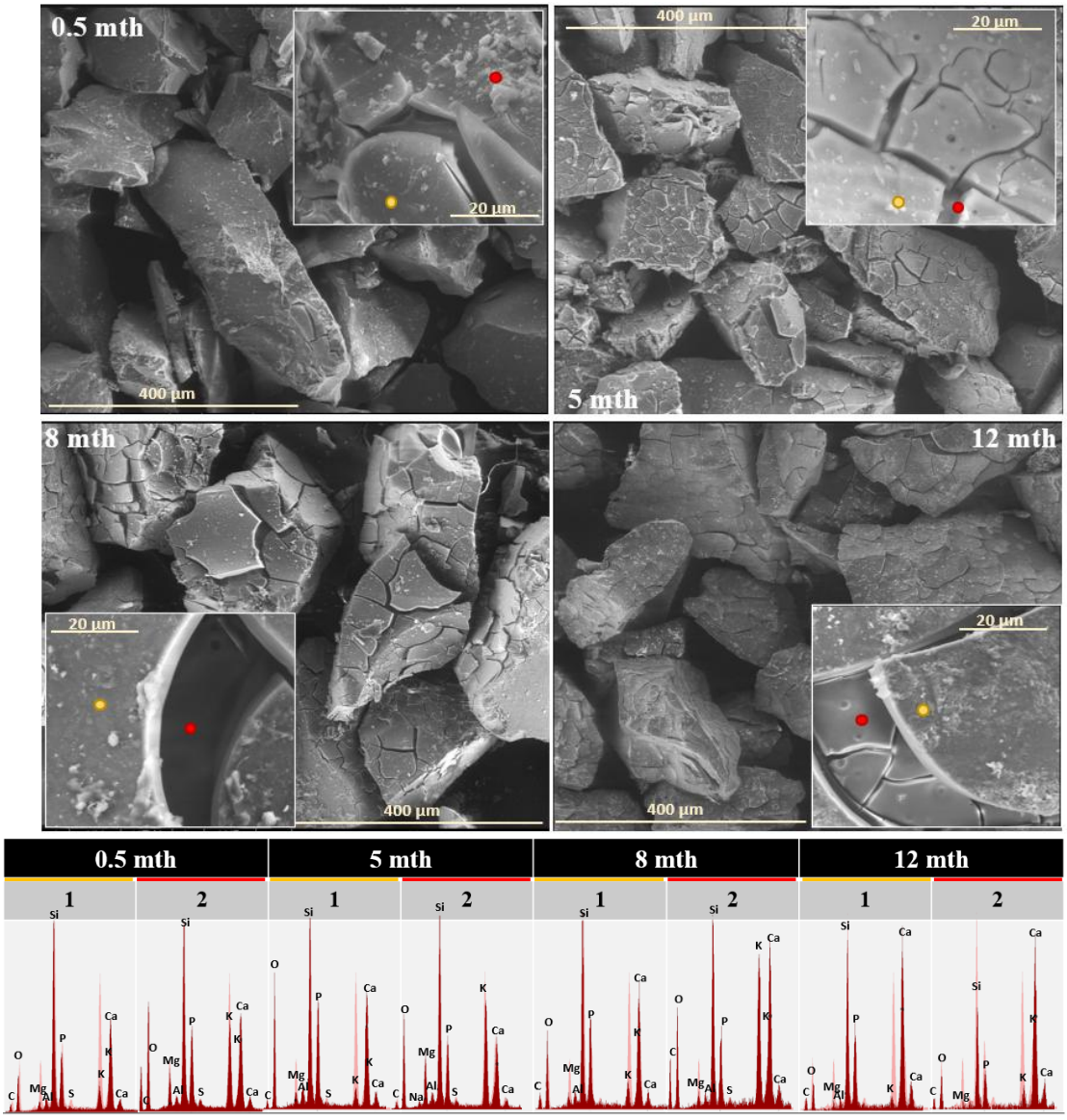


Fig. 64. Morphological evolution of the 3S_6PMC glass surface after 0.5, 5, 8, and 12 months of incubation in the universal substrate, accompanied by EDS spectra corresponding to selected surface regions (the bright spectrum represents intact glass and is included for reference purposes).

precipitates (Fig. 65, p.2; Fig. 66, p.1). The EDS spectrum collected from point 1 on Fig. 65 for the 0S_10PM sample indicates intensive potassium ion migration toward the glass surface, where it crystallizes – together with Mg^{2+} and $[PO_4]^{3-}$ ions—into the observed deposits (0.5 mth: p.2). Nevertheless, the overall chemical activity of these glasses appears to be lower compared to their behaviour in acidic peat. While the latter produced a reaction layer up to ~16.5 µm thick, the universal substrate still allows the presence of uncoated glass fragments in early incubation stages (Fig. 66, 0.5 mth: p.2), albeit already enriched in potassium. Although the KMgP-rich layer remains stable throughout the simulated spring period, increasing temperatures lead to its progressive degradation (Fig. 65, Fig. 66, 5 mth: p.3) – the freshly exposed regions of glass exhibit significantly reduced concentrations of all mobile constituents (Fig. 65, 5 mth: p.1; Fig. 66, 5 mth: p.2), the presence of locally formed CaP-type precipitates suggests inward calcium transport from the surrounding environment and its accumulation within silica-enriched surface

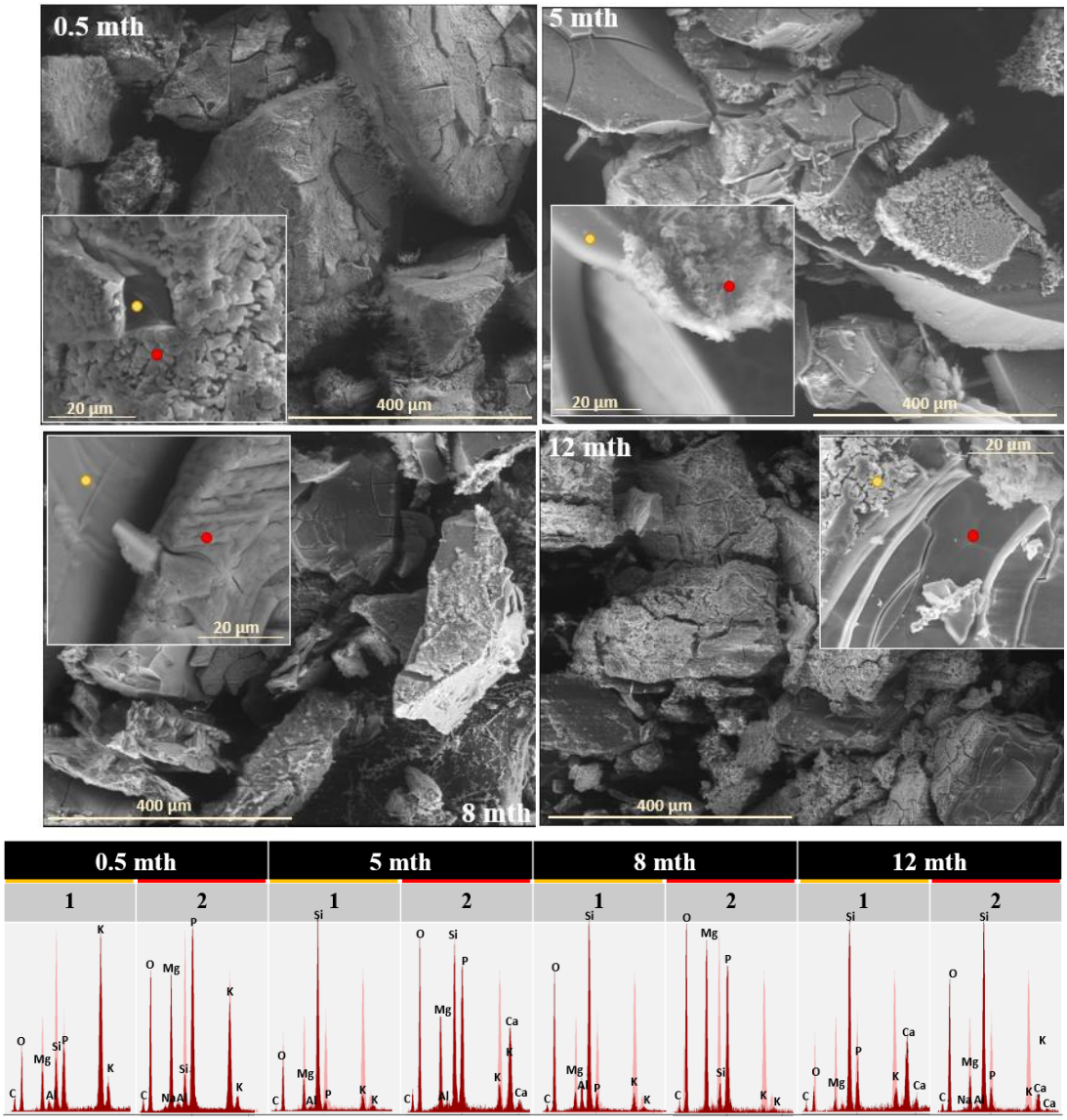


Fig. 65. Morphological evolution of the 0S_10PM glass surface after 0.5, 5, 8, and 12 months of incubation in the universal substrate, accompanied by EDS spectra corresponding to selected surface regions (the bright spectrum represents intact glass and is included for reference purposes).

zones (Fig. 65, 5 mth: p.2; Fig. 66,, 5 mth: p.1) ultimately altering the crystallization behaviour of the system.

The autumnal lower temperature conditions substantially intensify mechanical damage to the materials, manifesting not only as extended cracking but also as complete disintegration of sample fragments (Fig. 65, Fig. 66). The pronounced ion-exchange activity observed in this system is mirrored by a marked increase in local solution alkalinity and, consequently, the crystallization of distinctive, well-defined magnesium phosphate structures (Fig. 65, 8 mth: p.2; Fig. 66 – geometric crystallites marked by yellow 'x'). Calcium phosphate continues to precipitate concurrently as a secondary phase (Fig. 65, 8 mth, right-hand glass fragment; Fig. 66, 8 mth: p.1), forming a dense layer over the incubated surfaces. Notably, the chemical composition of glass areas devoid of secondary deposits indicates extensive leaching of nearly all mobile elements (Fig. 65, 8 mth: p.1; Fig. 66, 8

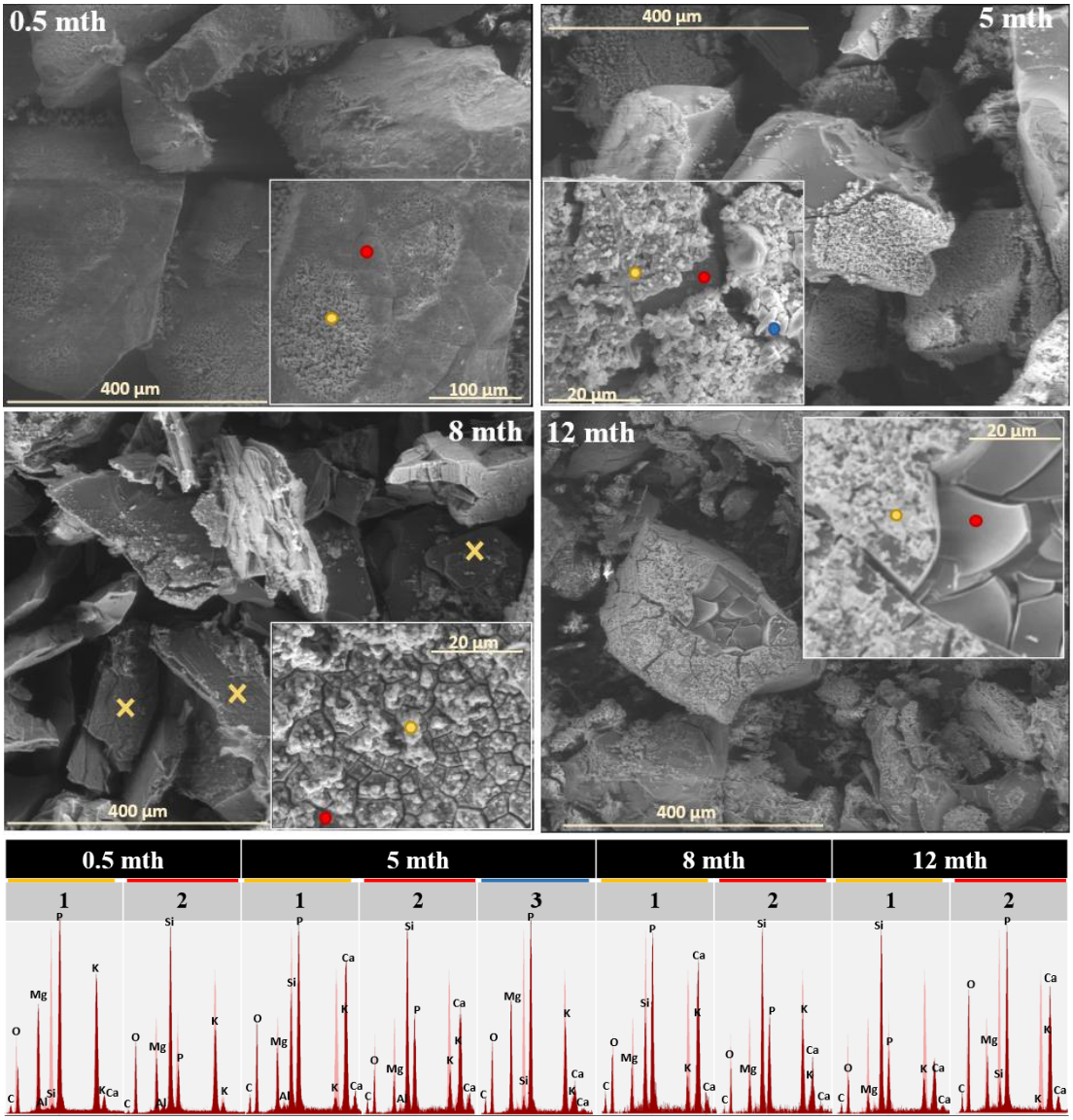


Fig. 66. Morphological evolution of the 3S_10PM glass surface after 0.5, 5, 8, and 12 months of incubation in the universal substrate, accompanied by EDS spectra corresponding to selected surface regions (the bright spectrum represents intact glass and is included for reference purposes).

mth: p.2), albeit to a significantly lesser extent than under acidic peat conditions, where a fully silica-rich leached layer was recorded at the same incubation stage.

Observations from the final incubation phase further corroborate previous findings: following the disintegration of the phosphate-rich surface layer and the depletion of mobile ions, Ca^{2+} ions accumulate in the corroded regions, eventually co-precipitating with phosphate units to form a compact CaP deposit that progressively covers the glass surface (Fig. 65, 12 mth: p.1; Fig. 66, 12 mth: p.1). However, this newly formed layer – as well as the altered glass zones beneath – exhibits a tendency toward cracking and mechanical failure, continuously exposing fresh material to the corrosive medium and perpetuating the leaching of mobile species (Fig. 65, 12 mth: p.2; Fig. 66, 12 mth: p.2).

Despite the observable differences in the behaviour of the incubated glasses across the two employed soil substrates – whose pH values differ only moderately (acidic peat: pH 3.5–4.5; universal substrate: pH 5.5–6.5) – it can once again be concluded that the

surface alteration processes closely resemble those well-documented for glass degradation under immersion conditions. The analysis of the *in vivo* experimental results confirms the presence of three principal mechanisms: (1) adsorption of a thin moisture film at the glass surface, (2) the simultaneous occurrence of three interrelated reactions – ion exchange, hydration, and hydrolysis – and (3) precipitation of a secondary surface layer.

Nevertheless, in most of the analysed cases, the flake-like surface regions exhibited partial release of the most mobile glass constituents (K^+, Mg^{2+}, SO_4^{2-}), albeit without the pronounced silica enrichment observed for samples incubated in acidic peat. This finding reinforces the hypothesis that ion exchange processes are significantly less intense under higher pH conditions, while at the same time suggesting a more substantial contribution of Si–O–Si bond hydrolysis, resulting in partial dissolution of the silica network into the surrounding medium along with mobile ions.

Even under the less acidic conditions of the universal substrate, a clear compositional dependence of glass weathering behaviour was observed, analogous to the trends reported for acidic peat exposure (as discussed in **P4**). Firstly, the presence of SO_3 as found to influence glass–substrate interfacial processes, although its effect was noticeably less pronounced than in the acidic medium. As previously emphasized in publication **P4**, sulfur's influence on glass–soil interactions arises indirectly – through increased network connectivity, which enhances the structural rigidity of the glass and thus increases its susceptibility to mechanical degradation. This effect is further amplified by the preferential location of [SO_4^{2-}] species within the structural voids of the vitreous matrix, where they contribute to internal stress development. In the acidic peat environment, sulfate-related effects were reflected in the deeper progression of the reaction front into the material, as a consequence of intensified cracking of near-surface regions. In contrast, within the universal substrate – where Si–O–Si hydrolysis also contributes to the alteration mechanism – the influence of sulfate incorporation is less substantial, although still perceptible in the form of enhanced fracture susceptibility.

Once again, the highest reactivity under *in vivo* conditions was exhibited by glasses with the greatest P_2O_5 content, which can be attributed to the contribution of hygroscopic [PO_4^{3-}] units. Notably, however, the impact of increased phosphate content appears to be reduced compared to the effects observed in acidic peat exposure. As with sulfate incorporation, this attenuated response likely results from a higher contribution of hydrolysis processes (and simultaneously lower participation of ion-exchange ones) in the alteration mechanism. Furthermore, consistent with previous observations, the chemically most complex system, XS_6PMC, again displayed the slowest onset of interaction with the soil substrate, most likely due to the well-known mixed alkaline-earth effect.

A form of indirect confirmation of the higher reactivity of the studied materials under more acidic conditions is presented in Fig. 67. Assuming that the thickness of the exfoliated flakes serves as a qualitative indicator of the corrosion depth, a rough estimation of the extent of glass degradation in both soil substrates may be performed based on SEM micrographs (cross-sectional preparation of the samples was not feasible due to the specific constraints of the experimental setup). Acknowledging the limitations of this rough, qualitative assessment, and considering that the flake thickness in samples exposed to the universal substrate is approximately 5–6 μm, whereas for those incubated in acidic peat it reaches ~10–15 μm, it can be inferred that the intensity of surface alteration processes is significantly greater in the latter environment.

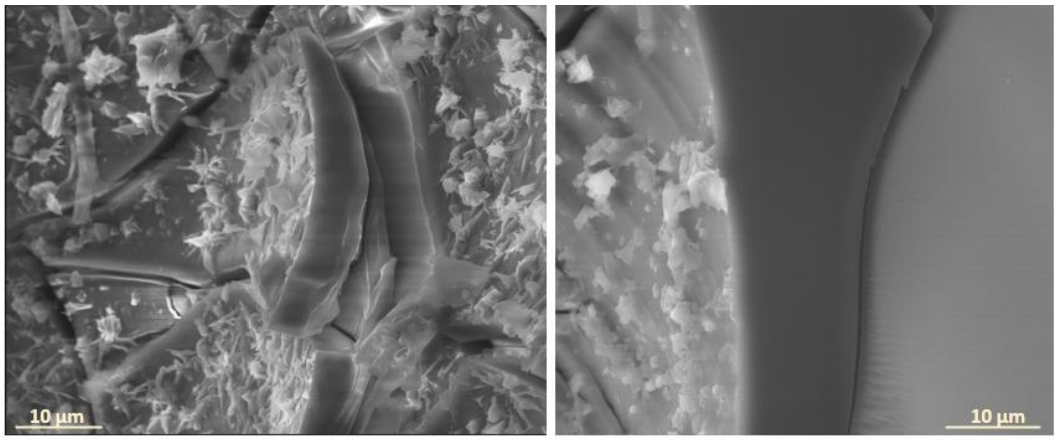


Fig. 67. Comparison of the thickness of exfoliated layers in glasses incubated in different soil substrates, based on sample 0S_6PC after 12 months in the universal substrate (left) and 9 months in acidic peat (right).

In summary, the *in vivo*-type experiment carried out in the universal soil substrate revealed a more pronounced influence of the soil environment on interfacial glass–solution interactions compared to that observed during incubation in acidic peat. a key distinguishing feature lies in the nature of the mechanical alterations formed in the near-surface regions – rather than the large, distinct flakes commonly developed in acidic media, the glasses incubated in the universal substrate exhibited networks of fine fissures forming small-scale flakes. These finer structures reflect, first and foremost, the markedly reduced extent of the ion exchange process: in contrast to the extensive surface disintegration and complete depletion of mobile ions (K^+, Mg^{2+}, SO_4^{2-}) observed under the strongly acidic conditions of peat, such extensive leaching was not evident in the higher-pH environment. Secondly, the presence of a network of fissures may also be interpreted as a manifestation of the parallel mechanism of Si–O–Si bond hydrolysis, commonly observed in glass–solution interactions. This hypothesis is supported by EDS spectra collected from selected surface regions, which indicate no significant silica enrichment in the altered layers, suggesting that part of the silica may also be released into the surrounding medium.

Furthermore, the lower acidity of the universal substrate results in a diminished rate of interdiffusion, leading to reduced alkalization of the contact solution and, consequently, a slightly lower intensity of crystallization processes and decreased phase diversity. In this case, the predominant crystalline product is calcium phosphate, known to precipitate over a broad pH range.

Despite the closed-system nature of this experimental setup, the findings from the entire *in vivo*-like study effectively capture the complexity and interdependence of the processes occurring at the soil–glass interface. These results underscore the pivotal role of soil pH and mineralogical composition, as well as glass chemistry and environmental variability, in dictating the course of glass–soil interactions.

Although the same sequence of surface processes – (1) moisture adsorption on the glass surface, (2) concurrent ion exchange, hydration, and hydrolysis, and (3) precipitation of secondary phases – was observed regardless of the substrate, their intensity varied depending on the soil characteristics. These variables modulated the dominant reaction pathways, favouring ion exchange in the case of acidic peat, and increasing the contribution of hydrolysis of Si–O–Si bonds with lower ion-exchange intensity in the case of the universal substrate.

The restricted water availability imposed by the experimental conditions – reflected in a high surface-area-to-volume (SA/V) ratio – resulted in rapid saturation of the contact solution with leached elements. This, in turn, promoted the precipitation of secondary phases, which occurred in both soil environments. From the perspective of targeted agricultural applications, this is a particularly valuable phenomenon, as it enables the temporary immobilization of excess nutrients, potentially reducing their immediate loss and allowing controlled re-release. Importantly, the identity of the crystallized phases was influenced not only by the solution pH but also by the interaction between the glass (more pronounced in the case of acidic peat incubation) and the soil compositions (more pronounced in the case of universal substrate incubation).

Crucially, these findings indicate that even minor modifications in the glass composition can be employed to fine-tune material behaviour in accordance with specific soil conditions. For example, the exclusion of Ca^{2+} from the glass composition could help avoid the precipitation of poorly soluble apatite-type phases in calcium-rich soils; altering the P_2O_5 content can be used to regulate nutrient release rates; and the incorporation of SO_3 groups may benefit sulfur-deficient soils or sulfur-demanding crops.

The above results, when considered alongside those presented in publication P4, emphasize the multifactorial and dynamic nature of glass degradation. The sequence and dominance of particular mechanisms remain inherently difficult to predict, highlighting the necessity of accounting for emergent behaviours in glass–soil systems. They also reinforce the need for further studies under more complex and variable environmental conditions to ensure comprehensive evaluation of the long-term behaviour of these materials in real-world agricultural contexts.

12 Structure of glasses after dissolution in citric acid solution

As highlighted in publications **P1** and **P2**[*], the glassy framework of the investigated materials (XS_6PM, XS_6PC, XS_6PMC, and XS_10PM), characterized by high silica content and elevated concentrations of both alkali and alkaline-earth oxides, is predominantly composed of metasilicate (Q^2_{Si}) and disilicate (Q^3_{Si}) units. This compositional profile is clearly reflected in the Raman spectra of these glasses, where the most prominent vibrational bands arise from the symmetric stretching modes of terminal Si–O^- bonds – vibrations inherently associated with the presence of alkali and alkaline-earth cations acting as network modifiers. Indeed, in all samples mentioned above, the most intense Raman band – positioned near 970 cm^{-1} – indicates the prevalence of Q^2_{Si} groupings, accompanied by a slightly less intense band near 1060 cm^{-1}, attributable to Q^3_{Si}.

Conversely, the findings reported in publications **P3** and **P4** unequivocally demonstrate that the primary factors governing the glass alteration process are the chemical composition of the material and the specific environmental conditions, particularly the nature of the aggressive medium. When exposed to such corrosive environments, the near-surface regions of glass undergo a range of reactions, including interdiffusion, hydration, and hydrolysis of Si–O linkages. The predominance of one mechanism over the others is strongly influenced by the pH of the attacking solution.

Given that glass alteration inherently induces structural reorganization, the investigation into the chemical activity of the tested silicate-phosphate glasses (**P3**, **P4**) was complemented by an in-depth structural analysis using Raman spectroscopy. Accordingly, spectra were collected for selected samples – specifically 3S_6PM and 3S_10PM – after

various durations of exposure to a 2% citric acid solution. These results are presented in Fig. 68 and Fig. 69[5].

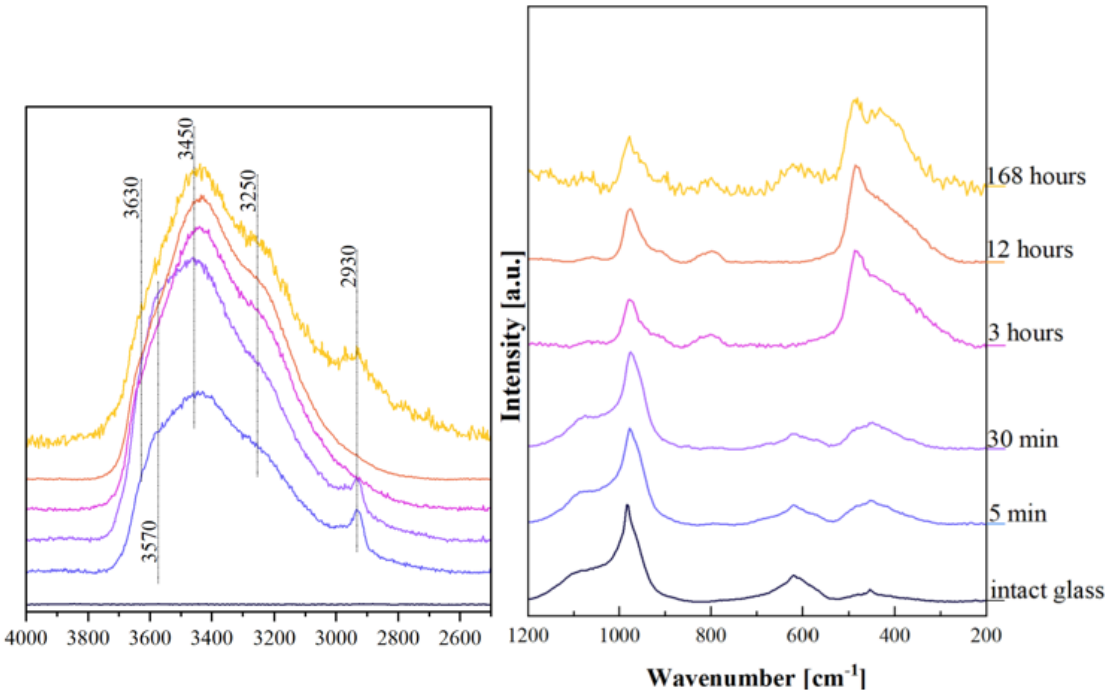


Fig. 68. Raman spectra of 3S_6PM glasses after various durations of exposure to 2% citric acid solution.

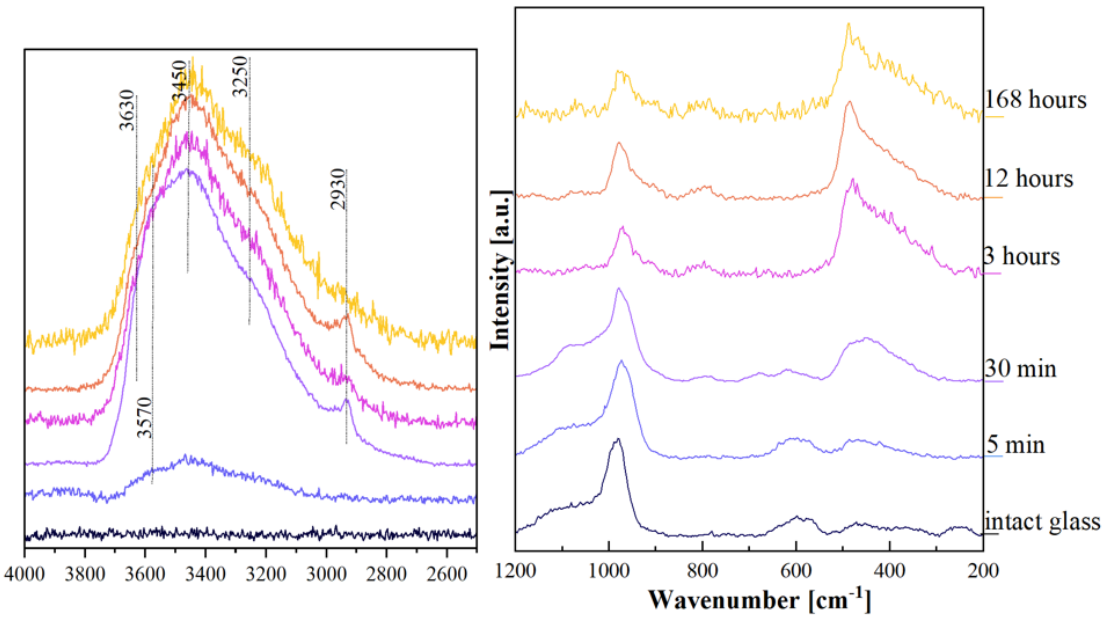


Fig. 69. Raman spectra of 3S_10PM glasses after various durations of exposure to 2% citric acid solution.

[5] The selection of these particular compositions for post-alteration structural analysis was guided by the outcomes of prior experiments on the kinetics of glass corrosion (as reported in publication **P3**).

To facilitate the interpretation of structural modifications induced by the acidic medium, a summary table has been compiled, assigning the observed vibrational bands to specific vibration modes within structural units/molecules, Tab. 24.

Tab. 24. Assignment of characteristic vibrational bands observed in Raman spectra of sulfate-bearing multicomponent silicate-phosphate glasses, [316,398–401].

Frequency range [cm^{-1}]	**Assignment**	**Ref.**
Pristine glass-related Raman vibration modes		
1200 – 850	Symmetric stretching vibrations of Si-O^- terminal bonds in silicate units: • 1100-1050 cm^{-1}: disilicate, Q^3_{Si}, units; • 1000-950 cm^{-1}: metasilicate, Q^2_{Si}, units; • 900 cm^{-1}: pyrosilicate, Q^1_{Si}, units; also: symmetric stretching vibrations of P-O bonds within the orthophosphate groups $[PO_4]^{3-}$, Q^0_P (~ 960-950 cm^{-1})	[317]
700 – 500	Bending motions of Si-O-Si bridges in Q^n_{Si} structural units (here – mainly the Q^2_{Si}), asymmetric bending vibrations of P–O^- in orthophosphate groups $(PO_4)^{3-}$ (~ 570 cm^{-1})	[317,403, 404]
500 – 350	Bending vibrations of O-P-O and P-O^- linkages in orthophosphate $(PO_4)^{3-}$, (~ 400 cm^{-1}) and pyrophosphate $(P_2O_7)^{4-}$, (~ 460 cm^{-1}) units, respectively	[314,403, 405]
Sulfate-specific Raman vibration modes		
984	Symmetric S-O stretching vibration, υ_{ss} (S-O)	[248,266, 267]
620	Asymmetric S-O-S bending vibration, δ_{as} (S-O-S)	
455	Symmetric S-O-S bending vibration, δ_{ss} (S-O-S)	
Glass alteration-related Raman vibration modes		
3630	Stretching mode of silanol groups (H-bonded to O of water), ν_s(SiO–H); And/or: asymmetric stretching mode of water, $\nu_3(H_2O)$	[398,400,401]
3570	Superimposition of OH vibrations of adsorbed water molecules and vicinal/geminal silanol groups	
3450	Symmetric stretching mode of water, $\nu_1(H_2O)$	
3250	First overtone of water bending mode, $2\nu_2(H_2O)$	

2930, 1640, 1430	Artifacts related to the remnants of unwashed citric acid
1200, 1070	Si–O-Si stretching motion, longitudinal and transversal optical modes (LO–TO splitting), ν_s(Si–O–Si)
975	Asymmetric stretching of Si–O in surface silanol groups, ν_{as}(O_3Si–OH)
800	bending of the Si–O–Si bridge, δ_{bend}(Si–O–Si)
610	"breathing" movement of the oxygen atoms in planar threefold Si–O–Si rings, defect band, D_2
495	"breathing" movement of the oxygen atoms in 4-membered Si-O-Si rings, defect band, D_1
450	rocking motion of SiO_2, δ_{rock}(Si–O–Si)
420	symmetric "breathing" modes of ≥5-fold Si–O–Si rings, δ_{breath}(Si–O–Si)

Remarkably, even after only five minutes of contact with the corrosive solution (2% citric acid, pH ~2), discernible structural changes are evident in the recorded Raman spectra of the tested ion-releasing glasses, Fig. 68, Fig. 69.

A broad, high-intensity band appears in the 3800–2800 cm^{-1} range, representing a convolution of multiple sub-bands, which collectively indicate the presence of water within the glass structure, Tab. 24. The dominant contribution to this feature is the symmetric stretching vibration of water molecules (~3450 cm^{-1}), while the low-frequency tail likely corresponds to the first overtone of the bending mode of H_2O, and a sharper, well-defined component – detectable in several spectra – can be attributed to residual citric acid from prior kinetic experiments that was not completely removed during sample preparation. Nonetheless, the most diagnostically informative portion of this composite feature lies in its high-wavenumber region (>3500 cm^{-1}), which is typically associated with silanol-related vibrational modes. Notably, only the spectra collected after the shortest exposure durations (5 minutes) exhibit a distinct inflection near 3570 cm^{-1}. This spectral shoulder is understood as a superimposition of two overlapping contributions: (i) the O–H vibrations of water molecules adsorbed on the glass surface and (ii) the stretching vibrations of hydroxyl groups associated with vicinal or geminal silanol species. Alternatively, the second component may arise from water molecules that remain physically adsorbed to the glass. As the duration of interaction with the acidic medium increases, this inflection feature gradually disappears, while the overall intensity of the water-related envelope increases. Simultaneously, a new shoulder emerges around 3630 cm^{-1}, which is assigned to the stretching vibration of hydrogen atoms bonded to oxygen within water molecules that are hydrogen-bonded to silanol groups. Given the band assignment (Tab. 24), the progressive replacement of the 3570 cm^{-1} inflection with the 3630 cm^{-1} shoulder suggests an increasing degree of silica hydration over time as well as reduction in surface curvature along with the prolonged exposure to the corrosive medium, as relatively lower number

of silanol groups may be detected within the laser-illuminated volume of the sample [398,401].

Progressive alterations in the vibrational spectrum of the tested glasses were also observed within the 1200–200 cm^{-1} range, which encompasses the bands associated with the vibrational modes of silicate and orthophosphate units present in the pristine materials. Notably, significant spectral changes become apparent after only five minutes of interaction with the leaching medium, as in both glass types, a new spectral feature emerges within the principal band (extending from 900 to 1200 cm^{-1}), manifesting as a distinct signal at 975 cm^{-1}, and attributed to the asymmetric stretching vibrations of Si–O bonds in surface silanol groups ($\nu_{as}(O_3Si–OH)$), Fig. 68, Fig. 69. Simultaneously, in the low-wavenumber region (<500 cm^{-1}), broad features develop around 450 cm^{-1} in both spectra, characteristic of amorphous silica and corresponding to Si–O–Si rocking vibrations (δ_{rock}(Si–O–Si)). Significantly, the Raman spectrum of the 3S_6PM sample no longer displays the sharp 982 cm^{-1} spectral feature indicative of sulfate species after just 5 minutes of exposure, which confirms the rapid leaching of sulfate groups from the near-surface region and underscores their high solubility in acidic environments (Fig. 68). More pronounced transformations, however, are observed in glasses with elevated P_2O_5 – content: specifically, the band associated with orthophosphate units (~570 cm^{-1}) becomes attenuated, and the signal attributed to Mg–O bending vibrations (~250 cm^{-1}) diminishes, indicating the release of magnesium from the glass matrix [265,314,316,398].

With extended exposure to the acidic medium, additional spectral modifications become evident, reflecting the continued structural evolution of the glasses.: after 30 minutes of interaction, subtle features appear at approximately 800 cm^{-1} and 610 cm^{-1}, along with a high-wavenumber inflection within the broad 450 cm^{-1} band at ~495 cm^{-1}, particularly pronounced in the sample with higher phosphate content P_2O_5 sample (Fig. 68, Fig. 69). All these emerging bands are characteristic of amorphous silica: the 800 cm^{-1} band corresponds to Si–O–Si bending vibrations with significant Si atomic displacement δ_{bend}(Si–O–Si), whereas the 610 and 495 cm^{-1} features are attributed to the "breathing" modes of oxygen atoms in 3- and 4-membered siloxane rings, respectively [398,400,401].

Prolonged exposure (≥ 3h) to citric acid results in more extensive structural reorganization: in both compositions, the 800 cm^{-1} band, corresponding to Si–O–Si bending in amorphous silica, increases in intensity. Concurrently, the band at 610 cm^{-1}, which signifies the presence of planar, threefold Si–O–Si rings, vanishes, while the overall profile of the 450–490 cm^{-1} band becomes increasingly asymmetric – a phenomenon marked by the dominance of the 495 cm^{-1} feature, indicative of fourfold siloxane rings, as well as the emergence of a low-wavenumber tail, which – according to literature – serves as a diagnostic indicator of higher-order siloxane rings (≥ fivefold). These trends are particularly evident in the samples subjected to prolonged interaction (168 hours / 7 days) with the acidic medium (Fig. 68, Fig. 69). Importantly, for exposure durations exceeding 3 hours, the spectral features characteristic of the pristine glasses – namely, the symmetric Si–NBO stretching vibrations associated with (Q^2_{Si}) and (Q^3_{Si}) units – disappear entirely. Instead, new bands emerge at approximately 1070 cm^{-1} and 1160 cm^{-1}, corresponding to Si–O–Si symmetric stretching vibrations ν_s(Si–O–Si) in a restructured, hydrated amorphous silica network [397,399,400].

The progressive appearance of these spectral features in Raman spectra recorded after varying durations of exposure provides compelling support for the dominant mechanism of interaction between the studied glasses and the simulated root-exudate solution, as

independently observed in both the 'in vitro' (**P3**) and 'in vivo' (**P4**) experimental series. Specifically, alkali and alkaline-earth cations, along with orthophosphate and sulfate groups, are progressively leached from the glass surface via ion exchange with protons from the surrounding medium. This leads to a systematic depletion of all mobile components from the near-surface region and promotes extensive hydration. As a consequence, silanol groups form and subsequently condense, yielding oligomeric and cyclic structures. These structures evolve further through the progressive formation of siloxane bridges, ultimately giving rise to a hydrous amorphous silica layer, via the well-documented polycondensation reaction, [397]:

$$\equiv Si - OH + HO - Si \equiv \leftrightarrow \equiv Si - O - Si \equiv + H_2O \qquad \text{Eq. (22}$$

Interestingly, literature reports suggest that the hydrolysis of Si–O–Si bonds can be monitored by Raman spectroscopy through the presence of a distinct spectral band near 670 cm^{-1} [398]. This band, although of currently uncertain structural origin, is considered a hallmark of the dissolution-dominated mechanism that typically occurs in alkaline conditions (high pH). The absence of this feature in all spectra collected in the present study supports the conclusion that no dissolution-driven structural breakdown has taken place under the employed experimental conditions.

Furthermore, it is worth emphasizing that, despite ongoing debate in the literature regarding the mechanism responsible for the formation of the crosslinked hydrous silica layer – whether it occurs via re-condensation of silanol groups or through a dissolution–reprecipitation process – the present findings strongly support the former scenario in relation to the tested materials. Under the experimental conditions applied (solution pH ~2), the solubility of silica is relatively low (in stark contrast to that in alkaline solutions with pH > 9), as confirmed by the results of the 'in vitro' dissolution experiments (**P3**). Additionally, the dynamic character of the experiment (350 rpm stirring) likely hindered the establishment of local supersaturation at the glass-solution interface, which would otherwise facilitate silica reprecipitation [119].

Taken together, the experimental results obtained in this complementary kinetic study are fully consistent with those previously reported in publications **P3** and **P4**, and thus serve as an important extension of the doctoral research on the chemical durability and alteration behaviour of the designed glasses.

13 Sulfur-bearing glass and conventional fertilizers – comparison

The final stage of the investigation concerning the chemical activity of the developed glass materials involved a comparative assessment of their behaviour upon contact with a solution simulating plant root exudates (2 wt.% citric acid solution), juxtaposed with a commercially available mineral fertilizer (Planta® universal fertilizer). For this purpose, a granulated fertilizer exhibiting a comparable nominal chemical composition (Tab. 25) was procured and subjected to an identical dissolution procedure, as described in publication **P3**, namely a 30-minute conventional immersion experiment in the above-mentioned acidic medium.

Tab. 25. Chemical composition of the commercially available universal mineral fertilizer [wt.%]

Component	SiO_2	P_2O_5	K_2O	MgO	CaO	SO_3	N_2
Acc. to manufacturer	–	8	15	3	5	32	10
XRF-measured	3.19	10.06	16.40	0.57	9.74	20.67	–

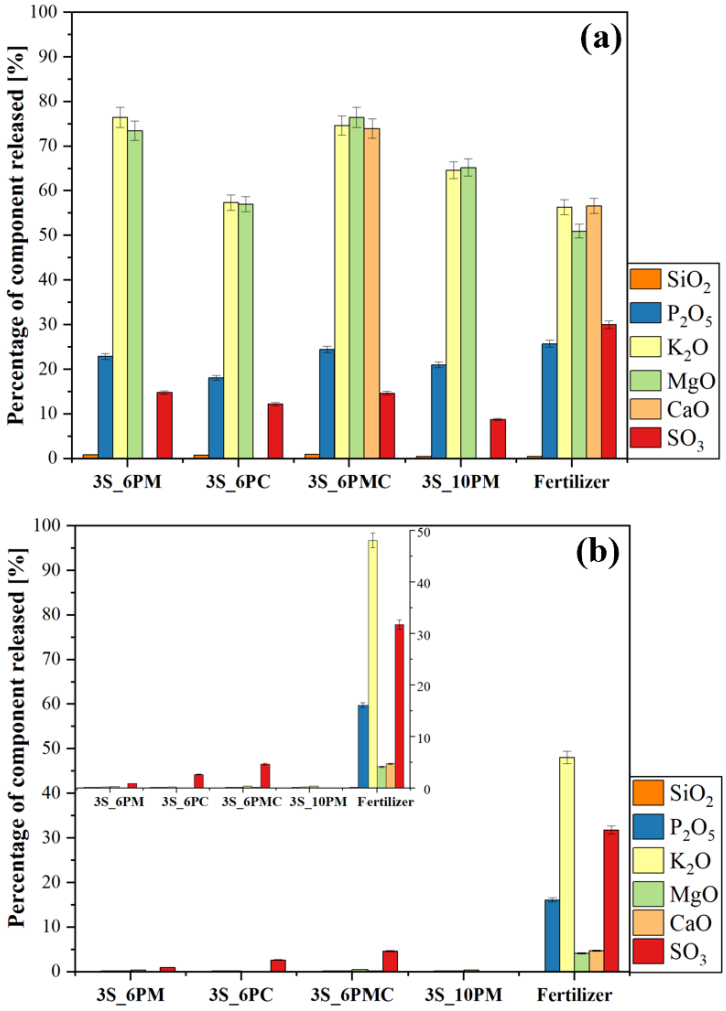


Fig. 70. Comparative release profiles of glass fertilizers versus the commercial mineral fertilizer in 2% citric acid solution (a) and distilled water (b).

The results of this experiment, compared with the data obtained for 3S-type glass fertilizer candidates from the studied systems (XS_6PM, XS_6PC, XS_6PMC, and XS_10PM), are presented in Fig. 70(a), while Fig. 70(b) illustrates the corresponding dissolution results for all aforementioned materials in distilled water under identical conditions (30-minute exposure).

As shown in Fig. 70, the glasses developed in the present study demonstrate the capacity to release structurally embedded nutrients under acidic conditions in quantities comparable to those released by the commercial mineral fertilizer of similar chemical composition. Undoubtedly, subjecting the tested conventional fertilizer to an extended 'in vivo' soil incubation study would yield more comprehensive insight into its long-term behaviour within the soil matrix and allow for a definitive comparison with the performance of the glass-based fertilizers, particularly in terms of nutrient release kinetics. Nevertheless, the current experiment confirms the markedly lower solubility of the synthesized vitreous materials in distilled water, thereby indicating a substantially reduced risk of over-fertilization and the associated environmental hazard of nutrient leaching into surrounding water bodies.

14 Lifecycle of vitreous sulfur carriers

The observed crystallization tendency of designed sulfur-bearing glasses prompted a detailed examination of material aging following prolonged laboratory storage. For this purpose, selected glass samples containing sulfur – specifically those of compositions previously studied under 'in vivo' conditions (3S_6PM, 3S_6PC, 3S_6PMC, and 3S_10PM) – were reanalysed after three years of ambient storage in sealed plastic zip bags under stable laboratory conditions (constant temperature and humidity). The microstructural assessment was conducted using SEM, and representative micrographs are presented in (Fig. 71. (a)-(d)).

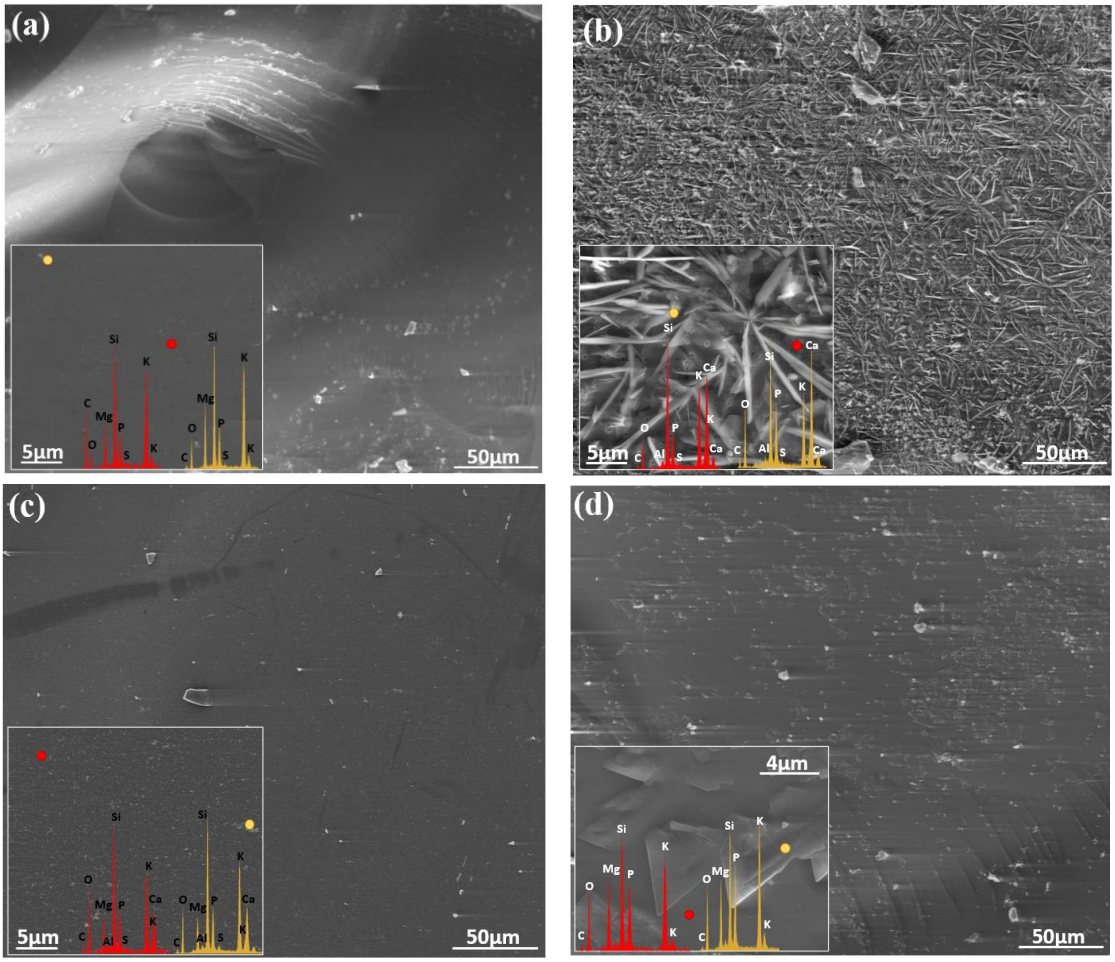


Fig. 71. SEM micrographs of 3-year-old glass samples: 3S_6PM (a), 3S_6PC (b), 3S_6PMC (c), and 3S_10PM (d), accompanied by EDS spectra collected from selected surface points.

As illustrated in the above micrographs, the surfaces of samples 3S_6PM and 3S_6PMC appear chemically homogeneous at the investigated sites and show no evidence of crystallites that would indicate atmospheric interaction (Fig. 71. (a) and (c)). In contrast, the surface of sample 3S_10PM – representing the composition previously shown to exhibit the highest chemical reactivity in soil environments – displays numerous well-defined geometric precipitates in the form of thin, plate-like structures (Fig. 71.(d)). EDS analysis of these secondary phases revealed elevated concentrations of Mg, K, and P relative to the parent glass composition, suggesting the formation of a double magnesium-potassium phosphate phase. The most pronounced alteration, however, was

observed on the surface of the 3S_6PC sample, which was entirely covered with star-shaped crystalline deposits. EDS results for these precipitates showed enrichment in Ca and P, pointing toward the formation of a calcium phosphate phase.

To precisely identify the secondary crystalline phases present on the surfaces of aged 3S_10PM and 3S_6PC samples, XRD analysis was performed, and the resulting diffractograms are shown in Fig. 72. (a), (b).

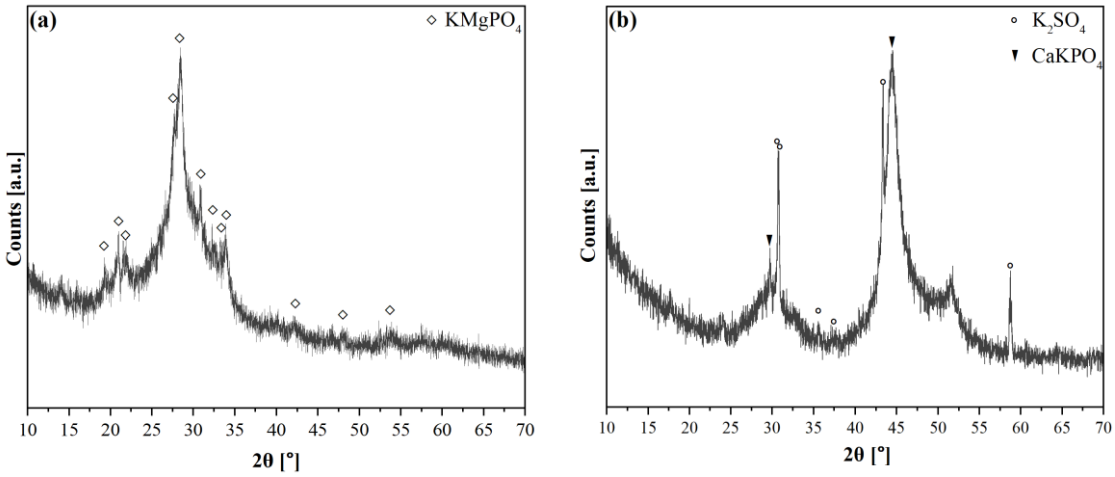


Fig. 72. XRD patterns of 3-year-old samples: 3S_10PM (a) and 3S_6PC (b).

The elevated background in both XRD patterns confirms the predominantly amorphous nature of the materials. Nevertheless, in both cases, weak but discernible crystalline reflections superimposed on the amorphous halo attest to partial devitrification. Despite the limited number and broadness of the observed peaks, phase identification for 3S_10PM indicates, with reasonable certainty, the presence of $KMgPO_4$ (Ref. 00-050-0149), consistent with the SEM-EDS findings. In contrast, although the XRD pattern of 3S_6PC exhibits more numerous and better-defined reflections, phase identification could only conclusively confirm the presence of K_2SO_4 (Ref. 00-024-0703). The assignment of the remaining peaks – unmatched to known sulfate phases – proved considerably more ambiguous, with at least three reflections not corresponding to any known crystalline compound. Among the possible candidates, $KCaPO_4$ (Ref. 98-002-7958) exhibited the best overall match, although this assignment only partially aligns with the EDS data, which did not indicate elevated potassium content in the star-shaped crystallites. Due to the limited number of identifiable reflections – or possibly due to database incompleteness—the attribution of $KCaPO_4$ remains uncertain. It is therefore not possible to unequivocally determine whether the observed surface phase indeed corresponds to this mixed phosphate. Alternatively, one might speculate that $KCaPO_4$ is in fact present within the sample volume, while its surface abundance lies below the detection threshold of the XRD method. It is also worth noting that not all reflections present in the diffractogram of 3S_6PC could be assigned.

To complement the microstructural and compositional data, Raman spectroscopy was employed to investigate the structural changes in the aged glasses. The resulting spectra are presented in Fig. 73. (a)-(d), which also, for comparative reasons, include spectra of freshly synthesized 3S_6PM and 3S_6PMC glasses – materials that, notably, did not exhibit secondary phase formation on their surfaces. For a reference, spectra of the fresh samples were also provided.

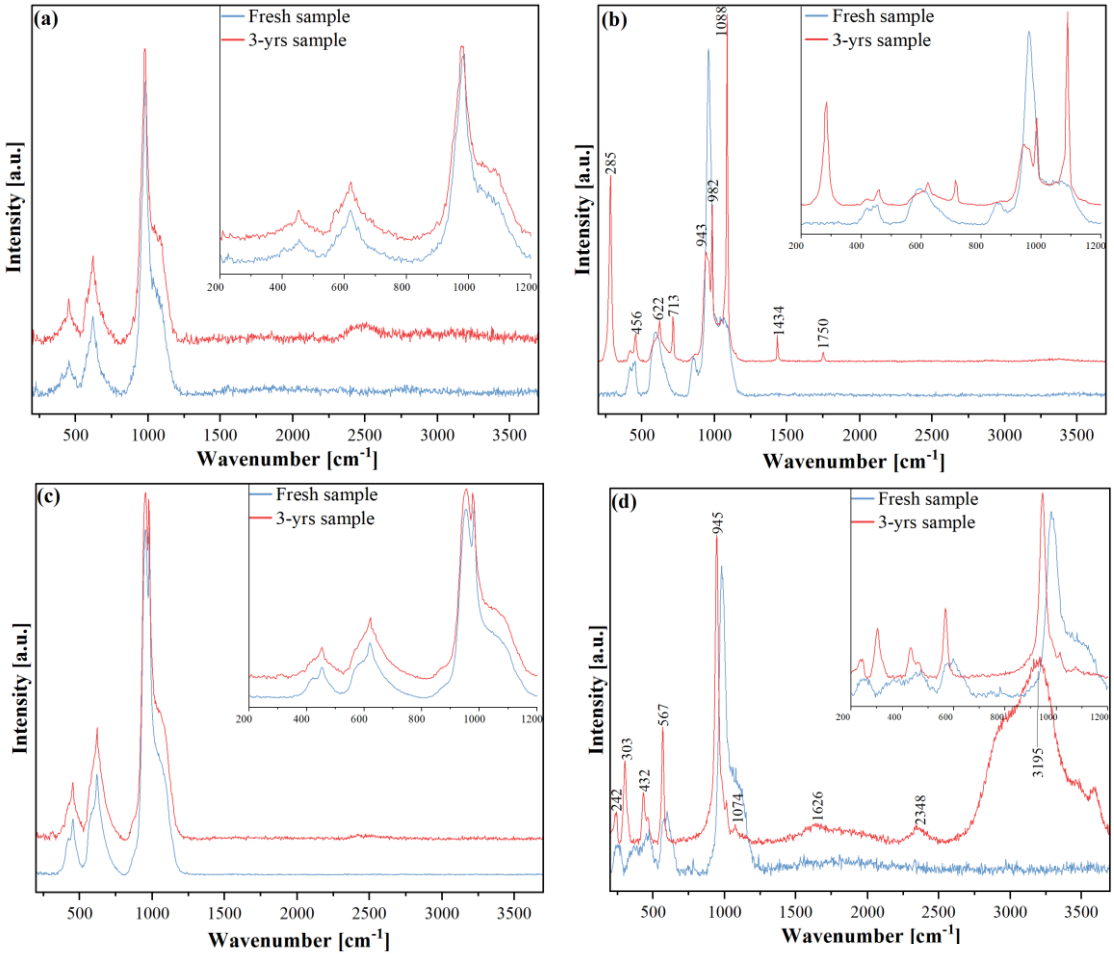


Fig. 73. Raman spectra of 3-year-old glasses (red lines): 3S_6PM (a), 3S_6PC (b), 3S_6PMC (c), and 3S_10PM (d), with corresponding spectra of freshly obtained samples (blue lines) included for reference.

The hypothesis derived from SEM and EDS analyses – namely, that the structure of 3S_6PM and 3S_6PMC glasses remained unchanged during storage – is corroborated by the Raman data (Fig. 73. (a) and (c)) – the spectra of the aged samples closely mirror those of their freshly synthesized counterparts, confirming structural stability over the 3-year storage period (see also publications **P1** and **P2*** for detailed structural discussions).

Conversely, the 3S_10PM glass, previously shown to exhibit the highest chemical activity in soil conditions, again demonstrated the most significant response to atmospheric exposure. This is evidenced by a broad, asymmetric, and complex band in the 2750–3500 cm^{-1} range (Fig. 73. (d)), characteristic of OH stretching vibrations. The high intensity and complex profile of this band suggest the overlapping of several vibrational modes, including fundamental H_2O stretching vibrations and their interactions with second-order transitions of similar symmetry and energy. Additionally, the broad band observed around 1600 cm^{-1} can be attributed to H_2O bending vibrations. The most prominent Raman feature, appearing at 945 cm^{-1}, is assigned to the symmetric stretching (v_1) mode of the $[PO_4]^{3-}$ species, while bands at 1074, 567, and 432 cm^{-1} correspond to the v_3 antisymmetric stretching, v_4 antisymmetric bending, and v_2 symmetric bending vibrations of the phosphate group, respectively. Meanwhile, lower frequency bands observed at 303 and 242 cm^{-1} can be attributed to Mg–O stretching vibrations and lattice modes involving Mg–O,

respectively [404,405]. Remarkably, all bands identified in the Raman spectrum of the aged 3S_10PM sample are consistent with the vibrational signature of struvite – a mineral isomorphous with magnesium potassium phosphate hexahydrate, $MgKPO_4 \cdot 6H_2O$ [405–407]. Although XRD analysis did not unambiguously confirm the presence of struvite within the sample bulk—likely due to the scarcity of well-defined reflections and the elevated background typical of amorphous substances – its formation is strongly supported by previous observations made during soil incubation experiments (publication **P4**), where struvite was the first phase to form, densely covering the glass surfaces. Since it is well known that struvite precipitates only under alkaline conditions [404], content compared to the 6P systems – may have facilitated moisture accumulation on the surface during storage. This, in turn, likely triggered ion exchange between mobile glass constituents and the condensed water film, leading to a localized pH increase and, consequently, the precipitation of a hydrated magnesium-potassium phosphate phase.

Similarly, the Raman spectrum of the 3-year-old 3S_6PC sample reveals pronounced differences compared to its freshly synthesized counterpart, with the sharpness and definition of the vibrational bands confirming the presence of crystalline phases within the material's structure (Fig. 73. (b)). Indeed, the bands located at 982, 622, and 456 cm^{-1} are characteristic of sulfate units, corresponding respectively to the symmetric stretching, and the antisymmetric and symmetric bending modes of the S–O bonds, thereby corroborating the conclusions drawn from XRD analysis, which suggested the presence of K_2SO_4 [251,264]. Unexpectedly, all other sharp and well-resolved bands detected in the Raman spectrum – specifically at 280, 713, 1088, 1434, and 1750 cm^{-1} – correspond closely to the well-established vibrational features of both synthetic and naturally occurring calcite [407]. Among these, the bands at 1435, 1085, and 711 cm^{-1} originate from internal vibrations of the CO_3^{2-} groups within the calcite crystal lattice, the intense signal at 1085 cm^{-1} is attributed to the symmetric stretching vibration (ν_1) of the carbonate ion, while the bands at 1435 cm^{-1} and 711 cm^{-1} are associated with its asymmetric stretching (ν_3) and symmetric bending (ν_4) modes, respectively. Then, the low-frequency band near 280 cm^{-1} arises from external vibrations of the carbonate units, involving translational and rotational oscillations of the anionic group relative to the surrounding cations, whereas the weak signal at 1749 cm^{-1} may be interpreted as a combination band ($\nu_1 + \nu_4$) [407]. Additionally, a vibrational feature located at approximately 943 cm^{-1}, corresponding to the symmetric stretching (ν_1) mode of the P–O bond in phosphate groups, is also observed in the spectrum of this aged sample [404,407]. Interestingly, an analogous spectrum was reported by Sánchez-Pastor et al. [407], during an experiment in which calcite crystallized within a column of silica hydrogel supplemented with Na_3PO_4 solution, in a result of which elongated calcite crystals were formed, with phosphate ions incorporated into their structure. Thus, the star-shaped surface phase commonly observed on the glasses from the XS_6PC series after soil incubation may, in fact, be more complex than initially presumed – possessing not only a phosphate character but also containing carbonate groups. Should this dual-phase character be confirmed for the crystalline precipitate on the surface of 3S_6PC, it would explain the difficulty in identifying the phase through XRD, as it may not be represented in the available crystallographic database. Nevertheless, a diffraction feature observed at $2\theta \approx 29.747°$ in the XRD pattern of this material aligns precisely with the most intense peak of the calcite reference pattern (Ref. 01-072-1651), lending further support to the hypothesis that a similar crystalline phase may be present on the sample surface.

Taken together, these findings suggest that, while the glasses representing the XS_6PM and XS_6PMC systems retain their amorphous character and show no signs of interaction with atmospheric components over three years of storage, those from the XS_6PC and XS_10PM series exhibit clear surface alterations indicative of such interactions. The reduced long-term stability of the latter materials is not unexpected: glasses with elevated P_2O_5 content are known to be more hygroscopic, accelerating alteration processes in aqueous environments. Concurrently, the incorporation of CaO as a network modifier – characteristics of the XS_6PC system – results in a more open, fragmented glass structure, which facilitates interaction with atmospheric species, particularly CO_2 due to the strong chemical affinity between calcium and carbonates. Analogously, the high affinity between CaO and P_2O_5 promotes the structural integration of phosphate ions into the resulting secondary phases [95]. Therefore, it may be concluded that glasses from the XS_6PC and XS_10PM systems possess a limited shelf-life, not exceeding three years, beyond which they begin to exhibit signs of aging – understood here as the precipitation of secondary crystalline phases on their surfaces. Although no such transformations have yet been observed in the XS_6PM and XS_6PMC samples, it cannot be ruled out that these materials may eventually undergo similar aging processes, albeit over longer timescales. These considerations underscore the importance of proper storage conditions for sulfur-bearing glasses, particularly minimizing their exposure to atmospheric moisture and gases, in order to preserve their structural integrity and prolong their functional lifespan.

15 Summary of the obtained results

As highlighted in the introduction to this dissertation, vitreous carriers of beneficial ions for agricultural applications must exhibit specific properties that distinguish them from materials intended for applications requiring high durability. For such glasses to serve as an alternative to commercially available fertilizers, they shall:

I. Demonstrate a tailored chemical composition that ensures the availability of essential macro- and micronutrients for plant nutrition while excluding the possibility of the heavy metals release into the soil environment;

II. Exhibit an amorphous nature, free from crystalline inclusions that would adversely affect their chemical activity and introduce unpredictability into the ion release process;

III. Feature an open, fragmented vitreous network that facilitates inward ingress of water molecules and ion exchange, forming the foundation of the material's action;

IV. Release beneficial components in the presence of organic acid solutions, which are key constituents of root exudates and microbial metabolites, while maintaining high resistance to water exposure, thereby preventing nutrient runoff;

V. Incorporate a mechanism that slows the release of ions trapped within their matrix, thereby prolonging the period over which nutrients are supplied to plants.

Therefore, this study endeavours to comprehend how the composition and structure of multicomponent sulfur-bearing silicate-phosphate glasses dictate their properties.

Through targeted property optimization, valuable insights can be gained into how the concentration of network formers, modifiers, and intermediates within the glass network determines their structural arrangement and, consequently, how specific structural units influence macroscopic properties, such as ion release rates and activity within the soil environment. As demonstrated throughout this dissertation and illustrated in Fig. 74, the aforementioned factors I–V interrelate, forming complex connections.

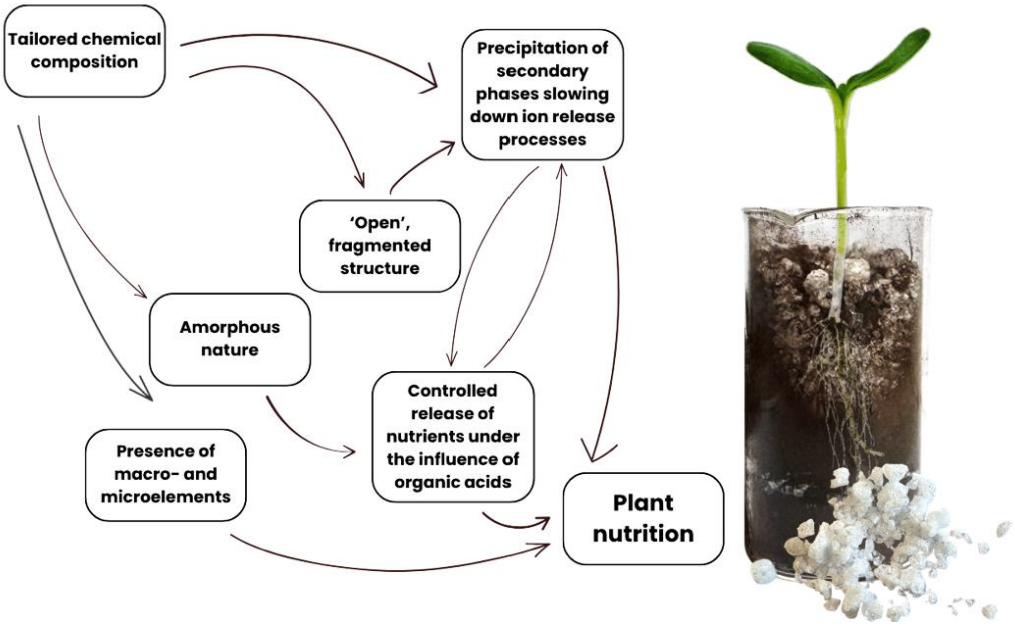


Fig. 74. Relationship between chemical composition, structure, and properties of sulfur-bearing glasses for agricultural applications.

To obtain materials meeting the set criteria, chemical compositions for multicomponent glasses with predominantly silicate characteristics were developed, incorporating essential plant nutrients such as phosphorus, potassium, magnesium, calcium, and sulfur into the vitreous matrix. The designed systems distinguished themselves by the ratios of these components, corresponding to the following chemical compositions:

- XS_6PM: $41SiO_2$-$6P_2O_5$-$20K_2O$-33CaO-SO_3
- XS_6PC: $41SiO_2$-$6P_2O_5$-$20K_2O$-33CaO-SO_3
- XS_6PMC: $41SiO_2$-$6P_2O_5$-$20K_2O$-16.5MgO-16.5CaO-SO_3
- XS_10PM: $41SiO_2$-$10P_2O_5$-$20K_2O$-29MgO-SO_3
- XS_10PC: $41SiO_2$-$10P_2O_5$-$20K_2O$-29CaO-SO_3
- XS_10PMC: $41SiO_2$-$10P_2O_5$-$20K_2O$-14.5MgO-14.5CaO-SO_3

Based on data from publications **P1**–**P3**, it was successfully demonstrated that materials with the designed chemical compositions could be obtained, exhibiting fully amorphous structures, however, using the metal plate cooling technique, amorphous structures were achieved only for the XS_6PM system. The glass-forming ability of the studied systems was improved when a slightly higher cooling rate was adopted through the fritting technique, which enabled the successful amorphization of most of the designed glass systems. Exceptions included the higher P_2O_5 and CaO-containing systems XS_10PC and

XS_10PMC, which still exhibited spontaneous crystallization during cooling, likely due to the high affinity between Ca^{2+} and $[PO_4]^{3-}$ ions, with the main crystalline phase detected being the calcium and potassium phosphate double salt, $KCaPO_4$.

Within these publications, comprehensive structural studies utilizing various spectroscopic techniques (Raman, FTIR, ^{29}Si and ^{31}P MAS-NMR, XAS), confirmed that the vitreous networks of all tested materials, selected as potential sulfur carriers for agricultural applications, exhibit unique frameworks characterized by fragmented chains or sheets of basic structural units, displaying significant potential for promoting the release of beneficial ions into the surrounding substrate.

Finally, the concluding publications **P3** and **P4**, which focused on the soil activity of the designed sulfate-bearing multicomponent silicate-phosphate glasses, deepened the understanding of the complex composition–structure–property relationships of the selected materials by highlighting the third critical aspect of this research – the simulated environment behaviour of the materials. As shown in these publications, the designed materials demonstrate high resistance to water, while releasing mobile components (K^+, Mg^{2+}, Ca^{2+}, SO_4^{2-}, PO_4^{3-}) in response to solutions simulating root exudates and microbial activity, leaving glass remnants as hydrated silica-altered layers. Additionally, these studies provided insights into the mechanisms slowing down their activity in soil environments, where secondary phases precipitate on the silica-enriched altered layers, temporarily binding excess components in the soil solution that are not utilized by plants.

The research conducted during this doctoral study not only validated the potential of the designed materials as carriers of essential ions, enriching the rhizosphere with deficient elements but also provided critical insights into the behaviour of sulfate ions within multicomponent silicate-phosphate glasses. As the primary subject of this investigation was the incorporation of sulfur in its sulfate form into the vitreous matrix, another focus of the present thesis was placed on understanding how this incorporation affects the properties of the final product.

As shown in the findings presented throughout this dissertation, the successful incorporation of sulfates into a silicate-based matrix is highly dependent on the chemical composition of the glass (and, consequently, its structure), with the incorporation of $[SO_4]^{2-}$ species parallelly influencing the properties of the final product. As regards the former of the listed relationships, analytical results revealed a correlation between both the content of phosphorus pentoxide in the vitreous matrix as well as the type of alkaline earth oxide network modifier (MgO/CaO), and the ability of multicomponent silicate-phosphate glasses to incorporate sulfur.

Glass composition vs sulfate capacity

(1) P_2O_5 content vs. sulfate capacity

As outlined in the introduction to this dissertation, literature suggests that the incorporation of sulfur into a vitreous matrix should be facilitated by an increase in P_2O_5 content – a hypothesis based on the premise that the sulfate capacity of any vitreous matrix is strongly influenced by the compatibility of the chemical parameters – such as cation field strength, the size and polarization of the polyhedra, and the strength of chemical bonds – of the cations involved in the host matrix. The higher similarity $[PO_4]$ and $[SO_4]$ tetrahedra, compared to the $[SiO_4]$ and $[SO_4]$ ones, should theoretically enhance the incorporation of sulfate species into the glass structure [262]. However, this was not observed for the materials under study. It is speculated that this effect might have been observed had

P_2O_5 been introduced to replace the second network former, SiO_2, rather than as a network modifier from the alkaline-earth metal oxide family. In that case, however, the resulting glasses would likely have exhibited insufficient network connectivity, leading to the rapid release of glass components into the surrounding environment.

On the other hand, glasses in the [10P] system demonstrated a higher degree of polymerization compared to materials with lower P_2O_5 content – phosphorus incorporated into the silicate-based vitreous matrix predominantly exists as orthophosphate units, and, analogous to sulfate groups, attract network modifiers for charge compensation, resulting in an overall enhancement of the connectivity of the silicate-based framework. In turn, an increase in the polymerization degree of the glass matrix (i.e., greater compactness) adversely impacts the material's ability to incorporate sulfate groups, which tend to occupy the voids within the matrix. This was clearly demonstrated by XRF analysis, which showed that the sulfate capacity of the 3S_10PM system was 0.8 mol.%, compared to the significantly higher value of 1.8 mol.% recorded for the lower-phosphorus 3S_6PM system. Not without significance for the incorporation of sulfate groups is also the competition between $[PO_4]^{3-}$ and $[SO_4]^{2-}$ units for the available network modifiers, which are essential for the presence of both charge-compensation-requiring species within the host matrix.

(2) Alkaline earth modifier type vs. sulfate capacity

The ability of the materials to incorporate sulfate species was also influenced, albeit to a lesser extent, by variations in the alkaline earth network modifiers used (MgO/CaO/MgO+CaO) – an influence that is well-documented, as sulfate solubility in the melt should depend on both the amount and type of network modifier incorporated [261]. Nonetheless, in the designed materials, the total content of all modifiers was kept constant, with the focus directed towards evaluating the impact of modifier type on sulfate incorporation potential. As highlighted in the introduction to this thesis, an increase in sulfate incorporation generally follows a trend based on the type of network modifier oxide: BaO > SrO > PbO > CaO > MgO > ZnO – a trend that is primarily governed by cation field strength, with bigger cations of lower CFS enhancing the system's ability to incorporate $[SO_4]^{2-}$ species [261].

Indeed, based on XRF-derived sulfate capacity results for the XS_6PC, XS_6PM, and XS_6PMC systems, which were approximately 2.1, 1.8, and 1.8 mol.%, respectively, the impact of the alkaline earth oxide type on the system's sulfate incorporation ability is apparent, albeit remains subtle. Notably, the observed differences align with variations in network connectivity for the studied systems, with the lowest NC values attributed to samples modified with CaO and the highest to those modified with MgO. The observed differences in network connectivity are, in turn, attributed to the varying sizes of the cations and, consequently, their cation field strength values (CFS_{Ca}= 0.36, CFS_{Mg}= 0.45-0.53 [201,281,408]) – factors that significantly influence the local structure of the glass, with larger cations (exhibiting lower CFS) more significantly promoting the depolymerization of the silicate network. Thus, the larger ionic radius of calcium likely contributes to the slightly enhanced sulfate incorporation ability of the XS_6PC system by causing more fragmentation of the network compared to the system modified with MgO, thereby expanding the inter-network spaces, or voids, where $[SO_4]^{2-}$ species are incorporated.

Remarkably, however, this reduced network connectivity is also accompanied by a decrease in the viscosity of the melt near the glass transition temperature, which facilitates

crystallization, as reflected in the XRD patterns of the XS_6PC samples, showing diffraction peaks of low intensity already for the baseline sample, n contrast to the fully amorphous XS_6PM system. Both of these effects – reduced network connectivity and the increase in sulfate incorporation – mirror the existence of a fine balance in selecting glass composition, demonstrating the apparent trade-off between optimizing sulfate capacity and achieving full amorphicity in the materials.

Sulfate addition vs. the glass properties

The in-depth studies conducted within this research have revealed that sulfur enters the vitreous matrix of the designed multicomponent silicate-phosphate glasses exclusively in its sulfate, $[SO_4]^{2-}$, form. These anions, which bear a negative charge, effectively scavenge network modifiers, to surround themselves with a shell of charge-compensators, thereby decreasing the concentration of such cations near the silicate/phosphate subnetworks. Moreover, these domains, of the $2K^+$– SO_4^{2-} character, exhibit independence within the silicate-based network, without forming linkages with either the silicon-oxygen or phosphor-oxygen frameworks. The presence of such groupings in the glass matrix significantly impacts the properties of the designed materials. Therefore, several general trends can be outlined regarding the response of the studied glass matrices to the incorporation of sulfate species:

(1) **Impact on amorphousness**: First, the incorporation of sulfate species into the structure of the materials adversely affects the ability to produce a fully amorphous product. Once the inherent capacity of a given glass system to incorporate sulfate species is exceeded, segregation occurs, with $2K^+$– SO_4^{2-} domains forming separate salt phases that exhibit high solubility in both aqueous and acidic solutions – thus, the surface presence of such precipitations poses a potential threat to the slow release of sulfate species into the environment. Additionally, high concentration of potassium-sulfate-type clusters is deemed as crystallization nuclei, promoting the bulk crystallization of the designed glasses.

(2) **Polymerization degree**: The addition of increasing amounts of sulfate species leads to a gradual yet rather subtle increase in the polymerization degree of the glass network, primarily within the silicon-oxygen subnetwork. This phenomenon arises from the nature of sulfate anions present in the vitreous matrix, as they attract network modifiers (K^+), subsequently reducing their concentration near the silicate/phosphate subnetworks. Thus, the presence of sulfates results in the conversion of non-bridging oxygens to bridging oxygens, gradually increasing the degree of polymerization in the glass framework.

(3) **Decreased stability**: Additionally, the presence of $[SO_4]^{2-}$ units in the structure enhances the rigidity of the silicate-based glass network, thereby reducing the overall stability of the material. This effect is reflected in the behaviour of the sulfur-bearing glasses in soil environments, where the presence of sulfate groupings was found to increase the materials' susceptibility to fracturing – a crucial process in the glass-soil interaction, as it shifts the reaction front deeper into the bulk glass.

As highlighted above, determining the relationship between the chemical composition, structure, and properties of the final product is critical for its intended application. The studies conducted on multicomponent silicate-phosphate glasses modified with sulfur

have provided insights into this relationship, both in terms of the materials' ability to incorporate sulfur and their suitability as vitreous carriers of useful ions (including sulfur) for plants. It was demonstrated that by manipulating primarily the content of phosphorus pentoxide, and also the type of network modifier from the alkaline earth family, not only can the sulfate capacity of these multicomponent silicate-phosphate glasses be tuned, but their overall behaviour in the intended application environment – namely, soil – can also be adjusted. Similarly, by adapting the SO_3 content itself, the structure of the final products can be subtly tailored, which in turn influences the glass-soil substrate interaction processes.

Considering the results presented in this work, it is concluded that all selected materials – representing the XS_6PM, XS_6PC, XS_6PMC, and XS_10PM systems – meet the requirements for vitreous carriers of useful ions for plants. These materials undoubtedly exhibit significant differences in sulfate capacity (with notably higher values for systems containing 6% P_2O_5) and chemical activity (enhanced activity observed for the 10P system, along with intense surface crystallization of calcium phosphate secondary phases in systems containing CaO as an alkaline earth network modifier, particularly when in contact with soil with high calcium content). Therefore, these materials can potentially be used for crops with varying nutritional needs, requiring different rates of ion release, or as agents for the revitalization of degraded lands. Nevertheless, the present studies clearly show that the chemical composition of glasses within the SiO_2– P_2O_5–K_2O–MgO–CaO–SO_3 can be tailored to enable effective application as slow-release vitreous carriers of sulfate ions for agricultural use. The final products are capable of sustained release of essential nutrients under acidic conditions, as encountered in the rhizosphere, while exhibiting sufficient resistance to leaching under neutral aqueous conditions.
Thus, the objectives set out in this work are considered fulfilled.

16 Future plans

In light of the promising findings presented in this work, which point to the high potential of the synthesized vitreous carriers as effective sources of macro- and micronutrients, the research plan has been extended to include a field-oriented experiment aimed at unequivocally verifying the suitability of these materials as alternative fertilizing agents. This experiment, initiated in June of the current year under the framework of the awarded *Preludium* project (No 2023/49/N/ST11/00299), involves the cultivation of Canasta lettuce seedlings under controlled environmental conditions (light exposure, temperature regime, and irrigation schedule), with the application of selected glass samples – specifically those compositions previously identified as effective nutrient carriers (XS_6PM, XS_6PC, XS_6PMC, and XS_10PM) – introduced into the soil substrate at three different concentrations (1%, 2%, and 4%), alongside an untreated control (0%). Throughout the experimental period, data reflecting seedling quality will be collected systematically, including measurements of leaf length, visual indicators of phytotoxicity (e.g., chlorosis and necrosis), and, upon completion of the growth cycle, harvested plant material will be dried and subjected to further analysis. This will include determination of total mineral content, final leaf moisture percentage, average leaf length and weight, visual assessment of plant health, and mortality records. The overarching aim of this evaluation is to determine the practical efficacy of the studied materials in promoting the growth and development of cultivated plants.

In parallel with this agronomic evaluation, a comprehensive aging study of the materials is also planned, with particular attention given to samples representing the XS_6PM and XS_6PMC systems, which previously exhibited no detectable secondary surface products arising from interaction with the ambient atmosphere. This study will be expanded to include more in-depth analysis of the XS_6PC and XS_10PM systems – those more susceptible to environmental interactions – in order to accurately determine the lifespan and long-term stability of these glass compositions. Should such materials be considered for large-scale production, the gathered data will offer valuable insight into storage conditions and shelf-life requirements for maintaining their structural and functional integrity.

Finally, future work will also explore the synthesis of glasses based on an inverted matrix system – namely, phosphate-silicate compositions – and subject them to comprehensive structural characterization as well as rigorous chemical activity testing. The goal of this investigation is to assess their viability as potential vitreous carriers of sulfur and other essential nutrients for agricultural applications.

.

17 References

[1] D.A. John, G.R. Babu, Lessons From the Aftermaths of Green Revolution on Food System and Health, Front Sustain Food Syst 5 (2021) 644559. https://doi.org/10.3389/fsufs.2021.644559.

[2] M. Wik, P. Pingali, S. Broca, Global Agricultural Performance: Past Trends and Future Prospects, Background Paper for the World Development Report (2008) 1–39. http://siteresources.worldbank.org/INTWDRS/Resources/477365-1327599046334/8394679-1327599874257/Pingali-Global_Agricultural_Performance.pdf.

[3] M. Nuruzzaman, M.M. Bahar, R. Naidu, Diffuse soil pollution from agriculture: Impacts and remediation, Science of the Total Environment 962 (2025) 178398. https://doi.org/10.1016/j.scitotenv.2025.178398.

[4] H. Ritchie, P. Rosado, M. Roser, Food and Agriculture Organization of the United Nations (2025) – with major processing by Our World in Data. "Sugar cane yields – FAO," (2025). OurWorldinData.org (accessed July 28, 2025).

[5] P.J.A. Withers, R. Sylvester-Bradley, D.L. Jones, J.R. Healey, P.J. Talboys, Feed the crop not the soil: Rethinking phosphorus management in the food chain, Environ Sci Technol 48 (2014) 6523–6530. https://doi.org/10.1021/es501670j.

[6] H.N. Pahalvi, L. Rafiya, S. Rashid, B. Nisar, A.N. Kamili, Chemical Fertilizers and Their Impact on Soil Health, in: Microbiota and Biofertilizers, Vol 2, Springer International Publishing, 2021: pp. 1–20. https://doi.org/10.1007/978-3-030-61010-4_1.

[7] P. Ahmad, M.R. Wani, M.M. Azooz, L.S. Phan Tran, Improvement of crops in the era of climatic changes, 2014. https://doi.org/10.1007/978-1-4614-8824-8.

[8] C.T. Kraamwinkel, A. Beaulieu, T. Dias, R.A. Howison, Planetary limits to soil degradation, Commun Earth Environ 2 (2021) 1–4. https://doi.org/10.1038/s43247-021-00323-3.

[9] P.M. Kopittke, B. Minasny, E. Pendall, C. Rumpel, B.A. McKenna, Healthy soil for healthy humans and a healthy planet, Crit Rev Environ Sci Technol 54 (2024) 210–221. https://doi.org/10.1080/10643389.2023.2228651.

[10] R.A. Lybrand, Connecting soils to life in conservation planning, nutrient cycling, and planetary science, Earth Sci Rev 237 (2023) 104247. https://doi.org/10.1016/j.earscirev.2022.104247.

[11] J. Telo da Gama, The Role of Soils in Sustainability, Climate Change, and Ecosystem Services: Challenges and Opportunities, Ecologies 4 (2023) 552–567. https://doi.org/10.3390/ecologies4030036.

[12] R. Tirado, M. Allsopp, Campaigning for sustainable agriculture, Greenpeace.Org (2012).

[13] F. Albornoz, Crop responses to nitrogen overfertilization: A review, Sci Hortic 205 (2016) 79–83. https://doi.org/10.1016/j.scienta.2016.04.026.

[14] J.M. Mogollón, A.F. Bouwman, A.H.W. Beusen, L. Lassaletta, H.J.M. van Grinsven, H. Westhoek, More efficient phosphorus use can avoid cropland expansion, Nat Food 2 (2021) 509–518. https://doi.org/10.1038/s43016-021-00303-y.

[15] S. Savci, An Agricultural Pollutant: Chemical Fertilizer, International Journal of Environmental Science and Development (2012) 73–80. https://doi.org/10.7763/ijesd.2012.v3.191.

[16] J.W. Erisman, J.N. Galloway, S. Seitzinger, A. Bleeker, N.B. Dise, A.M. Roxana Petrescu, A.M. Leach, W. de Vries, Consequences of human modification of the global nitrogen cycle, Philosophical Transactions of the Royal Society B: Biological Sciences 368 (2013). https://doi.org/10.1098/rstb.2013.0116.
[17] H.P. Jarvie, A.N. Sharpley, P.J.A. Withers, J.T. Scott, B.E. Haggard, C. Neal, Phosphorus Mitigation to Control River Eutrophication: Murky Waters, Inconvenient Truths, and "Postnormal" Science, J Environ Qual 42 (2013) 295–304. https://doi.org/10.2134/jeq2012.0085.
[18] K. Paustian, J. Lehmann, S. Ogle, D. Reay, G.P. Robertson, P. Smith, Climate-smart soils, Nature 532 (2016) 49–57. https://doi.org/10.1038/nature17174.
[19] A. Tkacz, P. Poole, Role of root microbiota in plant productivity, J Exp Bot 66 (2015) 2167–2175. https://doi.org/10.1093/jxb/erv157.
[20] P.M. Kopittke, B. Minasny, E. Pendall, C. Rumpel, B.A. McKenna, Healthy soil for healthy humans and a healthy planet, Crit Rev Environ Sci Technol 54 (2024) 210–221. https://doi.org/10.1080/10643389.2023.2228651.
[21] J. Lehmann, D.A. Bossio, I. Kögel-Knabner, M.C. Rillig, The concept and future prospects of soil health, Nat Rev Earth Environ 1 (2020) 544–553. https://doi.org/10.1038/s43017-020-0080-8.
[22] A. Merta-Staszczak, A. Zwyrzykowska, R. Kupczyński, Agrochemikalia w polskim rolnictwie w latach 1945-2010, Przemysl Chemiczny 96 (2017) 266–270. https://doi.org/10.15199/62.2017.2.2.
[23] A. Winiarski, KLASYFIKACJA I WYMAGANIA JAKOŚCIOWE DLA NAWOZÓW WE, Raporty PIB 2 (2006) 25–40. https://doi.org/10.26114/sir.iung.2006.02.02.
[24] PKN, Nawozy i środki wapnujące – Klasyfikacja. PN–EN 13535, (2003).
[25] J. Klem-Marciniak, E., Huculak-Mączka, M., Hoffman, K., Hoffmann, Effect of reaction time to receive fertilizer chelates, Proceedings of ECOpole 9 (2015) 15–17. https://doi.org/10.2429/proc.2015.9(2)073.
[26] H.J.M. Van Grinsven, H.F.M. Ten Berge, T. Dalgaard, B. Fraters, P. Durand, A. Hart, G. Hofman, B.H. Jacobsen, S.T.J. Lalor, J.P. Lesschen, B. Osterburg, K.G. Richards, A.K. Techen, F. Vertès, J. Webb, W.J. Willems, Management, regulation and environmental impacts of nitrogen fertilization in northwestern Europe under the Nitrates Directive; A benchmark study, Biogeosciences 9 (2012) 5143–5160. https://doi.org/10.5194/bg-9-5143-2012.
[27] Rozporządzenie 2019/1009 ustanawiające przepisy dotyczące udostępniania na rynku produktów nawozowych UE, zmieniające... - Dz.U.UE.L.2019.170.1 - OpenLEX, (n.d.). https://sip.lex.pl/akty-prawne/dzienniki-UE/rozporzadzenie-2019-1009-ustanawiajace-przepisy-dotyczace-udostepniania-na-69197503 (accessed April 3, 2025).
[28] K. Chojnacka, K. Moustakas, A. Witek-Krowiak, Bio-based fertilizers: A practical approach towards circular economy, Bioresour Technol 295 (2020) 122223. https://doi.org/10.1016/j.biortech.2019.122223.
[29] K. Kagan, K. Jonak, A. Wolińska, The Impact of Reduced N Fertilization Rates According to the "Farm to Fork" Strategy on the Environment and Human Health, Applied Sciences (Switzerland) 14 (2024) 10726. https://doi.org/10.3390/app142210726.

[30] S. Lesecq, G. Keeley, G. Dudnik, A. O'Riordan, Would digitalisation support transition towards more sustainable agriculture to meet the Green Deal ambition?, in: 2022 8th International Conference on Energy Efficiency and Agricultural Engineering, EE and AE 2022 - Proceedings, Institute of Electrical and Electronics Engineers Inc., 2022. https://doi.org/10.1109/EEAE53789.2022.9831296.

[31] S. Higgins, S.D. Keesstra, Ž. Kadziuliene, L. Jordan-Meille, D. Wall, A. Trinchera, H. Spiegel, T. Sandén, A. Baumgarten, J.L. Jensen, J. Hirte, F. Liebisch, S. Klages, P. Löw, K. Kuka, M. De Boever, K. D'Haene, S. Madenoglu, H. Özcan, W. Vervuurt, J. de Haan, W. van Geel, B. Stenberg, P. Denoroy, R. Mihelič, A. Astover, R. Mano, C. Sempiterno, F. Calouro, G. Valboa, H. Aronsson, T. Krogstad, S. Torma, J. Gabriel, P. Laszlo, N. Borchard, B. Adamczyk, A. Jacobs, B. Jurga, B. Smreczak, B. Huyghebaert, M. Abras, R. Kasparinskis, E. Mason, C. Chenu, Stocktake study of current fertilisation recommendations across Europe and discussion towards a more harmonised approach, Eur J Soil Sci 74 (2023) e13422. https://doi.org/10.1111/ejss.13422.

[32] F. Zulfiqar, M. Navarro, M. Ashraf, N.A. Akram, S. Munné-Bosch, Nanofertilizer use for sustainable agriculture: Advantages and limitations, Plant Science 289 (2019) 110270. https://doi.org/10.1016/j.plantsci.2019.110270.

[33] G.D. Avila-Quezada, A.P. Ingle, P. Golińska, M. Rai, Strategic applications of nano-fertilizers for sustainable agriculture: Benefits and bottlenecks, Nanotechnol Rev 11 (2022) 2123–2140. https://doi.org/10.1515/ntrev-2022-0126.

[34] E. Goldan, V. Nedeff, N. Barsan, M. Culea, M. Panainte-Lehadus, E. Mosnegutu, C. Tomozei, D. Chitimus, O. Irimia, Assessment of Manure Compost Used as Soil Amendment—A Review, Processes 11 (2023) 1167. https://doi.org/10.3390/pr11041167.

[35] Z. Jiang, H. Zheng, B. Xing, Environmental life cycle assessment of wheat production using chemical fertilizer, manure compost, and biochar-amended manure compost strategies, Science of the Total Environment 760 (2021) 143342. https://doi.org/10.1016/j.scitotenv.2020.143342.

[36] T. Hernandez, C. Chocano, M.D. Coll, C. Garcia, Composts as alternative to inorganic fertilization for cereal crops, Environmental Science and Pollution Research 26 (2019) 35340–35352. https://doi.org/10.1007/s11356-018-3898-6.

[37] K. (nauki rolnicze) Pilarski, A. (chemik) Pilarska, Parametry procesu kompostowania, Technika Rolnicza Ogrodnicza Leśna (2009) 16–17. http://agro.icm.edu.pl/agro/element/bwmeta1.element.agro-article-0e1abe65-30a9-4d25-82b5-2fe71a381eff.

[38] M. Allam, E. Radicetti, V. Quintarelli, V. Petroselli, S. Marinari, R. Mancinelli, Influence of Organic and Mineral Fertilizers on Soil Organic Carbon and Crop Productivity under Different Tillage Systems: A Meta-Analysis, Agriculture (Switzerland) 12 (2022) 1–19. https://doi.org/10.3390/agriculture12040464.

[39] G.L. Mumbach, L.C. Gatiboni, F.D. de Bona, D.E. Schmitt, J.C. Corrêa, C.A. Gabriel, D.J. Dall'Orsoletta, D.A. Iochims, Agronomic efficiency of organomineral fertilizer in sequential grain crops in southern Brazil, Agron J 112 (2020) 3037–3049. https://doi.org/10.1002/agj2.20238.

[40] Y. Bouhia, M. Hafidi, Y. Ouhdouch, Y. Zeroual, K. Lyamlouli, Organo-Mineral Fertilization Based on Olive Waste Sludge Compost and Various Phosphate Sources Improves Phosphorus Agronomic Efficiency, Zea mays Agro-

Physiological Traits, and Water Availability, Agronomy 13 (2023) 249. https://doi.org/10.3390/agronomy13010249.
[41] L. Chen, J. Kivelä, J. Helenius, A. Kangas, Meat bone meal as fertiliser for barley and oat, Agricultural and Food Science 20 (2011) 235–244. https://doi.org/10.2137/145960611797471552.
[42] EEA, The European environment — state and outlook 2015: synthesis report, European Environment Agency, Copenhagen, https://www.eea.europa.eu/soer-2015/synthesis/report/at_download/file, 2015.
[43] A.-K. H. Sabry, Synthetic fertilizers, role and hazards, Fertilizer Technology I: Synthesis (2015) 110–133. https://doi.org/10.13140/RG.2.1.2395.3366.
[44] I. Atemni, K. Hjouji, A. El Barnossi, A. Ainane, T. Ainane, M. Taleb, Z. Rais, Effect of Bone Meal Application on Soil Properties, Heavy Metal Accumulation, and Agronomic Traits of Pelargonium graveolens, J Soil Sci Plant Nutr 23 (2023) 6584–6595. https://doi.org/10.1007/s42729-023-01512-z.
[45] B.S. Jatana, C. Kitchens, C. Ray, N. Tharayil, Regulating the nutrient release rates from proteinaceous agricultural byproducts using organic amendments and its effect on soil chemical and microbiological properties, Biol Fertil Soils 56 (2020) 747–758. https://doi.org/10.1007/s00374-020-01446-z.
[46] S.E. Allen, D.A. Mays, Coated and other slow-release fertilizers for forages, in: Forage Fertilization, John Wiley & Sons, Ltd, 2015: pp. 559–582. https://doi.org/10.2134/1974.foragefertilization.c26.
[47] A.C.S. dos Santos, H.M. Henrique, V.L. Cardoso, M.H.M. Reis, Slow release fertilizer prepared with lignin and poly(vinyl acetate) bioblend, Int J Biol Macromol 185 (2021) 543–550. https://doi.org/10.1016/j.ijbiomac.2021.06.169.
[48] H. Tian, Z. Liu, M. Zhang, Y. Guo, L. Zheng, Y.C. Li, Biobased Polyurethane, Epoxy Resin, and Polyolefin Wax Composite Coating for Controlled-Release Fertilizer, ACS Appl Mater Interfaces 11 (2019) 5380–5392. https://doi.org/10.1021/acsami.8b16030.
[49] K. Lubkowski, A. Smorowska, M. Sawicka, E. Wróblewska, A. Dzienisz, M. Kowalska, M. Sadłowski, Ethylcellulose as a coating material in controlled-release fertilizers, Polish Journal of Chemical Technology 21 (2019) 52–58. https://doi.org/10.2478/pjct-2019-0010.
[50] P. Shan, D. Li, P. Cai, K. Zheng, H. Liu, Y. Lu, Z. Li, Z. Li, Direct fabrication of cross-linking polymer coatings from monomers via Triethylamine gas-mediated thiol-ene chemistry for sustained fertilizers release, Prog Org Coat 162 (2022) 106594. https://doi.org/10.1016/j.porgcoat.2021.106594.
[51] I.M. Bamatov, D.M. Bamatov, The influence of biodegradable polymer coated fertilizers on the agrochemical parameters of the soil, IOP Conf Ser Earth Environ Sci 548 (2020) 4–11. https://doi.org/10.1088/1755-1315/548/8/082069.
[52] C.A. Ezema, T. Ooi, K. Matsumoto, Heat-Press Technique for Coating Ammonium Nitrate Granules with Biodegradable Hydrophobic Polymer Blend of Poly(3-hydroxybutyrate- co-3-hydroxyhexanoate) and Poly(ϵ-caprolactone), ACS Agricultural Science and Technology 2 (2022) 1179–1186. https://doi.org/10.1021/acsagscitech.2c00061.
[53] T. El Assimi, R. Beniazza, M. Raihane, H. Ben Youcef, A. El Meziane, H. Kricheldorf, M. Lahcini, Overview on progress in polysaccharides and aliphatic

polyesters as coating of water-soluble fertilizers, J Coat Technol Res 19 (2022) 989–1007. https://doi.org/10.1007/s11998-022-00613-1.
[54] Haseeb-ur-Rehman, M.G. Asghar, R.M. Ikram, S. Hashim, S. Hussain, M. Irfan, K. Mubeen, M. Ali, M. Alam, M. Ali, I. Haider, M. Shakir, M. Skalicky, S.A. Alharbi, S. Alfarraj, Sulphur coated urea improves morphological and yield characteristics of transplanted rice (Oryza sativa L.) through enhanced nitrogen uptake, J King Saud Univ Sci 34 (2022) 101664. https://doi.org/10.1016/j.jksus.2021.101664.
[55] K.R.M. Ibrahim, F.E. Babadi, R. Yunus, Comparative performance of different urea coating materials for slow release, Particuology 17 (2014) 165–172. https://doi.org/10.1016/j.partic.2014.03.009.
[56] N. Sarhan, E.G. Arafa, N. Elgedawy, K.N.M. Elsayed, F. Mohamed, Urea intercalated encapsulated microalgae composite hydrogels for slow-release fertilizers, Sci Rep 14 (2024) 1–17. https://doi.org/10.1038/s41598-024-58875-1.
[57] M.A. Melaj, R.B. Gimenez, Hydrogels: An Effective Tool to Improve Nitrogen Use Efficiency in Crops, in: Polymers for Agri-Food Applications, Springer International Publishing, 2019: pp. 127–141. https://doi.org/10.1007/978-3-030-19416-1_8.
[58] R.A. Siegel, M.J. Rathbone, Overview of controlled release mechanisms, in: Fundamentals and Applications of Controlled Release Drug Delivery, Springer US, 2012: pp. 19–43. https://doi.org/10.1007/978-1-4614-0881-9_2.
[59] E.M. Ahmed, Hydrogel: Preparation, characterization, and applications: A review, J Adv Res 6 (2015) 105–121. https://doi.org/10.1016/j.jare.2013.07.006.
[60] A. Olad, H. Zebhi, D. Salari, A. Mirmohseni, A. Reyhani Tabar, Slow-release NPK fertilizer encapsulated by carboxymethyl cellulose-based nanocomposite with the function of water retention in soil, Materials Science and Engineering C 90 (2018) 333–340. https://doi.org/10.1016/j.msec.2018.04.083.
[61] D. França, Â.F. Medina, L.L. Messa, C.F. Souza, R. Faez, Chitosan spray-dried microcapsule and microsphere as fertilizer host for swellable − controlled release materials, Carbohydr Polym 196 (2018) 47–55. https://doi.org/10.1016/j.carbpol.2018.05.014.
[62] M.A. Melaj, M.E. Daraio, HPMC layered tablets modified with chitosan and xanthan as matrices for controlled-release fertilizers, J Appl Polym Sci 131 (2014). https://doi.org/10.1002/app.40839.
[63] Z. Zahra, Z. Habib, H. Hyun, H.M.A. Shahzad, Overview on Recent Developments in the Design, Application, and Impacts of Nanofertilizers in Agriculture, Sustainability (Switzerland) 14 (2022) 9397. https://doi.org/10.3390/su14159397.
[64] G. Sharma, A.R. Sharma, R. Bhavesh, J. Park, B. Ganbold, J.S. Nam, S.S. Lee, Biomolecule-mediated synthesis of selenium nanoparticles using dried vitis vinifera (raisin) extract, Molecules 19 (2014) 2761–2770. https://doi.org/10.3390/molecules19032761.
[65] H.S. Hussein, H.H. Shaarawy, N.H. Hussien, S.I. Hawash, Preparation of nanofertilizer blend from banana peels, Bull Natl Res Cent 43 (2019) 1–9. https://doi.org/10.1186/s42269-019-0058-1.
[66] P. Hydzik, Toksyczności nanocząstek - wybrane przykłady, (2012) 486–489.
[67] M.T. El-Saadony, A.S. ALmoshadak, M.E. Shafi, N.M. Albaqami, A.M. Saad, A.M. El-Tahan, E.S.M. Desoky, A.S.M. Elnahal, A. Almakas, T.A. Abd El-

Mageed, A.E. Taha, A.S. Elrys, A.M. Helmy, Vital roles of sustainable nano-fertilizers in improving plant quality and quantity-an updated review, Saudi J Biol Sci 28 (2021) 7349–7359. https://doi.org/10.1016/j.sjbs.2021.08.032.

[68] P. Goswami, S. Yadav, J. Mathur, Positive and negative effects of nanoparticles on plants and their applications in agriculture, Plant Science Today 6 (2019) 232–242.

[69] Z. Hossain, G. Mustafa, S. Komatsu, Plant responses to nanoparticle stress, Int J Mol Sci 16 (2015) 26644–26653. https://doi.org/10.3390/ijms161125980.

[70] D.H. Atha, H. Wang, E.J. Petersen, D. Cleveland, R.D. Holbrook, P. Jaruga, M. Dizdaroglu, B. Xing, B.C. Nelson, Copper oxide nanoparticle mediated DNA damage in terrestrial plant models, Environ Sci Technol 46 (2012) 1819–1827. https://doi.org/10.1021/es202660k.

[71] L. Otero-González, J.A. Field, R. Sierra-Alvarez, Fate and long-term inhibitory impact of ZnO nanoparticles during high-rate anaerobic wastewater treatment, J Environ Manage 135 (2014) 110–117. https://doi.org/10.1016/j.jenvman.2014.01.025.

[72] R. Paque, I. Alomia Herrera, J.L. Dixon, A. Molina, F. Zehetner, V. Vanacker, Constraining the Effect of Climate and Rock Porosity on Weathering Extent in the Volcanic Island of Santa Cruz (Galápagos, Ecuador), J Geophys Res Earth Surf 129 (2024). https://doi.org/10.1029/2024JF007651.

[73] P. Gierszewski, M.T. Karasiewicz, Współczesna aktywność wulkaniczna Ziemi, in: Idee i Praktyczny Uniwersalizm Geografii : Geografia Fizyczna, 2006: pp. 135–140. http://repozytorium.umk.pl/handle/item/595.

[74] D. Fiantis, F.I. Ginting, Gusnidar, M. Nelson, B. Minasny, Volcanic Ash, insecurity for the people but securing fertile soil for the future, Sustainability (Switzerland) 11 (2019). https://doi.org/10.3390/su11113072.

[75] K.L. Ferrier, J.W. Kirchner, Effects of physical erosion on chemical denudation rates: A numerical modeling study of soil-mantled hillslopes, Earth Planet Sci Lett 272 (2008) 591–599. https://doi.org/10.1016/j.epsl.2008.05.024.

[76] J. Viers, P. Oliva, J.L. Dandurand, B. Dupré, J. Gaillardet, Chemical Weathering Rates, CO2 Consumption, and Control Parameters Deduced from the Chemical Composition of Rivers, in: Treatise on Geochemistry, Pergamon, 2007: pp. 1–25. https://doi.org/10.1016/B978-008043751-4/00249-2.

[77] T. Marie-Pierre, N. Claude, C. Christophe, Rhizosphere impact on the dissolution of test minerals in a forest ecosystem, Geoderma 153 (2009) 147–154. https://doi.org/10.1016/j.geoderma.2009.07.023.

[78] F.D. Dakora, D.A. Phillips, Root exudates as mediators of mineral acquisition in low-nutrient environments, in: Food Security in Nutrient-Stressed Environments: Exploiting Plants' Genetic Capabilities, Springer, Dordrecht, 2002: pp. 201–213. https://doi.org/10.1007/978-94-017-1570-6_23.

[79] A. Yamagata, Y. Murata, K. Namba, T. Terada, S. Fukai, M. Shirouzu, Uptake mechanism of iron-phytosiderophore from the soil based on the structure of yellow stripe transporter, Nat Commun 13 (2022) 1–12. https://doi.org/10.1038/s41467-022-34930-1.

[80] L.D. M, P. Dasharath, M.M. H, K.J. D, P.N. G, K.P. K, P.M. O, K. Kuldeep, P.M. B, R. Asha, D. H, S.C. M, P. Suresh, Influence of phytosiderophore on iron and

zinc uptake and rhizospheric microbial activity, Afr J Microbiol Res 7 (2013) 5781–5788. https://doi.org/10.5897/ajmr2013.6461.
[81] V. RÖmheld, The role of phytosiderophores in acquisition of iron and other micronutrients in graminaceous species: An ecological approach, in: Iron Nutrition and Interactions in Plants, Springer, Dordrecht, 1991: pp. 159–166. https://doi.org/10.1007/978-94-011-3294-7_21.
[82] K. Wiatrowska, J. Komisarek, Sorpcja fosforu w glebach płowych i czarnych ziemiach w katenie falistej moreny dennej Pojezierza Poznańskiego, Polish Journal of Agronomy (2015) 25–32.
[83] A. Abrahão, H. Lambers, A.C.H.F. Sawaya, P. Mazzafera, R.S. Oliveira, Convergence of a specialized root trait in plants from nutrient-impoverished soils: phosphorus-acquisition strategy in a nonmycorrhizal cactus, Oecologia 176 (2014) 345–355. https://doi.org/10.1007/s00442-014-3033-4.
[84] Y.G. Zhu, G.L. Duan, B.D. Chen, X.H. Peng, Z. Chen, G.X. Sun, Mineral weathering and element cycling in soil-microorganism-plant system, Sci China Earth Sci 57 (2014) 888–896. https://doi.org/10.1007/s11430-014-4861-0.
[85] B. Morra, A.A. Olsen, Effect of common bean (Phaseolus vulgaris) on apatite weathering under elevated CO2, Chem Geol 558 (2020) 119887. https://doi.org/10.1016/j.chemgeo.2020.119887.
[86] H. Marschner, V. Römheld, Strategies of plants for acquisition of iron, Plant Soil 165 (1994) 261–274. https://doi.org/10.1007/BF00008069.
[87] G. Ranalli, E. Zanardini, C. Sorlini, Biodeterioration – Including Cultural Heritage, in: Encyclopedia of Microbiology, Third Edition, Elsevier, 2009: pp. 191–205. https://doi.org/10.1016/B978-012373944-5.00132-2.
[88] I.D.A. Ribeiro, C.G. Volpiano, L.K. Vargas, C.E. Granada, B.B. Lisboa, L.M.P. Passaglia, Use of Mineral Weathering Bacteria to Enhance Nutrient Availability in Crops: A Review, Front Plant Sci 11 (2020) 590774. https://doi.org/10.3389/fpls.2020.590774.
[89] V. Vandieken, M. Mußmann, H. Niemann, B.B. Jørgensen, Desulfuromonas svalbardensis sp. nov. and Desulfuromusa ferrireducens sp. nov., psychrophilic, Fe(III)-reducing bacteria isolated from Arctic sediments, Svalbard, Int J Syst Evol Microbiol 56 (2006) 1133–1139. https://doi.org/10.1099/ijs.0.63639-0.
[90] C. Calvaruso, M.P. Turpault, P. Frey-Klett, Root-associated bacteria contribute to mineral weathering and to mineral nutrition in trees: A budgeting analysis, Appl Environ Microbiol 72 (2006) 1258–1266. https://doi.org/10.1128/AEM.72.2.1258-1266.2006.
[91] J.R. Leake, A.L. Duran, K.E. Hardy, I. Johnson, D.J. Beerling, S.A. Banwart, M.M. Smits, Biological weathering in soil: the role of symbiotic root-associated fungi biosensing minerals and directing photosynthate-energy into grain-scale mineral weathering, Mineral Mag 72 (2008) 85–89. https://doi.org/10.1180/minmag.2008.072.1.85.
[92] A. Bhattacharjee, O. Qafoku, J.A. Richardson, L.N. Anderson, K. Schwarz, L.M. Bramer, G.X. Lomas, D.J. Orton, Z. Zhu, M.H. Engelhard, M.E. Bowden, W.C. Nelson, A. Jumpponen, J.K. Jansson, K.S. Hofmockel, C.R. Anderton, A Mineral-Doped Micromodel Platform Demonstrates Fungal Bridging of Carbon Hot Spots and Hyphal Transport of Mineral- Derived Nutrients, MSystems 7 (2022). https://doi.org/10.1128/msystems.00913-22.

[93] M.R. Grant, L.S. Tymon, G.L. Helms, L.S. Thomashow, C. Kent Keller, J.B. Harsh, Biofilm adaptation to iron availability in the presence of biotite and consequences for chemical weathering, Geobiology 14 (2016) 588–598. https://doi.org/10.1111/gbi.12187.
[94] A. Vujošević, S. Matijašević, S. Smiljanić, J. Nikolić, B. Zečević, V. Topalović, V. Savić, Polyphosphate glass as fertilizer for plant seedlings, Materials Protection 60 (2019) 96–104. https://doi.org/10.5937/zasmat1901096V.
[95] L. Stoch, I. Wacławska, M. Szumera, Phospho-silicate glasses, self-degradable in environment conditions, Adv Mat Res 39–40 (2008) 335–340. https://doi.org/10.4028/www.scientific.net/amr.39-40.335.
[96] B. Torrisi, A. Trinchera, E. Rea, M. Allegra, G. Roccuzzo, F. Intrigliolo, Effects of organo-mineral glass-matrix based fertilizers on citrus Fe chlorosis, European Journal of Agronomy 44 (2013) 32–37. https://doi.org/10.1016/j.eja.2012.07.007.
[97] J.H. da S. Soares, T.W. Boaventura, A.C.A. de Moura, L.C. da Silva, A.G. Filho, R.L. Landgraf, D.E. Christofoletti Mazzeo, A.C. de C. Bernardi, A.R.A. Nogueira, E.B. Ferreira, D. Manzani, Design and Performance of a Multicomponent Glass Fertilizer for Nutrient Delivery in Precision Agriculture, ACS Agricultural Science and Technology 5 (2025) 142–157. https://doi.org/10.1021/acsagscitech.4c00243.
[98] G. Wang, Q. Zhang, W. Du, R. Lin, J. Li, F. Ai, Y. Yin, R. Ji, X. Wang, H. Guo, In-situ immobilization of cadmium-polluted upland soil: A ten-year field study, Ecotoxicol Environ Saf 207 (2021) 111275. https://doi.org/10.1016/j.ecoenv.2020.111275.
[99] W. Wu, J. Wu, X. Liu, X. Chen, Y. Wu, S. Yu, Inorganic phosphorus fertilizer ameliorates maize growth by reducing metal uptake, improving soil enzyme activity and microbial community structure, Ecotoxicol Environ Saf 143 (2017) 322–329. https://doi.org/10.1016/j.ecoenv.2017.05.039.
[100] M. Romero, I. Padilla, L. Barbieri, F. Andreola, A. López-Delgado, Sustainable glasses in the SiO2–P2O5–CaO–K2O system from waste and concentrated solar power, Boletin de La Sociedad Espanola de Ceramica y Vidrio (2022). https://doi.org/10.1016/j.bsecv.2021.12.004.
[101] B. Mysen, P. Richet, Silicate Glasses and melts. Properties and Structure, 2005. www.elsevier.com/locate/petmissions.
[102] W. Vogel, G. Chemistry, B.H. New, Y. London, P. Tokyo, H. Kong, B. Budapest, Introduction to Glass Science, 1972. https://doi.org/10.1007/978-1-4757-0328-3.
[103] C.A. O'shaughnessy, The structure of alkali silicate glasses and melts: A multi-spectroscopic approach, (2019).
[104] H. Eckert, Structural characterization of bioactive glasses by solid state NMR, J Solgel Sci Technol 88 (2018) 263–295. https://doi.org/10.1007/s10971-018-4795-7.
[105] M. Sitarz, The structure of simple silicate glasses in the light of Middle Infrared spectroscopy studies, J Non Cryst Solids 357 (2011) 1603–1608. https://doi.org/10.1016/j.jnoncrysol.2011.01.007.
[106] J.E. Shelby, Introduction to Glass Science and Technology - Second Edition, 2005.
[107] Shangcong Cheng, Medium Range Ordering Structure and Silica Glass Transition, Glass Physics and Chemistry 45 (2019) 91–97. https://doi.org/10.1134/S1087659619020093.

[108] Q. Zhou, Y. Shi, B. Deng, J. Neuefeind, M. Bauchy, Experimental method to quantify the ring size distribution in silicate glasses and simulation validation thereof, Sci Adv 7 (2021) 1–11. https://doi.org/10.1126/sciadv.abh1761.
[109] E. Görlich, Stan szklisty, Wydawnictwo AGH, Kraków, 1989.
[110] M. Szumera, I. Wacławska, W. Mozgawa, M. Sitarz, Spectroscopic study of biologically active glasses, in: J Mol Struct, 2005: pp. 609–614. https://doi.org/10.1016/j.molstruc.2005.01.023.
[111] W. Mozgawa, M. Sitarz, M. Król, Spectroscopic characterization of silicate amorphous materials, in: Challenges and Advances in Computational Chemistry and Physics, Springer, 2019: pp. 457–481. https://doi.org/10.1007/978-3-030-01355-4_15.
[112] M. Edén, The split network analysis for exploring composition-structure correlations in multi-component glasses: I. Rationalizing bioactivity-composition trends of bioglasses, J Non Cryst Solids 357 (2011) 1595–1602. https://doi.org/10.1016/j.jnoncrysol.2010.11.098.
[113] C. Le Losq, M.R. Cicconi, G.N. Greaves, D.R. Neuville, Silicate Glass, 2019.
[114] A. Tilocca, A.N. Cormack, Structural effects of phosphorus inclusion in bioactive silicate glasses, Journal of Physical Chemistry B 111 (2007) 14256–14264. https://doi.org/10.1021/jp075677o.
[115] G. Calas, G.S. Henderson, J.F. Stebbins, THE STRUCTURE OF SILICATE GLASSES AND MELTS: SOME BASICS, 2006.
[116] S. Sen, J.F. Stebbins, S. Kroeker, I. Hung, Z. Gan, Evidence for Mixed Mg Coordination Environments in Silicate Glasses: Results from 25Mg NMR Spectroscopy at 35.2 T, Journal of Physical Chemistry B 127 (2023) 10659–10666. https://doi.org/10.1021/acs.jpcb.3c06419.
[117] V. Jain, Chemical durability of nuclear waste glasses - a review, Center For Nuclear Waste Regulatory Analyses (2012). https://www.nrc.gov/docs/ML0613/ML061310303.pdf.
[118] F. Alloteau, P. Lehuédé, O. Majérus, I. Biron, A. Dervanian, T. Charpentier, D. Caurant, New insight into atmospheric alteration of alkali-lime silicate glasses, Corros Sci 122 (2017) 12–25. https://doi.org/10.1016/j.corsci.2017.03.025.
[119] R. Zanini, G. Franceschin, E. Cattaruzza, A. Traviglia, A review of glass corrosion: the unique contribution of studying ancient glass to validate glass alteration models, Npj Mater Degrad 7 (2023). https://doi.org/10.1038/s41529-023-00355-4.
[120] L.L. Hench, D.E. Clark, Physical chemistry of glass surfaces, J Non Cryst Solids 28 (1978) 83–105. https://doi.org/10.1016/0022-3093(78)90077-7.
[121] M. De Bardi, H. Hutter, M. Schreiner, R. Bertoncello, Potash-lime-silica glass: Protection from weathering, Herit Sci 3 (2015) 1–9. https://doi.org/10.1186/s40494-015-0051-4.
[122] M. Ciecińska, D. Dorosz, E. Greiner-Wronowa, B. GRUSZKA, J. KUCHARSKI, M. LISIECKI, M. ŁĄCZKA, B. PROCYK, M. REBEN, S. SIWULSKI, M. ŚRODA, I. WACŁAWSKA, J. WASYLAK, ODPORNOŚĆ CHEMICZNA SZKŁA, in: Technologia Szkła : Właściwości Fizykochemiczne : Metody Badań, Cz. 1, Wyd. 2 pop, Polskie Towarzystwo Ceramiczne, Prace Komisji Nauk Ceramicznych, Polska Akademia Nauk. Oddział w Krakowie, Kraków, 2012: pp. 145–162.

[123] P. Tkaczyk, W. Bednarek, S. Dresler, J. Krzyszczak, P. Baranowski, C. Slawiński, Relationship between assimilable-nutrient content and physicochemical properties of topsoil, Int Agrophys 31 (2017) 551–562. https://doi.org/10.1515/intag-2016-0074.
[124] M.P. Turpault, C. Utérano, J.P. Boudot, J. Ranger, Influence of mature Douglas fir roots on the solid soil phase of the rhizosphere and its solution chemistry, Plant Soil 275 (2005) 327–336. https://doi.org/10.1007/S11104-005-2584-X/METRICS.
[125] C.-J. Li, J. Ma, Y. Li, Salt content in the rhizosphere of five psammophytes, Acta Ecologica Sinica 29 (2009) 4649–4655.
[126] S. Gin, J.M. Delaye, F. Angeli, S. Schuller, Aqueous alteration of silicate glass: state of knowledge and perspectives, Npj Mater Degrad 5 (2021). https://doi.org/10.1038/s41529-021-00190-5.
[127] S. Gin, L. Neill, M. Fournier, P. Frugier, T. Ducasse, M. Tribet, A. Abdelouas, B. Parruzot, J. Neeway, N. Wall, The controversial role of inter-diffusion in glass alteration, Chem Geol 440 (2016) 115–123. https://doi.org/10.1016/j.chemgeo.2016.07.014.
[128] Y. Kudriavtsev, R. Asomoza, Comparative analysis of corrosion of borosilicate glasses in water vapor, Solid State Ion 371 (2021) 115754. https://doi.org/10.1016/j.ssi.2021.115754.
[129] C. Lenting, O. Plümper, M. Kilburn, P. Guagliardo, M. Klinkenberg, T. Geisler, Towards a unifying mechanistic model for silicate glass corrosion, Npj Mater Degrad 2 (2018) 1–10. https://doi.org/10.1038/s41529-018-0048-z.
[130] G.S. Frankel, J.D. Vienna, J. Lian, J.R. Scully, S. Gin, J. V. Ryan, J. Wang, S.H. Kim, W. Windl, J. Du, A comparative review of the aqueous corrosion of glasses, crystalline ceramics, and metals, Npj Mater Degrad 2 (2018). https://doi.org/10.1038/s41529-018-0037-2.
[131] P. Frugier, S. Gin, Y. Minet, T. Chave, B. Bonin, N. Godon, J.E. Lartigue, P. Jollivet, A. Ayral, L. De Windt, G. Santarini, SON68 nuclear glass dissolution kinetics: Current state of knowledge and basis of the new GRAAL model, Journal of Nuclear Materials 380 (2008) 8–21. https://doi.org/10.1016/j.jnucmat.2008.06.044.
[132] S. Gin, P. Jollivet, M. Fournier, F. Angeli, P. Frugier, T. Charpentier, Origin and consequences of silicate glass passivation by surface layers, Nat Commun 6 (2015). https://doi.org/10.1038/ncomms7360.
[133] A. Verney-Carron, L. Sessegolo, A. Chabas, T. Lombardo, S. Rossano, A. Perez, V. Valbi, C. Boutillez, C. Muller, C. Vaulot, B. Trichereau, C. Loisel, Alteration of medieval stained glass windows in atmospheric medium: review and simplified alteration model, Npj Mater Degrad 7 (2023). https://doi.org/10.1038/s41529-023-00367-0.
[134] R. Conradt, Chemical durability of oxide glasses in aqueous solutions: A review, Journal of the American Ceramic Society 91 (2008) 728–735. https://doi.org/10.1111/j.1551-2916.2007.02101.x.
[135] J. Yliniemi, Surface Layer Alteration of Multi-Oxide Silicate Glasses at a Near-Neutral pH in the Presence of Citric and Tartaric Acid, Langmuir 38 (2022) 987–1000. https://doi.org/10.1021/acs.langmuir.1c02378.

[136] Y. Xiao, A.C. Lasaga, Ab initio quantum mechanical studies of the kinetics and mechanisms of quartz dissolution: OH- catalysis, Geochim Cosmochim Acta 60 (1996) 2283–2295. https://doi.org/10.1016/0016-7037(96)00101-9.
[137] D.R. Dunphy, S. Singer, A.W. Cook, B. Smarsly, D.A. Doshi, C.J. Blinker, Aqueous Stability of Mesoporous Silica Films Doped or Grafted with Aluminum Oxide, Langmuir 19 (2003) 10403–10408. https://doi.org/10.1021/la035183s.
[138] B.C. Bunker, Molecular mechanisms for corrosion of silica and silicate glasses, J Non Cryst Solids 179 (1994) 300–308. https://doi.org/10.1016/0022-3093(94)90708-0.
[139] T. Du, H. Li, G. Sant, M. Bauchy, New insights into the sol-gel condensation of silica by reactive molecular dynamics simulations, Journal of Chemical Physics 148 (2018) 234504. https://doi.org/10.1063/1.5027583.
[140] D.E. Clark, R.L. Schulz, G.G. Wiccks, A.R. Lodding, Waste glass alternation processes, surface layer evolution and rate limiting steps, in: Materials Research Society Symposium Proceedings, Publ by Materials Research Society, 1994: pp. 107–122. https://doi.org/10.1557/proc-333-107.
[141] N. Mascaraque, M. Bauchy, M.M. Smedskjaer, Correlating the Network Topology of Oxide Glasses with their Chemical Durability, Journal of Physical Chemistry B 121 (2017) 1139–1147. https://doi.org/10.1021/acs.jpcb.6b11371.
[142] N. Mascaraque, M. Bauchy, J.L.G. Fierro, S.J. Rzoska, M. Bockowski, M.M. Smedskjaer, Dissolution Kinetics of Hot Compressed Oxide Glasses, Journal of Physical Chemistry B 121 (2017) 9063–9072. https://doi.org/10.1021/acs.jpcb.7b04535.
[143] M. Wang, M.M. Smedskjaer, J.C. Mauro, G. Sant, M. Bauchy, Topological Origin of the Network Dilation Anomaly in Ion-Exchanged Glasses, Phys Rev Appl 8 (2017) 054040. https://doi.org/10.1103/PhysRevApplied.8.054040.
[144] A. Atila, Y. Ouldhnini, S. Ouaskit, A. Hasnaoui, Atomistic insights into the mixed-alkali effect in phosphosilicate glasses, Phys Rev B 105 (2022) 134101. https://doi.org/10.1103/PhysRevB.105.134101.
[145] A. Tilocca, Sodium migration pathways in multicomponent silicate glasses: Car-Parrinello molecular dynamics simulations, Journal of Chemical Physics 133 (2010) 14701. https://doi.org/10.1063/1.3456712.
[146] H. Mehrer, A.W. Imre, E. Tanguep-Nijokep, Diffusion and ionic conduction in oxide glasses, J Phys Conf Ser 106 (2008). https://doi.org/10.1088/1742-6596/106/1/012001.
[147] I. Elgayar, R. Hill, X. Chen, N. Bubb, D. Wood, Dielectric spectroscopy and dissolution studies of bioactive glasses, Int J Appl Glass Sci 8 (2017) 418–427. https://doi.org/10.1111/ijag.12324.
[148] F. Lodesani, M.C. Menziani, H. Hijiya, Y. Takato, S. Urata, A. Pedone, Structural origins of the Mixed Alkali Effect in Alkali Aluminosilicate Glasses: Molecular Dynamics Study and its Assessment, Sci Rep 10 (2020) 2906. https://doi.org/10.1038/s41598-020-59875-7.
[149] G.N. Greaves, EXAFS and the structure of glass, J Non Cryst Solids 71 (1985) 203–217. https://doi.org/10.1016/0022-3093(85)90289-3.
[150] B. Vessal, Cation microsegregation and ionic mobility in mixed alkali glasses, Nature 356 (1992) 167–169. https://doi.org/https://doi.org/10.1038/356504a0.

[151] A. Tilocca, Dynamical descriptors of bioactivity: A correlation between chemical durability and ion migration in biodegradable glasses, Physical Chemistry Chemical Physics 19 (2017) 6334–6337. https://doi.org/10.1039/c6cp07203h.
[152] D.S. Brauer, Bioactive glasses - Structure and properties, Angewandte Chemie - International Edition 54 (2015) 4160–4181. https://doi.org/10.1002/anie.201405310.
[153] A. Tilocca, A.N. Cormack, Surface signatures of bioactivity: MD simulations of 45S and 65S silicate glasses, Langmuir 26 (2010) 545–551. https://doi.org/10.1021/la902548f.
[154] S. Fagerlund, L. Hupa, M. Hupa, Dissolution patterns of biocompatible glasses in 2-Amino-2-hydroxymethyl- propane-1,3-diol (Tris) buffer, Acta Biomater 9 (2013) 5400–5410. https://doi.org/10.1016/j.actbio.2012.08.051.
[155] A. Tilocca, A.N. Cormack, Modeling the water-bioglass interface by Ab initio molecular dynamics simulations, ACS Appl Mater Interfaces 1 (2009) 1324–1333. https://doi.org/10.1021/am900198t.
[156] J.J. Sly, N.L. Clark, J.C. Mauro, Examining correlations between the dissolution rates and optical basicity of modified aluminoborate glasses, Journal of the American Ceramic Society (2025) 1–14. https://doi.org/10.1111/jace.20402.
[157] M.W.G. Lockyer, D. Holland, R. Dupree, NMR investigation of the structure of some bioactive and related glasses, J Non Cryst Solids 188 (1995) 207–219. https://doi.org/10.1016/0022-3093(95)00188-3.
[158] N.A. Elalaily, E.A. Saad, H.H. Mahmoud, A.Kh. Ghonaim, T.D. Abd-Elaziz, E. Hamed, F.M. Ezz-EIdin, Effect of dilute HF solutions on chemical, optical, and mechanical properties of soda-lime-silica glass, Egypt J Chem 50 (2007) 645–666. https://doi.org/10.1007/s10853-010-4679-x.
[159] M. Blochberger, L. Hupa, D.S. Brauer, Influence of zinc and magnesium substitution on ion release from Bioglass 45S5 at physiological and acidic pH, Biomedical Glasses 1 (2015) 93–107. https://doi.org/10.1515/bglass-2015-0009.
[160] R.D. SHANNON, Revised Effective Ionic Radii and Systematic Studies of Interatomie Distances in Halides and Chaleogenides, Acta Crystallographica Section A 32 (1976) 1052–1058. https://doi.org/10.1023/A:1018927109487.
[161] M.D. O'Donnell, R.G. Hill, Influence of strontium and the importance of glass chemistry and structure when designing bioactive glasses for bone regeneration, Acta Biomater 6 (2010) 2382–2385. https://doi.org/10.1016/j.actbio.2010.01.006.
[162] R. Brückner, M. Tylkowski, L. Hupa, D.S. Brauer, Controlling the ion release from mixed alkali bioactive glasses by varying modifier ionic radii and molar volume, J Mater Chem B 4 (2016) 3121–3134. https://doi.org/10.1039/c5tb02426a.
[163] M.F. DILMORE, D.E. CLARK, L.L. HENCH, Chemical Durability of Na2O-K2O-CaO-SiO2 Glasses, Journal of the American Ceramic Society 61 (1978) 439–443. https://doi.org/10.1111/j.1151-2916.1978.tb09355.x.
[164] A. Tilocca, A.N. Cormack, N.H. De Leeuw, The structure of bioactive silicate glasses: New insight from molecular dynamics simulations, Chemistry of Materials 19 (2007) 95–103. https://doi.org/10.1021/cm061631g.
[165] L. Stoch, Flexibility of structure and glass-forming ability: A chemical approach, in: Glass Physics and Chemistry, Springer, 2001: pp. 167–174. https://doi.org/10.1023/A:1011388528421.

[166] S. Lee, T. Nakano, T. Kasuga, Formation and structural analysis of 15MgO–15CaO–8P2O5–4SiO2 glass, J Non Cryst Solids 457 (2017) 73–76. https://doi.org/10.1016/j.jnoncrysol.2016.11.020.
[167] M. Kagan, G.K. Lockwood, S.H. Garofalini, Reactive simulations of the activation barrier to dissolution of amorphous silica in water, Physical Chemistry Chemical Physics 16 (2014) 9294–9301. https://doi.org/10.1039/c4cp00030g.
[168] M. Fournier, S. Gin, P. Frugier, Resumption of nuclear glass alteration: State of the art, Journal of Nuclear Materials 448 (2014) 348–363. https://doi.org/10.1016/j.jnucmat.2014.02.022.
[169] S. Gin, A.H. Mir, A. Jan, J.M. Delaye, E. Chauvet, Y. De Puydt, A. Gourgiotis, S. Kerisit, A General Mechanism for Gel Layer Formation on Borosilicate Glass under Aqueous Corrosion, Journal of Physical Chemistry C 124 (2020) 5132–5144. https://doi.org/10.1021/acs.jpcc.9b10491.
[170] P. Frugier, C. Martin, I. Ribet, T. Advocat, S. Gin, The effect of composition on the leaching of three nuclear waste glasses: R7T7, AVM and VRZ, Journal of Nuclear Materials 346 (2005) 194–207. https://doi.org/10.1016/j.jnucmat.2005.06.023.
[171] T. Chave, P. Frugier, S. Gin, A. Ayral, Glass-water interphase reactivity with calcium rich solutions, Geochim Cosmochim Acta 75 (2011) 4125–4139. https://doi.org/10.1016/j.gca.2011.05.005.
[172] N. Rajmohan, P. Frugier, S. Gin, Composition effects on synthetic glass alteration mechanisms: Part 1. Experiments, Chem Geol 279 (2010) 106–119. https://doi.org/10.1016/j.chemgeo.2010.10.010.
[173] M. Collin, M. Fournier, T. Charpentier, M. Moskura, S. Gin, Impact of alkali on the passivation of silicate glass, Npj Mater Degrad 2 (2018) 1–10. https://doi.org/10.1038/s41529-018-0036-3.
[174] K. Damodaran, S. Gin, S. Naranayasamy, J.M. Delaye, On the effect of Al on alumino-borosilicate glass chemical durability, Npj Mater Degrad 7 (2023) 1–9. https://doi.org/10.1038/s41529-023-00364-3.
[175] S. Gin, M. Collin, P. Jollivet, M. Fournier, Y. Minet, L. Dupuy, T. Mahadevan, S. Kerisit, J. Du, Dynamics of self-reorganization explains passivation of silicate glasses, Nat Commun 9 (2018) 1–9. https://doi.org/10.1038/s41467-018-04511-2.
[176] F. Angeli, M. Gaillard, P. Jollivet, T. Charpentier, Influence of glass composition and alteration solution on leached silicate glass structure: A solid-state NMR investigation, Geochim Cosmochim Acta 70 (2006) 2577–2590. https://doi.org/10.1016/j.gca.2006.02.023.
[177] D.E. Clark, R.L. Schulz, G.G. Wiccks, A.R. Lodding, Waste glass alternation processes, surface layer evolution and rate limiting steps, in: Materials Research Society Symposium Proceedings, Publ by Materials Research Society, 1994: pp. 107–122. https://doi.org/10.1557/proc-333-107.
[178] Y. Yu, Z. Bacsik, M. Edén, Contrasting in vitro apatite growth from bioactive glass surfaces with that of spontaneous precipitation, Materials 11 (2018) 1690. https://doi.org/10.3390/ma11091690.
[179] L.N. Niu, K. Jiao, T. Da Wang, W. Zhang, J. Camilleri, B.E. Bergeron, H.L. Feng, J. Mao, J.H. Chen, D.H. Pashley, F.R. Tay, A review of the bioactivity of hydraulic calcium silicate cements, J Dent 42 (2014) 517–533. https://doi.org/10.1016/j.jdent.2013.12.015.

[180] S. Gin, C. Guittonneau, N. Godon, D. Neff, D. Rebiscoul, M. Cabí, S. Mostefaoui, Nuclear glass durability: New insight into alteration layer properties, Journal of Physical Chemistry C 115 (2011) 18696–18706. https://doi.org/10.1021/jp205477q.
[181] O. Majérus, P. Lehuédé, I. Biron, F. Alloteau, S. Narayanasamy, D. Caurant, Glass alteration in atmospheric conditions: crossing perspectives from cultural heritage, glass industry, and nuclear waste management, Npj Mater Degrad 4 (2020) 1–16. https://doi.org/10.1038/s41529-020-00130-9.
[182] G.S. Frankel, J.D. Vienna, J. Lian, J.R. Scully, S. Gin, J. V. Ryan, J. Wang, S.H. Kim, W. Windl, J. Du, A comparative review of the aqueous corrosion of glasses, crystalline ceramics, and metals, Npj Mater Degrad 2 (2018). https://doi.org/10.1038/s41529-018-0037-2.
[183] G. Franceschin, R. Zanini, G. Iori, E. Longo, G. Divitini, G. Tromba, A. Traviglia, Non-destructive 3D exploration of silicate glass corrosion: a combined multiscale approach from the macro to the nanoscale, Physical Chemistry Chemical Physics 26 (2024) 9697–9707. https://doi.org/10.1039/d3cp05221d.
[184] L. Stoch, I. Wacławska, M. Ciecińska, Thermochemistry of biologically active glasses, in: J Therm Anal Calorim, 2001: pp. 341–350. https://doi.org/10.1023/A:1017948212869.
[185] I. Wacławska, M. Szumera, Thermal analysis of glasses for proecological applications, in: J Therm Anal Calorim, Springer, 2003: pp. 1065–1072. https://doi.org/10.1023/A:1025059424522.
[186] T. Oey, K.F. Frederiksen, N. Mascaraque, R. Youngman, M. Balonis, M.M. Smedskjaer, M. Bauchy, G. Sant, The role of the network-modifier's field-strength in the chemical durability of aluminoborate glasses, J Non Cryst Solids 505 (2019) 279–285. https://doi.org/10.1016/j.jnoncrysol.2018.11.019.
[187] J. Du, Y. Xiang, Investigating the structure-diffusion-bioactivity relationship of strontium containing bioactive glasses using molecular dynamics based computer simulations, J Non Cryst Solids 432 (2016) 35–40. https://doi.org/10.1016/j.jnoncrysol.2015.03.015.
[188] A. Tilocca, Structural models of bioactive glasses from molecular dynamics simulations, Proceedings of the Royal Society A: Mathematical, Physical and Engineering Sciences 465 (2009) 1003–1027. https://doi.org/10.1098/rspa.2008.0462.
[189] B. Mysen, P. Richet, Phosphorus in Silicate Systems, 2019. https://doi.org/10.1016/b978-0-444-63708-6.00013-2.
[190] M. Szumera, B. Łagowska, Spectroscopic Studies of MnO2 and SiO2 Containing Soil-Active Phosphate Glasses, J Appl Spectrosc 83 (2017) 951–958. https://doi.org/10.1007/s10812-017-0389-3.
[191] L. Stoch, Flexibility of structure as a criterion of glass formation and stability, Optica Applicata 30 (2000) 647–655.
[192] D. Stachel, A. Barz, Structure investigations of ultraphosphate glasses with some water content, Journal of Physics and Chemistry of Solids 68 (2007) 1021–1023. https://doi.org/10.1016/j.jpcs.2007.03.005.
[193] K. Meyer, A. Barz, D. Stachel, Effects of atmospheric humidity on the infrared reflectivity of vitreous P2O5 and ultraphosphate glasses, J Non Cryst Solids 191 (1995) 71–78. https://doi.org/10.1016/0022-3093(95)00301-0.

[194] A. Rodrigues, S. Fearn, T. Palomar, M. Vilarigues, Early stages of surface alteration of soda-rich-silicate glasses in the museum environment, Corros Sci 143 (2018) 362–375. https://doi.org/10.1016/j.corsci.2018.08.012.
[195] M. Melcher, M. Schreiner, Evaluation procedure for leaching studies on naturally weathered potash-lime-silica glasses with medieval composition by scanning electron microscopy, J Non Cryst Solids 351 (2005) 1210–1225. https://doi.org/10.1016/j.jnoncrysol.2005.02.020.
[196] X. Wang, S. Fagerlund, J. Massera, B. Södergård, L. Hupa, Do properties of bioactive glasses exhibit mixed alkali behavior?, J Mater Sci 52 (2017) 8986–8997. https://doi.org/10.1007/s10853-017-0915-y.
[197] L. Brázda, L. Hupa, M. Hupa, A. Helebrant, Influence of Na2O/K2O ratio on In Vitro properties of bioactive glass, in: 11th International Conference and Exhibition of the European Ceramic Society 2009, 2009: pp. 443–447. https://www-1scopus-1com-100002cim00e6.wbg2.bg.agh.edu.pl/record/display.uri?eid=2-s2.0-84878935506&origin=scopusAI (accessed May 9, 2025).
[198] W.H. Casey, H.R. Westrich, Control of dissolution rates of orthosilicate minerals by divalent metal-oxygen bonds, Nature 355 (1992) 157–159. https://doi.org/10.1038/355157a0.
[199] A. Tilocca, Sodium migration pathways in multicomponent silicate glasses: Car-Parrinello molecular dynamics simulations, Journal of Chemical Physics 133 (2010). https://doi.org/10.1063/1.3456712.
[200] S.J. Watts, R.G. Hill, M.D. O'Donnell, R. V. Law, Influence of magnesia on the structure and properties of bioactive glasses, J Non Cryst Solids 356 (2010) 517–524. https://doi.org/10.1016/j.jnoncrysol.2009.04.074.
[201] T. Labbilta, M. Mesnaoui, H. Aouad, Y. Abouliatim, M. Khouloud, L. Abielaala, Study of the effect of calcium substitution by magnesium in the vitreous system 3P2O5-2K2O-(1-x) CaO-x MgO, Materials 13 (2020) 2637. https://doi.org/10.3390/ma13112637.
[202] K. Shimoda, T. Nemoto, K. Saito, Local structure of magnesium in silicate glasses: A25Mg 3QMAS NMR study, Journal of Physical Chemistry B 112 (2008) 6747–6752. https://doi.org/10.1021/jp711417t.
[203] I. Wacławska, M. Szumera, Influence of MgO (CaO) on the structure of silicate-phosphate glasses : TA and NMR study, J Therm Anal Calorim 84 (2006) 185–190. https://doi.org/10.1007/s10973-005-7183-9.
[204] J. Grandgirard, D. Poinsot, L. Krespi, J.P. Nénon, A.M. Cortesero, On the Phase Separation and Crystallization of Glasses in the MgO–Al2O3 –SiO2 –TiO2 System, Entomol Exp Appl 103 (2002) 239–248. https://doi.org/10.1023/A.
[205] J.F. Stebbins, N. Kim, M.J. Andrejcak, P.M. Boymel, B.K. Zoitos, Characterization of phase separation and thermal history effects in magnesium silicate glass fibers by nuclear magnetic resonance spectroscopy, Journal of the American Ceramic Society 92 (2009) 68–74. https://doi.org/10.1111/j.1551-2916.2008.02844.x.
[206] X. Xu, X. Lao, Y. Deng, Z. Mao, Y. Zhao, W. Liao, Z. Wei, J. Liang, Y. Chen, The important role of phase separation in crystallization and sintering behaviors of cordierite glass-ceramics with different MgO content, Constr Build Mater 472 (2025) 140976. https://doi.org/10.1016/j.conbuildmat.2025.140976.

[207] J.M. Oliveira, R.N. Correia, M.H. Fernandes, J. Rocha, Influence of the CaO/MgO ratio on the structure of phase-separated glasses: A solid state29Si and31P MAS NMR study, J Non Cryst Solids 265 (2000) 221–229. https://doi.org/10.1016/S0022-3093(99)00957-6.
[208] B. Cagnon, S. Gin, M. Cabié, D. Daval, International Simple Glass (ISG) dissolution rate in a (Si, Ca)-rich environment at 90 °C and alkaline conditions, Journal of Nuclear Materials 603 (2025) 155426. https://doi.org/10.1016/j.jnucmat.2024.155426.
[209] P.J. Skrdla, P.D. Floyd, P.C. Dell'Orco, Predicting the solubility enhancement of amorphous drugs and related phenomena using basic thermodynamic principles and semi-empirical kinetic models, Int J Pharm 567 (2019) 118465. https://doi.org/10.1016/j.ijpharm.2019.118465.
[210] K. Grzybowska, S. Capaccioli, M. Paluch, Recent developments in the experimental investigations of relaxations in pharmaceuticals by dielectric techniques at ambient and elevated pressure, Adv Drug Deliv Rev 100 (2016) 158–182. https://doi.org/10.1016/j.addr.2015.12.008.
[211] T. Rouxel, What we can learn from crystals about the mechanical properties of glass, Journal of the Ceramic Society of Japan 130 (2022) 519–530. https://doi.org/10.2109/jcersj2.22067.
[212] A. Perez, D. Daval, M. Fournier, M. Vital, J.M. Delaye, S. Gin, Comparing the reactivity of glasses with their crystalline equivalents: The case study of plagioclase feldspar, Geochim Cosmochim Acta 254 (2019) 122–141. https://doi.org/10.1016/j.gca.2019.03.030.
[213] T.S. Mahadevan, S.H. Garofalini, Dissociative chemisorption of water onto silica surfaces and formation of hydronium ions (J. Phys. Chem. C (2008) 112C (1514)), Journal of Physical Chemistry C 112 (2008) 5694. https://doi.org/10.1021/jp8015134.
[214] F. Angeli, T. Charpentier, P. Jollivet, D. de Ligny, M. Bergler, A. Veber, S. Gin, H. Li, Effect of thermally induced structural disorder on the chemical durability of International Simple Glass, Npj Mater Degrad 2 (2018) 1–11. https://doi.org/10.1038/s41529-018-0052-3.
[215] R. Gislason, P. Sciences, Meteoric water-basalt interactions . I : A laboratory study, 51 (1987) 2827–2840.
[216] M. Montazerian, A. Shearer, J.C. Mauro, Perspectives on the impact of crystallization in bioactive glasses and glass-ceramics, International Journal of Ceramic Engineering and Science 6 (2024) e10194. https://doi.org/10.1002/ces2.10194.
[217] A. Nommeots-Nomm, A. Houaoui, A. Pradeepan Packiyanathar, X. Chen, M. Hokka, R. Hill, E. Pauthe, L. Petit, M. Boissière, J. Massera, Phosphate/oxyfluorophosphate glass crystallization and its impact on dissolution and cytotoxicity, Materials Science and Engineering C 117 (2020) 111269. https://doi.org/10.1016/j.msec.2020.111269.
[218] M. Hasanuzzaman, M. Fujita, H. Oku, K. Nahar, B. Hawrylak-Nowak, Phosphorus Nutrition: Plant Growth in Response to Deficiency and Excess, Plant Nutrients and Abiotic Stress Tolerance (2018) 1–590. https://doi.org/10.1007/978-981-10-9044-8.
[219] K.G. Raghothama, Phosphorus and Plants Nutrition: An Overwiev, Agronomy Monograph 46 (2005) 353–378.

[220] J. Shen, L. Yuan, J. Zhang, H. Li, Z. Bai, X. Chen, W. Zhang, F. Zhang, Phosphorus dynamics: From soil to plant, Plant Physiol 156 (2011) 997–1005. https://doi.org/10.1104/pp.111.175232.
[221] I. Ajmera, T. Charlie Hodgman, C. Lu, An integrative systems perspective on plant phosphate research, Genes (Basel) 10 (2019). https://doi.org/10.3390/genes10020139.
[222] X. Xu, X. Du, F. Wang, J. Sha, Q. Chen, G. Tian, Z. Zhu, S. Ge, Y. Jiang, Effects of Potassium Levels on Plant Growth, Accumulation and Distribution of Carbon, and Nitrate Metabolism in Apple Dwarf Rootstock Seedlings, Front Plant Sci 11 (2020) 534048. https://doi.org/10.3389/fpls.2020.00904.
[223] V. Römheld, E.A. Kirkby, Research on potassium in agriculture: Needs and prospects, Plant Soil 335 (2010) 155–180. https://doi.org/10.1007/s11104-010-0520-1.
[224] C. Zörb, M. Senbayram, E. Peiter, Potassium in agriculture - Status and perspectives, J Plant Physiol 171 (2014) 656–669. https://doi.org/10.1016/j.jplph.2013.08.008.
[225] A. Amtmann, F. Rubio, Potassium in Plants, in: ELS, Wiley, 2012. https://doi.org/10.1002/9780470015902.a0023737.
[226] M. Ishfaq, Y. Wang, M. Yan, Z. Wang, L. Wu, C. Li, X. Li, Physiological Essence of Magnesium in Plants and Its Widespread Deficiency in the Farming System of China, Front Plant Sci 13 (2022) 802274. https://doi.org/10.3389/fpls.2022.802274.
[227] N. Ahmed, B. Zhang, B. Bozdar, S. Chachar, M. Rai, J. Li, Y. Li, F. Hayat, Z. Chachar, P. Tu, The power of magnesium: unlocking the potential for increased yield, quality, and stress tolerance of horticultural crops, Front Plant Sci 14 (2023) 1285512. https://doi.org/10.3389/fpls.2023.1285512.
[228] X. Weng, H. Li, C. Ren, Y. Zhou, W. Zhu, S. Zhang, L. Liu, Calcium Regulates Growth and Nutrient Absorption in Poplar Seedlings, Front Plant Sci 13 (2022) 1–15. https://doi.org/10.3389/fpls.2022.887098.
[229] K. Thor, Calcium—nutrient and messenger, Front Plant Sci 10 (2019). https://doi.org/10.3389/fpls.2019.00440.
[230] M. Luyckx, J.F. Hausman, S. Lutts, G. Guerriero, Silicon and plants: Current knowledge and technological perspectives, Front Plant Sci 8 (2017). https://doi.org/10.3389/fpls.2017.00411.
[231] W. Zellner, B. Tubaña, F.A. Rodrigues, L.E. Datnoff, Silicon's Role in Plant Stress Reduction and Why This Element Is Not Used Routinely for Managing Plant Health, Plant Dis 105 (2021). https://doi.org/10.1094/PDIS-08-20-1797-FE.
[232] D. Coskun, R. Deshmukh, H. Sonah, J.G. Menzies, O. Reynolds, J.F. Ma, H.J. Kronzucker, R.R. Bélanger, The controversies of silicon's role in plant biology, New Phytologist 221 (2019) 67–85. https://doi.org/10.1111/nph.15343.
[233] J. Pavlovic, L. Kostic, P. Bosnic, E.A. Kirkby, M. Nikolic, Interactions of Silicon With Essential and Beneficial Elements in Plants, Front Plant Sci 12 (2021). https://doi.org/10.3389/fpls.2021.697592.
[234] R.K. Sharma, M.S. Cox, C. Oglesby, J.S. Dhillon, Revisiting the role of sulfur in crop production: A narrative review, J Agric Food Res 15 (2024) 101013. https://doi.org/10.1016/j.jafr.2024.101013.

[235] E.L.S. Hinckley, C.T. Driscoll, Sulfur fertiliser use in the Midwestern US increases as atmospheric sulfur deposition declines with improved air quality, Commun Earth Environ 3 (2022) 1–5. https://doi.org/10.1038/s43247-022-00662-9.
[236] M. Houhou, K.A. Joutei, C. Rais, L. Elghadraoui, S. Louahlia, Biomass partitioning and morphological parameters of Trigonella foenum-graecum submitted to sulfur deficiency, Indian J Plant Physiol 23 (2018) 118–127. https://doi.org/10.1007/s40502-018-0351-2.
[237] T. Zenda, S. Liu, A. Dong, H. Duan, Revisiting sulphur—the once neglected nutrient: It's roles in plant growth, metabolism, stress tolerance and crop production, Agriculture (Switzerland) 11 (2021). https://doi.org/10.3390/agriculture11070626.
[238] J. Eriksen, Chapter 2 Soil Sulfur Cycling in Temperate Agricultural Systems, Advances in Agronomy 102 (2009) 55–89. https://doi.org/10.1016/S0065-2113(09)01002-5.
[239] L.O. Fuentes-Lara, J. Medrano-Macías, F. Pérez-Labrada, E.N. Rivas-Martínez, E.L. García-Enciso, S. González-Morales, A. Juárez-Maldonado, F. Rincón-Sánchez, A. Benavides-Mendoza, From elemental sulfur to hydrogen sulfide in agricultural soils and plants, Molecules 24 (2019) 1–17. https://doi.org/10.3390/molecules24122282.
[240] M. Lewandowska, A. Sirko, Recent advances in understanding plant response to sulfur-deficiency stress, Acta Biochim Pol 55 (2008) 457–471. https://doi.org/10.18388/abp.2008_3051.
[241] M. Hasanuzzaman, M.H.M.B. Bhuyan, J.A. Mahmud, K. Nahar, S.M. Mohsin, K. Parvin, M. Fujita, Interaction of sulfur with phytohormones and signaling molecules in conferring abiotic stress tolerance to plants, Plant Signal Behav 13 (2018) e1477905. https://doi.org/10.1080/15592324.2018.1477905.
[242] C.M. Jantzen, M.E. Smith, D.K. Peeler, Dependency of sulfate solubility on melt composition and melt polymerization, in: Ceramic Transactions, 2005: pp. 141–152. https://doi.org/10.1002/9781118408438.ch13.
[243] Y. Morizet, M. Paris, I. Di Carlo, B. Scaillet, Effect of sulphur on the structure of silicate melts under oxidizing conditions, Chem Geol 358 (2013) 131–147. https://doi.org/10.1016/j.chemgeo.2013.09.004.
[244] D. Manara, A. Grandjean, O. Pinet, J.L. Dussossoy, D.R. Neuville, Factors influencing the sulphate incorporation in radioactive waste glasses, in: Materials Research Society Symposium Proceedings, 2006: pp. 377–384. https://doi.org/10.1557/proc-932-84.1.
[245] T. Tsujimura, X. Xue, M. Kanzaki, M.J. Walter, Sulfur speciation and network structural changes in sodium silicate glasses: Constraints from NMR and Raman spectroscopy, Geochim Cosmochim Acta 68 (2004) 5081–5101. https://doi.org/10.1016/j.gca.2004.08.029.
[246] S. Kopriva, M. Malagoli, H. Takahashi, Sulfur nutrition: Impacts on plant development, metabolism, and stress responses, J Exp Bot 70 (2019) 4069–4073. https://doi.org/10.1093/jxb/erz319.
[247] T. FÖRLAND, W.A. WEYL, Formation of a Sulfate Glass, Journal of the American Ceramic Society 33 (1950) 186–188. https://doi.org/10.1111/j.1151-2916.1950.tb12788.x.
[248] M. Handke, M. Rokita, A. Adamczyk, Krystalografia i krystalochemia dla ceramików, 2008.

[249] C. Calahoo, L. Wondraczek, Ionic glasses: Structure, properties and classification, Journal of Non-Crystalline Solids: X 8 (2020). https://doi.org/10.1016/j.nocx.2020.100054.
[250] D. Manara, A. Grandjean, O. Pinet, J.L. Dussossoy, D.R. Neuville, Sulfur behavior in silicate glasses and melts: Implications for sulfate incorporation in nuclear waste glasses as a function of alkali cation and V2O5 content, J Non Cryst Solids 353 (2007) 12–23. https://doi.org/10.1016/j.jnoncrysol.2006.09.041.
[251] S. V. Stefanovsky, O.I. Stefanovsky, I.L. Prusakov, M.I. Kadyko, A.A. Averin, B.S. Nikonov, Speciation of sulphate ions in sodium alumino(iron)phosphate glasses, J Non Cryst Solids 512 (2019) 81–89. https://doi.org/10.1016/j.jnoncrysol.2019.01.005.
[252] R.K. Mishra, K. V. Sudarsan, P. Sengupta, R.K. Vatsa, A.K. Tyagi, C.P. Kaushik, D. Das, K. Raj, Role of sulfate in structural modifications of sodium barium borosilicate glasses developed for nuclear waste immobilization, Journal of the American Ceramic Society 91 (2008) 3903–3907. https://doi.org/10.1111/j.1551-2916.2008.02773.x.
[253] P. Schantl, C. Majcenovic, REACTION TEXTURES IN Al2O3-SiO2 BRICKS INDUCED BY GASEOUS SOx ATTACK: NEW INSIGTHS FROM MINERALOGY AND THERMODYNAMIC MODELLING, in: Unified International Technical Conference on Refractories, UNITECR 2022 - Proceedings, 2022: pp. 74–81.
[254] D.B. Wang, Y.L. Xie, H. Chen, Immiscibility of sulfate and basic silicate melt under atmospheric pressure and distribution behavior of REEs in immiscible phase, Acta Petrologica et Mineralogica 42 (2023) 71–82. https://www-1scopus-1com-100002cpn0104.wbg2.bg.agh.edu.pl/record/display.uri?eid=2-s2.0-85183669901&origin=scopusAI (accessed May 19, 2025).
[255] M.C. Hutchinson, R.A. Brooker, J.H. Dilles, J. Blundy, The stability and composition of sulfate melts in arc magmas, Contributions to Mineralogy and Petrology 175 (2020) 1–25. https://doi.org/10.1007/s00410-020-01729-6.
[256] H. Cui, R. Zhong, Y. Xie, X. Wang, H. Chen, Melt–Fluid and Fluid–Fluid Immiscibility in a Na2SO4–SiO2–H2O System and Implications for the Formation of Rare Earth Deposits, Acta Geologica Sinica (English Edition) 95 (2021) 1604–1610. https://doi.org/10.1111/1755-6724.14795.
[257] J.M. Kleinsasser, A.C. Simon, B.A. Konecke, M.J. Kleinsasser, P. Beckmann, F. Holtz, Sulfide and sulfate saturation of dacitic melts as a function of oxygen fugacity, Geochim Cosmochim Acta 326 (2022) 1–16. https://doi.org/10.1016/j.gca.2022.03.032.
[258] H.S.C. O'Neill, J.A. Mavrogenes, The sulfate capacities of silicate melts, Geochim Cosmochim Acta 334 (2022) 368–382. https://doi.org/10.1016/j.gca.2022.06.020.
[259] P.A. Bingham, R.J. Hand, Sulphate incorporation and glass formation in phosphate systems for nuclear and toxic waste immobilization, Mater Res Bull 43 (2008) 1679–1693. https://doi.org/10.1016/j.materresbull.2007.07.024.
[260] K. Papadopoulos, SOLUBILITY OF SO3 IN SODA-LIME-SILICA MELTS., Physics and Chemistry of Glasses 14 (1973) 60–65. https://scholar.google.com/scholar_lookup?hl=en&volume=14&publication_year=1973&pages=60-

5&journal=Phys+Chem+Glasses&issue=3&author=K+Papadopoulos&title=The+solubility+of+SO3+in+soda-lime-silica+melts (accessed May 20, 2025).
[261] M. Ooura, T. Hanada, Compositional dependence of solubility of sulphate in silicate glasses, Glass Technology 39 (1998) 68–73.
[262] S. V Stefanovskii, Immobilising sulphate-bearing radioactive waste in glass, Phys. Chem. Mater. Treat 27 (1993) 157–167.
[263] X. Xu, R.E. Youngman, S. Kapoor, A. Goel, Structural drivers controlling sulfur solubility in alkali aluminoborosilicate glasses, Journal of the American Ceramic Society 104 (2021) 5030–5049. https://doi.org/10.1111/jace.17778.
[264] S. Vaishnav, A.C. Hannon, E.R. Barney, P.A. Bingham, Neutron Diffraction and Raman Studies of the Incorporation of Sulfate in Silicate Glasses, Journal of Physical Chemistry C 124 (2020) 5409–5424. https://doi.org/10.1021/acs.jpcc.9b10924.
[265] D.A. McKeown, I.S. Muller, H. Gan, I.L. Pegg, C.A. Kendziora, Raman studies of sulfur in borosilicate waste glasses: Sulfate environments, J Non Cryst Solids 288 (2001) 191–199. https://doi.org/10.1016/S0022-3093(01)00624-X.
[266] I.A. Sokolov, I. V. Murin, V.E. Kriyt, A.A. Pronkin, Structure and electrical conductivity of glasses in the Na 2O-Na2SO4-P2O5 system, Glass Physics and Chemistry 37 (2011) 351–361. https://doi.org/10.1134/S1087659611040158.
[267] V.G. Vyatchina, L.A. Perelyaeva, M.G. Zuev, I. V. Baklanova, V.L. Mamoshin, Vibrational spectra of sulfoborate glasses, Inorganic Materials 41 (2005) 1128–1130. https://doi.org/10.1007/s10789-005-0272-0.
[268] V.G. Vyatchina, L.A. Perelyaeva, M.G. Zuev, V.L. Mamoshin, I. V. Baklanova, Glass formation and vibrational spectra of glasses in the RSO 4-Na2B4O7-K2SO 4 (R = Mg, Ca, Sr, Ba) systems, Glass Physics and Chemistry 32 (2006) 634–637. https://doi.org/10.1134/S1087659606060071.
[269] Y. Morizet, S. Ory, I. Di Carlo, B. Scaillet, P. Echegut, The effect of sulphur on the glass transition temperature in anorthite-diopside eutectic glasses, Chem Geol 416 (2015) 11–18. https://doi.org/10.1016/j.chemgeo.2015.10.010.
[270] R. Saini, D.R. Neuville, R.E. Youngman, A. Goel, Deciphering the structural origins of high sulfur solubility in vanadium-containing borosilicate glasses, J Non Cryst Solids 619 (2023). https://doi.org/10.1016/j.jnoncrysol.2023.122554.
[271] L. Wu, L. Xu, F. Jiang, J. Lei, Y. Yang, Y. Teng, Y. Li, Microstructure, sulfate retention, and aqueous stability of barite-borosilicate glass-ceramics, Journal of Nuclear Materials 516 (2019) 152–159. https://doi.org/10.1016/j.jnucmat.2019.01.025.
[272] Jason M. Lonergan, Charmayne Lonergan, Joshua Silverstein, Pornsinee Cholsaipant, John McCloy, Thermal properties of sodium borosilicate glasses as a function of sulfur content, Journal of the American Ceramic Society 103 (2020) 3610–3619. https://doi.org/https://doi.org/10.1111/jace.17057.
[273] N. Hémono, F. Muñoz, Dissolution of SO3 within a lithium phosphate glass network and structure-property relationships, Physics and Chemistry of Glasses: European Journal of Glass Science and Technology Part B 51 (2010) 121–126.
[274] I. Wacławska, M. Szumera, Use of thermal analysis in the study of soil Pb immobilization, J Therm Anal Calorim 99 (2010) 873–877. https://doi.org/10.1007/s10973-009-0558-6.

[275] A. Lis-Krzyścin, Nawozy szkliste w uprawach ogrodniczych Zeszyty Naukowe Uniwersytetu Rolniczego im. Hugona Kołłątaja w Krakowie nr 497, Wydawnictwo Uniwersytetu Rolniczego w Krakowie, Krakow, 2012.
[276] I. Waclawska, M. Szumera, Reactivity of silicate-phosphate glasses in soil environment, J Alloys Compd 468 (2009) 246–253. https://doi.org/10.1016/j.jallcom.2007.12.093.
[277] J.D. Vienna, D.S. Kim, I.S. Muller, G.F. Piepel, A.A. Kruger, Toward understanding the effect of low-activity waste glass composition on sulfur solubility, Journal of the American Ceramic Society 97 (2014) 3135–3142. https://doi.org/10.1111/jace.13125.
[278] P.A. Bingham, S. Vaishnav, S.D. Forder, A. Scrimshire, B. Jaganathan, J. Rohini, J.C. Marra, K.M. Fox, E.M. Pierce, P. Workman, J.D. Vienna, Modelling the sulfate capacity of simulated radioactive waste borosilicate glasses, J Alloys Compd 695 (2017) 656–667. https://doi.org/10.1016/j.jallcom.2016.11.110.
[279] A. Berezicka, J. Sułowska, P. Jeleń, R. Lach, M. Szumera, Thermal behaviour of sulphate-bearing multicomponent silicate–phosphate glasses, J Therm Anal Calorim 148 (2023) 1381–1405. https://doi.org/10.1007/s10973-022-11498-y.
[280] A. Berezicka, M. Szumera, J. Sułowska, P. Jeleń, Z. Olejniczak, J. Stępień, M. Zając, S. Pollastri, L. Olivi, Unraveling the nature of sulfur-bearing silicate-phosphate glasses: Insights from multi-spectroscopic (Raman, MIR, 29Si, 31P MAS-NMR, XAS, XANES) investigation, Ceram Int 48 (2022) 4238–4254. https://doi.org/10.1016/j.ceramint.2021.10.216.
[281] A. Berezicka, J. Sułowska, P. Jeleń, S. Komarek, M. Szumera, Effect of sulfur addition on glass-forming ability, structure and thermal stability of multicomponent silicate-phosphate glasses, J Therm Anal Calorim 149 (2024) 10405–10427. https://doi.org/10.1007/s10973-023-12866-y.
[282] M. Mirsaneh, I.M. Reaney, P. V. Hatton, S. Bhakta, P.F. James, Effect of P2O5 on the early stage crystallization of K-fluorrichterite glass-ceramics, J Non Cryst Solids 354 (2008) 3362–3368. https://doi.org/10.1016/j.jnoncrysol.2008.02.003.
[283] Y. Shih, S. Sundararaman, S. Ispas, L. Huang, New interaction potentials for alkaline earth silicate and borate glasses, J Non Cryst Solids 565 (2021) 120853. https://doi.org/10.1016/j.jnoncrysol.2021.120853.
[284] T. Rouxel, N. Dély, J.C. Sangleboeuf, S. Dériano, M. LeFloch, B. Beuneu, S. Hampshire, Structure-property correlations in Y-Ca-Mg-sialon glasses: Physical and mechanical properties, Journal of the American Ceramic Society 88 (2005) 889–896. https://doi.org/10.1111/j.1551-2916.2005.00146.x.
[285] J. Kloužek, M. Arkosiová, L. Němec, Redox equilibria of sulphur in glass melts, Ceramics - Silikaty 50 (2006) 134–139.
[286] N.I. Min'ko, I.M. Binaliev, Science for Glass Production Role of Sodium Sulfate in Glass Technology, 69 (2012) 3–8.
[287] R.G.C. Beerkens, J. Van Der Schaaf, Gas release and foam formation during melting and fining of glass, Journal of the American Ceramic Society 89 (2006) 24–35. https://doi.org/10.1111/j.1551-2916.2005.00691.x.
[288] T. Komatsu, Design and control of crystallization in oxide glasses, J Non Cryst Solids 428 (2015) 156–175. https://doi.org/10.1016/j.jnoncrysol.2015.08.017.

[289] M. Sitarz, K. Bulat, A. Wajda, M. Szumera, Direct crystallization of silicate-phosphate glasses of NaCaPO 4-SiO2 system, in: J Therm Anal Calorim, Springer, 2013: pp. 1363–1368. https://doi.org/10.1007/s10973-013-3240-y.
[290] M. Sitarz, M. Szumera, Crystallization of silico-phosphate glasses, J Therm Anal Calorim 91 (2008) 255–260. https://doi.org/10.1007/s10973-007-8374-3.
[291] L. Stoch, Thermal analysis and thermochemistry of vitreous into crystalline state transition, in: J Therm Anal Calorim, Springer, 2004: pp. 7–16. https://doi.org/10.1023/B:JTAN.0000033182.90571.ce.
[292] L. Stoch, Thermochemistry of solids with flexible structures, J Therm Anal Calorim 54 (1998) 9–24. https://doi.org/10.1023/A:1010127129729.
[293] I. Avramov, T. Vassilev, I. Penkov, The glass transition temperature of silicate and borate glasses, J Non Cryst Solids 351 (2005) 472–476. https://doi.org/10.1016/j.jnoncrysol.2005.01.044.
[294] P. Stoch, M. Ciecinska, A. Stoch, Thermal properties of phosphate glasses for salt waste immobilization, J Therm Anal Calorim 117 (2014) 197–204. https://doi.org/10.1007/s10973-014-3698-2.
[295] L.P. Testasicca, R.L. Frost, X. Ruan, J. Lima, F.M. Belotti, R. Scholz, The application of high-temperature X-ray diffraction and infrared emission spectroscopy to the thermal decomposition of kröhnkite, J Therm Anal Calorim 126 (2016) 1089–1095. https://doi.org/10.1007/s10973-016-5644-y.
[296] A. Hrubý, Evaluation of glass-forming tendency by means of DTA, Czechoslovak Journal of Physics 22 (1972) 1187–1193. https://doi.org/10.1007/BF01690134.
[297] M.L.F. Nascimento, L.A. Souza, E.B. Ferreira, E.D. Zanotto, Can glass stability parameters infer glass forming ability?, J Non Cryst Solids 351 (2005) 3296–3308. https://doi.org/10.1016/j.jnoncrysol.2005.08.013.
[298] I. Avramov, E.D. Zanotto, M.O. Prado, Glass-forming ability versus stability of silicate glasses. II. Theoretical demonstration, J Non Cryst Solids 320 (2003) 9–20. https://doi.org/10.1016/S0022-3093(03)00081-4.
[299] D. Turnbull, Under What Conditions Can A Glass Be Formed?, Contemp Phys 10 (1969) 473–488. https://doi.org/10.1080/00107516908204405.
[300] Z.P. Lu, C.T. Liu, A new glass-forming ability criterion for bulk metallic glasses, Acta Mater 50 (2002) 3501–3512. https://doi.org/10.1016/S1359-6454(02)00166-0.
[301] E.D. Zanotto, Isothermal and adiabatic nucleation in glass, J Non Cryst Solids 89 (1987) 361–370. https://doi.org/10.1016/S0022-3093(87)80278-8.
[302] A. Kozmidis-Petrovic, J. Šesták, Forty years of the Hrubý glass-forming coefficient via DTA when comparing other criteria in relation to the glass stability and vitrification ability, in: J Therm Anal Calorim, Springer, 2012: pp. 997–1004. https://doi.org/10.1007/s10973-011-1926-6.
[303] I. Wacławska, M. Szumera, Thermal behaviour of Fe-doped silicate-phosphate glasses, in: J Therm Anal Calorim, Springer, 2010: pp. 423–427. https://doi.org/10.1007/s10973-010-0798-5.
[304] M. Szumera, I. Wacławska, Spectroscopic and thermal studies of silicate-phosphate glass, in: J Therm Anal Calorim, Springer, 2007: pp. 151–156. https://doi.org/10.1007/s10973-006-8118-9.

[305] L. Stoch, Structure and Crystallization of Multicomponent Glasses, High Temperature Materials and Processes 10 (1992) 245–264. https://doi.org/10.1515/HTMP.1992.10.4.245.
[306] L. Miladi, A. Oueslati, K. Guidara, Vibrational spectroscopic and dielectric properties investigations of phase transitions in KMgPO4 compound, J Mol Struct 1148 (2017) 404–411. https://doi.org/10.1016/j.molstruc.2017.07.047.
[307] L. Miladi, A. Oueslati, K. Guidara, Phase transition, conduction mechanism and modulus study of KMgPO4 compound, RSC Adv 6 (2016) 83280–83287. https://doi.org/10.1039/c6ra18560f.
[308] P. McMillan, A Raman spectroscopic study of glasses in the system CaO-MgO-SiO2., American Mineralogist 69 (1984) 645–659.
[309] H.N. Mills, Use of Fining Agents. Ceramic Engineering and Science Proceedings, in: W.J. Smothers (Ed.), 46th Conferenceon GlassProblems, 1986: pp. 404–409. https://doi.org/10.1002/9780470320327.ch7.
[310] Z. Wang, W. Yang, H. Liu, H. Jin, H. Chen, K. Su, Y. Tu, W. Wang, Thermochemical behavior of three sulfates (CaSO4, K2SO4 and Na2SO4) blended with cement raw materials (CaO-SiO2-Al2O3-Fe2O3) at high temperature, J Anal Appl Pyrolysis 142 (2019). https://doi.org/10.1016/j.jaap.2019.05.006.
[311] L. Pilon, Foams in Glass Manufacturing, in: Foam Engineering: Fundamentals and Applications, 2012: pp. 355–409. https://doi.org/10.1002/9781119954620.ch16.
[312] R. Youngman, NMR spectroscopy in glass science: A review of the elements, Materials 11 (2018) 476. https://doi.org/10.3390/ma11040476.
[313] M. Wilke, K. Klimm, S.C. Kohn, Spectroscopic studies on sulfur speciation in synthetic and natural glasses, Rev Mineral Geochem 73 (2011) 41–78. https://doi.org/10.2138/rmg.2011.73.3.
[314] S. Agathopoulos, D.U. Tulyaganov, J.M.G. Ventura, S. Kannan, A. Saranti, M.A. Karakassides, J.M.F. Ferreira, Structural analysis and devitrification of glasses based on the CaO-MgO-SiO2 system with B2O3, Na2O, CaF2 and P2O5 additives, J Non Cryst Solids 352 (2006) 322–328. https://doi.org/10.1016/j.jnoncrysol.2005.12.003.
[315] D.U. Tulyaganov, S. Agathopoulos, J.M. Ventura, M.A. Karakassides, O. Fabrichnaya, J.M.F. Ferreira, Synthesis of glass-ceramics in the CaO-MgO-SiO2 system with B2O3, P2O5, Na2O and CaF2 additives, J Eur Ceram Soc 26 (2006) 1463–1471. https://doi.org/10.1016/j.jeurceramsoc.2005.02.009.
[316] I. Wacławska, M. Szumera, J. Sułowska, Structural characterization of zinc-modified glasses from the SiO2-P2O5-K2O-CaO-MgO system, J Alloys Compd 666 (2016) 352–358. https://doi.org/10.1016/j.jallcom.2016.01.125.
[317] P. McMillan, Structural studies of silicate glasses and melts-applications and limitations of Raman spectroscopy, Contributions to Mineralogy and Petrology 69 (1984) 622–644. https://doi.org/10.1007/BF00307725.
[318] S. Agathopoulos, D.U. Tulyaganov, J.M.G. Ventura, S. Kannan, A. Saranti, M.A. Karakassides, J.M.F. Ferreira, Structural analysis and devitrification of glasses based on the CaO-MgO-SiO 2 system with B 2 O 3 , Na 2 O, CaF 2 and P 2 O 5 additives, (2006). https://doi.org/10.1016/j.jnoncrysol.2005.12.003.
[319] D.U. Tulyaganov, S. Agathopoulos, J.M. Ventura, M.A. Karakassides, O. Fabrichnaya, J.M.F. Ferreira, Synthesis of glass-ceramics in the CaO-MgO-SiO2

system with B2O3, P2O5, Na2O and CaF2 additives, J Eur Ceram Soc 26 (2006) 1463–1471. https://doi.org/10.1016/j.jeurceramsoc.2005.02.009.
[320] I. Wacławska, M. Szumera, J. Sułowska, Structural characterization of zinc-modified glasses from the SiO 2-P 2 O 5-K 2 O-CaO-MgO system, (2016). https://doi.org/10.1016/j.jallcom.2016.01.125.
[321] P. McMillan, Structural studies of silicate glasses and melts-applications and limitations of Raman spectroscopy., American Mineralogist 69 (1984) 622–644.
[322] B.O. Mysen, L.W. Finger, D. Virgo, F.A. Seifert, Curve-fitting of Raman spectra of silicate glasses., American Mineralogist 67 (1982) 686–695.
[323] D.A. Mckeown, I.S. Muller, H. Gan, I.L. Pegg, C.A. Kendziora, Raman studies of sulfur in borosilicate waste glasses: sulfate environments, n.d.
[324] Y. Morizet, E. Gennaro, S. Jego, Z. Zajacz, G. Iacono-Marziano, M. Pichavant, I. Di Carlo, C. Ferraina, P. Lesne, A Raman calibration for the quantification of SO42- groups dissolved in silicate glasses: Application to natural melt inclusions, American Mineralogist 102 (2017) 2065–2076. https://doi.org/10.2138/am-2017-6100.
[325] W. Jastrzbski, M. Sitarz, M. Rokita, K. Bułat, Infrared spectroscopy of different phosphates structures, Spectrochim Acta A Mol Biomol Spectrosc 79 (2011) 722–727. https://doi.org/10.1016/j.saa.2010.08.044.
[326] D.R. Neuville, Viscosity, structure and mixing in (Ca, Na) silicate melts, Chem Geol 229 (2006) 28–41. https://doi.org/10.1016/j.chemgeo.2006.01.008.
[327] D.R. Neuville, D. De Ligny, G.S. Henderson, Advances in Raman spectroscopy applied to earth and material sciences, Rev Mineral Geochem 78 (2014) 509–541. https://doi.org/10.2138/rmg.2013.78.13.
[328] B. Mysen, Structural behavior of Al3+ in silicate melts: In situ, high-temperature measurements as a function of bulk chemical composition, Geochim Cosmochim Acta 59 (1995) 455–474. https://doi.org/10.1016/0016-7037(95)00318-T.
[329] D.R. Neuville, Viscosity, structure and mixing in (Ca, Na) silicate melts, Chem Geol 229 (2006) 28–41. https://doi.org/10.1016/j.chemgeo.2006.01.008.
[330] B. Mysen, Structural behavior of Ai 3+ in silicate melts: In situ, high-temperature measurements as a function of bulk chemical composition, 1995.
[331] D.R. Neuville, D. De Ligny, G.S. Henderson, Advances in Raman spectroscopy applied to earth and material sciences, Rev Mineral Geochem 78 (2014) 509–541. https://doi.org/10.2138/rmg.2013.78.13.
[332] M. Sitarz, Influence of modifying cations on the structure and texture of silicate-phosphate glasses, J Mol Struct 887 (2008) 237–248. https://doi.org/10.1016/j.molstruc.2007.12.030.
[333] M. Sitarz, M. Rokita, M. Handke, E. Galuskin, Structural studies of the NaCaPO4 - SiO2 sol - gel derived materials, in: J Mol Struct, 2003: pp. 489–498. https://doi.org/10.1016/S0022-2860(03)00113-3.
[334] M. Szumera, I. Wacławska, W. Mozgawa, M. Sitarz, Spectroscopic study of biologically active glasses, (2005). https://doi.org/10.1016/j.molstruc.2005.01.023.
[335] W. Jastrzbski, M. Sitarz, M. Rokita, K. Bułat, Infrared spectroscopy of different phosphates structures, in: Spectrochim Acta A Mol Biomol Spectrosc, 2011: pp. 722–727. https://doi.org/10.1016/j.saa.2010.08.044.

[336] M. Sitarz, M. Rokita, M. Handke, E. Galuskin, Structural studies of the NaCaPO 4-SiO 2 sol-gel derived materials, (n.d.). https://doi.org/10.1016/S0022-2860(03)00113-3.
[337] S. V Stefanovsky, O.I. Stefanovsky, I.L. Prusakov, M.I. Kadyko, A.A. Averin, B.S. Nikonov, Speciation of sulphate ions in sodium alumino(iron)phosphate glasses, (2019). https://doi.org/10.1016/j.jnoncrysol.2019.01.005.
[338] A.G. Kalampounias, IR and Raman spectroscopic studies of sol-gel derived alkaline-earth silicate glasses, Bulletin of Materials Science 34 (2011) 299–303. https://doi.org/10.1007/s12034-011-0064-x.
[339] A.G. Kalampounias, IR and Raman spectroscopic studies of sol-gel derived alkaline-earth silicate glasses, 2011.
[340] M. Sitarz, Influence of modifying cations on the structure and texture of silicate-phosphate glasses, (n.d.). https://doi.org/10.1016/j.molstruc.2007.12.030.
[341] R.J. Kirkpatrick, R.K. Brow, Nuclear magnetic resonance investigation of the structures of phosphate and phosphate-containing glasses: A review, Solid State Nucl Magn Reson 5 (1995) 9–21. https://doi.org/10.1016/0926-2040(95)00042-O.
[342] W. -H Yang, R.J. Kirkpatrick, G. Turner, 31P and 29Si Magic-Angle Sample-Spinning NMR Investigation of the Structural Environment of Phosphorus in Alkaline-Earth Silicate Glasses, Journal of the American Ceramic Society 69 (1986) C-222-C-223. https://doi.org/10.1111/j.1151-2916.1986.tb07340.x.
[343] A. Belkébir, J. Rocha, A.P. Esculcas, P. Berthet, B. Gilbert, Z. Gabelica, G. Llabres, F. Wijzen, A. Rulmont, Structural characterization of glassy phases in the system Na2O-Ga2O3-P2O5 by MAS and solution NMR and vibrational spectroscopy: II. Structure of the phosphate network, Spectrochim Acta A Mol Biomol Spectrosc 56 (2000) 435–446. https://doi.org/10.1016/S1386-1425(99)00117-1.
[344] M. Yang, X. Cai, C. Wang, Z. Wang, F. Xue, C. Chu, J. Bai, Q. Liu, X. Ni, Highly Stable Amorphous (Pyro)phosphate Aggregates: Pyrophosphate as a Carrier for Bioactive Ions and Drugs in Bone Repair Applications, ACS Omega (2024). https://doi.org/10.1021/acsomega.4c01660.
[345] H. Aguiar, E.L. Solla, J. Serra, P. González, B. León, F. Malz, C. Jäger, Raman and NMR study of bioactive Na2O-MgO-CaO-P2O5-SiO2 glasses, J Non Cryst Solids 354 (2008) 5004–5008. https://doi.org/10.1016/j.jnoncrysol.2008.07.033.
[346] H. Maekawa, T. Maekawa, K. Kawamura, T. Yokokawa, The structural groups of alkali silicate glasses determined from 29Si MAS-NMR, J Non Cryst Solids 127 (1991) 53–64. https://doi.org/10.1016/0022-3093(91)90400-Z.
[347] B. Zagrajczuk, M. Dziadek, Z. Olejniczak, K. Cholewa-Kowalska, M. Laczka, Structural and chemical investigation of the gel-derived bioactive materials from the SiO2–CaO and SiO2-CaO-P2O5 systems, Ceram Int 43 (2017) 12742–12754. https://doi.org/10.1016/j.ceramint.2017.06.160.
[348] H. Maekawa, T. Maekawa, K. Kawamura, T. Yokokawa, The structural groups of alkali silicate glasses determined from 29Si MAS-NMR, J Non Cryst Solids 127 (1991) 53–64. https://doi.org/10.1016/0022-3093(91)90400-Z.
[349] B. Zagrajczuk, M. Dziadek, Z. Olejniczak, K. Cholewa-Kowalska, M. Laczka, Structural and chemical investigation of the gel-derived bioactive materials from the SiO2–CaO and SiO2-CaO-P2O5 systems, Ceram Int 43 (2017) 12742–12754. https://doi.org/10.1016/j.ceramint.2017.06.160.

[350] H. Grussaute, L. Montagne, G. Palavit, J.L. Bernard, Phosphate speciation in Na2O-CaO-P2O5-SiO2 and Na2O-TiO2-P2O5-SiO2 glasses, J Non Cryst Solids 263 (2000) 312–317. https://doi.org/10.1016/S0022-3093(99)00643-2.
[351] M.E. Fleet, X. Liu, S.L. Harmer, P.L. King, Sulfur K-edge XANES spectroscopy: Chemical state and content of sulfur in silicate glasses, Can Mineral 43 (2005) 1605–1618. https://doi.org/10.2113/gscanmin.43.5.1605.
[352] M.E. Fleet, X. Liu, S.L. Harmer, P.L. King, Sulfur K-edge XANES spectroscopy: Chemical state and content of sulfur in silicate glasses, Can Mineral 43 (2005) 1605–1618. https://doi.org/10.2113/gscanmin.43.5.1605.
[353] B. Debret, M. Andreani, A. Delacour, S. Rouméjon, N. Trcera, H. Williams, Assessing sulfur redox state and distribution in abyssal serpentinites using XANES spectroscopy, Earth Planet Sci Lett 466 (2017) 1–11. https://doi.org/10.1016/j.epsl.2017.02.029.
[354] A. Rohatgi, Web Plot Digitizer, V. 3.9 (2014) 1–17. http://arohatgi.info/WebPlotDigitizer.
[355] D.A. McKeown, I.S. Muller, H. Gan, I.L. Pegg, W.C. Stolte, Determination of sulfur environments in borosilicate waste glasses using X-ray absorption near-edge spectroscopy, J Non Cryst Solids 333 (2004) 74–84. https://doi.org/10.1016/j.jnoncrysol.2003.09.035.
[356] D. Li, G.M. Bancroft, M. Kasrai, M.E. Fleet, X. Feng, K. Tan, S K-and L-edge X-ray absorption spectroscopy of metal sulfides and sulfates: applications in mineralogy and geochemistry, The Canadian Mineralogist 33 (1995) 949–960.
[357] F. ME, XANES spectroscopy of sulfur in Earth materials, Can Mineral 43 (2005) 1811–1838.
[358] E.D. Ingall, J.A. Brandes, J.M. Diaz, M.D. De Jonge, D. Paterson, I. McNulty, W.C. Elliott, P. Northrup, Phosphorus K-edge XANES spectroscopy of mineral standards, J Synchrotron Radiat 18 (2011) 189–197. https://doi.org/10.1107/S0909049510045322.
[359] R. Franke, J. Hormes, The P K-near edge absorption spectra of phosphates, Physica B: Physics of Condensed Matter 216 (1995) 85–95. https://doi.org/10.1016/0921-4526(95)00446-7.
[360] Z. Yin, M. Kasrai, G.M. Bancroft, K.H. Tan, X. Feng, X-ray-absorption spectroscopic studies of sodium polyphosphate glasses, Phys Rev B 51 (1995) 742–750. https://doi.org/10.1103/PhysRevB.51.742.
[361] G.S. Henderson, A Si K-edge EXAFS / XANES, 183 (1995) 43–50.
[362] D. Li, G.M. Bancroft, M.E. Fleet, X.H. Feng, Silicon K-edge XANES spectra of silicate minerals, Phys Chem Miner 22 (1995) 115–122. https://doi.org/10.1007/BF00202471.
[363] D. Cabaret, M. Le Grand, A. Ramos, A.M. Flank, S. Rossano, L. Galoisy, G. Calas, D. Ghaleb, Medium range structure of borosilicate glasses from Si K-edge XANES: A combined approach based on multiple scattering and molecular dynamics calculations, J Non Cryst Solids 289 (2001) 1–8. https://doi.org/10.1016/S0022-3093(01)00733-5.
[364] M.E. Fleet, S. Muthupari, M. Kasrai, S. Prabakar, Sixfold coordinated Si in alkali and alkali-CaO silicophosphate glasses by Si K-edge XANES spectroscopy, J Non Cryst Solids 220 (1997) 85–92. https://doi.org/10.1016/S0022-3093(97)00222-6.

[365] D. Li, M. Peng, T. Murata, Coordination and local structure of magnesium in silicate minerals and glasses: Mg K-edge XANES study, Can Mineral 37 (1999) 199–206.
[366] B.J.A. Moulton, G.S. Henderson, C. Sonneville, C. O'Shaughnessy, L. Zuin, T. Regier, D. de Ligny, The structure of haplobasaltic glasses investigated using X-ray absorption near edge structure (XANES) spectroscopy at the Si, Al, Mg, and O K-edges and Ca, Si, and Al L2,3-edges, Chem Geol 420 (2016) 213–230. https://doi.org/10.1016/j.chemgeo.2015.11.016.
[367] Y. Morizet, N. Trcera, C. Larre, M. Rivoal, E. Le Menn, D. Vantelon, F. Gaillard, X-ray absorption spectroscopic investigation of the Ca and Mg environments in CO 2 -bearing silicate glasses, Chem Geol 510 (2019) 91–102. https://doi.org/10.1016/j.chemgeo.2019.02.014.
[368] P.G. Debenedetti, F.H. Stillinger, Supercooled liquids and the glass transition, Nature 410 (2001) 259–267.
[369] J. Liu, J. Wei, C. Liu, Effect of cooling rate on the crystallization and optical properties of silicate glasses containing ZnS, Ceram Int 49 (2023) 35414–35419. https://doi.org/10.1016/j.ceramint.2023.08.217.
[370] J. Ashwin, E. Bouchbinder, I. Procaccia, Cooling-rate dependence of the shear modulus of amorphous solids, Phys Rev E Stat Nonlin Soft Matter Phys 87 (2013) 1–5. https://doi.org/10.1103/PhysRevE.87.042310.
[371] K. Vollmayr, W. Kob, K. Binder, Cooling-rate effects in amorphous silica: A computer-simulation study, Phys Rev B Condens Matter Mater Phys 54 (1996) 15808–15827. https://doi.org/10.1103/PhysRevB.54.15808.
[372] Y. Wang, L. Qu, H. Li, H. Zhang, Y. Wang, Y. Lu, Effect of cooling rate on the microstructure of colloidal glass, Mater Trans 58 (2017) 420–422. https://doi.org/10.2320/matertrans.M2016408.
[373] Y. Lu, X. Lu, Z. Qin, J. Shen, Dependence of local order on cooling rate investigated in a colloidal glass, J Non Cryst Solids 420 (2015) 34–37. https://doi.org/10.1016/j.jnoncrysol.2015.04.014.
[374] Q. Wang, H. Chen, Y. Wang, J. Sun, Thermal shock effect on the glass thermal stress response and crack propagation, in: Procedia Eng, Elsevier Ltd, 2013: pp. 717–724. https://doi.org/10.1016/j.proeng.2013.08.118.
[375] L.A.G. Gray, C.B. Roth, Stability of polymer glasses vitrified under stress, Soft Matter 10 (2014) 1572–1578. https://doi.org/10.1039/c3sm52113c.
[376] V.M. Fokin, E.D. Zanotto, N.S. Yuritsyn, J.W.P. Schmelzer, Homogeneous crystal nucleation in silicate glasses: A 40 years perspective, J Non Cryst Solids 352 (2006) 2681–2714. https://doi.org/10.1016/j.jnoncrysol.2006.02.074.
[377] I. Waclawska, L. Stoch, Thermal behaviour of silicate-phosphate glasses in relation to their biochemical activity, J Therm Anal Calorim 65 (2001) 141–146. https://doi.org/10.1023/A:1011580702954.
[378] R. Brüning, T. Crowell, Method to determine the kinetics of a supercooled liquid by temperature scanning measurements applied to (Li,Na)acetate and GeO2, J Non Cryst Solids 248 (1999) 183–193. https://doi.org/10.1016/S0022-3093(99)00302-6.
[379] Y. Shi, O. Gulbiten, J. Neuefeind, D. Ma, A.P. Song, B. Wheaton, M. Bauchy, S.R. Elliott, Temperature-induced structural change through the glass transition of

silicate glass by neutron diffraction, Phys Rev B 101 (2020). https://doi.org/10.1103/PhysRevB.101.134106.
[380] C. Ṙssel, Nanocrystallization of CaF2 from Na2O/K 2O/CaO/CaF2/Al2O3/SiO2 glasses, Chemistry of Materials 17 (2005) 5843–5847. https://doi.org/10.1021/cm051430x.
[381] I. Avramov, C. Rüssel, N. Kolkovska, I. Georgiev, Crystallization kinetics and network rigidity, Journal of Physics Condensed Matter 20 (2008). https://doi.org/10.1088/0953-8984/20/33/335203.
[382] S. Chahal, K. Ramesh, Glass formation, thermal stability and fragility minimum in Ge-Te-Se glasses, Mater Res Bull 152 (2022) 111833. https://doi.org/10.1016/j.materresbull.2022.111833.
[383] C.A. Angell, Formation of glasses from liquids and biopolymers, Science (1979) 267 (1995) 1924–1935. https://doi.org/10.1126/science.267.5206.1924.
[384] R. Brüning, K. Samwer, Glass transition on long time scales, Phys Rev B 46 (1992) 11318–11322. https://doi.org/10.1103/PhysRevB.46.11318.
[385] E. Muller, K. Heide, E.D. Zanotto, Molecular structure and nucleation in silicate glasses, J Non Cryst Solids 155 (1993) 56–66. https://doi.org/10.1016/0022-3093(93)90471-9.
[386] A.M.B. Silva, C.M. Queiroz, S. Agathopoulos, R.N. Correia, M.H.V. Fernandes, J.M. Oliveira, Structure of SiO2-MgO-Na2O glasses by FTIR, Raman and 29Si MAS NMR, J Mol Struct 986 (2011) 16–21. https://doi.org/10.1016/j.molstruc.2010.11.023.
[387] Y.Q. Wu, C. Dai, G.C. Jiang, Local structure of calcium silicate melts from classical molecular dynamics simulation and a newly constructed thermodynamic model, Transactions of Nonferrous Metals Society of China (English Edition) 24 (2014) 1488–1499. https://doi.org/10.1016/S1003-6326(14)63217-9.
[388] B.N. Nelson, G.J. Exarhos, Vibrational spectroscopy of cation-site interactions in phosphate glasses, J Chem Phys 71 (1979) 2739–2747. https://doi.org/10.1063/1.438679.
[389] K. Zamanian, R. Taghizadeh-Mehrjardi, J. Tao, L. Fan, S. Raza, G. Guggenberger, Y. Kuzyakov, Acidification of European croplands by nitrogen fertilization: Consequences for carbonate losses, and soil health, Science of the Total Environment 924 (2024) 171631. https://doi.org/10.1016/j.scitotenv.2024.171631.
[390] B. Ulén, S. Pietrzak, B. Ramnerö, L. Strand, Agricultural soil acidity and phosphorus leaching risk at farm level in two focus areas, Acta Agric Scand B Soil Plant Sci 66 (2016) 359–368. https://doi.org/10.1080/09064710.2015.1126631.
[391] T. Palomar, Effect of soil pH on the degradation of silicate glasses, Int J Appl Glass Sci 8 (2017) 177–187. https://doi.org/10.1111/ijag.12226.
[392] P. Szterner, A. Antosik, J. Pagacz, P. Tymowicz-Grzyb, Morphology Control of Hydroxyapatite as a Potential Reinforcement for Orthopedic Biomaterials: The Hydrothermal Process, Crystals (Basel) 13 (2023). https://doi.org/10.3390/cryst13050793.
[393] D.P. McDonogh, P. Kirupananthan, D. Gebauer, Counterintuitive Crystallization: Rate Effects in Calcium Phosphate Nucleation at Near-Physiological pH, Cryst Growth Des 23 (2023) 7037–7043. https://doi.org/10.1021/acs.cgd.3c00851.
[394] O. Mekmene, T. Rouillon, S. Quillard, P. Pilet, J.M. Bouler, S. Pezennec, F. Gaucheron, Effects of citrate and NaCl on size, morphology, crystallinity and

microstructure of calcium phosphates obtained from aqueous solutions at acidic or near-neutral pH, Journal of Dairy Research 79 (2012) 238–248. https://doi.org/10.1017/S0022029912000076.
[395] P.Y. Putri, I. Ujike, N. Sandra, F. Ashar, EFFECT OF TEMPERATURE AND SOLUTION pH ON CALCIUM CARBONATE PRECIPITATION AS BIO-BASED REPAIR MATERIAL IN CONCRETE, International Journal of GEOMATE 26 (2024) 101–108. https://doi.org/10.21660/2024.114.g13453.
[396] W.C. Chen, C.P. Ju, W.H. Cheng, J.H. Chernlin, Green synthesis of calcium and phosphate compounds by varying ph value and ca/p atomic ratio using aqueous precipitations, Ceramics - Silikaty 57 (2013) 14–21.
[397] F.N. Türk, M.Ş.A. Eren, H. Arslanoğlu, Obtaining, Characterizing, and Evaluation of Potassium-Struvite (KMgPO4.6H2O) in Phosphorus Removal from Water: Investigation of Low-Cost Mgo Use, Water Conservation Science and Engineering 9 (2024) 1–14. https://doi.org/10.1007/s41101-024-00304-5.
[398] C. Lenting, T. Geisler, Corrosion of ternary borosilicate glass in acidic solution studied in operando by fluid-cell Raman spectroscopy, Npj Mater Degrad 5 (2021). https://doi.org/10.1038/s41529-021-00182-5.
[399] L. Robinet, D. Neff, A. Bouquillon, S. Pagès-Camagna, A. Verney-Carron, M.-P. Etcheverry, J. Tate, Raman spectrometry, a non-destructive solution to the study of glass and its alteration, 15th Triennial Conference, New Delhi, 22-26 September 2008: Preprints (ICOM Committee for Conservation) (2008) 224–231.
[400] K. Mishchik, Ultrafast laser-induced modification of optical glasses : a spectroscopy insight into the microscopic mechanisms Transformation photo-assist ´ ee de di ´ electriques pour l ' optique par laser ` a impulsions ultra-br ` etudes des m ´ ecanismes microscopiq, (2014) 1–185.
[401] T. Geisler, L. Dohmen, C. Lenting, M.B.K. Fritzsche, Real-time in situ observations of reaction and transport phenomena during silicate glass corrosion by fluid-cell Raman spectroscopy, Nat Mater 18 (2019) 342–348. https://doi.org/10.1038/s41563-019-0293-8.
[402] H. Wang, Z. Chen, L. Liu, Y. Sun, X. Wang, Roles of P2O5 addition on the viscosity and structure of CaO-SiO2-Al2O3-Na2O-P2O5 melts, ISIJ International 58 (2018) 1644–1649. https://doi.org/10.2355/isijinternational.ISIJINT-2018-138.
[403] S.A. Brawer, W.B. White, Raman spectroscopic investigation of the structure of silicate glasses. I. The binary alkali silicates, J Chem Phys 63 (1975) 2421–2432. https://doi.org/10.1063/1.431671.
[404] B. Mysen, Phosphorus speciation changes across the glass transition in highly polymerized alkali silicate glasses and melts, American Mineralogist 81 (1996) 1531–1534. https://doi.org/10.2138/am-1996-11-1226.
[405] H. Yang, H.J. Sun, R.T. Downs, Hazenite, KNaMg2(PO4)2l4H2O, a new biologically related phosphate mineral, from Mono Lake, California, U.S.A., American Mineralogist 96 (2011) 675–681. https://doi.org/10.2138/am.2011.3668.
[406] V. Stefov, B. Šoptrajanov, F. Spirovski, I. Kuzmanovski, H.D. Lutz, B. Engelen, Infrared and Raman spectra of magnesium ammonium phosphate hexahydrate (struvite) and its isomorphous analogues. I. Spectra of protiated and partially deuterated magnesium potassium phosphate hexahydrate, J Mol Struct 689 (2004) 1–10. https://doi.org/10.1016/j.molstruc.2003.08.019.

[407] F.S. Costa, F. Langenhorst, E. Kothe, Biomineralization of Nickel Struvite Linked to Metal Resistance in Streptomyces mirabilis, Molecules 27 (2022) 1–12. https://doi.org/10.3390/molecules27103061.
[408] N. Sánchez-Pastor, A.J. Pinto, P. del Buey Fernández, J.M. Astilleros, Crystallization of Calcium Carbonate and Calcium Phosphate Phases in Silica Hydrogel: Morphological and Compositional Characterization, Crystals (Basel) 14 (2024). https://doi.org/10.3390/cryst14070635.
[409] P. Jha, S.S. Danewalia, K. Singh, Influence of thermal stability on dielectric properties of SiO2–K2O–CaO–MgO glasses, J Therm Anal Calorim 128 (2017) 745–754. https://doi.org/10.1007/s10973-016-6013-6.

18 Attachments

1. **Publication P1**
2. **Publication P2***
3. **Publication P3**
4. **Publication P4**
5. **Authors' contribution statement**

1. Publication P1

Journal of Thermal Analysis and Calorimetry (2024) 149:10405–10427
https://doi.org/10.1007/s10973-023-12866-y

Effect of sulfur addition on glass-forming ability, structure and thermal stability of multicomponent silicate-phosphate glasses

Anna Berezicka[1] · Justyna Sułowska[1] · Piotr Jeleń[1] · Sebastian Komarek[1] · Magdalena Szumera[1]

Received: 20 July 2023 / Accepted: 25 December 2023 / Published online: 16 March 2024
© Akadémiai Kiadó, Budapest, Hungary 2024

Abstract

The incorporation of sulfate anions in a suitable host matrix has proven to be a challenging task for glass technologists around the world. Therefore, the present work reports on the solubility and retention of sulfate species, as an invaluable macronutrient for plants, in a multicomponent silicate-phosphate glasses from the SiO_2–P_2O_5–K_2O–MgO–CaO–XSO_3 system. Glasses containing target $[SO_4]^{2-}$ concentrations 0–5 mol.% were synthesized via high-temperature melt-quenching technique, the last stage of which constituted fritting the acquired melt in water. It was observed that this synthesis route broadened the glass-forming range of materials from the studied system, the sulfate capacity of which was determined to be ~ 2 mol.%. At higher $[SO_4]^{2-}$ concentrations, additional sulfur was retained in glasses as crystalline inclusions of sulfate salt. An in-depth insight into the materials' structure revealed that sulfate species exist in the vitreous matrix as units not bonded to either the silico-oxygen or phosphor-oxygen subnetworks, and their addition leads to a gradual increase in the polymerization degree of the former, and to the opposite effect as regards the latter. Thermal analysis of the tested glasses supported the structural studies and demonstrated that the addition of sulfur initially reduces materials' glass stability, leading to its increase after SO_3 content reaches 1 mol.%. It was also shown that $[SO_4]^{2-}$ species affect local environments of Si and Mg atoms indirectly, inducing changes in the medium-range structure beyond their first coordination spheres presumably involving the rearrangement of potassium cations within the vitreous matrix.

Keywords Silicate-phosphate glasses · Sulfur · Thermal analysis · Structure · Glass transition · Crystallization

Abbreviations

XRD	X-ray diffraction
XRF	X-ray fluorescence spectroscopy
DSC	Differential scanning calorimetry
T_g	Glass transformation temperature
T_x	Onset of glass crystallization peak
T_c	Maximum of glass crystallization peak
T_m	Glass melting temperature
ΔC_p	Molar heat capacity
K_A	Angell parameter
K_H	Hruby parameter
K_W	Weinberg parameter
RSI	Raman spectroscopy imaging
XAS	X-ray absorption spectroscopy

✉ Anna Berezicka
berezicka@agh.edu.pl

Justyna Sułowska
sulowska@agh.edu.pl

Piotr Jeleń
pjelen@agh.edu.pl

Sebastian Komarek
seko@agh.edu.pl

Magdalena Szumera
mszumera@agh.edu.pl

[1] Faculty of Materials Science and Ceramics, AGH University of Krakow, al. A. Mickiewicza 30, 30-059 Krakow, Poland

Introduction

It is estimated that to this day the amount of inorganic glass compositions, that have been produced since the discovery of the first man-made glass more than 5000 years ago in Mesopotamia, exceeds 2 000 000 [1]. Taking into account such a long history of this material unsurprising is the fact that almost any element of the periodic table was attempted to be introduced into the structure of an amorphous solid, often giving rise to unique formulations of constituents, coexistence of which is only possible in the flexible network of glass [2, 3]. One of such components which may be successfully incorporated into the framework of an oxide

glass, even despite that its chemical properties differ significantly from the ones of typical glass formers to the point of (creating common links is impossible) thereby excluding the possibility of formation of common links between their polyhedra, is sulfur.

Surely, sulfur as a constituent of amorphous solids and melts raises an interest of numerous branches of science: geochemical community seek to understand numerous processes (e.g., S degassing from volcanic eruptions, subsurface movements of magma or the origin of magmatic sulfide ores) through attaining knowledge of the solubility of sulfur species in silicate-based melts [4], glass technology has long drawn on knowledge of sulfate decomposition to promote melting, fining and homogenization of commercial glasses [5], while for radioactive waste management studies gaining an insight into the behavior of this, waste-load-limiting, ingredient in nuclear glass melts may constitute an invaluable technological clue to the optimization of a vitrification process [6, 7]. Furthermore, once the above list is complemented with the latest reports on sulfur-bearing vitreous materials group, starting from the evidence of sulfur-bearing amorphous material provided by the Curiosity rover which allowed to speculate on possible Martian surface processes and past or present habitability, through the mention of borophosphate glass enriched with $[SO_4]^{2-}$ as a candidate for new-generation solid-state electrolytes and finally to glassy carriers of bioavailable sulfur for plants, it may be said with some confidence that the topic itself receive incessant attention.

Nevertheless, despite this clear interest, there is still much unknown about this particular family of glasses and the collective body of research on this subject made hitherto only raises further questions. The reason for this is the inconsistency of the scientific data on the influence of sulfur addition on the evolution of the glass structure and, consequently, its properties. And so, while a substantial number of researchers claim that sulfur, being a constituent of a vitreous material, reside in the voids of its structure as isolated units surrounded only by modifier cations, and not linked to the spatial network [8–10], there are also premises that this particular element builds into the framework by forming the common bonds of the S–O–glass former cation type. As regards the latter notion, it finds favor in the works of Sokolov et al. [11] and Vyatchina et al. [12], who report on participation of $[SO_4]^{2-}$ ions in glass-former's subnetwork. Moreover, according to Hémono's et al. study [13], one should also consider a case that is somewhat intermediate between the two previously mentioned, that is the possibility of formation of two separate sublattices in the glass structure: the glass former-glass modifier as well as sulfate-glass modifier ones. Further ambiguities result from the unclear effect of $[SO_4]^{2-}$ anions on the direction of changes of glass polymerization degree. Again, while some researchers pointed out to the fact that incorporation of sulfates into the glass structure is accompanied by its depolymerization, formation of shorter chains and, at the same time, an increase of non-bridging oxygen atoms (NBOs) density [9, 11, 14] the others claimed that the effect is opposite and the presence of $[SO_4]^{2-}$ anions in the voids of the vitreous network may reduce the concentration of modifier cations in the surrounding of glass former's lattice, which in turn leads to its gradual polymerization [15–17].

Some ambiguities can also be found in the topic of thermal properties of glasses, and more specifically—regarding the influence of sulfur on glass transition temperature of vitreous materials. Lonergan et al. [18], who investigated properties of sodium borosilicate glasses as a function of sulfur content, noticed an increase in T_g along with $[SO_4]^{2-}$ introduction and such an observation he connected with the re-polymerization of the borosilicate glass framework induced precisely by the introduction of a new component into baseline glasses. Similar conclusions may be found in the studies of Xu et al. [16] as well as Manara et al. [7]. Both authors, after comparing values of T_g acquired for sulfur-free and sulfur-enriched glasses, postulated that addition of $[SO_4]^{2-}$ species, leading to the increased cross-linking of the glass backbone, results in shifting glass transformation effect toward higher temperatures. Nevertheless, according to the research of some authors, the influence of sulfur on glass transition temperature is entirely opposite to the above-reported [11, 13, 19, 20]. Sokolov et al. [11] explained the observed, and accompanied by $[SO_4]^{2-}$ addition, reduction of T_g by facilitating effect of highly polarized tetrahedral sulfate anions on the movements of glass structural units with respect to each other during heating procedure. Analogous, T_g-diminishing, influence of $[SO_4]^{2-}$ species was interpreted by Hémono et al. [13] as a manifestation of the lack of interaction between sulfate units and those formed by the other glass former. Yet another explanation is offered by Sadok et al. [19], claiming that the demonstrated reduction of glass transition temperature results from the shortening of phosphate chains and diminution of their cross-linking.

In spite of the aforesaid ambiguities, the literature data seem to be univocal in one aspect related to sulfate introduction into the vitreous matrix—an exceeding of the inherent, composition-dependent, sulfate capacity of a given glass results in adverse effect of phase separation and crystallization of sulfur-bearing phase [7, 14, 21]. Generally, such a phenomenon greatly limits the possible applications of sulfur carriers, especially when the fully amorphous character of such materials constitutes a necessary condition for their performance. For this particular reason, much effort has been made to widen the glass forming range of such materials. A known approach to attain this goal is to enhance glass capacity to host $[SO_4]^{2-}$ groupings through alternating such materials' composition, which is in accordance with

the notion that the compatibility between structural units of sulfate and those of other glass former oxides as well as the nature of glass modifiers substantially contribute to solubility of $[SO_4]^{2-}$ species in glass melts. Hitherto, it has been established that phosphate tetrahedra are the most adequate to coexist with sulfate ones, while the presence of low-field-strength, large cations promotes their incorporation [7, 22]. Less conventional strategy to ensure that amorphous nature of a material will be attained is through maneuvering the glass production route itself. According to a common theory in glass technology one can vitrify any substance provided that sufficiently high cooling rate is ensured. And although such a notion still raises controversies among glass scientists, it is indisputable that while there exist substances representing good glass-forming materials—e.g., SiO_2, P_2O_5 B_2O_3—for which the required rate of melt cooling is particularly low, some substances transform to an amorphous state only when quenched at considerably high rates (melts of mixed salts, for example) [23]. Clearly then an increment of melt cooling rate may be highly beneficial for vitrifying substances of high propensity toward crystallization. According to literature data, such an endeavor may be attained through many various routes [24–27], yet, the simplest and the most affordable technique constitutes the process of quenching the melt in a liquid medium (e.g., water).

Since our previous studies on sulfate-bearing silicate-based glasses clearly showed that it is a real endeavor to acquire fully amorphous materials once sulfur species participate in the formation of spatially polymerized vitreous network, the present research is aimed to investigate the overall effect of aforementioned processing route on glass-forming ability, glass stability, crystallization path, structure and, last but not least, the sulfate capacity of multicomponent silicate-phosphate soil-active glasses, intended as carriers of $[SO_4]^{2-}$ ions for plants. The aforementioned properties are particularly relevant for such materials, capable of the slow release of their components into the soil environment under the influence of biological solutions, what renders them fertilizers of positive influence on the natural environment. The presence of spontaneously formed crystalline phase, e.g., in the form of widely reported in the literature sulfate salt, exerts a negative impact on the nutrient-release mechanism as well as seriously affects solubility of such materials in soil substrate. Furthermore, to verify the theory that sulfate anions preferred association are the larger (e.g., Ca^{2+}) ions than the smaller (like K^+) ions, the subject of the present investigation constitutes multicomponent soil-active glasses from the SiO_2–P_2O_5–K_2O–MgO–CaO–SO_3 system containing three types of network modifiers. Such glasses, acquired by the water-quenching (fritting) method, will be then tested by means of XRD, XRF, DSC, FTIR and Raman spectroscopic techniques, followed by the detailed study of their devitrificates performed using XRD, RSI as well as XAS method, with the overall goal of resolving the intricacies of sulfur behavior in silicate-based vitreous materials.

Materials and methods

The focus of the present investigation constitutes sulfate-bearing silicate-phosphate glasses, distinguished by the presence of three different network modifiers and representing a composition of $41SiO_2$–$6P_2O_5$–$20K_2O$–16.5MgO–16.5CaO, to which SO_3 was added in amounts of 0, 0.5, 1, 3 or 5 mol.%. In order to examine the effect of solely $[SO_4]^{2-}$ addition on glass behavior the formulations were designed in such a manner that the contents of the core oxide components were kept constant in all the samples and the only variable between compositions constituted the SO_3 content.

Glass synthesis was carried out through traditional high-temperature melting of the designed batches. Accordingly, carefully weighed amounts of high purity raw materials (i.e., SiO_2, $(NH_4)_2HPO_4$, K_2CO_3, MgO, $CaCO_3$ and K_2SO_4 supplied by POCH, Poland) were mixed in a mortar with a pestle until the anticipated homogeneity was acquired (the total mass of glass batches was 60 g). So prepared batches were then transferred to ceramic crucibles, melted in an laboratory electric furnace at 1450 °C and, after completion of the heating program, quenched by pouring the melted material into the water-filled container (fritting).

The amorphous nature of the as-obtained samples, utterly important as regards glass fertilizers, was verified on the basis of powder X-ray diffraction measurements (PANalytical X-ray diffractometer X'Pert Pro with Cu lamp in the 2θ range 10–70°, with the step of the goniometer of 0.008° and the angular reproducibility of +/− 0.0002°), while to inspect their actual chemical composition an X-ray Fluorescence Spectrometry (ARL Advant 'XP spectrometer with normalizing glass sample composition to 100%) was utilized. The samples for the glass composition analysis were prepared using standard pellet method and the spectra obtained were developed quantitatively (reference-free) using the Omnian application package. Table 1 presents the molar contents of individual glass components, both nominal (in brackets) and determined by X-ray fluorescence (XRF). It is important to mention that the sample nomenclature, utilized in Table 1 and subsequently, follows a specific structure: the initial number represents the nominal molar content of SO_3, the subsequent letters indicate the alkaline earth oxides present in the glass compositions, and the letter F denotes the method of melt-quenching, specifically fritting.

An insight into the structure of materials was provided by means of FTIR as well as Raman spectroscopy methods. The measurements in the middle infrared region were taken via Bruke Vertex 70v vacuum spectrometer. The standard KBr pellet technique was applied, and 128 scans

Table 1 XRF-determined and nominal (in brackets) chemical composition of studied materials [mol.%]

Sample	SiO_2	P_2O_5	K_2O	MgO	CaO	SO_3
0S_MC_F	35.24 (41)	6.97 (6)	19.65 (20)	10.31 (16.5)	23.14 (16.5)	–
0.5S_MC_F	39.73 (41)	7.47 (6)	18.16 (20)	11.50 (16.5)	18.82 (16.5)	0.72 (0.5)
1S_MC_F	39.63 (41)	7.36 (6)	17.80 (20)	12.04 (16.5)	18.68 (16.5)	1.22 (1)
3S_MC_F	41.09 (41)	7.56 (6)	18.33 (20)	11.13 (16.5)	20.27 (16.5)	2.34 (3)
5S_MC_F	40.78 (41)	7.85 (6)	17.57 (20)	12.37 (16.5)	21.60 (16.5)	2.46 (5)

All the observed differences between nominal and XRF-determined content of glass components most probably result from volatility losses during the high-temperature melting process, possible impurities or fluctuations in the raw materials used as well as measurement errors, such as uncertainties in sample preparation, calibration, or instrumental drift

were acquired with a resolution of 4 cm^{-1}. Spectral deconvolution was executed employing the Levenberg–Marquardt algorithm, initializing the Gauss–Lorentz ratio at 0.5. The root mean square (RMS) noise after the curve fitting procedure was consistently below 0.1 for all samples. Meanwhile, Raman measurements were taken using the WITec Alpha 300 M + spectrometer. The measurements involved recording 4 accumulations, 20 s each, for every sample using Zeiss LD EC Epiplan 50 × objective as well as a 1800 grating with 488 nm diode laser.

X-ray absorption measurements were taken at the PEEM/XAS beamline of the SOLARIS National Science Centre, Poland [28], in the Mg and Si K-edge regions. The beamline used in this experiment is a bending magnet-based beamline that provides a soft X-ray energy range and is equipped with a plane grating monochromator that has a resolving power of $\Delta E/E$ better than 2.5×10^{-4}. The powdered glass samples were mounted on sample holders using adhesive carbon tape, and the data were collected under ambient conditions in the fluorescence mode. The collected spectra were normalized to a unit step for further analysis.

Alterations in thermal properties of studied materials as a function of sulfate content were monitored through the use of the STA 449 F3 Jupiter (NETZSCH) instrument which operates in the heat flux DSC mode and guarantees a temperature resolution of 0.001 K. The thermal measurements (differential scanning calorimetry) were taken at Faculty Laboratory of Thermophysical Research at Faculty of Material Science and Ceramics AGH University of Science and Technology. Powder samples of 31 mg, characterized by the grain size ranging from 0.1–0.3 mm, were placed in platinum crucibles and heated at a rate of 10 °C min^{-1} in the dynamic air atmosphere (80 mL min^{-1}. The temperature and heat calibrations of the instrument were performed using the melting temperatures and melting enthalpies of high-purity materials (Al, Zn, Sn, Au, Ag). The reference material constituted Al_2O_3, while the Netzsch Proteus Thermal Analysis Program (version 5.0.0.) was employed to determine the characteristic glass temperatures, namely glass transition temperature (T_g), the onset (T_x) and the maximum of the glass crystallization effect (T_c), as well as the values of molar heat capacity (ΔC_p). It should be noted that T_g was assessed as the midpoint of the relevant transformation step, while T_x and T_c were deducted from the onset and the maximum of the exothermic effect of glass crystallization, respectively.

Crystallization study was based on the in-depth analysis of glasses' devitrificates, the preparation of which involved grinding the portions of the synthesized samples to obtain the particles of 0.1–0.3 mm, and then subjecting them to 24 h of isothermal heating at the temperatures determined from the maxima of exothermic crystallization effects on DSC curves. The conditions applied in the isothermal crystallization experiment of glasses corresponded to those employed in the investigations using the DSC method. Therefore, the samples were introduced at room temperature and heated at a rate of 10 °C min^{-1} in an air atmosphere in a tube furnace to the specified crystallization temperature. An estimation of the relative contents of both amorphous and crystalline phases in the acquired devitrificates (internal ZnO standard method), as well as the identification of the types of the latter were carried out by X-ray diffractometry, using Philips X'Pert pro diffractometer (PANalytical X-ray diffractometer X'Pert Pro with Cu lamp in the 2θ range 10–70°).

Changes in the structure of studied materials, induced by the process of samples' thermal treatment, were tracked by virtue of Raman Imaging studies. The spectral maps of devitrified materials were collected via Confocal Raman Imaging system (WITec Alpha 300 M +) supplied with a 488 nm diode laser of approx. 650 mm spot, a 100 × ZEISS Epiplan Neofluar objective as well as 1800 grating. Raman images of the selected 40 × 40 µm areas on samples' surfaces were collected using the following scan parameters: 80 lines with 80 points for line and an integration time for a single spectrum of 1 s. In order to perform the necessary mathematical corrections the WITec Project Five 5.2 Plus software was exploited, while the true component analysis allowed to determine the chemical composition of the measured areas. Finally, by virtue of Raman Imaging studies, both maps of phases' distribution together with their respective spectra were acquired.

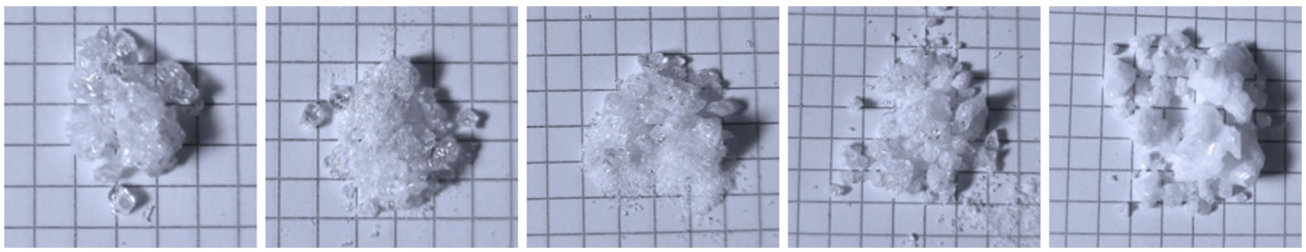


Fig. 1 Appearance of the as-synthesized materials loaded with, starting from the left: 0, 0.5, 1, 3 and 5 mol.% of SO_3

Results and discussion

Preliminary investigation of the obtained samples

The primary concern with processing the sulfate-bearing raw materials into a glass is its markedly low solubility in silicate-based melts that results in usually low concentrations of such species retained in the final product relative to the target. If one adds the significant volatility of sulfur species to the above equation it is not surprising that sulfate concentration in most acquired sulfur-containing silicate melts does not exceed 1 mol.% [14, 22]. Partitioning of sulfur in the molten salt phase (once its solubility limit is exceeded) has also been suggested as a mechanism for its low retention in the glass—volatilization of this element can occur from the salt layer even more readily than from the glass. Therefore, an attempt has been made to mitigate the problem of low sulfate solubility in silicate-based melts by fritting the acquired melts in the water-filled basket (in contradiction to the, previously studied, quenched in air and cooled on a steel plate materials [29]), according to the assumption that the slight increase of cooling rate provided by this particular method would allow to accelerate the vitrification process, decreasing at the same time the propensity of sulfate species to precipitate in the form of salt phase [30]. Accordingly, to test the effectiveness of this method, the preliminary examination of the as-synthesized materials, involving samples' visual examination as well as utilization of XRD and XRF methods, has been carried out.

In light of the foregoing, Fig. 1 depicts all the acquired samples, while Fig. 2 presents a column chart comparing the XRF-measured sulfate contents of studied, water-quenched, materials with those obtained by cooling melts of analogous composition on a steel plate.

The preliminary inspection of the melts before quenching indicated that the surface of the glass stayed clear of any secondary phases, the occurrence of which is commonly reported in the case of sulfate-bearing glasses.

It should be noted that as the glasses were cooled following high-temperature melting and fritting in water, cracking and shattering into small pieces were observed, likely resulting from thermal expansion mismatch stresses (Fig. 1). Furthermore, based on the performed visual investigation, it was established that the surfaces of all the glasses remained free of any secondary phases during melting and cooling. Importantly, all the obtained samples exhibited optical transparency, with the exception of the sample loaded with the highest sulfate content (5S_MC_F), which appeared cloudy. Based on previous experience with similar materials, it is well-established that such turbidity observed in as-synthesized samples serves as an indicator of the occurrence of spontaneous crystallization during the cooling of the melts.

The XRF analysis of the materials obtained through the water-quenching technique demonstrated that these samples exhibit significantly higher ability to retain sulfur in their structure (referred to as sulfate capacity) compared to those obtained by cooling the respective melts on a steel plate—the XS_MC_P series (Fig. 2) [31]. Given that, along with the fact that certain samples (0.5S_MC_F and 1S_MC_F) exhibited sulfur content exceeding the assumed value (and approaching the amount taking into account the volatility of SO_3), it can be concluded that the fritting process, which leads to the accelerated solidification of the melt, effectively traps volatile components within the glass structure, resulting in higher retained concentrations. It is also noteworthy that the 5S_MC_P sample obtained through cooling the melt on a steel plate exhibits an exceptionally high sulfur content. This phenomenon is attributed to the heterogeneity of this specific material, with regions near the surface exhibiting higher sulfur concentrations than the nominal content.

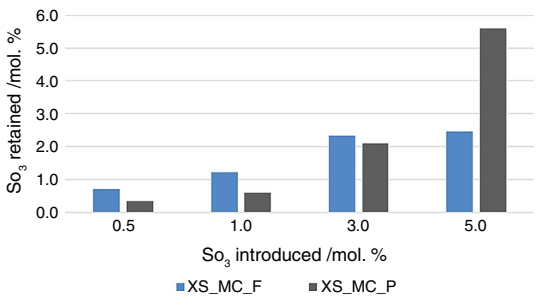


Fig. 2 Sulfate capacity of the as-synthesized glasses compared to that of analogous materials obtained through melt cooling on a steel plate (the XS_MC_P series of samples)

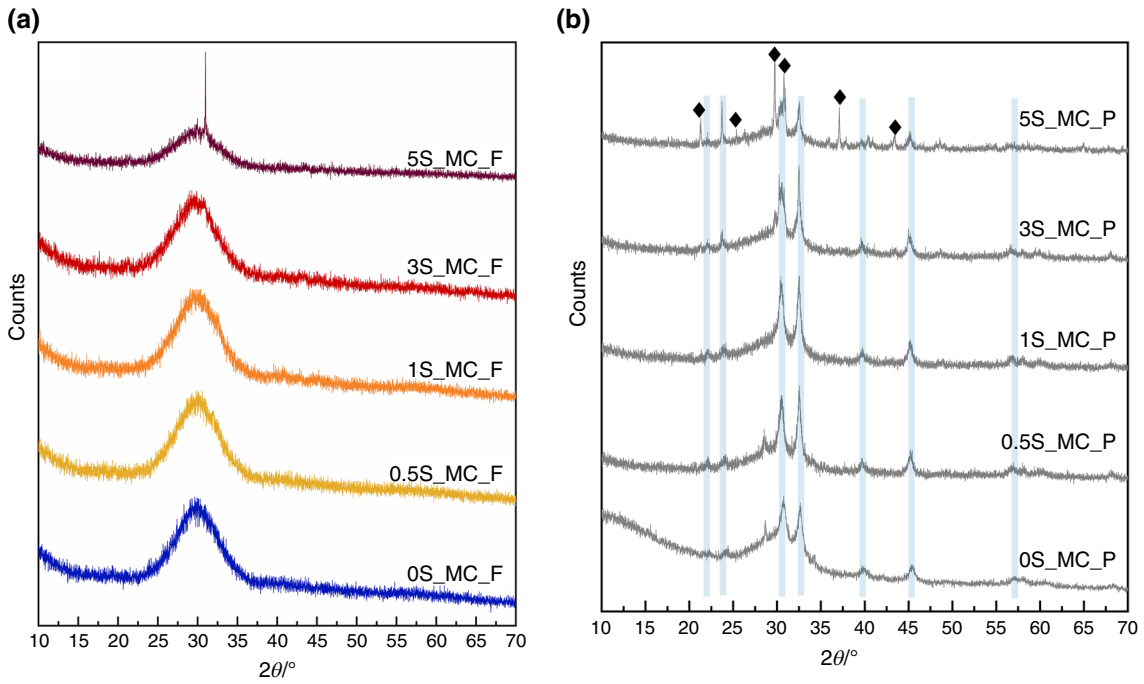


Fig. 3 X-ray diffraction patterns of the as-synthesized glass samples (**a**), along with the diffraction patterns of analogous materials obtained through melt cooling on a steel plate (the XS_MC_P series of samples, (**b**)). The diffraction peaks corresponding to the phase of $KCaPO_4$ (ref. 00-033-1002) are marked with light blue lines, while those characterizing the phase of K_2SO_4 (ref. 98-007-9777) are represented by black rhombi. It should be noted, that the reflection positioned at approximately 28.7°, observed in the X-ray patterns of both the 0S and 0.5S_MC_P samples, has not been assigned to any specific phase due to the absence of additional characteristic features and the limited information provided by this single peak

Such a phenomenon is not observed in the case of samples obtained through melt-fritting, which demonstrates the superiority of this process over plate-cooling.

It is of utmost importance, especially for glasses intended for contact with biological solutions, that they possess a fully amorphous character, since the presence of crystallites within the glass volume leads to a reduction of its chemical activity [32, 33]. Therefore, in order to verify the amorphous nature of the obtained samples, X-ray diffraction (XRD) method was employed, the results of which are presented in Fig. 3.

The addition of sulfate species (0.5−5 mol.%) into the base glass resulted in fully amorphous materials as revealed by XRD analysis (Fig. 3) as long as the sulfate loading does not exceeded 3 mol.%—beyond this threshold value a low-intensity reflection is visible on the broad amorphous halo of the respective sample (~ 30.97°), while above this level, at the same 2θ position, a well-defined narrow and sharp peak manifest itself on the still-raised background of the 5S_MC_F sample diffraction pattern. As the observed reflection is accompanied only by one additional peak (~ 30°) its origin cannot be accurately determined based on the available database. However, when comparing the position of these features to the 100% and 70%-intensity peaks of the potassium sulfate phase (30.99°, Ref. code: 98-007-9777), it can be reasonably inferred that it is precisely the K_2SO_4 crystallites that are present in the volume of the studied sample as soon as the inherent sulfate-capacity of this very system has been exceeded.

It is noteworthy to compare the X-ray diffraction patterns collected for the acquired samples with those measured for the materials of the analogous composition, but acquired through cooling the respective melts on a steel plate. Intriguingly, even in the base sample (i.e., without sulfate loading), discernible diffraction peaks are present, overlapping with a relatively high background featuring a characteristic halo at approximately 30°. Furthermore, in conjunction with the addition of SO_3, a simultaneous decrease in the background and an increase in peak intensities are observed, indicative of an elevated degree of crystallinity in plate-quenched materials. It is therefore clear that the cooling rate possible to achieve with the use of the plate-quenching method is insufficient to impede the ordering of structural elements into stable phases. On the contrary, exploiting the technique of fritting the melts in cooling medium (water) allows one to achieve the suitable conditions that promote the formation of pure amorphous solids.

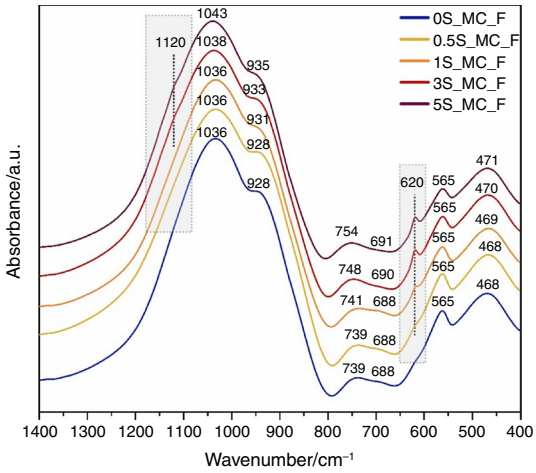


Fig. 4 Middle-infrared spectra of studied silicate-phosphate glasses

FTIR spectroscopy

It is widely acknowledged that the lack of long-range order in glasses prevents the application of X-ray diffraction analysis for investigating their structure. Nevertheless, characterization of the structural groups present in the obtained materials, as well as their variation with the sulfate addition, has been accomplished through the analysis of samples' vibrational spectra collected by means of two complementary techniques: FTIR and Raman spectroscopies. The results of the former are depicted in Fig. 4.

The FTIR spectrum of the sulfate-free, base glass (blue-colored, Fig. 4) exhibits three broad spectral features in the region between 1400 and 400 cm^{-1}, representing a superposition of bands attributable to various vibrations of silica and phosphorus oxygen bonds. Specifically, the following bands may be observed [34–37]:

- 1036 cm^{-1}—comprising the most intense spectral feature and resulting from a combination of Si–O (Si), Si–O(P) as well as P–O(P) asymmetric stretching modes;
- 928 cm^{-1}—representing the cation-modifiers-induced band, attributable to the asymmetric stretching vibrations of Si–O^- as well as P–O^- groups, the presence of which is a result of breaking Si–O–Si and P–O–P bridges;
- 739 cm^{-1} and its low-wavenumber shoulder at 688 cm^{-1}—constituting an overlap of the bands originating from symmetric stretching modes of oxygen bridges such as Si–O–Si and P–O–P;
- 565 cm^{-1}—ascribed to the O–P–O bending vibrations in PO_4^{3-} tetrahedra;
- 468 cm^{-1}—being an effect of rocking motion of the bridging oxygen atoms in the O–Si–O linkages, perpendicularly to the plane.

The presence of sulfate species manifests itself on the spectral envelope first in the form of a high-wavenumber shoulder on the 565 cm^{-1} feature (0.5S_MC_F sample), only to develop as a distinctive peak localized at 620 cm^{-1} as soon as 1 mol.% of $[SO_4]^{2-}$ is added to the glass batches. The intensity of this particular bands notably increases together with the increase of sulfate content, while its origin can be found in asymmetric bending vibrations (δ_{as}) of $[SO_4]^{2-}$ tetrahedra [9]. In the spectra of samples containing a minimum of 3 mol.% of sulfate species, an additional infrared-active sulfur-related vibration mode may be detected. This particular feature, appearing as a high-wavenumber shoulder on the most intense absorbance band (~1120 cm^{-1}), corresponds to the asymmetric stretching vibrations (υ_{as}) within the $[SO_4]^{2-}$ tetrahedra [9].

Seemingly, besides marking its presence in the respective spectra, the addition of sulfate species does not induce considerable alterations to the structure of studied materials (Fig. 4). However, a close examination of the acquired data shows that an incorporation of the increasing amounts of this particular component provokes subtle shifts of 1036, 928, 739, 688 and 468 cm^{-1} bands (that is bands related to vibration modes of the network formers-involving linkages) in the higher wavenumbers direction. Although this phenomenon is widely accepted as an indicator of increasing degree of glass network polymerization, considering the nuance of the observed changes, a complementary technique—Raman spectroscopy—was employed. It was thus assumed that Raman spectroscopy, being more sensitive to collective vibrational modes involving multiple atoms, would provide a deeper insight into the influence of sulfur on the evolution of the studied glasses' structure.

Raman spectroscopy

In order to gain an understanding of the effect of sulfate addition on the evolution of glass structure, the Raman data analysis should begin with the spectrum of pristine glasses. As can be seen in Fig. 5 the profile of the sulfur-free sample (0S_MC_F) is characterized by the presence of three distinctive regions: the high-, mid- as well as low-frequency area. The first of the foregoing, localized between 1200 and 800 cm^{-1}, is dominated by prominent bands, the broad character of which originates from the convolution of features associated with Si–O and P–O stretching vibrations. The energy positions of these very features, characteristic for network modifiers-containing glasses, is the higher, the less non-bridging oxygen atoms is linked to a silicate/phosphate tetrahedral unit [38]. The mid-range wavenumbers area (800–500 cm^{-1}) comprises bands of much less intensity that, according to the study of McMillan [38], are evident in all the classes of silicate units (disilicate, metasilicate as well as pyrosilicate) with the exception of those devoid of bridging

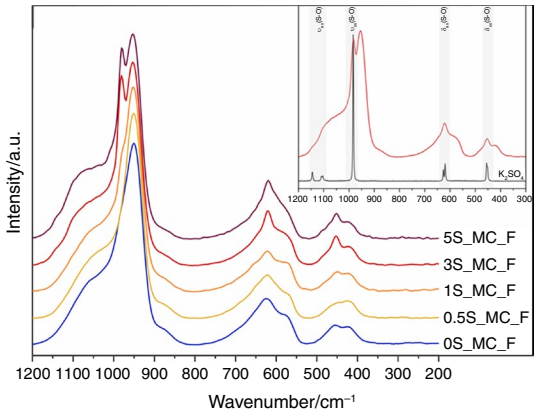


Fig. 5 Raman spectra obtained for the tested glasses, together with a comparison of band positions between the spectrum of crystalline K_2SO_4 and the spectrum of the selected sample—3S_MC_F (top right corner)

oxygen atoms—orthosilicate groupings. This particular observation indicated that it is the presence of Si–O–Si linkages in the structure which gives rise to the bands in the mid-frequency region and allowed to ascribe the main feature of this area to vibrations of inter-tetrahedral linkages [38, 39]. Based on the author's previous findings as well as existing literature relating to the glasses of similar composition, the last unascribed, shoulder-like, band of this waveforms area together with both of the low-intensity features constituting the low-frequency range should be attributed to the oscillations in ortho- (~420, 570 cm^{-1}) and pyrophosphate units (~470 cm^{-1}) (Fig. 5) [15, 40].

The addition of increasing amounts of sulfur into the studied glasses gives rise to the emergence of new bands in each of the frequency ranges, as seen in Fig. 5. Specifically, new bands at 1145^{-1} and 982 cm^{-1} appear in the high-frequency range, while in the mid- and low-frequency ranges, bands located at 618 and 460 cm^{-1}, respectively, were detected. The interpretation of these sulfur-related bands was performed by comparing them with spectral features of crystalline potassium sulfate (Fig. 5 above), which exhibits four basic vibrational modes of $[SO_4]$ tetrahedra. These modes include asymmetric S–O stretching modes at 1145 and 1107 cm^{-1}, symmetric S–O stretching modes near 984 cm^{-1}, asymmetric S–O-S bending modes at about 620 cm^{-1}, and symmetric S–O–S bending modes near 455 cm^{-1}. Notably, the S-related bands in the spectra of doped glasses correlate precisely to those detected for crystalline K_2SO_4 (Fig. 5 above). Thus, it may be assumed that sulfur exists in vitreous silicate-phosphate materials exclusively as sulfate anion, creating domains of structure comparable to that of crystalline sulfate. This conclusion is supported by the presence of distinct and well-defined sulfate-related bands appearing on the spectra of studied glasses as soon as 1 mol.% of $[SO_4]^{2-}$ species is present in their structure. Moreover, there are no spectral features assignable to more reduced sulfur species.

An initial analysis of the obtained spectra gives the apparent impression that, aside from the above-mentioned emergence of sharp and polarized sulfur-related features which significantly intensify as the sulfur content rises, the introduction of this element into the glass composition does not affect the vitreous framework. Nonetheless, a detailed analysis of the data reveals that as the sulfate content increases, a systematic shift of the high-frequency range bands toward the higher-energy positions may be observed, which is a generally acknowledged signal of silico-oxygen subnetwork polymerization. A confirmation of the foregoing may constitute the fact that along with sulfate loading the 800–500 cm^{-1} profile moves in the direction of lower wavenumbers (Fig. 5). Given that the energy positions of the bands constituting the mid-frequency range are the lower, the more bridging oxygens is present in the silicate structural unit, the detected shift implies an increase in the network connectivity of silicate subnetwork [38, 39]. Furthermore, noteworthy is the fact the intensity of the spectral features corresponding to the oscillations of orthophosphate units (~570 and 420 cm^{-1} bands) gradually increases, while those associated with the vibrations in the pyrophosphate groupings (~470 cm^{-1}) diminishes along with $[SO_4]^{2-}$ loading. Based on this observation, one may say with some confidence that while the addition of sulfate species induces an increase in the degree of polymerization of the silicon-oxygen sub-network, as regards the phosphor-oxygen one the observed effect is entirely opposite—a decreasing intensity of Q_P^1 at the expense of the Q_P^0 groupings implies that the connectivity of phosphor-oxygen framework slightly decreases along with $[SO_4]^{2-}$ incorporation.

Although the as-obtained spectra can give the general outlook on the glass structure evolution exerted by the introduction of sulfate species, it is believed that much more information may be extracted from the Raman data by the virtue of deconvolution procedure, separating such unresolved envelopes into individual component bands. Considering that the bands within the high-frequency envelope can convey both qualitative and quantitative information about individual silicate and phosphate structural units [41–43], and that, according to literature data, the mid-range features are sensitive to the Si–O–Si bond angle [38], the authors targeted the 1200–800 cm^{-1} range for the spectral decomposition process.

To decipher the acquired glass spectra the individual bands of selected profiles were approximated by Gaussian lines which are commonly used to model the broad distribution of both bond angles and distances in vitreous materials and are expected to accurately represent the spectral features. An exception to this approach was made for bands related

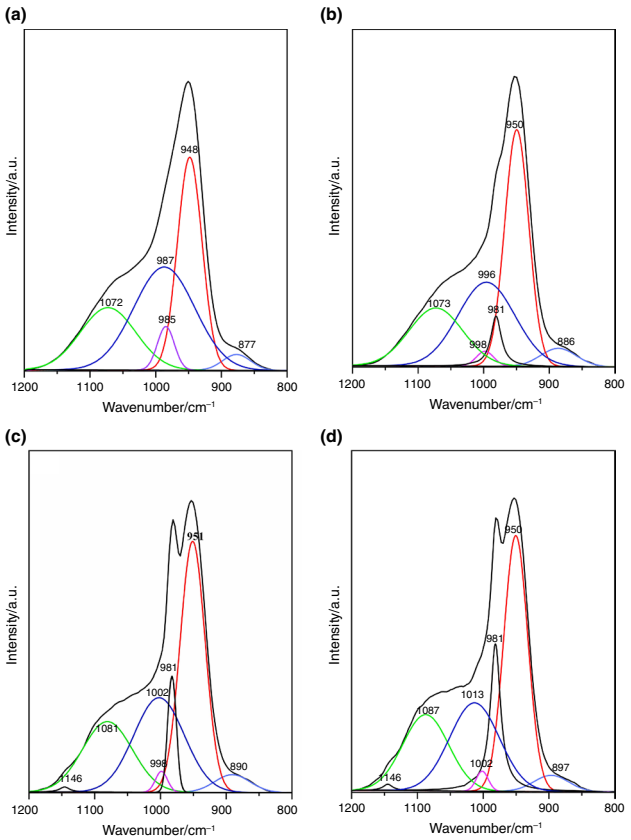


Fig. 6 Deconvoluted Raman spectra of selected silicate-phosphate glasses containing, from the left: 0% mol. SO_3, (base glass), (**a**); 1% mol. SO_3, (**b**); 3% mol. SO_3, (**c**); and 5% mol. SO_3, (**d**)

to sulfate species. Due to the known positions and limited distribution of S–O bond length and O–S–O bond angles, the spectral features associated with sulfur were modeled using Lorentzian functions [44].

The deconvolution procedure revealed the presence of five component bands in the spectrum of the sulfate-free glass (Fig. 6a–d) observed at 877, 948, 984, 986, and 1072 cm^{-1}. The interpretation of the detected features was based on the fact that the high-frequency spectral region of alkali and alkaline earth silicate-based glasses can be approximated by a certain combination of highly polarized Raman bands. These very bands, observed at 1100–1050 cm^{-1}, 1000–950 cm^{-1}, near 900 cm^{-1}, and near 850 cm^{-1}, dominate at disilicate, metasilicate, pyrosilicate, and orthosilicate compositions, respectively. From the foregoing it follows that the features localized at approx. 870, 990 and 1070 cm^{-1} originate from the symmetric silicon-oxygen stretching motions of silicate units that contain SiO_4 tetrahedra with three ($-SiO_3$ groups), two ($=SiO_2$ groups) and one ($\equiv SiO$ groups) non-bridging oxygens. It should be emphasized here that besides the silicate units, phosphate units are also present in the structure of the materials from the studied system, and must be taken into consideration when interpreting the obtained data. Therefore, given that vitreous P_2O_5 is considerably stronger Raman scatterer in comparison to v-SiO_2 [45] and hence—its bands manifest themselves on the Raman spectra in the form of well-defined features—the intense feature localized near 950 cm^{-1} should be assigned to Q^0_P orthophosphate units [42]. The final uninterpreted low-intensity band in the high-frequency region, localized at about 984 cm^{-1}, may originate from asymmetric stretching vibrations of P–O bonds in pyrophosphate Q^1_P units, the presence of which was suggested by the feature at around 470 cm^{-1} in the low-wavenumber region. As increasing amounts of sulfur were introduced into the structure studied glasses, not only did sulfate-related bands manifest themselves in the respective spectra and systematically increased in intensity (Fig. 6), but also the presence of sulfur species brought about some changes, particularly in the silico-oxygen subnetwork. It is noteworthy that all silicate structural units, namely Q^1_{Si}, Q^2_{Si}, and Q^3_{Si}, shifted in the direction of higher wavenumbers with increasing sulfur loading, confirming the previously suspected increase in the degree of polymerization of this particular framework. Apparently, the sulfur-related changes pertain also to phosphor-oxygen framework of tested materials since parallel with $[SO_4]^{2-}$ incorporation the slow diminishing of Q^1_P band may be observed.

To enable a quantitative investigation of the tested glasses' structure, an approach proposed by Wu et al. was adopted [41]. According to this method, the area of a given silicate unit-related band does not entirely reflect the actual content of Q^n due to the Raman scattering cross section in Raman spectra testing. Therefore, to calibrate the integrated Raman intensity caused by scattering, compositional-independent Raman scattering coefficients were used, as defined below:

$$S_n = \left(A_n/X_n\right)/\left(A_0/X_0\right), \quad n = 0, 1, 2, 3, 4$$

where S_n, A_n, and X_n denote the Raman scattering coefficients of Q^n, the peak area related to a given Q^n, as well as the molar fraction of Q^n, respectively. For the calculations of molar fractions of silicate units the Raman scattering coefficients calculated by Wu et al. [41, 46] were adopted (S_1, S_2, S_3, and S_4 equals 0.514, 0.242, 0.09, and 0.015, respectively). Given that there are limited data as regards the Raman scattering coefficients pertaining to various Q^n_P species, to represent the variations in the abundance of PO_4 structural units the following equation: $X_0/X_1 = A_0/A_1$ was used [42, 43]. The findings of this analysis are presented in Table 2 and Fig. 7.

Based on the results of the calculations presented in Table 2 and Fig. 7, it is clear that although an increase in the amount of sulfate introduced into the studied materials does not affect the concentration of Q^1 silicate groupings,

it causes a shift in the abundance of Q^2 and Q^3 units in the favor of the latter. It should also be emphasized that, considering the diminishing Q_P^1/Q_P^0 ratio, phosphor-oxygen subnetwork decreases in connectivity along with $[SO_4]^{2-}$ loading, which is in accordance with the previous observations.

The phenomenon of the opposing effect of sulfates on the silico-oxygen and phosphor-oxygen subnetworks, which was not observed in previous studies on similar materials, can be explained as follows: an in-depth analysis of the acquired spectra reveals that the concentration of Q_P^0 species increases at the expense of the Q_P^1 species. This is evident from the increase in the band originating from the oscillations of P–O pairs of Q_P^0 units and the concurrent decrease in the band assigned to the vibrations of such linkages belonging to Q_P^1 groupings. Such an observation unequivocally implies depolymerization of the phospho-oxygen subnetwork parallel with sulfate incorporation. This can be explained based on the study of Mysen et al. [43], who suggested that a change in silicate subnetwork polymerization is closely connected to the change in phosphate speciation. Oxygen species are exchanged between these types of groupings, so as soon as one becomes more polymerized, the connectivity of the other decreases [43]. Precisely such a phenomenon may be occurring here—the excess oxygen species lead to depolymerization of the phosphate subnetwork, observed as increased abundance of Q_P^0 groupings.

Interestingly, no such behavior was observed in our recent study [47] on similar materials that differed only by the lack of CaO network modifier oxide. A possible explanation for this discrepancy may be attributed to the diverse surroundings of phosphate units in both compositions. In the recent study, these groupings were charge-compensated by magnesium and potassium cations of coordination numbers (CN) 4 and/or 6 and 8, respectively, whereas in the present study, calcium ions, commonly known for their high affinity to phosphorus (CN ~ 6), play this role. It may be concluded then that although the number of high coordination number modifiers is enough to compensate for the excess oxygen species in the former case, the coordination environment of the latter is insufficient to fulfill this role. This results in an increasing O/P ratio and, as a consequence, the observed transition of $[P_2O_7]^{4-}$ complexes to $[PO_4]^{3-}$.

Thermal investigation of synthesized materials

Considering the vital role ascribed to avoiding crystallization of soil-active glasses, an attempt has been made to get a deep understanding of crystal phase formation process inside the amorphous structure of sulfate-bearing glasses. Therefore, on the basis of the DSC measurements, the characteristic glass temperatures have been determined, specifically: the glass transition temperature (T_g), the crystallization onset (T_x), and maximum temperature (T_c), as well as the melting temperature (T_m), which, due to great sensitivity to alterations in the chemical composition of the glass, allow one to track any changes in its thermal properties. The results of such thermal studies of acquired glass samples are presented in Fig. 8 as well as in Table 3.

Table 2 The molar content of individual silicate units in glasses characterized by increasing sulfur content, along with the relationship between Q_P^1 and Q_P^0 groupings in the tested materials

No	Q_{Si}^1	Q_{Si}^2	Q_{Si}^3	Q_P^1/Q_P^0
0S_MC_F	0.01	0.39	0.59	0.14
0.5S_MC_F	0.02	0.36	0.61	0.10
1S_MC_F	0.02	0.35	0.62	0.05
3S_MC_F	0.02	0.33	0.65	0.04
5S_MC_F	0.02	0.31	0.67	0.04

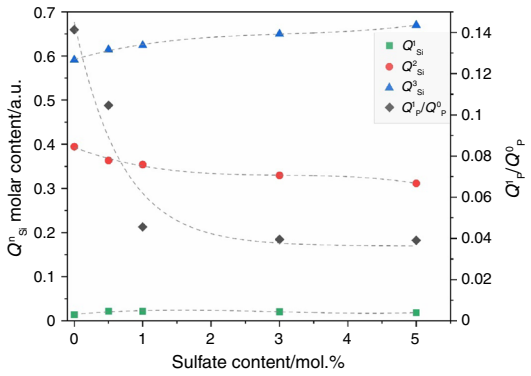


Fig. 7 Dependence between the molar content of individual silicate units and sulfate content, along with the changes in the Q_P^1/Q_P^0 ratio resulting from the addition of this component

The thermal investigation results (Fig. 8, Table 3) clearly demonstrate that the presence of increasing sulfur amounts in the structure of samples representing the tested system is mirrored in the acquired DSC curves as systematic changes in the positions of the glass transition temperature (T_g), exothermic crystallization peaks (T_c), and endothermic effect connected to melting of formed crystallites (T_m). The first trend to be noticed is that with the incorporation of $[SO_4]^{2-}$ species, a progressive shift of T_g toward higher temperature values takes place. The observed phenomenon is commonly attributed to an increasing degree of glass framework polymerization, since the augmentation of Si–O–Si cross-linking bridges strengthens the glass structure, thereby rendering the transition from a rigid solid state to a viscoelastic one more energetically demanding. Taking into account the results of structural investigations of glasses from the tested system (see "FTIR spectroscopy", "Raman spectroscopy" sections), the proposed theory appears to be well justified.

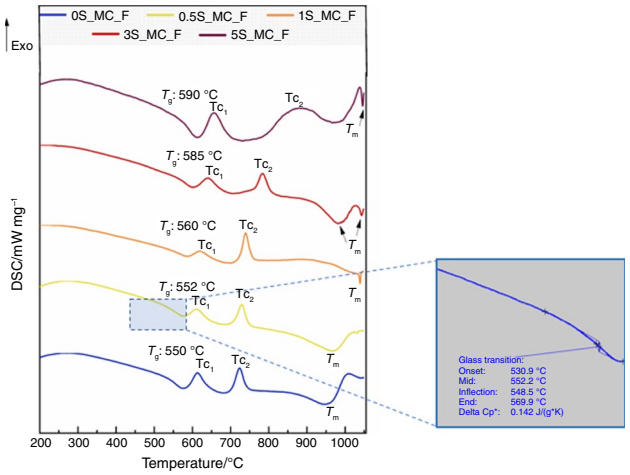


Fig. 8 DSC curves of the studied sulfate-bearing glasses recorded at a heating rate of 10 °C min^{-1}. On the right: an exemplary determination of the glass transition temperature in the Proteus software

Another trend that can be deduced from the obtained DSC curves relates to the changes in the molar heat capacity (ΔC_p) values of the obtained materials (Table 3). It is evident that the addition of the initial portion of sulfate species to the glass batches leads to a significant decrease in this peculiar parameter. However, as the loading of $[SO_4]^{2-}$ continues, the ΔC_p values systematically increase. In order to interpret such a phenomenon, it is important to mention that the value of ΔC_p serves as a measure of the degree of structural changes occurring during glass transformation and the glassy state's ability for stress relaxation, as discussed by Stoch et al. [48, 49]. Considering the above, the observed decrease in molar heat capacity in glasses loaded with the lowest tested amount of SO_3 can be attributed to the high covalency of bonds within the sulfate groups present in the voids of the vitreous network. These directional linkages may lead to higher internal structural strains, the accumulation of which results in higher energy accumulated in the glass network and less energy needed to break the bonds at the glass transition temperature. As gradual sulfate introduction induces a polymerization effect on the structure of the studied glasses, the subsequent increase in ΔC_p values can be attributed precisely to the enhanced connectivity of the vitreous framework, necessitating more energy for rearrangement during the glass transition.

Meanwhile, the characteristic glass parameters describing crystallization process, namely T_x (the onset of glass crystallization), T_{c1} as well as T_{c2}, undergo a gradual shift toward higher temperatures (Fig. 8) along with the introduction of increasing amounts of sulfate species into the glass batches. It is known that the crystallization of amorphous solids starts with the formation of crystals composed of chemical components relatively weakly bounded in the structure and easy to be free and mobile, and in consequence, the temperature of beginning of crystallization, and order of the crystal phases formation as well as its crystallization rate is determined by the strength of the chemical bonds in the structure of glass. Therefore, the observed trend in foregoing parameters should be interpreted as a manifestation of the formation of increasing amounts of strong Si–O–Si bridges and, again, confirms the theory regarding the polymerizing effect of sulfate addition on the silico-oxygen subnetwork of tested glasses.

In order to deepen the above-presented thermal characteristics of amorphous materials, based on the set of glass-specific temperatures, a complementary approach has been adapted, in which the relative positions of these effects are used to evaluate the thermal behavior of glasses. This very approach exploits certain formulas, developed by glass scientists, to numerically express the thermal stability of glasses, or, to be precise—the resistance of vitreous solid against devitrification on heating.

For the purposes of the present study, three quantitative measures of thermal glass stability (GS parameters) were selected, namely Angell's (K_A), Hruby's (K_H), as well as Weinberg's (K_W) parameters, defined by the following formulas (the symbols used in the equations correspond to the characteristic temperatures described in earlier considerations):

$$K_A = \left(T_x - T_g\right), [50]$$

$$K_H = \left(T_x - T_g\right)/\left(T_m - T_x\right), [51]$$

Table 3 Values of the characteristic temperatures and molar heat capacity of all the tested materials along with the calculated glass stability parameters

Sample	Temperature/DSC					Parameter			ΔC_p/ J g^{-1} K^{-1}
	T_g	T_x	T_{c1}	T_{c2}	T_m	Angell/K_A	Hruby/K_H	Weinberg/K_W	
0S_MC_F	550	586	613	723	947	36.1	0.100	0.038	0.375
0.5S_MC_F	552	586	611	729	969	34.2	0.089	0.035	0.142
1S_MC_F	564	594	618	739	1039	29.5	0.066	0.028	0.182
3S_MC_F	584	613	641	783	982 1043	29.4	0.080	0.030	0.285
5S_MC_F	589	625	657	880	1046	36.3	0.086	0.035	0.290

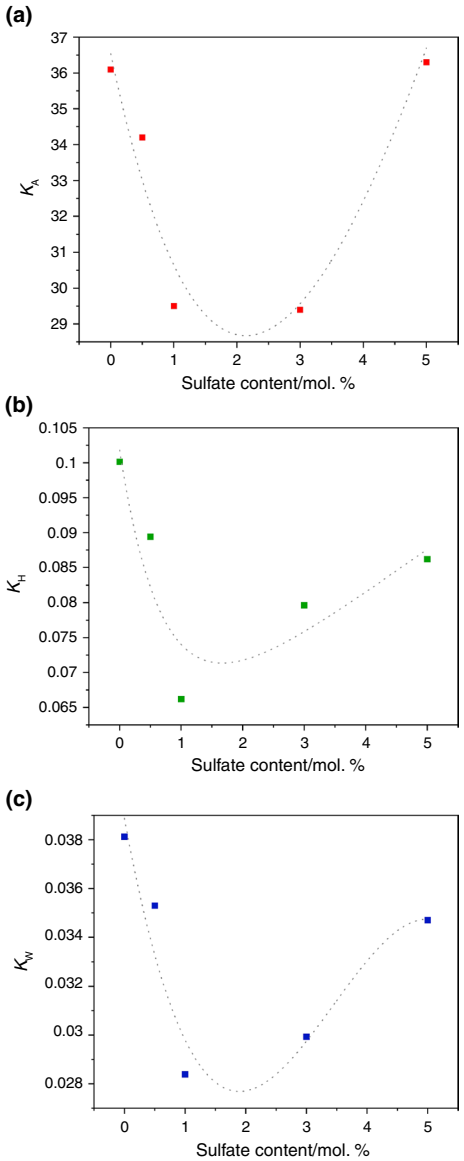


Fig. 9 Changes in the values of thermal stability parameters of the synthesized glasses: Angell (**a**), Hruby (**b**), and Weinberg (**c**) as a function of sulfur content in the materials' structure

$$K_W = \left(T_x - T_g\right)/T_m), [50]$$

It needs to be emphasized that the higher the values of all the adapted parameters, the higher is the stability of a glass against devitrification on heating. Meanwhile, the results presented in Fig. 9 clearly suggest that a progressive increase in sulfate content in the structure of tested glasses is followed by a subsequent decrease in each of the examined GS parameter. This trend continues until the amount of sulfur species reaches a value of 1 mol.%., after which the investigated properties begin to exhibit an increasing tendency. In order to explain this peculiar phenomenon it needs to be recalled that introduction of $[SO_4]^{2-}$ species to the glass structure augments the number of covalent bonds, which consequently leads to increasing rigidity of the glass' internal framework. Consequently, together with an increase of temperature, the formation of strains inside the structure proceeds, unloading of which is only possible through cracking of the bonds. This, in turn, leads to the decomposition of the vitreous framework and induces the process of glass crystallization.

On the other hand, an augmented network connectivity of glasses containing higher amounts of sulfate species, and hence—an increased strength of more polymerized chains—is in all likelihood the factor responsible for a higher energy barrier for the transformation of the glassy state into a crystalline state. As a result, the glass is less likely to undergo devitrification, which is mirrored by increased values of GS parameters in the case of samples loaded with both 3 and 5 mol.% of SO_3.

To summarize this section, it should be emphasized that the polymerizing influence of added sulfate groupings on the silicate-phosphate vitreous matrix is reflected in the changes of all the discussed parameters describing the thermal behavior of the glasses. Even though the initial addition of sulfur manifests itself through a decrease in certain investigated variables (ΔC_p, GS parameters), the increasing presence of strong Si–O–Si bonds, leading to the formation of an interconnected structure, hinders the glass from undergoing structural rearrangement and crystallization.

Analysis of the devitrificates

XRD study

It is known that the devitrification process can significantly impact the properties of amorphous materials, especially those, intended for interactions with biological fluids, by inhibiting the ability of the glass to release the useful ions, impacting their mechanical strength or degradation behavior. Therefore, it is believed that understanding the devitrification process allows one for better control and optimization of the manufacturing processes for glasses in order to develop strategies to either promote or inhibit devitrification based on the desired properties of the final product. In light of the foregoing following section contain the results of comprehensive analysis of devitrificates acquired through heat-treatment of glasses from the studied composition collected by means of XRD, Raman Spectroscopy Imaging and XAS techniques.

The results of the first mentioned technique—XRD analysis of the obtained materials combined with the Rietveld refinement tool to extract the quantitative information about the crystalline phases existing within the vitreous matrix—are presented in the figures and the table below (Figs. 10, 11, Table 4). It should be emphasized here that the data

concerning the type and, especially, the relative contributions of phases present in the residual glassy matrix after the isothermal heat-treatment process are purely indicative and should be considered with caution. This is related to the multicomponent nature of the materials from the tested system, and, as a result, the possibility of phase interactions such as numerous substitutions within the crystalline phases by different atoms present in the glass, leading to peak shifts, broadening, or splitting, as well as the high proportion of residual amorphous phase, which can mask or interfere with the diffraction peaks from the crystalline phases, making their identification and quantification more challenging.

The process of crystallization of vitreous materials, being in a liquid state of low viscosity, is primarily governed by three factors: the concentration of components in the melt, the Gibbs free energy of compound formation (ΔG_f^0), as well as the crystallochemical factor [52–54]. The second determinant mentioned above expresses the system's tendency to reach a state of minimal energy and, therefore, the probability of forming a specific crystalline phase, based on the chemical affinity between the components in the system. Meanwhile, the last of the above-listed factors—the crystallochemical one—constitutes an indicator of the strength of chemical bonds in the glass and can be expressed numerically as the difference in bond ionicity values (i_G) between oxygen and cations linked in a given oxygen bridge. Importantly, the smaller the difference in bond ionicity, the weaker the strength of the corresponding oxygen bridge, making it easier for these bonds to break during the glass crystallization process. Considering the above, it is not surprising that the primary crystallization product observed in all the investigated materials, regardless of the thermal treatment temperature, is dicalcium silicate alpha, characterized by the most negative ΔG value and composed of components connected by relatively weak and easy-to-break bonds (Tables 5, 6). Furthermore, since the Δi_G values of both magnesium and calcium cations with the silicate subnetwork are the lowest among those, listed in Table 6, the presence of protoenstatite and monticellite phases, as glass crystallization products in the lower temperatures range, is also well-justified.

Meanwhile, the observed variety of the thermal treatment products, as regards glasses processed at higher temperatures, is a direct consequence of the increased mobility of components, provoked not only by higher diffusion coefficients, but also—thermal destruction of the vitreous network. According to Stoch [52], this temperature-induced increase in component mobility leads to their rearrangement into phases whose chemical composition and structure reflect microregions (domains) within the parent glass, ultimately achieving an equilibrium phase composition, corresponding to that of the glass. Therefore, in addition to the aforementioned, representing silicate domains, phases of

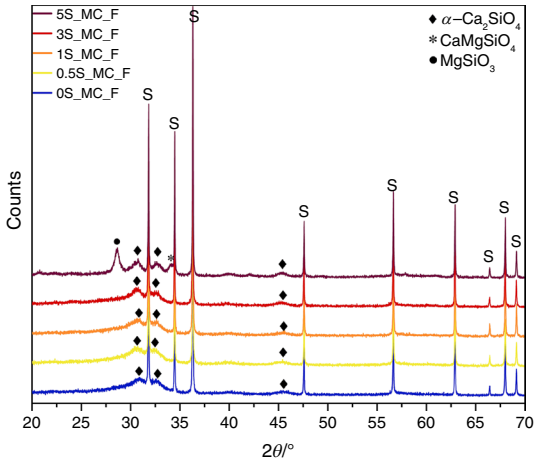


Fig. 10 X -ray diffraction patterns of the samples heat-treated at temperatures corresponding to the first crystallization peak on the DSC curves. The diffraction peaks originating from the internal standard, ZnO phase, have been labeled with the letter 'S'

dicalcium silicate, monticellite, and protoenstatite, the formation of additional ones, including calcium catena-silicate ($CaSiO_3$), dipotassium magnesium silicate (K_2MgSiO_4) and diopside ($CaMgSi_2O_6$) is observed, along with those, resulting from the ordering of phosphate (archerite, KH_2PO_4) as well as sulfate regions (dipotassium sulfate, K_2SO_4) within the glass.

The presence of the hydrogen-binding phosphate phase, as unexpected, deserves an explanation that, in all likelihood, could be as follows: the phosphate phase formed in the near-surface regions, when exposed to a humid environment, interacted with moisture from the air and, through hydrogenation reactions, facilitated the formation of the KH_2PO_4 phase. Worth emphasizing is also the presence of the sulfate phase, represented by K_2SO_4, which appears as a product of heat-treatment of all the sulfate-bearing samples processed at elevated temperatures, starting from the one modified with the smallest amount of $[SO_4]^{2-}$ ions (0.5S_MC_F) finally to this, loaded with 5 mol.% of this particular component.[1] Interestingly, the sulfate groupings present in the vitreous matrix do not contribute to the formation of phases with any of the glass components, except for potassium cations, confirming at the same time the results of the structural studies, which demonstrated that this very component is situated in the voids of the network as independent units, not linked to the silicate-phosphate network [15, 29].

[1] It should be recalled that while the presence of the K_2SO_4 phase was confidently identified based on characteristic peaks at approximately 28.0°, 20.5°, and 41.8°, obtaining a quantitative description of each crystalline phase emerged in the 5S_MC_F sample was not feasible due to the particular complexity of the corresponding X-ray diffraction pattern.

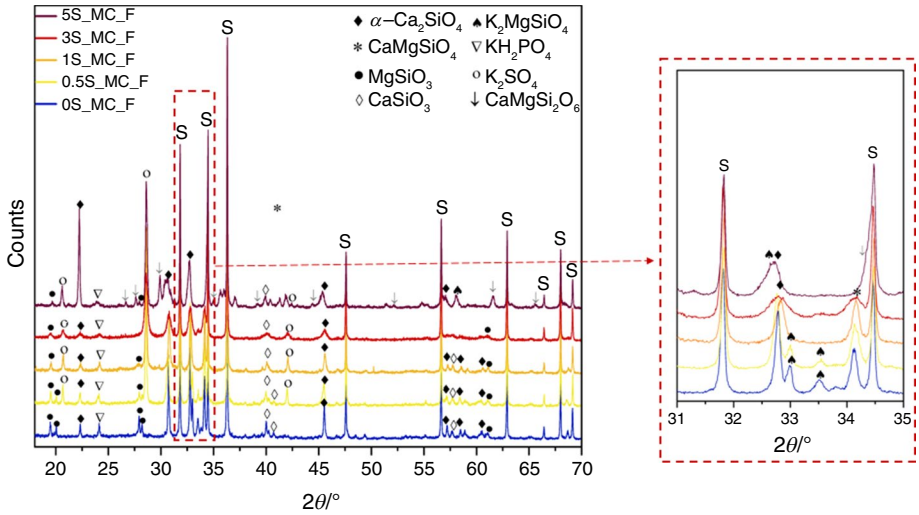


Fig. 11 X -ray diffraction patterns of the samples heat-treated at temperatures corresponding to the second crystallization peak on the DSC curves. The diffraction peaks originating from the internal standard, ZnO phase, have been labeled with the letter 'S'. On the right: an excerpt of the diffraction pattern showing the range of 31–35°

It is also worth noting that despite prolonged thermal treatment, all the tested materials exhibited a markedly high content of residual amorphous phase (94–99% and 73–89% for glasses processed at lower and higher temperatures, respectively). In light of the foregoing, it is highly probable that the preferential mechanism of studied materials' crystallization is the surface one, whereby the crystalline phase may predominantly form at the surface while the bulk of the material remains amorphous, resulting in an increased overall content of the latter in the samples. Interestingly, both in the case of glasses heat-treated at lower as well as at higher temperature ranges, the sample modified with a 3% addition of sulfate species exhibits the lowest proportion of crystalline phase (Table 4). This peculiarity should be regarded as a further evidence of the increased resistance to devitrification of this specific material, which, as a reminder, is attributed to the increasing degree of polymerization with the addition of $[SO_4]^{2-}$ anions.

Raman imaging study

For the purpose of further exploration of the obtained devitrificates, with particular emphasis on the distribution of identified phases within the material volume, the Raman Spectroscopy Imaging (RSI) technique has been employed. The surface mapping procedure was conducted on the cross sections of the selected samples: the base sample unmodified with sulfate addition, and the sample characterized by the highest investigated content of this component—5S_MC_F, both heat-treated at temperatures corresponding to the second crystallization peak on the respective DSC curves and polished to a flat surface. The resulting images, along with the Raman spectra representing the studied regions, are presented in Figs. 12, 13.

The analysis of the surface image of the base sample (Fig. 12) excluded the presence of distinct crystalline domains within the volume of the investigated devitrificate and unambiguously indicated the homogeneity of the material, despite the conducted thermal treatment process. Similar conclusions are provided by the analysis of the Raman spectrum corresponding to the studied surface area (Component 1), as it appears as analogous to that measured for the fully amorphous sample (see: "Raman spectroscopy" section). However, the presence of sharp peaks of low intensity, superimposed on the broad ones, characteristic for amorphous materials, suggested the existence of the small amounts of crystalline phase uniformly distributed within the volume of the investigated material. The positions of these peaks on the wavenumber axis (at around 665 and 1100 cm^{-1}), as well as literature data [56], indicate the highly probable presence of $MgSiO_3$ (protoenstatite) and/or $CaSiO_3$ (calcium catena-silicate) phase, giving rise to the observed narrow features in the obtained spectrum.

Similarly, on the surface of the sample loaded with the highest sulfur content (5S_MC_F), no areas representing distinct crystalline phases may be observed, and its spectrum (Component 1) exhibits close resemblance to the aforementioned spectrum of the base glass—the acquired Raman data indicate the presence of the sharp peaks corresponding to protoenstatite and/or calcium silicate phases at around 665, 1100 as well as ~ 870 cm^{-1} (Fig. 13). Additionally, the close examination of the obtained results revealed the spectral features commonly attributed to various types of vibrations in sulfate tetrahedra located around 980, 620, and 450 cm^{-1} and clearly indicating the occurrence of the sulfur-binding K_2SO_4 phase. Interestingly, the surface image of this particular sample revealed the presence of a crystalline phase situated within a crack on the glass surface (Fig. 13). The positions of the most intense peaks in the corresponding spectrum (Component 2) suggests that this very product of

Table 4 Types of crystallizing phases detected in the analyzed devitrificates heat-treated at temperatures corresponding to both crystallization peaks on the DSC curves

Sample	Phase	Formula	Reference code	Phase fraction/%
0S_MC_F	Dicalcium Silicate—alpha	Ca_2SiO_4	98-008-2998	2.2
0.5S_MC_F	Dicalcium Silicate—alpha	Ca_2SiO_4	98-008-2998	4.7
1S_MC_F	Dicalcium Silicate—alpha	Ca_2SiO_4	98-008-2998	5.6
3S_MC_F	Dicalcium Silicate—alpha	Ca_2SiO_4	98-008-2998	1.4
5S_MC_F	Dicalcium Silicate—alpha	Ca_2SiO_4	98-008-2998	2.9
	Protoenstatite	$MgSiO_3$	98-016-3891	0.6
	Monticellite	$CaMgSiO_4$	98-020-2285	0.2
0S_MC_F	Dicalcium Silicate—alpha	Ca_2SiO_4	98-008-2998	12.0
	Monticellite	$CaMgSiO_4$	98-020-2285	0.2
	Protoenstatite	$MgSiO_3$	98-016-3891	4.0
	Calcium Catena-Silicate	$CaSiO_3$	98-024-0449	0.7
	Dipotassium Magnesium Silicate	K_2MgSiO_4	98-008-32269	2.5
	Archerite	KH_2PO_4	98-002-4683	0.2
0.5S_MC_F	Dicalcium Silicate—alpha	Ca_2SiO_4	98-008-2998	13.3
	Monticellite	$CaMgSiO_4$	98-020-2285	0.3
	Protoenstatite	$MgSiO_3$	98-016-3891	5.4
	Calcium Catena-Silicate	$CaSiO_3$	98-024-0449	2.2
	Dipotassium Magnesium Silicate	K_2MgSiO_4	98-008-32269	1.8
	Archerite	KH_2PO_4	98-002-4683	0.5
	Dipotassium Sulfate (VI)—Alpha	K_2SO_4	98-000-2408	2.6
1S_MC_F	Dicalcium Silicate—alpha	Ca_2SiO_4	98-008-2998	11.8
	Monticellite	$CaMgSiO_4$	98-020-2285	0.4
	Protoenstatite	$MgSiO_3$	98-016-3891	2.1
	Calcium Catena-Silicate	$CaSiO_3$	98-024-0449	1.5
	Archerite	KH_2PO_4	98-002-4683	0.3
	Dipotassium Sulfate (VI)—Alpha	K_2SO_4	98-000-2408	2.7
3S_MC_F	Dicalcium Silicate—alpha	Ca_2SiO_4	98-008-2998	8.3
	Monticellite	$CaMgSiO_4$	98-020-2285	0.2
	Dipotassium Sulfate (VI)—Alpha	K_2SO_4	98-000-2408	2.3
5S_MC_F	Dicalcium Silicate—alpha	Ca_2SiO_4	98-008-2998	4.5
	Protoenstatite	$MgSiO_3$	98-016-3891	0.1
	Dipotassium Magnesium Silicate	K_2MgSiO_4	98-008-32269	1.4
	Dipotassium Sulfate (VI)—Alpha	K_2SO_4	98-000-2408	–*
	Diopside	$CaMgSi_2O_6$	98-003-0522	6.6

*The especially complex nature of the 5S_MC_F sample X-ray diffraction pattern, manifesting itself as the intricate features and overlapping peaks in the acquired data, hindered an accurate determination of the individual contribution of K_2SO_4 phase

crystallization has a form of orthosilicate, and, although its exact identification was challenging due to the complexity of the glass composition, considering the XRD analysis results together with literature data [57], one can deduce with some confidence that it is calcium silicate (Ca_2SiO_4) that emerged during the process of heat-treatment. It is worth emphasizing that the phenomenon of crystalline phase emergence within a crack on the glass surface is a direct consequence of an increased energy of this peculiar site compared to the bulk material, promoting at the same time the interaction of molecules or atoms with the crack surface and facilitating the reactions in the material, crystallization, as part of glass structure reconstruction and chemical component redistribution processes, being one of them.

The presence of such a minimal amount of crystalline phases in the bulk of both investigated glasses, along with its occurrence in a higher-energy sites, confirms the theory that it is the surface crystallization that constitutes the dominant mechanism of structure ordering as regards the materials from the studied system.

Table 5 Calculated Gibbs free energies of the formation of compounds from the oxides [55]

Crystalline phase	ΔG_f^0/kJ mol^{-1}		
	900 K	1000 K	1100 K
Ca_2SiO_4	− 2346	− 2376	− 2408
$MgSiO_3$	− 1613	− 1632	− 1652
K_2MgSiO_4	− 2098	− 2137	− 2180
$CaMgSiO_4$	− 2301	− 2329	− 2360
KH_2PO_4	− 2349	− 2651	− 2733
K_2SO_4	− 1135	− 1188	− 1245
$CaSiO_3$	− 1658	− 1679	− 1701

Table 6 Ionicity of the oxygen bridges present in the framework of studied materials

Type of the oxygen bridge	Δi_G	Type of the oxygen bridge	Δi_G
Mg–O–Si	0.241	Mg–O–P	0.357
K–O–Si	0.395	K–O–P	0.511
Ca–O–Si	0.279	Ca–O–P	0.395
K–O–S	0.621		

XAS study

Given the sensitivity of the X-ray absorption near edge structure (XANES) spectra to subtle variances in the materials' structure, and fact that changes exerted by the presence of $[SO_4]^{2-}$ species on the spatially polymerized silicate-phosphate network seem to be precisely the kind, an attempt has been made to track the sulfate-influenced changes in the local atomic environment of selected glass components employing the XAS technique. It should be mentioned here that the reason behind which the spectra were collected only at the magnesium and silicon K-edges is because the nearby facility operates in the range of soft X-rays enabling probing the surroundings only of the light elements. Hence, the local environments of the remaining elements constituting the internal framework of studied glasses were not possible to be investigated.

The collected spectra measured at the Mg edge of selected samples (for the measurement samples characterized by the lack of sulfate addition as well as these modified with its medium—1 mol.%—and the highest—5 mol.%—concentration have been selected) are displayed in Fig. 14a. Noteworthy is the fact that, despite the amorphous character of the tested samples, all the acquired spectra display the A-B-C triplet feature—a complex characteristic for various magnesium-bearing minerals—with the well-pronounced features A and B and the feature C appearing as a distinct shoulder at the higher-energy side of the aforesaid complex. Additionally, a broad oscillation (labeled as D, Fig. 14a) may be observed on each collected spectrum in the energy region localized about 30 eV above the absorption edge. From the in-depth analysis of the acquired data, it follows that sulfur species present in the vitreous network of studied materials do not influence the first coordination sphere of magnesium atoms, as the shapes and energy positions of both the peaks B (attributed to the electronic transition of ls to the empty bound 3p-like state within the first coordination sphere) and D (originating from the shape resonance of the first Mg-O coordination shell) remain unaltered irrespective of $[SO_4]^{2-}$ loading [58, 59]. On the contrary, peaks A and C related to the multiple scattering effects from the outermost coordination spheres around the absorbing magnesium atoms undergo slight changes along with sulfate introduction—it may be noticed that although the energy positions of these spectral features remain constant, both the former and the latter become more defined parallel as $[SO_4]^{2-}$ content increased. According to the literature such a change of these peaks' definition may be attributed to the alterations in the environment of alkali ions existing in the further proximity of the absorbing Mg atoms and this particular conclusion would be in agreement with our previous study which proved that in glasses of similar composition potassium ions adapt their localization to co-create sulfate domains once $[SO_4]^{2-}$ species are present in the structure [60].

Analogously, XANES spectra of tested glasses collected at silicon K-edge, characterized by the presence of three distinct features labeled here as A, B and C, seem not to be influenced by sulfate addition (Fig. 14b). As can be seen in Fig. 14b increasing amounts of sulfate species do not alter neither the energy position nor the overall appearance of the principal feature A, originating from the transition of Si ls electrons to the antibonding 3p-like state. Similarly the strong and broad feature designated as C and attributable to the transition of such electrons to the t_2 states occurs to one as insensitive to the presence of $[SO_4]^{2-}$ species [61, 62]. This apparent resemblance is not surprising given that both the mentioned spectral features constitute a direct consequence of the silicon first coordination sphere morphology and the commonly known tetrahedral coordination of silicon atoms by four oxygens is characteristic for the vast majority of silicates. On the other hand, the intermediate feature (labeled as B, Fig. 14b) clearly display certain discrepancies across the recorded spectra—it may be noticed that as the sulfur concentration raises, it diminishes and becomes less pronounced. To explain this peculiar phenomenon one needs to take into consideration that this shoulder-like feature stems from the 'symmetry-forbidden resonances' occurring in the distorted SiO_4 tetrahedra, in which mixing of the unoccupied 3p like features into the 3d states is possible. Noteworthy is the fact that such an asymmetry is peculiar not to the—paradoxically more regular—amorphous configurations but to the crystalline silicon

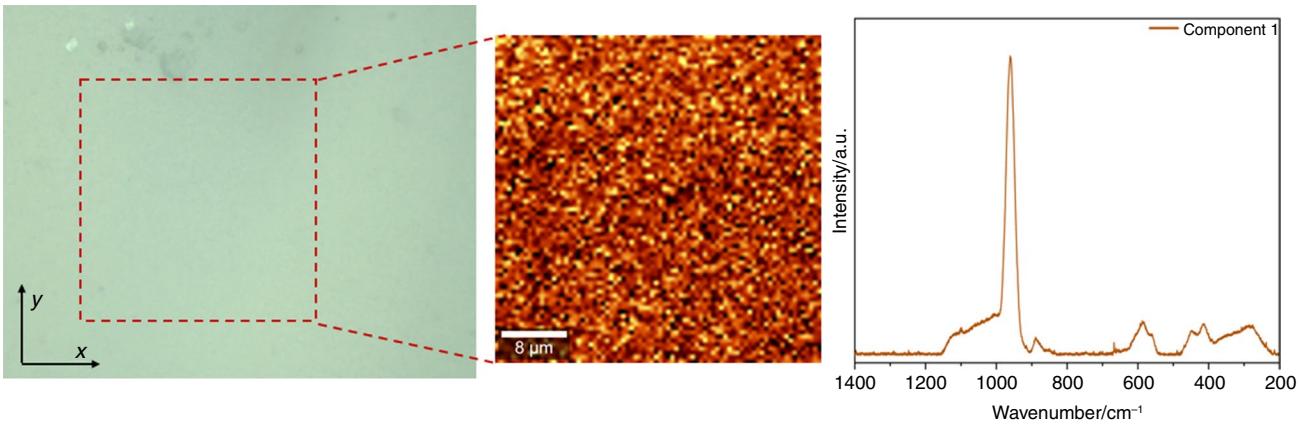


Fig. 12 The Raman maps of the surface fragment of the crystallized base glass (0S_MC_F), (left), and Raman spectra taken at detected region (right)

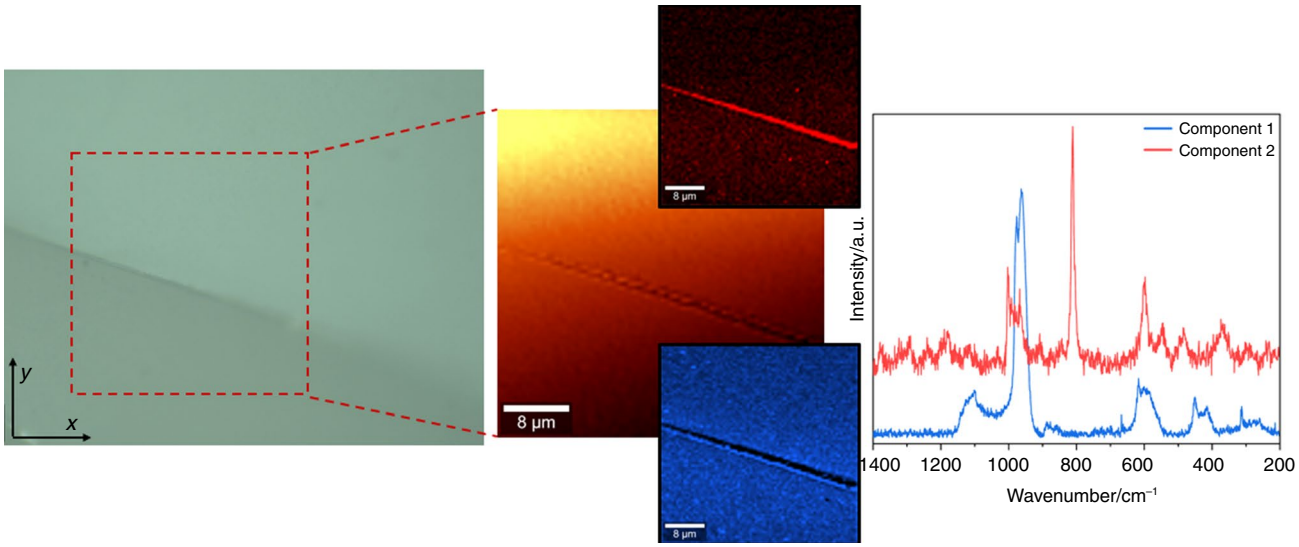


Fig. 13 The Raman maps of the surface fragment of the 5S_MC_F crystallized glass, (left), and Raman spectra taken at detected regions (right). Colors of the individual spectral lines correspond to those of surface regions, at which the data were collected

environment. Given the above, the observed diminishing of the B feature suggests that the factor causing the aforesaid distortion, most probably in the form of network modifiers, has been removed from the vicinity of glass-forming $[SiO_4]^{4-}$ anions as increasing amounts of $[SO_4]^{2-}$ species were introduced to the vitreous network of tested glasses [63].

In view of the fact that the XANES spectra are very sensitive for three-dimensional atomic configurations around the edge element, this particular method was utilized to collate data on the structure of not only amorphous but also devitrified samples.[2]

In Fig. 15a–c, Mg K-edge XANES spectra measured for the devitrified samples of synthesized glasses are presented and, analogously to the case of amorphous materials, the same A–D features may be observed in each of them. Despite the apparent similarity of acquired results an in-depth analysis showed that the conducted heat-treatment induced some changes emerging on recorded spectra: although the linewidth of the peak B remains consistent, its relative amplitude tends to increase slightly, feature A narrows and decreases in intensity while shoulder-like feature

[2] It should be emphasized that, to enable interpretation of the results, only samples heat-treated at comparable temperatures were selected for the XANES studies. Therefore, the sample with the highest sulfur content, annealed at the temperature of the second crystallization peak (approximately 890 °C), was not included in the conducted measurements.

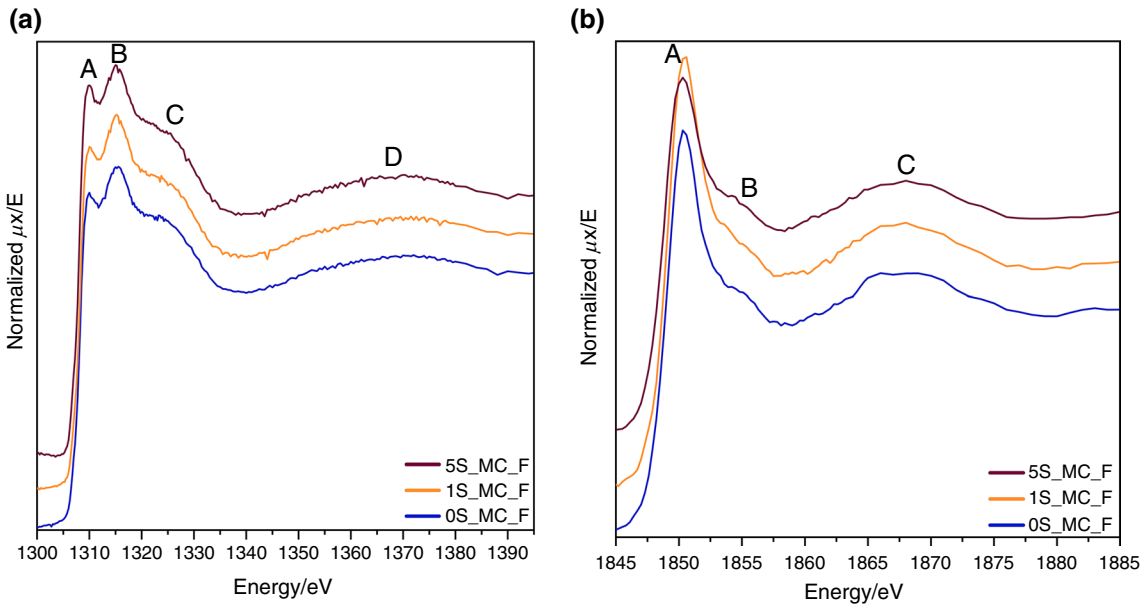


Fig. 14 Mg K-edge XANES spectra measured for the as-synthesized samples, with the main features labeled A to D, (**a**), and Si K-edge XANES spectra measured for the as-synthesized samples, with the main features labeled A to C, (**b**)

C becomes stronger and better pronounced. Noteworthy is also the fact that for the highest temperatures studied (above 730 °C) new features of weak intensities—labeled here as C' and D'—may be identified in the spectra of respective samples (Fig. 15). Judging by these spectral differences it is clear that not only the closest Mg surrounding, but also the further one, has been altered by the heat-treatment process. Since peak intensity in XAS technique mirrors the number of accessible multiple scattering pathways concerning the absorber atom as well as its first- and higher-order neighbors, the increased intensity of the peak B in heat-treated samples' spectra immediately suggest that the sites occupied by Mg become more structured parallel with temperature increase. Subsequently, according to the literature, the above-mentioned changes observed as regards the features related to the further Mg coordination spheres—A and C—may be indicative of an increased symmetry in the mean magnesium environment as well as an ordering of Mg-O polyhedra over medium-range distances within glass clusters. The presence of medium-range structural ordering extending beyond the first short-range Mg coordination sphere is also corroborated by the emergence of new features on the spectra of heat-treated samples which is the consequence of photoelectron interactions at larger distances. Worth highlighting is the fact that the above-described changes mark their presence more distinctly in the case of sulfur-free glasses' spectra while in those characterized by the highest $[SO_4]^{2-}$ amounts the influence of this peculiar addition seems much less pronounced. This particular observation corroborates the already-stated conclusion that sulfate localized in the voids of glass framework alters the local environment of magnesium cations but such an alteration is in all likelihood indirect as it involves cations of the further Mg coordination sphere.

It should be mentioned here that although the XAS technique is successfully used to deduce a coordination geometry of elements of interest, such an approach is not so straightforward as regards the Mg K-XANES, in the case of which even the subtlest modifications in the absorber's coordination environment or local electronegativity may result in remarkably different XANES spectra. However, given the high similarity between the acquired spectra of devitrified samples to those of silicates characterized by the presence of Mg in its octahedral form (diopside or protoenstatite) [58, 60] as well as the fact, that, as indicated by XRD results, such phases are among the products of induced crystallization, one may say with some confidence that Mg is mainly six-fold coordinated to oxygen atoms but the occurrence of tetrahedral magnesium units cannot be excluded.

Also, some differences between amorphous and heat-treated samples may be pointed out as regards the XANES results collected at the Si K-edge (Fig. 16). Noteworthy is the fact that all the acquired spectra show analogous evolution since both the features A and C display almost no alterations with temperature, while the shoulder-like feature B clearly becomes more distinctive and increase in intensity. The explanation lying behind the observed variations in the peak's B appearance is rather straightforward—as already stated, the intermediate features gain definition in

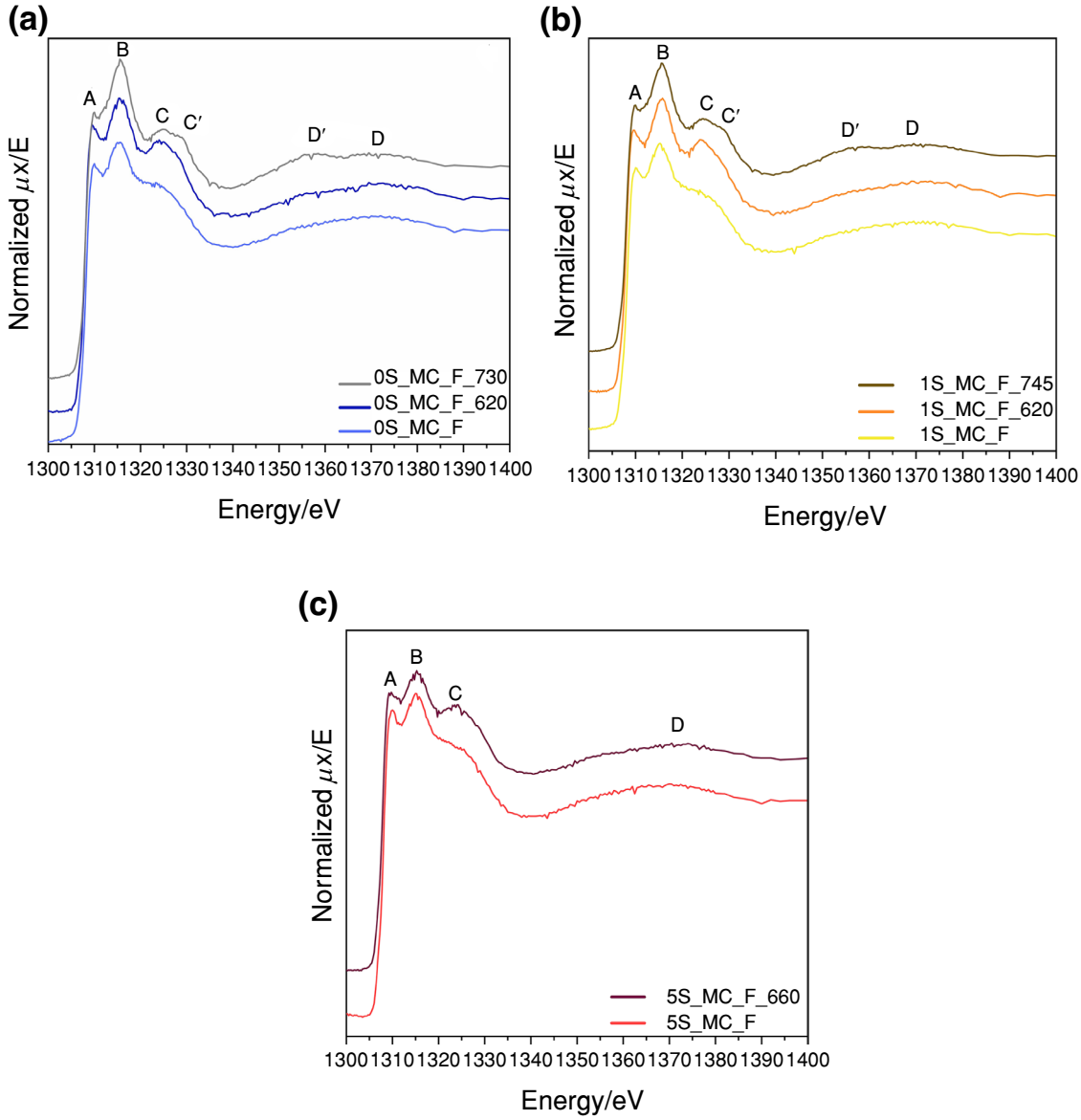


Fig. 15 The XANES spectra of the 0S_MC_F (**a**), 1S_MC_F (**b**) as well as 5S_MC_F (**c**) samples collected near the Mg K absorption edge. Lower curves represent those for the amorphous materials, where the upper ones correspond to their devitrificates, heat-treated at temperatures indicated in their sample names

the slightly distorted asymmetric silicon environment which enable spin-forbidden transitions of the 1 s electrons to the empty 3d states. Since this condition is fulfilled in the crystalline phases exhibiting structural ordering exceeding the first silicon-oxygen coordination sphere, it is not surprising that this particular feature increase in strength along with the heat-treatment temperature (Fig. 16), [63].

At the same time, the closest surrounding of silicon atoms, which, in both amorphous and crystalline silicates, consists of four oxygen atoms located at the corners of a tetrahedron, does not undergo significant changes with temperature and hence—the observed consistency of the white-line peak A as well as broad hump feature C in the spectra of heat-treated samples.

Worth mentioning here is the fact that the described changes of the feature B characteristics are less pronounced in the case of sulfate-bearing materials. By carrying on the argument regarding the relation between the prominence of this shoulder and the distortion of the SiO_4 tetrahedra it may be concluded that the presence of $[SO_4]^{2-}$ species indeed induce certain changes in the medium-range structure beyond the first coordination sphere of silicon atoms, which most probably involve the rearrangement of potassium cations in the glass vitreous matrix.

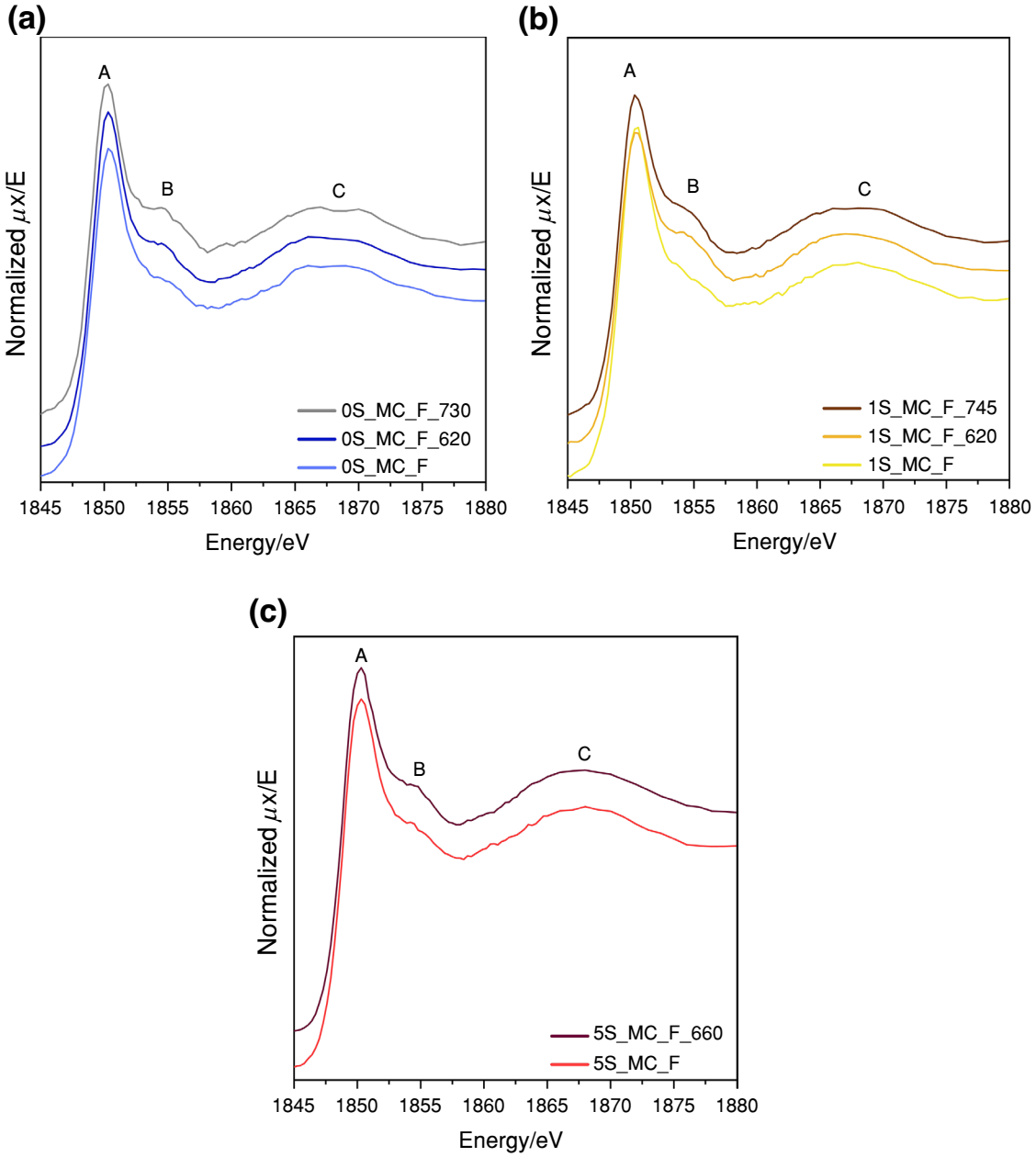


Fig. 16 The XANES spectra of the 0S_MC_F (**a**), 1S_MC_F (**b**) as well as 5S_MC_F (**c**) samples collected near the Si K absorption edge. Lower curves represent those for the amorphous materials, where the upper ones correspond to their devitrificates, heat-treated at temperatures indicated in their sample names

In-depth analysis of the acquired data showed that sulfate species present in the vitreous network of tested glasses alter the atomic configurations around the magnesium as well as silicon atoms and although the first coordination shell of tested absorbers remains intact irrespective of sulfur content, their further surrounding is evidently marked by the addition of this peculiar element. Most probably the registered changes pertain to variations in localization of potassium cations, which, in the presence of sulfate groupings, reorganize to assume the role of $[SO_4]^{2-}$ charge-compensators, reducing at the same time their concentration in the vicinity of magnesium/silicon coordination shell. Furthermore, from the XAS study it follows that both the magnesium local environment as well as the silicon one differs only by small modifications from their devitrified analogues and the observed alterations constitute a manifestation of increased degree of structural order that extended beyond the first coordination sphere of a given absorber.

Conclusions

A plethora of studies investigating sulfate-bearing silicate-based glasses have unequivocally demonstrated the arduous task of achieving fully amorphous materials when sulfur species are engaged in the formation of a spatially polymerized vitreous network. Therefore, the work presented in this article attempted to unearth the factors governing the solubility of $[SO_4]^{2-}$ anions in multicomponent silicate-phosphate glasses acquired through the process of quenching the melt in a liquid medium—a process known to be highly advantageous for vitrifying substances with a high tendency toward crystallization. Multiple analytical techniques exploited in the present study allowed to investigate the overall effect of aforementioned processing route on glass-forming ability, glass stability, crystallization path, structure and last but not least—sulfate capacity of the designed sulfur-bearing glasses and led to the following findings:

(1) The materials from the designed glass composition, SiO_2–P_2O_5–K_2O–MgO–CaO–SO_3, prepared via the process of quenching the melt in liquid medium, display a broad glass-forming range, as only the sample loaded with the highest amounts of sulfate species (5 mol.%) not only displayed turbidity but also exhibited distinctive, albeit low-intensity, peaks in its X-ray diffraction pattern, indicating the presence of crystalline phase (K_2SO_4). Verification of the sulfate capacity of the as-synthesized glasses, conducted due to the recognized volatility of sulfate species during glass melting and their tendency to segregate into separate salt phases, revealed that up to 2 mol.% of $[SO_4]^{2-}$ anions can be incorporated into the vitreous matrix of the studied materials before the crystallization of the sulfur-binding phase occurs.

(2) The addition of sulfate species leads to a gradual increase in the polymerization degree of the glass framework. This is evident from the systematic shift of high-frequency range bands toward higher-energy positions and the increased abundance of more polymerized Q^3_{Si} units, at the expense of less polymerized Q^2_{Si} units. The observed effect on the phosphor-oxygen subnetwork is entirely opposite (the decreasing concentration of Q^1_P groups is accompanied by an increase in Q^0_P groupings), which may be explained by the exchange of oxygen species between both silicate as well as phosphate subnetworks so that an increase in polymerization of one leads to a decrease in connectivity of the other. Moreover, the findings supported the notion of individuality of sulfate groupings within the glass network, as no linkages of the Si–O–S or P–O–S type were detected.

(3) The presence of increasing amounts of sulfur in the tested system leads to a progressive shift of the glass transition temperature (T_g) toward higher temperature values, confirming the conclusion drawn from the structural studies regarding the increased degree of glass framework polymerization with sulfate content. The analysis of the glass stability parameters, including Angell, Weinberg, and Hruby' parameters, revealed that the progressive increase in sulfate content in the tested glasses is followed by an initial decrease in each of the examined parameters and after the sulfur content reaches a value of 1 mol.%, the properties show an increasing tendency. The preliminary reduction of GS implies an increasing rigidity of the glass matrix leading to the development of internal strains, while their following augmentation reflects the enhanced network connectivity of glasses with higher sulfate content.

(4) The process of tested glasses' crystallization is governed by three factors: the concentration of components in the melt, the Gibbs free energy of compound formation (ΔG_f^0), as well as the strength of the bonds linking individual glass elements with its framework. The products of heat-treatment represented mostly silicate, but also phosphate as well as sulfate groupings, corresponding to the microregions present in the structure of a parent glass. Importantly, the sulfate groupings present in the vitreous matrix do not contribute to the formation of phases with any of the glass components, except for potassium cations, confirming at the same time the results of the structural studies, which demonstrated that this very component is situated in the voids of the network as independent units, not linked to the silicate-phosphate network.

(5) The preferential mechanism of the tested glasses' crystallization is the surface one. The analysis of the samples' surface images excluded the presence of distinct crystalline domains within the volume of the investigated devitrificates. Instead, small amounts of crystallization products (such as $CaSiO_3$, $MgSiO_3$, K_2SO_4) were found to be uniformly distributed within the volume of the studied glasses, while their greater concentration was revealed in higher-energy sites (cracks).

(6) The sulfate species localized in the voids of the glass framework alter the local environment of both the magnesium and silicon atoms. However, this alteration is likely to be indirect as it induces specific changes in the medium-range structure beyond the first coordination spheres of studied absorber atoms, presumably involving the rearrangement of potassium cations within the glass vitreous matrix.

The above presented findings underscore the significant influence of the processing route on the obtaining sulfate-bearing glasses of the fully amorphous nature and, by providing the results of a variety of analytical techniques, contribute to the better understanding of such intricate materials as those containing sulfate species in their matrix. As this unique group of glasses continues to intrigue researchers, the findings discussed here may serve as a foundation for future investigations in this field.

Acknowledgements The authors acknowledge the CERIC-ERIC Consortium for the access to experimental facilities. The part of the work related to the steel plate-cooled glasses (XS_MC_P series) was financed by the National Science Centre, Poland, project number 2018/31/D/ST8/03148, while the research on the water-quenched glasses (XS_MC_F series) was covered with funds from the grant No 2023/49/N/ST11/00299. The research was also partially supported by the program "Excellence initiative—research university" for the AGH University of Science and Technology (No 1588).

Authors' contribution The first draft of the present manuscript was written by Anna Berezicka, while Magdalena Szumera and Justyna Sułowska provided critical feedback and commented on the previous versions of manuscript. Anna Berezicka synthesized materials, collected the data, analyzed and interpreted them. Piotr Jeleń performed the measurements using the Raman Imaging technique, while Sebastian Komarek characterized the samples with XRD method. All authors discussed the results, helped shape the research as well as read and approved the final manuscript.

Funding This study was funded by Narodowe Centrum Nauki, 2018/31/D/ST8/03148, Justyna Sułowska, Narodowe Centrum Nauki, 2023/49/N/ST11/00299, Anna Berezicka, "Excellence initiative—research university" for the AGH University of Science and Technology, 1588, Magdalena Szumera.

References

1. Zanotto ED, Coutinho FAB. How many non-crystalline solids can be made from all the elements of the periodic table? J Non Cryst Solids. 2004;347:285–8.
2. Shakhgildyan G, Lipatiev A, Lotarev S, Fedotov S, Sigaev V. Glass: home of the periodic table. Front Chem. 2020;8:1–6.
3. Stoch L. Flexibility of structure as a criterion of glass formation and stability. Opt Appl. 2000;30:647–55.
4. Paris E, Giuli G, Carroll MR, Davoli I. The valence and speciation of sulfur in glasses by x-ray absorption spectroscopy. Can Miner. 2021;39:331–9.
5. Mills HN. Use of fining agents. In: Smothers WJ, editor. Ceramic engineering and science proceedings. 46th Conf Glas; 1986. p. 404–9.
6. Ojovan MI, Lee WE. Glassy wasteforms for nuclear waste immobilization. Metall Mater Trans A Phys Metall Mater Sci. 2011;42:837–51. https://doi.org/10.1007/s11661-010-0525-7.
7. Manara D, Grandjean A, Pinet O, Dussossoy JL, Neuville DR. Sulfur behavior in silicate glasses and melts: Implications for sulfate incorporation in nuclear waste glasses as a function of alkali cation and V2O5 content. J Non Cryst Solids. 2007;353:12–23.
8. McKeown DA, Muller IS, Gan H, Pegg IL, Kendziora CA. Raman studies of sulfur in borosilicate waste glasses: sulfate environments. J Non Cryst Solids. 2001;288:191–9.
9. Stefanovsky SV, Stefanovsky OI, Prusakov IL, Kadyko MI, Averin AA, Nikonov BS. Speciation of sulphate ions in sodium alumino(iron)phosphate glasses. J Non Cryst Solids. 2019;512:81–9. https://doi.org/10.1016/j.jnoncrysol.2019.01.005.
10. Vaishnav S, Hannon AC, Barney ER, Bingham PA. Neutron diffraction and Raman studies of the incorporation of sulfate in silicate glasses. J Phys Chem C Am Chem Soc. 2020;124:5409–24.
11. Sokolov IA, Murin IV, Kriyt VE, Pronkin AA. Structure and electrical conductivity of glasses in the Na 2O-Na2SO4-P2O5 system. Glas Phys Chem. 2011;37:351–61.
12. Vyatchina VG, Perelyaeva LA, Zuev MG, Baklanova IV, Mamoshin VL. Vibrational spectra of sulfoborate glasses. Inorg Mater. 2005;41:1128–30.
13. Hémono N, Muñoz F. Dissolution of SO3 within a lithium phosphate glass network and structure-property relationships. Phys Chem Glas Eur J Glas Sci Technol Part B. 2010;51:121–6.
14. Mishra RK, Sudarsan KV, Sengupta P, Vatsa RK, Tyagi AK, Kaushik CP, et al. Role of sulfate in structural modifications of sodium barium borosilicate glasses developed for nuclear waste immobilization. J Am Ceram Soc. 2008;91:3903–7.
15. Berezicka A, Szumera M, Sułowska J, Jeleń P, Olejniczak Z, Stępień J, et al. Unraveling the nature of sulfur-bearing silicate-phosphate glasses: insights from multi-spectroscopic (Raman, MIR, 29Si, 31P MAS-NMR, XAS, XANES) investigation. Ceram Int. 2022;48:4238–54. https://doi.org/10.1016/j.ceramint.2021.10.216.
16. Xu X, Youngman RE, Kapoor S, Goel A. Structural drivers controlling sulfur solubility in alkali aluminoborosilicate glasses. J Am Ceram Soc. 2021;104:5030–49.
17. Sułowska J, Madej D, Pokrzywka B, Szumera M, Kruk A. Structural and optical properties of pure and sulfur-doped silicate-phosphate glass. Molecules. 2021;26:1–28.
18. Lonergan JM, Lonergan C, Silverstein J, Cholsaipant P, McCloy J. Thermal properties of sodium borosilicate glasses as a function of sulfur content. J Am Ceram Soc. 2020;103:3610–9.
19. Sadok KH, Haouari M, Gallot-Lavallée O, Ben Ouada H. Effect of Na2SO4 substitution for Na2O on the structural and electrical properties of a sodium borophosphate glass. J Alloys Compd. 2019;778:878–88. https://doi.org/10.1016/j.jallcom.2018.11.203.
20. Wang X, Wu L, Li H, Xiao J, Cai X, Teng Y. Preparation and characterization of SO3-doped barium borosilicate glass-ceramics containing zirconolite and barite phases. Ceram Int. 2017;43:534–9. https://doi.org/10.1016/j.ceramint.2016.09.190.
21. Wu L, Wang X, Li H, Teng Y, Peng L. The effects of sulfate content on crystalline phase, microstructure, and chemical durability of zirconolite−barium borosilicate glass-ceramics. J Nucl Mater. 2016;478:303–9. https://doi.org/10.1016/j.jnucmat.2016.06.032.
22. Bingham PA, Vaishnav S, Forder SD, Scrimshire A, Jaganathan B, Rohini J, et al. Modelling the sulfate capacity of simulated radioactive waste borosilicate glasses. J Alloys Compd. 2017;695:656–67. https://doi.org/10.1016/j.jallcom.2016.11.110.
23. Bragg W. Chapter 2 - The glassy state. Structural Chemistry of Glasses. 2002. p. 13–76. https://doi.org/10.1016/B978-008043958-7/50020-0
24. Kiczenski TJ, Stebbins JF. The development of a rapid quenching device for the study of the dependence of glass structure on fictive temperature. Rev Sci Instrum. 2006;77:1–4.
25. Yue YZ, Christiansen JD, Jensen SL. Determination of the fictive temperature for a hyperquenched glass. Chem Phys Lett. 2002;357:20–4.
26. Bletskan DL. Glass-formation and crystallization in the system Ge-Te. Chalcogenide Lett. 2016;2:121–4.
27. Dabas P, Subramanian V, Hariharan K. Effect of quenching rate on the structure, ion transport, and crystallization kinetics in lithium-rich phosphate glass. J Mater Sci. 2014;49:134–41.

28. Zając M, Giela T, Freindl K, Kollbek K, Korecki J, Madej E, et al. The first experimental results from the 04BM (PEEM/XAS) beamline at Solaris. Nucl Instrum Methods Phys Res Sect B Beam Interact Mater Atoms. 2021;492:43–8. https://doi.org/10.1016/j.nimb.2020.12.024.
29. Berezicka A, Sułowska J, Jeleń P, Lach R, Szumera M. Thermal behaviour of sulphate-bearing multicomponent silicate–phosphate glasses. J Therm Anal Calorim. 2023;148:1381–405. https://doi.org/10.1007/s10973-022-11498-y.
30. McCloy JS, Riley BJ, Goel A, Liezers M, Schweiger MJ, Rodriguez CP, et al. Rhenium solubility in borosilicate nuclear waste glass: implications for the processing and immobilization of technetium-99. Environ Sci Technol. 2012;46:12616–22.
31. Berezicka AM, Secondary CA, Author C, Berezicka AM, Szumera M, Nauki NC, et al. Thermal behaviour of sulfate-bearing multicomponent silicate-phosphate glasses. J Therm Anal Calorim
32. Sitarz M, Bulat K, Wajda A, Szumera M. Direct crystallization of silicate-phosphate glasses of NaCaPO 4-SiO2 system. J Therm Anal Calorim. 2013. https://doi.org/10.1007/s10973-013-3240-y.
33. Erasmus EP, Sule R, Johnson OT, Massera J, Sigalas I. In vitro Evaluation of Porous borosilicate, borophosphate and phosphate bioactive glasses scaffolds fabricated using foaming agent for bone regeneration. Sci Rep [Internet]. 2018 [cited 2022 Jan 16];8. Available from: www.nature.com/scientificreports/
34. Wajda A, Sitarz M. Structural and microstructural studies of zinc-doped glasses from NaCaPO4-SiO2 system. J Non Cryst Solids. 2016;441:66–73.
35. Stoch L, Środa M. Infrared spectroscopy in the investigation of oxide glasses structure. J Mol Struct. 1999;511–512:77–84.
36. Jastrzbski W, Sitarz M, Rokita M, Bułat K. Infrared spectroscopy of different phosphates structures. Spectrochim Acta Part A Mol Biomol Spectrosc. 2011;79:722–7.
37. Szumera M, Wacławska I, Mozgawa W, Sitarz M. Spectroscopic study of biologically active glasses. J Mol Struct. 2005;744–747:609–14.
38. McMillan P. Structural studies of silicate glasses and melts-applications and limitations of Raman spectroscopy. Contrib Miner Petrol. 1984;69:622–44.
39. Furukawa T, Fox KE, White WB. Raman spectroscopic investigation of the structure of silicate glasses. III. Raman intensities and structural units in sodium silicate glasses. J Chem Phys. 1981;75:3226–37.
40. Wacławska I, Szumera M, Sułowska J. Structural characterization of zinc-modified glasses from the SiO2-P2O5-K2O-CaO-MgO system. J Alloys Compd. 2016;666:352–8. https://doi.org/10.1016/j.jallcom.2016.01.125.
41. Wu YQ, Dai C, Jiang GC. Local structure of calcium silicate melts from classical molecular dynamics simulation and a newly constructed thermodynamic model. Trans Nonferrous Met Soc China. 2014;24:1488–99. https://doi.org/10.1016/S1003-6326(14)63217-9.
42. Sun Y, Zhang Z, Liu L, Wang X. FTIR, Raman and NMR investigation of CaO-SiO<inf>2</inf>-P<inf>2</inf>O<inf>5</inf> and CaO-SiO<inf>2</inf>-TiO<inf>2</inf>-P<inf>2</inf>O<inf>5</inf> glasses. J Non Cryst Solids. 2015;420:26–33.
43. Mysen B. Phosphorus speciation changes across the glass transition in highly polymerized alkali silicate glasses and melts. Am Miner. 1996;81:1531–4.
44. Morizet Y, Gennaro E, Jego S, Zajacz Z, Iacono-Marziano G, Pichavant M, et al. A Raman calibration for the quantification of SO42- groups dissolved in silicate glasses: application to natural melt inclusions. Am Miner. 2017;102:2065–76.
45. Galeener FL, Mikkelsen JC, Geils RH, Mosby WJ. The relative Raman cross sections of vitreous SiO2, GeO 2, B2O3, and P2O5. Appl Phys Lett. 1978;32:34–6.
46. Wu YQ, Jiang GC, You JL, Hou HY, Chen H. Raman scattering coefficients of symmetrical stretching modes of microstructural units in sodium silicate melts. Wuli Xuebao/Acta Phys Sin. 2005;54:961–6.
47. Berezicka A, Szumera M, Sułowska J, Jeleń P, Olejniczak Z. Unraveling the nature of sulfur-bearing silicate-phosphate glasses: insights from multi-spectroscopic (Raman, MIR , 29 Si, P MAS-NMR, XAS, XANES) investigation.
48. Stoch L. Thermal analysis and thermochemistry of vitreous into crystalline state transition. J Therm Anal Calorim. 2004;77:7–16. https://doi.org/10.1023/B:JTAN.0000033182.90571.ce.
49. Stoch L. Thermochemistry of solids with flexible structures. J Therm Anal Calorim. 1998;54:9–24.
50. Nascimento MLF, Souza LA, Ferreira EB, Zanotto ED. Can glass stability parameters infer glass forming ability? J Non Cryst Solids. 2005;351:3296–308.
51. Hrubý A. Evaluation of glass-forming tendency by means of DTA. Czechoslov J Phys. 1972;22:1187–93.
52. Stoch L. Structure and crystallization of multicomponent glasses. High Temp Mater Process. 1992;10:245–64.
53. Stoch L, Stoch P. Crystal structures formation in glass from view of HRTEM. J Therm Anal Calorim. 2007;88:577–82.
54. Stoch L. Flexibility of structure and glass-forming ability: a chemical approach. Glas Phys Chem. 2001;27:167–74.
55. Barin I. Therrnochernical data of pure substances. In: Thermochemical data of pure substances. Hoboken: Wiley-VCH Verlag GmbH; 1995.
56. Kubicki JD, Hofmeister AM, Hemley RJ. Raman and infrared study of pressure-induced structural changes in MgSiO3, CaMgSi2O6, and CaSiO3 glasses. Am Miner. 1992;77:258–69.
57. Remy C, Reynard B, Madon M. Raman spectroscopic investigations of dicalcium silicate: polymorphs and high-temperature phase transformations. J Am Ceram Soc. 1997;80:413–23.
58. Li D, Peng M, Murata T. Coordination and local structure of magnesium in silicate minerals and glasses: Mg K-edge XANES study. Can Miner. 1999;37:199–206.
59. Morizet Y, Trcera N, Larre C, Rivoal M, Le Menn E, Vantelon D, et al. X-ray absorption spectroscopic investigation of the Ca and Mg environments in CO 2 -bearing silicate glasses. Chem Geol. 2019;510:91–102. https://doi.org/10.1016/j.chemgeo.2019.02.014.
60. Trcera N, Cabaret D, Rossano S, Farges F, Flank AM, Lagarde P. Experimental and theoretical study of the structural environment of magnesium in minerals and silicate glasses using X-ray absorption near-edge structure. Phys Chem Miner. 2009;36:241–57.
61. Li D, Bancroft GM, Fleet ME, Feng XH. Silicon K-edge XANES spectra of silicate minerals. Phys Chem Miner. 1995;22:115–22.
62. Li D, Bancroft GM, Fleet ME, Feng XH. Silicon K-edge XANES Spectra of silicate minerals. Phys Chem Miner. 1995;22:115–122. https://doi.org/10.1007/BF00202471
63. Thompson SP. Structural signatures of medium-range order in annealed laboratory silicates. Astron Astrophys. 2008;484:251–65.

Publisher's Note Springer Nature remains neutral with regard to jurisdictional claims in published maps and institutional affiliations.

Springer Nature or its licensor (e.g. a society or other partner) holds exclusive rights to this article under a publishing agreement with the author(s) or other rightsholder(s); author self-archiving of the accepted manuscript version of this article is solely governed by the terms of such publishing agreement and applicable law.

2. Publication P2*

Ceramics International

Phosphorus influence on sulfate capacity and structural evolution in multicomponent silicate-phosphate glasses

--Manuscript Draft--

Manuscript Number:	
Article Type:	Full length article
Keywords:	Sulfur-bearing glasses; glass fertilizers; silicate-phosphate glasses; structural studies
Corresponding Author:	Anna Maria Berezicka, MSc AGH University of Krakow Kraków, Małopolskie POLAND
First Author:	Anna Maria Berezicka, MSc
Order of Authors:	Anna Maria Berezicka, MSc
	Justyna Sułowska, PhD
	Piotr Jeleń, PhD
	Magdalena Szumera, DSc
Abstract:	Tailoring glasses to specific applications requires a deep understanding of the interplay between material composition and structure and how they define the properties of the final product. This mutual relationship, although relevant for all types of glasses intended for various uses, is particularly important for amorphous materials in contact with biotic systems, where an inappropriate dosage of useful ions released from the vitreous matrix may disrupt the course of vital biological processes. This study aims to decipher the structural evolution of multicomponent silicate-phosphate glasses in response to sulfur addition and to elucidate the role of phosphorus content in governing the sulfate capacity of these materials, intended as ecological SO_4^{2-} carriers for plants. To preliminarily characterize the fabricated SiO_2-P_2O_5-K_2O-MgO-SO_3 glasses, differing in P_2O_5 and sulfur content, the XRD, XRF, and SEM/EDS methods were employed. It was found that the higher-phosphorus system displays a significantly lower sulfate capacity than the one with a lower content of this network-forming component. Comprehensive spectroscopic investigations (FTIR, Raman, ^{29}Si and ^{31}P MAS-NMR, XAS methods) revealed that the incorporation of sulfate ions into the multicomponent silicate-phosphate glasses favours network polymerization, which involves both their subnetworks: not only the predominant silicon-oxygen network but also the phosphorus-oxygen one. The conclusion was drawn that the increased degree of polymerization of glasses with higher P_2O_5 content, and consequently their increased rigidity, hinders the formation of voids of size compatible with sulfate units, thereby limiting its incorporation into the glass network.
Opposed Reviewers:	Przemysław Jodłowski, DSc Cracow University of Technology pjodlowski@pk.edu.pl scientific background aligns closely with the general subject matter of the manuscript
	Mikołaj Szafran, Prof. Warsaw University of Technology szafran@ch.pw.edu.pl research experience in the field of inorganic glasses
	Marcin Kochanowicz, DSc Bialystok University of Technology m.kochanowicz@pb.edu.pl scientific background aligns closely with the general subject matter of the manuscript
	Barbara Pacewska, Prof. Warsaw University of Technology Pacewska@pw.edu.pl extensive research experience in the field of inorganic glasses

Powered by Editorial Manager® and ProduXion Manager® from Aries Systems Corporation

Phosphorus influence on sulfate capacity and structural evolution in multicomponent silicate-phosphate glasses

Anna Berezicka[a*], Justyna Sułowska[a], Piotr Jeleń[a], Magdalena Szumera[a]

[*]*corresponding author: berezicka@agh.edu.pl, phone: +48 884395101*

[a]*Faculty of Materials Science and Ceramics, AGH University of Science and Technology, al. A. Mickiewicza 30, 30-059 Krakow, Poland; e-mail addresses: berezicka@agh.edu.pl, mszumera@agh.edu.pl, sulowska@agh.edu.pl, pjelen@agh.edu.pl*

Dear Editor,

On behalf of my co-authors, I am pleased to submit our manuscript entitled *"Phosphorus influence on sulfate capacity and structural evolution in multicomponent silicate-phosphate glasses"* for consideration for publication in the *Ceramics International*.

Decades of intensive agriculture have depleted Earth's soil resources, significantly reducing fertility, disrupting biodiversity, and disturbing the balance of macro- and microelements. As members of the global scientific community, we have a responsibility to address these challenges and actively contribute to the restoration of soil ecosystems through the development of innovative materials for environmental protection. An innovative solution, aimed at sustainable management of croplands and preservation of bio-geochemical equilibrium, may constitute glassy carriers of macro-and microelements.

The present manuscript explores silicate-phosphate glasses within the SiO_2-P_2O_5-K_2O-MgO-SO_3 system, differing in P_2O_5 content and enriched with varying amounts of sulfur. Sulfur, an essential nutrient for proper plant development, has a largely unexplored impact on the vitreous framework of these materials. Therefore, this study aims to provide new insights into the structural evolution of multicomponent silicate-phosphate glasses in response to sulfur addition and to elucidate the role of phosphorus in governing the sulfate capacity of these glasses, which are intended as ecological SO_4^{2-} carriers for plants.

In light of the above, in the following pages of the manuscript, results from several experiments, using XRD, XRF, SEM-EDS methods as well as Raman, FTIR, ^{29}Si, ^{31}P MAS-NMR, XAS spectroscopic techniques, are demonstrated. This multifaceted approach allowed not only for the evaluation of the intrinsic ability of glasses in the studied systems to incorporate sulfate groups into their vitreous matrices, but more importantly, it enabled the authors to analyse the effect of sulfur incorporation on the silicate-phosphate glass framework.

The findings reveal that glasses with higher phosphorus content exhibit significantly lower sulfate capacity compared to those with reduced levels of this network-forming component. Furthermore, the progressive incorporation of sulfates into these multicomponent glasses promotes network polymerization involving not only the dominant silicon-oxygen subnetwork, but also the phosphorus-oxygen one. The research suggests that the increased degree of polymerization in glasses with higher P_2O_5 content leads to greater rigidity, which in turn restricts the formation of voids of sufficient size to accommodate sulfate units, thereby limiting their incorporation into the glass network.

While sulfur has long been recognized for its role as a refining agent in glass technology, its incorporation into a glass matrix remains relatively unexplored, leaving significant gaps in knowledge. This study addresses these gaps by providing a detailed analysis of the complex relationships between composition, structure, and properties in sulfur-bearing melts. These insights represent a valuable contribution to materials science, particularly given the potential of silicate-phosphate glasses to serve as ecological fertilizers, supplying essential macro- and microelements to plants.

In light of the growing global focus on restoring soil health and fertility, the findings presented in this article are expected to attract significant interest from researchers in related fields. We believe the study offers both fundamental and practical insights that align with current environmental and scientific priorities.

Sincerely yours,

Anna Berezicka

Author's Declaration

I, the undersigned, hereby declare under our ethical and legal responsibility that the submitted paper is original and has not been or is not being submitted to the peer review process to any other journal.

Author's Name: Anna Berezicka

Signed

Anna Berezicka

Manuscript Click here to view linked References

Phosphorus influence on sulfate capacity and structural evolution in multicomponent silicate-phosphate glasses

Anna Berezicka[a*], Justyna Sułowska[a], Piotr Jeleń[a], Magdalena Szumera[a]

*corresponding author: berezicka@agh.edu.pl, phone: +48 884395101
[a]Faculty of Materials Science and Ceramics, AGH University of Science and Technology, al. A. Mickiewicza 30, 30-059 Krakow, Poland; e-mail addresses: berezicka@agh.edu.pl, mszumera@agh.edu.pl, sulowska@agh.edu.pl, pjelen@agh.edu.pl

Tailoring glasses to specific applications requires a deep understanding of the interplay between material composition and structure and how they define the properties of the final product. This mutual relationship, although relevant for all types of glasses intended for various uses, is particularly important for amorphous materials in contact with biotic systems, where an inappropriate dosage of useful ions released from the vitreous matrix may disrupt the course of vital biological processes. This study aims to decipher the structural evolution of multicomponent silicate-phosphate glasses in response to sulfur addition and to elucidate the role of phosphorus content in governing the sulfate capacity of these materials, intended as ecological SO_4^{2-} carriers for plants. To preliminarily characterize the fabricated SiO_2-P_2O_5-K_2O-MgO-SO_3 glasses, differing in P_2O_5 and sulfur content, the XRD, XRF, and SEM/EDS methods were employed. It was found that the higher-phosphorus system displays a significantly lower sulfate capacity than the one with a lower content of this network-forming component. Comprehensive spectroscopic investigations (FTIR, Raman, ^{29}Si and ^{31}P MAS-NMR, XAS methods) revealed that the incorporation of sulfate ions into the multicomponent silicate-phosphate glasses favours network polymerization, which involves both their subnetworks: not only the predominant silicon-oxygen network but also the phosphorus-oxygen one. The conclusion was drawn that the increased degree of polymerization of glasses with higher P_2O_5 content, and consequently their increased rigidity, hinders the formation of voids of size compatible with sulfate units, thereby limiting its incorporation into the glass network.

Keywords

Sulfur-bearing glasses, glass fertilizers, silicate-phosphate glasses, structural studies

1 Introduction

Due to the structural flexibility of glasses, in the vitreous network one may enclose almost all Periodic Table elements, enabling the synthesis of compositions tailored to specific requirements and applications as well as providing a distinct advantage over crystalline substances [1–3]. Intriguingly, this glass-specific characteristic permits even the coexistence of components which differ in chemical properties and bond types with glass network anions (O^{2-}) to such a degree, that the occurrence of common bonds between polyhedra of these components is ruled out [3]. This allows for the successful design and application of materials such as bioglasses modified with not only 'classical' but also less-common elements indicated as therapeutic ions [4], glasses for optoelectronics facilitating the dissolution of large concentrations of RE ions [5], vitreous materials designed for the immobilization of hazardous waste, often consisting of radioactive elements [6], or glassy carriers of micro- and macroelements for plants [7–9]. An intriguing example of such chemical antagonism is found in sulfur-bearing silicate-based glasses, in which the [SO_4] and [SiO_4] units may coexist within the common vitreous network, despite restricted polymerization compatibility [10]. It should, however, be emphasized that, in general, the solubility of sulfur (as sulfate, SO_4^{2-}) in silicate-based matrices is rather limited and assumes values at levels around 1 wt.% [11,12]. It is of utmost importance, since at the SO_4^{2-} concentrations that exceed the solubility limit in the glass melt, sulfur precipitates as immiscible alkali and alkaline-earth crystalline sulfates. This issue presents several disadvantages, as the existence of such inhomogeneities impacts various physical and chemical properties of the final glass and often leads to its instability [13]. One major concern regarding sulfur-bearing glasses, particularly those interacting with the natural environment, is the high water solubility of the separated phase, which facilitates the elements' spontaneous release into the hydrosphere and their detrimental interaction with the environment [11,12]. In order to circumvent the solubility-limit complications, in recent years, significant research efforts have focused on developing efficient processes and glass formulations to enhance the loading of sulfate species into vitreous materials. It is now well estabilished that sulfur solubility in silicate melts is a function of two major factors: oxygen fugacity (fO_2) and melt composition [11,12,14,15]. Given that, the enhancement of the efficiency of the SO_4^{2-}-loading process relies on manipulating and controlling the vitrification atmosphere, where at high fO_2, S^{6+} dominates and is more soluble in silicate-based melts compared to S^{2-}, which predominates at low fO_2 [14]. Meanwhile, the second approach aiming at improving the sulfate capacity of glasses involves establishing the composition – structure – sulfur solubility relationships in glass matrices, and, since it’s more experimental than the first, it has spurred extensive research into advanced chemical compositions of SO_4^{2-}-carrying-glasses.

Owing to the presence of sulfur as a common component in radioactive wastes, the vast majority of such studies pertain to the topic of durable borosilicate glasses, widely applied for the immobilization of such hazardous products [16–19]. The stringent requirements for chemical resistance in such materials have resulted in less frequent exploration of sulfur-bearing phosphate and mixed silicate-phosphate glasses, employed in contexts where ion release into the environment is not only non-detrimental but also desirable. Interestingly, literature suggests that glasses composed entirely or partially of phosphate units, i.e., glasses of lower durability and hence greater potential in applications like glass fertilizers than the above-mentioned borosilicate ones, may exhibit an increased capability for incorporating sulfate units [12]. As per the findings of Stefanovsky et al. [20], the ability of a vitreous matrix to integrate [SO_4^{2-}]

units is contingent upon the compatibility between the crystallo-chemical parameters of the network-forming cations and those of sulfate species (i.e. the Dietzel field strength, the cation-oxygen binding energy, the bond strength and finally the dimensions along with the polarization of the polyhedra), enabling the arrangement of cations occurring in the glass in the following sequence [1]:S_{IV}^{6+}-P_{IV}^{5+}-V_{IV}^{5+}-B_{III}^{3+}-Si_{IV}^{4+}-B_{IV}^{3+}-Al_{IV}^{3+}-Zn_{IV}^{2+}. It should be noted that the closer the ions are to each other in the above series, the greater their ability to coexist in a common vitreous matrix, which would suggests that sulfate species exhibit significantly greater compatibility with phosphate units than with silicate ones [17]. Another study by Stefanovsky et al. [21] somewhat corroborated this theory, since as much as 6.6 wt.% (~7.8 mol.%) of sulfate ions were introduced into the matrix of alumino(iron) phosphate glasses without segregation of crystalline phase. However, similar to standard borosilicate glasses, [SO_4^{2-}] units retained their autonomous positions within the framework, exerting a depolymerizing effect on the phosphate network while increasing the fraction of pyro- (PO_3) and orthophosphate (PO_4) units. The statement that phosphate systems are more receptive to sulfate dissolution than silicate ones was further supported by Bobkova et al. [22], who studied various sulfate-bearing glass compositions, alkali-containing (Li_2O, Na_2O, K_2O) sulfate-phosphate glasses being one of them. Bobkova explained this phenomenon by suggesting that it is the lower synthesis temperature of phosphate-based systems compared to silicate ones that is responsible for their higher sulfate capacity. Conducted IR-based study also led her to conclude that $[SO_4]^{2-}$ units do not affect the degree of polymerization of the glass structural network, but, interestingly, she did not exclude the possibility of forming common bonds between sulfur and the glass-forming cations (e.g., Si–O–S or P–O–S). The phosphate-sulfate units interaction, although negated by many authors [23] was also proposed by Li et al. [24], who investigated the mutual bahaviour of these two components in the simulated low-level radioactive waste silicate glasses. Analyzing the spectra of glasses with increasing phosphorus content, he observed that in the spectrum of the sample with a 2.1 wt.% P_2O_5 (~ 1.2 mol.%) content, a characteristic band attributed to the vibrations of orthophosphate units appeared (not visible in glasses with lower content of this component). At the same time, the intensity of the band attributed to SO_4^{2-} species significantly increased, despite the sulfur content remaining constant. These observations led Li to conclude that, indeed, interaction between the analyzed groups occurs, although it is strongly dependent on their concentration in the melt. Meanwhile, the study of Sokolov et al. was much more specific, as based on the IR studies of glasses representing the Na_2O–Na_2SO_4–P_2O_5 system, the authors stated that presence of the $[SO_4]^{2-}$ units entails the development of the P–O–S bonds, which are predominantly terminal. According to Arkhipov et al. [25], however, the aforementioned interaction between sulfate and phosphate groups is minimal, as the data collected by the author in the analysis of glasses $0.4R_2SO_4*0.6NaPO_3$ (where R stands for Na, Li, or K) in the infrared region showed that it merely involves the sharing of the compensating cation between the negative charges of both groups (the first coordination sphere of R^+ cations consists of oxygen atoms from both sulfate tetrahedra and phosphate chains, forming a compound sulfate-phosphate anion).

The above-presented ambiguities raise a pressing question about the nature of interactions between [SO_4] and [PO_4] units, and prompt consideration of whether increased phosphorus content in the glass matrix indeed makes it more receptive to the addition of sulfate species. Since the answers to these inquiries may contribute to a deeper understanding of the relationship between the compositions of S-bearing glasses, their sulfate capacity and the behavior of this

[1] The Roman numeral subscripts denote the coordination number of the cation.

specific component in the melt, the aim of this study is to conduct a detailed analysis of the structure of glasses from analogous systems differing in phosphorus content: $41SiO_2$-$6(10)P_2O_5$-$20K_2O$-$33(29)MgO$ modified with the addition of SO_3, intended as glassy carriers of SO_4^{2-} ions for plants. This research continues and expands upon prior studies on the structural and compositional properties of phosphate-silicate glasses modified with sulfur, as presented in [!]. By building on these foundations, this study seeks to provide further insights into composition–structure–SO_4^{2-} solubility relationship and, consequently, enable the design of new glass compositions with increased capacity for this specific component.

2 Materials and Methods

2.1 Glass design and preparation

With the aim of investigating the composition-structure relationship, two groups of glasses differing in P_2O_5 content were designed, denoted as XS_6P and XS_10P. Here, X represents the nominal molar percentage of sulfate added to the base glasses, while the suffix 6P (or 10P) indicates the molar amount of P_2O_5 in each system (for example, a sample labelled as 1S_6P denotes a glass composition with nominal 6 mol.% P_2O_5 content, loaded with 1 mol.% of sulfate). As-designed glasses were then synthesized at the laboratory scale (~100g) by melting adequately weighed and homogenized raw materials of analytical grade purity (SiO_2, $(NH_4)_2HPO_4$, K_2CO_3, MgO, and K_2SO_4, all supplied by CHEMPUR, Poland) in ceramic crucibles placed in an electric chamber furnace under an air atmosphere at 1450°C. The resulting melts were quenched by pouring them into cold water to obtain amorphous materials as well as to hinder the spontaneous crystallization process.

2.2 Glass characterization methods

To verify the correspondence between nominal and actual contents of individual components incorporated into the glass matrix of the synthesized materials, an X-ray Fluorescence Spectrometry (XRF) was employed, using an ARL Advant'XP spectrometer. Preparation of the glass samples for composition analysis was conducted via standard pellet method, and the acquired spectra were quantitatively (reference-free) investigated using the PANanalytical Omnian application package, with sample compositions normalized to 100%. The nominal (in brackets) and XRF-acquired molar contents of the individual glass components are presented in Tab. 1.

Tab. 1 Chemical composition of all the synthesized silicate-phosphate glasses determined by XRF analysis [mol. %]. Nominal values are indicated in brackets.

	Sample	SiO_2	P_2O_5	K_2O	MgO	SO_3	Others
XS_6PI-series	0S_6P	39.17 (41)	7.57 (6)	29.62 (20)	21.23 (33)	0.00 (0)	2.41
	1S_6P	38.71 (41)	7.20 (6)	31.51 (20)	20.68 (33)	0.53 (1)	2.38
	3S_6P	37.09 (41)	7.03 (6)	33.98 (20)	20.96 (33)	1.66 (3)	2.28
	5S_6P	41.78 (41)	7.35 (6)	28.01 (20)	24.12 (33)	1.90 (5)	1.84
XS_10P-series	0S_10P	38.08 (41)	10.63 (10)	23.75 (20)	22.27 (29)	0.00 (0)	5.27
	1S_10P	39.30 (41)	10.65 (10)	21.35 (20)	23.91 (29)	0.28 (1)	5.52
	3S_10P	39.92 (41)	10.80 (10)	22.02 (20)	23.73 (29)	0.31 (3)	6.21
	5S_10P	41.21 (41)	11.19 (10)	21.72 (20)	24.08 (29)	0.47 (5)	6.34

The Scanning Electron Microscope (SEM) in combination with Energy Dispersive Spectroscopy (EDS) was utilized to countercheck the concentrations of oxide components within the studied materials, verify the homogeneity of the acquired glasses, and detect any visual changes generated by the sulfate addition. Observations were conducted under high vacuum conditions using a backscatter electron detector (BSE) with an accelerated voltage of 18 kV, employing the FEI Nova NanoSEM 200 scanning electron microscope. Given that sulfur addition often leads to the precipitation of crystalline sulfate-bearing phases, the amorphous

nature of the produced materials was assessed using X-ray diffraction (XRD). The measurements were performed with a PANalytical X-ray Diffractometer X'Pert Pro equipped with a Cu lamp, covering the 2θ range of 10–70° with a goniometer step size of 0.008° and an angular reproducibility of +/- 0.0002°. Detected crystalline phases were identified using the HighScore Plus software.

Complementary FTIR and Raman spectroscopy methods were employed to gain a comprehensive insight into the structure of the glass materials. Infrared measurements in the mid-IR region were conducted using a Bruker Vertex 70v vacuum spectrometer. The standard KBr pellet technique was utilized, with 128 scans taken at a resolution of 4 cm^{-1}. Raman spectroscopy investigation was carried out through WITec Alpha 300 M+ spectrometer, with 4 accumulations of 20 seconds each recorded for every sample using a Zeiss LD EC Epiplan 50x objective and an 1800 grating with a 488 nm diode laser.

To record high-resolution solid-state MAS-NMR spectra, an APOLLO console (Tecmag) and a 7 T / 89 mm superconducting magnet (Magnex) were used. A Bruker HP-WB high-speed MAS probe equipped with a 4 mm zirconia rotor and KEL-F cap was employed to spin the sample. A single 3 µs RF pulse corresponding to a π/2 flipping angle was applied. The ^{31}P MAS-NMR spectra were measured at a resonance frequency of 121.264 MHz, with the sample spinning at 6 kHz. The T1 relaxation times for ^{31}P were initially estimated to be about 3 s. The acquisition delay in accumulation was 10 s, and 256 scans were acquired. The ppm frequency scale was referenced to the ^{31}P resonance of 85% H_3PO_4. The ^{29}Si MAS-NMR spectra were measured at a resonance frequency of 59.515 MHz, with the sample spinning at 4 kHz. The T1 relaxation times for ^{29}Si were initially estimated to be about 10 s. The acquisition delay in accumulation was 30 s, and 256 scans were acquired. The ppm frequency scale was referenced to the ^{29}Si resonance of TMS (Tetramethylsilane). For the ^{31}P MAS-NMR spectra, the fitting uncertainties for line positions and linewidths were about 0.2 ppm, and the relative intensities had an accuracy of approximately 1%. For the ^{29}Si spectra, the corresponding uncertainties were 0.4 ppm and 1%, respectively.

X-ray absorption measurements for the Mg and Si K-edges were performed at the PEEM/XAS beamline of the SOLARIS National Science Centre in Poland [26]. This beamline, based on a bending magnet, provided a soft X-ray energy range and featured a plane grating monochromator with a resolving power (ΔE/E) better than $2.5x10^{-4}$. Powdered glass samples were affixed to sample holders using adhesive carbon tape, and data were collected in ambient conditions using total electron yield (TEY) mode.

K K-edge XANES spectra were obtained at the XAFS beamline at ELETTRA in Trieste, Italy [27], in fluorescence mode. A fixed exit Si (111) monochromator and a KETEK silicon drift detector (GmbH AXAS-M, Munich, Germany) with an 80 mm^2 active area were used. Energy calibration was conducted prior to the measurements. Powder samples were mounted on carbon tape and covered with Ultralene® film to prevent dispersion. Spectra were collected at room temperature and under vacuum conditions, with varying energy steps: a large step (5 eV) for the first 200 eV, a smaller step (0.2 eV) in the XANES region, and a constant k-step of 0.04 $Å^{-1}$ in the EXAFS region. For each sample, at least four spectra were collected and merged to improve the signal-to-noise ratio. All the obtained XAS spectra for the studied samples were normalized to the atomic background using the Athena software.

3 Results and discussion

3.1 Preliminary investigation of the as-synthesized glasses

Given the frequent observation reported by numerous researchers regarding the phenomenon of S-enriched layer precipitation on the surface of synthesized glasses [11,12,17], the samples were subjected to preliminary analysis using XRF, SEM with EDS composition analysis at specific points, as well as XRD method, all preceded by their visual inspection with the naked eye. The photographs of the as-synthesized glasses are presented in Fig. 1, while the graphical representation of the XRF results indicating the sulfate capacity of the materials is illustrated in Fig. 2.

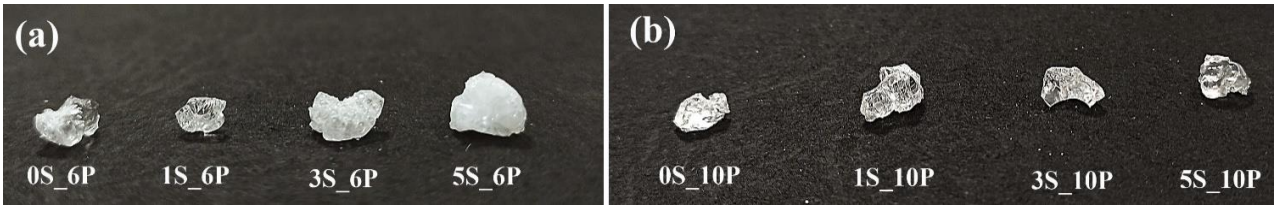


Fig. 1 Appearance of the synthesized glass samples representing the [6P] (a) and [10P] (b) systems.

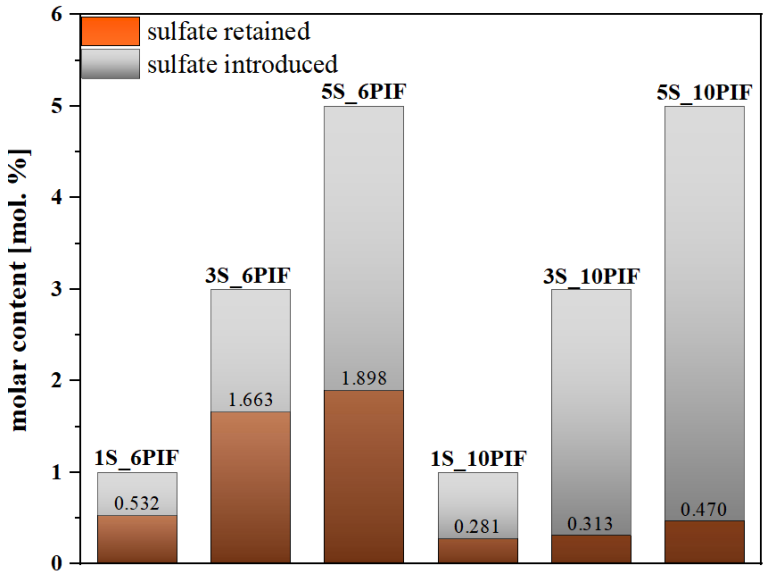


Fig. 1 Dependence of sulfate species introduced and retained in the glass matrices of studied materials.

Preliminary visual inspection of the sample surfaces confirmed the absence of any layer of crystalline products in all obtained glasses. The lack of a separated S-bearing salt on the exterior of the synthesized materials indicates that the sulfur quantities determined by the XRF method (Fig. 2) entirely reflect the amounts present within the bulk material [28]. It is, however, noteworthy that the glasses representing the XS_6P composition become increasingly more opaque with the addition of sulfate groups to the glass matrix (Fig. 1(a)), which is not observed in the system with higher P_2O_5 content (Fig. 1(b)), characterized by a significantly lower sulfate capacity than the former. Such an observation suggests that it is the relatively elevated amounts of SO_4^{2-} units in the XS_6P system, that is responsible for the observed opacity.

Fig. 2, which graphically presents the results of the XRF analysis, compares the amounts of sulfur introduced into the glassy matrix with those actually detected in the obtained materials, addressing the sulfate capacity of both examined glass systems. Contrary to expectations, the composition characterized by increased phosphorus content exhibits significantly lower ability to carry sulfate units – introduction of the highest dose, 5 mol. % of SO_3, resulted in the incorporation of approximately 40% of the initial amount in the XS_6P system, whereas four

times smaller quantities were detected for the one with higher P_2O_5 content, [10P]. Such results thus lead to the initial conclusion that even minor alterations in the composition of the investigated glasses exert a drastic influence on the ability of the vitreous matrix to incorporate SO_4^{2-} units. It is also noteworthy that for the system with 6 mol.% P_2O_5 content, the amount of sulfate species detected by the XRF method for the sample 5S_6P is similar to that analysed for the sample 3S_6P. Accordingly, these values likely delineate the sulfate capacity limit of this system. In contrast, such a phenomenon is not observed for the XS_10P composition, indicating that the capacity of this matrix to accommodate SO_4^{2-} species has not been reached in this case. Meanwhile, the microphotographs of the selected samples, taken to enhance the conducted visual investigation, are presented in Fig. 3 (a)-(f).

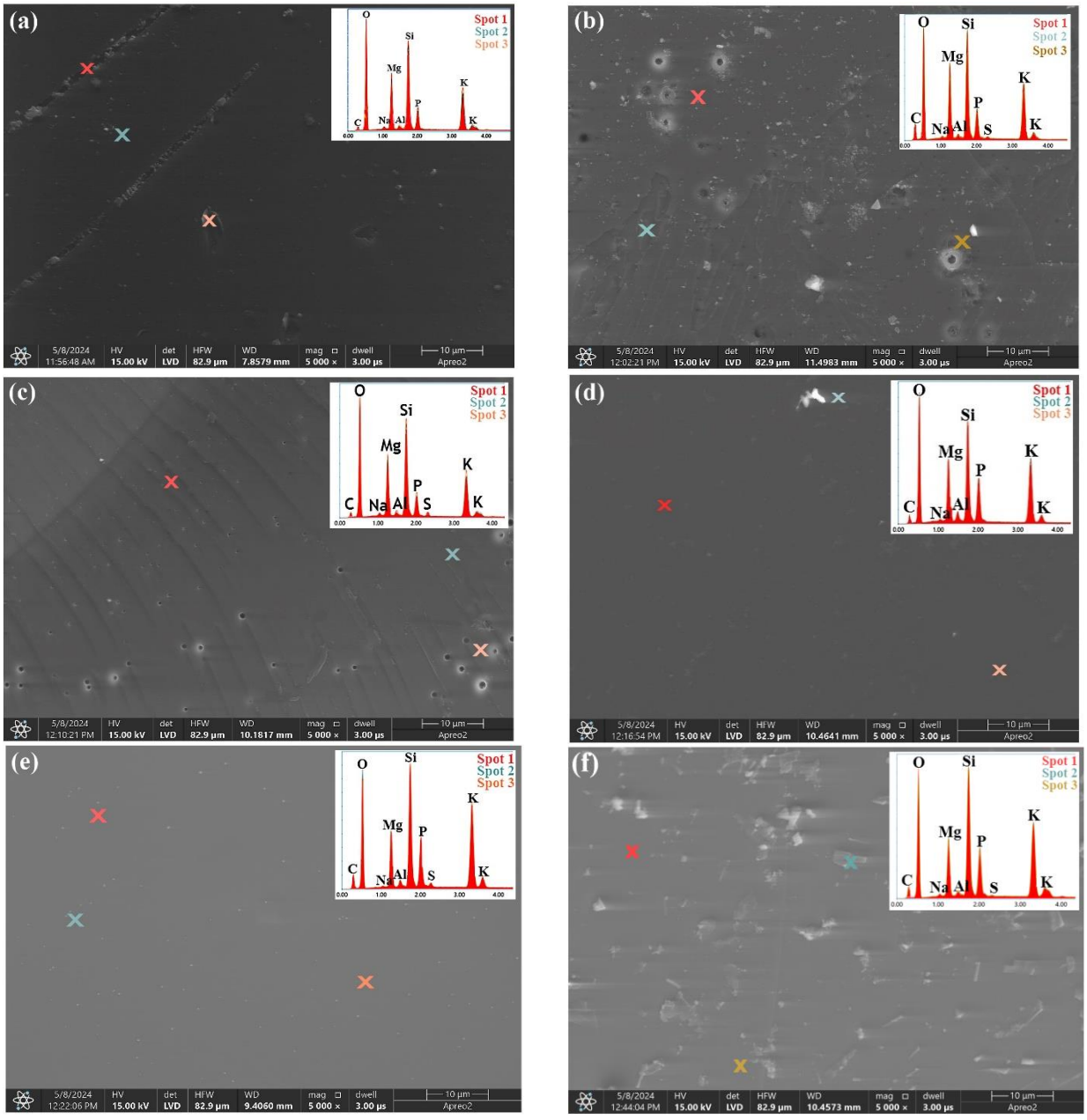


Fig. 3 SEM microphotographs of selected samples representing both studied systems: [6P] ((a) 0 mol.%, (b) 3 mol.%, (c) 5 mol.%) and [10P] ((d) 0 mol.%, (e) 3 mol.%, (f) 5 mol.%). The EDS spectra presented are a compilation of data collected from three distinct points on each sample's surface.

SEM analysis of the surfaces of as-synthesized materials indicated a homogeneous distribution of all elements within the vitreous matrix, confirmation of which constituted EDS spectra taken at different points within the studied regions. The overlapping of these signals reflects high level of similarity in the composition of the examined spots (Fig. 3). Importantly, the examined surfaces showed no presence of any crystalline forms. The only observed peculiarities constituted the geometric shapes visible in the microphotograph of sample 5S_10P (Fig. 3 (f)), however, considering that their composition does not deviate from other points on the glass surface, they should be attributed to cracking, as a consequence of the glass processing method (fritting in cold water).

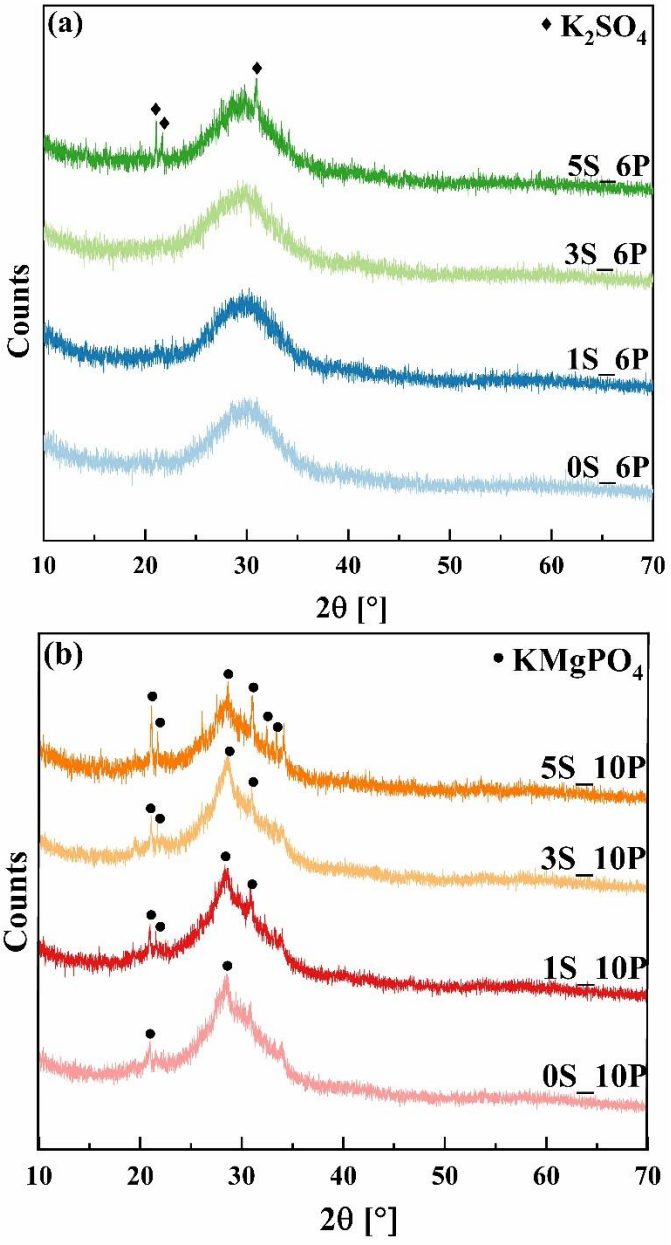


Fig. 2 Diffraction patterns acquired for all synthesized glasses, representing the [6P] (a) and [10P] (b) systems. The reflections corresponding to the identified crystalline phases are marked with circle and rhombus symbols.

In the final step of the preliminary analysis of the obtained materials, the XRD method was employed as a tool allowing for the unequivocal assessment of the amorphous nature of a material. Accordingly, diffraction patterns of all synthesized samples, representing both examined systems are presented in Fig. 4 (a), (b).

Analysis of the diffraction patterns of samples from the XS_6P composition demonstrates that materials visually assessed as transparent indeed exhibit a fully amorphous character (0S_6P, 1S_6P), as evidenced by the characteristic halo typical of the glassy state, and located at an angular position of 2 theta ~ 30° (Fig. 4 (a)). Interestingly, the XRD pattern of the optically opaque sample, modified with a 3 mol.% addition of sulfate units, shows no reflections indicative of crystalline phases. Partially crystalline character is, on the other hand, attributed to the sample with the highest sulfur content, 5S_6P – sharp reflections observed in its diffraction pattern likely origin from the presence of K_2SO_4 (Ref. 01-083-0682). It should be emphasized however that the exact analysis is hindered by the low quantity and intensity of these features. Significantly, the precipitation of sulfate-bearing compound is considered an indicator of exceeding the sulfate capacity of an investigated system [19,29,30].

The absence of visually perceptible surface sulfate layers (see Fig. 1) suggests a liquid-liquid phase separation within the volume of the glassy matrix [31]. This leads to the precipitation of excess SO_4^{2-} species from the glassy matrix and the formation of numerous droplets within the cooling melt, which organize themselves into a crystalline sulfate phase. This phenomenon explains the XRD results of the 5S_6P specimen, indicating the presence of K_2SO_4 within its glassy matrix. Furthermore, the lack of reflections in the diffraction pattern of the 3S_6P sample, despite the observed opacity, may indicate a minimal content of the precipitated phase, not surpassing the detection threshold of the XRD method. Such a statement would be in accordance with the earlier hypothesis that the introduction of 3 mol.% sulfate units into the melt is a limiting amount, defining the sulfate capacity of this system.

A completely different set of conclusions arises from the analysis of the diffraction patterns obtained for samples representing the system with increased phosphorus content (Fig. 4 (b)). Despite a clearly noticeable background raise around the 2θ angle ~ 30°, indicating predominantly amorphous nature of these materials, each XRD pattern shows reflections pointing to the presence of crystalline phase within their volume. It is important to emphasize here, however, that the relatively broad peak widths of the observed diffraction features suggest small crystallite sizes, which contribute to the full optical transparency of these materials (see Fig. 1). Only the diffraction pattern of the sample doped with the highest introduced dose of sulfur (5S_10P) exhibits relatively low background and significantly narrower reflections, signifying an increased fraction of crystalline phase within the vitreous matrix. Interestingly, the interpretation of these reflections points not to the presence of the sulfate-binding K_2SO_4 compound, as observed in the XS_6P system, but instead to an orthophosphate phase $KMgPO_4$ (Ref. 98-005-0926).

The diffraction patterns obtained for the composition with higher P_2O_5 content do not provide a definitive answer regarding the sulfate capacity of this system – the absence of sulfate-phase-related reflections may indicate that the solubility limit of SO_4^{2-} units in the [10P] matrix has not been exceeded. Yet, it is equally plausible that the sulfate capacity has been reached for this system, but the very small amount of these units accommodated within the structure of these materials is below the detection limit of the XRD method. Nonetheless, it is certain that this threshold is significantly lower than in the case of the system with a 6 mol.% content of P_2O_5.

3.2 Raman and FTIR spectroscopic investigations

It is well-established that vitreous silica exhibits a broad distribution of Si-O-Si bond angles, ranging from 170 to 130 degrees, with the most probable angles falling within the range of 155 to 140 degrees. This variability results in vibrational spectra characterized by broad, often poorly resolved band envelopes, with bandwidths sometimes exceeding those of comparable crystalline compounds by up to tenfold [32]. Therefore, to facilitate the elucidation of structural information, both Raman and Infrared Spectroscopy techniques were employed complementarily in this study, providing a comprehensive understanding of the structures of the acquired amorphous samples.

To investigate the changes in the bonding environment of each designed glass composition induced by the addition of sulfate, the samples were initially characterized using FTIR spectroscopy. The obtained absorption spectra are depicted in Fig. 5 (a), (b).

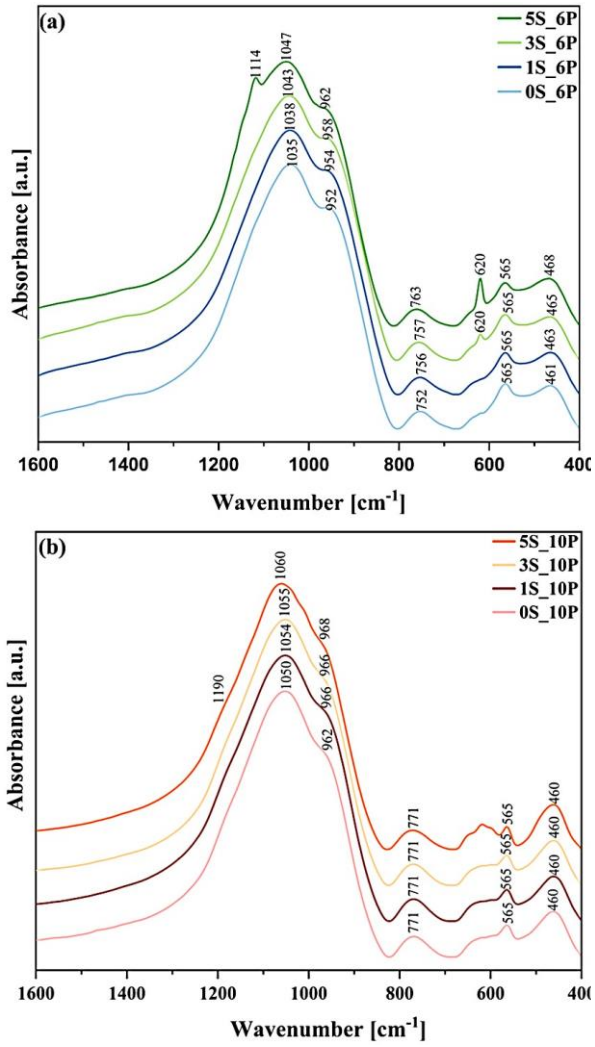


Fig. 3 Mid-infrared spectra of all synthesized glasses from the [6P] (a) and [10P] (b) systems.

All the obtained infrared spectra, regardless of the phosphorus content in the glassy matrix and the sulfate loading, consist of three spectral regions characteristic of silicate-based glasses: the most intense high wavenumber area (1300 – 800 cm^{-1}), where various stretching vibrations of Si-O and P-O groups overlap; the low-frequency region (700 – 400 cm^{-1}), primarily resulting from bending vibrations of these groups; and the least intense mid-frequency part of the spectrum (800 – 700 cm^{-1}), originating from symmetric stretching vibrations of Si-O-Si connections [32,33].

The preliminary analysis of the obtained spectra primarily yields two conclusions about the structure of the studied materials. Firstly, inspection of the spectral envelopes indicates a higher degree of network polymerization in glasses representing the system with increased phosphorus content [10P]. This is evidenced by spectral features characteristic of groups forming the silicate network (1050, 963, 770, 462 cm^{-1}) emerging at higher wavenumber frequencies compared to analogous samples from the [6P] system (1035, 952, 752, 460 cm^{-1}). This phenomenon has been previously observed by numerous researchers [34,35] and results from the preferential localization of network-modifier cations nearby charge-compensation requiring [PO_4^{3-}] units, thereby promoting an increase in the degree of polymerization of the modifier-depleted silicate framework of the glasses. The second conclusion drawn from the preliminary analysis of the spectra is that concurrent with sulfate loading, new, well-defined bands appear in the FTIR signals of glasses representing the [6P] system, specifically at 1114 cm^{-1} and 620 cm^{-1}, corresponding respectively to the asymmetric stretching mode (ν_{as}) and bending mode (δ_{as}) of SO_4^{2-} ions (Fig. 5 (a)). It should be emphasized that no bands indicating the presence of such groups were observed in the spectra of glasses characterized by increased phosphorus content, likely due to their significantly lower sulfate capacity compared to materials from the [6P] system.

Interestingly, the overall shape of the obtained spectra does not change with the addition of increasing amounts of sulfur into the structure of the studied materials, suggesting that the skeleton of the glass network remains unchanged. Only a more detailed analysis of band positions in the infrared spectra indicates the effect of increasing amounts of SO_4^{2-} groups in the glass matrices. It is noticeable that with sulfate loading, features associated with asymmetric vibrations of Si-O-Si connections and those corresponding to antisymmetric stretching of Si-

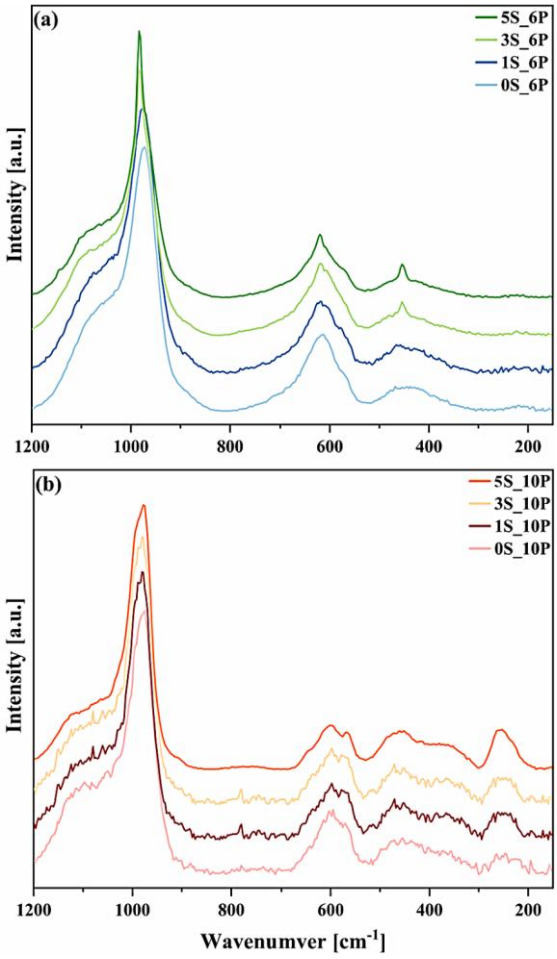


Fig. 4 Raman spectra of the glasses representing the XS_6P (a) as well as XS_10P (b) compositions.

O-non-bridging bonds in Q^2_{Si} silicate units shift towards higher wavenumbers (from 1035 to 1047 cm^{-1} and 952 to 962 cm^{-1} in the [6P] system, and from 1050 to 1060 cm^{-1} and 963 to 967 cm^{-1} in the [10P] system). Although these changes are not drastic, they unequivocally indicate a subtle increase in the degree of polymerization of the silicon-oxygen subnetworks in both studied glass compositions [36]. Similar behavior is observed for bands corresponding to symmetric stretching (752 to 763 cm^{-1}) as well as bending (460 to 468 cm^{-1}) vibration motions of silicon-oxygen linkages, but only in the spectra of glasses from the [6P] system, which reflects a greater scale of sulfate-related changes in these materials, Fig. 5 (a) [37–39]. The effect of introducing sulfate species into the network of materials characterized by an increased phosphorus content is most pronounced in the spectrum of a specimen doped with the highest amount of the new component – 5S_10P. It can be observed that the band corresponding to vibrations of $Si\text{-}O^-$ in Q^2_{Si} units (~960 cm^{-1}) flattens slightly, and, at approximately 1010 cm^{-1}, a shoulder-like feature overlapping the most intense band of the spectrum is observed, originating from analogous vibrations but in groupings with a higher degree of polymerization, Q^3_{Si} (Fig. 5 (b))[40]. Furthermore, the intensity of a spectral feature visible in the 670 – 600 cm^{-1} range of wavenumbers, attributable to Si-O-Si bending modes, increases. Both of these changes confirm that, despite significantly lower sulfur content, also the silicon-oxygen subnetwork of glasses from the [10P] system undergoes evolution towards a subtly increased degree of polymerization, as a result of the [SO_4^{2-}] addition.

Unfortunately, the overlap of bands originating from phosphate groups with those corresponding to the much more abundant silicate units hindered the assessment of sulfur's impact on the phosphorus-oxygen subnetwork. Nonetheless, the existence of the former, in the form of orthophosphate species, has been corroborated by the band observed at about 570 cm^{-1}, attributable to the P-O bending mode [36,38]. Therefore, in order to reveal this influence and also conduct a more thorough analysis of sulfate's effect on the glasses from both studied systems, supplementary Raman spectroscopy data analysis was performed.

The compilation of the obtained spectral profiles for samples from the XS_6P and XS_10P systems is presented in Fig. 6 (a), (b), respectively.

In order to monitor and thoroughly comprehend the structural evolution arising from the introduction of a new component into the matrix of multicomponent silicate-based glasses, the analysis of acquired spectra commenced with the base, sulfate-free, samples. It should be noted that similarly to the spectra obtained using infrared spectroscopy, Raman scattering patterns

represent an assemblage of bands originating from various vibrational modes of network formers' structural units with different degrees of polymerization (Q^nspecies). Given that, as well as the well-understood wavenumber positions of individual structural units, the spectral profiles were analyzed by dividing them into three main regions: the high-frequency region (1200 – 800 cm^{-1}), I; an intermediate-frequency region (800 – 500 cm^{-1}), II; and the low-frequency region (500 – 150 cm^{-1}), III, Fig. 7.

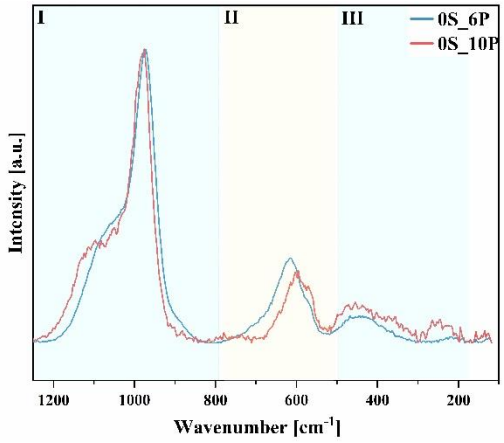


Fig. 5 Three regions distinguished in the obtained spectra of sulfur-free glasses: the high-frequency region (1200 – 800 cm^{-1}), I; the intermediate-frequency region (800 – 500 cm^{-1}), II; and the low-frequency region (500 – 150 cm^{-1}).

The high waveform area of silicate-based glasses presents the least controversy regarding band assignment. It is well-established that this region comprises a compilation of highly polarized features, exact positions of which depend on the number of non-bridging oxygens (NBOs) within the silicate tetrahedron. Depending on whether the glass composition is predominantly disilicate, metasilicate, pyrosilicate, or orthosilicate, the major Raman bands are typically observed within specific ranges: 1100-1050 cm^{-1}, 1000-950 cm^{-1}, around 900 cm^{-1}, or near 850 cm^{-1} [41]. Therefore, based on the position of the most intense spectral feature in this region, it can be concluded that the dominant structure-forming species in both base glasses are represented by Q^2_{Si} and Q^3_{Si} silicate units. Assigning individual bands to specific vibrational motions is considerably more speculative in both the mid- and low-frequency regions, where the intensities of spectral features are generally diminished. However, according to one hypothesis, the broad band in the former region reflects the presence of Si-O-Si bridges, and its position shifts towards higher wavenumbers as the degree of glass polymerization decreases. The spectral frequencies of this feature, ~620 cm^{-1} for the XS_6P system and ~600 cm^{-1} for the XS_10P system, support the theory that the tested glasses predominantly contain linkages of the ≡SiO and $=SiO_2$ type [36,41,42]. It is also noteworthy that the slightly lower wavenumber position of this band in the 0S_10P glass spectrum suggests an increased degree of polymerization in glasses representing the higher phosphorus oxide composition (Fig. 7). The shoulder of this broad band (~570 cm^{-1}), along with the weak feature localized near 390 cm^{-1} within the low-frequency range of the acquired spectra, indicate the presence of the orthophosphate PO_4^{3-} units (Q^0_P), while the 460 cm^{-1} one represents the diphosphate $P_2O_7^{4-}$ (Q^1_P) complexes [9,36,40,43]. An additonal feature localized at around 230 cm^{-1}, scarcely detectable in the glasses representing the XS_6P system, should be attributed to M-O bending modes (where M denotes a network modifier) and lattice vibrations [44–46].

The analysis of spectral assemblages of materials representing both studied systems (Fig. 6 (a), (b)) allows to conclude that, indeed, glass composition greatly influences sulfate incorporation into the vitreous matrix. While the observed spectral alterations resulting from [SO_4^{2-}] incorporation are rather small in the case of the XS_6P series, they are entirely invisible when considering the XS_10P system. Undoubtedly, sulfate species manifest their presence in the spectra of lower-phosphorus glasses – not only that new, well-defined, bands emerge on the spectral envelopes with increased amounts of this ingredient introduced (1143 cm^{-1}, asymmetric S-O stretching vibration; 982 cm^{-1}, symmetric S-O stretching vibration; 620 cm^{-1}, asymmetric S-O-S bending vibration; 453 cm^{-1}, symmetric S-O-S bending vibration, [15,16,28,29]), but

also the high-frequency spectral profile shifts towards higher wavenumber values, signifying an augmentation of the degree of framework polymerization (Fig. 6 (a)). Neither of these changes are evident in the second tested system (Fig. 6 (b)).

Given the disordered nature of glasses, which results in broad, asymmetric, and overlapping vibrational responses, analyzing sulfate-related structural changes poses significant challenges. Thus, to gain further insight, a decomposition of the high-frequency range of the acquired spectra has been conducted, according to a belief that relative intensities of bands within this area could be utilized to quantitatively describe the structures of the tested materials [47–50]. The glass spectra were deciphered following an approach proposed by Mysen et al. [51], wherein the individual bands of selected profiles were approximated by Gaussian lines, known for accurately representing the broad distribution of bond angles and distances in vitreous materials. An exception to this approach was made for bands related to sulfate species, which, due to limited distribution of S-O bond length and O-S-O bond angles, were modeled using Lorentzian functions [52]. Since the areas of Raman bands are known to not fully represent the contributions of individual structural units forming the vitreous network, the abundance of various Q_{Si}^n species depending on sulfate addition can be calculated using the approach proposed by Wu et al. [48,53]. According to their studies, determining the mole fractions, X_n, of different structural units, Q_{Si}^n, should be calibrated by the Raman composition-independent scattering coefficient, S_n (where S_1, S_2, S_3, and S_4 equals 0.514, 0.242, 0.09, and 0.015, respectively), based on the following equation, (1) [2]:

$$X_n = ({}^{A_n}/_{S_n})/(\sum_{n=0}^{4} {}^{A_n}/_{S_n}) \qquad (1)$$

Where A_n denote the band area of the given Q_{Si}^n units. Since this approach only pertains to various silicate species, a simple formula was employed to quantify phosphate units, expressing the Q_P^0/Q_P^1 ratio as follows, (2), [43,50]:

$${}^{A_0}/_{A_1} = {}^{X_0}/_{X_1} \qquad (2)$$

The resulting decomposed spectral envelopes of the selected glasses, the mole fractions of various Q^n species as a function of sulfate content as well as the description of the individual bands are presented in the Fig. 8**.**, Tab. 2 and Tab. 3, respectively.

[2] It is important to note that while the conducted calculations offer valuable insights into the trends in the abundance of structural units in the studied glasses, they do not yield exact quantitative values. Therefore, the assessment of these values was carried out using MAS-NMR studies, the results of which are presented in the subsequent section of the manuscript (see 3.3 ^{31}P and ^{29}Si MAS-NMR study).

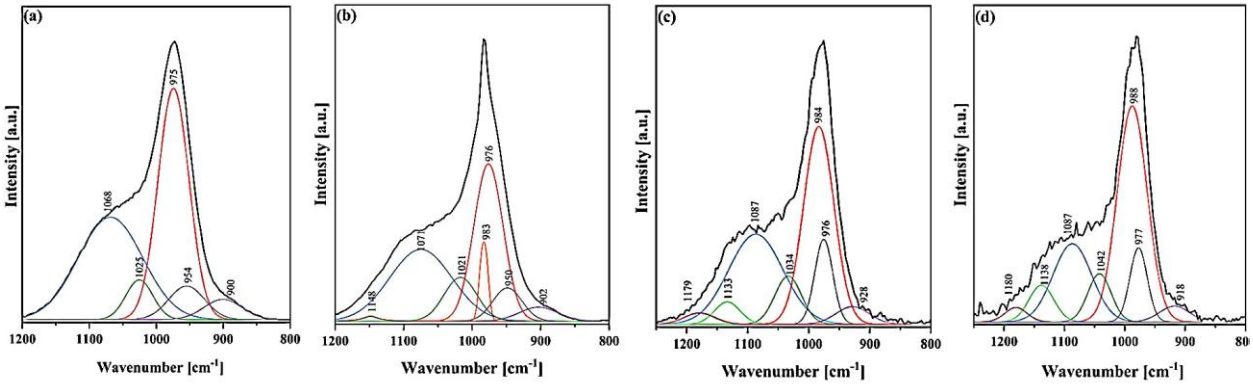


Fig. 6 The exemplary deconvoluted spectra of the glasses modified with 0 mol% SO_3 (a), (c) and 3 mol% SO_3 (b), (d), representing both studied systems.

Tab. 2 Mole fractions of various Q_{Si}^n units along with Q_P^0/Q_P^1 ratios.

Sulfate content [mol. %]		Q_{Si}^n molar content				
		X_1	X_2	X_3	X_4	Q_P^0/Q_P^1
XS_6P	0	0.014	0.285	0.701		1.119
	1	0.012	0.273	0.715		0.929
	3	0.015	0.267	0.718		0.673
	5	0.012	0.250	0.738		0.543
XS_10P	0	0.010	0.210	0.460	0.320	1.203
	1	0.008	0.222	0.307	0.463	1.173
	3	0.007	0.219	0.274	0.500	1.152
	5	0.006	0.194	0.217	0.583	0.977

Tab. 3 Assignments of the detected bands in the decomposed Raman spectra

Wavenumber [cm^{-1}]		**Band assignment**	**Reference**
XS_6P	XS_10P		
~ 900	~ 930	Symmetric Si-O$^-$ stretching in Q_{Si}^1 units	[9,49,50,54]
~ 950	~ 975	Symmetric P-O$^-$ stretching in Q_P^0 units	[49,50,55,56]
~ 975	~ 985	Symmetric Si-O$^-$ stretching in Q_{Si}^2 units	[9,49,50,54]
~ 983	–	Symmetric S-O stretching vibration	[15,29]
~ 1025	~ 1035	P-O$^-$ stretching in $P_2O_7^{4-}$ complexes	[36,43,50,57]
~ 1070	~ 1085	Symmetric Si-O$^-$ stretching in Q_{Si}^3 units	[9,49,50,54]
–	~ 1135	Si-O^0 stretching in Q_{Si}^4 unit	[9,43,51,58,59]
~ 1145	–	Asymmetric S-O stretching vibration	[15,29]
–	~ 1180	Asymmetric Si-O-Si stretching mode	[47,60]

The performed procedure unveiled the presence of five component bands in the case of XS_6P system, whereas as many as seven were detected in the higher-phosphorus one (Fig. 8). Worth noting is the fact that while the existence of Q_{Si}^1, Q_{Si}^2, Q_{Si}^3, Q_P^0 and Q_P^1 structural units is the common feature of both the studied formulations, only the materials characterised by elevated phosphorus levels display the band related to the vibrational mode of fully polymerized, Q_{Si}^4, silicate units. This observation should serve as confirmation of a slighlty increased degree of polymerisation of these glasses compared to those, representing the XS_6P system, and is consistent with the common notion that, in the presence of phosphate species, network modifiers (alkalis/alkaline earths) undergo a transfer from the silicate complexes to the immediate surroundings of ortho- and diphosphates, leading to the repolymerization of the silicate network [61,62]. Such a finding should also serve as a confirmation of the XRF data pointing to an increased sulfate capacity of the [6P] system, which, due to the reduced connectivity of the framework, is capable of accomodating an elevated number of [SO_4^{2-}] species (Fig. 2).

As suspected based on the intial spectral analysis, the conducted decomposition procedure did not reveal any bands that could be attributed to the vibrational movements of sulfate species in the case of XS_10P system, contrary to the lower-phosphorus one. In the latter, the sulfate-related features grew in intesity in parallel with the sulfate loading, suggesting that an increasing number of species are localizing themselves in the voids of the vitreous matrix (Fig. 8 (b)).

Irrespective of this, the presence of [SO_4^{2-}] species is evident in both studied systems through systematic changes in the molar fractions of individual silicate as well as phosphate structural units (Tab. 2). It is clear that along the introduction of increasing amounts of sulfate units into the structures of the tested materials, the molar fraction of the most polymerized species (Q_{Si}^3 in the case of the XS_6P system and Q_{Si}^4 as regards the XS_10P one) increases at the expense of those with fewer oxygen bridges. Notwithstanding, it is important to emphasize that this effect is rather subtle in both tested formulations. Although the response of the phosphorus-oxygen subnetwork to increasing sulfur content is analogous – in both glass formulations, a rise in Q_P^1 units, accompanied by a decrease in those lacking oxygen bridges, Q_P^0, is observed (as illustrated by the declining Q_P^0/Q_P^1 ratio, Tab. 2) – the scale of subnetwork changes is diminished in the [10P] system. In this composition, the Q_P^0/Q_P^1 ratio reduces only from approximately 1.20 to 0.98, as opposed to the [6P] system, where it drops from nearly 1.12 to 0.54. Such findings unambiguously indicate that the introduced [SO_4^{2-}] groupings, albeit slightly, enhance the framework's degree of polymerization. This phenomenon, as explained by the authors [63], is closely related to the exchange of charge-compensating network modifying cations between the network-forming silicate and phosphate units and the newly-introduced sulfate species, thus resulting in the polymerization of the glass network.

3.3 ^{31}P and ^{29}Si MAS-NMR study

In complex chemical glass and melt systems, vibrational spectroscopy suffers from extensive band overlap, making band assignments not always unequivocal. In light of the above, the MAS-NMR data of vitreous materials was employed as a critical constraint, enabling to separate the influence of SO_3 on the silicon-oxygen subnetwork from the one it has on the phosphorus-oxygen subnetwork, as well as providing clear-cut and quantitative answers about the extent of network polymerization in relation to sulfate content.

The compilation of MAS-NMR spectra comparing the chemical environments of the network formers in both studied systems ([6P] and [10P]), is presented in Fig. 9 (^{29}Si MAS-NMR), as well as Fig. 10 (^{31}P MAS-NMR), respectively.

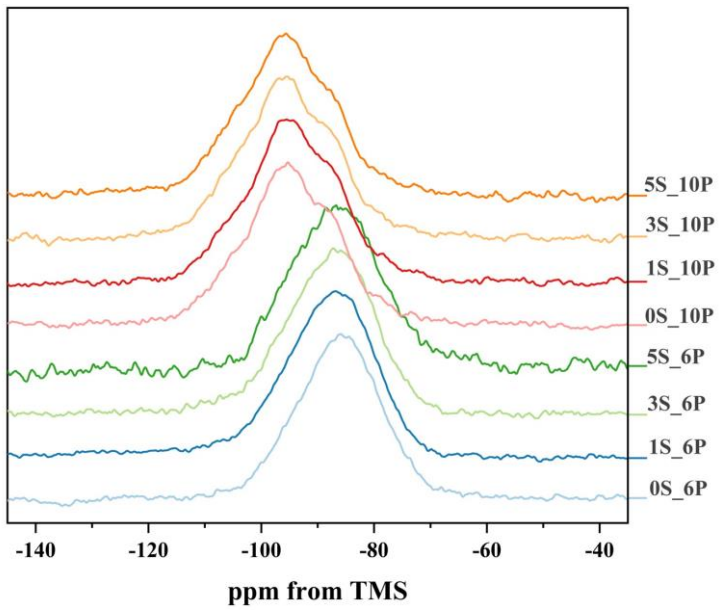


Fig. 7 ^{29}Si MAS-NMR spectra recorded for the obtained glasses from the [6P] (a) as well as the [10P] (b) systems, respectively.

The obtained spectra clearly reflect differences in the distribution of the primary structural units of the glasses (SiO_4 and PO_4) depending on the amount of P_2O_5 introduced into the glass matrix. The shift of the main resonance in the ^{29}Si MAS-NMR spectra, located at around -85 ppm for glasses with lower P_2O_5 content, to around -95 ppm for glasses representing the [10P] system, confirms the Raman spectroscopy finding of an increased degree of polymerization in the latter (Fig. 9 (b)). The pronounced asymmetry of this spectral feature observed for glasses with increased P_2O_5 content indicates a greater diversity in the chemical environment of silicon compared to the [6P] system. Importantly, the position of the observed resonance on the chemical shift axis (between -100 and -70 ppm for the [6P] system and between -110 and -75 ppm for the [10P] system) in both cases suggests the presence of the silicate tetrahedra sharing three oxygen atoms, Q^3_{Si}, besides those existing in the middle of the silicon-oxygen chains Q^2_{Si} [61,64]. It should be noted that the already-mentioned subtle influence of sulfate groups on the structure of the obtained glasses (see section on Raman spectroscopy) renders the preliminary analysis of the NMR signals limited in detail regarding the evolution of the glass framework with sulfate loading. Nonetheless, it can be observed that the position of the main spectral feature in both systems shifts slightly towards more negative chemical shifts (-85.5 to -86.8 ppm for the [6P] system and -94.8 to -95.9 ppm for the [10P] system), and its left-side asymmetry increases slightly with the addition of sulfate groups. Such a direction of spectral changes is commonly ascribed to an increasing degree of polymerization of the silicon-oxygen subnetwork.

Similar conclusions can be drawn from the analysis of the MAS-NMR spectra obtained for phosphorus nuclei (Fig. 10) – the chemical environments of this network former differ significantly between the studied systems, and the spectral changes resulting from the addition of sulfur to the glass matrix are difficult to discern during a preliminary analysis of the spectra.

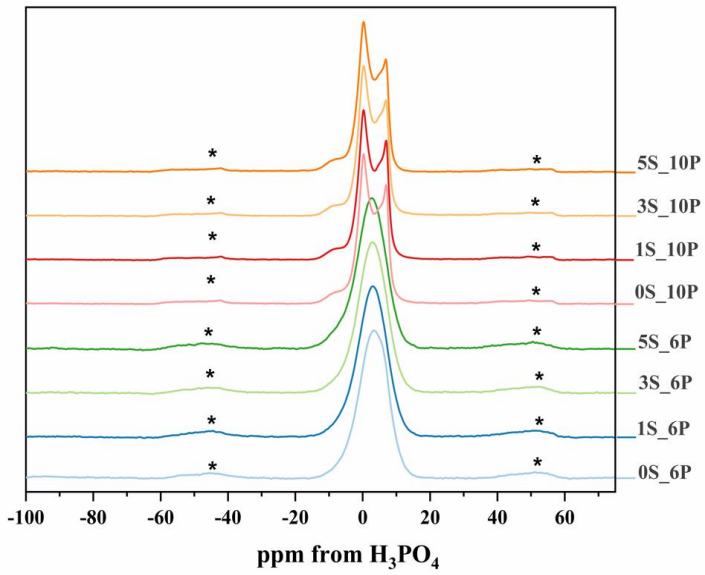


Fig. 8 ^{31}P MAS-NMR of all the studied glasses from the [6P] (a) and [10P] (b) compositions, respectively. The spinning sidebands are marked with asterisks.

While the position of the recorded spectral features in both cases is analogous and indicative of phosphate units mainly in the form of isolated tetrahedra Q^0_P (-10 to 10 ppm), the most notable difference distinguishing glasses with lower and higher phosphorus oxide content is the disordered (amorphous) character of the chemical environment of P atoms in the former, contrasted with the well-defined, highly ordered nature of phosphorus sites in the latter (Fig. 10). Furthermore, a preliminary analysis of the spectra suggests that the introduction of sulfate groups into the glass structure leads to two main observations: a slight shift of the main resonance towards more negative chemical shift values in glasses of the [6P] system, and a subtle increase in the left-side shoulder of the main spectral feature (~ –8.7 ppm) in glasses with higher phosphorus oxide content. Both the former and the latter changes, implying a gradually increasing presence of units with fewer non-bridging oxygens (NBO), Q^1_P, point to a subtle increase in the degree of polymerization of the phosphorus-oxygen subnetwork with sulfate loading.

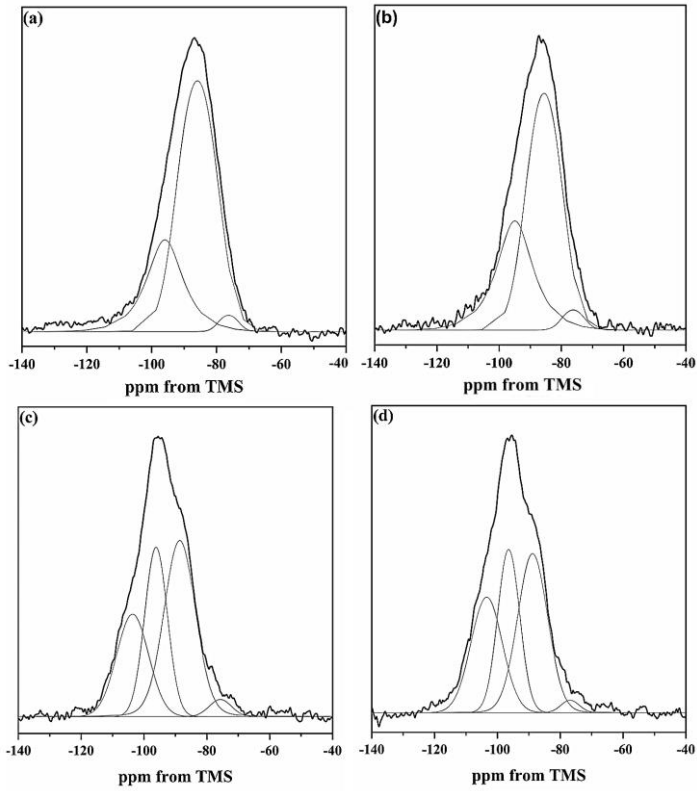


Fig. 9 Decomposed ^{29}Si MAS-NMR spectra of selected glasses from both studied systems, modified with 1 mol.% (a, c) and 3 mol.% (b, d) of SO_3.

To gain deeper insights into the chemical environments of both studied network formers in studied glass compositions, and primarily – to analyse the impact of sulfur addition on the distribution of the identified sites, all obtained spectra were subjected to a deconvolution procedure. This involved fitting the spectral regions with a set of bands described by the Voigt function, which proved optimal for describing most NMR spectra. The only deviation from this approach

constituted the ^{31}P MAS-NMR spectra of the [10P] system, which featured narrow, well-defined resonances best suited to description by the Lorentzian function. Exemplary results of spectral decomposition for selected glass samples from both systems are presented in Fig. 11 and Fig. 12. Moreover, by utilizing the NMR method's capability to directly quantify the contributions of specific structural units in the materials, the percentage distributions of the detected species are summarized in Tab. 4.

Tab. 4 The percentage distributions of the detected species based on the MAS-NMR spectra decomposition.

Distribution of the silicate units								
	Sulfur content [mol. %]							
	0		1		3		5	
[6P]								
Q_{Si}^1	–	–	–	–	–	–	-67.8	5.2%*
Q_{Si}^2	-84.5	75.4%	-85.4	71.2%	-85.4	68.9%	-83.9	61.6%
Q_{Si}^3	-93.2	24.6%	-94.8	28.8%	-94.6	31.1%	-93.1	33.2%
[10P]								
Q_{Si}^1	-75.9	2.7%	-75.7	2.9%	-76.9	1.9%	-77.6	1.0%
Q_{Si}^2	-89.4	46.1%	-88.6	43.3%	-88.8	39.4%	-88.4	32.7%
Q_{Si}^3	-96.9	27.4%	-96.2	29.0%	-96.4	29.2%	-95.9	33.2%
Q_{Si}^4	-104.3	23.8%	-103.6	24.8%	-103.4	29.5%	-103.0	33.1%
Distribution of the phosphate units								
	Sulfur content [mol. %]							
	0		1		3		5	
[6P]								
Q_P^0	3.6	91.1%	3.2	89.9%	3.4	84.9%	3.1	76.4%
Q_P^1	-4.9	8.9%	-4.6	10.1%	-2.8	15.1%	-2.2	23.6%
[10P]								
Q_P^0	7.0	13.2%	7.0	15.1%	7.0	14.2%	7.0	12.9%
$Q_P^{0\prime}$	4.6	30.3%	5.0	27.5%	5.1	27.2%	5.0	25.6%
$Q_P^{0\prime\prime}$	0.2	53.4%	0.3	53.4%	0.3	54.1%	0.3	56.9%
Q_P^1	-8.4	3.1%	-8.6	4.0%	-8.4	4.4%	-8.1	5.6%

* The presence of small fraction of the Q_{Si}^1 units only in the structure of glass modified with the highest sulfate content in the [6P] system may be an effect of so called disproportionation reaction, in which part of the Q_{Si}^2 species transforms into more Q_{Si}^3 and Q_{Si}^1 according to a following equation: $2Q_{Si}^2=Q_{Si}^1+Q_{Si}^3$ [37,48].

As indicated by the decomposition procedure, the recorded ^{29}Si MAS-NMR spectra of glasses representing the [6P] system consist of 2 components (with the exception of the sample modified with the highest content of sulfate units, 5S_6P, where 3 components were detected). In contrast, spectra belonging to the higher phosphorus oxide content system comprise as many as 4 bands, depicting chemically inequivalent chemical sites of Si atoms (Fig. 11). Considering that the centroid position of chemical shifts becomes more negative with increasing shielding effect, indicative of more bridging oxygen atoms surrounding the central silicon atom in Q_{Si}^n units, resonances detected at chemical shift positions around -70, -85, -95, and -105 ppm were assigned respectively to tetrahedral SiO_4 units containing 3, 2, 1, and 0 NBOs (Q_{Si}^1, Q_{Si}^2, Q_{Si}^3, and Q_{Si}^4 units), see Fig. 9, Tab. 4, [65–68].

It is worth emphasizing that despite the detected differences in the types of chemical sites of Si atoms in both studied systems, the silicate network in each case is predominantly formed by Q^2_{Si} units occurring in the central part of the silica chains, accompanied by a smaller quantity of Q^3_{Si} species, which constitute the two-dimensional part of the glass network. Importantly, in both studied systems, the introduction of sulfate units (although it does not cause drastic shifts in band positions) leads to a systematic increase in the concentration of components characteristic for structures with higher polymerization degree (Q^3_{Si} in the [6P] system and Q^3_{Si} and Q^4_{Si} in the [10P] system), at the expense of those with a higher proportion of non-bridging oxygens (Q^2_{Si}, Q^1_{Si}). Although this effect is rather subtle, undoubtedly provides clear confirmation of the Raman spectroscopy findings and indicates a gradually increasing degree of the silicate subnetwork's connectivity along with sulfate loading in both tested systems.

Similar to the ^{29}Si MAS-NMR spectra, the decomposition of the ^{31}P MAS-NMR spectra also signified a greater variability of chemical sites in the structure of the [10P] glasses, compared to those from the XS_6P composition (Fig. 12, Tab. 4).

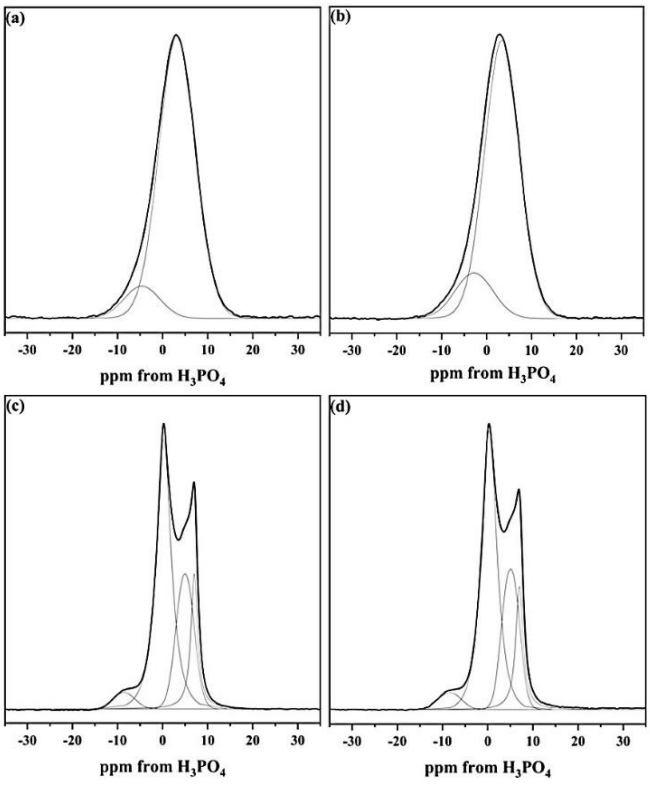


Fig. 10 Decomposed ^{31}P MAS-NMR spectra of selected glasses from both studied systems, modified with 1 mol.% (a, c) and 3 mol.% (b, d) of SO_3.

While in both cases the dominant type of phosphorus environment is that in which the network former is surrounded by four NBOs, Q^0_P, [67,69] in the glass structure representing the [10P] system, there are as many as three chemically inequivalent orthophosphate sites (Tab. 4). The origin of the main resonance observed in the MAS-NMR spectra of glasses from the [6P] system at chemical shifts around +3.6 ppm, and the analogous feature emerging in the [10P] composition at approximately +4.6 ppm, can be deduced by considering that pure K_3PO_4 exhibits a signal at about +11.7 ppm, whereas Mg_3PO_4 – around 0.0 ppm. Thus, the intermediate position between these values suggests the presence of orthophosphate sites in the tested systems, charge-compensated by both K^+ and Mg^{2+} cations [70,71]. Interestingly, similarly well-defined resonances observed in the spectra of [10P] glasses at about +7.0 ppm, positioned between the characteristic resonance of orthophosphate units coordinated by potassium ions (+11.7 ppm) and those surrounded by magnesium ions (+0.0 ppm), indicate a [PO_4^{3-}] sites surrounded by a mixture of K^+ and Mg^{2+} cations (Fig. 12).

The presence of two distinct spectral components of analogous origin can be attributed to different levels of site ordering – while the first one, of a wider observed full width at half maximum (FWHM), observed at +4.6 ppm, mirrors an amorphous nature of [PO_4^{3-}] units, the atoms constituting the well-defined and sharp second site at +7.0 ppm exhibit a higher degree

of organization, manifested in a narrower distribution of bridging angles, bond lengths, or third neighbour environments of the orthophosphate units in this site.

Similarly, the sharp and narrow resonance observed at a chemical shift of approximately +0.2 ppm points to a more regular environment of orthophosphate units compared to that observed in vitreous materials. As mentioned above, its position suggests that the second coordination sphere of [PO_4^{3-}] tetrahedra in this case consists of magnesium ions [71]. The last detected spectral component, emerging at chemical shifts around -4.9 ppm for glasses from the [6P] system and -8.9 ppm for those with higher P_2O_5 content, indicates that phosphate units with slightly higher connectivity—diphosphate units—are present in both studied compositions [67,72,73].

It should be emphasized that, similarly as it was observed in the case of ^{29}Si MAS-NMR spectra, the relative contributions of the ^{31}P MAS-NMR spectral components vary with increasing [SO_4^{2-}] content in the glassy matrix of the studied materials: as manifested by a decrease in the relative contribution of Q^0_P units in both compositions, in favour of the more polymerized, Q^1_P, ones, the connectivity of the phosphorus-oxygen framework also increases (Tab. 4). Nevertheless, as found in the case of the Raman study (see 3.3 ^{31}P and ^{29}Si MAS-NMR study), the overall [SO_4^{2-}]-related polymerizing effect is rather delicate and, judging by the scale of changes in Q^0_P units concentration changes upon sulfate introduction, is more pronounced as regards the [6P] system. Moreover, in the materials representing the [10P] composition, a gradual decrease in the proportion of disordered units coordinated by a mixture of K^+ and Mg^{2+} cations is noted, implying a gradual increment in their structural ordering parallel to sulfate units addition. Interestingly, a rise in the proportion of orthophosphate sites surrounded solely by Mg^{2+} cations was found. The explanation for this phenomenon lies in the preferential coordination of sulfate groups by K^+ cations, thus, the gradual increase in the proportion of [SO_4^{2-}] tetrahedra is accompanied by a concomitant decrease in the availability of these charge-compensators, resulting in an increased proportion of orthophosphate sites coordinated by the remaining network-modifying ions, specifically Mg^{2+}.

The results from the decomposition of the acquired MAS-NMR spectra can offer further insights into the impact of sulfur addition on the structure of the studied glasses, specifically regarding changes in network connectivity, NC. This parameter is critical for describing the structure-property relationship of glasses, particularly those intended for use in biological environments, as it directly influences the polymerization degree of the network. This, in turn, affects the degradation, solubility, and release of essential cations in biological solutions [74–76]. The NC parameter denotes the average number of bridging oxygen (BO) atoms per network-forming element and is calculated straightforwardly from the glass composition using the method outlined by Edén [77]. This calculation involves the molar quantities (x) of oxides employed in fabricating the glass compositions, as specified by the following equation [78–80], (1)[3]:

$$\{NC\}_{theor} = \{4xSiO_2 + 6xP_2O_5 - 2(xK_2O + xMgO) + 4xSO_2\}/xSiO_2 \qquad (1)$$

[3] Notably, the performed calculations of $\{NC\}_{theor}$ took into consideration the non-uniform distribution of BO/NBO in the structure of the investigated materials and the pronounced preference for P-NBO contacts, resulting in the predominance of Q_P^0 units in the phosphorus-oxygen subnetwork. Therefore, as a parameter describing the network connectivity of the synthesized materials, the average number of BO atoms per silicon tetrahedron was utilized instead of the total sum of Si and P tetrahedra [79,80]. Furthermore, the calculations assumed that [SO_4^{2-}] species enter the glass network exclusively as isolated tetrahedral units, with modifier cations such as K^+ required to maintain charge balance, thereby enhancing the connectivity of the silicate subnetwork, as indicated by the term $+4xSO_2$.

Meanwhile, the experimental values of this parameter, $\{NC\}_{exp}$, were obtained using the proportions of Q_{Si}^n and Q_P^n units derived from the decomposition of MAS-NMR spectra, according to the equations proposed by Eckert [67], (2),(3),(4):

$$\{NC\}_{Si} = 4 \times f\left(Si^{(4)}\right) + 3 \times f\left(Si^{(3)}\right) + 2 \times f\left(Si^{(2)}\right) + 1 \times f\left(Si^{(1)}\right) \quad (2)$$

$$\{NC\}_P = 3 \times f\left(P^{(3)}\right) + 2 \times f\left(P^{(2)}\right) + 1 \times f\left(P^{(1)}\right) \quad (3)$$

$$\{NC\}_{exp} = \{2xP_2O_5 \times \{NC\}_P + xSiO_2 \times \{NC\}_{Si}\}/xSiO_2 \quad (4)$$

The comparison of network connectivity calculations for each of the glass samples from both studied systems is depicted in Fig. 13.

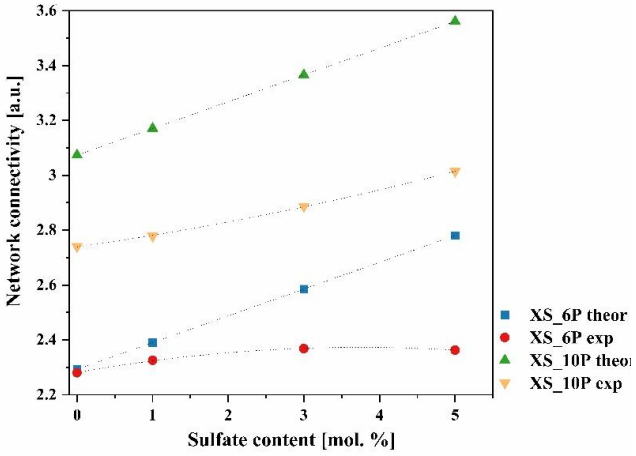


Fig. 11 Network connectivity of studied glass compositions as a function of sulfate content.

Upon analysing the obtained NC results, it is noteworthy that in both studied glass systems, the $\{NC\}_{exp}$ values are lower than $\{NC\}_{theor}$ with a markedly greater difference observed in the XS_10P system (Fig. 13). This phenomenon directly results from the lower content of sulfate groups detected in the glass network compared to the assumed values. Consequently, these units bind fewer charge-compensating K^+ cations, leading to a smaller-than-expected increase in the polymerization of the silicate subnetwork. This discrepancy between $\{NC\}_{theor}$ and $\{NC\}_{exp}$ is more pronounced in the phosphorus-enriched system, where the sulfate capacity is considerably lower compared to the [6P] glasses.

Worth emphasizing is that the $\{NC\}_{exp}$ results confirm earlier spectroscopic studies, indicating that all examined glasses are primarily structured by Q_{Si}^2 units, accompanied by the Q_{Si}^3 sites, and that materials representing the [10P] system show a higher proportion of the latter, thus exhibiting a greater degree of polymerization (Fig. 13).

While it is the glasses structured predominantly by Q_{Si}^2 and Q_{Si}^3 units, that are known for their biologically active behavior, NC values exceeding approximately 2.7 are widely believed to confer significant resistance to degradation in biological fluids, primarily due to the consequent hydrolysis requirement of numerous Si-O-Si bonds [81,82]. Considering this, it can be speculated that a system with a 6% molar phosphorus content and higher network fragmentation may serve as a superior candidate as a potential carrier of useful ions in biological environments. Importantly, as indicated by the computed results, the addition of sulfate groups influences the network formation of the studied materials – in both cases, NC rises in parallel with sulfate loading (Fig. 13). The observed phenomenon, as previously mentioned (see section 3.2 Raman and FTIR spectroscopic investigations), is linked to the modifier scavenging effect of $[SO_4^{2-}]$ units, which enhances the degree of polymerization within the glass subnetworks. It is important to note, however, that these changes are relatively minor, highlighting the limited impact of the subtle amounts of sulfur introduced into the matrices of both systems.

3.4 Insights from XAS Spectroscopy

Considering that XAS technique is a powerful method to get an insight into the atomic environment of a specific element, irrespective of whether the system is ordered or displays an amorphous nature, this tool has been employed to track the changes in the closest surrounding of the main network-former of the studied materials – Si atoms [83]. Additionally, since charge-compensation-requiring sulfate species influence the distribution of network-modifying cations in the glass matrix, the atomic environments of both K and Mg atoms have been monitored to capture the subtle changes induced by [SO_4^{2-}] addition.

Given the above, the spectra collected at the K-edge of the main glass network former, silicon, for selected samples from both studied systems are presented in Fig. 14.

Initial assessment of the obtained spectra does not indicate significant differences between them, regardless of the studied system or the sulfur content in the glass – the collected data revealed the presence of analogous spectral features A, B, and C in each of the tested samples (Fig. 14). The appearance of identical characteristics A (the white line, originating from a 1s → 3p transition) and C (associated with transitions of Si 1s electrons to the t_2 state, which pertains to the empty Si 3d state) in all the spectra is not surprising, given that both these features correspond to the first coordination sphere of silicon atom, and the SiO_4 tetrahedron is a fundamental structural unit of all silicates, whether crystalline or amorphous [84–86]. Therefore, structural changes occurring in silicate-based minerals and glasses usually manifest themselves in the energy region between the above-mentioned features (~ 1850-1860 eV) – the spectral characteristics emerging there provide evidence of structural order beyond the first Si-O coordination shell [84]. As regards the XS_6P system, the intermediate region is represented only by the broad shoulder-like feature B (known to be responsive to multiple scattering effects of oxygen atoms situated at Si-O distances exceeding 3.3Å [87]), and is not influenced by sulfur addition into the glass matrix (Fig. 14). Interestingly, in the XAS spectrum of the 0S_10P sample, additional features, labeled here as *d* and *e*, can be observed within this intermediate energy range (Fig. 14). According to Thompson [84], these characteristics appear as prominent in configurations, where SiO_4 tetrahedra are slightly distorted, resulting in the mixing of empty 3p-like features with the 3d states, thereby producing symmetry-forbidden shape resonances. Considering this, along with the observation that the mentioned characteristics diminish upon the inclusion of increasing amounts of sulfur into the glass matrix (Fig. 14), and the spectra subsequently revert to resembling those typical of amorphous silicates (exhibiting distinct features A, B, and C), it can be reasonably inferred that the addition of sulfur induces a reorganization of elements in the further coordination spheres of silicon atoms, most likely

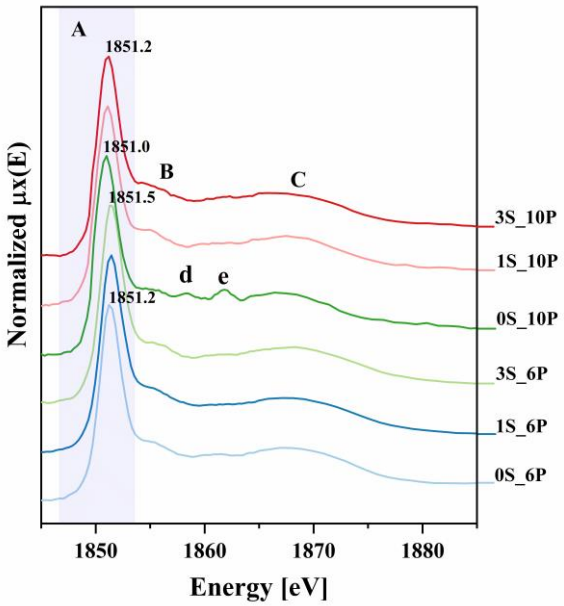


Fig. 12 Silicon K-edge XANES spectra of selected glass samples from both the [6P] (a) and [10P] (b) systems, each loaded with 0, 1, and 3 mol. % of sulfur species. The white line, feature A, is marked in blue color.

network-modifying cations, being the cause of the aforementioned distortion of the SiO_4 tetrahedra.

The analysis of the obtained spectra provides another important piece of information - within each of the examined systems, the position of the edge feature A shifts slightly towards higher energy values with the addition of sulfur (1851.2 → 1851.5 eV and 1851.0 → 1851.2 eV for the XS_6P and XS_10P systems, respectively, Fig. 14). This phenomenon is commonly explained in the literature by the increasing degree of polymerization of the silicon-oxygen subnetwork in glasses [85,88,89] or, alternatively, according to Li et al. [90], it may suggest changes in the chemical parameters of the investigated materials (e.g. an increase in silicon-silicon or silicon-oxygen bond length, or a decrease in Si-O-Si bond angle). Nevertheless, considering the results from other spectroscopic methods, the former theory appears to be the most applicable.

Although both K and Mg in silicate melts are typically classified as network-modifying cations and are believed to exhibit similar behaviours, the structural environment of Mg^{2+} differs from that of K^+, leading to distinct impacts exerted on their sites by sulfate anions. To investigate this influence, XANES spectra at the Mg K-edge as well as K K-edge of the selected glasses from both the studied systems were collected and are presented in Fig. 15 and Fig. 16, respectively.

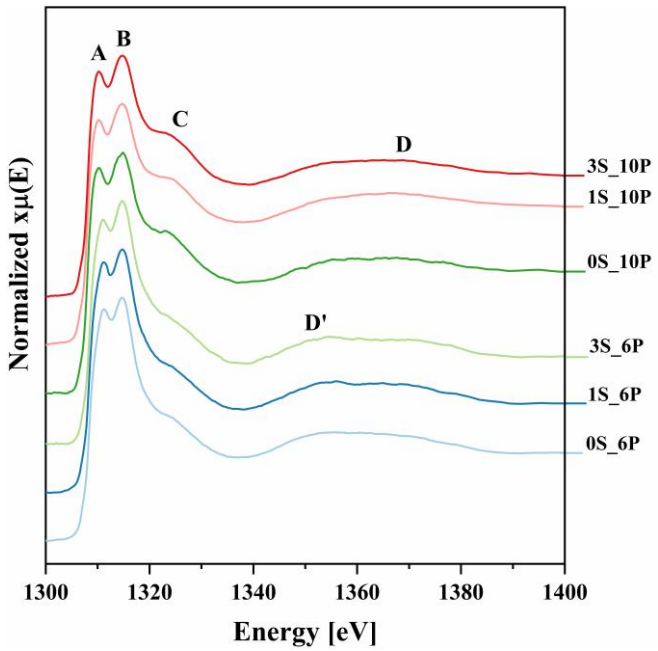


Fig. 13 Magnesium K-edge XANES spectra of selected glass samples from both the [6P] (a) and [10P] (b) systems, each loaded with 0, 1, and 3 mol. % of sulfur species.

All the acquired Mg K-edge XANES spectra of the selected samples representing both studied systems exhibit significant similarity and correspond to previous studies on magnesium-containing glasses, with their spectral line shapes comparable to those, reported in the literature [91,92], (Fig. 15). The near-edge regions of the recorded signals are composed of four main features denoted here as A, B, C and D, with a faint peak D' appearing as a lower-energy shoulder on the last of these spectral characteristics. Notably, this vague feature is observed exclusively in glasses from the [6P] system (Fig. 15). According to previous studies on analogous materials, feature A should be attributed to the transition of 1s electrons to empty 3p states (or, alternatively, as some suggest [93], to multiple scattering resonances from the outer shells), while characteristics B and D are associated with the first coordination shell of magnesium atoms, and originate from the 1s → 3p transitions and first shell resonances, respectively. Peaks C and D', on the other hand, emerge due to multiple scattering effects from coordination spheres around the absorbing Mg [84,94]. Importantly, despite the apparent resemblance of the acquired [6P] and [10P] spectra, two minor differences should be noted: firstly, all the mentioned features emerge at lower energy values

for the XS_10P system compared to the XS_6P one, and secondly, in the former composition, peak C is somewhat more prominent, while the D' and D features merge into one broader spectral characteristics (Fig. 15). Given the robust dependency of Mg near-edge structure on local electronegativity and multiple scattering, which allows for differentiation between structures exhibiting even slight modifications in their coordination, the observed variances, albeit subtle, mirror the variances in the Mg environment in the investigated glass compositions [92,95]. Such differences pertain both to the first, as well as the further coordination spheres of magnesium atoms, which may be deduced based on the changes regarding features A and C: the differences in the position of the lowest-energy peak, labelled here as A, as highly sensitive to bond length, polyhedral distortion degree, and the coordination number of Mg (the first resonance tends to shift to higher energy by up to 1 eV with an alteration in the CN from $^{[4]}$Mg to $^{[6]}$Mg or $^{[6]}$Mg to $^{[8]}$Mg [91]), imply the variations in the first short-range coordination shell of O around Mg [84], whereas the disparities in the line-shape of the C feature, arising from interactions of the photoelectron at extended distances, reflects the alterations in the structural ordering beyond the first-shell short-range one [84], (Fig. 15). And while the differences resulting from energy positions of peak A indicate a higher CN of Mg atoms in [6P] glasses compared to the [10P] one (as indicated by XRD magnesium cations in the [10P] system co-create the $KMgPO_4$ domains, where are bonded to oxygen atoms in a 4- or 5-coordinate geometry, while in the [6P] formulation, most likely, besides co-forming alike regions, the coordinate metasilicate units, existing in octahedral geometry, [96]), these, reflected by peak C definition suggest increased regularity of the Mg environment in the higher-phosphorus system [91]. Given that the number of features in the near-edge region mirrors the number of scattering pathways [91], the additional feature D' in the case of [6P] glasses' spectra confirms the more diverse, less ordered, character of the Mg regions.

Attention should also be directed towards the changes exerted on the spectra as an effect of [SO_4^{2-}] species introduction – upon sulfate loading the spectral feature C in both tested systems loses its definition (Fig. 15). As related to the multiple scattering effects, the variations of peak C mirror a rearrangements of network components situated at extended distances to Mg atoms, demonstrating simultaneously an indirect impact of the presence of [SO_4^{2-}] – the environment of magnesium changes, as the environment of the structural units coordinated by it changes [84]. It should be highlighted however that this sulfur-related spectral change is more pronounced as regards the [6P] system, implying a slightly greater scale of structure alterations in this composition (Fig. 15). Having said that, the overall impact of [SO_4^{2-}] species content on the magnesium surroundings is minor, what aligns with the current understanding that these units do not interact with Mg^{2+} cations, and the observed spectral changes likely arise from interactions between sulfate groupings and other cations, indirectly influencing the Mg sites in studied glasses.

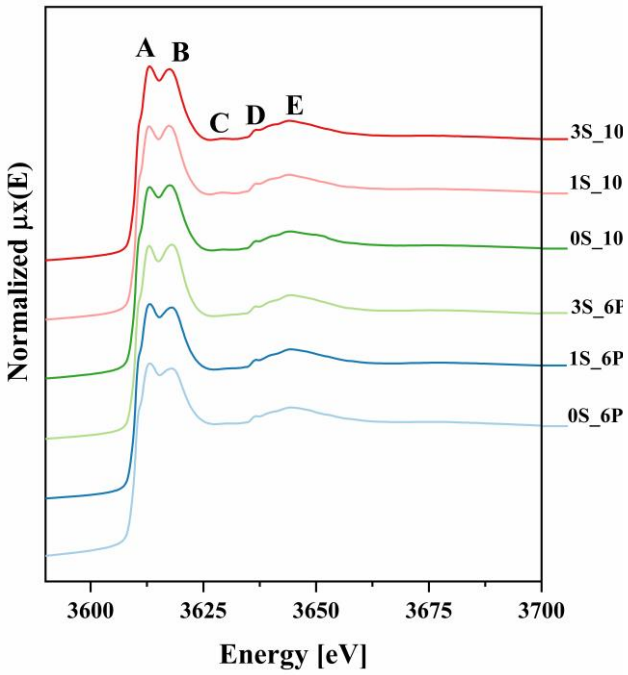


Fig. 14 Potassium K-edge XANES spectra of selected glass samples from both the [6P] (a) and [10P] (b) systems, each loaded with 0, 1, and 3 mol. % of sulfur species.

Tab. 1 Comparison of the A/B intensity ratio in XAS spectra across all studied glasses.

Glass name	A/B relation
0S_6P	1.03
1S_6P	1.02
5S_6P	0.99
0S_10P	0.98
1S_10P	0.99
5S_10P	1.01

Analogously as it was observed as regards the Si and Mg K-edges XANES spectra, the preliminary analysis of the data displayed in the Fig. 16 implies that all acquired spectra, regardless of the tested system or sulfate content, exhibit high level of similarity. Indeed, the registered signals consist of strong edge feature A (~3613 eV), originating from the transition of 1s electrons to the empty 3p states, distinctive post-edge peak B (~3617 eV) corresponding to [1s3p] excitation of K, and three significantly weaker features related to the multiple scattering processes: C (~3629 eV), low intensity peak D (~3636 eV), and broad spectral feature E (~3645 eV) [97,98]. Given that it is oxygen atoms that primarily contribute to the K K-edge spectrum, the observed consistency in the collected data, indicated by the comparable sequence of peaks, suggests a high degree of similarity in the first-shell structure around potassium cations across all the studied materials [99]. Nevertheless, the slight differences in peak positions in the near-edge region between analogous glasses representing lower- and higher-phosphorus systems (Fig. 16) suggest some variability in the potassium surroundings within the glassy matrix of the investigated materials. According to Ragoen et al. [83], the observed shift in the peak A position to higher energy values may indicate a reduction in K-O distances in the glasses of the XS_10P system (3613.13 eV) compared to those in the XS_6P system (3613.10 eV). The presence of shorter K-O distances in the former is not unexpected, given the higher connectivity of the 10P-glasses' framework (see 3.2 Raman and FTIR spectroscopic investigations), which forces potassium cations into smaller sites and restricts their ability to relax within their environment. It is also noteworthy to consider the amplitude ratio of the most prominent peaks in the acquired spectra – features A and B (Tab. 5). It is evident that upon sulfate loading, the A/B ratio decreases for the XS_6P system, whereas the opposite effect is observed for the higher-phosphorus glass formulation. According to Geng et al. [100], this phenomenon should be attributed to changes in the coordination number of potassium ions in the material, with the decreasing intensity ratio of peaks A/B indicating an increasing K-O coordination number.

Initially, the XS_10P system exhibits a slightly higher coordination number of potassium cations in relation to oxygen atoms (Tab. 5) than the [6P] one, likely due to the larger concentration of charge-compensation-requiring orthophosphate units (which have a higher K-O coordination number compared to potassium atoms in the vicinity of Q^2_{Si} and Q^3_{Si} units). However, upon the addition of the first portion of sulfate anions to both glass formulations, the coordination number in the XS_6P system increases, while the higher-phosphorus system shows the opposite trend. Since sulfur content is the only variable introduced into both systems, this observed effect must be attributed to this specific addition. It is therefore believed that the slightly raising coordination number of potassium in the XS_6P system is specifically linked to the presence of a increasing number of K_2SO_4-like regions, (where K may adopt 9 or 10-coordination with oxygen), at the expense of K_3PO_4-like configurations (where K typically occupies sites of 6 or 7-coordinate geometry in relation to oxygen) [96]. Following this line of reasoning, the decrease in the coordination number of potassium in the [10P] composition is likely associated with an increasing ratio of crystalline $KMgPO_4$ regions (where two K sites are present, coordinated by 5 and 7 oxygen atoms, respectively), at the expense of the aforementioned K_3PO_4-like configurations [96]. In contrast to the [6P] system, an increase in K-O coordination number associated with the presence of sulfate units is not observed in the [10P] composition (Tab. 5), possibly due to lower quantities of incorporated [SO_4^{2-}] species compared to the former.

The XANES insights underscore that among the studied elements (Mg, Si, and K), only the immediate environment of potassium is altered by the introduction of sulfur. This emphasizes that it is precisely K^+ cations that act as the charge compensators for sulfate units in the vitreous matrices of the studied glasses.

4 Conclusions

The subtle intricacies between glass composition and its polymeric structure necessitate an in-depth understanding, to tailor material properties that align with intended functionalities. Glass fertilizers, as representatives of vitreous materials that biodegrade in living ecosystems, are expected to exhibit a unique framework characterized by fragmented chains or sheets of basic structural units, and thus – facilitating the release of beneficial cations into the surrounding substrate. Therefore, multicomponent silicate-phosphate glasses, enriched with sulfate units known as macroelements, vital for plant organisms, underwent thorough examination: initially, by a set of preliminary investigative tools, commonly employed to assess fundamental properties of synthesized glasses (XRF for chemical composition, SEM-EDS for homogeneity, and XRD for amorphousness), and then via various spectroscopic techniques (Raman, FTIR, ^{29}Si and ^{31}P MAS-NMR, XAS), enabling description of the acquired materials in terms of structural concepts.

Maximizing sulfate retention in glass while maintaining its complete amorphous nature is crucial for glasses intended as carriers of sulfur ions for plants. The more so that partial crystallinity of such materials may limit their solubility in the soil environment and thus - disrupt the process of releasing essential ions. Although the exact proportion of crystalline phases that adversely affect the chemical activity of glass is not well understood, diffraction patterns of the synthesized materials revealed that only glasses from the [6P] system exhibited full amorphicity (except for the sample doped with 5 mol. % sulfate additive), whereas the [10P] system contained higher-order regions of $KMgPO_4$ composition.

The XRF analysis revealed that sulfate capacity of studied materials is highly dependent on melt composition – it was found that the amount of sulfate species retained within the glass dropped from 1.9 to 0.5 mol. % in the 5S-glasses as the P_2O_5 content increased from 6 to 10 mol.%. Given that orthophosphate units, the predominant form of phosphorus in the tested matrices, require charge compensation, it was hypothesized that sulfate solubility correlates with the availability of remaining alkali/alkaline earth cations in the glass.

The combined results from FTIR, Raman, and MAS-NMR techniques clearly demonstrated that, in addition to the availability of network-modifying elements, also the degree of glass polymerization influences sulfate incorporation. The XS_6P system, with its more fragmented and flexible framework primarily composed of Q^2_{Si} units, exhibited a greater capacity to accommodate sulfate units within voids of compatible size, than its higher-phosphorus analogue. Importantly, this relationship between glass polymerization and sulfate incorporation has been found to operate bidirectionally—increasing sulfur content in the glass matrix correlates with higher values of network connectivity. This phenomenon originates from the alkali cation-scavenging effect of newly introduced [SO_4^{2-}] groups, resulting in an increase in the concentration of more polymerized glass-forming units at the expense of those with a lower non-bridging oxygen fraction. Although this effect applies to the silicon-oxygen frameworks of both studied systems, its significance is evident only in the [6P] system regarding the phosphorus-oxygen subnetwork, while in the [10P] system, it is rather marginal. Nonetheless, the observed sulfur-related polymerizing effect is relatively minor in all studied cases, as insignificant is the actual amount of the [SO_4^{2-}] species introduced to both compositions.

The structural studies were completed with XAS investigation, which enabled the establishment of the influence of sulfate species addition on the nearest environments of Mg, Si, and K atoms. It was found that while the presence of [SO_4^{2-}] groups has only an indirect impact on the first two, affecting the distant elements in magnesium surrounding and promoting the polymerization of the silicate subnetwork, its influence on the potassium environment is the most pronounced. Specifically, sulfate addition alters the K-O coordination number in both studied systems, but the observed effect is opposite: while in the [6P] composition sulfate addition resulted in its slight enhancement due to formation of an increased number of K_2SO_4-like regions (of higher CN) at the expense of K_3PO_4-like ones, in the [10P] system this parameter was gradually reduced, likely as a consequence of a raising fraction of crystalline $KMgPO_4$ phase (of lower CN). It was simultaneously confirmed that sulfate groups preferentially localize within the voids of the studied glass network near K^+ cations, rather than Mg^{2+} ones.

Ultimately, the presented study demonstrates how adjusting the P_2O_5 content can influence the final product's structure and sulfate capacity, revealing the ways in which sulfur, as an unconventional component, alters the connectivity of the silicate-based framework. This insight into the composition-structure relationship will pave the way for future research aimed at creating chemically active glasses that can effectively carry and release beneficial ions in natural environments.

Acknowledgements

The authors acknowledge the CERIC-ERIC Consortium for the access to experimental facilities. The authors would also like to express their gratitude for the XRD, XRF, SEM-EDS and MAS-NMR analyses to PhD Sebastian Komarek, DSc. Bartosz Handke, PhD Agnieszka Wojteczko and PhD Mariusz Gackowski, respectively (Faculty of Materials Science and Ceramics, AGH University of Science and Technology in Krakow and Jerzy Haber Institute of Catalysis and Surface Chemistry, Polish Academy of Sciences, Poland). This work was financed by the National Science Centre, Poland, project number 2023/49/N/ST11/00299 and partially supported by the programs "Excellence initiative—research university" for the AGH University of Krakow (No 9785) and "Excellence initiative – research university" for the AGH University of Krakow (No 8874).

Author Contributions:

Writing - original draft and editing, data curation, conceptualization, formal analysis, funding acquisition, investigation, methodology, project administration, visualization, A. Berezicka; conceptualization, critical review, funding acquisition, investigation, methodology, supervision, J. Sułowska; critical review, funding acquisition, investigation, methodology P. Jeleń; critical review, funding acquisition, investigation, methodology, project administration, supervision, M. Szumera

Data availability

The data supporting the findings of this study are publicly available and can be accessed at https://doi.org/10.58032/AGH/G1EYFN

References

[1] L. Stoch, Thermochemistry of solids with flexible structures, J Therm Anal Calorim 54 (1998) 9–24. https://doi.org/10.1023/A:1010127129729.

[2] G. Shakhgildyan, A. Lipatiev, S. Lotarev, S. Fedotov, V. Sigaev, Glass: Home of the periodic table, Front Chem 8 (2020) 1–6. https://doi.org/10.3389/fchem.2020.00384.

[3] L. Stoch, Flexibility of structure and glass-forming ability: A chemical approach, in: Glass Physics and Chemistry, Springer, 2001: pp. 167–174. https://doi.org/10.1023/A:1011388528421.

[4] U. Pantulap, M. Arango-Ospina, A.R. Boccaccini, Bioactive glasses incorporating less-common ions to improve biological and physical properties, J Mater Sci Mater Med 33 (2022). https://doi.org/10.1007/s10856-021-06626-3.

[5] D. Dorosz, Rare earth ions doped aluminosilicate and phosphate double clad optical fibres, 56 (2008) 103–111.

[6] J.S. Mccloy, S. Schuller, Vitrification ofwastes: fromunwanted to controlled crystallization, a review, Comptes Rendus Géoscience 354 (2022) 121–160. https://doi.org/https://doi.org/10.5802/crgeos.111.

[7] I. Wacławska, M. Szumera, Thermal behaviour of Fe-doped silicate-phosphate glasses, in: J Therm Anal Calorim, Springer, 2010: pp. 423–427. https://doi.org/10.1007/s10973-010-0798-5.

[8] M. Szumera, I. Wacławska, Thermal study of Mn-containing silicate-phosphate glasses, in: J Therm Anal Calorim, Kluwer Academic Publishers, 2012: pp. 583–588. https://doi.org/10.1007/s10973-011-1941-7.

[9] I. Wacławska, M. Szumera, J. Sułowska, Structural characterization of zinc-modified glasses from the SiO 2-P 2 O 5-K 2 O-CaO-MgO system, (2016). https://doi.org/10.1016/j.jallcom.2016.01.125.

[10] R.K. Mishra, K. V. Sudarsan, P. Sengupta, R.K. Vatsa, A.K. Tyagi, C.P. Kaushik, D. Das, K. Raj, Role of sulfate in structural modifications of sodium barium borosilicate glasses developed for nuclear waste immobilization, Journal of the American Ceramic Society 91 (2008) 3903–3907. https://doi.org/10.1111/j.1551-2916.2008.02773.x.

[11] C.M. Jantzen, M.E. Smith, D.K. Peeler, Dependency of sulfate solubility on melt composition and melt polymerization, in: Ceramic Transactions, 2005: pp. 141–152. https://doi.org/10.1002/9781118408438.ch13.

[12] P.A. Bingham, R.J. Hand, Sulphate incorporation and glass formation in phosphate systems for nuclear and toxic waste immobilization, Mater Res Bull 43 (2008) 1679–1693. https://doi.org/10.1016/j.materresbull.2007.07.024.

[13] Y. Oba, R. Motokawa, K. Kaneko, T. Nagai, Y. Tsuchikawa, T. Shinohara, J.D. Parker, Y. Okamoto, Neutron resonance absorption imaging of simulated high-level radioactive waste in borosilicate glass, Sci Rep 13 (2023) 1–8. https://doi.org/10.1038/s41598-023-37157-2.

[14] Y. Morizet, M. Paris, I. Di Carlo, B. Scaillet, Effect of sulphur on the structure of silicate melts under oxidizing conditions, Chem Geol 358 (2013) 131–147. https://doi.org/10.1016/j.chemgeo.2013.09.004.

[15] T. Tsujimura, X. Xue, M. Kanzaki, M.J. Walter, Sulfur speciation and network structural changes in sodium silicate glasses: Constraints from NMR and Raman spectroscopy, Geochim Cosmochim Acta 68 (2004) 5081–5101. https://doi.org/10.1016/j.gca.2004.08.029.

[16] D.A. Mckeown, I.S. Muller, H. Gan, I.L. Pegg, C.A. Kendziora, Raman studies of sulfur in borosilicate waste glasses: sulfate environments, n.d.

[17] D. Manara, A. Grandjean, O. Pinet, J.L. Dussossoy, D.R. Neuville, Sulfur behavior in silicate glasses and melts: Implications for sulfate incorporation in nuclear waste glasses as a function of alkali cation and V2O5 content, J Non Cryst Solids 353 (2007) 12–23. https://doi.org/10.1016/j.jnoncrysol.2006.09.041.

[18] Y. Morizet, S. Ory, I. Di Carlo, B. Scaillet, P. Echegut, The effect of sulphur on the glass transition temperature in anorthite-diopside eutectic glasses, Chem Geol 416 (2015) 11–18. https://doi.org/10.1016/j.chemgeo.2015.10.010.

[19] C.P. Kaushik, R.K. Mishra, P. Sengupta, A. Kumar, D. Das, G.B. Kale, K. Raj, Barium borosilicate glass - a potential matrix for immobilization of sulfate bearing high-level radioactive liquid waste, Journal of Nuclear Materials 358 (2006) 129–138. https://doi.org/10.1016/j.jnucmat.2006.07.004.

[20] S.V. Stefanovskij, F.A. Lifanov, Glasses for immobilization of sulphate-containing radioactive wastes, Radiokhimiya 31 (1989) 129–134.
[21] S. V Stefanovsky, O.I. Stefanovsky, I.L. Prusakov, M.I. Kadyko, A.A. Averin, B.S. Nikonov, Speciation of sulphate ions in sodium alumino(iron)phosphate glasses, (2019). https://doi.org/10.1016/j.jnoncrysol.2019.01.005.
[22] N.M. Bobkova, E.E. Trusova, Structure of Sulfate-Containing Glasses and the Structural State of SO3 Groups in Them (Review), Glass and Ceramics (English Translation of Steklo i Keramika) 74 (2017) 153–157. https://doi.org/10.1007/s10717-017-9951-y.
[23] N. Hémono, F. Muñoz, Dissolution of SO3 within a lithium phosphate glass network and structure-property relationships, Physics and Chemistry of Glasses: European Journal of Glass Science and Technology Part B 51 (2010) 121–126.
[24] H. Li, J.G. Darab, D.W. Matson, P.A. Smith, P. Hrma, Y. Chen, J. Liu, Phosphate-Sulfate Interaction in Simulated Low-level Radioactive Waste Glasses, MRS Online Proceedings Library (OPL) 412 (1995) 141–148. https://doi.org/https://doi.org/10.1557/PROC-412-141.
[25] V.G. Arkhipov, L. V Ivanova, V.L. Mamoshin, P.I. Buler, O.I. Lushchai, L.M. Galnykina, A spectroscopic study of structural features in alkali-bearing sulfate-phosphate glasses, J Appl Spectrosc 45 (1986) 976–978. https://doi.org/10.1007/BF00663524.
[26] B. Ravel, M. Newville, ATHENA, ARTEMIS, HEPHAESTUS: Data analysis for X-ray absorption spectroscopy using IFEFFIT, in: J Synchrotron Radiat, J Synchrotron Radiat, 2005: pp. 537–541. https://doi.org/10.1107/S0909049505012719.
[27] A. Di Cicco, G. Aquilanti, M. Minicucci, E. Principi, N. Novello, A. Cognigni, L. Olivi, Novel XAFS capabilities at ELETTRA synchrotron light source, in: J Phys Conf Ser, Institute of Physics Publishing, 2009. https://doi.org/10.1088/1742-6596/190/1/012043.
[28] S. Vaishnav, A.C. Hannon, E.R. Barney, P.A. Bingham, Neutron Diffraction and Raman Studies of the Incorporation of Sulfate in Silicate Glasses, Journal of Physical Chemistry C 124 (2020) 5409–5424. https://doi.org/10.1021/acs.jpcc.9b10924.
[29] P.A. Bingham, S. Vaishnav, S.D. Forder, A. Scrimshire, B. Jaganathan, J. Rohini, J.C. Marra, K.M. Fox, E.M. Pierce, P. Workman, J.D. Vienna, Modelling the sulfate capacity of simulated radioactive waste borosilicate glasses, J Alloys Compd 695 (2017) 656–667. https://doi.org/10.1016/j.jallcom.2016.11.110.
[30] Jason M. Lonergan, Charmayne Lonergan, Joshua Silverstein, Pornsinee Cholsaipant, John McCloy, Thermal properties of sodium borosilicate glasses as a function of sulfur content, Journal of the American Ceramic Society 103 (2020) 3610–3619. https://doi.org/https://doi.org/10.1111/jace.17057.
[31] S. Tan, The incorporation and solubility of sulphate, chloride and molybdate anions in borosilicate and aluminosilicate glasses, Immobilisation Science Laboratory (2015) 254.
[32] W.R. Taylor, Application of infrared spectroscopy to studies of silicate glass structure: Examples from the melilite glasses and the systems Na2O-SiO2 and Na2O-Al2O3-SiO2, Proceedings of the Indian Academy of Sciences - Earth and Planetary Sciences 99 (1990) 99–117. https://doi.org/10.1007/BF02871899.
[33] M. Szumera, I. Wacławska, Spectroscopic and thermal studies of silicate-phosphate glass, in: J Therm Anal Calorim, 2007: pp. 151–156. https://doi.org/10.1007/s10973-006-8118-9.
[34] J.D. Jia Ding, Y.C. Youkuo Chen, W.C. Wei Chen, L.H. Lili Hu, G.B. G. Boulon, Effect of P2O5 addition on the structural and spectroscopic properties of sodium

aluminosilicate glass, Chinese Optics Letters 10 (2012) 071602–071605. https://doi.org/10.3788/col201210.071602.

[35] B. Piriou, P. McMillan, The high-frequency vibrational spectra of vitreous and crystalline orthosilicates., American Mineralogist 68 (1983) 426–443.

[36] H. Wang, Z. Chen, L. Liu, Y. Sun, X. Wang, Roles of P2O5 addition on the viscosity and structure of CaO-SiO2-Al2O3-Na2O-P2O5 melts, ISIJ International 58 (2018) 1644–1649. https://doi.org/10.2355/isijinternational.ISIJINT-2018-138.

[37] A.M.B. Silva, C.M. Queiroz, S. Agathopoulos, R.N. Correia, M.H.V. Fernandes, J.M. Oliveira, Structure of SiO2-MgO-Na2O glasses by FTIR, Raman and 29Si MAS NMR, J Mol Struct 986 (2011) 16–21. https://doi.org/10.1016/j.molstruc.2010.11.023.

[38] M.D. O'Donnell, S.J. Watts, R.G. Hill, R. V. Law, The effect of phosphate content on the bioactivity of soda-lime- phosphosilicate glasses, J Mater Sci Mater Med 20 (2009) 1611–1618. https://doi.org/10.1007/s10856-009-3732-2.

[39] I. Lebecq, F. Désanglois, A. Leriche, C. Follet-Houttemane, Compositional dependence on the in vitro bioactivity of invert or conventional bioglasses in the Si-Ca-Na-P system, J Biomed Mater Res A 83 (2007) 156–168. https://doi.org/10.1002/jbm.a.31228.

[40] S. Agathopoulos, D.U. Tulyaganov, J.M.G. Ventura, S. Kannan, A. Saranti, M.A. Karakassides, J.M.F. Ferreira, Structural analysis and devitrification of glasses based on the CaO-MgO-SiO 2 system with B 2 O 3 , Na 2 O, CaF 2 and P 2 O 5 additives, (2006). https://doi.org/10.1016/j.jnoncrysol.2005.12.003.

[41] P. McMillan, Structural studies of silicate glasses and melts-applications and limitations of Raman spectroscopy, Contributions to Mineralogy and Petrology 69 (1984) 622–644. https://doi.org/10.1007/BF00307725.

[42] T. Furukawa, K.E. Fox, W.B. White, Raman spectroscopic investigation of the structure of silicate glasses. III. Raman intensities and structural units in sodium silicate glasses, J Chem Phys 75 (1981) 3226–3237. https://doi.org/10.1063/1.442472.

[43] B. Mysen, Phosphorus speciation changes across the glass transition in highly polymerized alkali silicate glasses and melts, American Mineralogist 81 (1996) 1531–1534. https://doi.org/10.2138/am-1996-11-1226.

[44] F. Spirovski, I. Kuzmanovski, H.D. Lutz, B. Engelen, Infrared and Raman spectra of magnesium ammonium phosphate hexahydrate (struvite) and its isomorphous analogues . I . Spectra of protiated and partially deuterated magnesium potassium phosphate hexahydrate, 689 (2004) 1–10. https://doi.org/10.1016/j.molstruc.2003.08.019.

[45] X. Hu, L. Liu, S. Zhai, The structure-Raman spectra relationships of Mg 3 (PO 4) 2 polymorphs : A comprehensive experimental and DFT study, Spectrochim Acta A Mol Biomol Spectrosc 245 (2021) 118906. https://doi.org/10.1016/j.saa.2020.118906.

[46] L. Miladi, A. Oueslati, K. Guidara, Vibrational spectroscopic and dielectric properties investigations of phase transitions in KMgPO4 compound, J Mol Struct 1148 (2017) 404–411. https://doi.org/10.1016/j.molstruc.2017.07.047.

[47] D. Matson, S. Sharma, J. Philpotts, The structure of high-silica alkali-silicate glasses. A Raman spectroscopic investigation, J Non Cryst Solids 58 (1983) 323–352. https://doi.org/10.1016/S0251-1088(83)90297-8.

[48] Y.Q. Wu, C. Dai, G.C. Jiang, Local structure of calcium silicate melts from classical molecular dynamics simulation and a newly constructed thermodynamic model, Transactions of Nonferrous Metals Society of China (English Edition) 24 (2014) 1488–1499. https://doi.org/10.1016/S1003-6326(14)63217-9.

[49] C. Liu, R. Zhang, X. Zhao, J. Jia, Y. Min, Quantification of phosphorus structures in CaO–SiO2–P2O5 glasses via Raman spectroscopy, J Non Cryst Solids 557 (2021) 120579. https://doi.org/10.1016/j.jnoncrysol.2020.120579.

[50] Y. Sun, Z. Zhang, L. Liu, X. Wang, FTIR, Raman and NMR investigation of CaO–SiO2–P2O5 and CaO–SiO2–TiO2–P2O5 glasses, J Non Cryst Solids 420 (2015) 26–33. https://doi.org/10.1016/j.jnoncrysol.2015.04.017.

[51] B.O. Mysen, L.W. Finger, D. Virgo, F.A. Seifert, Curve-fitting of Raman spectra of silicate glasses., American Mineralogist 67 (1982) 686–695.

[52] Y. Morizet, E. Gennaro, S. Jego, Z. Zajacz, G. Iacono-Marziano, M. Pichavant, I. Di Carlo, C. Ferraina, P. Lesne, A Raman calibration for the quantification of SO42- groups dissolved in silicate glasses: Application to natural melt inclusions, American Mineralogist 102 (2017) 2065–2076. https://doi.org/10.2138/am-2017-6100.

[53] Y.Q. Wu, G.C. Jiang, J.L. You, H.Y. Hou, H. Chen, Raman scattering coefficients of symmetrical stretching modes of microstructural units in sodium silicate melts, Wuli Xuebao/Acta Physica Sinica 54 (2005) 961–966. https://doi.org/10.7498/aps.54.961.

[54] B.O. Mysen, J.D. Frantz, Silicate melts at magmatic temperatures: in-situ structure determination to 1651°C and effect of temperature and bulk composition on the mixing behavior of structural units, Contributions to Mineralogy and Petrology 117 (1994) 1–14. https://doi.org/10.1007/BF00307725.

[55] F. Wang, Y. Wang, Q. Liao, J. Zhang, W. Zhao, Y. Yuan, H. Zhu, L. Li, Y. Zhu, Immobilization of a simulated HLW in phosphate based glasses/glass-ceramics by melt-quenching process, J Non Cryst Solids 545 (2020). https://doi.org/10.1016/j.jnoncrysol.2020.120246.

[56] T. Okura, T. Miyachi, H. Monma, Properties and vibrational spectra of magnesium phosphate glasses for nuclear waste immobilization, J Eur Ceram Soc 26 (2006) 831–836. https://doi.org/10.1016/j.jeurceramsoc.2005.07.031.

[57] G.E.B.Jr. and C.W.P. W.E. JACKSON, X-ray absorption study of the potassium coordination environment in glasses from the NaAlSi3O8-KAlSi3O8 binary, J Non Cryst Solids 93 (1987) 311–322.

[58] M. Gajek, M. Leśniak, M. Sitarz, E. Stodolak-Zych, A. Rapacz-Kmita, The crystallization and structure features of glass within the K2O–MgO–CaO–Al2O3–SiO2-(BaO) system, J Mol Struct 1220 (2020) 128747. https://doi.org/10.1016/j.molstruc.2020.128747.

[59] N. Zotov, H. Keppler, The influence of water on the structure of hydrous sodium tetrasilicate glasses, American Mineralogist 83 (1998) 823–834. https://doi.org/10.2138/am-1998-7-814.

[60] M. Szumera, Molybdenum modified phosphate glasses studied by 31P MAS NMR and Raman spectroscopy, Spectrochim Acta A Mol Biomol Spectrosc 137 (2015) 111–115. https://doi.org/10.1016/j.saa.2014.08.038.

[61] B.O. Mysen, G.D. Cody, Silicate-phosphate interactions in silicate glasses and melts: II. Quantitative, high-temperature structure of P-bearing alkali aluminosilicate melts, Geochim Cosmochim Acta 65 (2001) 2413–2431. https://doi.org/10.1016/S0016-7037(01)00598-1.

[62] H. Grussaute, L. Montagne, G. Palavit, J.L. Bernard, Phosphate speciation in Na2O-CaO-P2O5-SiO2 and Na2O-TiO2-P2O5-SiO2 glasses, J Non Cryst Solids 263 (2000) 312–317. https://doi.org/10.1016/S0022-3093(99)00643-2.

[63] A. Berezicka, M. Szumera, J. Sułowska, P. Jeleń, Z. Olejniczak, J. Stępień, M. Zając, S. Pollastri, L. Olivi, Unraveling the nature of sulfur-bearing silicate-phosphate glasses: Insights from multi-spectroscopic (Raman, MIR, 29Si, 31P MAS-NMR, XAS, XANES) investigation, Ceram Int 48 (2022) 4238–4254. https://doi.org/10.1016/j.ceramint.2021.10.216.

[64] G.D. Cody, B. Mysen, G. Sághi-Szabó, J.A. Tossell, Silicate-phosphate interactions in silicate glasses and melts: I. A multinuclear (27Al,29Si,31P) MAS NMR and ab initio chemical shielding (31P) study of phosphorous speciation in silicate glasses, Geochim Cosmochim Acta 65 (2001) 2395–2411. https://doi.org/10.1016/S0016-7037(01)00597-X.

[65] H. Maekawa, T. Maekawa, K. Kawamura, T. Yokokawa, The structural groups of alkali silicate glasses determined from 29Si MAS-NMR, J Non Cryst Solids 127 (1991) 53–64. https://doi.org/10.1016/0022-3093(91)90400-Z.

[66] R. Dupree, D. Holland, P.W. McMillan, R.F. Pettifer, The structure of soda-silica glasses: A mas NMR study, J Non Cryst Solids 68 (1984) 399–410. https://doi.org/10.1016/0022-3093(84)90020-6.

[67] H. Eckert, Structural characterization of bioactive glasses by solid state NMR, J Solgel Sci Technol 88 (2018) 263–295. https://doi.org/10.1007/s10971-018-4795-7.

[68] W.J. Malfait, W.E. Halter, Y. Morizet, B.H. Meier, R. Verel, Structural control on bulk melt properties: Single and double quantum 29Si NMR spectroscopy on alkali-silicate glasses, Geochim Cosmochim Acta 71 (2007) 6002–6018. https://doi.org/10.1016/j.gca.2007.09.011.

[69] I. Wacławska, M. Szumera, Influence of MgO (CaO) on the structure of silicate-phosphate glasses : TA and NMR study, J Therm Anal Calorim 84 (2006) 185–190. https://doi.org/10.1007/s10973-005-7183-9.

[70] M. Yang, X. Cai, C. Wang, Z. Wang, F. Xue, C. Chu, J. Bai, Q. Liu, X. Ni, Highly Stable Amorphous (Pyro)phosphate Aggregates: Pyrophosphate as a Carrier for Bioactive Ions and Drugs in Bone Repair Applications, ACS Omega (2024). https://doi.org/10.1021/acsomega.4c01660.

[71] H. Aguiar, E.L. Solla, J. Serra, P. González, B. León, F. Malz, C. Jäger, Raman and NMR study of bioactive Na2O-MgO-CaO-P2O5-SiO2 glasses, J Non Cryst Solids 354 (2008) 5004–5008. https://doi.org/10.1016/j.jnoncrysol.2008.07.033.

[72] I. Wacławska, M. Szumera, Influence of MgO (CaO) on the structure of silicate-phosphate glasses : TA and NMR study, J Therm Anal Calorim 84 (2006) 185–190. https://doi.org/10.1007/s10973-005-7183-9.

[73] R.J. Kirkpatrick, R.K. Brow, Nuclear magnetic resonance investigation of the structures of phosphate and phosphate-containing glasses: A review, Solid State Nucl Magn Reson 5 (1995) 9–21. https://doi.org/10.1016/0926-2040(95)00042-O.

[74] M.D. O'Donnell, S.J. Watts, R. V Law, R.G. Hill, Effect of P2O5 content in two series of soda lime phosphosilicate glasses on structure and properties - Part I: NMR, J Non Cryst Solids 354 (2008) 3554–3560. https://doi.org/10.1016/j.jnoncrysol.2008.03.034.

[75] J.K. Christie, R.I. Ainsworth, N.H. De Leeuw, Investigating structural features which control the dissolution of bioactive phosphate glasses: Beyond the network connectivity, J Non Cryst Solids 432 (2016) 31–34. https://doi.org/10.1016/J.JNONCRYSOL.2015.01.016.

[76] M. Edén, The split network analysis for exploring composition-structure correlations in multi-component glasses: I. Rationalizing bioactivity-composition trends of bioglasses,

J Non Cryst Solids 357 (2011) 1595–1602. https://doi.org/10.1016/j.jnoncrysol.2010.11.098.

[77] M. Edén, The split network analysis for exploring composition-structure correlations in multi-component glasses: I. Rationalizing bioactivity-composition trends of bioglasses, J Non Cryst Solids 357 (2011) 1595–1602. https://doi.org/10.1016/j.jnoncrysol.2010.11.098.

[78] M.D. O'Donnell, S.J. Watts, R. V. Law, R.G. Hill, Effect of P2O5 content in two series of soda lime phosphosilicate glasses on structure and properties - Part I: NMR, J Non Cryst Solids 354 (2008) 3554–3560. https://doi.org/10.1016/j.jnoncrysol.2008.03.034.

[79] M. Edén, The split network analysis for exploring composition-structure correlations in multi-component glasses: I. Rationalizing bioactivity-composition trends of bioglasses, J Non Cryst Solids 357 (2011) 1595–1602. https://doi.org/10.1016/j.jnoncrysol.2010.11.098.

[80] Y. Yu, R. Mathew, M. Edén, Quantitative composition – bioactivity relationships of phosphosilicate glasses : Bearings from the phosphorus content and network polymerization, J Non Cryst Solids (2018) 1–12. https://doi.org/10.1016/j.jnoncrysol.2018.07.060.

[81] R.G. Hill, D.S. Brauer, Predicting the bioactivity of glasses using the network connectivity or split network models, J Non Cryst Solids 357 (2011) 3884–3887. https://doi.org/10.1016/j.jnoncrysol.2011.07.025.

[82] R. Mathew, B. Stevensson, A. Tilocca, M. Edén, Toward a rational design of bioactive glasses with optimal structural features: Composition-structure correlations unveiled by solid-state NMR and MD simulations, Journal of Physical Chemistry B 118 (2014) 833–844. https://doi.org/10.1021/jp409652k.

[83] C. Ragoen, L. Cormier, A.I. Bidegaray, S. Vives, F. Henneman, N. Trcera, S. Godet, A XANES investigation of the network-modifier cations environment before and after the Na+/K+ ion-exchange in silicate glasses, J Non Cryst Solids 479 (2018) 97–104. https://doi.org/10.1016/j.jnoncrysol.2017.10.021.

[84] S.P. Thompson, Structural signatures of medium-range order in annealed laboratory silicates, Astron Astrophys 484 (2008) 251–265. https://doi.org/10.1051/0004-6361:20078675.

[85] G.S. Henderson, F.M.F. De Groot, B.J.A. Moulton, X-ray absorption near-edge structure (XANES) spectroscopy, Rev Mineral Geochem 78 (2014) 75–138. https://doi.org/10.2138/rmg.2014.78.3.

[86] O. Takahashi, Y. Tamenori, T. Suenaga, T. Ikeda-Fukazawa, J. Matsuno, A. Tsuchiyama, XANES spectra of forsterite in crystal, surface, and amorphous states, AIP Adv 8 (2018). https://doi.org/10.1063/1.5017245.

[87] D. Cabaret, M. Le Grand, A. Ramos, A.M. Flank, S. Rossano, L. Galoisy, G. Calas, D. Ghaleb, Medium range structure of borosilicate glasses from Si K-edge XANES: A combined approach based on multiple scattering and molecular dynamics calculations, J Non Cryst Solids 289 (2001) 1–8. https://doi.org/10.1016/S0022-3093(01)00733-5.

[88] D. Li, G.M. Bancroft, M.E. Fleet, X.H. Feng, Silicon K-edge XANES spectra of silicate minerals, Phys Chem Miner 22 (1995) 115–122. https://doi.org/10.1007/BF00202471.

[89] G.S. Henderson, A Si K-edge EXAFS / XANES, 183 (1995) 43–50.

[90] D. Li, G.M. Bancroft, M. Kasrai, M.E. Fleet, X.H. Feng, K.H. Tan, B.X. Yang, High-resolution Si K- and L2,3-edge XANES of α-quartz and stishovite, Solid State Commun 87 (1993) 613–617. https://doi.org/10.1016/0038-1098(93)90123-5.

[91] P. Ildefonse, G. Calas, A.M. Flank, P. Lagarde, Low Z elements (Mg, Al, and Si) K-edge X-ray absorption spectroscopy in minerals and disordered systems, Nuclear Inst. and Methods in Physics Research, B 97 (1995) 172–175. https://doi.org/10.1016/0168-583X(94)00710-1.

[92] Y. Morizet, N. Trcera, C. Larre, M. Rivoal, E. Le Menn, D. Vantelon, F. Gaillard, X-ray absorption spectroscopic investigation of the Ca and Mg environments in CO 2 -bearing silicate glasses, Chem Geol 510 (2019) 91–102. https://doi.org/10.1016/j.chemgeo.2019.02.014.

[93] N. Trcera, D. Cabaret, S. Rossano, F. Farges, A.M. Flank, P. Lagarde, Experimental and theoretical study of the structural environment of magnesium in minerals and silicate glasses using X-ray absorption near-edge structure, Phys Chem Miner 36 (2009) 241–257. https://doi.org/10.1007/s00269-008-0273-z.

[94] D. Li, M. Peng, T. Murata, Coordination and local structure of magnesium in silicate minerals and glasses: Mg K-edge XANES study, Can Mineral 37 (1999) 199–206.

[95] G. ichiro Yamamoto, A. Kyono, S. Okada, Temperature dependence of amorphous magnesium carbonate structure studied by PDF and XAFS analyses, Sci Rep 11 (2021) 1–8. https://doi.org/10.1038/s41598-021-02261-8.

[96] A. Jain, S.P. Ong, G. Hautier, W. Chen, W.D. Richards, S. Dacek, S. Cholia, D. Gunter, D. Skinner, G. Ceder, K.A. Persson, Commentary: The materials project: A materials genome approach to accelerating materials innovation, APL Mater 1 (2013) 11002. https://doi.org/10.1063/1.4812323.

[97] W. Li, X.M. Liu, Y. Hu, Potassium and Calcium K-Edge XANES in Chemical Compounds and Minerals: Implications for Geological Phase Identification, Geostand Geoanal Res 44 (2020) 805–819. https://doi.org/10.1111/ggr.12351.

[98] G.J. Padežnik, A. Kodre, I. Arčon, R. Prešeren, K-edge x-ray-absorption spectrum of potassium, Phys Rev A 64 (2001) 1–5. https://doi.org/10.1103/PhysRevA.64.022508.

[99] G. Cibin, A. Mottana, A. Marcelli, M.F. Brigatti, Potassium coordination in trioctahedral micas investigated by K-edge XANES spectroscopy, Mineral Petrol 85 (2005) 67–87. https://doi.org/10.1007/s00710-005-0099-z.

[100] Www.kemkes.go.id, Atomistic structure of alkali-silica reaction products refined from X-ray diffraction and micro X-ray absorption data, Satukan Tekad Menuju Indonesia Sehat 105958 (2020).

Declaration of interests

☒The authors declare that they have no known competing financial interests or personal relationships that could have appeared to influence the work reported in this paper.

☐The authors declare the following financial interests/personal relationships which may be considered as potential competing interests:

3. Publication P3

molecules

MDPI

Article

Alteration of Sulfur-Bearing Silicate-Phosphate (Agri)Glasses in Soil Environment: Structural Characterization and Chemical Reactivity of Fertilizer Glasses: Insights from 'In Vitro' Studies

Anna Berezicka *, Justyna Sułowska and Magdalena Szumera *

Faculty of Materials Science and Ceramics, AGH University of Krakow, Al. A. Mickiewicza 30, 30-059 Krakow, Poland; sulowska@agh.edu.pl

* Correspondence: berezicka@agh.edu.pl (A.B.); mszumera@agh.edu.pl (M.S.)

Abstract: Vitreous carriers of essential nutrients should release elements in response to plant demand, minimizing over-fertilization risks. This study focused on designing and characterizing sulfate-bearing slow-release fertilizers based on four glass series ($41SiO_2 \cdot 6(10)P_2O_5 \cdot 20K_2O$–$33(29)MgO/CaO/MgO + CaO$) with increasing sulfate content. Structural analysis identified a network dominated by Q^2_{Si} units, with some Q^3_{Si} species and isolated Q^0_P units. This fragmented structure resulted in high solubility in acidic environments while maintaining water resistance. Such dual behavior is a direct consequence of the delicate balance between depolymerized silicate chains and isolated orthophosphate units, which ensure rapid ion exchange under acidic conditions while preventing uncontrolled leaching in neutral media. Nutrient leaching depended on SO_3 content, affecting matrix rigidity, and on the type of alkaline earth modifier and P_2O_5 content. Dissolution kinetics showed an initial rapid release phase, followed by stabilization governed by silicate hydrolysis. Thermal analysis linked network flexibility to dissolution behavior—CaO promoted an open structure with high SiO_2 release, MgO increased rigidity, while their co-addition reduced ion diffusion and silica dissolution. The thermal behavior of the glasses provided indirect insight into their structural rigidity, revealing how compositional variations influence the mechanical stability of the network. This structural rigidity, inferred from glass transition and crystallization phenomena, was found to correlate with the selective dissolution profiles observed in acidic versus neutral environments. These results reveal complex interactions between composition, structure, and nutrient release, shaping the agricultural potential of these glasses.

Keywords: slow-release fertilizers; sulfate-bearing glasses; nutrient leaching; glass structure; dissolution kinetics

check for updates

Academic Editors: Loredana Maiuolo and Paola Costanzo

Received: 26 February 2025
Revised: 31 March 2025
Accepted: 3 April 2025
Published: 9 April 2025

Citation: Berezicka, A.; Sułowska, J.; Szumera, M. Alteration of Sulfur-Bearing Silicate-Phosphate (Agri)Glasses in Soil Environment: Structural Characterization and Chemical Reactivity of Fertilizer Glasses: Insights from 'In Vitro' Studies. *Molecules* **2025**, *30*, 1684. https://doi.org/10.3390/molecules30081684

Copyright: © 2025 by the authors. Licensee MDPI, Basel, Switzerland. This article is an open access article distributed under the terms and conditions of the Creative Commons Attribution (CC BY) license (https://creativecommons.org/licenses/by/4.0/).

1. Introduction

The concept of glass fertilizers originated from the observation of natural processes and an effort to replicate them. Volcanic activity, despite its destructive impact, has given rise to some of the most fertile soils on Earth, which owe their unique properties to the presence of volcanic glass—one of the first components to undergo weathering. As glass decomposes, essential cations are gradually released into the soil, making them bioavailable for plant uptake [1–3].

While mineral weathering plays a crucial role in sustaining long-term soil fertility, it alone may not provide a sufficient supply of nutrients to support optimal plant growth or soil revitalization. Remarkedly, soil is far from being an inert medium; it is a complex,

living ecosystem teeming with microorganisms that work in symbiosis to maintain nutrient availability. Both plants as well as rhizosphere bacteria and fungi contribute to this process and respond to nutrient deficiencies by exuding organic acids, sugars, vitamins, inorganic ions, and enzymes, among other compounds, to mobilize nutrients from soil minerals, further enhancing nutrient cycling [4–6].

A well-designed glass fertilizer integrates seamlessly into this dynamic system, responding to the biochemical signals of the rhizosphere while preserving the delicate biogeochemical balance essential for sustainable soil health [3,7–13].

Achieving this 'proper design' is critical to ensuring the final product exhibits the desired properties. However, despite the apparent simplicity of the glass fertilizer concept, its fabrication presents significant challenges. The final material must meet several key requirements:

- Targeted composition—the glass must incorporate specific macro- and micronutrients to address existing soil deficiencies effectively;
- Amorphous structure—the material should exist in a fully vitreous state to enhance its solubility and reactivity compared to its crystalline counterparts;
- Selective solubility—rather than dissolving readily in water, the glass should respond to acidic exudates from plant roots and soil microorganisms, ensuring nutrients are released only when needed;
- Slow release—nutrient leaching should occur gradually throughout the entire plant development cycle, providing a sustained supply of essential elements.

Regarding the first of the aforementioned requirements, extensive research has shown that a silicon-oxygen matrix provides a highly adaptable framework capable of accommodating a wide range of beneficial ions [3,14–19]. These include not only well-established macronutrients such as PO_4^{3-}, K^+, Mg^{2+}, or Ca^{2+}, but also less conventional ones, such as SO_4^{2-}, recently acknowledged as the fourth major nutrient element, alongside NPK—a designation well justified by its critical role in protein structure and synthesis, enzyme and vitamin function, and plant defense mechanisms against stress and pests [20–30].

While achieving the first requirement may seem straightforward, it is inherently linked to the second—the selected components must not only be beneficial for the intended application but also capable of forming a stable vitreous network. Although it is commonly believed that any material can be transformed into a glass if cooled rapidly enough from the molten state to prevent nucleation and crystal growth, obtaining fully amorphous materials is often far more complex [31–36]. This difficulty arises from the fact that a glassy state represents a departure from the thermodynamically favored, long-range periodic lattice arrangement. Hence, even if a liquid is successfully frozen into a glass by restricting atomic mobility and preventing rearrangement into equilibrium lattice sites, the system will gradually and imperceptibly shift toward its energy minimum over time [37–41]. This challenge becomes particularly pronounced in multicomponent systems, where elements with substantial differences in bonding nature and chemical properties must coexist within a common network. Such structural incompatibilities introduce internal stresses that lower the energy barrier for nucleation, increasing the likelihood of crystallization. This issue is especially relevant for SiO_2–P_2O_5-based glass fertilizers and sulfate-containing oxide glass systems, both of which exhibit a strong tendency toward phase separation or crystallization [42–44]. The requirement of obtaining fully amorphous carriers of essential nutrients is not arbitrary. The glassy state, being a higher-energy configuration, is significantly more soluble than its crystalline counterpart, in which the presence of long-range order and the absence of strained, reactive Si–O–Si bonds confer superior chemical durability by limiting hydrolysis sites and restricting water penetration into the bulk [45–50]. Thus, ensuring an

amorphous structure is critical to enhancing the controlled release of useful ions, making glass fertilizers' behavior effective and predictable in their intended applications.

Careful selection of chemical composition is also crucial for meeting the third and fourth prerequisites. Unlike crystalline soil minerals, which weather too slowly to support plant growth, or conventional mineral fertilizers, which release nutrients rapidly and hence are prone to leaching losses, glass fertilizers can strike a balance—offering a controlled, responsive supply of essential elements. In the case of conventional mineral fertilizers, even regular rainfall can cause excessive and uncontrolled nutrient release from their chemical structure, leading to losses and potential environmental pollution. This release is dictated by plant-driven biochemical signals, primarily the exudation of weak organic acids, ensuring nutrients become available precisely when they are needed [51–56].

The sustained nutrient release from glass fertilizers is driven by processes occurring in their near-surface regions under the influence of chemically active soil components. The release rate is primarily governed by the concentration of exogenous protonated species (H^+ or H_3O^+) in the surrounding environment as well as the structural characteristics of the glass matrix. Specifically, the degree of network connectivity and its openness dictate the susceptibility of Si–O–Si linkages to hydrolysis and water infiltration, respectively, both controlling the pace of dissolution and the availability of nutrients over time [57–59].

Remarkedly, such chemical activity of glass fertilizers is inherently tied to their structural characteristics, which, in turn, are dictated by material's chemical composition—emphasizing the fundamental composition–structure–property relationship. Since glass chemical activity is founded on the gradual release of its constituents into the soil solution, it is significantly influenced by the degree of network cross-linking and the strength of the bonds between network formers and modifier cations [60,61]. Consequently, the transition from highly soil-reactive to chemically inert glass compositions can primarily be controlled by adjusting the content of network-forming oxides, particularly SiO_2 and P_2O_5 [62].

As demonstrated by Edèn [63], materials with an 'disconnected' network—composed predominantly of disrupted silicate chains (primarily Q^2_{Si} tetrahedra, with minor Q^3_{Si} and Q^1_{Si} contributions)—exhibit enhanced interaction with biological solutions compared to three-dimensional networks dominated by Q^3_{Si} and Q^4_{Si} species. It is worth emphasizing that in the Q^n notation, used to describe the structure of silicate (or phosphate) glasses, Q stands for 'quaternary', while n indicates the number of bridging oxygens (BO, bridging oxygens) in a given SiO_4 or PO_4 polyhedron (meaning that the remaining 4−n are non-bridging oxygens, NBO). Since a bridging oxygen (BO) links two adjacent tetrahedra, these factors reflect the overall network connectivity (NC) of the glass: n = 2 corresponds to infinite chains or rings, n = 3 represents sheet-like structures, and n = 4 refers to a three-dimensional network framework. Furthermore, compositions exhibiting the strongest response to biological fluids typically have a network connectivity (NC) of approximately 2–3 [60]—such a loosely connected structure facilitates the surface penetration of physiological solutions into the glass, granting access to modifier ions embedded within the matrix, thereby distinguishing bioactive (or soil-active) glasses from their conventional counterparts [64].

The influence of P_2O_5 content on glass structure and, consequently, its chemical activity is more complex than that of silicon. Generally, when phosphorus is primarily present as isolated Q^0_P species, charge-balanced by modifier cations, and the silicate subnetwork maintains an NC within the chemically active range (≈2–3), an increase in its content enhances glass's interaction with biological solutions [63]. This is attributed to the facile release of isolated PO_4^{3-} groups, which concurrently accelerate the formation of a metastable layer of slow dissolution on the glass surface—an essential factor in regulating the slow-release properties of glass fertilizers [60,62]. However, excessive phosphorus concentrations can

deplete the reservoir of available modifier cations, leading to the clustering of orthophosphate tetrahedra and the emergence of Q^1_P and Q^2_P species. This structural shift significantly reduces glass solubility and reactivity in biological environments, as demonstrated by Edèn [63] and further corroborated by Ting et al. [65], who observed that the presence of polyphosphate chains markedly increased resistance to physiological fluids. Additionally, mixed-network glasses with high P_2O_5 and low SiO_2 content exhibit improved mechanical and thermo-mechanical properties, which can be fine-tuned by adjusting silica levels in the composition [66,67].

An alternative approach to modifying the glass structure—and consequently its susceptibility to degradation in biological environments—involves adjusting the proportion of glass components that alter the vitreous network by converting bridging oxygens (BOs), which ionically-covalently link adjacent polyhedra, into non-bridging oxygens (NBOs). This transformation results in the formation of Si(P)-O-M^+ linkages, where M^+ represents a modifier cation. The incorporation of increasing amounts of such network constituents, typically alkali or alkaline earth metal oxides, into an initially fully polymerized silicate glass structure, leads to a reduction in network connectivity, thereby enhancing the material's susceptibility to dissolution [62,64,68].

Equally crucial for the intended application is the nature of the bonds between modifier cations and the glass network components. The predominantly ionic character of Si(P)-O-M^+ linkages weakens the overall structural integrity and chemical resistance of the glass, making these elements the first to be released upon exposure to a corrosive medium [14,15,43,62,69]. Interestingly, despite their analogous role in modifying the vitreous matrix, different cations can induce significant structural variations. Factors such as ionic radius, field strength, oxidation state, coordination number, and bonding type with the glass network collectively influence material properties, including connectivity, density, hardness, thermal behavior, framework rigidity, and stability [59,70,71]. For instance, substituting Mg^{2+} with the larger Ca^{2+} expands the silicon-oxygen backbone, increasing its permeability to protonated exogenous species, thereby facilitating ion exchange and dissolution [59]. Furthermore, when a glass contains a mixture of alkali and/or alkaline earth ions, it may exhibit nonlinear behavior relative to compositions containing only a single type of modifier ion—a phenomenon known as the mixed-alkali or mixed-alkaline earth effect [70–72]. In such cases, ion diffusion may be hindered due to the presence of modifier cations of different sizes occupying non-interchangeable sites—coordination environments within the glass matrix that are structurally and energetically optimized for specific cation types and thus cannot be effectively occupied by different cations due to mismatched ionic radii, charge densities, or bonding preferences—which ultimately disrupts ion migration pathways and suppresses ionic mobility, a hallmark of the mixed-alkaline earth effect, thereby affecting the chemical activity of the glass [70].

While the effects of the above-mentioned network components on the chemical activity of silicate-phosphate glasses—though highly dependent on composition and concentration—are relatively well understood, the influence of sulfur remains an open question. Due to the poor miscibility between silica-rich and sulfur-rich liquids under low-pressure conditions [73], incorporating [SO_4^{2-}] species into the vitreous network presents a considerable challenge. Moreover, to the best of the authors' knowledge, no studies have yet established a direct link between the composition-dependent structure of sulfate-bearing silicate-phosphate glasses and their chemical activity.

Thus, the primary objective of this study is to elucidate the intricate relationships between glass composition, structural evolution, and chemical reactivity in sulfate-containing silicate-phosphate systems. The following sections present a preliminary investigation of various glass formulations, an analysis of their structural transformations, and an as-

Molecules **2025**, *30*, 1684 5 of 37

containing silicate-phosphate systems. The following sections present a preliminary investigation of various glass formulations, an analysis of their structural transformations, and an assessment of their chemical activity in relevant solutions. These findings aim to provide essential guidelines for the rational design and characterization of materials intended for environmental protection.

2. Results and Discussion

2.1. Preliminary Glass Investigation

Prior to evaluating the potential of the designed glasses as slow-release vitreous fertilizers, a preliminary analysis was conducted to comprehensively understand the composition–structure–property relationships within the context of the tested samples.

2.1.1. Assessing the Amorphous Nature of Glasses (XRD)

While induced crystallization is a well-established method for tailoring and controlling the final properties of vitreous materials, spontaneous crystallization constitutes a highly undesirable phenomenon in glasses intended for interaction with biotic systems [50]. A high content of biologically relevant ions (e.g., macro- and micronutrients), which simultaneously act as glass network modifiers, weakens and fragments the structure, while the increased mobility of structural units further promotes their ordering into critical-size nuclei. Not only can crystalline phases, being thermodynamically more stable than their amorphous counterparts, significantly reduce the chemical reactivity of the final product, but the uncontrolled nature of spontaneous crystallization also renders the ion release process unreliable and difficult to predict [48,50,59]. Therefore, XRD analysis was performed not only to verify the amorphous nature of the tested samples but also to track changes induced by the incorporation of sulfur-containing species into the system. The resulting diffractograms of selected glasses (both base samples and those loaded with 3 mol.% sulfate species) are presented in Figure 1.

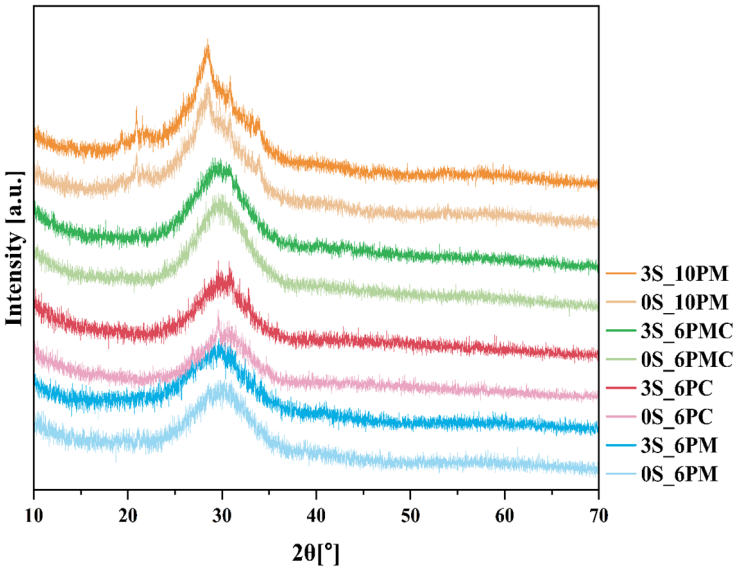


Figure 1. Diffraction patterns of selected samples, including the base composition and those loaded with 3 mol.% sulfate species, from all tested glass formulations.

The primary conclusion drawn from the data presented in Figure 1 is that, while all acquired diffractograms exhibit an elevated background in the 2θ range of 20–40°, characteristic of an amorphous nature, the samples representing the enhanced P_2O_5 composition (XS_10PM) also display slightly sharper, more defined reflections, superimposed on the registered halo, indicative of the presence of a crystalline phase embedded within the predominant vitreous matrix.

Given that the early stages of multicomponent glass crystallization are typically governed by diffusion-driven rearrangement of the most mobile and/or weakly bonded species in the structure, and considering that P_2O_5 in silicate-based melts generally integrates into the matrix as orthophosphate units, the observed tendency toward spontaneous crystallization in the [10P] composition is unsurprising [59,74–76]. This is further supported by the fact that the reflections observed in the diffractograms of both the 0S and 3S_10PM samples indicate the presence of the orthophosphate phase, $KMgPO_4$ (Ref. 98-005-0926). On the other hand, phosphate regions in the matrices of lower P_2O_5 materials are more diluted within the glass volume, thereby limiting nucleation and restricting the formation of crystalline orthophosphates. The only deviation from this trend is observed in the [6P] composition containing CaO, whose diffractogram exhibits a few low-intensity reflections (at approximately 29.65°, 30.95°, and 33.02° 2θ), suggesting the presence of a small fraction of crystallites (Figure 1). Although the number of detected reflections is limited, their low intensity and overlap with the broad amorphous background prevent definitive phase identification and make their attribution debatable. Considering both the observed peak positions and the aforementioned [PO_4^{3-}] mobility, it is plausible that the phase under evaluation corresponds to potassium calcium phosphate, $K_4Ca(PO_4)_2$ (Ref. 00-046-0629).

To elucidate the greater crystallization propensity of the XS_6PC system compared to the other [6P] compositions, it is important to highlight the stronger depolymerizing effect of CaO relative to MgO, which consequently increases the tendency of the resulting melt to reorganize during cooling. Furthermore, while MgO is known to act as a network modifier, fragmenting the silicate structure, it also exhibits a dual role in the vitreous matrix, as [MgO_4^{2-}] units can contribute to network formation [59,77,78].

Lastly, the effect of sulfate's addition on the development of crystalline phases in the studied materials must be considered. A thorough analysis of the recorded diffractograms, along with the authors' previous research on this phenomenon [79–81], suggests an increasing tendency for crystallization with a higher incorporation of sulfate units in the glass. However, one cannot see the effect of SO_3 content on the progressively more intense and sharper reflections in the XRD patterns of the XS_6PC and XS_10PM systems (Figure 1). This effect arises from the incorporation of sulfate groupings into the flexible amorphous matrix, understood as a loosely cross-linked glass network capable of local structural rearrangements under external stimuli, such as compositional changes or thermal fluctuations. The presence of [SO_4^{2-}] tetrahedral units, characterized by highly covalent S–O bonds, disrupts the structural compatibility within the predominantly ionic-covalent silicate framework. These covalent linkages introduce localized distortions and generate internal stresses, which cannot be fully relaxed within a rigid network. As a result, the accumulated stress lowers the energy barrier for atomic rearrangement, enhancing the tendency for spontaneous ordering and ultimately facilitating the formation of critical-size nuclei within the glass matrix [42,82].

2.1.2. Characterization of Thermal Properties

Investigating the thermal behavior of glasses intended for application in biotic environments is of utmost importance. From a technological standpoint, it facilitates the selection of appropriate synthesis temperatures to minimize the risk of spontaneous crystallization, a phenomenon known to reduce glass reactivity in contact solutions, while from an application perspective, differential scanning calorimetry (DSC) analysis serves as an invaluable tool for assessing thermal stability—an essential parameter in the preliminary evaluation of glass chemical activity, as both the crystallization tendency and the release of network-forming elements into the surrounding solution primarily depend on those structural components whose bonds are most susceptible to breaking [15,83].

Figure 2 presents the DSC curves, revealing a glass transition followed by a single-stage crystallization event for all glass compositions, except for the system containing both CaO and MgO as alkaline earth modifiers—in this case, two exothermic peaks are observed, reflecting the multicomponent nature of this particular formulation. Notably, while the glass transition and crystallization events in the [6P] series are well-defined, these effects appear significantly less distinct in the [10P] system.

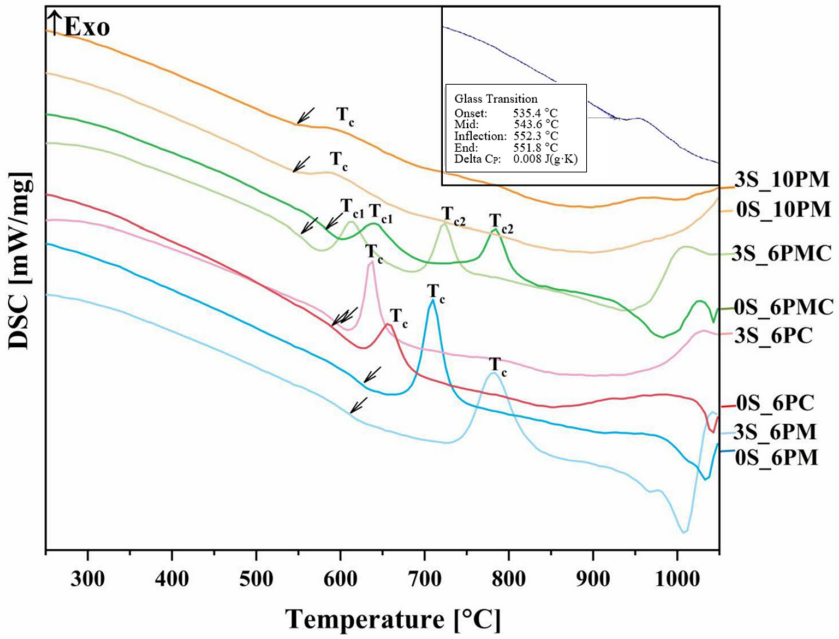


Figure 2. DSC curves of samples from all tested systems: base glasses and those doped with 3 mol.% sulfate. Note: T_g values were determined from the inflection points of the DSC signals (right upper corner).

Since the glass transition, manifested as an endothermic baseline shift in the DSC curve, reflects structural relaxation within the vitreous network—its magnitude and temperature being dependent on the nature and concentration of the network-constituting components—the subtlety of this effect may, however, indicate a more rigid internal framework in [10P] glasses. According to Stoch [42,43], glass network rigidity can be influenced by the presence of highly covalent bonds within its structure, but this effect is not straightforward and must be considered in the context of other structural factors. Given this, and considering the complex relationship between [SiO_4] and [PO_4] units in terms of polymerization compatibility, the increased P_2O_5 content could contribute to internal stresses within the mixed network, potentially leading to some degree of structural destabilization. However, this effect requires further investigation to fully understand its impact.

This, in turn, results in a less pronounced and narrow-range glass transition, characterized by the breaking of strained chemical bonds, followed by the ordering of a random glass structure. Nevertheless, the direct correlation between glass transition behavior and network rigidity remains uncertain. This phenomenon is further reflected in the weak crystallization peak height of the [10P] series observed across all studied systems, rather than the low crystallization temperature itself, which should rather be interpreted as an indicator of a slower crystallization rate (small crystal growth rate) and the difficulty of crystallizing these glasses. This trend is expected due to the higher concentration of glass-forming oxides (SiO_2 + P_2O_5) compared to other formulations, which generally increases the resistance to crystallization.

This phenomenon is further supported by the Angell glass stability parameter (K_A), which quantifies the material's propensity for crystallization. The Angell parameter is defined as the difference between the onset of crystallization temperature (T_x) and the glass transition temperature (T_g) ($K_A = T_x - T_g$). The term ($T_x - T_g$) in this equation reflects the material's resistance to crystallization, where a smaller interval indicates a higher tendency for crystallization (Figure 2, Table 1).

Table 1. DSC-registered parameters (T_g, T_x, and Angell parameter values) for all tested samples across the studied compositions.

No	Thermal Parameter		
	T_g	T_x	Angell (K_A)
	[°C]		[a.u.]
0S_6PM	613	750	137.0
1S_6PM	615	741	126.2
3S_6PM	624	689	65.1
5S_6PM	636	687	50.8
0S_6PC	595	624	28.9
1S_6PC	594	615	21.1
3S_6PC	608	635	26.5
5S_6PC	626	663	36.6
0S_6PMC	550	586	36.1
1S_6PMC	564	594	29.5
3S_6PMC	584	613	29.4
5S_6PMC	589	625	36.3
0S_10PM	544	556	12.1
1S_10PM	544	552	7.3
3S_10PM	546	573	27.0
5S_10PM	549	601	51.6

The highest characteristic temperatures together with the highest glass stability parameter are exhibited by the XS_6PM system (Table 1). The lower P_2O_5 content, combined with a slightly higher MgO concentration—known for its ability to bond the structure through its capacity to exist in either tetrahedral or octahedral coordination—makes the structure both cohesive and simultaneously more flexible than its higher P_2O_5 counterpart. This flexibility allows for structural rearrangement during the glass transition without disrupting the continuity of the network [78,84–86].

In contrast to MgO, CaO acts exclusively as a network modifier, leading to relatively lower T_g values observed in the XS_6PC system (Table 1). Notably, the extensive fragmentation of Si-O-Si polymeric chains in this modifier-rich system facilitated rapid structural reorganization immediately after the glass transition, which is reflected by the narrow temperature range between T_g and T_x in the recorded DSC curves of the respective samples and the observed tendency for their spontaneous crystallization, as evidenced by the XRD data presented above (Figure 1).

Meanwhile, introducing both alkaline earth network modifiers into the system placed the XS_6PMC glasses between the XS_6PM and XS_6PC compositions in terms of thermal stability parameters but simultaneously results in lower registered T_g values (Table 1).

The intermediate K_A values relative to the endpoint compositions are understandable and can be directly attributed to the network-forming capabilities of Mg^{2+} as well as its stronger bond to oxygen, which is expected given the higher field strength and smaller ionic radius of magnesium compared to calcium. However, the cause of the more than 50 °C lower T_g values for the XS_6PMC system compared to the other [6P] systems remains unclear. Drawing on the work of Kjeldsen et al. [84] and Swansbury et al. [70], it is plausible to hypothesize that this phenomenon may be linked to the mixed alkaline earth effect (MAEE)—the coexistence of Mg^{2+} and Ca^{2+} ions appears to influence the dynamic properties of the glass, potentially impeding the cooperative rearrangement of atoms within the common framework as the system approaches the glass transition, and, subsequently, promoting structural relaxation via bond breakage during the as-accelerated glass transition [42,70,84]. It is important to discuss the impact of sulfate unit addition on the thermal stability of the tested materials, understood as their resistance to devitrification. As shown in Figure 3, the data clearly indicate that the addition of [SO_4^{2-}] species increased the melt's propensity for ordering its elements and promoting the crystallization of the amorphous material. However, this declining trend continued throughout the entire composition range only for the XS_6PM system, while for the other compositions, a threshold value of sulfate content can be identified, beyond which the trend reversed (an increase in sulfur content leads to enhanced thermal stability). This effect can be attributed to the largest proportion of the amorphous phase in the XS_6PM composition (see Figure 1 as well as the authors' previous studies on akin materials [79,81])—the absence of a stabilizing crystalline phase led to a gradual weakening of the glass's internal structure with the introduction of sulfate units, which, by augmenting the number of covalent bonds, progressively increased the rigidity of the internal framework and enhance the system's tendency for ordering due to bond breaking. While this phenomenon was observed in all studied systems upon the initial addition of [SO_4^{2-}], the increasing network ordering along with sulfur content in the remaining compositions (evidenced by distinct reflections in the XRD patterns for XS_6PC and XS_6PMC systems at 5 mol.% nominal SO_3 content and for the [10P] system, already in the base sample, see [81] as well as Figure 1) led to an improvement in thermal stability, as reflected by the inversion of the trend (a higher energy barrier for the transformation from a glassy to a crystalline state).

Molecules **2025**, *30*, 1684 10 of 37

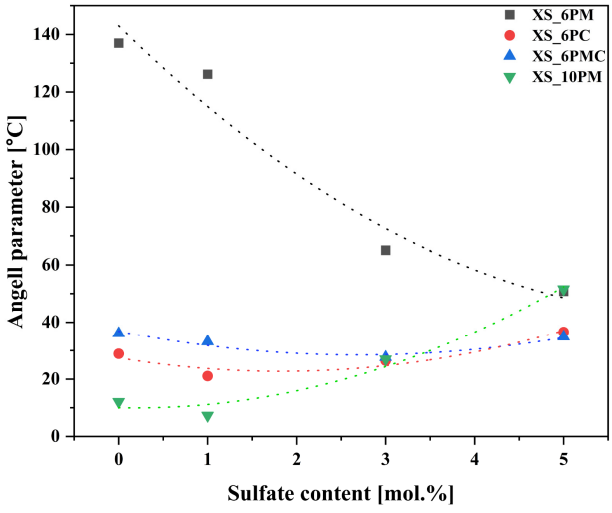


Figure 3. Variation of the Angell parameter across the studied glass compositions. The nominal SO_3 content is used on the *x*-axis as a reference to distinguish between the samples and does not represent the experimentally measured sulfur concentrations (see Table 3 in Section 4.1).

Figure 3. Variation of the Angell parameter across the studied glass compositions. The nominal SO_3 content is used on the *x*-axis as a reference to distinguish between the samples and does not represent the experimentally measured sulfur concentrations (see Table 3 in Section 4.1).

2.1.3. Structural Analysis of Glasses via ^{29}Si and ^{31}P MAS-NMR Spectroscopy

A key factor that transforms a material traditionally considered inert (e.g., conventional window glass) into one that exhibits chemical activity in biological systems is its fragmented structure. This structural characteristic facilitates the penetration of water molecules into the vitreous network, particularly at sites occupied by network modifiers, thereby enabling the systematic release of ions into the surrounding medium [59,87–89].

Therefore, to assess the potential of the designed glasses as vitreous carriers of bene-

2.1.3. Structural Analysis of Glasses via ^{29}Si and ^{31}P MAS-NMR Spectroscopy

A key factor that transforms a material traditionally considered inert (e.g., conventional window glass) into one that exhibits chemical activity in biological systems is its fragmented structure. This structural characteristic facilitates the penetration of water molecules into the vitreous network, particularly at sites occupied by network modifiers, thereby enabling the systematic release of ions into the surrounding medium [59,87–89].

Therefore, to assess the potential of the designed glasses as vitreous carriers of beneficial ions, ^{29}Si and ^{31}P MAS-NMR spectroscopy was employed to characterize the vitreous framework of the tested systems. The compilation of MAS-NMR spectra comparing the chemical environments of the network formers in both studied systems ([6P] and [10P]) is presented in Figure 4a (^{29}Si MAS-NMR) as well as Figure 4b (^{31}P MAS-NMR), respectively.

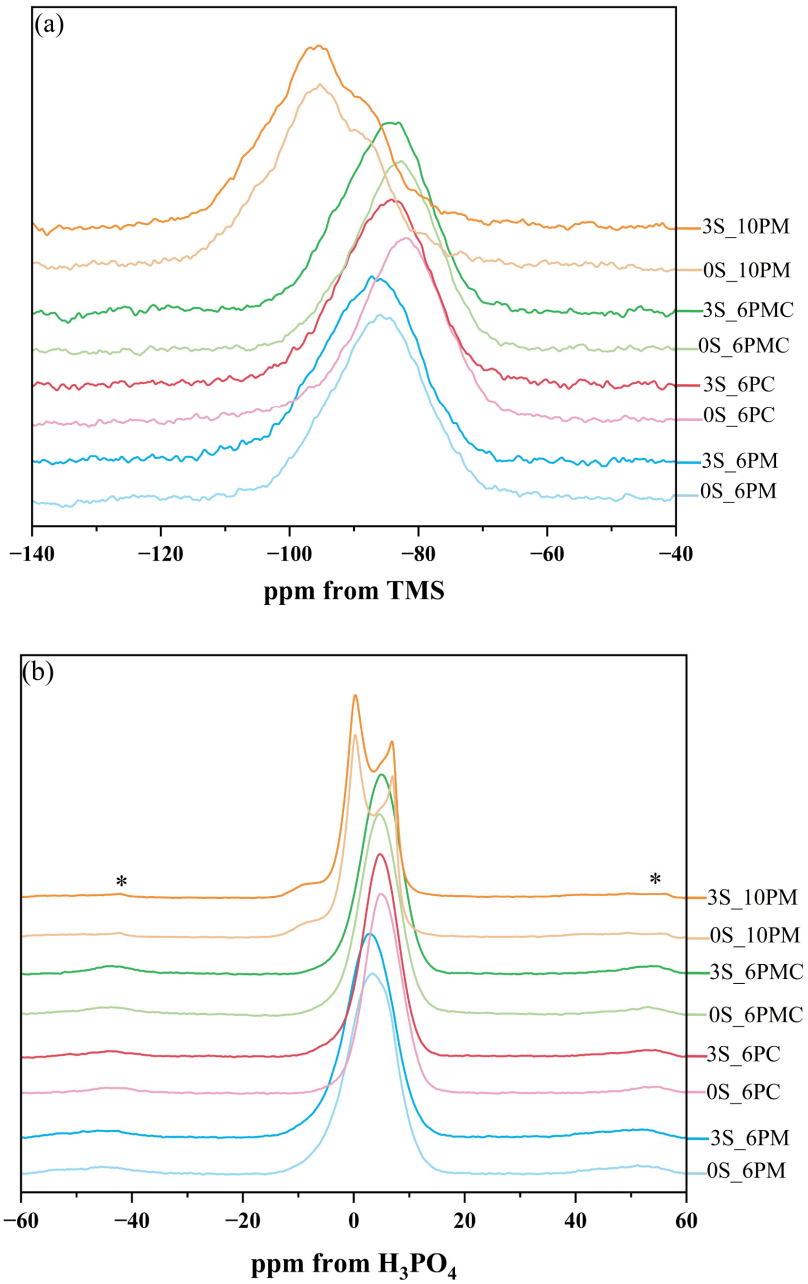


Figure 4. ^{29}Si (**a**) and ^{31}P (**b**) MAS-NMR spectra of the studied glasses (base and those loaded with 3 mol.% sulfate species) for all tested compositions. Spinning sidebands are marked with asterisks.

The obtained ^{29}Si MAS-NMR results reveal distinct differences in the distribution of fundamental structural units between the studied compositions, particularly when comparing the [6P] and [10P] series. In glasses with lower P_2O_5 content, the positions of the main resonance peaks (ranging from the least negative values: −82.1 ppm for 0S_6PC, −82.9 ppm for 0S_6PMC, and −85.4 ppm for 0S_6PM) indicate a predominantly metasilicate network, primarily composed of Q^2_{Si} species arranged in chains. (The fundamental structural unit of silicate glasses is the SiO_4 tetrahedron, which can be linked to adjacent SiO_4 tetrahedra via Si–O–Si bonds, commonly known as bridging oxygens. These structural units are classified as Q^n species, where n denotes the number of bridging oxygen atoms attached to a given tetrahedron.) In contrast, the spectrum of the [10P] system exhibits significant asymmetry, suggesting a more chemically diverse structure. While Q^2_{Si} units (−88.7 ppm) remain present, the well-defined resonance at −95.4 ppm signifies the existence of disilicate Q^3_{Si} groups. Additionally, a slight rightward inflection near −78.6 ppm reflects a minor contribution of pyrosilicate Q^1_{Si} units (linked via a single bridging oxygen), while a subtle leftward shoulder at −107.2 ppm indicates the presence of fully polymerized Q^4_{Si} species within the glass network [90–95].

Similar trends emerge from the analysis of the ^{31}P MAS-NMR spectra (Figure 4b). The signals recorded for glasses with a 6 mol.% P_2O_5 content consisted of a single broad resonance, whose position—starting from more positive values—was noted at 4.9 ppm for 0S_6PC and 0S_6PMC and 3.5 ppm for the 0S_6PM system and confirms the exclusive presence of orthophosphate units. Conversely, the resonance observed for the XS_10PM system deviated entirely from this pattern, instead exhibiting two distinct maxima (6.9 and 0.2 ppm), which indicate the existence of two chemically distinct orthophosphate environments in these materials [94,96–98].

Beyond providing an initial structural characterization of the synthesized glasses, these results also offer insights into the impact of [SO_4^{2-}] incorporation on the structural evolution of the materials. A comparison of the ^{29}Si MAS-NMR resonance positions between the base glasses and those containing 3 mol.% sulfates (shifting to −84.3 ppm for 3S_6PC, −84.11 ppm for 3S_6PMC, −86.5 ppm for 3S_6PM, and −89.3/−95.9 ppm for 3S_10PM) suggests a slight polymerizing effect of [SO_4^{2-}] addition on the silicate framework. A similar, albeit significantly weaker, influence of these groups was observed on the phosphorus-oxygen subnetwork, where a displacement of the main resonance towards more negative values, exceeding 0.5 ppm, was only noted for the 0S_6PM system (3.5 → 2.7 ppm). In the XS_6PC system, the shift was minimal (4.9 → 4.7 ppm), while in the XS_6PMC one, the resonance moved toward more positive ppm values (4.9 → 5.0 ppm). Notably, no alike transition was observed in the XS_10P system.

The obtained results, in line with the general assumption that glasses with a predominantly metasilicate structure tend to interact with biological environments, allow for a preliminary classification of all synthesized glasses as potentially chemically active. Nevertheless, a significantly more reliable measure of such reactivity is the degree of polymerization of the glass network, commonly expressed as network connectivity (NC) [76,99,100]. This parameter, defined as the average number of bridging oxygens (BO) per network-forming element, provides a more quantitative assessment of the structural integrity of the glass framework. The experimental values of network connectivity, $\{NC\}_{exp}$, can be determined based on the exact proportions of individual Q^n_{Si} and Q^n_P species, following the equations proposed by Eckert, [101], (1)–(3):

$$\{NC\}_{Si} = 4 \times f\left(Si^{(4)}\right) + 3 \times f\left(Si^{(3)}\right) + 2 \times f\left(Si^{(2)}\right) + 1 \times f\left(Si^{(1)}\right) \quad (1)$$

$$\{NC\}_{P} = 3 \times f\left(P^{(3)}\right) + 2 \times f\left(P^{(2)}\right) + 1 \times f\left(P^{(1)}\right) \quad (2)$$

$$\{NC\}_{Si} = 4 \times f\left(Si^{(4)}\right) + 3 \times f\left(Si^{(3)}\right) + 2 \times f\left(Si^{(2)}\right) + 1 \times f\left(Si^{(1)}\right) \quad (1)$$

$$\{NC\}_{P} = 3 \times f\left(P^{(3)}\right) + 2 \times f\left(P^{(2)}\right) + 1 \times f\left(P^{(1)}\right) \quad (2)$$

$$\{NC\}_{exp} = \{2xP_2O_5 \times \{NC\}_P + xSiO_2 \times \{NC\}_{Si}\}/xSiO_2 \quad (3)$$

Therefore, to extract the data necessary for calculations based on Equations (1)–(3) and asses the relative abundance of individual structural units within the glass network as well as the impact of sulfate species' addition on their distribution, the obtained signals were subjected to a deconvolution procedure. Accordingly, spectral regions were fitted with a set of bands modeled using the Voigt function, which was deemed optimal for approximating most NMR signals. The only exception was the ^{31}P MAS-NMR spectra recorded for the [10P] system, where narrow, well-defined resonances were best described by the Lorentzian function. Representative deconvolution results for selected samples from the XS_6PMC system are presented in Figure 5, while a comparison of network connectivity calculations for all glass samples from both studied systems is depicted in Figure 6.

Therefore, to extract the data necessary for calculations based on Equations (1)–(3) and asses the relative abundance of individual structural units within the glass network as well as the impact of sulfate species' addition on their distribution, the obtained signals were subjected to a deconvolution procedure. Accordingly, spectral regions were fitted with a set of bands modeled using the Voigt function, which was deemed optimal for approximating most NMR signals. The only exception was the ^{31}P MAS-NMR spectra recorded for the [10P] system, where narrow, well-defined resonances were best described by the Lorentzian function. Representative deconvolution results for selected samples from the XS_6PMC system are presented in Figure 5, while a comparison of network connectivity calculations for all glass samples from both studied systems is depicted in Figure 6.

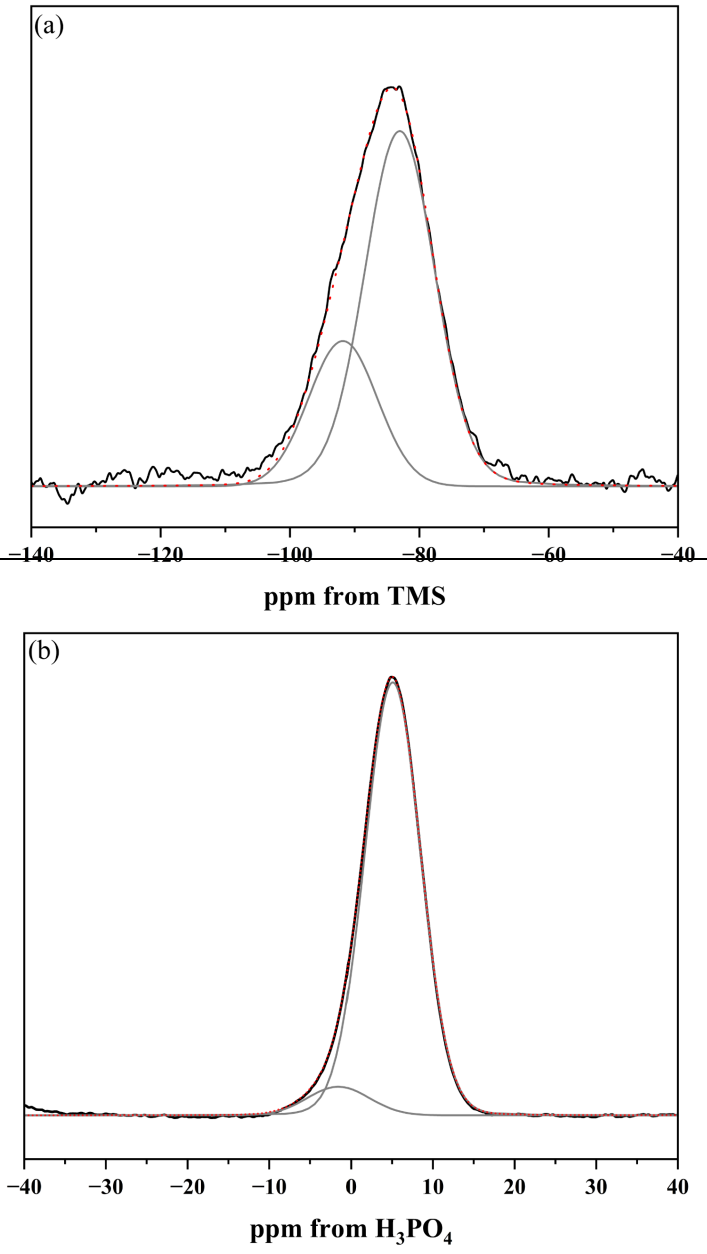


Figure 5. Representative ^{29}Si (**a**) and ^{31}P (**b**) MAS-NMR spectra of the selected 3S_6PMC sample. The original experimental spectrum is shown in red, while the fitted envelope obtained from spectral deconvolution is marked in black.

Figure 5. Representative ^{29}Si (**a**) and ^{31}P (**b**) MAS-NMR spectra of the selected 3S_6PMC sample. The original experimental spectrum is shown in red, while the fitted envelope obtained from spectral deconvolution is marked in black.

Upon analyzing the obtained network connectivity results, it is evident that the previously stated assumption regarding the higher degree of polymerization in glasses with increased P_2O_5 content holds true, as the acquired NC values for XS_10PM samples were

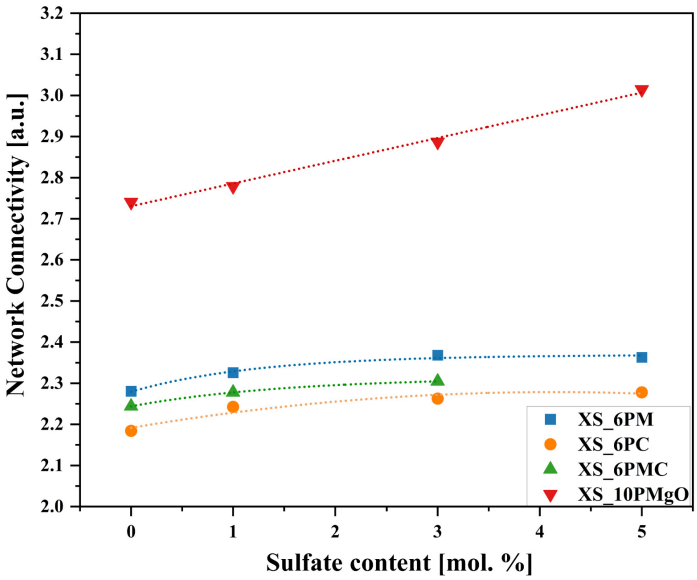


Figure 6. Calculated network connectivity values for the studied glass compositions. The data are plotted against the nominal SO_3 content, used here solely to distinguish between the samples. Please note that these values do not represent experimentally measured sulfur concentrations, which are provided in Table 3 (see Section 4.1). The NC value for the 5S_6PMC glass is not available due to the specimen's instability, which prevented the acquisition of both 29Si and 31P MAS NMR spectra.

Upon analyzing the obtained network connectivity results, it is evident that the previously stated assumption regarding the higher degree of polymerization in glasses with increased P_2O_5 content holds true, as the acquired NC values for XS_10PM samples were significantly higher than those representing the [6P] series (Figure 6). The markedly higher crosslinking observed in the [10P] system should be attributed precisely to its increased P_2O_5 content. It is well established that raising the concentration of this network former, without a concurrent increase in modifier oxides necessary for charge balancing the newly formed orthophosphate units, drives the redistribution of M^+/M^{2+} cations away from the silicate framework and toward $[PO_4^{3-}]$ units. This reorganization of network elements alters the Q^n_{Si} species distribution, ultimately enhancing the connectivity of the silicon-oxygen network [59,102,103]. Additionally, the presence of MgO as the sole alkaline earth network modifier in the [10P] system played a crucial role. As discussed earlier, this particular oxide exhibits characteristics of both a network modifier and former, and thus, a fraction of this component incorporates into the glass matrix as $[MgO_4^{2-}]$ species, which require charge compensation from nearby cations. Given that, similar to $[PO_4^{3-}]$ units, this process effectively increases silicon-oxygen NC; unsurprisingly, the highest Si–O–Si connectivity among all studied [6P] compositions was observed for the XS_6PM system (Figure 6).

Following this reasoning, it becomes evident that CaO exerted a significantly stronger depolymerizing effect on the silicon-oxygen network, which is reflected in the progressive decrease in NC from the XS_6PM system, through the XS_6PMC system (containing an equal ratio of MgO and CaO), to the XS_6PC system (which contains only CaO)—further confirming the sole network-modifying role of calcium oxide (Figure 6). This evident parallel increase in the connectivity of the silicon-oxygen backbone together with an increase in MgO content across the [6P] compositions clearly contradicts the conventional classification of MgO as a network-disrupting component in vitreous systems. Such a statement finds confirmation in the literature data, as according to Jha et al. [86], its role is content-dependent—at concentrations where both MgO and CaO act as network modifiers, differences in glass properties arise from their distinct ionic sizes and field strengths, known

to affect the local structure of glasses (e.g., the incorporation of larger cations into the glass structure can enhance the depolymerization of the silicate network [104–106]). However, at higher concentrations, MgO begins to form its own network by scavenging modifier cations for charge balancing, thereby reducing the number of non-bridging oxygens in the system. A more detailed perspective is provided by Watts et al. [107], who quantified the network-forming and modifying roles of MgO based on ^{29}Si MAS-NMR deconvolution of silicate-based glasses, where MgO was gradually replaced by CaO. Regardless of composition, their findings indicated that while 86% of MgO acts as a traditional network modifier, up to 14% incorporates into the vitreous network as tetrahedral MgO_4 units, effectively removing modifier cations for charge compensation and promoting network polymerization. Although this behavior may not be universal across all MgO-containing silicate glasses, Watts' findings suggest that in highly disrupted silicate systems—such as those in her study and the present work—MgO can exhibit a dual, concentration-dependent role. This statement may thus serve as an explanation for the observed decrease in NC as MgO content decreases from XS_6PM through XS_6PMC to its absence in XS_6PC systems.

Despite the above-discussed differences, all the studied systems shared two key similarities—firstly, they all exhibited a similar response to increasing sulfate content, with NC following an upward trend across all materials. The explanation for this behavior mirrors that of the previously discussed [PO_4^{3-}] units: sulfur is introduced into the compositions exclusively as tetrahedral [SO_4^{2-}] species, which attract network modifiers. This redistribution of M^+/M^{2+} cations disrupts the silicate subnetwork's continuity, reduces their concentration near the Si-O-Si framework, and favors the formation of more polymerized Q^3_{Si} units.

The second observed similarity, based on the NC trend, is that the values of this parameter for all tested glasses indicate that the silicate network in each case was predominantly formed by Q^2_{Si} units forming silicon-oxygen chains/rings, with a smaller proportion of Q^3_{Si} species constituting the two-dimensional part of the network [59]. This metasilicate-based, open, and fragmented structure places these compositions in the category of glasses that are prone to disintegration in biotic environments. The only system that may raise concerns regarding its potential to interact with aquatic solutions is the [10P] system, where NC exceeds the established threshold for bioactivity (>2.7 [74,99,108]).

Nonetheless, it is important to emphasize here that the network connectivity parameter alone does not capture all the structural aspects that influence glass solubility [59]. The interaction of a vitreous material with a solution is also strongly influenced by the nature of the cross-links (the strength of bonds between modifiers and the silicate-based vitreous matrix) and the P_2O_5 content, which, when incorporated into the vitreous matrix as orthophosphate units, directly contribute to the enhanced chemical activity of the glass [3,15,16,74,99,108]. Therefore, to further complete the composition–structure–property relationship and unequivocally assess the potential of the tested compositions as vitreous carriers of useful ions, both 'in vivo' and 'in vitro' experiments were conducted.

2.2. Glass Dissolution Studies ('In Vitro' Experiment)

The concept of vitreous fertilizers is based on the controlled release of nutrients in response to plant demand. This interaction between the rhizosphere, soil microorganisms, and the macro-/micronutrient carrier relies on the secretion of low-molecular-weight organic acids, which mobilize elements encapsulated within the glass matrix [52,109,110]. Therefore, to assess the leaching behavior of the designed materials in relation to their chemical composition, an 'in vitro' experiment was conducted using a solution that simulates these organic exudates, and the results are presented in Figures 7–11.

sulfate-bearing phase was observed at 5 mol.% SO_3 in both melt-quenched and fritted XS_6PM samples [80], whereas for XS_6PC and XS_6PMC compositions, crystallization occurred at 3 mol.% in melt-quenched glasses, with the fritting process extending this limit to 5 mol.% [79,81].

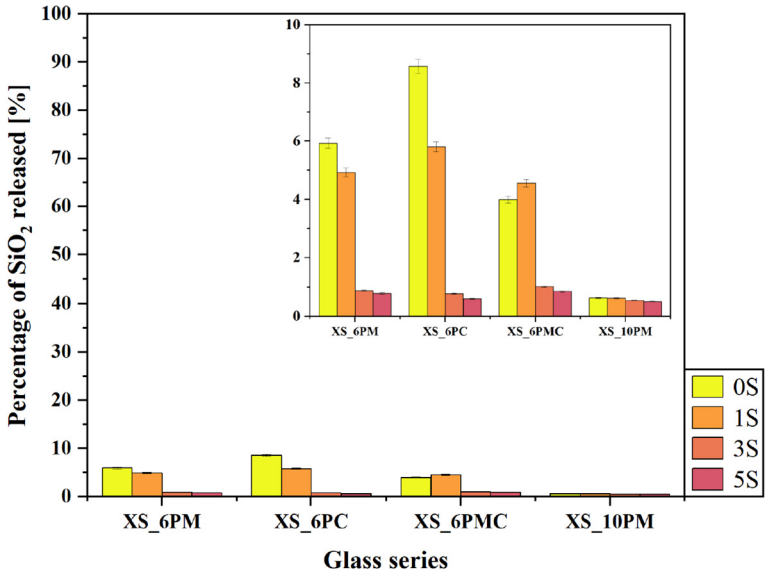
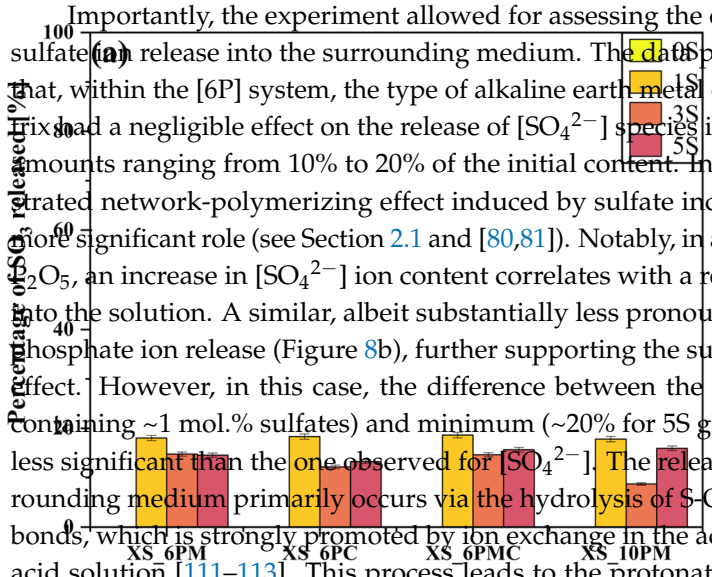


Figure 7. Percentage of SiO_2 released into the citric acid solution for all studied systems.

Importantly, the experiment allowed for assessing the effect of glass composition on sulfate ion release into the surrounding medium. The data presented in Figure 8a indicate that, within the [6P] system, the type of alkaline earth metal oxide modifying the glass matrix had a negligible effect on the release of $[SO_4^{2-}]$ species into the solution, with leached amounts ranging from 10% to 20% of the initial content. Instead, the previously demonstrated network-polymerizing effect induced by sulfate incorporation appears to play a more significant role (see Section 2.1 and [80,81]). Notably, in all systems containing 6 mol.% P_2O_5, an increase in $[SO_4^{2-}]$ ion content correlates with a reduced release of this species into the solution. A similar, albeit substantially less pronounced, trend was observed for phosphate ion release (Figure 8b), further supporting the sulfate-induced polymerization effect. However, in this case, the difference between the maximum (~26% for glasses containing ~1 mol.% sulfates) and minimum (~20% for 5S glasses) phosphate release was less significant than the one observed for $[SO_4^{2-}]$. The release of both anions into the surrounding medium primarily occurs via the hydrolysis of S-O-K^+ and P-O-K^+/Mg^{2+}/Ca^{2+} bonds, which is strongly promoted by ion exchange in the acidic environment of the citric acid solution [111–113]. This process leads to the protonation of phosphate and sulfate units into $H_2PO_4^-$/HPO_4^{2-} and HSO_4^-, respectively. The sulfate-induced densification of the glass network, therefore, acts as a kinetic barrier, restricting the transport of these relatively large anions to the glass–solution interface. Consequently, the observed leached ion concentrations primarily originate from near-surface regions rather than the glass bulk.



Although the network-polymerizing influence of $[SO_4^{2-}]$ species is also reflected in the release of other glass components of [6P] glasses into the surrounding medium (Figures 7 and 9a,b), it is most pronounced in the data presenting silica release (Figure 7), where a sharp decline in SiO_2 concentration in the leachate was observed for all glasses beyond the threshold of 1 mol.% SO_3 (dropping from an average of 6% to just ~1% of the initial content). Numerous scientific reports identify ~1 mol.% SO_3 as the maximum amount that can be accommodated within the free volume of a silicate-based vitreous framework without triggering crystalline phase precipitation [114,115]. Therefore, a certain correlation can be established between the solubility limits reported in the literature and the data presented in Figure 7. In the systems studied, the precipitation of K_2SO_4 as a sulfate-bearing phase was observed at 5 mol.% SO_3 in both melt-quenched and fritted XS_6PM samples [80], whereas for XS_6PC and XS_6PMC compositions, crystallization

occurred at 3 mol.% in melt-quenched glasses, with the fritting process extending this limit to 5 mol.% [79,81].

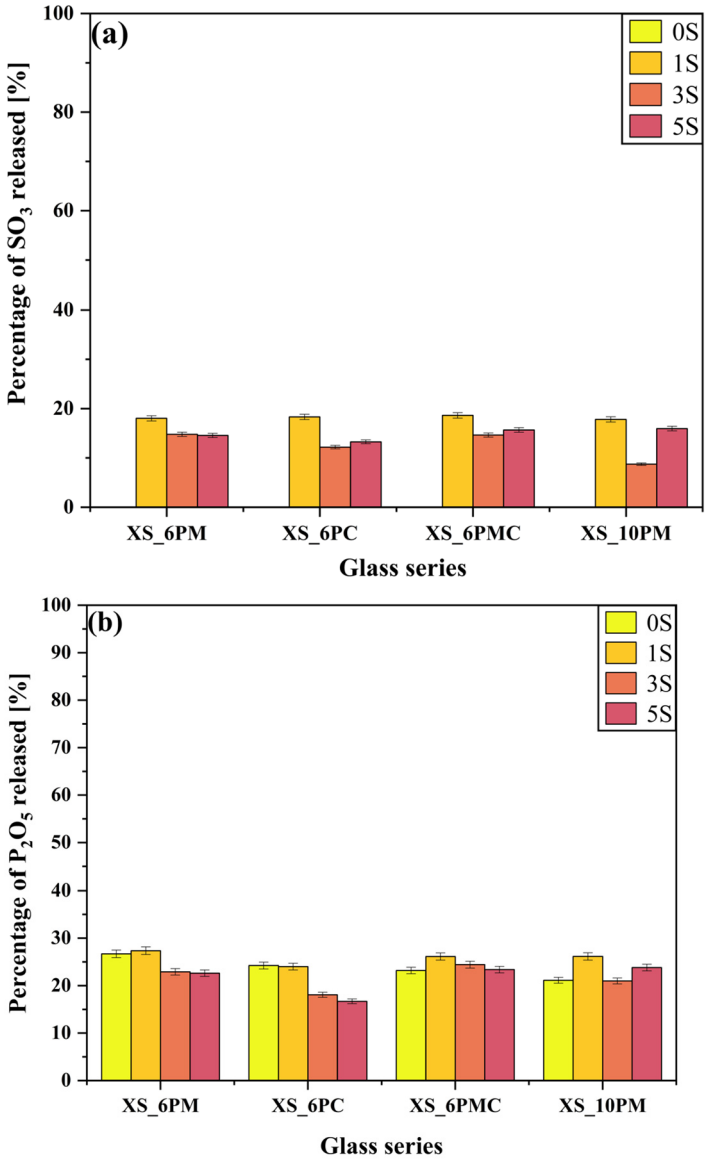
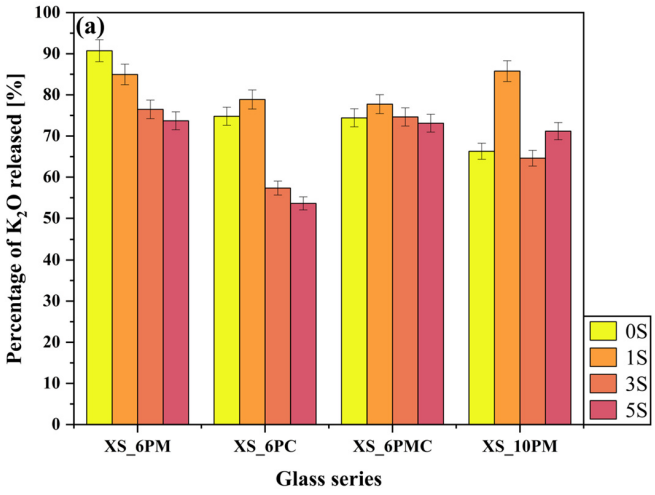


Figure 8. Percentage of SO_3 (**a**) and P_2O_5 (**b**) released into the citric acid solution for all studied systems.

Beyond the confirmed sulfur-induced polymerization effect, which reduces silica extraction from the glass matrix [80,81], another crucial factor must be then considered—the progressive ordering of the internal glass structure with increasing [SO_4^{2-}] content. Although such structural rearrangements toward a more stable, crystalline-like configuration do not manifest as distinct reflections in the XRD patterns (Figure 1), they undoubtedly enhance the formation of strong, low-strain, hydrolysis-resistant Si–O–Si linkages, ultimately influencing the durability of the glass network [31,42]. This hypothesis is further supported by the stark contrast in dissolution rates between quartz and amorphous silica in pure water, which are 4.2×10^{-14} and 9.0×10^{-13} mol/m^2, respectively, underscoring the profound influence of network geometry on dissolution kinetics [45]. Unsurprisingly, the highest silica release was observed for the XS_6PC system, which exhibited the greatest proportion of chain-like Q^2_{Si} units—more susceptible to bond cleavage than the more highly networked Q^3_{Si} units (see Section 2.1.3). As in previous cases, the leached Si most likely orig-

inates from near-surface regions, where defect concentrations, including undercoordinated Si atoms, are highest, resulting in increased reactivity [116].



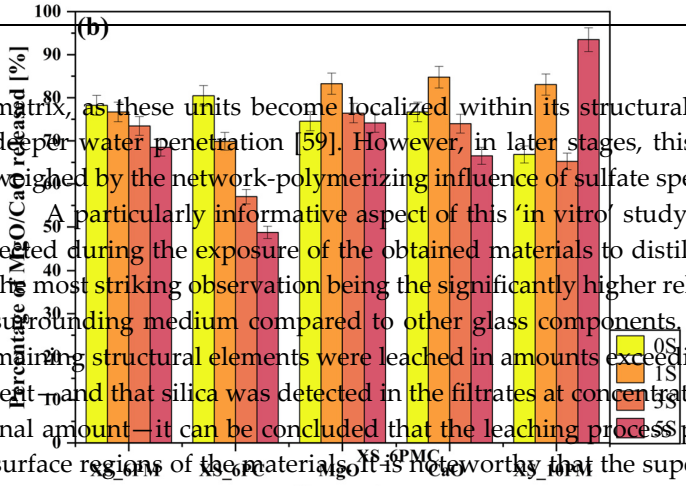


Figure 9. Percentage of K_2O (**a**) and MgO/CaO (**b**) released into the citric acid solution for all studied systems.

matrix, as these units become localized within its structural voids, thereby facilitating deeper water penetration [59]. However, in later stages, this effect was gradually outweighed by the network-polymerizing influence of sulfate species.

A particularly informative aspect of this 'in vitro' study is the analysis of data collected during the exposure of the obtained materials to distilled water (Figure 10), with the most striking observation being the significantly higher release of sulfate ions into the surrounding medium compared to other glass components. Given that none of the remaining structural elements were leached in amounts exceeding 0.5% of their initial content and that silica was detected in the filtrates at concentrations below 0.1% of its original amount—it can be concluded that the leaching process primarily affected the near-surface regions of the materials. It is noteworthy that the superficial glass area was characterized not only by the presence of weaker bonded atoms and chemically reactive sites (such as non-bridging oxygens, three-coordinated Si, and strained Si–O bonds) but also by a slightly higher concentration of network modifiers compared to the bulk glass [117–119].

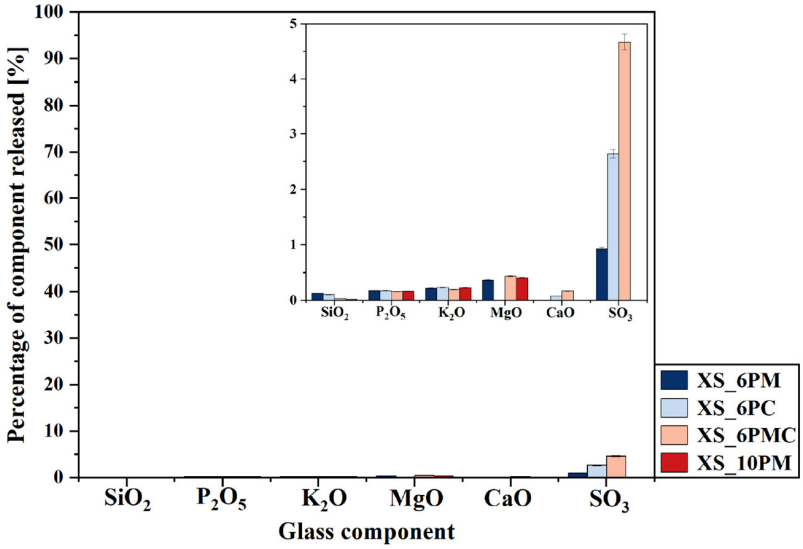


Figure 10. Percentages of glass elements released into distilled water for all studied systems.

This assumption leads to the conclusion that the sulfate ions released in such large quantities also originate from the outermost layers of the samples, suggesting at the same time a non-uniform distribution of sulfate units within the glass volume. This interpretation aligns with literature reports describing the tendency of sulfates to form a so-called

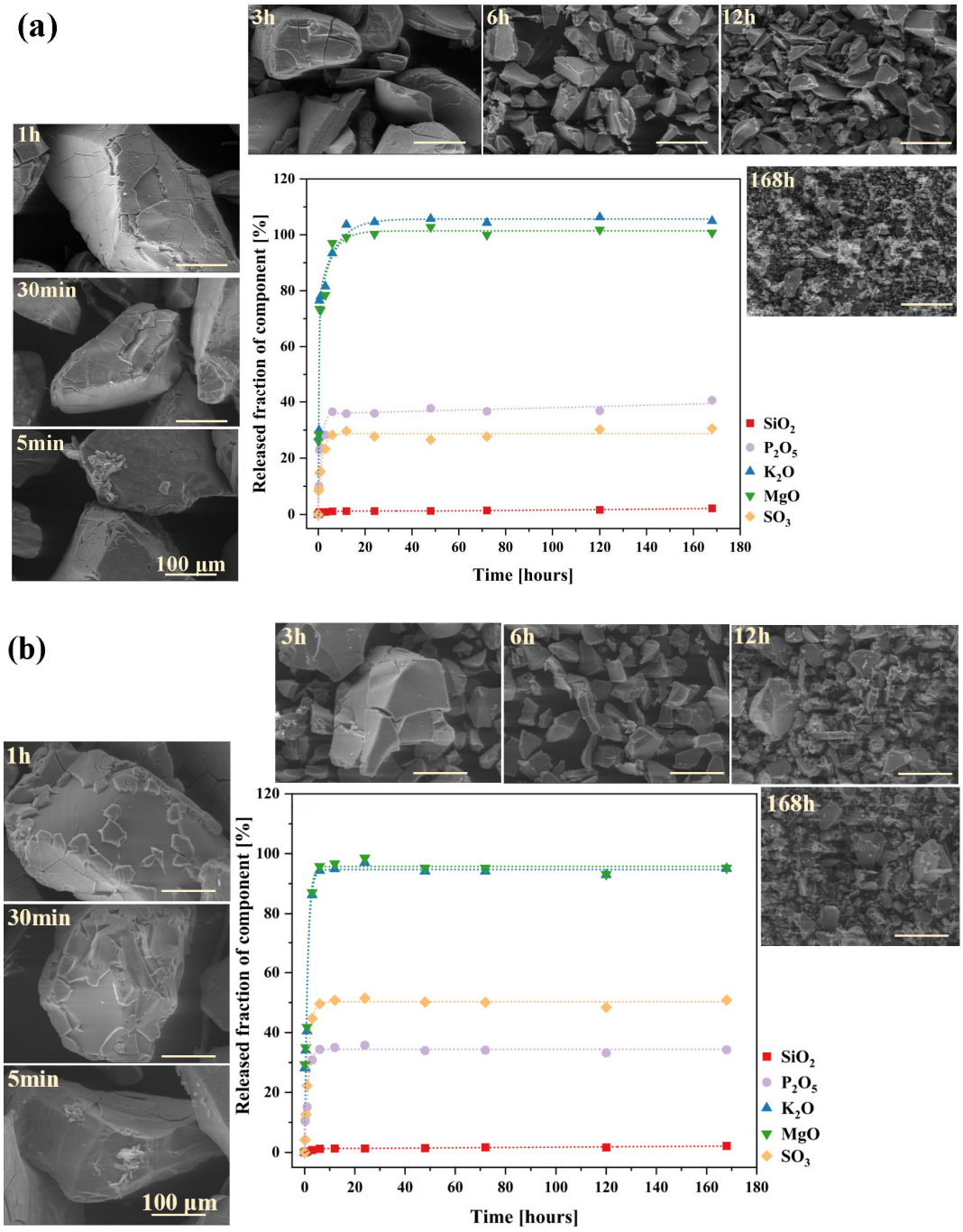


Figure 11. Ion dissolution profiles of 3S_6PM (**a**) and 3S_10PM (**b**) glasses in 2% citric acid under dynamic leaching conditions as a function of immersion time, accompanied by micrographs from selected surface points, illustrating surface changes at various stages of the experiment. It should be stressed that the percentages of K_2O and P_2O_5 released in the case of XS_6PM system were noted to slightly exceed 100% due to the limitations of the XRF analysis (in the pearl method used, the samples were heated to 1100 °C, potentially leading to the volatility of certain glass components and resulting in inaccuracies in the measured values). The micrographs were taken at 1000× magnification, with the scale bar corresponding to 100 µm.

Particular attention should be paid to the release data of the most mobile glass components—potassium ions (K^+), present in all systems, as well as alkaline earth metal ions (Mg^{2+} and/or Ca^{2+})—in this case, too, the increasing degree of cross-linking in the silicate framework, driven by the rising concentration of $[SO_4^{2-}]$ units, appears to hinder the transport of these species toward the surface (Figure 9a,b). It is well known that the redriving force for further dissolution (2) [57,134,135]. According to Equations (4) and (5)

Molecules 2025, 30, 1684 18 of 37

The observed rate drop in glass corrosion kinetics is typically attributed to two main phenomena: the formation of a passivating silica gel layer on the outermost glass surface in contact with the solution (1), or a decrease in reaction affinity due to saturation effects, where high concentrations of dissolved species in the leachate reduce the thermodynamic

lease of cations from the glass network occurs through interactions with positively charged exogenous species, such as H^+ and H_3O^+. Given that alkali metal ions have a lower charge than alkaline earth metal ones, the interdiffusion process typically favors the former [71]. Nonetheless, the investigated glasses within the [6P] series did not follow this general trend, as all network modifier cations were released in comparable amounts (generally between 70–80% of their initial content). The observed lack of preferential leaching of any specific modifier cation can be attributed to the dynamic character of the experiment as well as the MAS-NMR-confirmed open framework of these glasses and the resulting high concentration of hydrophilic non-bridging oxygen atoms, both of which promote deep water penetration [59].

The relationships discussed above were not observed for the glasses representing the [10P] system, with one exception—the silica release profile, where the sulfate-related network-polymerizing effect was again apparent. As the sulfur content in the matrix increased, the release of Si into the solution slightly decreased (Figure 7); however, this effect was rather subtle, as the recorded decline was only from 0.6% to 0.5% of the initial content. In contrast, analysis of the release data for other ions does not reveal a similar influence of sulfate incorporation on their leaching behavior, as was the case for the [6P] series (Figures 7 and 9). This lack of such correlation can be attributed to the increasing instability of the [10P] system with higher sulfate loading, which arises not only from the greater rigidity of the Si-O-Si glass backbone—and consequently, structural stresses—but also from the partial crystallinity of samples representing the higher P_2O_5 series, complicating the unequivocal description of ion release data. Undoubtedly then, in these glasses, DSC-confirmed structural instability plays a more dominant role in governing ion release than the presence of silicon-oxygen network-polymerizing sulfate groups.

Analyzing the 'in vitro' experimental data, it is worth noting a few cases where an initial increase in the release of a given element (e.g., K^+ in the case of sample 1S_6PC) was observed compared to the base sample, followed by a subsequent decline. This phenomenon can likely be attributed to a slight expanding effect of [SO_4^{2-}] species on the glass matrix, as these units become localized within its structural voids, thereby facilitating deeper water penetration [59]. However, in later stages, this effect was gradually outweighed by the network-polymerizing influence of sulfate species.

A particularly informative aspect of this 'in vitro' study is the analysis of data collected during the exposure of the obtained materials to distilled water (Figure 10), with the most striking observation being the significantly higher release of sulfate ions into the surrounding medium compared to other glass components. Given that none of the remaining structural elements were leached in amounts exceeding 0.5% of their initial content—and that silica was detected in the filtrates at concentrations below 0.1% of its original amount—it can be concluded that the leaching process primarily affected the near-surface regions of the materials. It is noteworthy that the superficial glass area was characterized not only by the presence of weaker bonded atoms and chemically reactive sites (such as non-bridging oxygens, three-coordinated Si, and strained Si-O bonds) but also by a slightly higher concentration of network modifiers compared to the bulk glass [117–119].

This assumption leads to the conclusion that the sulfate ions released in such large quantities also originate from the outermost layers of the samples, suggesting at the same time a non-uniform distribution of sulfate units within the glass volume. This interpretation aligns with literature reports describing the tendency of sulfates to form a so-called 'sulfate gall' on the surface of silicate melts [114,120–122], further supporting the notion of [SO_4^{2-}] species migrating toward the surface [123]. Moreover, the highest sulfate ion concentrations were detected in the filtrates of the 3S_6PC and 3S_6PMC samples, whose melts exhibited

the lowest viscosities, potentially facilitating the migration of sulfur species towards the surface. Finally, it is crucial to emphasize the inherently high solubility of sulfate ions in aqueous environments, which, combined with their presence in the glass matrix as isolated units unbound to the network, further enhances the mobility of sulfur species into the surrounding medium [124,125].

Nevertheless, comparing the release of glass matrix components into a corrosive acidic medium (pH~2) versus neutral distilled water clearly demonstrates the high resistance of the investigated materials to the latter. The concentrations of all glass constituents in the water leachate were significantly lower, indicating that the studied materials exhibited enhanced reactivity in environments mimicking root exudates and microbial secretions. These results confirm that the structure of each designed glass composition permitted the penetration of exogenous H^+ and H_3O^+ species into the matrix, facilitating ion exchange and the subsequent liberation of all mobile glass constituents, while silica remained largely retained, with its release not exceeding 10% of the initial content. It is important to emphasize that the 'in vitro' experiment, conducted in accordance with Regulation (EC) No 2003/2003 of the European Parliament and of the Council of 13 October 2003 on fertilizers [126], serves as a reliable tool for assessing the leaching potential of specific ions from the tested materials into solutions that simulate those secreted in the rhizosphere. However, as this method does not fully predict or model long-term nutrient leaching, a dissolution kinetics study was conducted to provide deeper insights into release profiles—critical for ensuring a sustained nutrient supply to plants.

2.3. Simulation of Long-Term Glass Dissolution (Dissolution Kinetic Studies)

The selection of glass compositions for the study of glass dissolution kinetics was guided by the following criteria:

- The glasses should exhibit the highest possible sulfate capacity without exceeding the critical [SO_4^{2-}] ion concentration, beyond which the precipitation of a highly soluble sulfate-bearing crystalline phase occurs (as observed in the XS_6PM system at a nominal 5 mol.% sulfate loading [80,81]), leading to its immediate release into the environment when the material is used in its intended applications;
- The glasses should contain comparable concentrations of sulfate ions;
- The P_2O_5 content is one of the key factors influencing the chemical reactivity of similar materials [59,74,103,127].

Considering these criteria, along with the analogous behavior observed for all [6P] glasses in the 'in vitro' experiment, the glasses 3S_6PM and 3S_10PM—both containing MgO as an alkaline earth metal modifier—were selected for further study. This selection enables the investigation of phosphorus content effects on dissolution kinetics while minimizing potential influences arising from variations in the characteristics of network-modifying cations on the release rate of glass components into the solution.

The shape of the corrosion kinetic curves obtained for both analyzed systems reflects two well-known kinetic regimes in glass dissolution studies in aqueous solutions [57,128,129], as shown in Figure 11a,b. The initial, highly intensive release of mobile species (K^+, Mg^{2+}) is associated with interdiffusion, where these cations undergo ion exchange with H^+/H_3O^+ from the contacting solution, leaving the near-surface region of the glass depleted of these elements. The recorded release profiles of the network modifiers follow a $t^{\frac{1}{2}}$ dependence, a clear indicator of a transport-controlled process [130–132]. Surprisingly, larger PO_4^{3-} and SO_4^{2-} ions, which do not participate in proton exchange, are released following the same trend. Their initially rapid leaching can be attributed to their structural role in the glass matrix, where they exist as isolated units rather than being

integrated into the silicate-based network; hence, their dissolution does not require the hydrolysis of silicon-oxygen bonds [59,133].

After approximately three hours of the initial rate regime, a noticeable decline (rate drop) appeared on the dissolution kinetic curves of the above-mentioned elements. Beyond this point, and continuing until the end of the experiment, a stable but nonzero residual release rate was observed (Figure 11a,b).

The observed rate drop in glass corrosion kinetics is typically attributed to two main phenomena: the formation of a passivating silica gel layer on the outermost glass surface in contact with the solution (1), or a decrease in reaction affinity due to saturation effects, where high concentrations of dissolved species in the leachate reduce the thermodynamic driving force for further dissolution (2) [57,134,135]. According to Equations (4) and (5) [136,137], hydration of the dealkalized glass surface layer is a natural consequence of the ion exchange process (as evidenced by the Si-rich layer depleted of mobile components, observed in micrographs of both glasses after 1h of long-term dissolution experiment; Figure 12a,b: yellow spectra, compared to the red ones, which represent initial compositions of the freshly exposed glass surfaces) and may lead to the reorganization of newly formed Si-OH groups into a more condensed, porous layer (6) and (7). However, even if such a passivating layer were to form, the ongoing disintegration of glass fragments (and the delaminating nature of its corrosion process, observable in Figures 11 and 12 at the 1 h stage for both glasses) would continuously remove this surface area, exposing deeper regions of the glass and renewing the release of its components.

$$\equiv Si - O^{-} - M^{+}_{(glass)} + H^{+}_{(sol.)} \rightarrow \equiv Si - OH_{(glass)} + M^{+}_{(sol.)} (\equiv \text{represents the silica bonds}) \quad (4)$$

$$\equiv Si - O - M^{+}_{(glass)} + H_3O^{+}_{(sol.)} \rightarrow \equiv Si - OH_{(glass)} + M^{+}_{(sol.)} + H_2O \quad (5)$$

$$\equiv Si - O - Si \equiv_{(glass)} + OH^{-}_{(sol.)} \rightleftharpoons \equiv Si - OH_{(glass)} + \equiv Si - O^{-}_{(glass)} \quad (6)$$

$$\equiv Si - OH_{(glass)} + HO - Si \equiv_{(glass)} \rightleftharpoons \equiv Si - O - Si \equiv_{(glass)} + H_2O \quad (7)$$

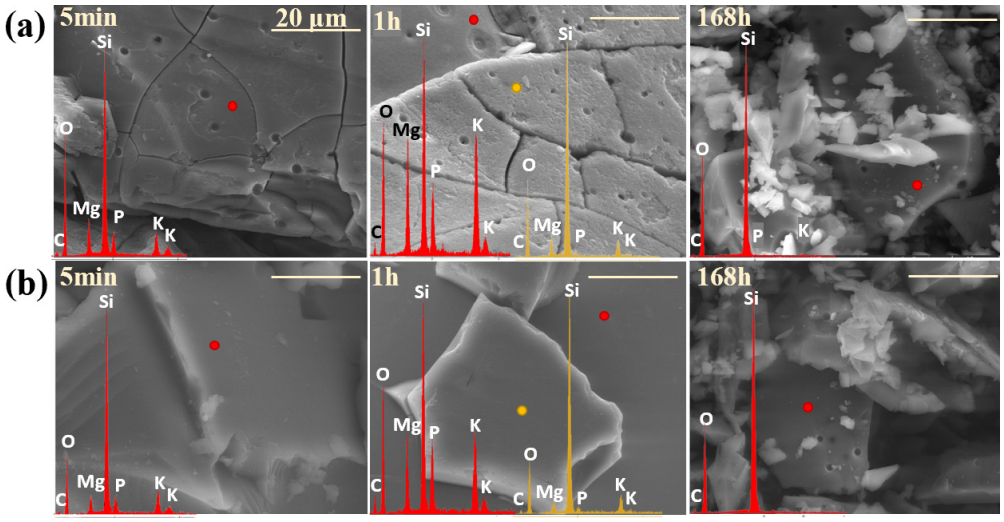


Figure 12. Micrographs and corresponding EDS spectra of 3S_6PM (**a**) and 3S_10PM (**b**) samples at different stages of long-term dissolution in 2% citric acid under dynamic leaching conditions: 5 min, 1 h, and 168 h. The micrographs were taken at 10,000× magnification, with the scale bar corresponding to 20 µm. The colors of the EDS spectra (yellow and red) correspond to the marked points in the respective micrographs, where the analyses were performed.

Hence, a hypothesis based on affinity effects appears more plausible, as the observed rate drop coincided with the depletion of a significant portion of mobile components from both glasses (~90% K^+ and ~95% Mg^{2+}). Nonetheless, the experimental conditions must be considered—specifically, the high dilution used in the dissolution tests, which suggests that saturation of the leachant with mobile species is unlikely [132]. Instead, the authors propose an alternative explanation for the observed rate drop under the given conditions: the open, fragmented structure of the designed materials facilitated the rapid leaching of mobile species from the most accessible regions of the glass via preferential ion transport pathways. The remaining, unreleased fraction of these elements was confined within less water-accessible regions of the glass network. Their liberation required the hydrolysis of strong ionic-covalent Si-O-Si bonds, which became the rate-limiting step in this kinetic regime. This conclusion is supported by the SiO_2 release kinetics curves (Figure 13).

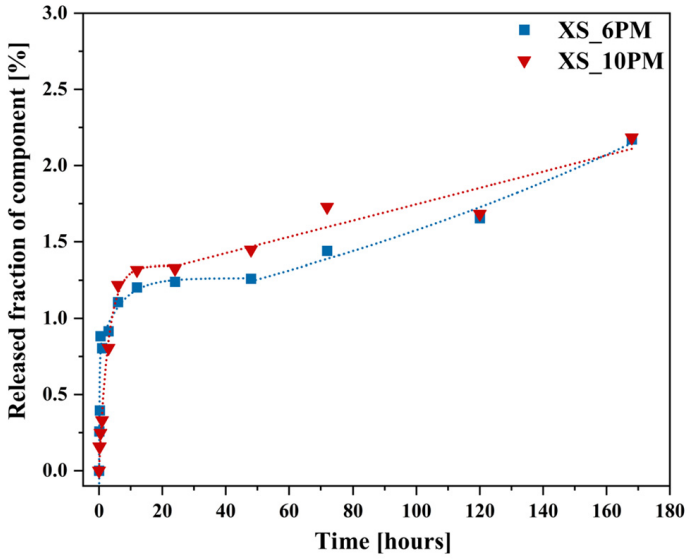


Figure 13. SiO_2 dissolution profiles of 3S_6PM and 3S_10PM glasses in 2% citric acid under dynamic leaching conditions as a function of immersion time.

The dissolution profiles of silicon from both investigated glasses, despite an initial sharp release episode—likely attributed to the leaching of surface-exposed, loosely bound, or less network-integrated silica species [138,139]—did not follow the trends observed for the other glass constituents. After six hours of the experiment, a rate drop was observed; however, instead of stabilizing, the kinetic curve exhibited a gradual upward trend, increasing almost linearly with time, albeit at a slower rate than in the initial regime (Figure 13). According to [130–132], such a linear t^1 dependence is indicative of a network hydrolysis process controlled by an interfacial reaction. The slowdown in the release of mobile glass components coincides with the moment when the rate of proton–metal exchange reactions decreases the overall glass dissolution rate, with kinetics now limited by the dissolution of the hydrated Si-O-Si framework [140]. Further insights can be drawn from the mass loss profiles of the studied glass samples throughout the experiment (Figure 14).

The curves presented in Figure 14 exhibit a similar trend to the release profiles of mobile components (Figure 11), with the key difference being that the slowdown occurred after 12 h rather than 6, as observed for the latter. Additionally, SEM micrographs displayed in Figure 11, taken at various exposure times to the aggressive solution, reveal a progressive exfoliation of surface fragments over time, accompanied by a noticeable reduction in the size of leached particles. These findings suggest that the delamination of the outermost glass layers—where surface dealkalization results in the formation of a mechanically

weaker, silica-rich layer prone to detachment [140–142]—gradually exposed deeper yet intact regions of the glass, thereby sustaining the leaching of network-forming components and contributing to continuous mass loss.

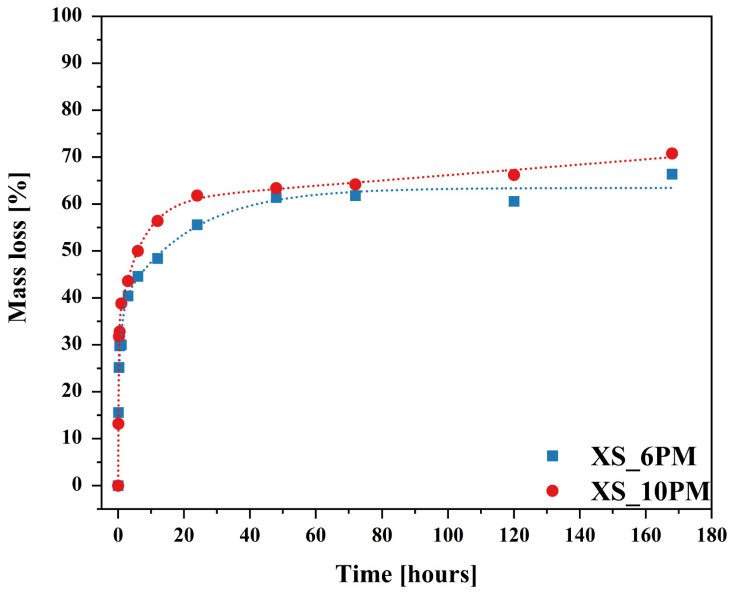


Figure 14. Mass loss curves of 3S_6PM and 3S_10PM glasses under dynamic leaching in a citric acid solution as a function of immersion time.

It is also important to note the changes in the pH of the leachate as the leaching process progressed for both glass compositions (Figure 15), which closely corresponded with the results obtained by ICP-OES, showing a similar upward trend following the square root of time function (Figure 11).

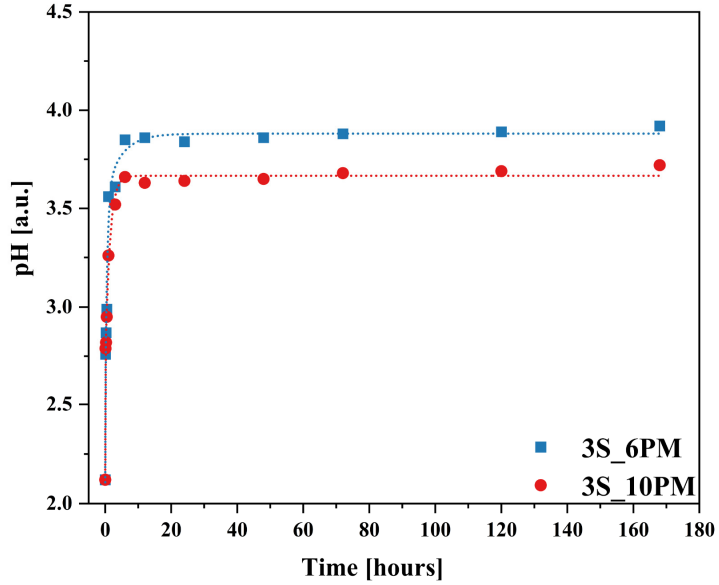


Figure 15. pH-change profiles of 3S_6PM and 3S_10PM glasses under dynamic leaching in citric acid as a function of immersion time.

The sharp increase in the release of mobile components into the solution during the first 6 h of the experiment (initial rate regime) coincided with a sudden rise in pH observed within this time range. After this period, once pH values reached 3.85 (for the XS_6PM system) and 3.66 (for the XS_10PM system), pH changed only slightly, ultimately

stabilizing at 3.92 and 3.72, respectively (Figure 15). This observed increase in pH is a direct consequence of the interdiffusion process—proton consumption from the contact solution during the glass dealkalization led to the formation of hydroxyl groups in the leachate, subsequently raising its pH. The rate of glass transformation is therefore dependent on the concentration of available protons in the contacting solution. Although the pH variation profiles over the course of the experiment were similar for both systems, the samples representing the [10P] series showed a slightly smaller increase in pH compared to the other tested composition (Figure 15). This difference can be directly attributed to the higher content of orthophosphate [PO_4^{3-}] species in these glasses (see Section 2.1.3), whose mildly acidic nature may counterbalance the alkaline environment induced by the release of alkali or alkaline earth ions [43,143].

Additionally, to characterize the behavior of the designed materials in a neutral medium, an analogous experiment was conducted using distilled water, with the results presented in Figure 16a,b and Figure 17. Interestingly, the obtained ion release profiles in the surrounding solution resembled those recorded for Si rather than for the mobile network-forming components. After an initial, more rapid release regime lasting approximately 3 h, which indicates the leaching of surface-exposed, loosely bound ions into the solution, the release rate slowed down, followed by a subsequent increase at 72 h (Figure 16a,b).

It is well established that an alkaline medium promotes network dissolution, in which OH^- ions attack the silicate network. During this process, new hydroxyl ions are generated, making the hydrolysis of the Si-O-Si glass backbone self-perpetuating, thus leading to the release of increasing amounts of glass components into the surrounding solution. However, it should be noted that these processes are most intense at pH values around 9 or higher [36,91–93], so the observed pH increase (Figure 17) in the case of the studied glasses is unlikely to be the cause of the renewed release after 72 h. Instead, the observed effect is more likely due to the previously mentioned exfoliation mechanism—peeling of hydrated surface flakes—which exposed previously unaffected areas of the glass, thereby further enhancing the release of the weakest, surface-bound components (Figure 16a,b: a slight decrease in K^+ concentration was noticeable when comparing the EDS spectra of glasses after 30 min and 168 h).

It should be emphasized here that none of the components of the tested materials were leached into the surrounding solution in amounts exceeding 3.5% of their initial content in the glass. This finding highlights the significant resistance of the synthesized samples to the action of water.

Furthermore, following the approach used by Labbilta et al. [9,144,145], the initial dissolution rates (V_0) of the studied glasses were calculated using the slope of the linear fit ($V_0 = dm/dt$) from the mass loss dissolution curves (Figure 14). For comparison, the V_0 values obtained for Si release in citric acid solution are also displayed in Table 2.

Table 2. Initial dissolution rates (V_0) of the 3S_6PM and 3S_10PM glasses, determined from the mass loss curves registered during leaching studies in citric acid and distilled water. For comparison, the V_0 values corresponding to SiO_2 release in citric acid solution are also included.

	Glass	
	3S_6PM	**3S_10PM**
	V_0 [g/h]	
Citric acid, 2%	0.432	0.576
Distilled water	0.018	0.024
Si initial release rate (citric acid)	0.006	0.001

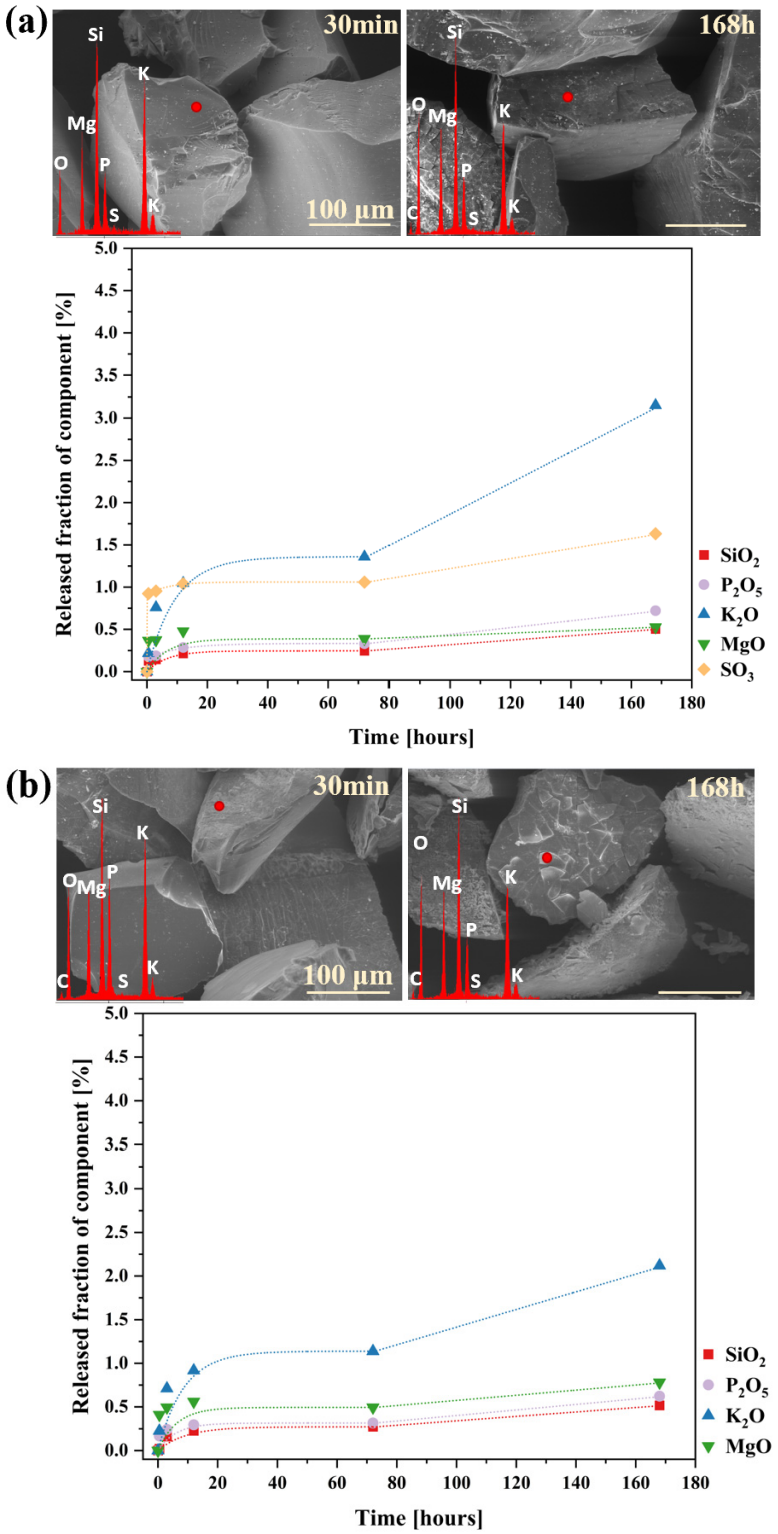


Figure 16. Ion dissolution profiles of 3S_6PM (**a**) and 3S_10PM (**b**) glasses in distilled water under dynamic leaching conditions as a function of immersion time, accompanied by micrographs and EDS data from selected surface points, illustrating surface changes at various stages of the experiment. The absence of [SO_4^{2-}] ion release profiles in the case of the 3S_10PM sample was due to the concentrations of this component in its leachate being below the sulfur detection limit of the ICP-OES method. The micrographs were taken at 1000× magnification, with the scale bar corresponding to 100 µm.

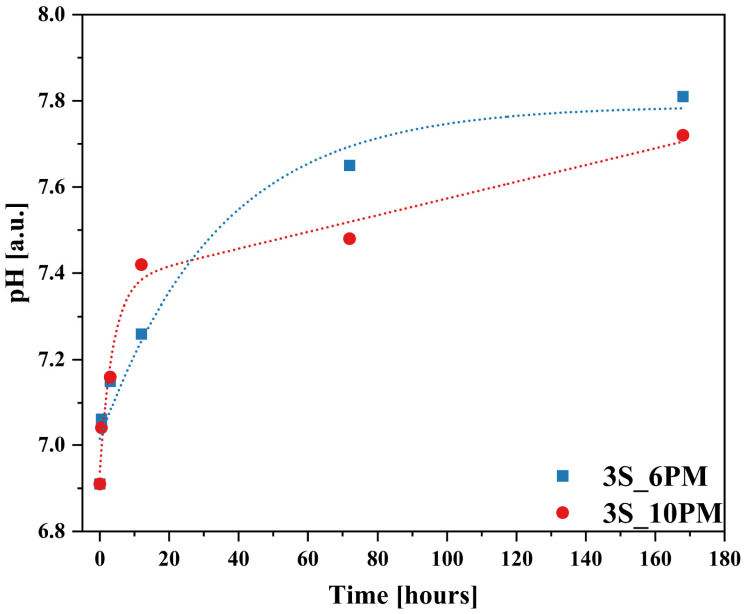


Figure 17. pH-change profiles of 3S_6PM and 3S_10PM glasses under dynamic leaching in distilled water as a function of immersion time.

The data presented in Table 2 clearly demonstrate that the chemical resistance of the glasses was influenced not only by the characteristics of the corrosive medium but also by the composition and structure of the glass itself. Significantly higher values of initial dissolution rates (V_0) observed for the citric acid solution, compared to those for Si release from the glasses, support the theory of an open, fragmented silica-oxygen network in the tested materials. This structure facilitated the leaching of ions localized within its voids while undergoing only limited hydrolysis, as confirmed by the negligible V_0 values derived from the Si release curves. The elevated V_0 values obtained in the acidic medium are primarily attributed to intense ion exchange processes within the pH range it represents, in contrast to distilled water, where only surface dealkalization occurs in the case of the tested samples. Furthermore, the higher initial dissolution rates observed for the [10P] sample, in both acidic and aqueous environments, coupled with the lower V_0 for Si release, confirm a greater chemical reactivity, resulting from the presence of a larger number of independent [PO_4^{3-}] units prone to leaching, and simultaneously, an enhanced degree of polymerization of its silicon-oxygen subnetwork, as indicated by MAS-NMR studies.

It is important to emphasize that the data presented in this subsection reflect ion leaching profiles under dynamic conditions in highly acidic solutions, which, while accelerating ion exchange processes, do not directly replicate natural soil environments [140,146]. Instead, they illustrate general trends in the behavior of the studied materials. Additionally, these data were obtained without accounting for the complexities of the final application environment, such as the presence of exogenous elements, seasonal temperature fluctuations, or variations in water availability, all of which can influence ion transport. To address these factors, future studies will extend this investigation by evaluating material performance and assessing ion release dynamics under conditions that more closely mimic natural soil environments.

3. Conclusions

The structure of glass is inherently not in thermodynamic equilibrium, making it susceptible to chemical reactions that can lead to degradation over time. While this characteristic is often regarded as a major drawback, in the case of materials designed as vitreous carriers of plant-essential ions, it is precisely what enables their functionality. Such ma-

terials should release the elements encapsulated within their vitreous matrix in response to plant demand—triggered by organic acids secreted by root systems or soil microorganisms. This controlled release minimizes the risk of over-fertilization and, consequently, nutrient runoff, which could otherwise disrupt the biogeochemical equilibrium of the soil environment. Thus, this study aimed to design and synthesize vitreous carriers of micro- and macroelements, with a particular focus on sulfur-containing compositions, as potential fertilizers of a slow-release mechanism.

This study has demonstrated that the melt fritting method successfully yields amorphous materials, with only the XS_6PC and XS_10PM samples exhibiting subtle reflections indicative of the presence of stable phases, likely double potassium-calcium and potassium-magnesium phosphates, respectively. Notably, the tendency of these systems to reorganize was amplified by sulfate incorporation, which—by occupying voids in the matrix—induced structural stresses that lowered the energy barrier for crystallization.

It was confirmed that the alteration behavior of the tested glasses can be tailored at the compositional level. Even a slight variation in the type of alkaline earth network modifier was shown to influence the material's structure and, consequently, its ion-release profile. MAS-NMR analysis revealed that all synthesized glasses ($41SiO_2$–$6(10)P_2O_5$–$20K_2O$–$33(29)MgO/CaO/MgO + CaO$) exhibited an open network, primarily composed of Q^2_{Si} silicate tetrahedra (short chains or rings), with minor contributions from Q^3_{Si} species and, in higher P_2O_5-content formulations, traces of Q^1_{Si}/Q^4_{Si} units, whereas the phosphorus-oxygen subnetwork was exclusively composed of isolated Q^0_P phosphate species. An experiment simulating exposure to acidic exudates from plant roots and microorganisms confirmed that this fragmented network facilitates ion exchange, with Si–O–Si hydrolysis occurring only at later stages of glass–solution interactions. Additionally, the incorporation of sulfur subtly modulated network cross-linking via the K^+-scavenging effect of [$SO_4{}^{2-}$] species, which enhanced polymerization of the silicate backbone, which was further demonstrated via the 'in vitro' experiment, where this increased network connectivity translated into a reduced tendency to release mobile components into the solution.

Remarkedly, the conducted experiment also revealed that glass reactivity is not solely dictated by Q^n species distribution or framework stability but is strongly influenced by the surrounding environment—despite high solubility in acidic conditions, all tested glasses exhibited significant resistance to distilled water, as evidenced by the minimal leaching of matrix components.

A correlation between thermal behavior and chemical reactivity was also established: the presence of CaO, acting exclusively as a network modifier, led to the formation of the most fragmented and open network, reflected in the lowest thermal stability of the Si–O–Si backbone and its pronounced tendency to crystallize into more stable phases. This low stability and high network openness resulted in the highest SiO_2 release, serving as an indicator of overall glass degradation. Conversely, MgO, acting both as a network modifier and a former present in the XS_6PM system, increased network polymerization, enhancing silicate backbone rigidity and reducing Si release. Meanwhile, the co-addition of MgO and CaO seemed to induce a mixed alkaline earth effect, known to increase the activation energy for ionic diffusion, as the respective samples exhibited the lowest glass transition temperature and chemical reactivity in terms of silica dissolution among the [6P] series. Given the highest NC of all the studied formulations, unsurprisingly, the XS_10P samples released SiO_2 in the lowest amounts, despite their lowest thermal stability, stemming from the high concentration of incompatible [$SiO_4{}^{4-}$, $PO_4{}^{3-}$] and [$SO_4{}^{2-}$] species within the common framework. Additionally, the incorporation of sulfate units was evidenced to indirectly impact the behavior of the tested materials in the solutions used—the resulting

increase in the network connectivity and rigidity and simultaneous decrease in thermal stability diminished their susceptibility to dissolution in acidic environments.

Meanwhile, dissolution kinetics studies provided insights into nutrient release profiles, which are essential for ensuring a steady supply of nutrients to plants: after an initial rapid dissolution rate in citric acid (strongly intensified by higher P_2O_5 content), the release of beneficial elements stabilized and became dependent on the hydrolysis of the silicate backbone. Importantly, the dissolution curves followed a $t^{1}/^{2}$ dependency (indicative of diffusion-controlled ion exchange), indicating that the process is governed by interdiffusion reactions. Furthermore, preliminary observations suggest that these materials underwent surface cracking, flaking, and exfoliation, which further enhanced ion leaching by increasing the contact area with the surrounding solution.

The present study employed laboratory experiments to gain a deeper understanding of the composition–structure–property relationship in sulfate-bearing multicomponent silicate-phosphate glasses—an essential foundation for future investigations under soil-conditions. The findings confirm that the synthesized glasses meet all the key requirements for potential glass fertilizers. Not only did they exhibit an amorphous nature, but they also possessed an open, fragmented network that facilitated water infiltration. Moreover, the designed materials demonstrated high resistance to water while selectively releasing their constituents in acidic solutions that simulated root exudates.

Overall, these findings establish a foundation for the rational design of sulfate-bearing silicate-phosphate glasses with controlled chemical activity, and—recognizing that laboratory data may not fully capture the complexities of the application environment—will pave the way for further studies aimed at evaluating their long-term behavior under realistic soil conditions.

4. Materials and Methods

4.1. Glass Design, Synthesis, and Preliminary Characterization (XRF, XRD, DSC, MAS-NMR)

In order to design vitreous carriers for macro- and micronutrients displaying prolonged release characteristics, raw materials were selected as sources of phosphorus ($(NH_4)_3PO_4$), potassium (K_2CO_3), magnesium (MgO), calcium (CaO), and sulfur (K_2SO_4). Additionally, silica (SiO_2) was chosen as the primary structural component of the glass matrix, serving as a matrix for these elements. To assess the feasibility of controlling the release of nutrients into the soil environment through the appropriate selection of glass matrix components, four formulations were developed based on previous experimental findings [3,16,80,81,96], which exhibited the highest potential for application as sulfate-bearing vitreous carriers of beneficial nutrients. The molar percentages of individual oxides in each formulation were as follows (X represents the molar percentage of SO_3 introduced into the formulations; in this study, X = 0, 1, 3, or 5 mol.%):

- XS_6PM system: $41SiO_2 \cdot 6P_2O_5 \cdot 20K_2O \cdot 33MgO \cdot XSO_3$
- XS_6PC system: $41SiO_2 \cdot 6P_2O_5 \cdot 20K_2O \cdot 33CaO \cdot XSO_3$
- XS_6PMC system: $41SiO_2 \cdot 6P_2O_5 \cdot 20K_2O \cdot 16.5MgO \cdot 16.5CaO \cdot XSO_3$
- XS_10PM system: $41SiO_2 \cdot 10P_2O_5 \cdot 20K_2O \cdot 29MgO \cdot XSO_3$

It is important to emphasize that samples representing the XS_10PC and XS_10PMC compositions were also prepared to explore a selected range of possible combinations within the chosen P_2O_5 content regimes. However, the resulting materials exhibited the highest fraction of crystalline phases in their amorphous matrices, rendering them unsuitable for further testing (Figure 18).

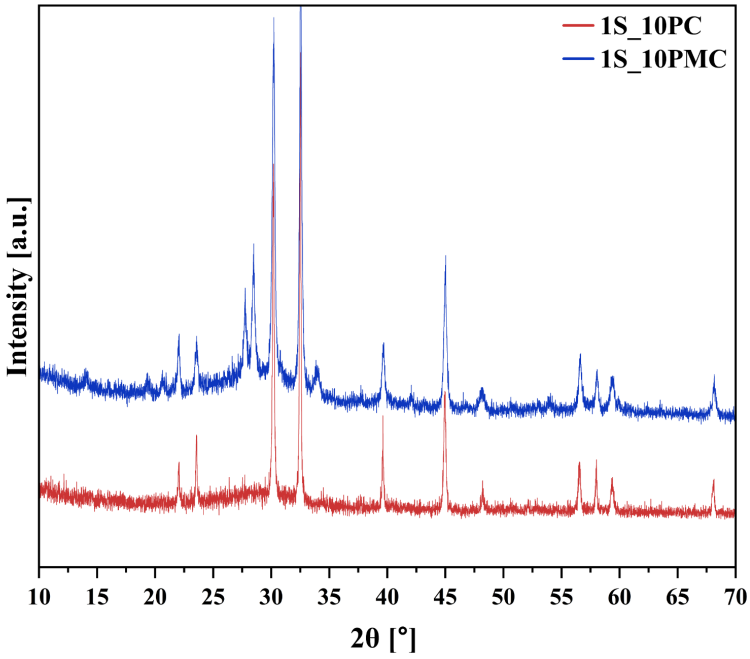


Figure 18. Diffraction patterns of 1S_10PC and 1S_10PMC samples.

The designed glasses were synthesized on a laboratory scale (~100 g) by melting precisely weighed (to an accuracy of 0.001 g) and homogenized (using a mortar and pestle) raw materials of analytical grade purity (SiO_2, $(NH_4)_2HPO_4$, K_2CO_3, MgO, and K_2SO_4, all supplied by CHEMPUR, Piekary Śląskie, Poland). The synthesis was carried out in ceramic crucibles placed in an electric chamber furnace under an air atmosphere at 1450 °C. The resulting melts were rapidly quenched by pouring them into cold water to obtain fully amorphous materials and to simultaneously suppress spontaneous crystallization [81]. The actual oxide compositions of the synthesized glasses were verified using X-ray fluorescence spectrometry (XRF) with an ARL Perform'X spectrometer, at the accredited testing laboratory FerroCarbo (Krakow, Poland). Samples for measurement were prepared from homogenized glass material in the form of either pressed or fused pellets (~10 g of glass). Potential losses associated with the high-temperature synthesis of the glasses were accounted for in the calculations, resulting in a measured composition that exhibited a high degree of consistency with the nominal values. The fusion method involved pre-calcination and melting of the samples in a fluxer.

Notably, the total oxide contents determined for the sulfur-containing silicate-phosphate glasses representing the XS_6PM and XS_10PM systems did not sum to 100%. This discrepancy likely resulted from the volatility of certain glass components during the fusion process at 1100 °C, which occurred as part of the XRF pearl preparation method.

The XRF-determined molar contents of individual glass components are presented in Table 3.

To verify the amorphous nature of the synthesized materials, the samples were ground into a powder form (<0.1 mm) and analyzed using X-ray diffraction (XRD) on a PANalytical X'Pert Pro diffractometer equipped with a Cu anode (Malvern, UK). Data were collected over the 2θ range of 10–70° with a goniometer step size of 0.008° and an angular reproducibility of ±0.0002°. Crystalline phases, if present, were identified using the HighScore Plus software (https://www.malvernpanalytical.com/en/products/category/software/x-ray-diffraction-software/highscore-with-plus-option, accessed on 2 April 2025).

Table 3. Measured compositions of the synthesized specimens. Registered minor discrepancies between the expected and actual amounts of glass components are attributed to inherent measurement uncertainties and potential volatilization during the heating process.

No	SiO_2	P_2O_5	K_2O	MgO	CaO	SO_3
0S_6PM	41.42 (±0.40)	6.75 (±0.09)	20.42 (±0.00)	30.17 (±0.45)	–	–
1S_6PM	37.39 (±0.41)	5.96 (±0.09)	19.53 (±0.00)	31.72 (±46)	–	0.84 (±0.12)
3S_6PM	40.00 (±0.41)	6.92 (±0.09)	20.63 (±0.00)	32.67 (±0.46)	–	1.84 (±0.14)
5S_6PM	41.60 (±0.40)	6.49 (±0.40)	17.69 (±0.00)	33.44 (±0.40)	–	1.59 (±0.40)
0S_6PC	39.11 (±0.44)	6.29 (±0.09)	18.88 (±0.00)	–	33.63 (±0.71)	–
1S_6PC	38.28 (±0.45)	6.14 (±0.10)	17.21 (±0.00)	–	35.79 (±0.73)	1.00 (±0.16)
3S_6PC	37.90 (±0.45)	6.46 (±0.09)	18.40 (±0.00)	–	35.12 (±0.72)	2.05 (±0.13)
5S_6PC	43.25 (±0.45)	6.10 (±0.01)	15.03 (±0.00)	–	37.42 (±0.72)	1.39 (±0.15)
0S_6PMC	39.91 (±0.41)	6.33 (±0.09)	18.40 (±0.00)	15.46 (±0.34)	18.16 (±0.44)	–
1S_6PMC	38.20 (±0.42)	6.33 (±0.09)	19.59 (±0.00)	15.53 (±0.33)	18.09 (±0.56)	0.95 (±0.12)
3S_6PMC	38.08 (±0.09)	6.64 (±0.09)	18.92 (±0.00)	16.57 (±0.34)	20.15 (±0.45)	1.76 (±0.15)
5S_6PMC	41.70 (±0.42)	6.46 (±0.09)	16.41 (±0.00)	16.32 (±0.35)	20.89 (±0.56)	1.40 (±0.14)
0S_10PM	38.11 (±0.40)	11.01 (±0.08)	21.56 (±0.00)	29.12 (±0.44)	–	–
1S_10PM	39.00 (±0.42)	10.89 (±0.09)	19.95 (±0.00)	28.98 (±0.50)	–	0.25 (±0.05)
3S_10PM	39.37 (±0.42)	11.02 (±0.09)	21.14 (±0.00)	29.35 (±0.47)	–	0.83 (±0.10)
5S_10PM	42.29 (±0.41)	11.48 (±0.08)	22.29 (±0.00)	24.71 (±0.46)	–	0.48 (±0.07)

Thermal property variations as a function of sulfate content were examined using a STA 449 F3 Jupiter (NETZSCH, Selb, Germany) instrument operating in heat-flux DSC mode, with a temperature resolution of 0.001 K, at the Thermophysical Research Laboratory of the Faculty of Materials Science and Ceramics, AGH University of Krakow. To conduct differential scanning calorimetry (DSC) measurements, powder samples (31 mg) with grain sizes ranging from 0.1 to 0.3 mm were placed in platinum crucibles and heated at a rate of 10 °C min^{-1} in a dynamic air atmosphere (80 mL min^{-1}). The instrument temperature sensor was calibrated using the melting temperatures of high-purity reference materials (Al, Zn, Sn, Au, Ag), and sensitivity for enthalpy and heat capacity determinations was calibrated with synthetic sapphire (α-Al_2O_3) standard references. The Netzsch Proteus Thermal Analysis Program (version 5.0.0) was used to determine the characteristic glass transition temperature (T_g), the onset (T_x), and the maximum (T_c) of the glass crystallization effect. T_g was determined as the midpoint of the relevant transformation step, while T_x and T_c were derived from the onset and maximum of the exothermic crystallization peak, respectively.

High-resolution solid-state ^{29}Si and ^{31}P MAS-NMR spectra were recorded using an APOLLO console (Tecmag, Houston, TX, USA) and a 7 T/89 mm superconducting magnet (Magnex, Oxford, UK) at the Jerzy Haber Institute of Catalysis and Surface Chemistry, Polish Academy of Sciences. A Bruker HP-WB high-speed MAS probe, equipped with a 4 mm zirconia rotor and KEL-F cap, was employed for sample spinning. A single 3 µs RF pulse, corresponding to a $\pi/2$ flipping angle, was applied. The ^{31}P MAS-NMR spectra were measured at a resonance frequency of 121.264 MHz, with the sample spinning at 6 kHz. The initial ^{31}P T1 relaxation time was estimated to be approximately 3 s. The acquisition delay was set to 10 s, with 256 scans acquired. The ppm frequency scale was referenced to the ^{31}P resonance of 85% H_3PO_4. For the ^{29}Si MAS-NMR spectra, measurements were taken at a resonance frequency of 59.515 MHz, with the sample spinning at 4 kHz. The initial ^{29}Si T1 relaxation time was estimated to be approximately 10 s, with an acquisition delay of 30 s and 256 scans. The ppm frequency scale was referenced to the ^{29}Si resonance of TMS (Tetramethylsilane). For the ^{31}P MAS-NMR spectra, the uncertainties in line positions and linewidths were about 0.2 ppm, while the relative intensities had an accuracy of

approximately 1%. For the ^{29}Si spectra, the corresponding uncertainties were 0.4 ppm and 1%, respectively.

4.2. Glass Dissolution Studies ('In Vitro' Conditions)

The assessment of behavior of the designed materials in a solution simulating plant root exudates (hereafter referred to as the 'in vitro' experiment) was conducted in accordance with Regulation (EC) 2003/2003 on fertilizers, which provides guidelines for Member States regarding sampling and analytical methods for fertilizers [126]. Glass fractions of 0.1–0.3 mm were carefully weighed (to an accuracy of 0.001 g) to obtain 1 g specimens, which were placed in glass beakers. To each beaker, 100 (±1) mL of 2% citric acid solution was added, a common root exudate suitable for simulating plant action. The beakers were then covered with a watch glass and placed on magnetic stirrers, where they were mixed for 30 min at 300 rpm at room temperature. After this period, the contents of the beakers were immediately filtered into a dry container through a dry, phosphate-free filter paper. The collected filtrates were analyzed for pH using a Mettler Toledo pH meter and subsequently subjected to analysis via inductively coupled plasma optical emission spectroscopy (ICP-OES, PerkinElmer Optima 2000 DV, Norwalk, CA, USA) at the Accredited Hydrogeochemical Laboratory of AGH University of Krakow (Certificate No. AB 1050). The same procedure was applied to assess the solubility of the synthesized samples in distilled water, although this test was conducted only on selected samples representing all systems with 3 mol.% SO_3 content.

The authors find it necessary to clarify the use of the term 'in vitro' in the context of this study, as it is traditionally associated with medical research. Notably, in soil science, specialists consider the soil environment a 'living entity' due to its complex biological activity and interactions with microorganisms. Based on this perspective, the term 'in vitro' refers here to laboratory-based experiments conducted outside soil system, such as dissolution studies of glass fertilizers in simulated environments (e.g., solutions that mimic soil conditions). However, to underscore the distinction from traditional biological applications, this term is presented in apostrophes throughout the manuscript.

4.3. Experimental Approach to Glass Dissolution Kinetics

The dissolution kinetics of selected glasses in a 2% citric acid solution was investigated for two compositions—3S_6PM and 3S_10PM. The experiment commenced by weighing glass fractions (0.1–0.3 mm) to a precision of 0.001 g, resulting in 1 g specimens of each composition. Twelve replicate samples (12 × 1 g) were prepared for each composition, placed in glass beakers, and 100 (±1) mL of 2% citric acid solution was added to each. The beakers were then covered with watch glasses and placed on magnetic stirrers, where they were stirred for 30 min at 300 rpm and room temperature. At intervals of 5, 15, and 30 min and 1 h, 3 h, 6 h, 12 h, 24 h, 48 h, 72 h, 120 h, and 168 h, leachates were collected by filtration through dry, phosphate-free corrugated filter paper, followed by pH measurement and composition analysis using ICP-OES. An analogous experiment was conducted to estimate the dissolution kinetics in distilled water, but with a lower frequency of sampling, at 30 min, 3 h, 12 h, 72 h, and 168 h. Additionally, selected residues left on the filter (after 5, 30, and 60 min and 6 h, 12 h, and 168 h of dissolution in citric acid, and after 30 min and 168 h in distilled water) were carefully cleaned by ultrasonic treatment to remove any remnants of corrosive solution. The residues were then weighed to a precision of 0.001 g and analyzed using Scanning Electron Microscopy (SEM) with Energy Dispersive X-ray Spectroscopy (EDS) for qualitative and semi-quantitative analyses at selected points on the sample surfaces. Observations were conducted under high-vacuum conditions using a backscatter electron detector (BSE) with an accelerated voltage of 18 kV employing a NOVA

NANO SEM 200 (FEI EUROPE, Eindhoven, The Netherlands) coupled with an EDAX EDS analyzer in the Laboratory of Scanning Microscopy and Microanalysis at the Faculty of Materials Science and Ceramics, AGH University of Krakow.

Author Contributions: Conceptualization, M.S. and A.B.; Methodology, A.B. and M.S.; Software, A.B. and M.S.; Validation, A.B., M.S. and J.S.; Formal Analysis, A.B., M.S. and J.S.; Investigation, A.B.; Resources, A.B.; Data Curation, A.B. and M.S.; Writing—Original Draft Preparation, A.B.; Writing—Review and Editing, A.B. and M.S.; Visualization, A.B.; Supervision, A.B. and M.S.; Project Administration, A.B. and M.S.; Funding Acquisition, A.B. and M.S. All authors have read and agreed to the published version of the manuscript.

Funding: This work was financed by the National Science Centre, Poland, project number 2023/49/N/ST11/00299, and partially supported by the program 'Excellence initiative—research university' for the AGH University of Krakow (No 9785).

Institutional Review Board Statement: Not applicable.

Informed Consent Statement: Not applicable.

Data Availability Statement: The data presented in this study are available on request from the corresponding author.

Acknowledgments: The authors would like to express their gratitude for the XRD and XRF analyses to Sebastian Komarek and Bartosz Handke, respectively (Faculty of Materials Science and Ceramics, AGH University of Krakow, Poland). The authors also gratefully acknowledge Mariusz Gackowski for his assistance with the MAS-NMR measurements and Dorota Rutkowska-Żbik for her guidance and support during the internship. The authors also extend their gratitude to the Jerzy Haber Institute of Catalysis and Surface Chemistry, Polish Academy of Sciences, for providing the facilities necessary to conduct this research as part of the internship program.

Conflicts of Interest: The authors declare no conflicts of interest.

References

1. Fiantis, D.; Ginting, F.I.; Gusnidar; Nelson, M.; Minasny, B. Volcanic Ash, insecurity for the people but securing fertile soil for the future. *Sustainability* **2019**, *11*, 3072. [CrossRef]
2. Neall, V.E. Land use and land cover. In *Encyclopaedia of Life Support Systems*; UNESCO: Paris, France, 2006; Volume 1, pp. 1–24.
3. Stoch, L.; Wacławska, I.; Szumera, M. Phospho-silicate glasses, self-degradable in environment conditions. *Adv. Mater. Res.* **2008**, *39–40*, 335–340. [CrossRef]
4. Dakora, F.D.; Phillips, D.A. Root exudates as mediators of mineral acquisition in low-nutrient environments. *Plant Soil* **2002**, *245*, 35–47. [CrossRef]
5. Vega, N.W.O. A review on beneficial effects of Rhizosphere bacteria on soil nutrient availability and plant nutrient uptake. *Nac. Agron.-Medellín* **2007**, *60*, 3621–3643.
6. Wang, H.-Y.; Shen, Q.-H.; Zhou, J.-M.; Wang, J.; Du, C.-W.; Chen, X.-Q. Plants use alternative strategies to utilize nonexchangeable potassium in minerals. *Plant Soil* **2011**, *343*, 209–220. [CrossRef]
7. Stoch, L.; Wacławska, I.; Ciecińska, M. Thermochemistry of biologically active glasses. *J. Therm. Anal. Calorim.* **2001**, *65*, 341–350. [CrossRef]
8. Labbilta, T.; Ait-El-Mokhtar, M.; Abouliatim, Y.; Khouloud, M.; Meddich, A.; Mesnaoui, M. Innovative formulations of phosphate glasses as controlled-release fertilizers to improve tomato crop growth, yield and fruit quality. *Molecules* **2021**, *26*, 3928. [CrossRef]
9. Labbilta, T.; Ait-El-Mokhtar, M.; Harech, M.A.; Anasser, I.; Abouliatim, Y.; Khouloud, M.; Meddich, A.; Mesnaoui, M. Advancing controlled-release phosphate glasses as sustainable fertilizers: Microelement-enhanced formulations and dissolution behavior analysis. *J. Non-Cryst. Solids* **2024**, *625*, 122765. [CrossRef]
10. Ouis, M.A.; Abd-Eladl, M.; Abou-Baker, N.H. Evaluation of Agriglass as an Environment Friendly Slow Release Fertilizer. *Silicon* **2018**, *10*, 293–299. [CrossRef]
11. Mandal, B.; Hazra, G.; Ghosh, G.K.; Das, T. Leaching pattern of phosphate glass fertilizers with different compositions under Soxhlet distillation conditions. *Cerâmica* **2020**, *66*, 250–255. [CrossRef]
12. Sava, B.A.; Boroica, L.; Sava, M.; Elisa, M.; Vasiliu, C.I.; Nastase, F.; Nastase, C.; Medianu, R. Potassium phosphate glasses used as agro-fertilizers with controlled solubility. *J. Optoelectron. Adv. Mater.* **2011**, *13*, 1534–1541.

13. Cacini, S.; Rinaldi, S.; Massa, D.; Nesi, B.; Epifani, R.; Trinchera, A. The effect of a glass matrix fertilizer and compost amendment on plant growth and mineral nutrition of two container-grown *Rose* spp. cultivars. *Sci. Hortic.* **2020**, *274*, 109660. [CrossRef]
14. Waclawska, I.; Stoch, L. Thermal behaviour of silicate-phosphate glasses in relation to their biochemical activity. *J. Therm. Anal. Calorim.* **2001**, *65*, 141–146. [CrossRef]
15. Wacławska, I.; Szumera, M. Thermal analysis of glasses for proecological applications. *J. Therm. Anal. Calorim.* **2003**, *72*, 1065–1072. [CrossRef]
16. Szumera, M.; Wacławska, I. Spectroscopic and Thermal Studies of Silicate-Phosphate Glass. *Proc. J. Therm. Anal. Calorim.* **2007**, *88*, 151–156. [CrossRef]
17. Szumera, M.; Wacławska, I. Effect of molybdenum addition on the thermal properties of silicate–phosphate glasses. *J. Therm. Anal. Calorim.* **2012**, *109*, 649–655. [CrossRef]
18. Szumera, M.; Wacławska, I.; Sułowska, J. Thermal properties of MnO_2 and SiO_2 containing phosphate glasses. *J. Therm. Anal. Calorim.* **2016**, *123*, 1083–1089. [CrossRef]
19. Wacławska, I.; Szumera, M.; Stoch, P.; Sitarz, M. Structural role of Fe in the soil active glasses. *Spectrochim. Acta Part A Mol. Biomol. Spectrosc.* **2011**, *79*, 728–732. [CrossRef]
20. Hawkesford, M.; Horst, W.; Kichey, T.; Lambers, H.; Schjoerring, J.; Skrumsager Møller, I.; White, P. Functions of macronutrients. In *Marschner's Mineral Nutrition of Higher Plants*, 3rd ed.; Marschner, P., Ed.; Elsevier Ltd.: Amsterdam, The Netherlands, 2012; pp. 135–189. [CrossRef]
21. Shen, J.; Yuan, L.; Zhang, J.; Li, H.; Bai, Z.; Chen, X.; Zhang, W.; Zhang, F. Phosphorus dynamics: From soil to plant. *Plant Physiol.* **2011**, *156*, 997–1005. [CrossRef]
22. Zhu, Y.-X.; Gong, H.-J.; Yin, J.-L. Role of silicon in mediating salt tolerance in plants: A Review. *Plants* **2019**, *8*, 147. [CrossRef]
23. Jarvie, H.P.; Sharpley, A.N.; Withers, P.J.A.; Scott, J.T.; Haggard, B.E.; Neal, C. Phosphorus Mitigation to Control River Eutrophication: Murky Waters, Inconvenient Truths, and "Postnormal" Science. *J. Environ. Qual.* **2013**, *42*, 295–304. [CrossRef] [PubMed]
24. White, P.J.; Broadley, M.R. Calcium in plants. *Ann. Bot.* **2003**, *92*, 487–511. [CrossRef] [PubMed]
25. Zellener, W.; Tubaña, B.; Rodrigues, F.A.; Datnoff, L.E. Silicon's Role in Plant Stress Reduction and Why This Element Is Not Used Routinely for Managing Plant Health. *Plant Dis.* **2021**, *105*, 2033–2049. [CrossRef]
26. Cordell, D.; Drangert, J.-O.; White, S. The story of phosphorus: Global food security and food for thought. *Glob. Environ. Change* **2009**, *19*, 292–305. [CrossRef]
27. Wang, M.; Zheng, Q.; Shen, Q.; Guo, S. The critical role of potassium in plant stress response. *Int. J. Mol. Sci.* **2013**, *14*, 7370–7390. [CrossRef]
28. Yan, B.; Hou, Y. Effect of Soil Magnesium on Plants: A Review. *IOP Conf. Ser. Earth Environ. Sci.* **2018**, *170*, 022168. [CrossRef]
29. Dahl, C.; Hell, R.; Knaff, D.; Leustek, T. (Eds.) *Sulfur Metabolism in Phototrophic Organisms*; Springer: Berlin, Germany, 2008; Volume 27.
30. Jamal, A.; Moon, Y.S.; Abdin, M.Z. Sulphur—A general overview and interaction with nitrogen. *Aust. J. Crop Sci.* **2010**, *4*, 523–529.
31. Stoch, L. Thermal analysis and thermochemistry of vitreous into crystalline state transition. *J. Therm. Anal. Calorim.* **2004**, *77*, 7–16. [CrossRef]
32. Weinberg, M.C. Glass-forming ability and glass stability in simple systems. *J. Non-Cryst. Solids* **1994**, *167*, 81–88. [CrossRef]
33. Turnbull, D. Under What Conditions Can a Glass Be Formed? *Contemp. Phys.* **1969**, *10*, 473–488. [CrossRef]
34. Zanotto, E.D.; Cassar, D.R. The race within supercooled liquids—Relaxation versus crystallization. *J. Chem. Phys.* **2018**, *149*, 024503. [CrossRef] [PubMed]
35. Uhlmann, D.R. A Kinetic Treatment of Glass Transition. *J. Non-Cryst. Solids* **1972**, *7*, 337–348. [CrossRef]
36. Richet, P.; Toplis, M.J. Thermodynamic aspects of the glass transition of silicates. *Comptes Rendus l'Académie Sci.-Ser. IV-Phys. Astrophys.* **2001**, *2*, 191–202. [CrossRef]
37. Vogel, W. *Introduction to Glass Science*; Springer: New York, NY, USA, 1972. [CrossRef]
38. Kawasaki, T.; Tanaka, H. Structural evolution in the aging process of supercooled colloidal liquids. *Phys. Rev. E* **2014**, *89*, 062315. [CrossRef]
39. Johari, G.; Shanker, R.M. On determining the relaxation time of glass and amorphous pharmaceuticals' stability from thermodynamic data. *Thermochim. Acta* **2010**, *511*, 89–95. [CrossRef]
40. Riechers, B.; Roed, L.A.; Mehri, S.; Ingebrigtsen, T.S.; Hecksher, T.; Dyre, J.C.; Niss, K. Predicting nonlinear physical aging of glasses from equilibrium relaxation via the material time. *Sci. Adv.* **2022**, *8*, eabl9809. [CrossRef]
41. Krishnan, N.M.A.; Wang, B.; Le Pape, Y.; Sant, G.; Bauchy, M. Irradiation-driven amorphous-to-glassy transition in quartz: The crucial role of the medium-range order in crystallization. *Phys. Rev. Mater.* **2017**, *1*, 053405. [CrossRef]
42. Stoch, L. Flexibility of structure and glass-forming ability: A chemical approach. *Glass Phys. Chem.* **2001**, *27*, 167–174. [CrossRef]
43. Stoch, L. Flexibility of structure as a criterion of glass formation and stability. *Opt. Appl.* **2000**, *30*, 647–655.

44. Manara, D.; Grandjean, A.; Pinet, O.; Dussossoy, J.; Neuville, D. Sulfur behavior in silicate glasses and melts: Implications for sulfate incorporation in nuclear waste glasses as a function of alkali cation and V_2O_5 content. *J. Non-Cryst. Solids* **2007**, *353*, 12–23. [CrossRef]
45. Diallo, B.; Topka, K.C.; Puyo, M.; Lebesgue, C.; Genevois, C.; Laloo, R.; Samelor, D.; Lecoq, H.; Allix, M.; Vergnes, H.; et al. Network hydration, ordering and composition interplay of chemical vapor deposited amorphous silica films from tetraethyl orthosilicate. *J. Mater. Res. Technol.* **2021**, *13*, 534–547. [CrossRef]
46. Awazu, K.; Kawazoe, H. Strained Si–O–Si bonds in amorphous SiO_2 materials: A family member of active centers in radio, photo, and chemical responses. *J. Appl. Phys.* **2003**, *94*, 6243–6262. [CrossRef]
47. Fabert, M.; Ojha, N.; Erasmus, E.; Hannula, M.; Hokka, M.; Hyttinen, J.; Rocherullé, J.; Sigalas, I.; Massera, J. Crystallization and sintering of borosilicate bioactive glasses for application in tissue engineering. *J. Mater. Chem. B* **2017**, *5*, 4514–4525. [CrossRef] [PubMed]
48. Filho, O.P.; Latorre, G.P.; Hench, L.L. Effect of crystallization on apatite-layer formation of bioactive glass 45S5. *J. Biomed. Mater. Res.* **1996**, *30*, 509–514. [CrossRef]
49. Sitarz, M.; Bulat, K.; Szumera, M. Influence of modifiers and glass-forming ions on the crystallization of glasses of the $NaCaPO_4$–SiO_2 system. *J. Therm. Anal. Calorim.* **2012**, *109*, 577–584. [CrossRef]
50. Montazerian, M.; Shearer, A.; Mauro, J.C. Perspectives on the impact of crystallization in bioactive glasses and glass-ceramics. *Int. J. Ceram. Eng. Sci.* **2024**, *6*, e10194. [CrossRef]
51. Weaver, J.L.; DePriest, P.T.; Plymale, A.E.; Pearce, C.I.; Arey, B.; Koestler, R.J. Microbial interactions with silicate glasses. *npj Mater. Degrad.* **2021**, *5*, 11. [CrossRef]
52. Mimmo, T.; Pii, Y.; Valentinuzzi, F.; Astolfi, S.; Lehto, N.; Robinson, B.; Brunetto, G.; Terzano, R.; Cesco, S. Nutrient availability in the rhizosphere: A review. *Acta Hortic.* **2018**, *1217*, 13–28. [CrossRef]
53. Vancea, C.; Mosoarca, G.; Popa, S. A sustainable solution to obtain p-k-mn glass fertilizers from cheap and readily available wastes. *Int. J. Environ. Res. Public Health* **2021**, *18*, 6585. [CrossRef]
54. Hassan, M.K.; McInroy, J.A.; Kloepper, J.W. The interactions of rhizodeposits with plant growth-promoting rhizobacteria in the rhizosphere: A review. *Agriculture* **2019**, *9*, 142. [CrossRef]
55. Gent, M.P.N.; Parrish, Z.D.; White, J.C. Nutrient Uptake among Subspecies of Cucurbita Pepo L. Is Related to Exudation of Citric Acid. *JASHS* **2005**, *130*, 782–788. [CrossRef]
56. Balemi, T.; Negisho, K. Management of soil phosphorus and plant adaptation mechanisms to phosphorus stress for sustainable crop production: A review. *J. Soil Sci. Plant Nutr.* **2012**, *12*, 547–562. [CrossRef]
57. Gin, S.; Delaye, J.-M.; Angeli, F.; Schuller, S. Aqueous alteration of silicate glass: State of knowledge and perspectives. *NPJ Mater. Degrad.* **2021**, *5*, 42. [CrossRef]
58. Zanini, R.; Franceschin, G.; Cattaruzza, E.; Traviglia, A. A review of glass corrosion: The unique contribution of studying ancient glass to validate glass alteration models. *npj Mater. Degrad.* **2023**, *7*, 38. [CrossRef]
59. Brauer, D.S. Bioactive glasses—Structure and properties. *Angew. Chem. Int. Ed. Engl.* **2015**, *54*, 4160–4181. [CrossRef]
60. Tilocca, A.; Cormack, A.N.; de Leeuw, N.H. The structure of bioactive silicate glasses: New insight from molecular dynamics simulations. *Chem. Mater.* **2007**, *19*, 95–103. [CrossRef]
61. Wacławska, I.; Środa, M.; Stoch, L. Thermal Methods Applied to the Glass Transition of Mixed Network $AlPO_4$-BPO_4-SiO_2 Glasses. *Proc. J. Therm. Anal. Calorim.* **2001**, *65*, 661–667. [CrossRef]
62. Waclawska, I.; Szumera, M. Reactivity of silicate–phosphate glasses in soil environment. *J. Alloys Compd.* **2009**, *468*, 246–253. [CrossRef]
63. Edén, M. The split network analysis for exploring composition–structure correlations in multi-component glasses: I. Rationalizing bioactivity-composition trends of bioglasses. *J. Non-Cryst. Solids* **2011**, *357*, 1595–1602. [CrossRef]
64. Moulton, B.J.A.; Henderson, G.S. Glasses: Alkali and Alkaline-Earth Silicates. *Encycl. Mater. Tech. Ceram. Glas.* **2021**, *2*, 462–482. [CrossRef]
65. Ting, H.; Page, S.J.; Poologasundarampillai, G.; Chen, S.; Yu, B.; Hanna, J.V.; Jones, J.R. Phosphate content affects structure and bioactivity of sol-gel silicate bioactive glasses. *Int. J. Appl. Glass Sci.* **2017**, *8*, 372–382. [CrossRef]
66. Zeng, H.; Jiang, Q.; Liu, Z.; Li, X.; Ren, J.; Chen, G.; Liu, F.; Peng, S. Unique sodium phosphosilicate glasses designed through extended topological constraint theory. *J. Phys. Chem. B* **2014**, *118*, 5177–5183. [CrossRef] [PubMed]
67. das Dores, D.R.S.; da Silva, V.R.; Silva, G.H.; De Oliveira, V.H.; Ludwig, Z.M.d.C.; Bell, M.J.V.; Ludwig, V.; Pontuschka, W.M.; dos Anjos, V.C. On the influence of low silica content on phosphates glasses doped with Erbium Ions. *Quarks Braz. Electron. J. Phys. Chem. Mater. Sci.* **2020**, *3*, 41–49. [CrossRef]
68. Wallace, K.E.; Hill, R.G.; Pembroke, J.T.; Brown, C.J.; Hatton, P.V. Influence of sodium oxide content on bioactive glass properties. *J. Mater. Sci. Mater. Med.* **1999**, *10*, 697–701. [CrossRef]
69. Stoch, L. The significance of structural factors in thermal dissociation of solids. *Thermochim. Acta* **1985**, *92*, 97–100. [CrossRef]

70. Laura, S.; Mountjoy, G. Homogeneity of modifier ion distributions and the mixed alkaline earth effect in MgO–CaO–SiO_2 silicate glasses using molecular dynamics. *Eur. J. Glass Sci. Technol. Part B* **2018**, *58*, 165–170.
71. Yang, R.; Liu, H.; Ding, Z.; Zheng, J.; Mauro, J.C.; Kim, S.H.; Zheng, Q. Chemical durability of borosilicate pharmaceutical glasses: Mixed alkaline earth effect with varying [MgO]/[CaO] ratio. *J. Am. Ceram. Soc.* **2021**, *104*, 3973–3981. [CrossRef]
72. Garza-Garcia, M.; Lopez-Cuevas, J.; Gutierrez-Chavarria, C.A.; Rendon-Angeles, J.C.; Valle-Fuentes, J.F. Study of a Mixed Alkaline–Earth Effect on Some Properties of Glasses of the CaO-MgO-Al_2O_3-SiO_2 System. *Bol. Soc. Esp. Ceram. Vidr.* **2007**, *46*, 153–162.
73. Manara, D.; Grandjean, A.; Pinet, O.; Dussossoy, J.; Neuville, D. Factors influencing the sulphate incorporation in radioactive waste glasses. *MRS Proc.* **2006**, *932*, 377–384. [CrossRef]
74. Hill, R.G.; Brauer, D.S. Predicting the bioactivity of glasses using the network connectivity or split network models. *J. Non-Cryst. Solids* **2011**, *357*, 3884–3887. [CrossRef]
75. Stoch, L. Structure and Crystallization of Multicomponent Glasses. *High Temp. Mater. Processes* **1992**, *10*, 245–264. [CrossRef]
76. O'donnell, M.D.; Watts, S.; Law, R.; Hill, R. Effect of P_2O_5 content in two series of soda lime phosphosilicate glasses on structure and properties—Part I: NMR. *J. Non-Cryst. Solids* **2008**, *354*, 3554–3560. [CrossRef]
77. Deng, B.; Shi, Y.; Zhou, Q.; Bauchy, M. Revealing the structural role of MgO in aluminosilicate glasses. *Acta Mater.* **2022**, *222*, 117417. [CrossRef]
78. Jha, P.; Singh, K. Effect of MgO on bioactivity, hardness, structural and optical properties of SiO_2–K_2O–CaO–MgO glasses. *Ceram. Int.* **2016**, *42*, 436–444. [CrossRef]
79. Berezicka, A.; Sułowska, J.; Jeleń, P.; Lach, R.; Szumera, M. Thermal behaviour of sulphate-bearing multicomponent silicate–phosphate glasses. *J. Therm. Anal. Calorim.* **2023**, *148*, 1381–1405. [CrossRef]
80. Berezicka, A.; Szumera, M.; Sułowska, J.; Jeleń, P.; Olejniczak, Z.; Stępień, J.; Zając, M.; Pollastri, S.; Olivi, L. Unraveling the nature of sulfur-bearing silicate-phosphate glasses: Insights from multi-spectroscopic (Raman, MIR, 29Si, 31P MAS-NMR, XAS, XANES) investigation. *Ceram. Int.* **2022**, *48*, 4238–4254. [CrossRef]
81. Berezicka, A.; Sułowska, J.; Jeleń, P.; Komarek, S.; Szumera, M. Effect of sulfur addition on glass-forming ability, structure and thermal stability of multicomponent silicate-phosphate glasses. *J. Therm. Anal. Calorim.* **2024**, *149*, 10405–10427. [CrossRef]
82. Jiang, H.-R.; Hu, J.-Y.; Neuber, N.; Bochtler, B.; Adam, B.; Riegler, S.S.; Frey, M.; Ruschel, L.; Lu, W.-F.; Feng, A.-H.; et al. Effect of sulfur on the glass-forming ability, phase transformation, and thermal stability of Cu-Zr-Al bulk metallic glass. *Acta Mater.* **2021**, *212*, 116923. [CrossRef]
83. Reben, M.; Wacławska, I.; Paluszkiewicz, C.; Środa, M. Thermal and Structural Studies of Nanocrystallization of Oxyfluoride Glasses. *Proc. J. Therm. Anal. Calorim.* **2007**, *88*, 285–289. [CrossRef]
84. Kjeldsen, J.; Smedskjaer, M.M.; Mauro, J.C.; Youngman, R.E.; Huang, L.; Yue, Y. Mixed alkaline earth effect in sodium aluminosilicate glasses. *J. Non-Cryst. Solids* **2013**, *369*, 61–68. [CrossRef]
85. Rouxel, T.; Dély, N.; Sangleboeuf, J.C.; Dériano, S.; LeFloch, M.; Beuneu, B. Structure-property correlations in Y-Ca-Mg-sialon glasses: Physical and mechanical properties. *J. Am. Ceram. Soc.* **2005**, *88*, 889–896. [CrossRef]
86. Jha, P.; Danewalia, S.S.; Singh, K. Influence of thermal stability on dielectric properties of SiO_2–K_2O–CaO–MgO glasses. *J. Therm. Anal. Calorim.* **2017**, *128*, 745–754. [CrossRef]
87. Mysen, B.; Richet, P. *Silicate Glasses and Melts*; Elsevier: Amsterdam, The Netherlands, 2018; pp. 1–720. [CrossRef]
88. Shelby, J.E. *Introduction to Glass Science and Technology*, 2nd ed.; Royal Society of Chemistry: London, UK, 2005; Volume 1.
89. Elgayar, I.; Hill, R.; Chen, X.; Bubb, N.; Wood, D. Dielectric spectroscopy and dissolution studies of bioactive glasses. *Int. J. Appl. Glass Sci.* **2017**, *8*, 418–427. [CrossRef]
90. Cody, G.D.; Mysen, B.; Sághi-Szabó, G.; Tossell, J.A. Silicate-phosphate interactions in silicate glasses and melts: I. A multinuclear (27 Al, 29 Si, 31 P) MAS NMR and ab initio chemical shielding (31 P) study of phosphorous speciation in silicate glasses. *Geochim. Cosmochim. Acta* **2001**, *65*, 2395–2411. [CrossRef]
91. Mysen, B.O.; Cody, G.D. Silicate-phosphate interactions in silicate glasses and melts: II. quantitative, high-temperature structure of P-bearing alkali aluminosilicate melts. *Geochim. Cosmochim. Acta* **2001**, *65*, 2413–2431. [CrossRef]
92. Maekawa, H.; Maekawa, T.; Kawamura, K.; Yokokawa, T. The structural groups of alkali silicate glasses determined from 29Si MAS-NMR. *J. Non-Cryst. Solids* **1991**, *127*, 53–64. [CrossRef]
93. Dupree, R.; Holland, D.; McMillan, P.; Pettifer, R. The structure of soda-silica glasses: A mas NMR study. *J. Non-Cryst. Solids* **1984**, *68*, 399–410. [CrossRef]
94. Mathew, R.; Turdean-Ionescu, C.; Stevensson, B.; Izquierdo-Barba, I.; García, A.; Arcos, D.; Vallet-Regí, M.; Edén, M. Direct Probing of the Phosphate-Ion Distribution in Bioactive Silicate Glasses by Solid-State NMR: Evidence for Transitions between Random/Clustered Scenarios. *Chem. Mater.* **2013**, *25*, 1877–1885. [CrossRef]
95. Malfait, W.J.; Halter, W.E.; Morizet, Y.; Meier, B.H.; Verel, R. Structural control on bulk melt properties: Single and double quantum 29Si NMR spectroscopy on alkali-silicate glasses. *Geochim. Cosmochim. Acta* **2007**, *71*, 6002–6018. [CrossRef]

96. Wacławska, I.; Szumera, M. Influence of MgO (CaO) on the structure of silicate-phosphate glasses. *J. Therm. Anal. Calorim.* **2006**, *84*, 185–190. [CrossRef]
97. Yang, M.; Cai, X.; Wang, C.; Wang, Z.; Xue, F.; Chu, C.; Bai, J.; Liu, Q.; Ni, X. Highly Stable Amorphous (Pyro)phosphate Aggregates: Pyrophosphate as a Carrier for Bioactive Ions and Drugs in Bone Repair Applications. *ACS Omega* **2024**, *9*, 23724–23740. [CrossRef] [PubMed]
98. Aguiar, H.; Solla, E.; Serra, J.; González, P.; León, B.; Malz, F.; Jäger, C. Raman and NMR study of bioactive Na_2O–MgO–CaO–P_2O_5–SiO_2 glasses. *J. Non-Cryst. Solids* **2008**, *354*, 5004–5008. [CrossRef]
99. Christie, J.K.; Ainsworth, R.I.; de Leeuw, N.H. Investigating structural features which control the dissolution of bioactive phosphate glasses: Beyond the network connectivity. *J. Non-Cryst. Solids* **2016**, *432*, 31–34. [CrossRef]
100. Akunna, C.; Cerruti, M. Structural Connectivity and Bioactivity in Sol–Gel Silicate Glass Design. *Acta Biomater* **2024**, *188*, 374–392. [CrossRef]
101. Eckert, H. Structural characterization of bioactive glasses by solid state NMR. *J. Sol-Gel Sci. Technol.* **2018**, *88*, 263–295. [CrossRef]
102. Wang, H.; Chen, Z.; Liu, L.; Sun, Y.; Wang, X. Roles of P_2O_5 addition on the viscosity and structure of CaO-SiO_2-Al_2O_3-Na_2O-P_2O_5 melts. *ISIJ Int.* **2018**, *58*, 1644–1649. [CrossRef]
103. Tilocca, A.; Cormack, A.N. Structural Effects of Phosphorus Inclusion in Bioactive Silicate Glasses. *J. Phys. Chem. B* **2007**, *111*, 14256–14264. [CrossRef]
104. Kim, E.J.; Kim, Y.-H.; Lee, S.K. Pressure-Induced Structural Transitions in Na–Li Silicate Glasses under Compression. *J. Phys. Chem. C* **2019**, *123*, 26608–26622. [CrossRef]
105. Abdullah, T.K. Study of the Redox and Acid-Base Properties of Soda-Lime Silicate Glass: Application to the High Temperature Corrosion of Ni-Based Alloys and Ceramic Materials. August 2018. Available online: http://www.culture.gouv.fr/culture/infos-pratiques/droits/protection.htm (accessed on 7 February 2025).
106. Atila, A.; Ghardi, E.M.; Ouaskit, S.; Hasnaoui, A. Atomistic insights into the impact of charge balancing cations on the structure and properties of aluminosilicate glasses. *Phys. Rev. B* **2019**, *100*, 144109. [CrossRef]
107. Watts, S.; Hill, R.; Onnell, O.; Law, R. Influence of magnesia on the structure and properties of bioactive glasses. *J. Non-Cryst. Solids* **2010**, *356*, 517–524. [CrossRef]
108. O'donnell, M.D.; Watts, S.J.; Hill, R.G.; Law, R.V. The effect of phosphate content on the bioactivity of soda-lime-phosphosilicate glasses. *J. Mater. Sci. Mater. Med.* **2009**, *20*, 1611–1618. [CrossRef] [PubMed]
109. Zhu, H.; Bing, H.; Wu, Y.; Sun, H.; Zhou, J. Low molecular weight organic acids regulate soil phosphorus availability in the soils of subalpine forests, eastern Tibetan Plateau. *CATENA* **2021**, *203*, 105328. [CrossRef]
110. Sokolova, T.A. Low-Molecular-Weight Organic Acids in Soils: Sources, Composition, Concentrations, and Functions: A Review. *Eurasian Soil Sci.* **2020**, *53*, 580–594. [CrossRef]
111. Othman, S.M.; Sarsam, S.I.; Ismail, S.A. Gypsum and limestone dissolution within fatha formation (*Middle miocene*) at various ph solutions: A laboratory study. *Iraqi Geol. J.* **2020**, *53*, 71–88. [CrossRef]
112. Kiran-Yildirim, B.; Gencaslan, A.; Titiz-Sargut, S. Thermodynamic Models and Central Composite Design for Calcium Sulfate Dihydrate Solubility. *Chem. Eng. Technol.* **2020**, *43*, 1124–1136. [CrossRef]
113. Böschel, D.; Henning, S.; Michler, G.H.; Roggendorf, H.; Syrowatka, F.; Trempler, J. Characterisation of Gel Layers on Corroded Sodium Disilicate Glasses by Scanning Electron Microscopy and EDX Profiling. *Eur. J. Glass Sci. Technol. Part B* **2007**, *48*, 267–270.
114. Jantzen, C.M.; Smith, M.E.; Peeler, D.K. Dependency of sulfate solubility on melt composition and melt polymerization. *Ceram. Trans.* **2005**, *168*, 141–152. [CrossRef]
115. Bingham, P.; Hand, R. Sulphate incorporation and glass formation in phosphate systems for nuclear and toxic waste immobilization. *Mater. Res. Bull.* **2008**, *43*, 1679–1693. [CrossRef]
116. Mahadevan, T.S.; Du, J. Evaluating Water Reactivity at Silica Surfaces Using Reactive Potentials. *J. Phys. Chem. C* **2018**, *122*, 9875–9885. [CrossRef]
117. Feuston, B.P.; Garofalini, S.H. Topological and bonding defects in vitreous silica surfaces. *J. Chem. Phys.* **1989**, *91*, 564–570. [CrossRef]
118. Zemek, J.; Jiricek, P.; Gedeon, O.; Lesiak, B.; Jozwik, A. Electron irradiated potassium-silicate glass surfaces investigated by XPS. *J. Non-Cryst. Solids* **2005**, *351*, 1665–1674. [CrossRef]
119. Ashtekar, S.; Nguyen, D.; Zhao, K.; Lyding, J.; Wang, W.H.; Gruebele, M. Communication: An obligatory glass surface. *J. Chem. Phys.* **2012**, *137*, 141102. [CrossRef] [PubMed]
120. Henderson, G.S.; de Groot, F.M.; Moulton, B.J. X-ray absorption near-edge structure (XANES) spectroscopy. *Rev. Miner. Geochem.* **2014**, *78*, 75–138. [CrossRef]
121. Bingham, P.A.; Hyatt, N.C.; Hand, R.J.; Forder, S.D. Vitrification of UK intermediate level radioactive wastes arising from site decommissioning. Initial laboratory trials. *Glass Technol. Eur. J. Glass Sci. Technol. Part A* **2013**, *54*, 1–19.
122. Nienhuis, E.T.; Saleh, M.; Marcial, J.; Kriegsman, K.; Lonergan, J.; Lipton, A.S.; Guo, X.; McCloy, J.S. Structural characterization of ZnSO4-K2SO4-NaCl glasses. *J. Non-Cryst. Solids* **2019**, *524*, 119639. [CrossRef]

123. Meng, Z.; Hong, W.; Wang, Y.; Jiang, H. Model of diffusion of sulfur in soda-lime-silicate glass: An experimental and comparative study. *J. Wuhan Univ. Technol. Sci. Ed.* **2017**, *32*, 76–79. [CrossRef]
124. Al-Otaibi, F.A. Dissolution behavior of corrosive anions from sabkha soil southern kuwait under long term leaching. *Int. J. GEOMATE* **2020**, *19*, 138–144. [CrossRef]
125. Li, S.; Sun, K.; Zhao, Y.; Nie, G.; Song, S. Purification and rapid dissolution of potassium sulfate in aqueous solutions. *RSC Adv.* **2019**, *9*, 2156–2161. [CrossRef]
126. European Council. *Regulation (EC) 2003/2003 Relating to Fertilisers*; European Council: Brussels, Belgium, 2003.
127. Fábián, M.; Kovács, Z.; Lábár, J.L.; Sulyok, A.; Horváth, Z.E.; Székács, I.; Kis, V.K. Network structure and thermal properties of bioactive (SiO_2–CaO–Na_2O–P_2O_5) glasses. *J. Mater. Sci.* **2020**, *55*, 2303–2320. [CrossRef]
128. Gin, S.; Mir, A.H.; Jan, A.; Delaye, J.-M.; Chauvet, E.; De Puydt, Y.; Gourgiotis, A.; Kerisit, S.N. A General Mechanism for Gel Layer Formation on Borosilicate Glass under Aqueous Corrosion. *J. Phys. Chem. C* **2020**, *124*, 5132–5144. [CrossRef]
129. Thorpe, C.L.; Neeway, J.J.; Pearce, C.I.; Hand, R.J.; Fisher, A.J.; Walling, S.A.; Hyatt, N.C.; Kruger, A.A.; Schweiger, M.; Kosson, D.S.; et al. Forty years of durability assessment of nuclear waste glass by standard methods. *npj Mater. Degrad.* **2021**, *5*, 61. [CrossRef]
130. Hench, L.; Clark, D. Physical chemistry of glass surfaces. *J. Non-Cryst. Solids* **1978**, *28*, 83–105. [CrossRef]
131. Rodrigues, A.; Fearn, S.; Palomar, T.; Vilarigues, M. Early stages of surface alteration of soda-rich-silicate glasses in the museum environment. *Corros. Sci.* **2018**, *143*, 362–375. [CrossRef]
132. Delahaye, F.; Montagne, L.; Palavit, G.; Touray, J.C.; Baillif, P. Acid dissolution of sodium–calcium metaphosphate glasses. *J. Non-Cryst. Solids* **1998**, *242*, 25–32. [CrossRef]
133. Vaishnav, S.; Hannon, A.C.; Barney, E.R.; Bingham, P.A. Neutron Diffraction and Raman Studies of the Incorporation of Sulfate in Silicate Glasses. *J. Phys. Chem. C* **2020**, *124*, 5409–5424. [CrossRef]
134. Backhouse, D.J.; Fisher, A.J.; Neeway, J.J.; Corkhill, C.L.; Hyatt, N.C.; Hand, R.J. Corrosion of the International Simple Glass under acidic to hyperalkaline conditions. *npj Mater. Degrad.* **2018**, *2*, 29. [CrossRef]
135. Chave, T.; Frugier, P.; Gin, S.; Ayral, A. Glass–water interphase reactivity with calcium rich solutions. *Geochim. Cosmochim. Acta* **2011**, *75*, 4125–4139. [CrossRef]
136. Verney-Carron, A.; Sessegolo, L.; Chabas, A.; Lombardo, T.; Rossano, S.; Perez, A.; Valbi, V.; Boutillez, C.; Muller, C.; Vaulot, C.; et al. Alteration of medieval stained glass windows in atmospheric medium: Review and simplified alteration model. *npj Mater. Degrad.* **2023**, *7*, 49. [CrossRef]
137. Bates, J.K.; Cunnane, J.C.; Bradley, C.R. *High-Level Waste Borosilicate Glass, A Compendium of Corrosion Characteristics*; United States Department of Energy Office of Waste Management: Washington, DC, USA, 1994; Volume I.
138. Zhang, Z.; Kob, W.; Ispas, S. First-principles study of the surface of silica and sodium silicate glasses. *Phys. Rev. B* **2021**, *103*, 184201. [CrossRef]
139. Agnello, G.; Youngman, R.; Lamberson, L.; Smith, N.; LaCourse, W.; Cormack, A.N. Bulk structures of silica-rich calcium aluminosilicate (CAS) glasses along the molar CaO/Al_2O_3 = 1 join via molecular dynamics (MD) simulation. *J. Non-Cryst. Solids* **2019**, *519*, 119450. [CrossRef]
140. Snellings, R. Surface chemistry of calcium aluminosilicate glasses. *J. Am. Ceram. Soc.* **2015**, *98*, 303–314. [CrossRef]
141. De Bardi, M.; Hutter, H.; Schreiner, M.; Bertoncello, R. Potash-lime-silica glass: Protection from weathering. *Herit. Sci.* **2015**, *3*, 22. [CrossRef]
142. Guadagnino, E.; Zuccato, D. Delamination propensity of pharmaceutical glass containers by accelerated testing with different extraction media. *PDA J. Pharm. Sci. Technol.* **2012**, *66*, 116–125. [CrossRef]
143. Elalaily, N.A.; Zahran, A.H.; Saad, E.A.; Sallam, O.I.; Ezz-Eldin, F.M. Corrosion and Infrared Study of Some γ-Irradiated Lead-Phosphate Glasses Doped with MoO_3. *Silicon* **2018**, *10*, 1613–1623. [CrossRef]
144. Labbilta, T.; Ait-El-Mokhtar, M.; Abouliatim, Y.; Khouloud, M.; Meddich, A.; Mesnaoui, M. Elaboration and characterization of vitreous fertilizers and study of their impact on the growth, photosynthesis and yield of wheat (*Triticum durum* L.). *Materials* **2021**, *14*, 1295. [CrossRef]
145. Labbilta, T.; Mesnaoui, M.; Aouad, H.; Abouliatim, Y.; Khouloud, M.; Abielaala, L. Study of the effect of calcium substitution by magnesium in the vitreous system $3P_2O_5$-$2K_2O$-(1 − x) CaO-x MgO. *Materials* **2020**, *13*, 2637. [CrossRef]
146. Esquivel-Upshaw, J.; Dieng, F.; Clark, A.; Neal, D.; Anusavice, K. Surface degradation of dental ceramics as a function of environmental pH. *J. Dent. Res.* **2013**, *92*, 467–471. [CrossRef]

Disclaimer/Publisher's Note: The statements, opinions and data contained in all publications are solely those of the individual author(s) and contributor(s) and not of MDPI and/or the editor(s). MDPI and/or the editor(s) disclaim responsibility for any injury to people or property resulting from any ideas, methods, instructions or products referred to in the content.

4. Publication P4

molecules

MDPI

Article

Alteration of Sulfur-Bearing Silicate–Phosphate (Agri)Glasses in Soil Environment: Chemical Interactions and Biological Response

Anna Berezicka *, Agnieszka Wojteczko, Justyna Sułowska and Magdalena Szumera *

Faculty of Materials Science and Ceramics, AGH University of Krakow, al. A. Mickiewicza 30, 30-059 Krakow, Poland; agdudek@agh.edu.pl (A.W.); sulowska@agh.edu.pl (J.S.)
* Correspondence: berezicka@agh.edu.pl (A.B.); mszumera@agh.edu.pl (M.S.)

Abstract: Glasses exposed to soil environments are of interest across various scientific fields, from nuclear waste containment to archaeological preservation and nutrient-delivery systems for plants. While immersion experiments provide valuable insights into the ion release kinetics in root- and microbe-exuded solutions, they fail to replicate the complexities of nutrient leaching in real soil conditions. To address this, the degradation behavior of nutrient-bearing glasses ($41SiO_2 \cdot 6(10)P_2O_5 \cdot 20K_2O \cdot 33(29)MgO/CaO/MgO + CaO$) with increasing sulfate contents was investigated through a soil incubation experiment simulating Central European weather variability. A comprehensive approach, combining SEM observations and EDS semi-quantitative analysis, revealed that acidic peat strongly promoted ion exchange, where protons from the medium replaced network cations. The glass composition played a crucial role in the fracture behavior: sulfate incorporation increased the network rigidity, making the glasses more prone to mechanical degradation and accelerating the reaction front advancement. The P_2O_5 content was also a key factor in modulating the reactivity, with higher concentrations intensifying interactions with the soil medium. Limited water availability accelerated the solution saturation, leading to secondary phase precipitation and temporary nutrient immobilization. These findings demonstrate that glass reactivity can be fine-tuned through composition adjustments and highlight the dynamic nature of glass–soil interactions, including seasonal variations in nutrient release under acidic conditions.

Keywords: glass–soil interactions; nutrient-bearing glasses; ion exchange; sulfate incorporation; fertilizer; soil incubation experiment

check for updates

Academic Editors: Loredana Maiuolo and Paola Costanzo

Received: 3 March 2025
Revised: 9 April 2025
Accepted: 11 April 2025
Published: 16 April 2025

Citation: Berezicka, A.; Wojteczko, A.; Sułowska, J.; Szumera, M. Alteration of Sulfur-Bearing Silicate–Phosphate (Agri)Glasses in Soil Environment: Chemical Interactions and Biological Response. *Molecules* **2025**, *30*, 1790. https://doi.org/10.3390/molecules30081790

Copyright: © 2025 by the authors. Licensee MDPI, Basel, Switzerland. This article is an open access article distributed under the terms and conditions of the Creative Commons Attribution (CC BY) license (https://creativecommons.org/licenses/by/4.0/).

1. Introduction

Despite the unprecedented level of understanding of the amorphous state, glass still poses a challenge to scientists at both the microscopic and thermodynamic levels. Microscopically, its random network lacks the long-range order characteristic of crystalline solids, while thermodynamically, it is a nonequilibrium material that undergoes slow structural relaxation, progressively reaching lower free-energy minima [1]. This intrinsic tendency to minimize free energy makes glass susceptible to irreversible transformation upon contact with liquid media, potentially leading to degradation over time [2,3]. Such alterations may be imperceptibly slow [4], but according to Grambow's hypothesis [5], they never cease due to the metastable nature of the material. The resistance of glass to this irreversible damage and the mechanisms governing its alteration are critical for numerous fields, starting from applications requiring superior chemical durability, such as

nuclear waste storage, cultural heritage preservation, and optical fibers, where moisture-induced degradation can severely impact the performance, to applications where controlled dissolution is desirable, like in the case of biomedical glasses for bone regeneration [6–10], or, significantly less studied, vitreous fertilizers—materials designed to supply plants with a variety of macro- and microelements essential for optimal growth and development [11–16].

Interestingly, despite extensive research on glass corrosion, efforts to develop a universal model describing the interactions and reactions between aqueous solutions and vitreous materials have failed, incapable of capturing the vast variability in glass compositions, structures, bonding characteristics, and thermal histories, as well as the wide range of environmental factors influencing the alteration process [3,17–19]. Indeed, the macroscopic response of a glass in contact with a corrosive medium arises from the aggregation of numerous atomistic-level mechanisms, encompassing species originating from both the solution and the glass itself. Nevertheless, the commonly proposed mechanisms of glass alteration share fundamental steps that, at the molecular level, proceed in a similar manner for all silicate-based glasses. These sequential stages include (1) the adsorption of water onto the glass surface, (2) the simultaneous occurrence of three competing reactions: hydration, hydrolysis, and ion exchange, and (3), in some cases, the precipitation of secondary phases on the altered glass surface [18,20–23].

Expanding on this simplified mechanism of glass interaction with the contacting solution, shortly after the initial water molecules adhere to the glass's outermost regions, they interact with adsorption sites, leading to the breakage of surface chemical bonds and the formation of a hydroxylated surface. This process is followed by the penetration of water into the glassy matrix—a step that marks the onset of irreversible material degradation. In glasses with loosely structured vitreous networks, characterized by the presence of sufficiently large openings that facilitate molecular water infiltration, hydration occurs, allowing H_2O to enter the glass as an intact solvent. Conversely, in glasses with highly interconnected networks, where water penetration is hindered, the glass–solvent interaction is predominantly limited to hydrolysis, involving the cleavage of Si-O-Si backbone-forming linkages in favor of Si-OH bonds, and gradually leading to network depolymerization. The third mechanism, ion exchange (or interdiffusion), entails the replacement of network modifiers by H^+/H_3O^+ ions from the surrounding solution and results in the depletion of these elements in the affected area. As a consequence of these processes, a silica-rich alteration layer forms at the interface between the glass and the corrosive medium, with its morphology and composition strongly influenced by both the intrinsic properties of the glass and the environmental conditions. Under specific circumstances that promote the accumulation of a thin interfacial film of solution supersaturated with respect to leached mobile glass components, the precipitation of secondary phases may occur at the outermost region of the altered glass—a phenomenon known to affect the further evolution of interactions at the glass–solution interface [7,8,10,23–25].

The aforementioned processes are highly nuanced, with their progression best elucidated in the context of glasses undergoing corrosion immersed in aqueous environments. In contrast, significantly less research has been devoted to amorphous materials exposed to soil media. This disparity is unsurprising, given the challenges of analyzing glass degradation in this biotic system, where multiple variables—such as the soil composition, moisture fluctuations, temperature changes, pH variations, and chemical diversity—interact in intricate ways [26–30].

The complexity and interconnected nature of soil corrosion-affecting parameters make the process of glass alteration difficult to fully comprehend. In acidic conditions, degradation primarily occurs through ion exchange, leading to an alkali-depleted surface and, in some cases, the formation of a hydrated gel that temporarily slows further alteration [3,4].

According to Palomar [31], such glasses often exhibit networks of isolated or interconnected fissures on their surfaces. Conversely, alkaline soils induce a more aggressive attack by the corrosive medium, manifesting itself through the breakdown of the Si-O-Si-based vitreous network and the removal of silica into the adjacent solution. In this case, the outermost glass layer may assume the form of either a very thin alteration crust [31] or finely laminated layers [3,4,32–34]. Numerous studies indicate that the prevalent phenomenon of the degradation of vitreous samples subjected to moist soil is the development of hydrated dealkalinization layers enriched with silica [3,4]. In contrast, when water availability is low, the removal of modifier cations from the glass matrix causes a rapid increase in the pH of the contact solution, subsequently accelerating the deterioration of the silicon–oxygen backbone [35]. Under frequent rainfall conditions, these processes occur differently: the leached ions are washed away from the subsurface area, maintaining a near-neutral pH and preventing the onset of alkaline-driven corrosion [35]. Additionally, alternating rain and drought cycles, along with seasonal and daily temperature fluctuations, significantly influence glass weathering, since not only do they affect ion exchange, but they also promote the formation of secondary corrosion products and contribute to shrinkage-induced cracking in the alteration zone [3,35–38].

Beyond soil environment-related factors influencing glass deterioration, another crucial aspect is its composition and, consequently, its structure. Indeed, it is well established that a low-silica, alkali-rich composition results in an open network—a feature of utmost importance for enhanced water penetration. And while the durability of silicate-based glasses inversely correlates with the quantity of alkali network modifiers, the same is not necessarily true for alkaline-earth oxide cations. In fact, glass resistance to corrosive media improves with their addition, provided it does not exceed approximately 15 mol.% [4]. Interestingly, the incorporation of a second network former, such as P_2O_5, does not always enhance the durability of silicate–phosphate glasses. Conversely, it has been found that unless the P_2O_5 content is sufficient to facilitate the formation of a highly connected phosphorus–oxygen subnetwork, an increase in the [PO_4^{3-}] species concentration—when present as isolated or corner-connected tetrahedra—not only fails to reinforce the glass structure but also increases the glass reactivity [4,6,39].

Also of great significance in glass–soil interactions is the role of additives and trace elements, as even minor compositional variations can lead to substantial differences in durability. Among these, sulfur is particularly noteworthy—a component rarely incorporated into the vitreous framework but increasingly relevant not only in modern glass technology but also in plant nutrition, as, due to the significant reduction in SO_2 emissions into the atmosphere, the primary sulfur source in the rhizosphere has declined [40–46]. Given that, to the best of the authors' knowledge, no studies have examined the chemical behavior of sulfate-bearing glasses in soil environments, the present study aims to address this knowledge gap by providing integrated insights into the alteration of sulfur-bearing multicomponent silicate–phosphate glasses.

2. Results and Discussion

2.1. Surface Alteration Trends Across the Studied Glass Compositions

This section aims to provide scientific insight into the weathering mechanisms of glass fertilizers under environmental conditions relevant to their intended application. Understanding these processes is essential for evaluating how glass–soil interactions influence the release of macro- and microelements. Given its ability to capture both chemical and physical transformations at the material's surface, SEM-EDS was selected as the most effective technique for monitoring such interactions throughout the incubation process.

The extent and scale of the changes occurring on the surfaces of the incubated glasses in contact with the soil solution were evaluated by examining the surface layer cracking, identifying the presence and characteristics of secondary precipitated phases, and analyzing the ion leaching intensity from superficial glass regions using EDS data. The collected data are presented descriptively in Table 1, accompanied by micrographs (Figures 1–8) depicting incubated samples from all the studied compositions modified with 0 and 3 mol% sulfate units, after 2 weeks, as well as at 5, 8, and 12 months of incubation.

Table 1. Summary of surface characteristics of glass samples after soil incubation, detailing the types of crystalline phases identified and the extent of the surface fragmentation.

Month	0.5	1	2	3	4	5	6	7	8	9	10	11	12
0S_6PM	M	I	I	N	M	H	E	H	E	H	E	H	H
	MP	KMP	MP	MP	MP	MP	MP	MP	MP	MP	MP	MP	MP
	Localized leaching							Intense leaching					
3S_6PM	I	N	I	M	M	M	M	E	E	E	H	H	E
	-	KMP	MP	MP	MP	MP	MP	MP	MP	MP	MP	MP	MP
	Localized leaching							Intense leaching					
0S_6PC	N	I	I	I	M	N	M	M	E	M	H	H	H
	CP small precipitate deposit										Thinning of the CP deposit		
	Localized leaching							Intense leaching					
3S_6PC	M	I	M	E	H	E	E	E	H	H	E	E	E
	CaP small precipitate deposit										Thinning of the CaP deposit		
	Localized leaching							Intense leaching					
0S_6PMC	N	M	N	M	M	M	H	H	E	E	H	H	E
	-	CP	MP	MP CC	CP CC	CC	CP CC	CP	CP	CP	CP	CC	CP
	Localized leaching							Intense leaching					
3S_6PMC	I	I	I	*	*	E	E	E	E	E	E	E	E
	-	CC	MP CC	KMP CC	KMP CC	KMP CC	CP	CP	CP	CP	-	-	-
	Localized leaching							Intense leaching					
0S_10PM	E	E	E	E	E	E	C	C	M	H	H	C	M
	KMP	KMP	KMP	KMP	KMP	KMP	-	-	-	-	-	-	-
	Localized leaching							Intense leaching					
3S_10PM	E	E	E	E	E	C	C	C	C	C	C	C	C
	KMP	KMP MP	KMP	KMP	KMP	KMP MP	MP	MP	MP	MP	MP	MP	MP
	Localized leaching							Intense leaching					

Legend: Types of crystals suggested by the semi-quantitative SEM-EDS analysis: MP—magnesium phosphate, KMP—potassium magnesium phosphate, CP—calcium phosphate, CC—calcium carbonate. Surface condition (fragmentation/cracking): N: no visible cracks—no shading, I: isolated cracks—light pink, M: moderate concentration of cracks—light red, H: high concentration of cracks—red, E: cracks covering the entire surface of all fragments—dark red, C: complete fragmentation of glass pieces—gray. Shaded fields indicate areas where dense layers of crystallites uniformly covered the glass surface. * Note that the evaluation of the surface condition at 3 and 4 months of incubation was not possible due to the dense layer of precipitation products, which obscured detailed assessment.

For glasses representing the XS_6PM system, the initial incubation period (first two months) under simulated spring conditions was marked by the intense crystallization of secondary products in the form of small (~5 µm) magnesium phosphate crystallites, which formed a discontinuous layer covering the entire surface of the granules. Nevertheless, while precipitates were already observed on the surface of the baseline sample after just two weeks (Figure 1: 0.5 mth), in the sulfate-bearing counterpart, the first signs of interaction with the soil solution appeared as localized cracks in the most weathering-prone areas (marked with a dashed line). Similar secondary phases were only observed from the

second month onward, persisting until the end of the experiment (Table 1). The leaching of mobile components occurred at a low intensity and remained localized within the cracked regions (Figure 2). These processes continued in a similar manner throughout the months simulating spring conditions.

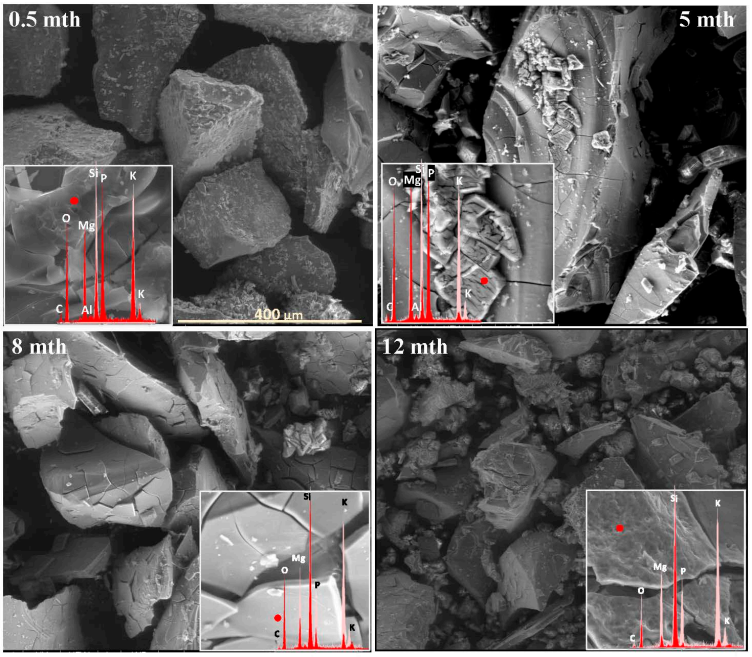


Figure 1. Micrographs illustrating surface changes in the 0S_6PM glass after 0.5, 5, 8, and 12 months of incubation, accompanied by EDS spectra from selected surface points (red spectra) compared with the spectrum of the unaltered glass (light-pink spectrum). The main microphotographs were taken at 350× magnification, while the inset images were captured at 5000×. The scale bar shown in the first image (400 µm) applies to all other images in the figure.

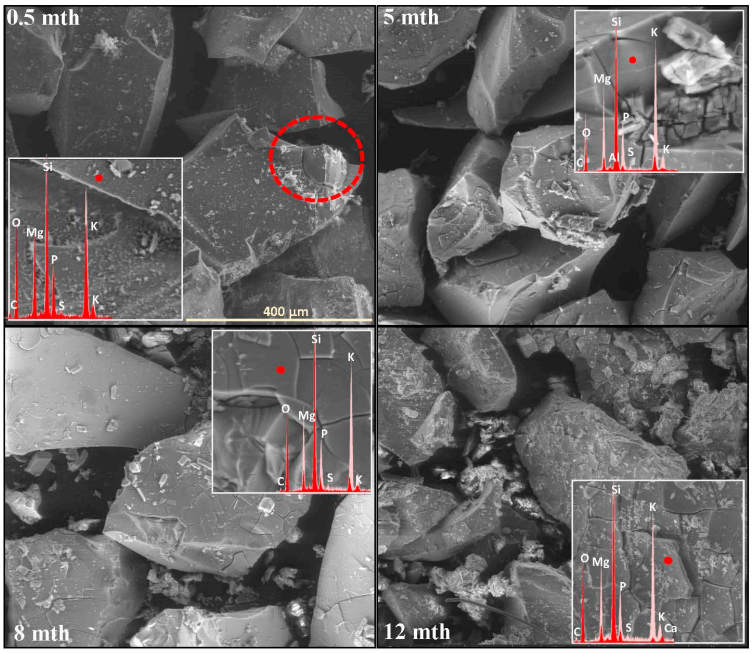


Figure 2. Micrographs illustrating surface changes in the 3S_6PM glass after 0.5, 5, 8, and 12 months of incubation, accompanied by EDS spectra from selected surface points (red spectrum) compared with the spectrum of the unaltered glass (light-pink spectrum). The main microphotographs were taken at 350× magnification, while the inset images were captured at 5000×. The scale bar shown in the first image (400 µm) applies to all other images in the figure.

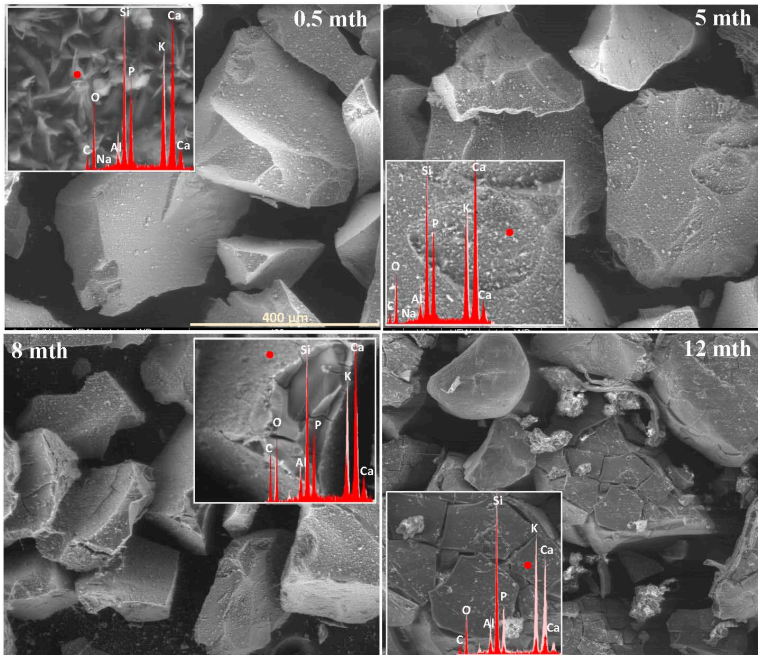


Figure 3. Micrographs illustrating surface changes in the 0S_6PC glass after 0.5, 5, 8, and 12 months of incubation, accompanied by EDS spectra from selected surface points (red spectrum) compared with the spectrum of the unaltered glass (light-pink spectrum). The main microphotographs were taken at 350× magnification, while the inset images were captured at 5000×. The scale bar shown in the first image (400 µm) applies to all other images in the figure.

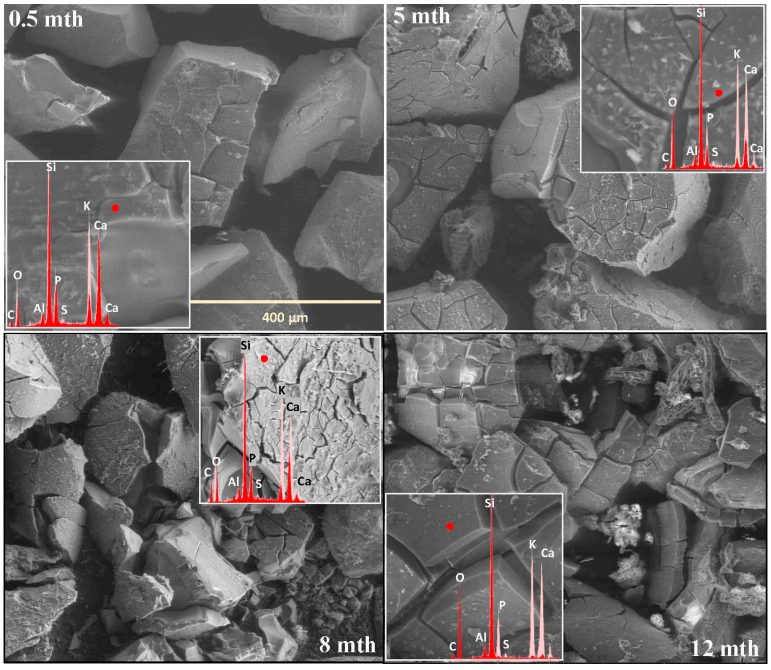


Figure 4. Micrographs illustrating surface changes in the 3S_6PC glass after 0.5, 5, 8, and 12 months of incubation, accompanied by EDS spectra from selected surface points (red spectrum) compared with the spectrum of the unaltered glass (light-pink spectrum). The main microphotographs were taken at 350× magnification, while the inset images were captured at 5000×. The scale bar shown in the first image (400 µm) applies to all other images in the figure.

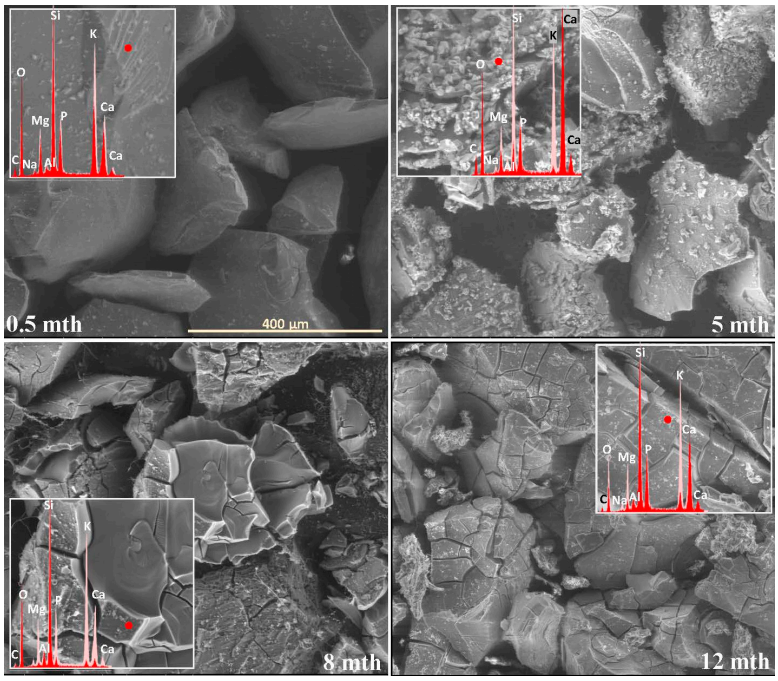


Figure 5. Micrographs illustrating surface changes in the 0S_6PMC glass after 0.5, 5, 8, and 12 months of incubation, accompanied by EDS spectra from selected surface points (red spectrum) compared with the spectrum of the unaltered glass (light-pink spectrum). The main microphotographs were taken at 350× magnification, while the inset images were captured at 5000×. The scale bar shown in the first image (400 µm) applies to all other images in the figure.

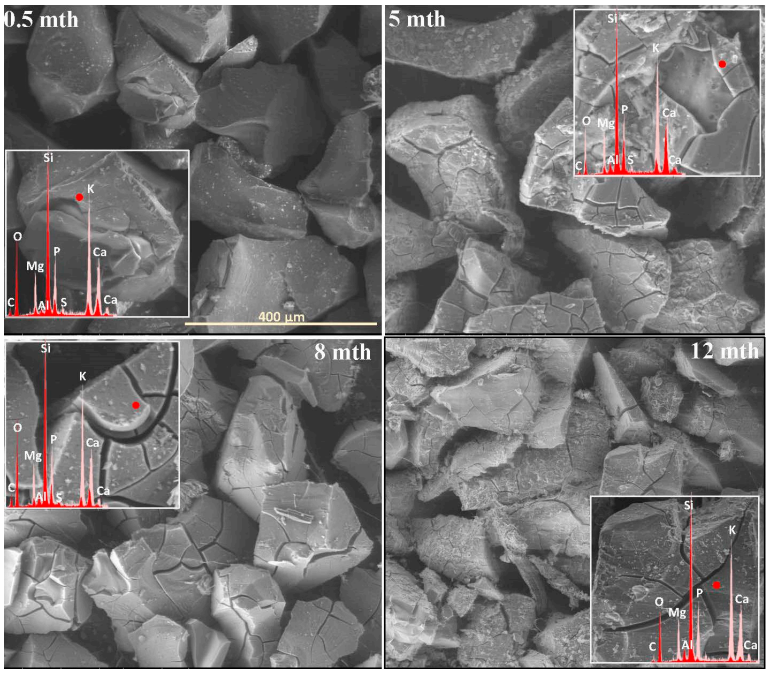


Figure 6. Micrographs illustrating surface changes in the 3S_6PMC glass after 0.5, 5, 8, and 12 months of incubation, accompanied by EDS spectra from selected surface points (red spectrum) compared with the spectrum of the unaltered glass (light-pink spectrum). The main microphotographs were taken at 350× magnification, while the inset images were captured at 5000×. The scale bar shown in the first image (400 µm) applies to all other images in the figure.

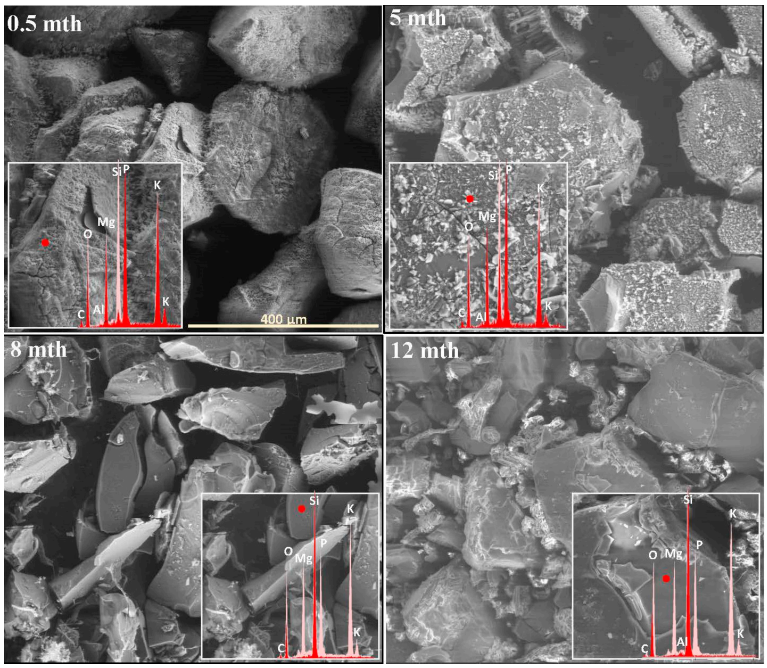


Figure 7. Micrographs illustrating surface changes in the 0S_10PM glass after 0.5, 5, 8, and 12 months of incubation, accompanied by EDS spectra from selected surface points (red spectrum) compared with the spectrum of the unaltered glass (light-pink spectrum). The main microphotographs were taken at 350× magnification, while the inset images were captured at 5000×. The scale bar shown in the first image (400 µm) applies to all other images in the figure.

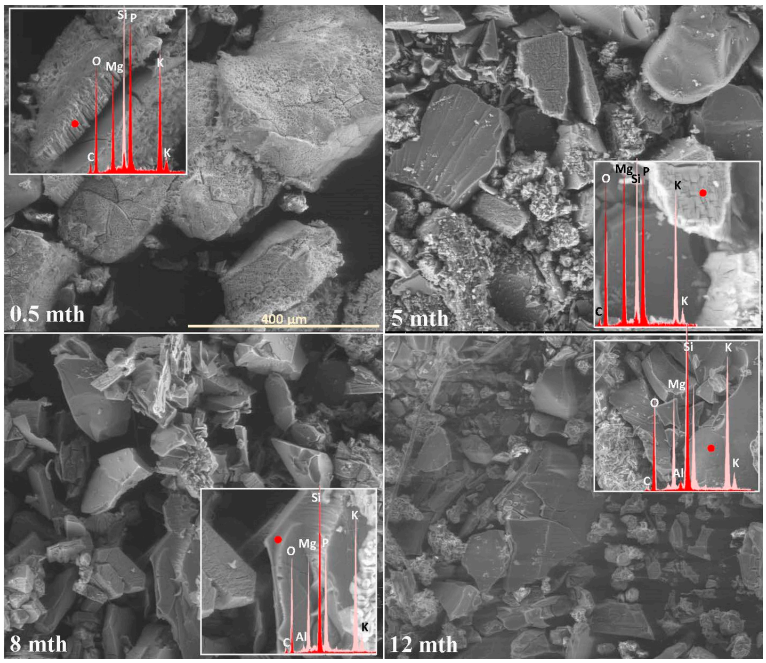


Figure 8. Micrographs illustrating surface changes in the 3S_10PM glass after 0.5, 5, 8, and 12 months of incubation, accompanied by EDS spectra from selected surface points (red spectrum) compared with the spectrum of the unaltered glass (light-pink spectrum). The main microphotographs were taken at 350× magnification, while the inset images were captured at 5000×. The scale bar shown in the first image (400 µm) applies to all other images in the figure.

It is only with the temperature increase imposed by the simulated summer conditions (starting from the fourth month) that a distinct intensification of surface processes was observed. The entire outer layer of glass exposed to the soil medium developed a network

of cracked, Si-enriched scales with only residual amounts of mobile ions, indicating an enhancement of ion exchange processes with the contact solution. This leaching intensification was noticeable from the fifth month in the baseline sample and from the third month in the sulfate-doped variant (Table 1; Figures 1 and 2: 5 mth). Precipitation processes also became significantly more pronounced, as evidenced by the presence of large (40–50 μm), well-defined characteristic crystals composed of small subunits with visible gaps between them, of a chemical composition corresponding to magnesium phosphate (Figure 2: 5 mth: EDS spectrum). Additionally, on the surface of the baseline glass, distinct etch pits (marked with red circles) suggest the localized dissolution of the Si-O-Si glass network.

As the incubation progressed and temperatures dropped during the simulated autumn (after the seventh month), the Si-rich crust, initially forming as cracked scales, began to visibly disintegrate, exposing deeper layers of the material to direct contact with the soil solution and subsequently shifting the reaction front further into the glass structure (Figures 1 and 2: 8 mth). Interestingly, the large precipitated magnesium phosphate crystals also responded to the temperature shift, undergoing mechanical decohesion—an effect particularly pronounced in the sulfate-doped glass.

The further temperature drop associated with the transition to winter-like simulated conditions, along with daily fluctuations around 0 °C, appeared to accelerate the fragmentation not only of the glass surface but also of entire sample fragments (Figures 1 and 2: 12 mth).

Analogous to the MgO-containing system, the XS_6PC series also exhibited high reactivity in the acidic soil environment. However, while the baseline glass primarily developed a network of small, star-shaped precipitates (~5 μm in diameter), whose composition suggests the formation of calcium phosphate (Figure 3: 0.5 mth), the 3S_6PC sample exhibited additional features. In this case, besides localized precipitations of a similar nature, the surface also developed flaking cracks, indicating the localized release of mobile glass components (K^+) into the contact solution (Figure 4: 0.5 mth).

As in the previous case, the temperature increase associated with simulated summer conditions appeared to intensify the processes at the glass–soil interface. For the base glass, this effect was largely limited to a slight enhancement in the surface cracking and further calcium phosphate crystallization, forming a discontinuous but dense network of secondary products covering the incubated fragments. In contrast, the 3S_6PC sample underwent extensive fracturing of the still-phosphate-coated surface, accompanied by a significant intensification of the leaching process, which began as early as the fourth month of incubation. In the baseline glass, in contrast, this effect was delayed, becoming noticeable only after six months (Figures 3 and 4: 5 mth; Table 1).

The temperature drop during the transition from summer to autumn further accelerated the fragmentation of the altered layers. Nonetheless, in the sulfate-free sample, this phenomenon remained largely confined to areas most susceptible to weathering, such as edges and granules with highly developed surfaces. In contrast, the [SO_4^{2-}]-modified glass underwent extensive disintegration, affecting not only the surface layer but also entire fragments of the material (Figures 3 and 4: 8 mth). Despite these transformations, the superficial regions of incubated granules in both cases remained coated with a discontinuous layer of calcium phosphates.

With the onset of simulated winter conditions, the mechanical degradation intensified, though the effect was significantly more pronounced in the sulfate-containing sample (Figures 3 and 4: 12 mth). Notably, during this period of increased surface degradation, the previously observed phosphate deposits were no longer present, and only localized precipitates could be detected, which may suggest either the gradual dissolution of these secondary phases in the acidic peat environment or their mechanical decohesion.

Meanwhile, the baseline sample representing the mixed-alkaline-earth system appeared to exhibit the least interaction with the soil solution among all the tested compositions after two weeks of incubation, as no visible cracks or precipitates were observed on its surface (Figure 5: 0.5 mth). In contrast, its sulfate-modified counterpart showed localized fractures, characterized by the leaching of the most mobile glass components (Figure 6: 0.5 mth). Remarkedly, as the incubation progressed under simulated spring conditions, the presence of the most diverse secondary phases among all the tested systems was observed, reflecting the intricate interactions between the glass matrix constituents in the complex composition of the XS_6PMC system. Although both glass types developed magnesium phosphate and calcium carbonate phases, the baseline sample also exhibited calcium phosphate precipitates, while the sulfate-doped one formed double magnesium–potassium phosphates (Table 1). Notably, these secondary phases initially appeared as localized deposits, densely covering the surfaces of the 0S_6PMC and 3S_6PMC glasses between the 4th and 6th and 2nd and 4th months of incubation, respectively.

For the base glass, an increase in temperature promoted crystallization, accompanied by progressive surface fracturing (Figure 5: 5 mth). Conversely, in the sulfate-doped sample, summer-like conditions primarily drove mechanical surface degradation, leading to the intensified leaching of the mobile glass constituents into the surrounding solution (Figure 6: 5 mth, Table 1). The transition to autumn- and, subsequently, winter-like conditions significantly impacted the cohesion of the superficial glass layers, exacerbating both fracturing and mechanical disintegration. This process exposed the deeper, still-intact glass regions to the action of the soil solution (Figures 5 and 6: 8,12 mth). During these simulated seasons, secondary phase precipitation was observed only sporadically, and predominantly in the form of calcium phosphate (with a single instance of calcium carbonate precipitation observed in the baseline sample) (Table 1).

Clearly, samples from the 10P series exhibited the highest reactivity in the soil environment, as evidenced by the pronounced surface cracking and the formation of a thick (~15 μm) needle-like layer of double magnesium–potassium phosphates from the earliest observation stage (Figures 7 and 8: 0.5 mth).

The transition to summer-like conditions resulted in the gradual disappearance of this dense precipitate layer, occurring after the 6th and 5th months for the 0S and 3S_10M samples, respectively (Table 1). In both cases, this phase coincided with significant fragmentation of the incubated granules, indicating that the surface layer decohesion was primarily mechanical, though partial dissolution in the acidic peat environment cannot be excluded (Figures 7 and 8: 5 mth). From the 5th month onward, a notable shift in the precipitation pattern of the sulfate-modified sample was observed, with the emergence of large, well-defined magnesium phosphate crystals, whereas the base glass no longer exhibited a tendency towards further crystallization. At this stage, both samples also showed a marked intensification of mobile ion leaching (Table 1). As the incubation progressed and the temperatures continued to drop, the fragmentation of the incubated material was further exacerbated, along with the mechanical decohesion of the precipitated phases—an effect particularly pronounced in the 3S_10PM sample (Figures 7 and 8: 8,12 mth).

The data presented in Table 1 reveal a strong correlation between the degree of surface layer disintegration and both the intensity of the mobile ion leaching into the surrounding solution and the decohesion or thinning of the secondary precipitated phases. In all the studied systems, these effects manifested at earlier incubation stages and with greater intensity in the 3S samples compared to their baseline glass counterparts (Table 1). Consequently, the collected data suggest that sulfate species indirectly influence glass–soil solution interactions by enhancing the material's susceptibility to fracturing and subsequently promoting the decohesion of the altered superficial layers during incubation.

This observation aligns with the DSC and MAS-NMR results discussed in the authors' preceding study on the same materials and pointing to a reduction in thermal stability and an increase in network connectivity with increasing sulfur contents. Such structural modifications translate into the enhanced rigidity of the silicon–oxygen backbone, resulting, in turn, in a greater propensity for the surface cracking and exfoliation of the incubated specimens.

In the XS_6PM system, this effect was initially less pronounced between the 0S and 3S glasses but became evident in the later experiment stages—likely due to the already relatively high polymerization degree of the baseline glass (and its associated structural stresses) compared to other compositions within the [6P] series. Conversely, in the XS_6PC and XS_6PMC systems, the intensified fracturing of the 3S specimens was apparent throughout all the incubation stages. While numerous studies have reported that CaO-rich glasses exhibit lower susceptibility to cracking [47,48], attributed to the greater flexibility of the Si-O-Si framework when modified by calcium oxide compared to MgO [49], the introduction of highly covalent sulfate species occupying matrix voids reduces this initial elasticity. As a result, the network becomes more rigid, mirrored by the registered intensified surface fracturing. Glasses from the 10P system, which exhibited the highest degree of polymerization and the lowest thermal stability, appeared to be the most reactive, as from the earliest stages of incubation, the XS_10P samples displayed extensive fracturing across their entire surfaces. Nevertheless, even in this highly active system, the [SO_4^{2-}] addition further accelerated the interfacial degradation by promoting glass granule decohesion; however, similar to the XS_6PM system, this effect became most pronounced during the later incubation stages.

2.2. Sequence of Glass Component Release into Soil Solution

The release of glass matrix components from the XS_6PM system began with alkali ions, as evidenced in Figure 9a, where newly exposed—via fracturing—surfaces exhibit significantly increased K^+ contents. This phenomenon is indicative of the preferential partitioning of this particular element in the process of ion exchange, making it the first to migrate toward near-surface regions (Figure 9a: red spectrum). Subsequently, albeit at a slower rate compared to K^+, Mg^{2+} and PO_4^{3-} ions were released, leaving behind a Si-enriched hydrated layer (Figure 9a: blue spectrum), which, in further stages, may either lose moisture during dry periods, leading to mechanical decohesion, or retain hydration and transition into a silica gel phase, which is progressively depleted of all mobile glass constituents (Figure 9a: yellow spectrum).

Similar to the base composition, the sulfate-modified glass also exhibited the preferential release of potassium ions, as already after two weeks of incubation, the SEM-EDS analysis of the selected surface region of the 3S_6M sample revealed a slight depletion of K^+ from the glass matrix, while the concentrations of the other major glass components remained unchanged (Figure 9b).

Further interpretation of the SEM-EDS data suggests that sulfate ions were the next species released into the soil solution. The region exposed following the disintegration of the altered layer was characterized by a reduced concentration of both K^+ and SO_4^{2-}, while the levels of other mobile species, such as Mg^{2+} and PO_4^{3-}, remained unchanged (Figure 9a: red spectrum). The reduced leaching tendency of Mg^{2+} and PO_4^{3-} was likely due to the rapid attainment of supersaturation in the thin moisture film adhering to the glass surface, thereby diminishing the reaction affinity. Apparently, the subsequent precipitation of magnesium phosphates (Figure 9a: yellow spectrum) depleted these ions from the contact solution, restoring the leaching potential, as evidenced by the near-complete depletion of mobile glass constituents in the Si-rich altered layer (Figure 9a: blue spectrum).

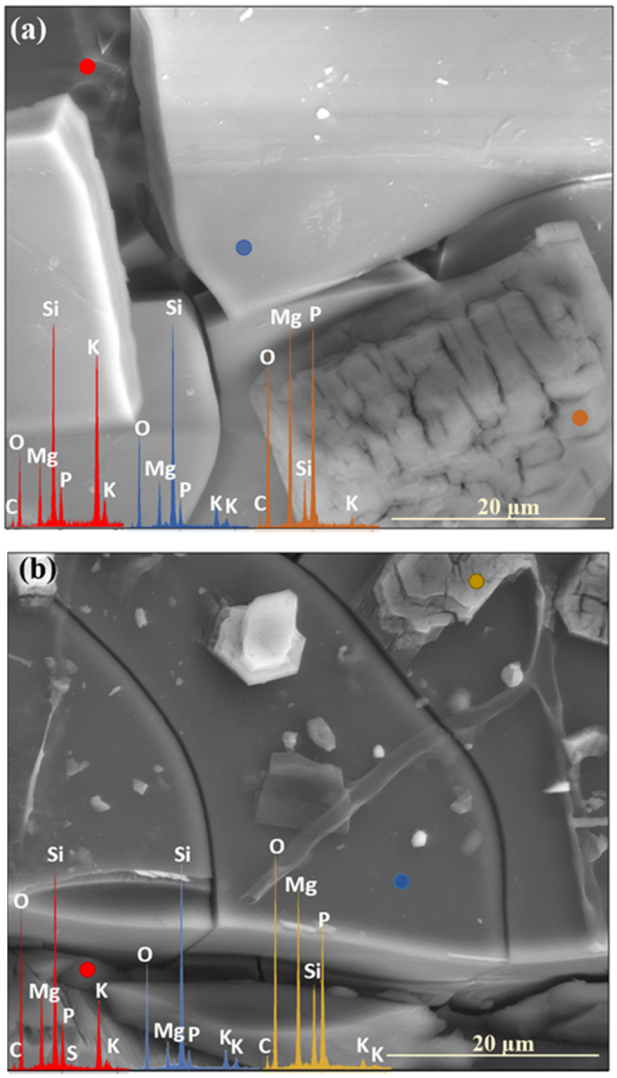


Figure 9. Micrographs and EDS spectra of selected surface points on 0S_6PM (**a**) and 3S_6PM (**b**) glasses after 8 months of incubation, illustrating the sequences of element release from the studied samples. The microphotographs were taken at 5000× magnification.

Analogous to the MgO-containing system, the XS_6PC series also exhibited the preferential leaching of potassium ions into the contact solution. Observations conducted after two weeks of incubation revealed a slight depletion of K^+ relative to its initial concentration, accompanied by the accumulation of Ca^{2+} ions in the superficial regions of the tested glasses (Figure 5: 0.5 mth). Notably, phosphate ions (PO_4^{3-}) also concentrated in the near-surface regions, eventually coprecipitating with Ca^{2+} to form a thin layer of calcium phosphates (Figure 5: 5 mth).

Although a similar tendency for calcium retention within the hydrated Si-rich altered layer was previously reported by Chave et al. [50], who proposed the passivating effect of this phase, in the present study, no such diffusion barrier effect was observed, even when the entire glass surface was covered with a precipitate layer (Figure 5: 8 mth—diminished K^+ concentration). This discrepancy is likely attributed to the discontinuous nature of the registered secondary product, which did not form a uniform protective coating, as well as to the pronounced propensity of the superficial glass regions to crack and exfoliate under cyclic wet–dry conditions, which facilitated the progression of the reaction front deeper into the pristine glass, ultimately accelerating the glass alteration process (Figure 10a).

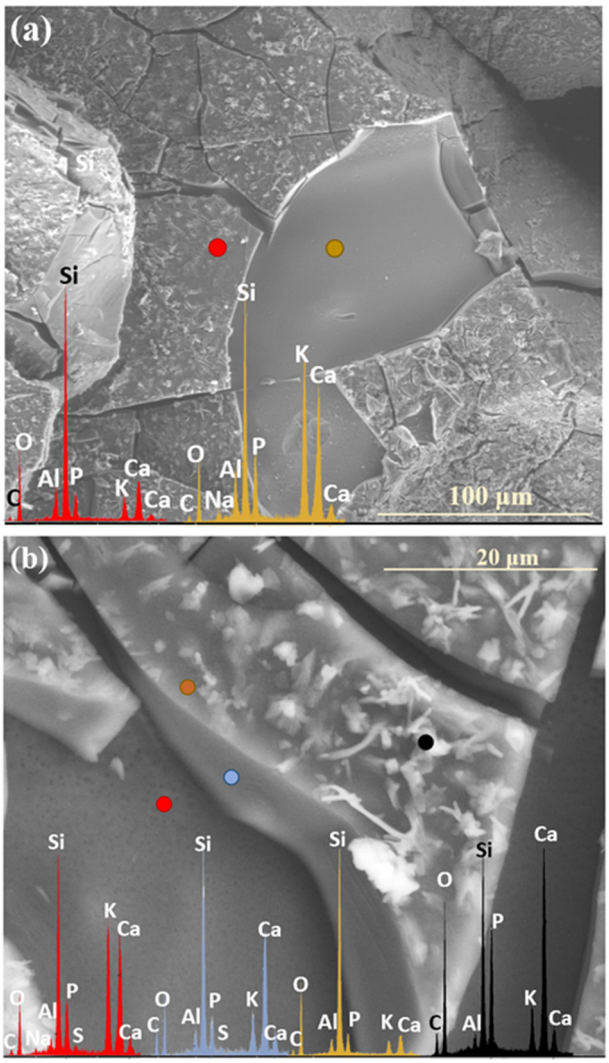


Figure 10. Micrographs and EDS spectra of selected surface points on 0S_6PC (**a**) and 3S_6PC (**b**) glasses after 7 and 5 months of incubation, respectively, illustrating the sequences of element release from the studied samples. The microphotographs were taken at 1000× (**a**) and 5000× (**b**) magnification.

When evaluating the preferential release of K^+ over Ca^{2+}, the mineralogical profile of the soil environment must also be considered. The significantly higher concentration of calcium ions in peat soil (Table 2) likely reduces the driving force for Ca^{2+} leaching, further emphasizing the complexity of soil–glass interactions and the importance of environmental variables in governing glass dissolution mechanisms.

SEM-EDS analysis of selected points on the surface of the 3S_6PC sample (Figure 10b) suggests that the sequential release of K^+ and SO_4^{2-} ions follows a pattern analogous to that observed in the 3S_6PM system. The sulfate ion concentration gradually decreases from the freshly exposed glass surface (red spectrum), through the altered layer (blue spectrum), and into the Si-enriched crust (yellow spectrum), highlighting the progressive modification of the outermost glass regions during incubation.

Similar to the previously discussed systems, the XS_6PMC series also exhibited the highest mobility of K^+ ions, the increased concentration of which was detected in the near-surface regions, newly exposed due to the decohesion of the altered layer (Figure 11a: red spectrum). This observation further supports the preferential involvement of K^+ in interdiffusion processes, leading to its early transport toward the glass surface as the first matrix element to be released. In contrast, the edge region of the resulting cavity is

predominantly silica-enriched, containing only residual amounts of other mobile ions (K^+, Mg^{2+}, Ca^{2+}, PO_4^{3-}) (blue spectrum).

Table 2. Chemical composition of the soil substrate used (mol. %).

Soil Composition, mol.%			
SiO_2	38.64	P_2O_5	0.88
CaO	27.72	Na_2O	0.62
SO_3	8.94	MnO	0.21
Fe_2O_3	6.28	Br	0.20
Al_2O_3	5.02	ZnO	0.20
Cl	3.80	PbO	0.19
MgO	3.09	SrO	0.13
K_2O	2.68	ZrO_2	0.10
		TiO_2	1.30

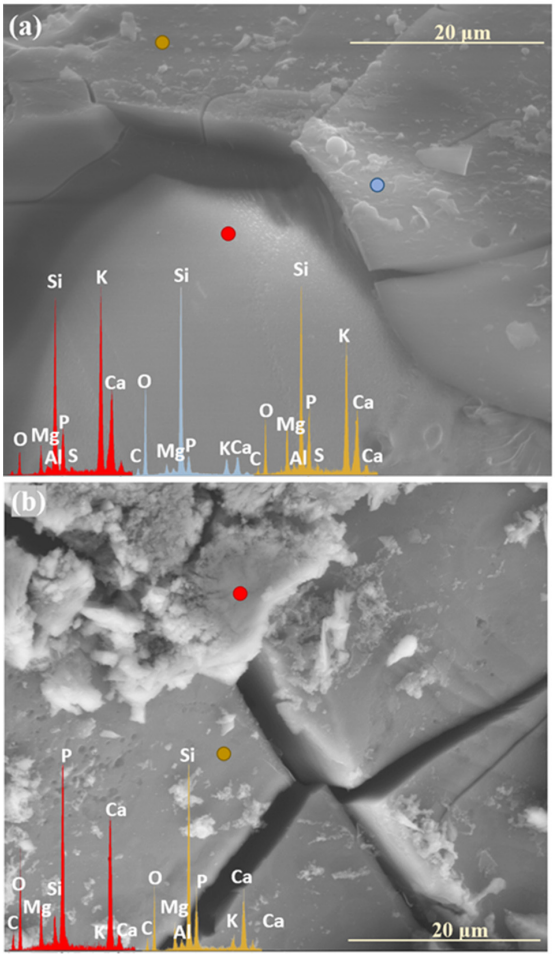


Figure 11. Micrographs and EDS spectra of selected surface points on 3S_6PMC (**a**) and 0S_6PMC (**b**) glasses after 0.5 and 7 months of incubation, respectively, illustrating the sequences of element release from the studied samples. The microphotographs were taken at 5000× magnification.

Analogous SEM-EDS analyses conducted on the base glass of this system revealed a trend similar to that observed in the XS_6PC samples, marked by the accumulation of Ca^{2+} and [PO_4^{3-}] ions in the near-surface regions (Figure 11b: yellow spectrum). This behavior is attributed to the rapid attainment of supersaturation in the contact solution with respect to these components, promoting their precipitation as secondary phases (red spectrum).

Interestingly, in the 10P system, which exhibited the highest overall reactivity, no preferential release of any specific mobile glass constituents into the soil solution was

observed, and all the major ions (K^+, Mg^{2+}, PO_4^{3-}, and SO_4^{2-}) appeared to leach simultaneously instead (Figure 12: yellow spectrum). Notably, the retention of these ions within the hydrated silica layer varied depending on the type of secondary crystalline phase that formed at different incubation stages. In the early phase of the experiment, when double magnesium–potassium phosphates precipitated, K^+ was preferentially retained within the altered zone (Figure 13a), while during the later months, which favored the crystallization of magnesium phosphate, Mg^{2+} and PO_4^{3-} accumulated within the altered layer (Figure 13b).

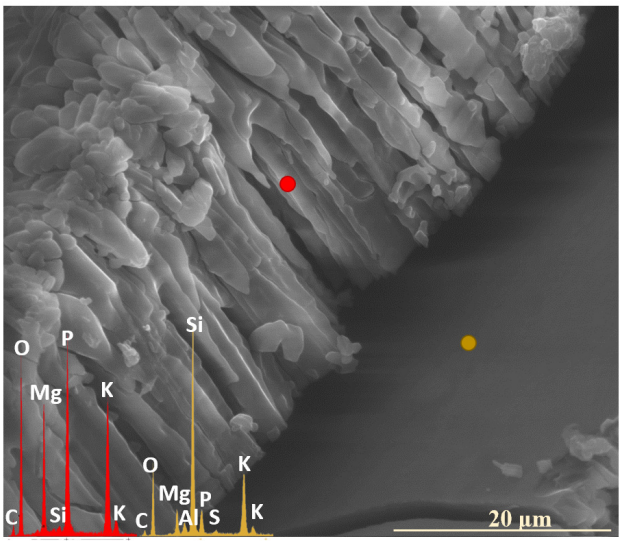


Figure 12. Micrograph and EDS spectra of selected surface points on 3S_10PM glass after 0.5 month of incubation, illustrating the sequence of element release from the studied sample. The microphotograph was taken at 5000× magnification.

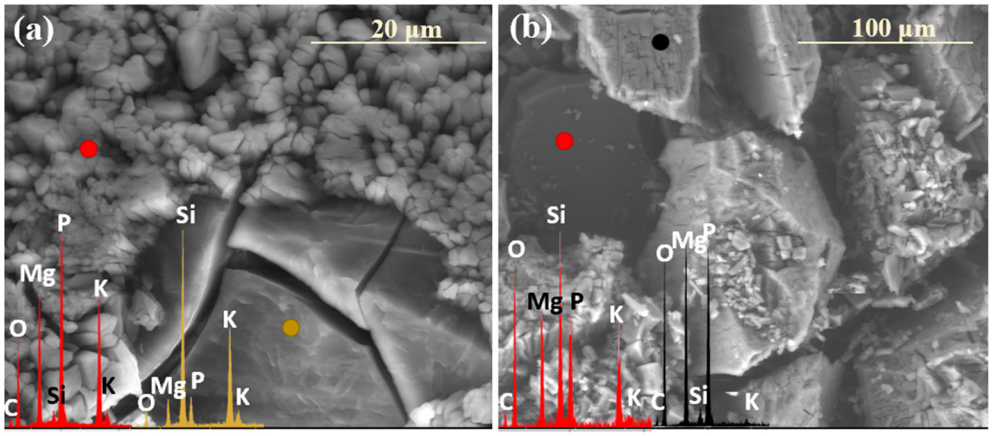


Figure 13. Micrographs and EDS spectra of selected surface points on 3S_10PM glass after 3 months (**a**) and 5 months (**b**) of incubation, illustrating the retention of ions within the hydrated silica layer.

Remarkedly, SO_4^{2-} species were predominantly released during the initial incubation stages, likely due to their high leachability under acidic conditions [51,52]. In all glasses representing the [6P] series, sulfur was detected in the EDS spectra only up to the 2nd month of incubation (or up to the 3rd month in the XS_6PC system), whereas at later stages, it appeared only sporadically, primarily in freshly exposed areas following surface exfoliation (Figure 14). In contrast, in the highly reactive XS_10PM system, this element was detected only in the first two weeks, confirming the most rapid leaching dynamics of the higher P_2O_5 composition among all the studied compositions (Figure 12: yellow spectrum).

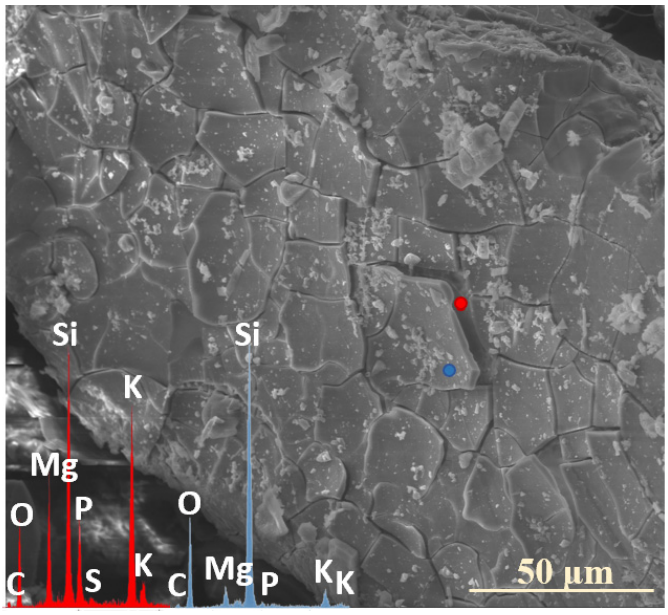


Figure 14. Micrograph of the 3S_6PM glass surface after 12 months of incubation, showing the presence of SO_4^{2-} species on the freshly exposed glass surface. The microphotograph was taken at 5000× magnification.

Given that, according to the observations carried out, K^+ leaches preferentially, followed by alkaline-earth cations (Mg^{2+}, Ca^{2+}) and PO_4^{3-} and SO_4^{2-} species, while the silicon–oxygen framework remains largely intact, the registered elemental release patterns suggest a selective, incongruent dissolution process. This acidic pH-driven, selective removal of mobile glass components leads to the rapid saturation of the limited-contact soil solution with the leached ions. As a result, glass constituents exceeding their solubility limit in the surrounding medium precipitate onto the outermost surface regions, forming a layer of secondary minerals.

2.3. Characterization of Precipitation Layers

Analyzing the data presented in Table 1, it becomes evident that the primary factor governing the formation of precipitating secondary phases is the chemical composition of the given glass. Accordingly, the presence of magnesium phosphates, as well as of double phosphates of potassium and magnesium in systems containing MgO as an alkaline-earth network modifier, is to be expected. Interestingly, for compositions with reduced P_2O_5 contents, the latter phase appeared only sporadically during the first month of the experiment (Figure 15a), whereas in the 10P series, it predominated, covering the entire superficial area of granules with a dense, thick (~16 µm) layer (Figure 15b).

Notably, while potassium struvite typically crystallizes into irregular tetrahedral shapes (disphenoids) when synthesized, the gel diffusion method tends to produce the characteristic needle-like morphology, analogous to the one observed in this study. It can therefore be inferred that the initial hydration of the surface layers of incubated glasses promotes the organization of leached ions (K^+, Mg^{2+}, PO_4^{3-}) into the double-phosphate structure detected. Additionally, as reported by Türk et al. [53], the coprecipitation of potassium to form struvite is favored under slightly alkaline conditions (pH < 8), whereas magnesium phosphate crystallizes at higher pH values. This observation underscores the critical role of the contact solution's pH in governing the crystallizing phase and offers valuable insights into the sequence of secondary product formation [54,55].

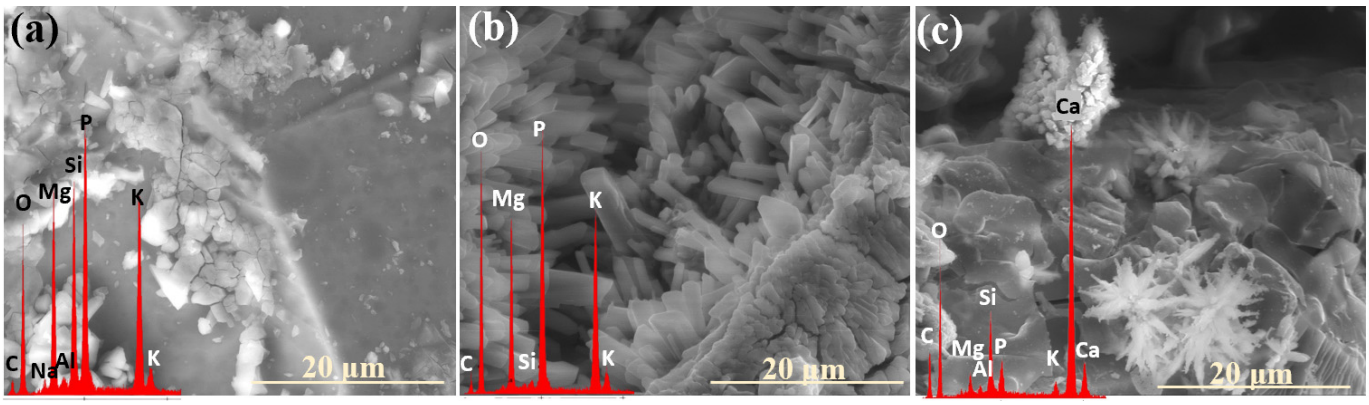


Figure 15. Exemplary secondary phases detected during the glass incubation experiment: double magnesium–potassium phosphates on the surfaces of 0S_6PM (**a**) and 0S_10PM (**b**) samples, as well as calcium carbonate observed on the 3S_6PMC glass (**c**). The microphotographs were taken at 5000× magnification.

During the early stages of the experiment, when the alkalization of the contact solution was minimal due to localized and less intense ion leaching, the formation of double phosphates was promoted. In contrast, at later stages, higher pH values in the thin moisture film adhering to the glass surfaces favored the precipitation of $Mg_3(PO_4)_2$. Furthermore, samples from the [10P] system were found to alkalize the surrounding environment to a lesser extent than those with lower P_2O_5 contents (as evidenced by long-term pH monitoring, the results of which are discussed in the authors' preceding study on the same materials, serving as a complementary investigation to this work), which explains the tendency of the XS_10PM glasses to preferentially form a potassium-containing struvite analogue, while magnesium phosphate appears in the XS_6PM system. Also worth emphasizing is the fact that not only the type of the crystal itself but also its morphology and habit are pH-dependent [53].

Based on the research of Prywer et al. [56], who studied struvite isomorphous phases, one may infer the conditions under which the observed $Mg_3(PO_4)_2$ phase was formed. It has been established that at lower pH values, single, poorly defined crystals are generally observed (as seen in Figure 1: 0.5 mth), whereas an increase in the pH promotes the precipitation of distinct, porous forms exhibiting a unique morphology that gives the impression of a structure composed of smaller subunits (Figure 9a: yellow spectrum).

While both the above-discussed phosphates are known to form in alkaline conditions, calcium phosphate precipitates over a broad pH range; however, depending on the acid/base properties of the environment, it can adopt various sizes, morphologies, and degrees of crystallinity [57–61].

Remarkedly, the 'desert-rose' form exhibiting poor crystallinity, observed with varying intensity in the XS_6PC system throughout the experiment, is promoted when the solution is slightly acidic (pH ~ 5–6) [59]. Such a statement, in turn, would suggest that CaO-containing compositions induce only the mild alkalization of the surrounding environment; but, given that the Ca^{2+} ions tended to accumulate in the superficial regions of the glass (Figure 10b: black spectrum) and therefore did not contribute to the formation of $Ca^{2+}(OH^-)_2$ species in the contact solution, this conclusion appears well founded.

In contrast, in the XS_6PMC system, which is more prone to alkalizing the contact solution due to the additional presence of Mg^{2+} cations, another poorly crystalline form of calcium phosphate was observed: agglomerates of cloudlike, shapeless granules, known to precipitate at higher pH values of ~7.5 [57] (Figure 11b: red spectrum). Interestingly, in this system, the dendrite-like calcium carbonate formations were also locally observed

(Figure 15c), with their presence indicating the involvement of carbonate ions in the contact solution (from either biotic or atmospheric sources) and a mildly alkaline environment (pH ~ 8–9) [60,61]. It is important to highlight that in this most complex composition, all the aforementioned phases were observed, reflecting the multicomponent nature of the system and the intricate relationships between the individual components of the glass matrix, as well as their diverse local effects on the pH of the contact solution.

It was observed that in none of the cases did the precipitated layer of secondary minerals establish a complete physical barrier to ion exchange processes. In the [6P]-series compositions, crystallization products settled on the altered glass surfaces in a fragmented, discontinuous manner, rather than forming an impermeable shield (Figure 3: 5 mth). Conversely, in the higher-P_2O_5 compositions, the precipitation layer exhibited the potential to act as a diffusion barrier; however, the presence of extensive cracking disrupted its integrity, enabling water penetration and consequently facilitating the transport of exogenous protonated species toward the pristine glass (Figure 12).

Furthermore, in both cases, the precipitates demonstrated a pronounced tendency toward decohesion or mechanical disintegration, particularly under temperature fluctuations associated with seasonal transitions from warmer to colder periods (Figure 16a). Additionally, the structurally distinct nature of the precipitated layer, relative to the outermost altered glass surface, likely introduced additional stress, further exacerbating the cracking and mechanical separation (Figure 16b).

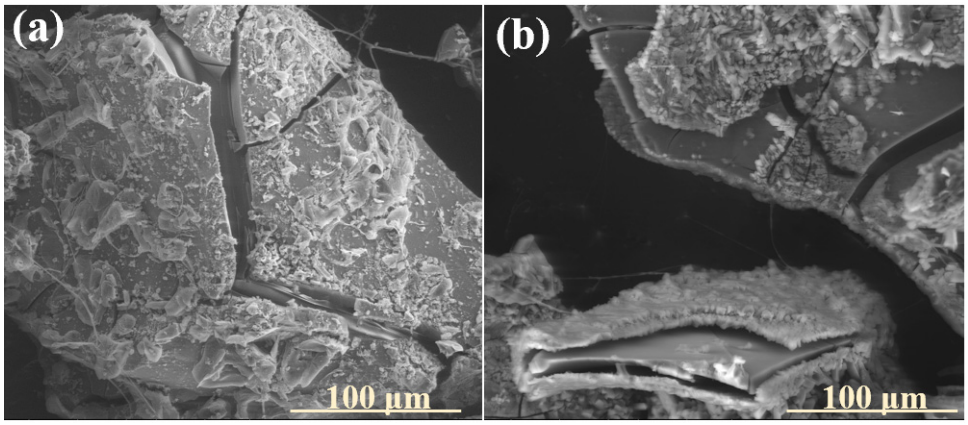


Figure 16. Micrographs of the surfaces of 3S_6PMC (**a**) and 3S_10PM (**b**) glasses after 6 months and 4 months of incubation, respectively, showing the tendency for the decohesion or mechanical disintegration of the precipitation layers. The microphotographs were taken at 1000× magnification.

Notably, sulfate species were found to play no role in the formation of secondary phases accumulating on the glass surface. Due to their relatively low concentration compared to other glass constituents, sulfate ions do not oversaturate the contact solution but instead migrate away from the glass surface and diffuse into the surrounding soil substrate.

2.4. Mechanism of Glass–Soil Interaction

Given the above considerations, the observed interaction between glass and the soil substrate appears to occupy an intermediate position between two well-documented glass deterioration processes: degradation in liquid media (where rapid dealkalization occurs through ion exchange with exogenous positively charged species from the surrounding solution, and the released glass components are promptly removed from the material's immediate vicinity—limiting oversaturation of the adjacent solution and, consequently, secondary phase precipitation), and alteration under atmospheric conditions (e.g., RH < 100%, where instead of being leached into a bulk liquid, glass constituents are redistributed within the hydrated alteration layer, modifying its composition and porosity differently, compared to aqueous

environments). Conversely, in the temperate mid-European climate, such as that of Poland, the soil moisture conditions fluctuate on short time scales, influenced by weather patterns and seasonal changes. As a result, potential vitreous fertilizers may experience discontinuous exposure to aqueous media, undergoing alternating cycles of wet and dry conditions of varying durations, creating a dynamic and non-static corrosion environment.

Accordingly, the conditions imposed on the samples during the 'in vivo' experiment were designed to replicate this periodic variability, allowing for a more accurate prediction of their behavior in real-field applications. This fluctuation in the environmental conditions explains the layered structure observed in the near-surface regions of the incubated glasses throughout the experiment: periods of increased water availability promoted interdiffusion processes, facilitating the penetration of hydrogenated species from the solution into the glass while simultaneously driving the outward migration of mobile glass constituents. This dynamic exchange leads to the formation of diffusion (alteration) layers, akin to those observed in glass corrosion under liquid immersion. Following this stage of heightened water supply, subsequent dry periods induce the progressive dehydration of the altered zone, weakening the superficial glass regions and rendering them preferential planes along which the decohesion of the alteration layers occurs (Figure 17). Beyond periodic soil wetting episodes, this mechanical separation of glass fragments was particularly evident immediately after temperature drops associated with the transition from summer to autumn, highlighting the differing thermal expansion coefficients of the bulk glass and the weathered layer. While numerous studies have reported the diffusion-blocking function of the outermost altered glass layer [7,18,62,63], the present experiment suggests a contrasting behavior: the brittle, Si-enriched superficial zone—prone to fracturing both parallel and perpendicular to the glass surface—created a unique network of pathways that facilitated water penetration toward the pristine glass. However, the most impactful factor appeared to be the scaling phenomenon itself, which directly accelerated glass–soil interactions by exposing fresh, unaltered surfaces to the corrosive effects of the soil solution (Figure 17).

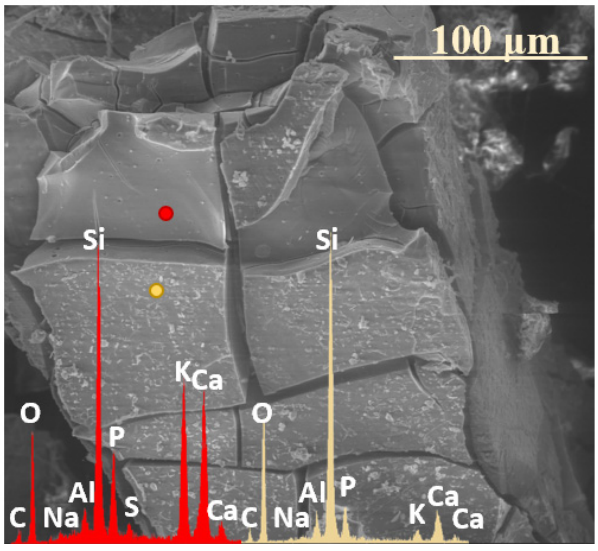


Figure 17. Micrograph illustrating the progression of the reaction front into the bulk glass through the decohesion of alteration layers, based on the observations of the 3S_6PC glass after 11 months of incubation. The microphotograph was taken at 1000× magnification.

It is postulated that these alternating episodes of wetting and drying, coupled with cyclic temperature fluctuations (on both the diurnal and seasonal scales), establish a self-reinforcing feedback loop. As surface scaling advances the alteration front deeper into the pristine glass, the increased exposure to soil moisture enhances ion leaching, subsequently

leading to the formation of a hydrated silica crust. During dry periods, this crust contracts and readily disintegrates, perpetuating the cycle. This hypothesis is further supported by the observed correlation between the extent of the surface fragmentation and the quantity of the leached mobile glass elements (Table 1).

The conditions employed in the conducted experiment—namely, the high surface-area-to-volume (SA/V) ratio, indicative of solution-dominated conditions, and the closed-system character of the incubation—exerted a significant influence on the processes occurring at the glass surfaces. Due to the acidic nature of the soil substrate (peat) and the resulting abundance of hydrogenated species (H^+, H_3O^+) in the contact solution, the predominant alteration mechanism involved interdiffusion, leading to the progressive hydration of the superficial material layers, as described by Equations (1) and (2), illustrating the predominant reactions involved in the glass corrosion process [25,64]:

$$\equiv Si - O^- - M^+_{(glass)} + H^+_{(sol.)} \rightarrow \equiv Si - OH_{(glass)} + M^+_{(sol.)} (\equiv \text{represents the silica bonds}) \quad (1)$$

$$\equiv Si - O - M^+_{(glass)} + H_3O^+_{(sol.)} \rightarrow \equiv Si - OH_{(glass)} + M^+_{(sol.)} + H_2O \quad (2)$$

$$\equiv Si - O - Si \equiv_{(glass)} + OH^-_{(sol.)} \rightleftharpoons \equiv Si - OH_{(glass)} + \equiv Si - O^-_{(glass)} \quad (3)$$

$$\equiv Si - OH_{(glass)} + HO - Si \equiv_{(glass)} \rightleftharpoons \equiv Si - O - Si \equiv_{(glass)} + H_2O \quad (4)$$

Another direct consequence of reduced water availability was the rapid alkalization of the contact solution, driven by proton consumption and the subsequent formation of K^+OH^- species (alternatively $Mg^{2+}2(OH^-)$, with the less frequent appearance of $Ca^{2+}2(OH^-)$ as Ca^{2+} ions, which were found to be retained in the near-surface glass regions). As-generated alkaline conditions lead to substantially more aggressive attacks directly affecting the silicate backbone via Si-O-Si bond hydrolysis (Equation (3)). Such visible marks of glass network dissolution resulting from the prolonged action of the alkaline medium in irregular surface areas constitute pits, occasionally detected on the tested material surfaces (see Figure 2: 8 mth, left upper corner).

Despite the ion exchange process facilitating the hydration of the superficial glass region (Equation (4)), the formation of a distinct, gel-like, Si-enriched layer was only sporadically evidenced (Figure 18). It is believed that the periodic wet–dry cycles inhibited the stabilization of this alteration product—either due to water evaporation or the systematic exfoliation of the silica crust. Consequently, the occasional presence of silica gel was primarily observed under winter-like conditions, where the lack of air circulation (imposed by the limitations of the climate chamber) allowed for prolonged moisture retention.

Notably, the surface alteration processes recorded in this experiment exhibit substantial similarities to those well documented for glass deterioration in immersion conditions, as the analysis of the 'in vivo' experimental results confirms the occurrence of three key processes [18,19,65–67]: (1) the adsorption of a thin layer of moisture at the superficial glass area, (2) the proceeding of three parallel and interconnected reactions: ion exchange, hydration, and hydrolysis, as well as (3) the precipitation of the secondary product layer. However, the primary distinguishing factor between glass weathering in a soil medium versus a liquid environment is the water availability, which emerged as the critical factor governing the rate of glass alteration under the experimental conditions. In addition to the moisture dynamics, the glass composition is also known to play a role in controlling the reactions between glass constituents and environmental species, further influencing the overall alteration behavior.

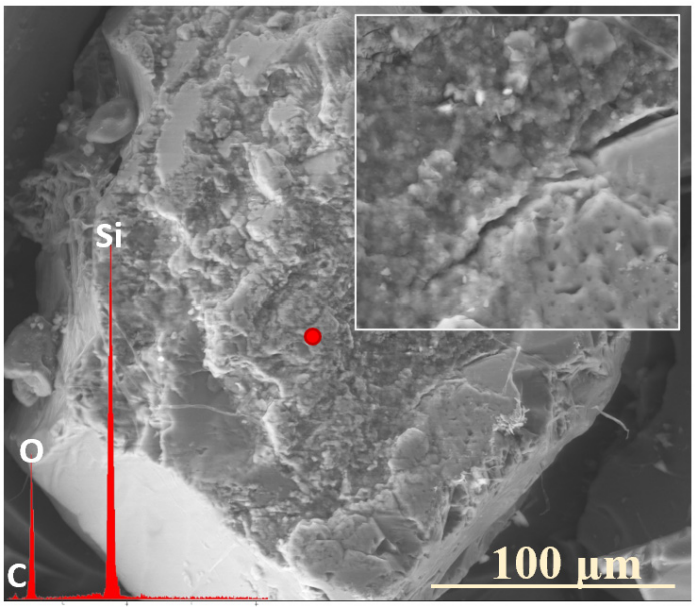


Figure 18. Silica gel layer observed on the surface of 3S_10PM glass after 10 months of incubation. The microphotograph was taken at 1000× magnification.

In this study, however, only minor differences were observed in the behavior of the tested compositions in the soil environment, when comparing compositions belonging to the same series: 6P compositions. As discussed in Section 2.1, these differences primarily manifest in the material's tendency to undergo fracturing, a process significantly intensified by the presence of sulfate units. Nonetheless, among the 6P compositions, the system that exhibited the lowest initial reactivity appears to be the XS_6PMC variant. This phenomenon can be attributed to the well-documented mixed-alkali-/-alkaline-earth effect, which increases the activation energy required for ion hopping between sites within the vitreous matrix, thereby hindering the ionic diffusion process [68,69]. Clearly, the P_2O_5 content plays a far greater role in controlling the glass reactivity than the specific type of alkaline-earth oxide modifier, as evidenced by the 10P system, which, despite having the highest network connectivity, was found to be the most chemically active. It is well known that introducing phosphorus pentoxide into silicate-based glass matrices enhances their hygroscopic properties while simultaneously reducing their resistance to humidity, as phosphate glasses are notorious for their rapid deterioration upon exposure to atmospheric moisture due to the presence of readily hydrated P-O-P bridges [14,15,68,70–72]. Therefore, it is assumed that the strong hydrophilic nature of [PO_4^{3-}] species renders these glasses highly susceptible to moisture-induced degradation; the more water molecules adsorbed at the surface, the deeper and faster the hydrolysis and hydration processes and the higher the chemical potential of the adsorbed 'solution', ultimately accelerating the leaching of mobile cations (Figure 19). Importantly, these considerations remain valid as long as phosphorus enters the vitreous matrix predominantly in the form of isolated Q_P^0 units, which, as indicated by previous research on similar materials, applies to glasses containing up to 15 mol% P_2O_5 [15,73,74]. Beyond this threshold, the structural role of phosphorus may undergo a significant shift, potentially reversing its effect on the overall glass reactivity, particularly in the presence of Fe as an introduced micronutrient [75,76].

Clearly, for glasses with the same P_2O_5 contents, variations in the type of network-modifying alkaline-earth oxide influence their interaction with the soil environment not only by affecting their propensity for fracturing but also by determining the nature of the crystallizing secondary phases and their further role in the glass–soil interface reactions. In the XS_6PM system, the precipitated magnesium phosphates appeared as large, well-

defined crystals scattered across the glass surface, and their localized distribution did not present a significant barrier to ion exchange. Similarly, in the XS_6PMC system, the secondary phases also formed in a dispersed manner, and even during periods of increased precipitation, the resulting layer remained discontinuous. In contrast, calcium phosphates in the XS_6PC system initially formed a more distinct barrier, but only during the early stages of incubation, when the lack of cracks and the absence of surface mechanical degradation had not yet facilitated the advancement of the reaction front into the deeper glass matrix. Notably, in the 10P system, the precipitation layer appeared dense and uniform; however, the glass itself exhibited a high degree of fracturing, which enhanced the accessibility of the contact solution to the glass surface.

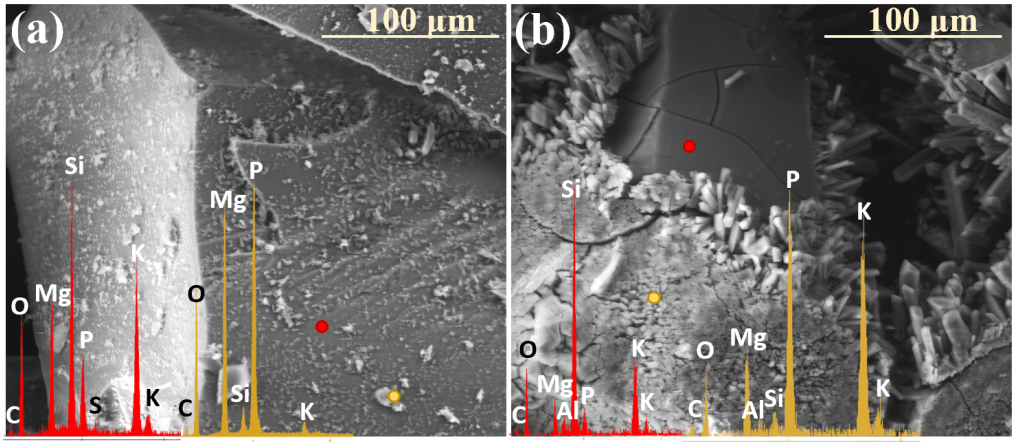


Figure 19. Comparison of the chemical activities of glasses with lower (**a**) and higher (**b**) P_2O_5 contents, based on 3S_6PM and 3S_10PM samples after 2 months of incubation. The microphotographs were taken at 1000× magnification.

Importantly, it may be claimed that the existence of a superficial area of secondary phases is responsible for regulating the release of nutrients into the soil environment by virtue of the temporary immobilization of the elements within the composition of such a precipitation layer itself. It should be noted that all the observed phases display low solubility in water, preventing nutrient runoff, and are characterized by much higher acidic pH values in the environment [53,77–79].

From a practical standpoint, this precipitation-driven ion retention may be considered a natural strategy for controlled nutrient release, as the remobilization of useful ions is triggered under the influence of roots'/microorganisms' acidic exudates. However, it must be stressed that calcium phosphates belonging to the apatite family exhibit the lowest solubility in acidic environments compared to other observed phases. This characteristic should be carefully considered when designing CaO-containing vitreous fertilizers, as the re-release of immobilized nutrients from these phases is expected to be the slowest [77].

2.5. Influence of Soil Environment

It is crucial to highlight the multitude and complexity of factors influencing the processes occurring at the soil–glass interface. Many of these factors, due to their inherently unpredictable nature, cannot always be fully accounted for when describing such interactions. Beyond the evident impact of seasonal or even daily weather fluctuations—which significantly affect the soil moisture levels, the concentrations of dissolved organic and inorganic compounds, and, consequently, parameters such as the electrical conductivity (EC) and redox potential (Eh)—the chemical and mineralogical properties of the soil itself play a pivotal role in shaping these processes.

A compelling confirmation of this influence is the observed effect of the glass composition on the ion mobility within the application environment. The acidic peat substrate used in the incubation experiments, characterized by a significant calcium ion content, may have aided in both the retention of these ions within the silica-enriched hydrated layer and the crystallization of secondary calcium phosphates. Conversely, the presence of exogenous carbonate ions—either biotically generated or derived from atmospheric CO_2—promoted the formation of calcium carbonate precipitates.

Furthermore, the application of glasses in soil environments necessitates the consideration of biotic glass alteration, a process known to substantially contribute to the degradation of vitreous materials. Interestingly, microbial colonization was observed on the surfaces of some of the tested glasses (Figure 20). Given that microorganisms are particularly prone to adhering to mineral surfaces rich in bioavailable elements, this form of biotic weathering may serve as an additional indication of the potential utility of such materials in agricultural or environmental applications [80]. Notably, this research direction remains an active area of the authors' ongoing scientific investigations, aiming to further explore the interplay between the glass composition–structure properties, biotic interactions, and long-term material stability.

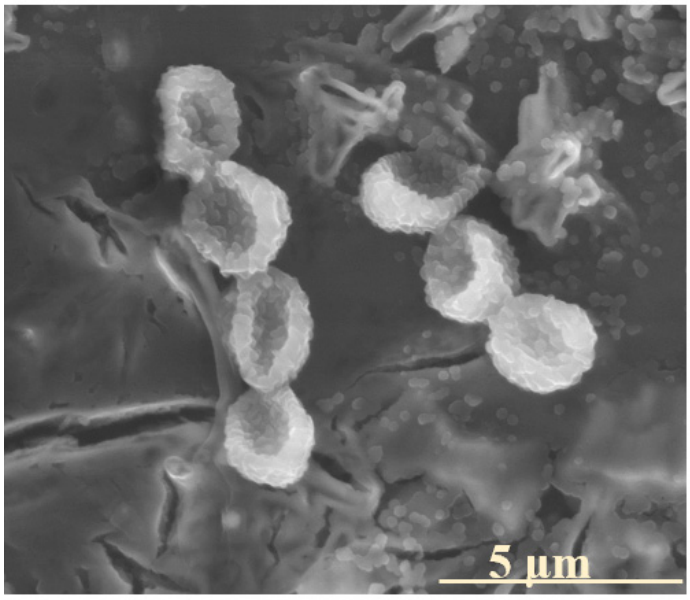


Figure 20. Detected biotic colonization on the surface of exemplary 0S_6PM glass after 4 months of incubation. The microphotograph was taken at 10,000× magnification.

3. Materials and Methods

3.1. Definitions

The authors would like to emphasize that, in this study, various terms describing phenomena that alter the physicochemical properties of glass (e.g., weathering, corrosion, alteration, degradation, and deterioration), despite having distinct nuances, are used interchangeably for simplicity.

Nonetheless, it is important to note that the term dissolution specifically refers to the rupture of Si-O-Si bonds and the breakdown of the silica network, whereas leaching denotes the initial degradation step involving the loss of alkali- and alkaline-earth metal ions that are ionically bonded to the silica framework—a process that precedes network dissolution [3,42]. Weathering refers to degradation resulting from prolonged exposure to water in the environment, both in the vapor and liquid states [3,42,43], while deterioration is defined as changes in the chemical composition of glass over time [44]. Moreover, the

terms 'dissolution' and 'corrosion' should be used specifically when describing the transformation of glass into solely aqueous species and both solid alteration products and aqueous species, respectively.

Given its relevance to this study, the term slow-release fertilizer also requires clarification. According to the Association of American Plant Food Control Officials (AAPFCO), slow-release fertilizers are characterized by delayed nutrient availability and delivery following application, and their rate of macro-/microelement release is slower compared to that of conventional fertilizers, providing nutrients in a readily available form [45,46].

Additionally, the authors find it necessary to clarify the use of the terms 'in vitro' and 'in vivo' in the context of this study, as these are traditionally associated with medical research. Notably, in soil science, specialists consider the soil environment a 'living entity' due to its complex biological activity and interactions with microorganisms. Based on this perspective, we define the terms as follows:

- The term 'in vitro' refers here to laboratory-based experiments conducted outside the soil system, such as dissolution studies of glass fertilizers in simulated environments (e.g., solutions that mimic soil conditions);
- The term 'in vivo' refers here to experiments performed within a biotic soil environment, such as soil incubation studies, where glass fertilizers interact with actual soil conditions to simulate real-world scenarios.

To underscore the distinction from traditional biological applications, both terms are presented in quotation marks throughout the manuscript. This highlights their adapted use in studying glass fertilizers under controlled soil conditions.

3.2. Synthesis and Compositional Analysis of the Designed Glass Fertilizers

To evaluate the potential of vitreous carriers for macro- and micronutrients with prolonged-release properties, four of the most promising formulations were selected based on previous experimental findings as well as insights from related research [15,16,49,81–84].

The molar percentages of the individual oxides in each formulation are as follows (where X represents the molar percentage of SO_3 introduced, with values of X = 0, 1, 3, or 5 mol% in this study):

- The XS_6PM system: $41SiO_2 \cdot 6P_2O_5 \cdot 20K_2O \cdot 33MgO \cdot XSO_3$;
- The XS_6PC system: $41SiO_2 \cdot 6P_2O_5 \cdot 20K_2O \cdot 33CaO \cdot XSO_3$;
- The XS_6PMC system: $41SiO_2 \cdot 6P_2O_5 \cdot 20K_2O \cdot 16.5MgO \cdot 16.5CaO \cdot XSO_3$;
- The XS_10PM system: $41SiO_2 \cdot 10P_2O_5 \cdot 20K_2O \cdot 29MgO \cdot XSO_3$.

The above glass formulations were synthesized on a laboratory scale (~100 g) through a high-temperature melting process, utilizing raw materials of analytical-grade purity, including SiO_2, $(NH_4)_2HPO_4$, K_2CO_3, MgO, and K_2SO_4, all sourced from CHEMPUR (Poland). To ensure compositional accuracy, the precursor materials were meticulously weighed to a precision of 0.001 g and subsequently homogenized using a mortar and pestle. The synthesis was conducted in ceramic crucibles under ambient atmospheric conditions within an electric chamber furnace, maintaining a temperature of 1450 °C. The resulting molten glasses were subjected to rapid quenching in cold water, a process designed to achieve a fully amorphous structure while simultaneously inhibiting spontaneous crystallization [83].

The actual oxide compositions of the obtained glass samples were determined through X-ray fluorescence spectrometry (XRF) using an ARL Perform'X spectrometer (Thermo Fisher Scientific, Ecublens, Switzerland) at the accredited FerroCarbo testing laboratory. For XRF measurements, the samples—derived from homogenized glass material—were prepared in the form of fused pellets (~10 g of glass). The fusion method involved a preliminary calcination step followed by high-temperature melting in a fluxer (1100 °C)

to produce analytical pearls. The XRF-determined molar contents of the individual glass components are presented in Table 3.

Table 3. Measured compositions of the synthesized specimens. Registered minor discrepancies between the expected and actual amounts of glass components are attributed to inherent measurement uncertainties and potential volatilization during the heating process.

No.	SiO_2	P_2O_5	K_2O	MgO	CaO	SO_3
0S_6PM	41.42 (±0.40)	6.75 (±0.09)	20.42 (±0.00)	30.17 (±0.45)	-	-
1S_6PM	37.39 (±0.41)	5.96 (±0.09)	19.53 (±0.00)	31.72 (±46)	-	0.84 (±0.12)
3S_6PM	40.00 (±0.41)	6.92 (±0.09)	20.63 (±0.00)	32.67 (±0.46)	-	1.84 (±0.14)
5S_6PM	41.60 (±0.40)	6.49 (±0.40)	17.69 (±0.00)	33.44 (±0.40)	-	1.59 (±0.40)
0S_6PC	39.11 (±0.44)	6.29 (±0.09)	18.88 (±0.00)	-	33.63 (±0.71)	-
1S_6PC	38.28 (±0.45)	6.14 (±0.10)	17.21 (±0.00)	-	35.79 (±0.73)	1.00 (±0.16)
3S_6PC	37.90 (±0.45)	6.46 (±0.09)	18.40 (±0.00)	-	35.12 (±0.72)	2.05 (±0.13)
5S_6PC	43.25 (±0.45)	6.10 (±0.01)	15.03 (±0.00)	-	37.42 (±0.72)	1.39 (±0.15)
0S_6PMC	39.91 (±0.41)	6.33 (±0.09)	18.40 (±0.00)	15.46 (±0.34)	18.16 (±0.44)	-
1S_6PMC	38.20 (±0.42)	6.33 (±0.09)	19.59 (±0.00)	15.53 (±0.33)	18.09 (±0.56)	0.95 (±0.12)
3S_6PMC	38.08 (±0.09)	6.64 (±0.09)	18.92 (±0.00)	16.57 (±0.34)	20.15 (±0.45)	1.76 (±0.15)
5S_6PMC	41.70 (±0.42)	6.46 (±0.09)	16.41 (±0.00)	16.32 (±0.35)	20.89 (±0.56)	1.40 (±0.14)
0S_10PM	38.11 (±0.40)	11.01 (±0.08)	21.56 (±0.00)	29.12 (±0.44)	-	-
1S_10PM	39.00 (±0.42)	10.89 (±0.09)	19.95 (±0.00)	28.98 (±0.50)	-	0.25 (±0.05)
3S_10PM	39.37 (±0.42)	11.02 (±0.09)	21.14 (±0.00)	29.35 (±0.47)	-	0.83 (±0.10)
5S_10PM	42.29 (±0.41)	11.48 (±0.08)	22.29 (±0.00)	24.71 (±0.46)	-	0.48 (±0.07)

3.3. Soil Incubation Experiment ('In Vivo' Simulation)

To investigate the long-term nutrient release mechanisms under conditions that closely mimic real-field scenarios, yet on a laboratory scale, selected glasses representing all the synthesized compositions—incorporating 3% mol. sulfate and a base for comparison—were incubated in a soil medium. Poland, one of the largest agricultural producers in the European Union (EU), holds the largest agricultural area within the Baltic Sea drainage basin and is a key cereal producer. However, the country faces challenges related to increased soil acidity, primarily driven by inefficient and excessive nitrogen (N) fertilization, a problem also common in many European nations [84–86]. Therefore, as a representative medium, acidic peat was chosen, with a pH range of 3.5–4.5, and the composition (determined by X-ray fluorescence using an ARL Advant'XP spectrometer with the standard pellet method) is presented in Table 3.

Glass samples (fraction: 0.1–0.3 mm), 15 of each composition, were affixed to square pieces of carbon tape (approximately 5 × 5 mm), placed in plastic containers, and evenly mixed with the soil substrate. As-prepared specimens were then incubated in a climate chamber (Binder KMF constant climate chamber) for a 12-month period under variable climatic conditions simulating the average yearly temperature fluctuations in Poland (Table 4), with the soil watered with distilled water once a month. In the soil incubation experiments, water was not applied as a fixed volume but was instead sprayed onto the substrate until the soil surface visibly darkened—indicating the adsorption of moisture by soil particles—while avoiding the accumulation of free liquid at the bottom of the container. This corresponded to an approximate volume of a few milliliters per sample and was intended to emulate natural moisture conditions, in which water is retained in the upper soil layers before gradually percolating downwards. Such an approach ensured localized interactions between the glass particles and soil-bound water, without inducing artificial waterlogging effects.

Table 4. Characterization of simulated seasonal climatic conditions.

Simulated Seasons	Spring (Mar–May)	Summer (Jun–Aug)	Autumn (Sep–Nov)	Winter (Dec–Feb)
Day/night average temperature (°C)	13.5/3.8	23.1/13.8	13.2/5.5	1.8/−4.2
Average humidity (%)	71	71	79	- *

* The average humidity data for the winter period could not be simulated in the experiment due to chamber limitations, as the chamber was unable to control air humidity at temperatures below 0 °C.

The incubated samples were extracted from the soil substrate at various time intervals: after 2 weeks, and then monthly until the end of the experiment, to assess both the qualitative changes and alterations in the chemical compositions of the surfaces of the materials using SEM (NOVA NANO SEM 200, FEI EUROPE, Eindhoven, The Netherlands) with EDS (EDAX) in the Laboratory of Scanning Microscopy and Microanalysis at the Faculty of Materials Science and Ceramics, AGH University of Krakow. The chemical compositions of different regions on the glass surfaces were determined by EDS from at least two different spots.

To assess the applicability of the EDS data for semi-quantitative analysis, the results obtained via XRF (the pearl method) were compared with those derived from the averaged EDS analysis at three distinct points on the surface of a representative, non-altered glass sample (3S_6PM). The obtained data are presented in Table 5.

Table 5. Comparison between the chemical composition of the selected sample obtained via XRF and SEM-EDS method.

Data Origin	SiO_2	P_2O_5	K_2O	MgO	SO_3
XRF	40.00 (±0.40)	6.92 (±0.08)	20.63 (±0.00)	32.67 (±0.59)	1.84 (±0.14)
SEM-EDS	44.64 (±0.34)	7.70 (±0.23)	19.15 (±1.96)	27.02 (±2.17)	1.49 (±0.45)

The similarity between the compared datasets suggests that the SEM-EDS analysis was highly effective for the semi-quantitative analysis, enabling the study of the surface variations on the glass throughout the 'in vivo' experiment. The observed deviations may have resulted from the impinging electron beam, which could have locally heated the specimens during the analysis.

4. Conclusions

In light of the pressing challenges facing modern agriculture—namely, the need to sustain a growing global population while the arable land availability declines and soil fertility diminishes—developing innovative strategies to replenish essential macro- and micronutrients in the soil has become imperative. Ensuring and maintaining soil health is fundamental not only for supporting plant growth and productivity but also for preserving the intricate balance of microbial communities that drive key biochemical processes within Earth's most diverse habitats. A promising approach to addressing this challenge lies in the application of glassy fertilizers, which offer controlled and prolonged nutrient release, mitigating the risks of overfertilization and nutrient runoff—factors that can severely disrupt the biogeochemical equilibrium of soil ecosystems. Importantly, the inherent flexibility of the glassy state enables the encapsulation of a diverse array of macro- and micronutrients within an amorphous matrix, including elements that, due to their crystallo-chemical incompatibilities, cannot readily co-exist in the crystalline phase (e.g., [SiO_4] and [SO_4] tetrahedra [86–88]).

The present study centered on a soil incubation experiment of sulfate-bearing multicomponent silicate–phosphate glasses to deepen the understanding of the intricate composition–structure–property relationships within the selected composition. By focusing on the third crucial link in this chain—their real-environment behavior—this work provides

insights into the mechanisms governing their interactions in soil conditions, setting the foundation for further research on their agronomic potential.

From the results obtained, the weathering behavior of the tested glasses can be effectively controlled at the compositional level. Even subtle modifications, such as altering the type of alkaline-earth network modifier or adjusting the SO_3 and P_2O_5 contents, significantly influence the material's reactivity.

MgO is known to play a dual role in glass systems, depending on its concentration, acting as either a network modifier or a former, which, in turn, increases the degree of polymerization and enhances the structural rigidity of the silicate–oxygen backbone. This reinforcement of the network architecture, evident in the XS_6PM formulation, contributed to the formation of cracks and fissures, ultimately facilitating the deeper penetration of the soil solution into the glass matrix. In contrast, the presence of CaO generally resulted in a more flexible glass network, which, in the case of the XS_6PC system, exhibited greater resistance to mechanical fracturing and a slightly reduced reactivity in the soil environment, as evidenced by the slower advancement of the reaction front into the bulk glass. The co-introduction of MgO and CaO may lead to a mixed-alkaline-earth effect, manifesting itself as an increase in the activation energy for ionic diffusion. In the formulations containing both MgO and CaO, this effect was reflected in a modest delay in the chemical reactivity compared to the other compositions.

Although indirectly, sulfate incorporation was also found to influence the material's behavior in soil. The resulting increase in the network connectivity enhanced the structural rigidity, which, in turn, made the glasses more susceptible to mechanical damage (an effect further amplified by the positioning of the $[SO_4^{2-}]$ species within voids of the glass matrix, inducing additional structural stresses). In the soil environment, sulfate-related effects were reflected in the deeper progression of the reaction front into the material. Notably, glasses with the highest P_2O_5 contents exhibited the greatest reactivity under 'in vivo' conditions. This not only stemmed from the significant contribution of hygroscopic $[PO_4^{3-}]$ units but also, in all likelihood, from the high concentration of the crystallo-chemically incompatible $[SiO_4^{4-}]$, $[PO_4^{3-}]$, and $[SO_4^{2-}]$ species within the framework, which destabilized the backbone structure and consequently led to the highest rates of interdiffusion reactions. Given that the propensity for glass cracking, flaking, and exfoliation directly correlates with the ion leaching intensity—by increasing the material's contact area with the soil solution—it is evident that precise compositional modifications can be employed to regulate nutrient release rates.

Another key factor influencing the reaction kinetics at the glass–soil solution interface was the immobilization of released ions within a precipitation layer, the nature of which was strongly dependent on both the glass composition and the pH of the surrounding medium. The registered effect is of utter importance given the intended materials' application: as the fraction of nutrients not directly utilized by plants accumulates in the soil solution, excess ions are expected to precipitate as secondary phases on the glass surface. Importantly, the composition-dependent nature of these secondary phases dictates their subsequent dissolution rates, thereby influencing the long-term availability of both micro- and macronutrients in acidic soil environments.

A particularly crucial aspect of this study, from the perspective of utilizing these materials as glassy carriers of essential nutrients, was determining the sequential release of the matrix constituents into the soil medium. The findings revealed that K^+ ions, possessing low cationic field strength and resulting in a strong tendency to diffuse toward the glass surface, were leached preferentially, followed by the release of alkaline-earth cations and $[PO_4^{3-}]$ and $[SO_4^{2-}]$ species, whereas the silicon–oxygen backbone remained largely intact over the duration of the experiment. Notably, in all the tested cases, the $[SO_4^{2-}]$ species

were released in the early stages of the incubation, likely due to their high solubility in acidic conditions. Furthermore, the dissolution was found to be selective, with the formation of a silica-rich crust that retained residual, unleached ions, confirming an incongruent dissolution mechanism.

Despite the controlled nature of this closed-system study, the findings successfully captured the complex and interdependent processes occurring at the soil–glass interface, emphasizing the critical roles of the soil pH, the glass composition, and environmental variability in governing glass–soil interactions. The acidic nature of the peat dictated the primary reaction mechanisms, favoring ion exchange, while limited water availability led to rapid solution saturation with leached elements, promoting the precipitation of secondary phases. Notably, the identity of these crystallized phases was strongly influenced by both the solution pH and the interplay between the glass and soil compositions, whereas surface characteristics—such as roughness, microdefects, and compositional heterogeneities—played a decisive role in governing the timing and localization of the glass–solution interactions.

These findings highlight the multifactorial nature of glass degradation, where the sequence of events and the predominance of specific processes remain difficult to predict with certainty, underscoring the necessity of considering unforeseen phenomena when assessing glass–soil interactions, as well as the importance of further investigations under more dynamic and complex environmental conditions.

Final Remarks

The findings from this study provide valuable insights into the long-term alteration mechanisms of glass, which can aid in the development of more accurate predictive models for understanding the complex behavior of glass materials under various environmental conditions. Furthermore, these insights may prove crucial in the design of advanced vitreous fertilizers, optimizing their nutrient release profiles while minimizing their environmental impact.

Author Contributions: Conceptualization, M.S. and A.B.; methodology, A.B., J.S. and M.S.; software, A.B. and A.W.; validation, A.B. and A.W.; formal analysis, A.B. and M.S.; investigation, A.B. and J.S.; resources, A.B.; data curation, A.B. and M.S.; writing—original draft preparation, A.B.; writing—review and editing, A.B. and M.S.; visualization, A.B.; supervision, A.B. and M.S.; project administration, A.B. and M.S.; funding acquisition, A.B. and M.S. All authors have read and agreed to the published version of the manuscript.

Funding: This work was financed by the National Science Centre, Poland, project number 2023/49/N/ST11/00299, and was partially supported by the program 'Excellence initiative—research university' for the AGH University of Krakow (No. 9785).

Institutional Review Board Statement: Not applicable.

Informed Consent Statement: Not applicable.

Data Availability Statement: The data presented in this study are available upon request from the corresponding author.

Acknowledgments: The authors would like to express their gratitude to the Laboratory of Scanning Microscopy and Microanalysis at the Faculty of Materials Science and Ceramics, AGH University of Krakow, for providing access to the SEM-EDS facilities essential for this research.

Conflicts of Interest: The authors declare no conflicts of interest.

References

1. Mauro, J.C. Decoding the glass genome. *Curr. Opin. Solid State Mater. Sci.* **2018**, *22*, 58–64. [CrossRef]
2. Yanagishima, T.; Russo, J.; Tanaka, H. Common mechanism of thermodynamic and mechanical origin for ageing and crystallization of glasses. *Nat. Commun.* **2017**, *8*, 15954. [CrossRef] [PubMed]
3. Zanini, R.; Franceschin, G.; Cattaruzza, E.; Traviglia, A. A review of glass corrosion: The unique contribution of studying ancient glass to validate glass alteration models. *NPJ Mater. Degrad.* **2023**, *7*, 38. [CrossRef]
4. Jackson, C.M.; Greenfield, D.; Howie, L.A. An assessment of compositional and morphological changes in model archaeological glasses in an acid burial matrix. *Archaeometry* **2012**, *54*, 489–507. [CrossRef]
5. Gin, S.; Guo, X.; Delaye, J.-M.; Angeli, F.; Damodaran, K.; Testud, V.; Du, J.; Kerisit, S.; Kim, S.H. Insights into the mechanisms controlling the residual corrosion rate of borosilicate glasses. *NPJ Mater. Degrad.* **2020**, *4*, 41. [CrossRef]
6. Brauer, D.S. Bioactive Glasses—Structure and Properties. *Angew. Chem. Int. Ed. Engl.* **2015**, *54*, 4160–4181. [CrossRef]
7. Hench, L.; Clark, D. Physical chemistry of glass surfaces. *J. Non Cryst. Solids* **1978**, *28*, 83–105. [CrossRef]
8. Christie, J.K.; Ainsworth, R.I.; de Leeuw, N.H. Investigating structural features which control the dissolution of bioactive phosphate glasses: Beyond the network connectivity. *J. Non Cryst. Solids* **2016**, *432*, 31–34. [CrossRef]
9. Tilocca, A.; Cormack, A.N.; de Leeuw, N.H. The Structure of bioactive silicate glasses: New insight from molecular dynamics simulations. *Chem. Mater.* **2007**, *19*, 95–103. [CrossRef]
10. Hill, R.G.; Brauer, D.S. Predicting the bioactivity of glasses using the network connectivity or split network models. *J. Non Cryst. Solids* **2011**, *357*, 3884–3887. [CrossRef]
11. Labbilta, T.; Ait-El-Mokhtar, M.; Abouliatim, Y.; Khouloud, M.; Meddich, A.; Mesnaoui, M. Elaboration and Characterization of Vitreous Fertilizers and Study of Their Impact on the Growth, Photosynthesis, and Yield of Wheat (*Triticum durum* L.). *Materials* **2021**, *14*, 1295. [CrossRef]
12. D'Amato, R.; De Feudis, M.; Troni, E.; Gualtieri, S.; Soldati, R.; Famiani, F.; Businelli, D. Agronomic potential of two different glass-based materials as novel inorganic slow-release iron fertilizers. *J. Sci. Food Agric.* **2021**, *102*, 1660–1664. [CrossRef] [PubMed]
13. Ouis, M.A.; Abd-Eladl, M.; Abou-Baker, N.H. Evaluation of Agriglass as an Environment Friendly Slow Release Fertilizer. *Silicon* **2016**, *10*, 293–299. [CrossRef]
14. Waclawska, I.; Stoch, L. Thermal behaviour of silicate-phosphate glasses in relation to their biochemical activity. *J. Therm. Anal. Calorim.* **2001**, *65*, 141–146. [CrossRef]
15. Waclawska, I.; Szumera, M. Reactivity of silicate–phosphate glasses in soil environment. *J. Alloys Compd.* **2009**, *468*, 246–253. [CrossRef]
16. Stoch, L.; Wacławska, I.; Szumera, M. Phospho-silicate glasses, self-degradable in environment conditions. *Adv. Mater. Res.* **2008**, *39–40*, 335–340. [CrossRef]
17. Conradt, R. Chemical durability of oxide glasses in aqueous solutions: A review. *J. Am. Ceram. Soc.* **2007**, *91*, 728–735. [CrossRef]
18. Gin, S.; Delaye, J.-M.; Angeli, F.; Schuller, S. Aqueous alteration of silicate glass: State of knowledge and perspectives. *NPJ Mater. Degrad.* **2021**, *5*, 42. [CrossRef]
19. Hellmann, R.; Icenhower, R.J.P. Mechanisms of Glass Corrosion by Aqueous Solutions. *Encycl. Glass Sci. Technol. Hist. Cult.* **2021**, *1*, 647–662. [CrossRef]
20. Rodrigues, A.; Fearn, S.; Palomar, T.; Vilarigues, M. Early stages of surface alteration of soda-rich-silicate glasses in the museum environment. *Corros. Sci.* **2018**, *143*, 362–375. [CrossRef]
21. Thorpe, C.L.; Neeway, J.J.; Pearce, C.I.; Hand, R.J.; Fisher, A.J.; Walling, S.A.; Hyatt, N.C.; Kruger, A.A.; Schweiger, M.; Kosson, D.S.; et al. Forty years of durability assessment of nuclear waste glass by standard methods. *NPJ Mater. Degrad.* **2021**, *5*, 61. [CrossRef]
22. Gin, S.; Mir, A.H.; Jan, A.; Delaye, J.-M.; Chauvet, E.; De Puydt, Y.; Gourgiotis, A.; Kerisit, S.N. A General Mechanism for Gel Layer Formation on Borosilicate Glass under Aqueous Corrosion. *J. Phys. Chem. C* **2020**, *124*, 5132–5144. [CrossRef]
23. Frankel, G.S.; Vienna, J.D.; Lian, J.; Scully, J.R.; Gin, S.; Ryan, J.V.; Wang, J.; Kim, S.H.; Windl, W.; Du, J. A comparative review of the aqueous corrosion of glasses, crystalline ceramics, and metals. *NPJ Mater. Degrad.* **2018**, *2*, 15. [CrossRef]
24. Bunker, B. Molecular mechanisms for corrosion of silica and silicate glasses. *J. Non Cryst. Solids* **1994**, *179*, 300–308. [CrossRef]
25. Bates, J.K.; Bradley, C.R.; Buck, E.C.; Cunnane, J.C.; Ebert, W.L.; Feng, X.; Mazer, J.J.; Wronkiewicz, D.J. *High-Level Waste Boro-Silicate Glass, A Compendium of Corrosion Characteristics*; United States Department of Energy Office of Waste Management: Washington, DC, USA, 1994.
26. McNear, D.H. The Rhizosphere—Roots, Soil and Everything In Between. *Nat. Educ. Knowl.* **2013**, *4*, 1.
27. Palomar, T.; Garcia-Heras, M.; Villegas, M.-A. Model historical glasses under simulated burial conditions. *Coalition* **2012**, *23*, 2–6.
28. Cox, G.A.; Ford, B.A. The long-term corrosion of glass by ground-water. *J. Mater. Sci.* **1993**, *28*, 5637–5647. [CrossRef]
29. Zacharias, N.; Palamara, E.; Kordali, R.; Muros, V. Archaeological glass corrosion studies: Composition, environment and content. *Sci. Cult.* **2020**, *6*, 53–67. [CrossRef]

30. Friedrich, K.T.; Degryse, P. Soil vs. glass: An integrated approach towards the characterization of soil as a burial environment for the glassware of Cucagna Castle (Friuli, Italy). *STAR: Sci. Technol. Archaeol. Res.* **2019**, *5*, 138–156. [CrossRef]
31. Palomar, T. Effect of soil pH on the degradation of silicate glasses. *Int. J. Appl. Glas. Sci.* **2017**, *8*, 177–187. [CrossRef]
32. Roemich, H.; Gerlach, S.; Mottner, P.; Mees, F.; Jacobs, P.; van Dyck, D.; Carbó, T.D. Results from burial experiments with simulated medieval glasses. *MRS Proc.* **2003**, *757*, 97–108. [CrossRef]
33. Odegaard, N.; Watkinson, G. Post-Depositional Changes in Archaeological Ceramics and Glass. *Handb. Archeol. Sci.* **2023**, *2*, 1103–1116. [CrossRef]
34. Schalm, O.; Anaf, W. Laminated Altered Layers in Historical Glass: Density Variations of Silica Nanoparticle Random Packings as Explanation for the Observed Lamellae. *J Non Cryst Solids* **2016**, *442*, 1–16. [CrossRef]
35. De Bardi, M.; Hutter, H.; Schreiner, M.; Bertoncello, R. Potash-lime-silica glass: Protection from weathering. *Herit. Sci.* **2015**, *3*, 1–9. [CrossRef]
36. Ojovan, M.I.; Lee, W.E.; Kalmykov, S.N. Performance of Wasteform Materials. In *An Introduction to Nuclear Waste Immobilisation*; Elsevier: Amsterdam, The Netherlands, 2019; pp. 433–461. [CrossRef]
37. Perera, G.; Doremus, R.H. Dissolution Rates of Commercial Soda–Lime and Pyrex Borosilicate Glasses: Influence of Solution pH. *J. Am. Ceram. Soc.* **1991**, *74*, 1554–1558. [CrossRef]
38. Xing, S.-B.; Muller, I.S.; Pegg, I.L. Non-Linearity in Glass Composition Dependence of Dissolution Rates: Effect of Solution pH. *MRS Proc.* **1993**, *333*, 549. [CrossRef]
39. Cheng, X.; Brow, R.K.; Chen, G. The dissolution behavior in alkaline solutions of a borosilicate glass with and without P_2O_5. *J. Am. Ceram. Soc.* **2017**, *100*, 4519–4532. [CrossRef]
40. Westervelt, D.M.; Fiore, A.M.; Baublitz, C.B.; Correa, G. Impact of Regional Northern Hemisphere Mid-Latitude Anthropogenic Sulfur Dioxide Emissions on Local and Remote Tropospheric Oxidants. *Atmos. Chem. Phys.* **2021**, *21*, 6799–6810. [CrossRef]
41. Aas, W.; Mortier, A.; Bowersox, V.; Cherian, R.; Faluvegi, G.; Fagerli, H.; Hand, J.; Klimont, Z.; Galy-Lacaux, C.; Lehmann, C.M.B.; et al. Global and Regional Trends of Atmospheric Sulfur. *Sci. Rep.* **2019**, *9*, 1–11. [CrossRef]
42. Rebroš, M.; Jamnický, M.; Lokaj, J.; Kadlečíkova, M. Weathering of the crystal glass in moist and polluted atmospheres. *Ceram. Silik.* **2006**, *50*, 44–50.
43. Papadopoulos, N.; Drosou, C.A. Influence of weather conditions on glass properties. *J. Univ. Chem. Technol. Metall.* **2012**, *47*, 429–438.
44. Gueli, A.M.; Pasquale, S.; Tanasi, D.; Hassam, S.; Lemasson, Q.; Moignard, B.; Pacheco, C.; Pichon, L.; Stella, G.; Politi, G. Weathering and deterioration of archeological glasses from late Roman Sicily. *Int. J. Appl. Glas. Sci.* **2020**, *11*, 215–225. [CrossRef]
45. Kalita, A.; Elayarajan, M.; Janaki, P.; Suganya, S.; Sankari, A.; Parameswari, E. Organo-monomers coated slow-release fertilizers: Current understanding and future prospects. *Int. J. Biol. Macromol.* **2024**, *274*, 133320. [CrossRef] [PubMed]
46. Trenkel, M.E. *Controlled-Release and Stabilized Fertilizers in Agriculture*; International Fertilizer Industry Association: Paris, France, 1997.
47. Palomar, T.; Redol, P.; Almeida, I.C.; da Silva, E.P.; Vilarigues, M. The influence of environment in the alteration of the stained-glass windows in portuguese monuments. *Heritage* **2018**, *1*, 365–376. [CrossRef]
48. Huisman, D.; Pols, S.; Joosten, I.; van Os, B.; Smit, A. Degradation processes in colourless Roman glass: Cases from the Bocholtz burial. *J. Archaeol. Sci.* **2008**, *35*, 398–411. [CrossRef]
49. Wacławska, I.; Szumera, M. Influence of MgO (CaO) on the structure of silicate-phosphate glasses. *J. Therm. Anal. Calorim.* **2006**, *84*, 185–190. [CrossRef]
50. Chave, T.; Frugier, P.; Gin, S.; Ayral, A. Glass–water interphase reactivity with calcium rich solutions. *Geochim. Cosmochim. Acta* **2011**, *75*, 4125–4139. [CrossRef]
51. Othman, S.M.; Sarsam, S.I.; Ismail, S.A. Gypsum and limestone dissolution within fatha formation (middle miocene) at various ph solutions: A laboratory study. *Iraqi Geol. J.* **2020**, *53*, 71–88. [CrossRef]
52. Kiran-Yildirim, B.; Gencaslan, A.; Titiz-Sargut, S. Thermodynamic Models and Central Composite Design for Calcium Sulfate Dihydrate Solubility. *Chem. Eng. Technol.* **2020**, *43*, 1124–1136. [CrossRef]
53. Türk, F.N.; Eren, M.Ş.A.; Arslanoğlu, H. Obtaining, Characterizing, and Evaluation of Potassium-Struvite ($KMgPO_4.6H_2O$) in Phosphorus Removal from Water: Investigation of Low-Cost Mgo Use. *Water Conserv. Sci. Eng.* **2024**, *9*, 68. [CrossRef]
54. Banks, E.; Chianelli, R.; Korenstein, R.J.I.C. Crystal chemistry of struvite analogs of the type MgMPO4. 6H2O (M+= potassium (1+), rubidium (1+), cesium (1+), thallium (1+), ammonium (1+). *Inorg. Chem.* **1975**, *14*, 1634–1639. [CrossRef]
55. Mathew, M.; Schroeder, L.W. Crystal structure of a struvite analogue, $MgKPO_4.6H_2O$. *Acta Crystallogr. Sect. B Struct. Crystallogr. Cryst. Chem.* **1979**, *35*, 11–13. [CrossRef]
56. Prywer, J.; Torzewska, A.; Płociński, T. Unique surface and internal structure of struvite crystals formed by Proteus mirabilis. *Urol. Res.* **2012**, *40*, 699–707. [CrossRef] [PubMed]
57. Szterner, P.; Antosik, A.; Pagacz, J.; Tymowicz-Grzyb, P. Morphology Control of Hydroxyapatite as a Potential Reinforcement for Orthopedic Biomaterials: The Hydrothermal Process. *Crystals* **2023**, *13*, 793. [CrossRef]
58. McDonogh, D.P.; Kirupananthan, P.; Gebauer, D. Counterintuitive Crystallization: Rate Effects in Calcium Phosphate Nucleation at Near-Physiological pH. *Cryst. Growth Des.* **2023**, *23*, 7037–7043. [CrossRef]

59. Mekmene, O.; Rouillon, T.; Quillard, S.; Pilet, P.; Bouler, J.-M.; Pezennec, S.; Gaucheron, F. Effects of citrate and NaCl on size, morphology, crystallinity and microstructure of calcium phosphates obtained from aqueous solutions at acidic or near-neutral pH. *J. Dairy Res.* **2012**, *79*, 238–248. [CrossRef]
60. Putri, P.Y. Effect of temperature and solution PH on calcium carbonate precipitation as bio-based repair material in concrete. *Int. J. Geomate* **2024**, *26*, 101–108. [CrossRef]
61. Chen, W.C.; Ju, C.P.; Cheng, W.H.; Chernlin, J.H. Green synthesis of calcium and phosphate compounds by varying ph value and ca/p atomic ratio using aqueous precipitations. *Ceram. Silik.* **2013**, *57*, 14–21.
62. Gin, S.; Jollivet, P.; Fournier, M.; Angeli, F.; Frugier, P.; Charpentier, T. Origin and consequences of silicate glass passivation by surface layers. *Nat. Commun.* **2015**, *6*, 6360. [CrossRef]
63. Cailleteau, C.; Angeli, F.; Devreux, F.; Gin, S.; Jestin, J.; Jollivet, P.; Spalla, O. Insight into silicate-glass corrosion mechanisms. *Nat. Mater.* **2008**, *7*, 978–983. [CrossRef]
64. Verney-Carron, A.; Sessegolo, L.; Chabas, A.; Lombardo, T.; Rossano, S.; Perez, A.; Valbi, V.; Boutillez, C.; Muller, C.; Vaulot, C.; et al. Alteration of medieval stained glass windows in atmospheric medium: Review and simplified alteration model. *NPJ Mater. Degrad.* **2023**, *7*, 49. [CrossRef]
65. Abdelouas, A.; Neeway, J.; Grambow, B. Chemical Durability of Glasses. In *Springer Handbook of Glass. Springer Handbooks*; Musgraves, J.D., Hu, J., Calvez, L., Eds.; Springer: Cham, Switzerland, 2019; ISBN 9783319937281.
66. Hellmann, R.; Cotte, S.; Cadel, E.; Malladi, S.; Karlsson, L.S.; Lozano-Perez, S.; Cabié, M.; Seyeux, A. Nanometre-Scale Evidence for Interfacial Dissolution–Reprecipitation Control of Silicate Glass Corrosion. *Nat. Mater.* **2015**, *14*, 307–311. [CrossRef]
67. Sterpenich, J.; Libourel, G. Water Diffusion in Silicate Glasses under Natural Weathering Conditions: Evidence from Buried Medieval Stained Glasses. *J. Non Cryst. Solids* **2006**, *352*, 5446–5451. [CrossRef]
68. Elgayar, I.; Hill, R.; Chen, X.; Bubb, N.; Wood, D. Dielectric spectroscopy and dissolution studies of bioactive glasses. *Int. J. Appl. Glas. Sci.* **2017**, *8*, 418–427. [CrossRef]
69. Tilocca, A. Sodium migration pathways in multicomponent silicate glasses: Car–Parrinello molecular dynamics simulations. *J. Chem. Phys.* **2010**, *133*, 014701. [CrossRef] [PubMed]
70. Bouabdalli, E.M.; El Jouad, M.; Touhtouh, S.; Hajjaji, A. First investigation of the effect of strontium oxide on the structure of phosphate glasses using molecular dynamics simulations. *Comput. Mater. Sci.* **2023**, *220*, 112068. [CrossRef]
71. Meyer, K.; Barz, A.; Stachel, D. Effects of atmospheric humidity on the infrared reflectivity of vitreous P2O5 and ultraphosphate glasses. *J. Non Cryst. Solids* **1995**, *191*, 71–78. [CrossRef]
72. Stachel, D.; Barz, A. Structure investigations of ultraphosphate glasses with some water content. *J. Phys. Chem. Solids* **2007**, *68*, 1021–1023. [CrossRef]
73. Wacławska, I.; Szumera, M.; Stoch, P.; Sitarz, M. Structural role of Fe in the soil active glasses. *Spectrochim. Acta Part A Mol. Biomol. Spectrosc.* **2011**, *79*, 728–732. [CrossRef]
74. Wacławska, I.; Szumera, M. Thermal analysis of glasses for proecological applications. *J. Therm. Anal. Calorim.* **2003**, *72*, 1065–1072. [CrossRef]
75. Goj, P.; Stoch, P. Molecular dynamics simulations of P_2O_5-Fe_2O_3-FeO-Na_2O glasses. *J. Non Cryst. Solids* **2018**, *500*, 70–77. [CrossRef]
76. Stoch, P.; Goj, P.; Ciecińska, M.; Jeleń, P.; Błachowski, A.; Stoch, A.; Krakowiak, I. Influence of aluminum on structural properties of iron-polyphosphate glasses. *Ceram. Int.* **2020**, *46*, 19146–19157. [CrossRef]
77. Valle, S.F.; Giroto, A.S.; Dombinov, V.; Robles-Aguilar, A.A.; Jablonowski, N.D.; Ribeiro, C. Struvite-based composites for slow-release fertilization: A case study in sand. *Sci. Rep.* **2022**, *12*, 14176. [CrossRef] [PubMed]
78. Wang, L.; Nancollas, G.H. Calcium Orthophosphates: Crystallization and Dissolution. *Chem. Rev.* **2008**, *108*, 4628–4669. [CrossRef] [PubMed]
79. Kilic, S.; Toprak, G.; Ozdemir, E. Stability of $CaCO_3$ in $Ca(OH)_2$ solution. *Int. J. Miner. Process.* **2016**, *147*, 1–9. [CrossRef]
80. Weaver, J.L.; DePriest, P.T.; Plymale, A.E.; Pearce, C.I.; Arey, B.; Koestler, R.J. Microbial interactions with silicate glasses. *NPJ Mater. Degrad.* **2021**, *5*, 11. [CrossRef]
81. Berezicka, A.; Sułowska, J.; Jeleń, P.; Komarek, S.; Szumera, M. Effect of sulfur addition on glass-forming ability, structure and thermal stability of multicomponent silicate-phosphate glasses. *J. Therm. Anal. Calorim.* **2024**, *149*, 10405–10427. [CrossRef]
82. Berezicka, A.; Sułowska, J.; Szumera, M. Alteration of Sulfur-Bearing Silicate-Phosphate (Agri)Glasses in Soil Environment: Structural Characterization and Chemical Reactivity of Fertilizer Glasses: Insights from 'In Vitro' Studies. *Molecules* **2025**, *30*, 1684. [CrossRef]
83. Ulén, B.; Pietrzak, S.; Ramnerö, B.; Strand, L. Agricultural soil acidity and phosphorus leaching risk at farm level in two focus areas. *Acta Agric. Scand. Sect. B Soil Plant Sci.* **2016**, *66*, 359–368. [CrossRef]
84. Zamanian, K.; Taghizadeh-Mehrjardi, R.; Tao, J.; Fan, L.; Raza, S.; Guggenberger, G.; Kuzyakov, Y. Acidification of European croplands by nitrogen fertilization: Consequences for carbonate losses, and soil health. *Sci. Total. Environ.* **2024**, *924*, 171631. [CrossRef]

85. Tkaczyk, P.; Bednarek, W.; Dresler, S.; Krzyszczak, J.; Baranowski, P.; Sławiński, C. Relationship between assimilable-nutrient content and physicochemical properties of topsoil. *Int. Agrophysics* **2017**, *31*, 551–562. [CrossRef]
86. Stoch, L. Flexibility of structure as a criterion of glass formation and stability. *Opt. Appl.* **2000**, *30*, 647–655.
87. Stoch, L. Flexibility of Structure and Glass-Forming Ability: A Chemical Approach. *Glas. Phys. Chem.* **2001**, *27*, 167–174. [CrossRef]
88. Berezicka, A.; Szumera, M.; Sułowska, J.; Jeleń, P.; Olejniczak, Z.; Stępień, J.; Zając, M.; Pollastri, S.; Olivi, L. Unraveling the nature of sulfur-bearing silicate-phosphate glasses: Insights from multi-spectroscopic (Raman, MIR, 29Si, 31P MAS-NMR, XAS, XANES) investigation. *Ceram. Int.* **2022**, *48*, 4238–4254. [CrossRef]

Disclaimer/Publisher's Note: The statements, opinions and data contained in all publications are solely those of the individual author(s) and contributor(s) and not of MDPI and/or the editor(s). MDPI and/or the editor(s) disclaim responsibility for any injury to people or property resulting from any ideas, methods, instructions or products referred to in the content.

5. Authors' contribution statement

Udział procentowy autorów w powstaniu publikacji

Effect of sulfur addition on glass-forming ability, structure and thermal stability of multicomponent silicate-phosphate glasses

Journal of Thermal Analysis and Calorimetry, Volume 149, pages 10405–10427, (2024)

Autorzy: Anna Berezicka, Justyna Sułowska, Piotr Jeleń, Sebastian Komarek, Magdalena Szumera

Anna Berezicka	40%	Anna Berezicka
Justyna Sułowska	30%	Justyna Sułowska
Piotr Jeleń	10%	Piotr Jeleń
Sebastian Komarek	10%	Komarek
Magdalena Szumera	10%	Szumera

Udział procentowy autorów w powstaniu publikacji

Alteration of Sulfur-Bearing Silicate-Phosphate (Agri)Glasses in Soil Environment: Structural Characterization and Chemical Reactivity of Fertilizer Glasses: Insights from 'In Vitro' Studies

Molecules 2025, 30, 1684

Autorzy: Anna Berezicka, Justyna Sułowska, Magdalena Szumera

Anna Berezicka	50%	Anna Berezicka
Justyna Sułowska	10%	Justyna Sułowska
Magdalena Szumera	40%	

Udział procentowy autorów w powstaniu publikacji

Alteration of Sulfur-Bearing Silicate–Phosphate (Agri)Glasses in Soil Environment: Chemical Interactions and Biological Response

Molecules 2025, 30, 1790

Autorzy: Anna Berezicka, Agnieszka Wojteczko, Justyna Sułowska, Magdalena Szumera

Anna Berezicka	50%	Anna Berezicka
Agnieszka Wojteczko	10%	Agnieszka Wojteczko
Justyna Sułowska	10%	Justyna Sułowska
Magdalena Szumera	30%	